Transactions of the ASME

Journal of Engineering for Power (ISSN 0022-0825) is edited and published quarterly at the offices of The American Society of Mechanical Engineers, United Engineering Center, 345 E. 47th St., New York, N. Y. 10017. ASME-TWX No. 710-581-5267, New York. Second Class postage paid at New York, N.Y., and at additional mailing offices.
CHANGES OF ADDRESS must be received at Society headquarters seven weeks before they are to be effective. Please send old label and new address.
PRICES: To members, $36.00, annually; to nonmembers, $72.00. Single copies, $24.00 each. Add $6.00 for postage to countries outside the United States and Canada.
STATEMENT from By-Laws. The Society shall not be responsible for statements or opinions advanced in papers or ... printed in its publications (B 7.1, para. 3).

INDEXED by the Engineering Index, Inc.

Journal of Engineering for Power

Published Quarterly by The American Society of Mechanical Engineers
VOLUME 105 • NUMBER 2 • APRIL 1983

TECHNICAL PAPERS

(Contents continued on p. 264)

(Contents Continued)

ANNOUNCEMENTS

The Influence of Trailing Edge Ejection on the Base Pressure in Transonic Turbine Cascades

C. H. Sieverding
von Karman Institute for Fluid Dynamics,
Rhode Saint Genèse, Belgium

This paper summarizes the results of base pressure studies on transonic turbine blades in the presence of an ejection of coolant flow from a slot in the trailing edge. The first part of the paper reports on tests carried out on a enlarged model of the overhang section of a typical transonic cascade. This model provides valuable information about the detailed trailing edge pressure distribution and points to an asymmetric evolution of the base pressure on both sides of the slot in the presence of a bleed. The second part of the paper presents experimental results from cascade tests covering an outlet Mach number range $M_{2,is}$ = 0.5 to 1.35. These experiments underline the importance of the coolant flow impact on the base pressure and confirm the asymmetry of the base pressure with respect to the cooling slot. Tests with different coolant flow gases point to the significance of a proper simulation of the density ratio between coolant flow and main flow.

Introduction

The progress in the design of highly efficient gas turbines over the last 30 years has been closely related to the introduction of blade cooling methods since the early 1950s. The use of blade cooling in conjunction with improved blade material allows the gas temperatures to increase from ~1050 K in 1950 to ~1800 K at present. Throughout, there has existed the problem of elaborating cooling schemes for which the benefit of an increased inlet temperature was not weighed out by the associated aerodynamic efficiency penalties, such as the losses due to the mixing between coolant and main flow.

In many cooled blade designs the coolant is discharged partially or entirely through the trailing edge into the main flow. This solves not only the problem of cooling the trailing edge, but it is also considered to be an efficient way to mix the coolant flow with the main flow.

An important experimental research program concerning the aerodynamic effect of trailing edge cooling on the flow in turbine bladings was carried out by NASA [1–4]. This work as well as some other experimental investigations of less importance [5–8] concentrates on the investigation of the effect of different trailing edge geometries and cooling slot geometries on the overall performance of straight and annular cascades and complete stages. It appears, however, that the effect of a trailing edge bleed on the flow in the immediate neighbourhood of the trailing edge has not yet been studied in great detail, possibly because of the small dimensions of the trailing edge. A research group at Liverpool University has attempted to fill this gap by experiments on a single airfoil at incidence in a straight duct [9]. The similarity between this flow and the cascade flow is, however, not very convincing.

In continuation of an investigation concerning the base pressure in transonic cascades [10], the von Karman Institute started in 1977 a similar experimental program on the influence of trailing edge coolant ejection on the base pressure in transonic cascades. In the first part of the program, tests were carried out on an enlarged model representing the region of uncovered turning downstream of the throat of a transonic turbine blade. The dimensions of this model allowed a detailed instrumentation of the trailing edge. The model was tested only at supersonic downstream conditions. The main flow and the coolant flow were connected to the same air supply. The second part of the tests was carried out on a nozzle cascade with similar characteristics as the model. The much smaller dimension of the trailing edge of the cascade blades set automatically a limit to the instrumentation of the trailing edge. Based on the model test results, the in-

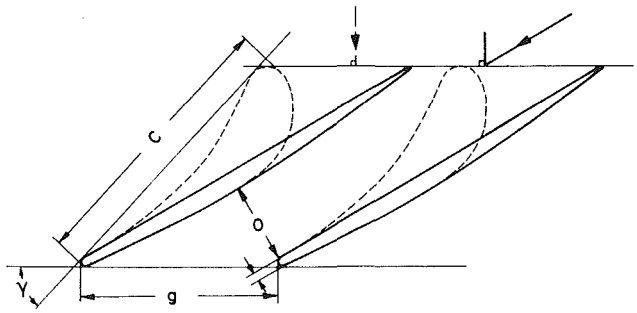

Fig. 1 Similitude between model and transonic turbine blade

Contributed by the Gas Turbine Division of THE AMERICAN SOCIETY OF MECHANICAL ENGINEERS and presented at the 27th International Gas Turbine Conference and Exhibit, London, England, April 18–22, 1982. Manuscript received at ASME Headquarters December 3, 1981. Paper No. 82-GT-50.

strumentation could be greatly reduced without loosing its validity with respect to measuring a representative base pressure. The cascade tests covered an outlet Mach number range from $M_2 = 0.5$ to 1.4. The use of different gases for the coolant flow (air, carbondioxide, and air-freon mixtures) allowed to vary both the density ratios and the blowing rates.

Model Tests

Model Description. The model is derived from a cascade with the following main characteristics (Fig. 1):

- Pitch to chord ratio, g/c 0.71
- Gauging angle, $\beta_2^* = \arcsin 0/g$ 23.7°
- Stagger angle, γ 47.5°
- Trailing edge thickness to throat, $te/0$ 0.12
- Trailing edge wedge angle, δ_{te} 4.5°
- Suction side turning downstream of throat, ϵ 4.5°

Note: the turning is concentrated near the throat, 70 percent of the region of uncovered turning are straight.

The advantage of the model is that it requires a much smaller tunnel height than the corresponding nozzle cascade.

The set-up of the model in the wind tunnel is shown in Fig. 2. The model presents a cascade reduced to only two passages. The lower tunnel wall plays the role of the pressure side of the first channel. The central blade is the cooled blade. The cooling air enters the blade through the lugs supporting the blade in the perspex side walls. The height of the cooling passage inside the blade decreases continuously towards the trailing edge and reaches, at 25 mm from the trailing edge, the final height of 2 mm, which represents one-third of the total trailing edge height. The slot covers 80 percent of the total blade height of 100 mm. Two structural support webs placed at ±20 mm from the midblade height assure a constant slot width for all bleeds.

It is obvious that a model with only two passages cannot simulate correctly the periodic downstream conditions of a cascade with a great number of blades. The outlet periodicity can be improved, however, by the use of tailboards. The velocity of the outlet flow field is controlled by the inclination angle, δ, of the tailboards. A turning of the tailboards in clockwise direction (δ-positive) increases the velocity while a counterclockwise turning (δ-negative) reduces the velocity. At $\delta = 0$, the tailboards are horizontal and parallel to the pressure side of the blades. The model is appropriate only for testing at supersonic outlet flow conditions.

The end wall boundary layer along the upper inlet nozzle block is blown off in front of the upper blade in order to allow the development of a new boundary layer on the blade.

The central blade is provided with a very dense instrumentation of pressure tappings. The trailing edge was instrumented with 6 tappings of 0.3-mm dia on each side of the slot (Fig. 2).

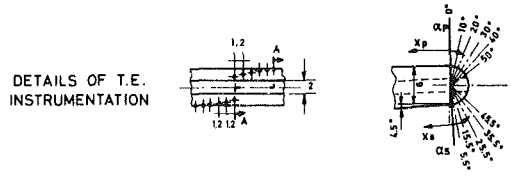

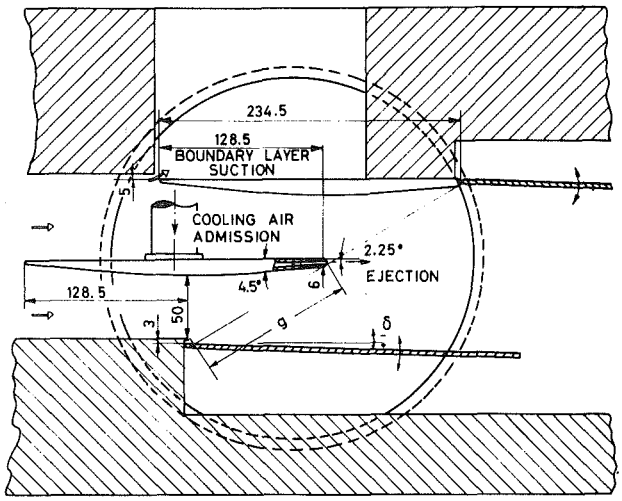

Fig. 2 Set-up of model in test section

Test Conditions.

- Fluid for primary and coolant flow : air
- Total temperature of primary flow and coolant flow: $T_0 \cong 280$ K
- Total upstream pressure for primary flows (for all tests : $P_{01} = 2.5$ bar
- Reynolds number (based on inlet flow conditions and chord length): Re = $9 \cdot 10^6$
- Turbulence level: Tu = 1 percent
- Blade surface: polished
- State of boundary layer at trailing edge: turbulent.

Model Test Results. The nonperiodicity of the outlet flow is still quite strong in spite of the use of tailboards. In fact, the location of the suction side shock boundary layer interaction on the central and upper blades differs by as much as 17 percent of the region of uncovered turning. It is therefore preferable to characterize the flow conditions by the tailboard angle, δ, rather than by an arbitrary definition of the downstream Mach number. The lack of a well-defined relation between blade flow and downstream Mach number is not important since the aim of this test series focuses on the study of the influence of a base bleed on the pressure distribution around the trailing edge and the trailing edge shock patterns. The tailboard angle was varied from $\delta = -2$ deg, to +6 deg.

Nomenclature

c = chord
d = slot width
g = pitch
h = blade height
M = Mach number throat
p = pressure
p_b = base pressure
p_b^* = base pressure at zero bleed
te = trailing edge thickness
x,y = coordinates
β_2^* = gauging angle ($\beta_2^* = \arcsin 0/g$)
γ = stagger angle
δ = tailboard angle
δ_{te} = trailing edge wedge angle
ϵ = suction side turning downstream of throat
ρ = density

Subscripts

1 = upstream
2 = downstream
0 = total
c = coolant flow
is = isentropic
l = local
m = main
s = static

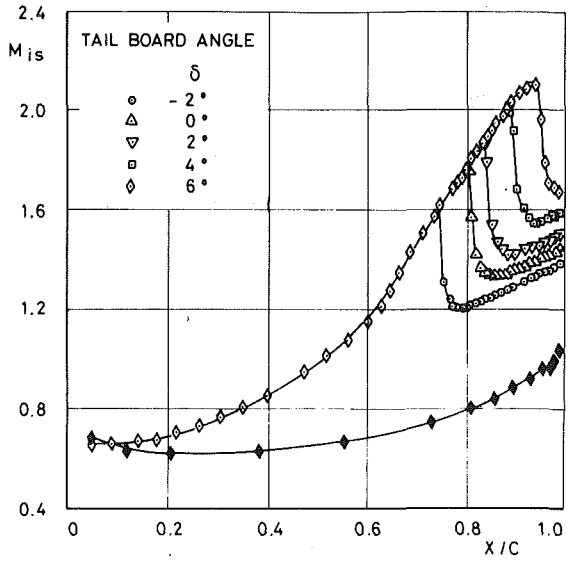

Fig. 3 Blade velocity distributions for model

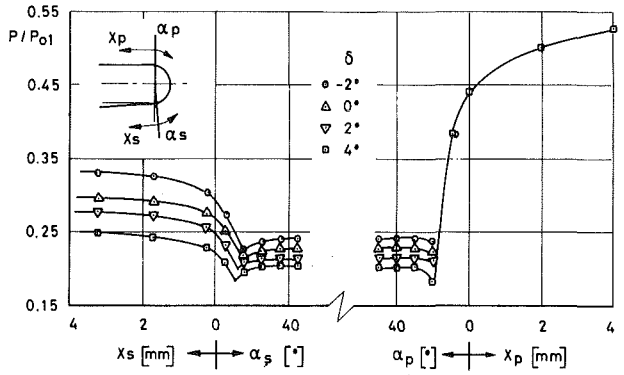

Fig. 4 Pressure distributions around trailing edge at zero bleed

Tests Without Bleed. The blade velocity distributions in fig. 3 have all the characteristic features of the flow through a convergent transonic turbine cascade. The pressure rise through the shocks impinging on the suction side is comparable to that in actual cascades with the same suction side profile downstream of the throat. The sharp increase of the pressure is typical for turbulent boundary layers. As the cascade is choked, the pressure side velocity distributions can be presented by a unique curve for all tailboard inclinations.

The pressure distributions around the trailing edge corresponding to the blade velocity distributions are presented in Fig. 4. They are very similar to those obtained on a previously tested solid flat-plate model [10]. The flow from the pressure side and the suction side overexpands slightly before separating from the trailing edge. However, due to a smaller number of pressure tappings, the separation shock strength is not as well defined as in [10]. The base pressure is constant over approximately 70 percent of the trailing edge circumference.

Tests with bleed. The parameter used to characterize the coolant flow is the pressure ratio between the total pressure of the coolant, P_{0c}, measured in the cooling air admission tubes, and the trailing edge base pressure in absence of a coolant ejection, p_b^*. For the case where the coolant pressure, P_{0c}, equals the inlet stagnation pressure of the main flow, P_{01}, the coolant mass flow amounts to 3.2 percent of the main mass flow. In case of no loss in the blades, the coolant mass flow would have been 4 percent.

The influence of a base bleed on the trailing edge shock

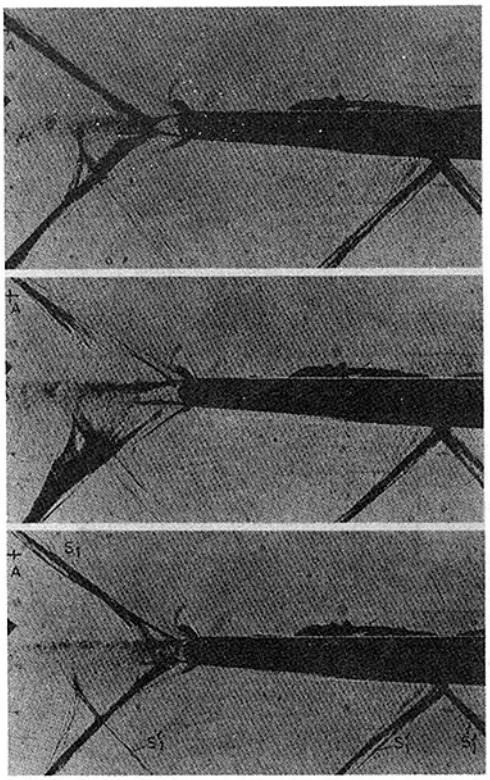

Fig. 5 Influence of bleed on trailing edge shock configuration at tailboard angle $\delta = -2$ deg (from top to bottom: $P_{0_c}/P_b^* = 1.0$, 1.5, and 3.0)

configuration is clearly demonstrated by the schlieren photographs in Fig. 5. These visualizations are taken for the lowest outlet Mach number realized in the model tests. A further decrease of the outlet velocity would have caused the double reflected trailing edge shock S_1' (S_1' is reflected from the suction side of the central blade onto the tailboard and from there back into the flow) to interfere with the base flow of the central cooled blade. The picture for zero bleed shows the usual flow patterns with a fairly well-defined reattachment region and corresponding wake shocks at a distance of two to four times the trailing edge radius from the base. The effect of a moderate bleed (injection pressure ratio $P_{0c}/P_1^* = 1.5$) widens the wake and reduces the expansion of the pressure side and suction side flow around the trailing edge (see modification of the direction of the free shear layers between Fig. 5(*a*) and 5(*b*) which is equivalent to an increase of the base pressure. The recompression starts almost immediately behind the trailing edge and extends over a slightly bigger distance than the isobaric mixing zone plus the reattachment region for the zero bleed case. At high coolant injection ratios, the expansion angle around the trailing edge increases again, indicating a decrease of the base pressure (Fig. 5(*c*). The coolant splits the base region into two separated small dead water regions. Due to a difference between the directions of the slot axis and the wake, the two dead air regions are asymmetric. Since the trailing edge thickness for each part is only 1/3 of the total thickness, it is not unexpected that the trailing edge shocks are closer to the blade than in the case of zero bleed. At some distance away from the wake the shock displacement can be estimated by comparing its position with respect to the reference point A indicated on each photograph.

The influence of the coolant flow ejection on the pressure distribution around the trailing edge is presented in Fig. 6 for two downstream flow conditions, corresponding to the tailboard inclinations $\delta = -2$ deg and $+4$ deg. The highest

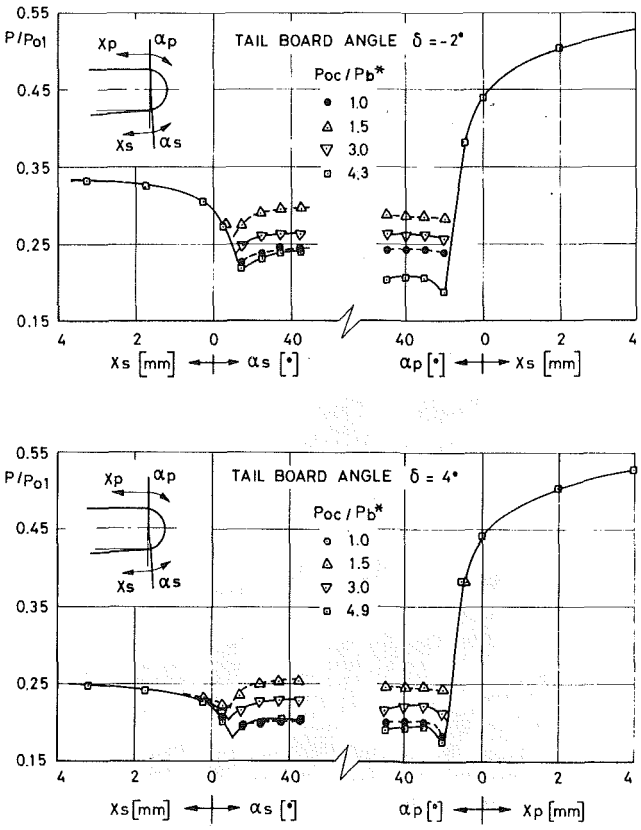

Fig. 6 Influence of coolant flow on base pressure distribution

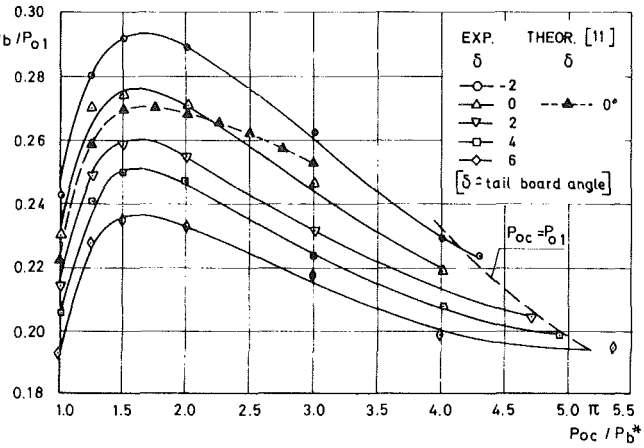

Fig. 7 Base pressure variation versus injection pressure ratio

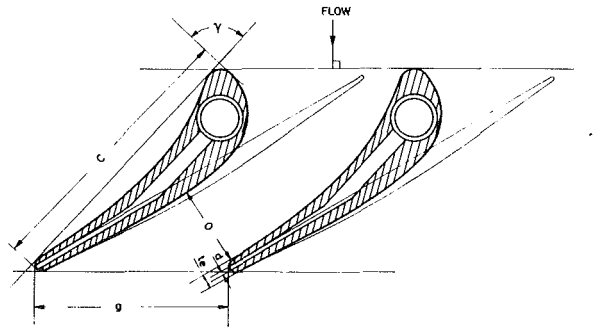

Fig. 8 Cooled nozzle blade

injection pressure ratio, P_{0c}/P_b^*, corresponds to the case where the coolant pressure is approximately equal to the inlet total pressure of the main flow. The left side of the figures presents the flow coming from the suction side of the blade, the right side the flow from the pressure side. The data confirm the findings from the Schlieren photograhs: the bleed influences strongly the base pressure level and causes an asymmetry of the pressure distribution with respect to the slot. The effect of the asymmetry was observed for all tail board angles, δ. The data show that the asymmetry depends both on the injection pressure ratio and the difference between the wake angle and the coolant jet angle (the wake angle varies with the outlet Mach number). One of the objectives of the cascade tests will be to evaluate the significance of this effect over a wide range of outlet Mach numbers.

With respect to the pressure distribution over each partial base, one notices that the pressure is fairly constant except for the small regions which are affected by the trailing edge separation shocks.

With respect to the second test series (cascade tests), it can be concluded that: (*a*) the base pressure has to be measured on both sides of the slot and (*b*) one single pressure tapping on each side of the slot is sufficient to obtain a representative value for the base pressure.

Figure 7 summarizes the results of all base pressure measurements for the model tests. The average base pressure is defined arbitrarily as the arithmetic mean value of three pressure readings on each side of the slot. The angular position of these pressure tappings around the trailing is: α_p = 30, 40, 50 deg and α_s = 45.5, 35.5, 25.5 deg (see Fig. 2). All curves indicate a maximum value of the base pressure for an injection pressure ratio P_{0c}/P_b^* = 1.5 to 1.7. The curves indicate also the existence of a minimum base pressure at high injection rates. For δ = 0, the base pressure was also calculated with the method of Carriere [11]. The predicted base pressure is superimposed on the experimental results in Fig. 7. The agreement is fairly good. This is, in fact, somewhat surprising since the prediction method is supposed to handle only very small blowing rates. The reason for this limitation is the assumption of an isobaric mixing zone behind the base. This assumption very soon becomes obsolete with increasing blowing. This was already indicated by the Schlieren photographs and is confirmed by static pressure traverses along the wake center line.

Cascade Tests

Cascade Geometry. The blade used for the cascade tests is shown in Fig. 8. The model has been superimposed for comparison. The main characteristics of the cascade are indicated below:

– chord length, c	64.6 mm
– aspect ratio, h/c	0.77
– pitch chord ratio, g/c	0.72
– gauging angle, β_2^* = arc sin $0/g$	24.9°
– stagger angle, γ	47.5°
– trailing edge thickness to throat, te/0	0.153
– trailing edge wedge angle, δ_{te}	7°
– suction side turning downstream of the throat, ϵ	7°
– number of blades in cascade, N	6

The blades were designed using cubic spline functions. The blade coordinates are given in the appendix.

Three of the six cascade blades were provided with cooling passages. The trailing edge slot covers 80 percent of the blade height, it has a width of 1 mm compared to a trailing edge of 3 mm, and its axis is parallel to the tangent to the mean camber line. Also high blowing rates did not lead to a noticeable deformation of the slot. Two of the blades were instrumented

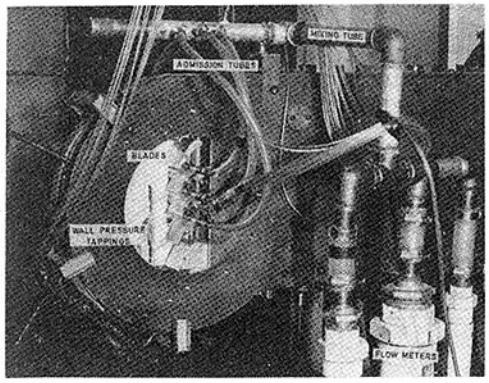

Fig. 9 Cascade set-up in wind tunnel

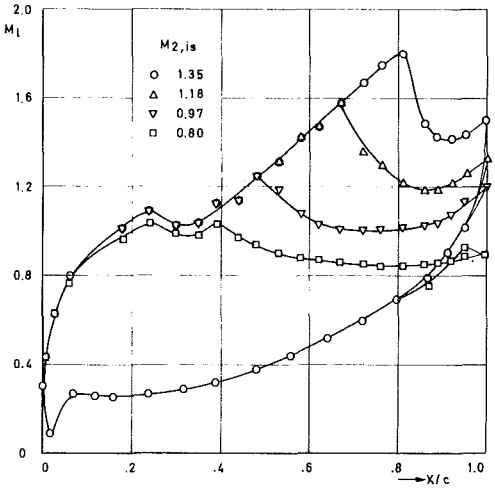

Fig. 10 Blade velocity distributions

identically in order to check the flow periodicity. The base pressure was measured on each blade by two tappings (positioned symmetrically with respect to mid span) on both sides of the slot. The doubling of the base pressure tappings should allow cross-checks to minimize errors due to small leaks and inadequate response time through clogging of the fine pressure tubes. Figure 9 shows a photograph of the cascade set up in the wind tunnel.

Test Conditions.

- Fluid for primary flow : air
- Fluid for coolant flow : air, carbondioxide and air-freon mixtures (freon-CCL_2F_2)
- Total temperature of primary flow : T_{01} = 270-280 K
- Total temperature of coolant flow: T_{0_c} = 285-295 K (the carbondioxide and the freon pass through a heat exchanger before going on board of the cooled blades)
- Total pressure of primary flow : variable with outlet Mach number from 1.1 bar (absolute pressure) at $M_2 = 0.5$. to 3.0 bar for $M_2 = 1.35$
- Total pressure of coolant flow from $P_{0c} = P_b^*$ to $P_{0c} = P_{01}$
- Inlet flow angle : $\beta_1 = 90$ deg
- Reynolds number based on outlet flow conditions and chord length : approximate linear variation from $\mathrm{Re} = 1.5 \cdot 10^5$ at $M_2 = 0.5$ to $\mathrm{Re} = 2.35 \cdot 10^5$ at $M_2 = 1.35$
- Turbulence level : $\mathrm{Tu} \cong 1$ percent
- Blade surface roughness : polished.

Cascade Results.

Tests Without Bleed. A preliminary test series was conducted on a cascade with six blank blades to check the overall

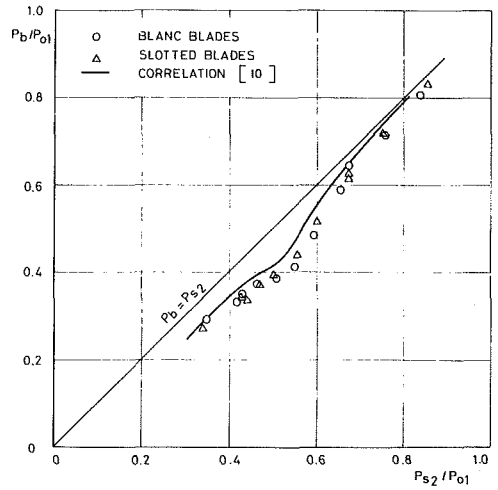

Fig. 11 Base pressure-downstream pressure relation

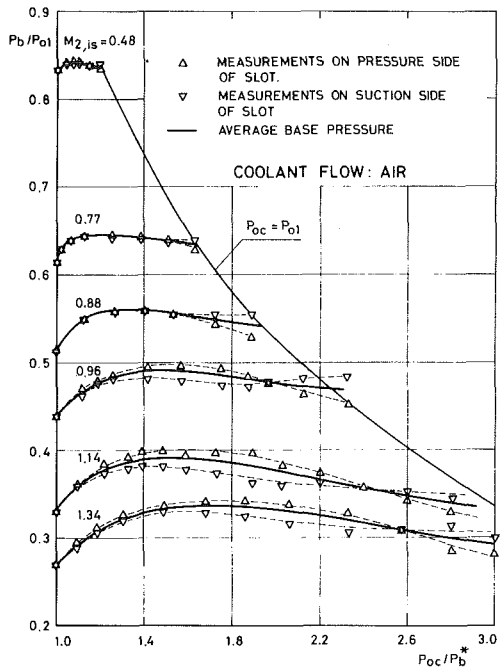

Fig. 12 Asymmetric base pressure evolution on both sides of slot

flow behaviour by means of oil flow visualizations, Schlieren photographs and blade velocity distributions. Due to lack of space, it is not possible to reproduce all the results.

The oil flow visualizations served to get a rough idea about the extension of secondary flows across the span. By comparison with test results on a similar previously investigated nozzle blade (including both oil flow visualizations and spanwise traverses) [12], it can be concluded that the secondary loss distribution in the trailing edge plane is characterized by a loss maximum at about 13 percent distance from the wall and that two-dimensional flow conditions exist over approximately 50 percent of the blade height.

The degree of the outlet flow nonperiodicity, expressed as

$$f = \frac{\bar{M}_{2,1\text{ pitch}} - \bar{M}_{2,3\text{ pitches}}}{\bar{M}_{2,3\text{ pitches}}}$$

varies between f = 1 and 2 percent for $M_2 \leq 1.3$ and $f = 2 \rightarrow 3$ percent for $M_2 > 1.3$. The outlet Mach numbers are based on wall pressure tappings taken at a distance $x/c = 0.5$ from

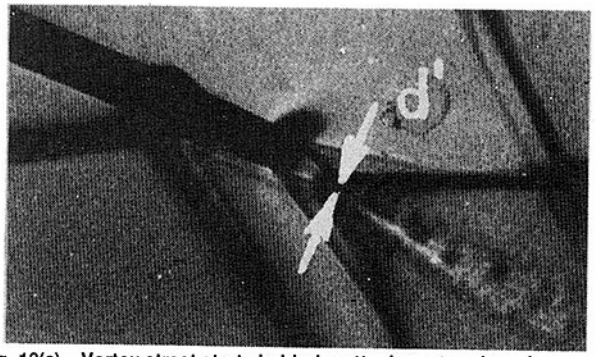

Fig. 13(*a*) Vortex street starts behind reattachment region of pressure side and suction side flow, Heinemann and Butefish (13)

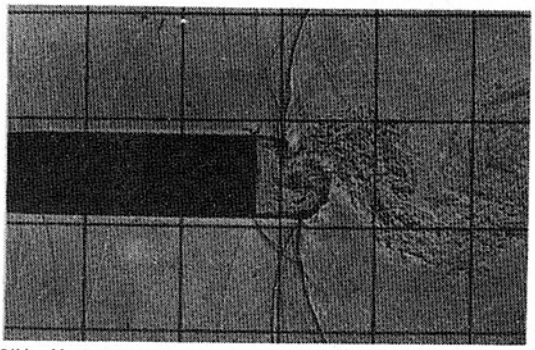

Fig. 13(*b*) Vortex street starts immediately downstream of trailing edge, Dyment and Gryson (14)

Fig. 13 Different types of wakes flows

the trailing edge. The measurements cover the three central passages.

The velocity distributions in Fig. 10 give some insight into the channel flow behavior. The retardation of the rear suction side velocity at subsonic outlet Mach numbers and the strong shock induced deceleration at transonic and supersonic Mach numbers are the result of the combined effect of a thick trailing edge and a weak rear suction side curvature. Schlieren photographs show that the shock impingement on the suction side causes a local boundary layer separation. The advantage of a weak rear suction side curvature lies in the fact that it limits the velocity difference across the trailing edge and therewith the trailing edge shock strength. This is also expressed by the fact that the suction side flow undergoes a slight acceleration around the trailing edge (the base pressure is lower than the suction side pressure before separation at the trailing edge) rather than a recompression as in the case of blades with strong rear suction side curvatures.

The base pressure-downstream pressure relation is presented in Fig. 11. The figure includes not only the data from the blank blades but also from the tests on the cooled blades at zero bleed. The presence of the trailing edge slot does not seem to influence the base pressure. The base pressure correlation by Sieverding [10] is shown for comparison.

Tests With Trailing Edge Bleed. The discharge coefficient of the trailing edge slot was determined prior to the cascade tests by ejecting air through the cooled blades to the ambient atmosphere. The flow conditions of the coolant flow were measured in the coolant feed tubes of the blades. The discharge coefficient, c_d, changes slightly with the leaving velocity at the exit of the slot from $c_d = 0.78$ at Mach number $M = 0.5$ to $c_d = 0.81$ at $M = 1.0$ (the Mach number is based on the pressure ratio P_{atm}/P_{01}). The value of c_d is measured with an accuracy of ± 3 percent. The two dimensionlity of the

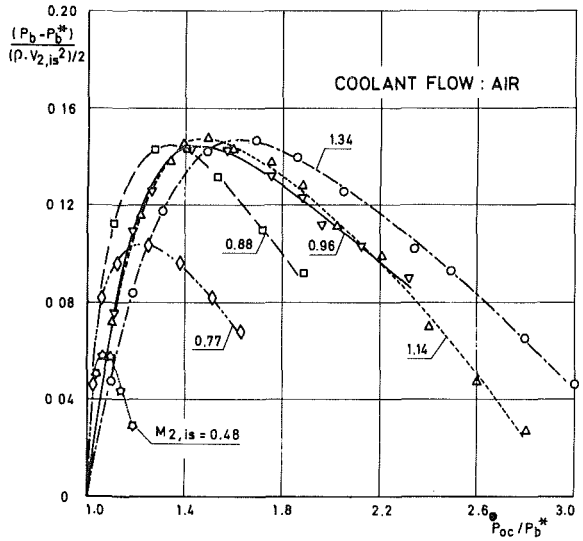

Fig. 14 Base pressure rise in percent of downstream dynamic head

bleed flow was controlled by measuring the velocity profile at the slot exit at various spanwise locations. The coolant jet is nearly two dimensional across 75 percent of the slot length. At midspan, the mass-averaged total pressure at slot exit is 5 to 8 percent lower than the total pressure in the coolant feed tubes. For convenience, it was preferred to use the total pressure in the feed tubes, P_{0c}, rather than the mass-averaged slot exit total pressure to describe the influence of the coolant flow on the base flow.

A first test series was performed with air as coolant flow. The maximum temperature difference between primary flow and coolant flow is of the order of 20 K. As already indicated by the model tests, the influence of the bleed on the base pressure is quite different for the suction side and pressure side of the slot (Fig. 12). The suction side value increases slower than the pressure side value, but it drops off less rapidly past the maximum, p_b, and exceeds the pressure side value at high injection pressure ratios. Similar tendencies are observed for the injection of carbondioxide and freon-air mixtures.

A tentative description of the flow mechanism leading to the pressure difference at the trailing edge base is given. At zero bleed, the outer flow entrains some fluid from the base region through an ejector effect. The amount of entrained fluid is different for both sides and depends on the free stream velocity and the boundary layer momentum thickness on each side of the trailing edge. For reasons of continuity, an amount equivalent to that entrained from the base region is to be returned to it. The driving force for this reverse flow is a pressure difference between the flow near the trailing edge base and the reattachment region at the merging of the flows from the suction side and pressure side. These effects create recirculating flows at the trailing edge base.

However, the trailing edge region cannot necessarily be looked at as a zone with two coexisting stationary recirculating regions. In fact, the flow is shed off the trailing edge in an unsteady motion which results in the formation of alternating vortices. Depending on the geometry of the base and the external flow conditions, the vortex street starts more or less close to the base leaving a smaller or bigger place for a stationary recirculation zone. At supersonic downstream conditions with a well-established oblique trailing edge shock system, the vortex street starts apparently somewhere at the end of the confluence region between the pressure side and suction side flow (see Schlieren photographs, Fig. 13(*a*), taken from [13]). In this case, there exists an important recirculation zone between the base and the confluence region. At subsonic

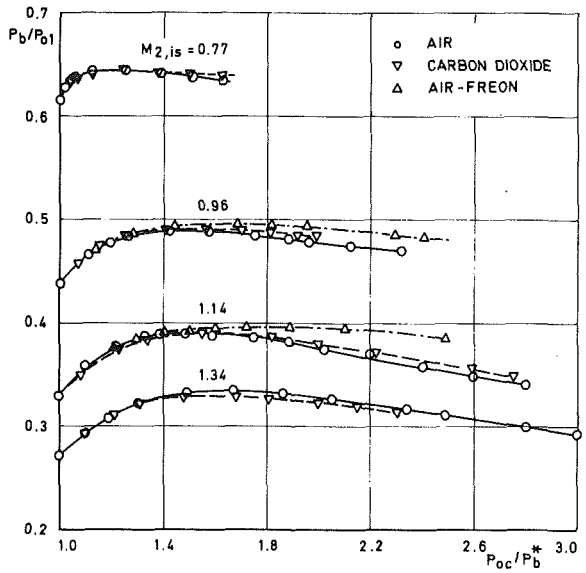

Fig. 15 Effect of density ratio ρ_c/ρ_m on base pressure evolution

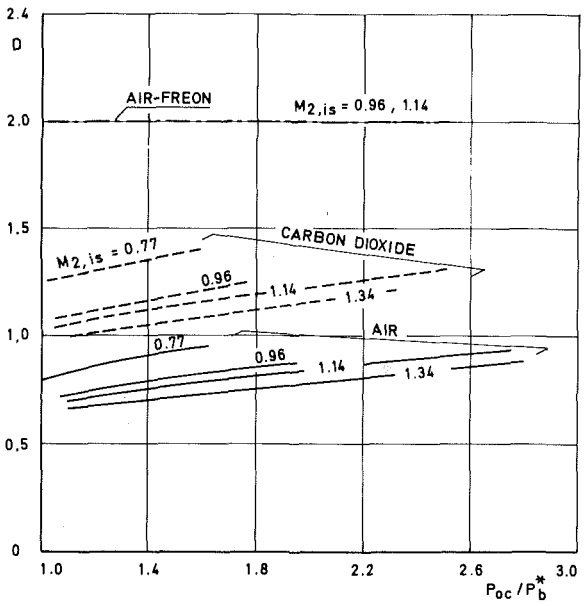

Fig. 16 Density ratios for coolant fluids in Fig. 15

and transonic free stream conditions, the situation might be quite different as indicated in Fig. 13(*b*). This figure shows an ultra-short duration shadowgraph of the flow behind a rectangular trailing edge at a free stream Mach number M = 0.77, taken by Dyment & Gryson [14]. In this example, the vortex street starts almost immediately behind the base. Hence the entrainment of the fluid and the corresponding reverse flow is highly unsteady.

Similar flow patterns as those in Fig. 13(*b*) were reproduced at VKI in a water table. These tests alow some qualitative conclusions as to the trailing edge bleed on the wake structure. At low coolant ejection rates, the coolant is entirely under the influence of the oscillating motion of the trailing edge vortices, and is entrained alternatively by the pressure side and suction side flow. The formation of the vortices is slightly delayed. The entrainment of the coolant flow must lead to a reduction of the reverse flow and therewith to an increase of the base pressure. The time-averaged pressure remains the same on both sides of the slot. This corresponds to a first regime where the coolant flow is injected with negligeable momentum transport.

The second flow regime is one in which the momentum of the coolant flow is eventually sufficient to overcome the adverse pressure gradient. With further momentum increase, the coolant flow can escape directly downstream without being entrained by the outer flows. During this second regime, the position of the vortices is shifted gradually downstream. Stable dead air regions are formed at the trailing edge on both sides of the slot, and the base pressure may be different on each side. Such behaviour depends on three factors : (*i*) coolant flow and outer flow velocities; (*ii*) boundary layer momentum thickness at separation from the coolant slot edge and the outer trailing edge; (*iii*) angle between coolant flow and outer flows. At the end of the second regime, the base pressures should be near their maximum value. It was not possible to verify this point directly through wake traverses behind the cascade blades, since the static pressure probe dimensions would have been too big compared to the width of the wake in the reattachment zone. However, in a first approximation one may assume that for subsonic outlet flow the pressure after reattachment is equal to the average downstream pressure. With this assumption, the minimum coolant flow pressure ratio to obtain maximum base pressure rise should be approximately $P_{0c}/P_b^* = P_{s2}/P_b^*$. This results in the present cascade in $P_{0c}/P_b^* = 1.09$ for $M_{2,is} = 0.77$ and $P_{0c}/P_b^* = 1.17$ for $M_{2,is} = 0.88$ (from Fig. 11). Figure 12 shows that most of the base pressure rise is indeed accomplished for the above values of the injection pressure ratio.

At high injection rates, corresponding to the third regime, the magnitude of the momentum of the coolant is significant compared to the main flow, and the coolant flow then behaves similar to the main flow. We deal with two entirely separate and, in most cases, different trailing edge flows. A vortex street is formed behind each of the small trailing edges, and the base pressures will in general start to decrease.

The aforementioned considerations about the effect of a trailing edge bleed on the wake structure at subsonic and transonic velocities can easily be extended to the case of a fully supersonic trailing edge flow with large recirculation zones between the base and the reattachment region.

For a better appreciation of the relative changes of the base pressure, Fig. 14 presents the variation of P_b with respect to the base pressure at zero bleed P_b^*, nondimensionalized by the downstream dynamic head $(\rho \cdot V^2_{2,is})/2$. The maximum base pressure rise due to coolant injection varies from 5.5 percent at $M_{2,is} = 0.48$ to 14.5 percent at $M_{2,is} = 0.88$, and then stays constant for the whole Mach number range investigated here, i.e., up to $M_{2,is} = 1.34$. The position of the maximum shifts with increasing downstream Mach number to higher injection pressure ratios P_{0c}/P_b^*.

The big temperatuare difference between main flow and coolant flow in real engines implies that the density ratio between main and coolant flow is typically of the order 1.5 to 2. Such density ratios can be simulated in cold flow cascade tunnels by using gases of different densities. In the present investigation, the influence of a density variation was examined by using, besides air, also carbondioxide and air-freon mixtures as coolant fluids. The carbondioxide coolant fluid was used for the downstream Mach numbers $M_{2,is}$ = 0.77, 0.96, 1.14, and 1.34; the air-freon coolant fluid for $M_{2,is}$ = 0.96 and 1.14. Figure 15 presents the results of these tests. The mean base pressure is plotted again versus the injection pressure ratio, P_{0c}/P_b^*. The corresponding density ratios $D = \rho_c/\rho_m$ (ρ_c = density of coolant flow, ρ_m = density of main flow) in Fig. 16 have been calculated using for main and coolant flow the base pressure at zero bleed as reference pressure rather than the actual base pressure in presence of coolant ejection. D increases slightly with P_{0c}/P_b^* for pure air and pure carbondioxide. The density ratios are in the ranges $0.65 < D < 0.95$ and $1.0 < D < 1.4$, respectively. The

density of the coolant carbondioxide is in average 40 percent to 55 percent higher than the density of the coolant air. The air-freon mixture was chosen such as to obtain a constant density ratio $D = 2$ for all tests.

Figure 15 shows that the density ratio, D, has relatively little influence on the base pressure, P_b, up to the maximum value of P_b. The drop off of the base pressure at high injection rates is, however, much slower for the air-freon coolant with $D = 2$ than for the pure air coolant with $D < 1$.

At last, it should be mentioned that the trailing edge coolant ejection has only a very limited effect on the blade velocity distribution. The shock impingement point on the suction side shifts slightly upstream, at maximum base pressure hardly 1 to 2 percent of the chord length, at maximum injection, 2 to 5 percent (increasing from $M = 0.96$ to 1.34). The shock intensity does not seem to be affected.

Conclusions

The main results of the present study can be summarized as follows:

1 The ejection of coolant flow through the trailing edge affects considerably the base pressure in turbine cascades. The maximum base pressure rise can be as high as 15 percent of the downstream dynamic head at transonic and low supersonic outlet Mach numbers. The maximum base pressure occurs when the momentum of the coolant flow is just about strong enough to overcome the adverse pressure gradient.

2 The basebleed can cause significant differences between the pressure side and the suction side of the trailing edge slot. Since the difference depends partially on the angle between coolant jet and wake, it is possible to minimize this pressure difference for the design injection pressure ratio.

3 The relation $P_b/P_{01} = f(P_{0c}/P_b^*)$ is little affected by the density ratio between coolant and main stream as long as the injection ratio is smaller than that at which the maximum base pressure occurs. The drop-off of the base pressure at high injection pressure ratios is, however, slower for high density ratios. This result could be essential for the choice of the optimum combination of a slot width and injection pressure ratio.

4 The influence of the trailing edge bleed on the blade pressure distribution is of minor importance. At transonic and supersonic downstream Mach numbers, there is a slight upstream shift of the shock interference point on the blade suction side, but the shock intensity does not seem to be influenced.

Acknowledgments

The author would like to express his sincere thanks to SNECMA who contributed to the financing of the first part (i.e., model tests) of this work.

References

1 Prust, H. W., et al., "Cold Air Investigation of a Turbine With Stator Blade Trailing Edge Slot Ejection, Part II: Detailed Stator Performance," NASA TM X 1963, 1970.

2 Prust, H. W., et al., "Flow Conditions Around the Exit and Downstream of Certain Stator Blading With Various Trailing Edge Thicknesses and Geometries," NASA TM-X-2659, 1972.

3 Prust, H. W., "Cold Flow Study of the Effect on Turbine Stator Blade Aerodynamic Performance of Coolant Ejection From Various Trailing Edge Slot Geometries, Part II: Comparison of Experimental and Analytical Results," NASA TM-X-3190, 1975.

4 Prust, H. W., et al., "Cold Air Study of the Effect of Turbine Stator Blade Aerodynamic Performance of Coolant Ejection From Various Trailing Edge Slot Geometries," NASA TM-X-3000, 1974.

5 Lokai, V. I., and Kumirov, B. A., "Losses in Turbine Cascades With Cooling Air Discharge and Various Trailing Edge Geometries," *Izv. Vuz. Aviats. Tekn.*, Vol. 16, No. 3, 1973.

6 Barry, B., "The Aerodynamic Penalties Associated With Turbine Blade Cooling," *Turbine Blade Cooling*, VKI LS 83, Jan. 1976.

7 Venediktov, V. D., "Investigating a Turbine Stage With Cooling Air Leaving Through Slots in the Concave Surfaces of the Nozzle Blades," *Teploenergetika*, Vol. 19, No. 7, 1972, pp. 15-19.

8 Lawaczek, O., "The Influence of Jets of Cooling Air Exhausted From the Trailing Edges of a Supercritical Turbine Cascade on the Aerodynamic Data," AGARD CP 229, Paper No. 30, 1977.

9 Abdul-Kadir, F. F., and Gibbings, J. C., The transonic flow past a blunt base. U. Liverpool.

10 Sieverding, C., Stanislas, M., and Snoeck, J., "The Base Pressure Problem in Transonic Turbine Cascades. ASME JOURNAL OF ENGINEERING FOR POWER, Vol. 102, No. 3, 1980, pp. 711-718.

11 Carriere, P., and Sirieix, M., "Facteur d'influence du recollement d'un ecoulement supersonique," *Xme Congr. Int. de Mecanique Appl.*, Stresa, 1960.

12 Marchal, Ph., and Sieverding, C. H., "Secondary Flows Within Turbomachinery Bladings," AGARD CP 214, Paper No. 11, 1977.

13 Heinemann, H-J., and Butefisch, K. A., "Determination of the Vortex Shedding Frequency of Cascades With Different Trailing Edge Thicknesses, AGARD CP 227, Paper No. 35, 1977.

14 Dyment, A., and Gryson, P., "Etude d'ecoulements turbulents subsoniques et supercritiques par visualisation ultra-rapide," AGARD CP 227, Paper No. 28, 1977.

APPENDIX

Blade Coordinates

X [mm]	$Y_{\text{suction-s}}$ [mm]	$Y_{\text{pressure-s}}$ [mm]
0.	4.00	4.00
0.20	5.80	2.50
0.50	6.99	1.80
1.00	8.35	1.00
2.00	10.33	0.24
3.00	11.80	0.00
4,00	12.85	0.05
5.00	13.70	0.32
6.00	14.40	0.79
7.00	14.90	1.20
8.50	15.61	1.79
10.00	16.08	2.39
11.50	16.30	2.89
13.00	16.49	3.31
15.00	16.61	3.85
17.00	16.60	4.31
20.00	16.30	4.85
23.00	15.80	5.28
26.00	15.28	5.45
29.00	14.53	5.45
32.00	13.71	5.40
35.00	12.89	5.18
38.00	12.00	4.86
41.00	11.02	4.50
44.00	10.00	3.05
47.00	9.92	3.50
50.00	7.85	2.90
53.00	6.80	2.30
56.00	5.65	1.55
58.00	4.90	1.10
60.00	4.14	0.60
61.00	3.75	0.35
62.00	3.30	0.10
62.50	3.10	0.00
63.00	2.90	0.10
63.50	2.60	0.35
63.80	2.20	0.70
64.00	1.50	1.50

I. Ariga
Professor.

N. Kasai
Postgraduate Student.

S. Masuda
Associate Professor.

Faculty of Science
and Technology,
Keio University,
Yokohama, Japan

Y. Watanabe
Power Plant
Overhaul Center,
Japan Air Lines,
Tokyo, Japan

I. Watanabe
Professor,
Faculty of Engineering,
Kanto-Gakuin University,
Yokohama, Japan
Mem. ASME

The Effect of Inlet Distortion on the Performance Characteristics of a Centrifugal Compressor

The present paper concerns itself with the effects of total pressure (and thus velocity) distortion on performance characteristics and surge margin of centrifugal compressors. Both radial and circumferential distortions were investigated. The performance tests as well as the velocity measurements within the impeller passages were carried out with a low-speed compressor test rig with the inlet honeycomb as the distortion generators and compared with the case of "no distortion" as a datum. The results indicated that the inlet distortion exerted unfavorable influences on the efficiency and the surge margin of the given compressor, though the influence of the radial distortion was much stronger than that of the circumferential one. Various distortion indices were further examined in order to correlate the performance to the inlet distortion.

Introduction

In recent years, centrifugal compressors has been increasingly utilized for various purposes, and the spatial restrictions become inherent with the growing width of applications. Consequently, the flow nonuniformity is frequently generated at the impeller inlet.

This is generally known as "inlet distortion," which is divided mainly into "radial distortion" and "circumferential distortion." The former one is further subdivided into "tip distortion" and "hub distortion," corresponding to the regions where the total pressure defect exists near a hub or a shroud side.

These may actually occur in the following cases:

1 Hub distortion – axisymmetric obstacles at a center portion of an inlet, such as a tachometer pick up, a hub cover, etc., or axisymmetric boundary layers of a return channel of multistage compressor.

2 Tip distortion – axisymmetric boundary layers of an inlet duct or a return channel or axisymmetric obstacles such as an orifice plate.

3 Circumferential distortion – nonaxisymmetric obstacles such as struts or a bending duct.

With regard to an axial compressor, the effect of inlet distortions on its performance characteristics has been widely investigated, and it has been reported that the compressor performance was deteriorated due to the inlet distortions and at the same time the flow range became narrower. Distortion indices which may be correlated to the compressor performance have also been variously discussed as to axial compressors, and many proposals have been made.

Only a few data about the inlet distortions of centrifugal compressors are available up to now [1, 2], although the nonuniformity of inlet flow appears frequently.

In this paper, total pressure distortions are investigated where the velocity is nonuniform and the static pressure is uniform at the inlet. Three kinds of distorted velocity profiles, including two radial distortions and one circumferential distortion together with the undistorted profile, are artificially given at the impeller inlet.

In the following section, the results of the performance tests as well as the velocity measurements within the impeller passage are reported, and the effects of inlet distortion on performances and flow range are clarified. The distortion index is also discussed.

Experimental Equipments and Methods

The test compressor configuration is shown in Fig. 1. Since its details were given in the reference [3], only the main points

Contributed by the Gas Turbine Division of THE AMERICAN SOCIETY OF MECHANICAL ENGINEERS and presented at the 27th International Gas Turbine Conference and Exhibit, London, England, April 18–22, 1982, Manuscript received at ASME Headquarters December 7, 1981. Paper No. 82-GT-92.

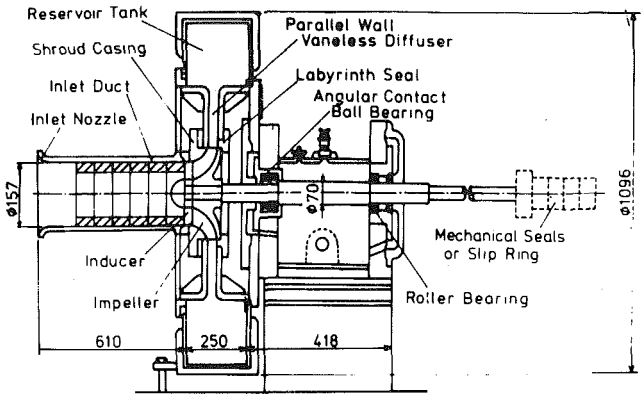

Fig. 1 Compressor configuration

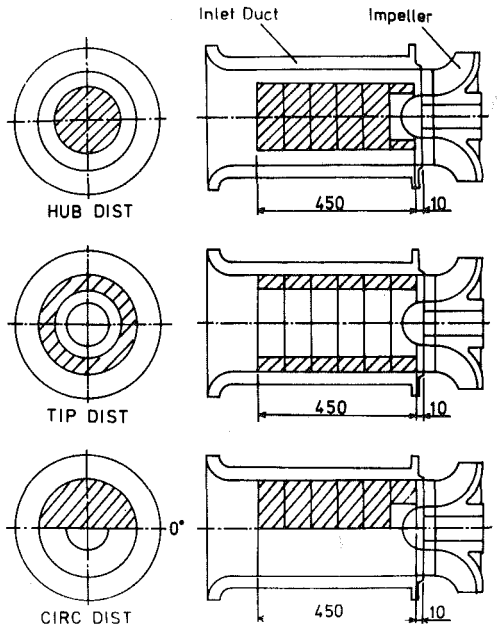

Fig. 2 Setting location of distortion generater

are to be repeated in the following. This compressor is driven by an eddy-current motor and its rotational speed can be changed from standstill to 6300 rpm continuously.

The pressure signals from the rotating impeller is lead through the pipes buried in the shaft to the sealed channels consisted of four mechanical seals, then onto a stationary manometer. The electrical signals of the rotating hot-wire probe are transmitted through a five poles slip ring unit to a constant temperature anemometer.

The compressor specifications are illustrated in Table 1. An impeller with straight blades employed in the present study has a diffusion ratio, C_{2r}/C_{1m}, of 1.0. An inducer has a parabolic camber line and is designed such that shockless inlet condition along the span at an inducer leading edge is attained at the design point.

Table 1 Compressor specifications

Shape of blade	Radial straight
Dia. of impeller outlet	270mm
Inner dia of impeller inlet	81mm
Outer dia of impeller inlet	157mm
Blade height of impeller outlet	16.9mm
Number of blades	12
Blade thickness	3mm
Rotation speed at design point	6000rpm
Flow coefficient at design point C_{2r}/U_2	0.4
Static pressure ratio at design point	1.04

Table 2 Kinds of distortion

Distortion pattern	Blocked area ratio	Distortion generator
No dist. (No Distortion)	0	No honeycomb
Hub dist. (Hub Distortion)	1/2	Cylindrical honeycomb at the hub side
Tip dist. (Tip Distortion)	1/2	Cylindrical honeycomb at the shroud side
Circ dist. (Circumferential Distortion)	1/2	Fan-shaped honeycomb

Nomenclature

C = absolute velocity [m/s]
H = total head [m]
Δh_{in} = shock loss at the impeller
h = length along blade height
h_t = distance from hub to shroud along quasi-orthogonal line
i = incidence angle [deg]
l_1 = curvilinear coordinate measured along shroud surface
l_{1-2} = total length of impeller measured along shroud surface
l_{inc} = total length of inducer
m = mass flow rate [kg/s]
N = rotational speed [rpm]
N_0 = corrected speed $(=N\sqrt{T_0/T_a})$ [rpm]
P = pressure [Pa]
R = gas constant [Nm/kg k]
T = temperature [K]
u = peripheral speed [m/s]
W = relative velocity [m/s]
β = inducer inlet angle [deg]
η_{imp} = impeller efficiency

$$= \frac{\frac{\kappa}{\kappa-1}RT_1\left\{\left(\frac{P_{t1}}{P_{t2}}\right)^{\frac{\kappa-1}{\kappa}}-1\right\}}{\mu u_2^2}$$

θ = circumferential location [deg]
ϕ = flow coefficient (c_{2r}/u_2)
μ = slip factor
κ = ratio of specific heats

Subscripts

0 = standard condition
1 = impeller inlet condition
2 = impeller outlet condition
a = atmospheric condition
m = axial component
m^* = through flow component
r = radial component
s = static
t = total
u = peripheral component
s = surge point

Superscript

$-$ = mass average

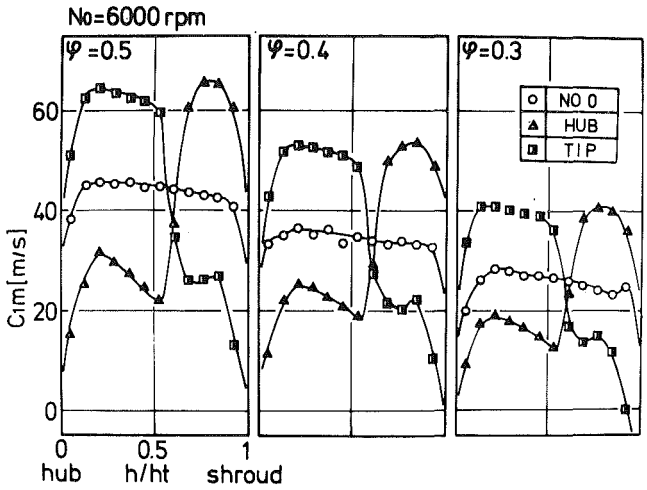

Fig. 3 Axial velocity distributions for no/radial distortions at the inducer inlet (N_0 = 6000rpm, ϕ = 0.50, 0.40, 0.30)

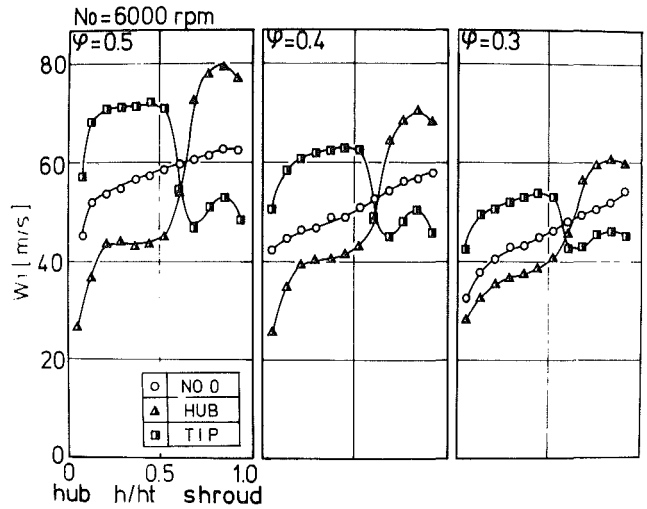

Fig. 4 Relative velocity distributions for no/radial distortions at the inducer inlet (N_0 = 6000rpm, ϕ = 0.50, 0.40, 0.30)

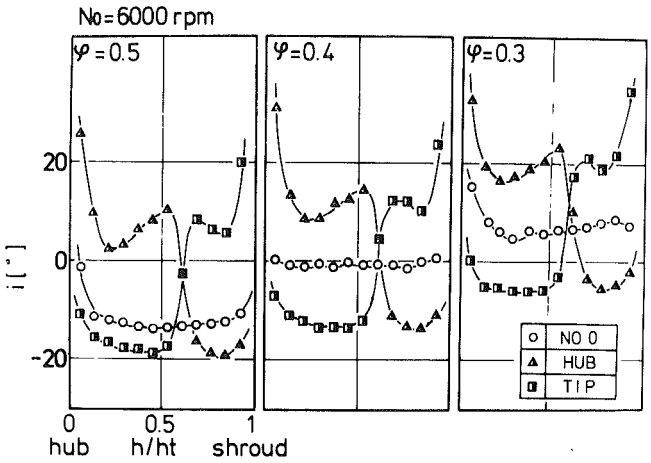

Fig. 5 Incidence angle distortions for no/radial distortions at the inducer inlet (N_0 = 6000rpm, ϕ = 0.50, 0.40, 0.30)

The experiments were carried out in the ranges of the corrected speeds N_0 = 6000, 5000, 4000 rpm and the flow coefficients ϕ = 0.3, 0.4, 0.5. Several kinds of distortion are used in the experiments, as shown in Table 2.

The test cross sections were at locations 5 mm upstream of the inducer leading edge and downstream of the impeller, respectively. The measurement points in those sections were selected at twelve sites for the inlet and nine sites for the outlet between the hub and shroud sides. Especially in the case of Circ dist, six circumferential locations were adopted, as shown in Fig. 2. A kiel probe and three holes yaw probe were used for the measurements of time-averaged total pressure and flow angle.

Concerning the relative flow patterns in the impeller, two probes, a three holes yaw probe for the time-averaged value and a hot-wire probe for the time dependent value were traversed in the meridional direction at the mid-passage.

The static pressure taps were placed along the shroud casing from the inlet to the outlet. To detect the surge phenomenon, pressure transducer was installed on the shroud casing of the inducer throat.

Inlet Conditions

The typical inlet distortion patterns of the radial distortions for the corrected speed N_0 = 6000 rpm are given in Fig. 3, 4, and 5 for three values of flow coefficient including the design value of ϕ = 0.4. Figure 3 shows the distributions of axial velocities measured at the location of 5 mm upstream of the impeller inlet. Their nonuniformities increase with increasing flow rate because the pressure loss generated by the distortion generator is proportional to the square of the velocity. Figure 4 shows the relative velocity distribution at the inlet section. While the defects of the axial velocity for the hub and the tip distortions are nearly equal as seen in the previous figure, those of the relative velocity become somewhat greater for the hub distortion than for the tip distortion due to the effect of the circumferential velocity. The corresponding incidence angle distributions are shown in Fig. 5. For all three inlet conditions, the average values vary from negative for the larger flow rate to positive for the smaller flow rate, being nearly zero for the design condition. The local portion of the negative incidence, where the inflow attains toward the suction side of the inducer blade, exists in the region of higher axial velocities, i.e., in the shroud region for the hub distortion and in the hub region for the tip distortion. The appearance of such negative incidences on the blading may be related to the unfavorable operating conditions.

The circumferential distributions of the axial and the relative velocities for the circumferential distortion are shown in Fig. 6 and Fig. 7, in which the mass-averaged values in the hub-shroud section are plotted. As shown in the figure, the honeycomb is placed at the circumferential location between 0 and 180 deg. The difference between the maximum and the minimum velocities are again remarkable with increasing flow rate. In Fig. 7, corresponding incidence angle distributions are shown, where the negative incidence angle can be seen in the circumferential range without the blockage on the flow due to the existence of honeycomb.

Performance Characteristics

In Fig. 8, the total pressure ratios of the impeller are plotted against the mass flow function for the three distortions as well as the undistorted cases. The highest pressure ratio is obtained in case of No dist. (no distortion) and it falls gradually in the order of Circ dist. (circumferential distortion), Tip dist. (tip distortion) and Hub dist. (hub distortion). This degeneration becomes more remarkable when the mass flow function increases, and there seems no effect of the inlet distortion at the smallest mass flow function shown in the figure. These tendencies are recognized equally for all three rotational speeds, though the effect of distortion slightly grows as the rotational speed increases.

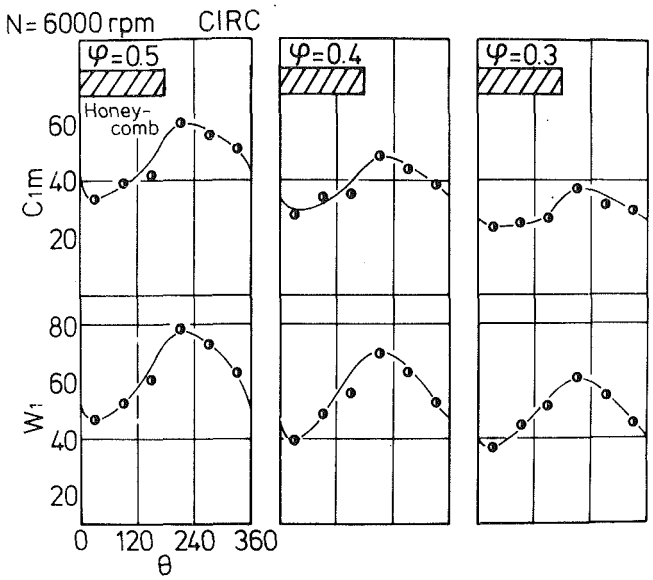

Fig. 6 Axial and relative velocity distributions for circumferential distortion at the impeller inlet (N_0 = 6000rpm, ϕ = 0.50, 0.40, 0.30)

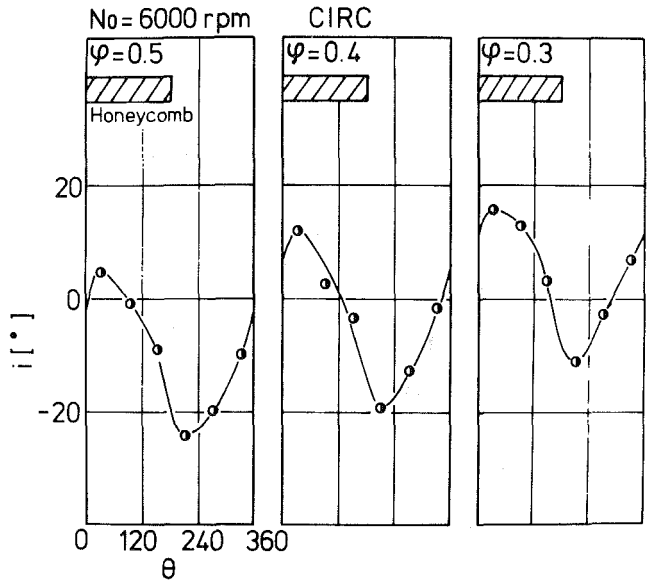

Fig. 7 Incidence angle distributions for circumferential distortion at the impeller inlet (N_0 = 6000rpm, ϕ = 0.50, 0.40, 0.30)

The violent surge lines are also shown in the same figure. Unlike the total pressure ratio, the violent surge limit is the highest for the No dist. and it moves to the lower flow rate in the order of Hub dist., Tip dist. and Circ dist. Although these results reflect the effect of distortion itself, we must not fail to notice an influence of duct resistance associated with the inlet honeycomb, too. Mild surge limit at corrected speed N_0 = 5000 rpm is shown by arrow marks in Fig. 8. The tendency of mild surge limits differs from that of violent surge. On these subjects, we will discuss later.

Figure 9 shows the variation of the impeller efficiency for N_0 = 6000 rpm. In accordance with the total pressure ratio, Circ dist. has the smallest influence, the peak efficiency and the corresponding flow coefficient as well as the off-design variations being the same as those for No dist. The radial distortions, on the other hand, have remarkable influences on the impeller efficiencies. Tip dist. shows the lowest efficiency in almost all the range of flow coefficients tested. The more striking features are seen in the efficiency curve for Hub dist., which is characterized by the efficiency higher than that for

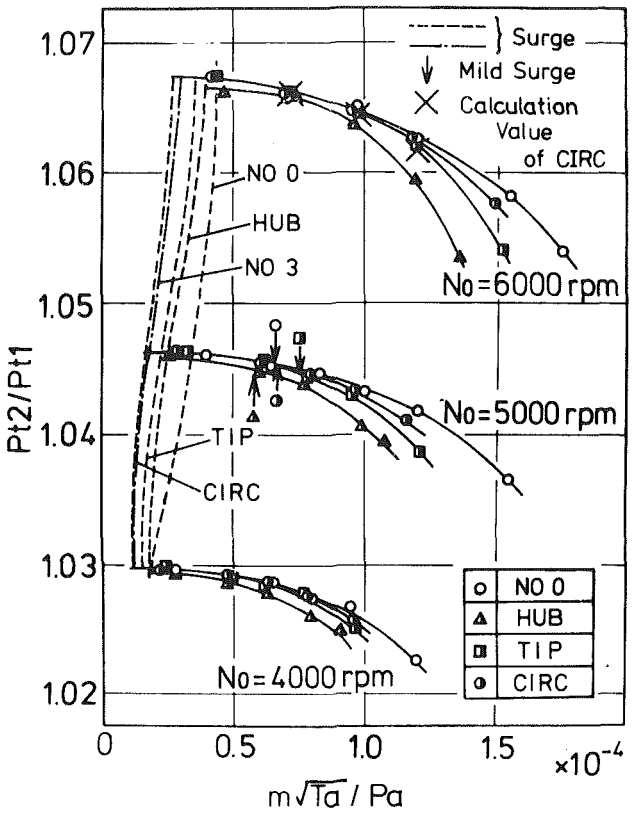

Fig. 8 Comparison of performance curves with various distortions

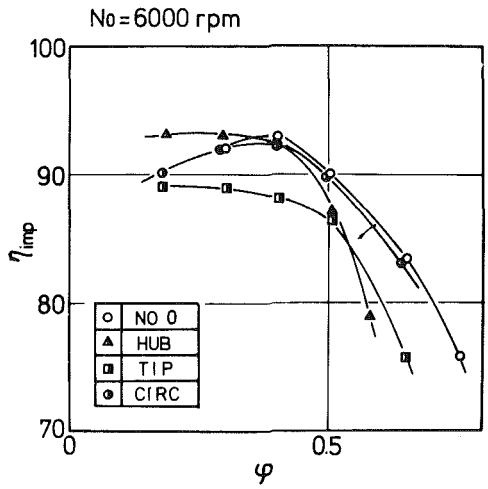

Fig. 9 Impeller efficiency

No dist. at the small flow rate (ϕ < 0.4) and the steep decrease at the large flow rate.

Mean Flow Pattern Within the Impeller Passage

In order to examine the behavior of the distorted velocity profile within the impeller passage, the time-averaged velocities were measured by the three hole yaw probe mounted on the rotating impeller for ϕ = 0.40 and N_0 = 5000 rpm. The typical results obtained within the inducer are given in Fig. 10, together with the velocity profile just upstream of the inducer. In the case of the radial distortions, the velocity profile given at the inlet is maintained to the downstream end of the inducer. Since the circumferential distortion is seen from the rotating frame as the periodic flow, the time-averaged velocity profile within the inducer is apparently the same as that of No dist.

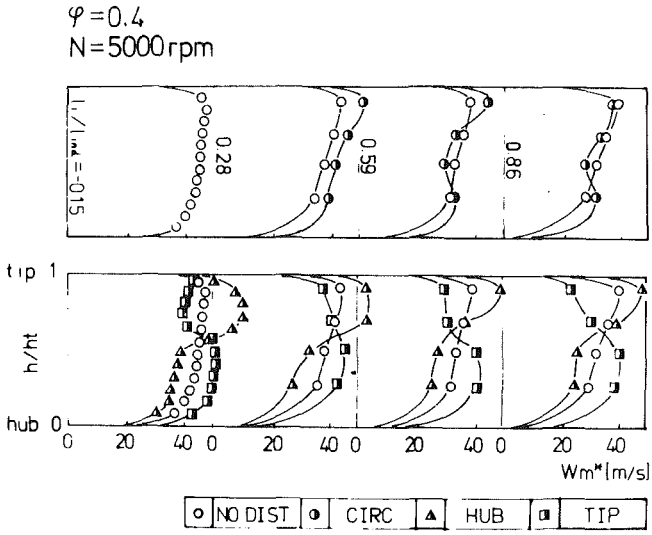

Fig. 10 The velocity profile within the inducer (N_0 = 5000rpm, ϕ = 0.40)

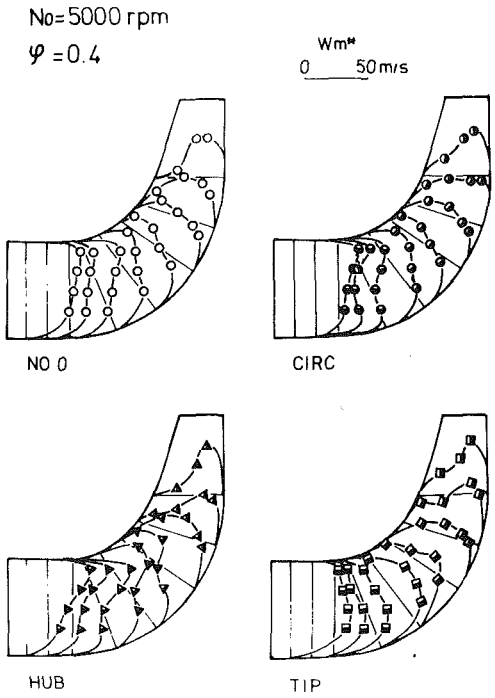

Fig. 11 The velocity profile within the impeller passage (N_0 = 5000rpm, ϕ = 0.40)

Figure 11 shows the development of velocity profile further downstream within the impeller passage. In all cases, the velocity profiles at the second half of the impeller become nearly the same, with the velocity peak being near the hub side. Without distortion, the peak exists near the shroud side at the first half of the impeller and it moves to the hub side in the downstream direction. These tendencies are intensified in case of Hub dist., where the initial velocity near the shroud side is artificially increased. In the case of Tip dist., the velocity profile remains almostly unchanged, with the velocity peak lying always near the hub side. The flow development of Circ dist. is hardly distinguishable from that of No dist. in the time mean manner.

Outlet Velocity Profile

The radial component of the absolute velocities at the location of 5 mm downstream of the impeller outlet are given

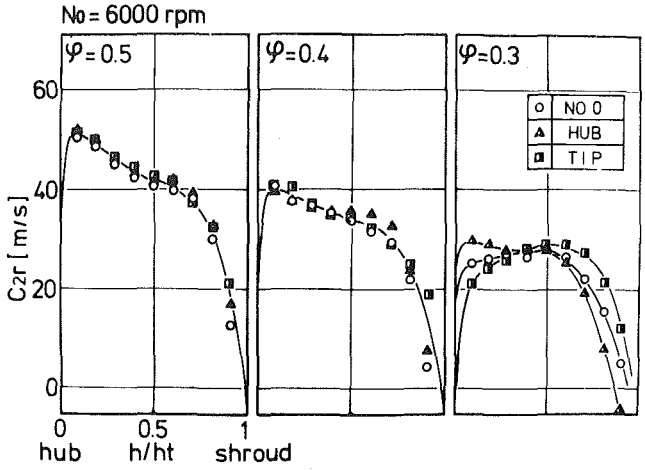

Fig. 12 Radial velocity distributions for no/radial distortions at the impeller outlet (N_0 = 6000rpm, ϕ = 0.50, 0.40, 0.30)

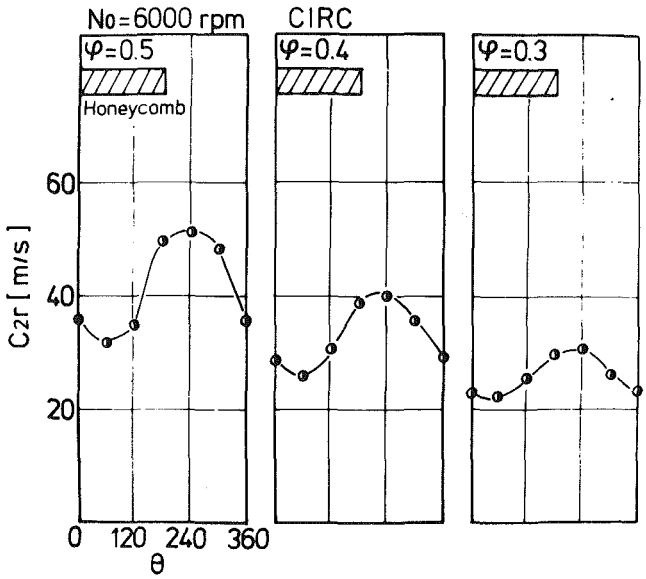

Fig. 13 Radial velocity distribution of circumferential distortion at the impeller outlet (N_0 = 6000rpm, ϕ = 0.50, 0.40, 0.30)

in Figs. 12 and 13 for the radial and the circumferential distortions, respectively. As seen in Fig. 12, the outlet velocity profiles of the radial distortions leave no traces of the inlet conditions except for the smallest flow rate (ϕ = 0.30). One of the interesting results is seen in Fig. 12 for ϕ = 0.30, where the effect of inlet conditions is remarkable, though the velocity profiles are entirely different from those given at the inlet. Since the complete measurement of flow development through the whole passage of the impeller was performed only for ϕ = 0.40, it is difficult to clear up the causes, but the remarkable difference of the impeller efficiency at small flow rates shown in Fig. 9 may be closely related to the distinct feature of the outlet velocity profile.

The outlet velocity distributions for the circumferential distortion shown in Fig. 13 exhibit another interesting result. In contrast to the radial distortions, the traces of the inlet distortion are clearly found at the outlet. It is also worth noticing that the defect of the outlet velocity exists just at the same angular position as given at the inlet, in spite of the rotating impeller lying between them (see Fig. 6).

Time Dependent Measurement of Circ Dist.

As explained earlier, the time-averaged measurements in

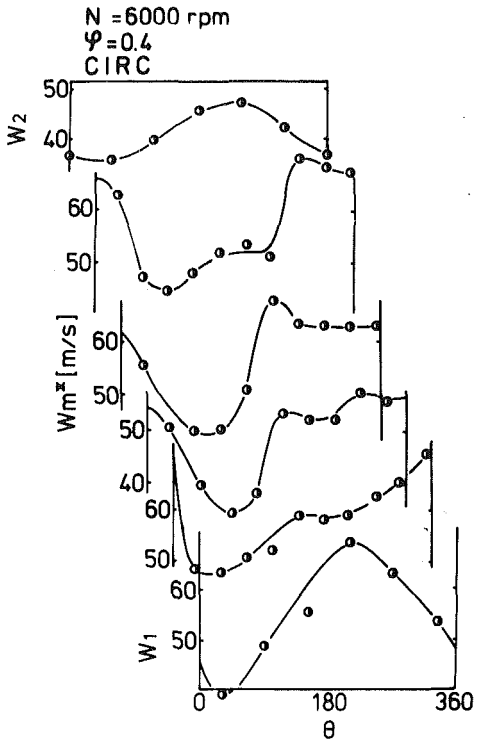

Fig. 14 Through flow velocity distribution within impeller channel by hot-wire, including relative velocity distribution at the impeller inlet and outlet (N_0 = 6000rpm, ϕ = 0.40)

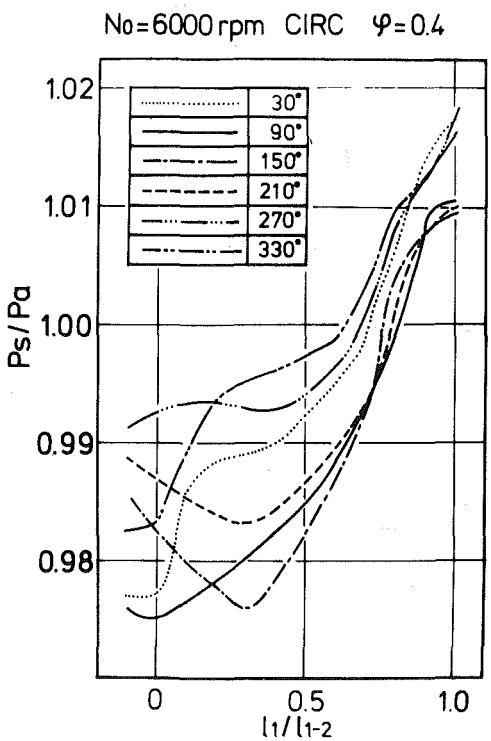

Fig. 15 Shroud surface static pressure distribution for circumferential distortion (N_0 = 6000rpm, ϕ = 0.40)

the impeller passage for the circumferential distortions exhibit no appreciable difference as compared with the undistorted case. The results of the time dependent measurements of the through flow velocity within the impeller channel W_m. are shown in Fig. 14, together with the relative velocities W_1 and W_2 at the inlet and the outlet cross sections, respectively. W_m.

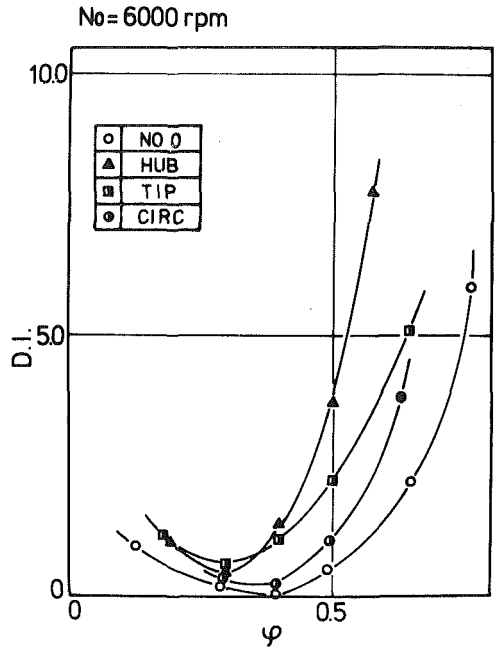

Fig. 16 Distortion index DI plotted against the flow coefficient for four distortions (N_0 = 6000rpm)

was obtained using the rotating hot-wire probe fixed at the mid point of the channel cross section and one cycle of the time dependent signals was converted into the function of angular positions measured from the fixed origin in the stationary frame. The velocity profiles within the impeller are well coincided with those at the inlet and the outlet, which means that the flow associated with the circumferential distortion is spatial within the entire flow region including the rotating impeller if it is observed from the stationary frame of reference. The whole length of an impeller channel accepts the periodic variation of flow rates simultaneously and one channel of the impeller experiences the small and large flow rates alternatively as it rotates passing through the angular regions of low and high velocities.

Figure 15 shows the static pressure distribution along the radial lines on the shroud casing. At the circumferential locations θ = 150 and 210 deg, which correspond to the region near the minimum velocity, the static pressure once decreases to the minimum at the first quarter of the impeller and then increases. On the other hand, it increases monotonously in the region near maximum velocity, say at θ = 330 deg.

The two figures suggest the possibility of extending the idea of "parallel compressor" model, which was proposed by Doyle [4], Reid [5], and Roberts [6] for axial compressors, to centrifugal compressors with the circumferential distortions. In one period of time when a channel rotates through the region behind the honeycomb, it acts as if it were operating steadily at a point lying in the region of small flow rate on the undistorted performance map. In the rest of one cycle, the channel acts as if it were operating at another point lying in the region of larger flow rate.

On the basis of this model, the total pressure ratio for the circumferential distortion is estimated using the following relation

$$\mathrm{Pr}'(\phi) = \frac{\int_{\phi_{\min}}^{\phi_{\max}} \mathrm{Pr}(\phi)\,\phi\,d\phi}{\phi(\phi_{\max} - \phi_{\min})} \tag{1}$$

where Pr and Pr′ are the total pressure ratios for the undistorted condition and for the circumferential distortions,

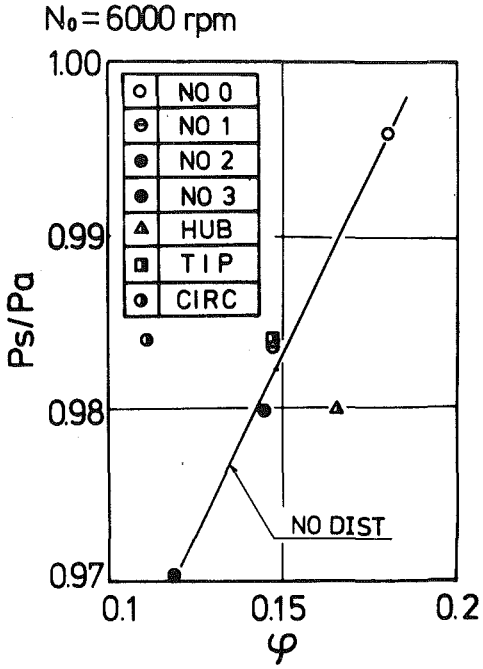

Fig. 17 Relation of static pressures upstream of the impeller inlet with flow coefficients at violent surge point (N_0 = 6000rpm)

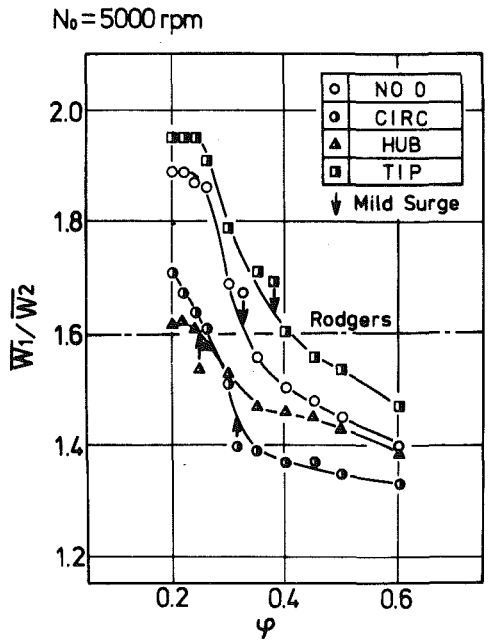

Fig. 18 Relation of mild surge points with ratio of inlet average relative velocity to outlet one

respectively and ϕ_{max} and ϕ_{min} are the maximum and the minimum values of the local flow coefficients for the circumferential distortion at a given mean flow coefficient. The calculated values are plotted in Fig. 8, which shows good correlation with the measured results, and supports the applicability of the "parallel compressor" model to centrifugal compressors with the circumferential distortions. It is also clear that the effect of circumferential distortions on performance characteristics is dependent not only on the pattern of distortion but also on the shape of the performance curve for undistorted conditions. As the first approximation, the total pressure ratio is improved or deteriorated by the circumferential distortions according to the sign of $d\text{Pr}/d\phi$ of the undistorted curve at the mean operation point.

The direct application of this model to the radial distortions is impossible because the region of high and low velocities are not isolated in those cases but mixed within one channel of the impeller, and it may cause the additional complexity, such as loading distribution, secondary flows, leakage, and so on.

Distortion Index

It is desirable to have a single parameter which correlates performance characteristics with the patterns of inlet distortions uniquely. Such a parameter is called "distortion index" and many proposals have been made on the distortion indices for axial compressors with the circumferential distortions as summarized in [7]. Since we are dealing with the centrifugal compressor with the radial and circumferential distortions together, we tried to find a new index which is applicable to these cases.

As stated before, some parts of the inducer blading have nonzero incidence angle, though it is equal to zero in the mean. Shock loss associated with it may be considered as one of the major factors causing the additional losses due to distortions of both types. So, we have tried to relate a new index with the shock loss of the inducer. O'Neil et al. [8] suggested that the shock loss is proportional to the square of the relative peripheral velocity, ΔW, at the leading edge of the inducer. The distortion index may then be defined as

$$DI = \frac{\Delta h_{in}}{H_1} \tag{2}$$

where

$$\Delta h_{in} = \zeta_{in} \frac{\Delta W^2}{2g} \tag{3}$$

$$\Delta W = W_{1u} - W_{1m} \cdot \tan\beta \tag{4}$$

H_1 = inlet total head

Here the shock head coefficient is determined experimentally, and $\zeta_{in} = 0.6$ from the present experiment.

Figure 16 shows the relation between DI and ϕ for all cases of distortions tested. Comparison with the total pressure ratio given in Fig. 16 indicates that DI is the suitable parameter for estimating the total pressure ratio with inlet distortions.

Surge Margin

Surge regions are divided into "Mild surge" and "Violent surge." In the former case, pressure fluctuations detected only by a pressure transducer are still small, and in the later case, the large fluctuations are observed anywhere in the machine, accompanied with the vibration of a compressor.

Violent Surge. As already shown in Fig. 8, the violent surge margin is affected by the inlet distortions. It is well known, however, that a surge margin is also related to a flow resistance of an entire compressor passage, which varies with the distortion generators in the present cases. Hence, it was tried to investigate the effects of inlet distortion patterns, themselves, on the surge margin except for the differences of the resistance through the distortion generators.

Figure 17 indicates the relation between the flow coefficients on the violent surge line and the inlet static pressure normalized by the atmospheric pressure at $\phi = 0.40$. The latter is related to the flow resistance through the honeycomb section. As references, the three additional undistorted conditions, No. 1, No. 2, and No. 3, are included herein. They are generated by the one, two, and three pieces of full shaped honeycomb of 75-mm thick, which are installed in series in the inlet pipe, respectively, and they can generate the uniform flows with different resistances. The performances for them were agreed almostly with that for No. 0 as shown in Fig. 8.

The results of four kinds of undistorted conditions lie on a single straight line, which indicates that the resistance alone reduces the violent surge flow rate. The resistance of the three distorted conditions are nearly equal to those of No. 1 and No. 2, and these five results may be compared in order to examine the effect of distortion with the same level of resistance. It is clear from this comparison that the violent surge flow rate is reduced by Circ dist, increased by Hub dist. and unaffected by Tip dist.

Mild Surge. Rodgers [9] proposed that a compressor stall, and consequently a mild surge, could be related with a diffusion factor defined as a ratio of inlet and outlet relative velocities (W_1/W_2), and gave $W_1/W_2 = 1.6$ as the criterion for occurrence of a mild surge. It is interesting to examine whether his criterion is applicable also to the distorted cases. In Fig. 18, the diffusion factors, which are evaluated from the mass flow average of relative velocities, are given as the functions of the flow coefficients and the mild surge limits are shown by the arrows.

It is clearly seen in this figure that mild surge of a radial distortion is well predicted by Rodger's criterion, but it can not directly be applied to circumferential distortion.

Conclusion

In the present paper the authors experimentally investigated the effects of inlet total pressure distortion, i.e., radial and circumferential distortions on the performance characteristics and surge margin of a centrifugal compressor. Various distortion indices were also examined in order to correlate the performance to the inlet distortion. The results are summarised as follows:

1 Compared with undistorted case, total pressure ratios fall in the order of circumferential, tip and hub distortions.

2 Distortion index, *DI*, employing the shock loss of the inducer,

$$DI = \frac{\Delta h_{in}}{H_1}$$

is the suitable parameter for estimating the total pressure ratio with inlet distortions.

3 At the impeller outlet, the circumferential inlet distortion remains at the same circumferential location, while the effect of radial distortion almost disappears, except for small flow rate.

4 "Parallel compressor" model can be applied to centrifugal compressors with circumferential distortions.

5 Violent surge is prompted by hub distortion and restrained by circumferential distortion, while it is unaffected by tip distortion if they are compared in the same level of duct resistance.

6 A mild surge limit of radial distortion is well predicted by Rodger's criterion, while it is not directly applicable to circumferential distortion.

References

1 Livshitz, S. I., "Aerodynamics of Centrifugal Compressor," *Mechanical Engineering*, 1966.

2 Benvenuti, E., Bonciani, L., Corradini, U., "Inlet Flow Distortions on Industrial Centrifugal Compressor Stages Experimental Investigations and Evaluation of Effects on Performance," AGARD Conference, Paper No. 282, 1980.

3 Mizuki, S., Ariga, I., and Watanabe, I., "Investigation Concerning the Blade Loading of Centrifugal Impellers," ASME Paper No. 74-GT-143, 1974.

4 Doyle, M. D. C., and Horlock, J. H., "Circumferential Asymmetry in Axial Flow Compressors," *Journal of the Royal Aeronautical Society*, Vol. 70, 1966, pp. 956–957.

5 Reid, C., "The Response of Axial Flow Compressors to Intake Flow Distortion," ASME Paper No. 69-GT-29, 1969.

6 Roberts, F., Plourde, G. A., and Smakula. F., "Insights into Axial Compressor Response to Distortion," AIAA Paper No. 68-595, 1968.

7 Graber, E. J., Jr., and Braithwaite, W. M., "Summary of Recent Investigations of Inlet Flow Distortion Effects on Engine Stability," AIAA Paper No. 74-236, 1974.

8 O'Neil, P. P., and Wickli, H. E., "Predicting Process Gas Performance of Centrifugal Compressors From Air Test Data," ASME *Journal of Engineering for Industry*, Series B, Vol. 84, 1962, pp. 248–264.

9 Rodgers, C., "Impeller Stalling as Influenced by Diffusion Limitations," ASME *Journal of Fluids Engineering*, Series I, Vol. 99, 1977, pp. 84–93.

A Mixed-Flow Cascade Passage Design Procedure Based on a Power Series Expansion

R. A. Novak
Consultant, Aerodynamics.

G. Haymann-Haber
(Formerly) Technical Engineer.

General Electric Company,
Aircraft Engine Group,
Lynn, Mass. 01910

Flow passage design and analysis procedures employing a TAYLOR series expansion across the flow field were first suggested as far back as 1908. With very few exceptions the early work addressed only the problem of symmetrical convergent-divergent passages. A generalization and an extension of the approach permits it to be used for the design of arbitrary cascade passages in subsonic, supersonic, or mixed-flow regimes. The method will give fast, realistic solutions in situations where shock-free flow is meaningful, and where the cascade gap-chord ratio is not excessive. It assumes inviscid, irrotational flow and employs a fourth-order TAYLOR series expansion across the cascade passage. Numerous examples are given, with comparisons with experimental data and other analytic solutions.

Introduction

The use of a power series expansion to represent the flow field in a nozzle or cascade passage is not new. A comparatively recent paper by DeCuypere [1] cites references (not repeated here) which go back to 1908. They include such names as G. I. Taylor, Hall, Oswatitsch, Rothstein, Sauer. With few exceptions, the earlier efforts were directed at the design or analysis of Laval nozzles.

Reference [2] is the first instance discovered in which a TAYLOR series expansion was used for cascade design. It dealt only with radially oriented cascades, i.e., centrifugal compressor diffusers. The present effort was sparked by the discovery of the 1952 paper by Wu and Brown [3]. Reference [3] restricted itself to rectilinear stationary turbine cascades. Reference [4] includes a nearly literal rewrite of the Wu and Brown formulation for a rotating cylindrical coordinate system.

Wu and Brown (and [4]) use a second-order TAYLOR series. This is surprisingly effective within the blade passage itself for closely spaced cascades such as those characteristic of most turbine nozzles and centrifugal compressors. For cascades of wider spacing, particularly in the region of the leading and trailing edges, higher-order terms must be included to assure a more realistic representation of the flow field. Many of the earlier efforts directed toward the Laval nozzle problem did, in fact, employ expansions up to fourth order; because the geometry was symmetric, however, only half of the coefficients of the expansion were required.

Most currently available cascade programs are direct, or analysis, programs. They provide, when successful, blade surface pressure or Mach number for a cascade of prescribed geometry. In the design of a turbomachine blade row, it is most often the case that an indirect, or design, technique would be more useful. The quasi-three-dimensional design technique currently used by nearly everyone usually starts with, for example, a meridional-plane streamline curvature solution. This, typically, results from input of annulus geometry, blade thickness distribution, upstream and downstream boundary conditions, rotative speed, estimated losses, a blade stacking axis, and an intrablade angular momentum addition rate. The solution gives average meridional-plane velocity components, pressures, and temperatures, and establishes the presumed rotationally symmetric streamtube thickness distribution for each streamtube. It is a fact that there is one, and only one, blade shape for each streamtube which will satisfy the input constraints listed above (we except consideration of viscous, Coriolis-induced stream surface twist, and secondary flow phenomena). Within additional overall assumptions which will be discussed below, it has been the objective of the present effort to devise a blade-to-blade design technique which will quickly develop the unique blade shape implied by the meridional-plane input specifications. This could then be treated as a preliminary version of a final blade shape, to be modified in accordance with the designer's perception of neglected real flow effects.

It should be kept in mind that, strictly speaking, we will be discussing a channel design process, not a blade design process. Alternatively, one can consider that the "blade" developed by the process is the blade proper plus the upstream and downstream stagnation streamline locus. In the upstream and downstream regions, the stagnation streamline shape results from the specification of zero blade thickness and zero angular momentum change. The computation process inside and outside the blade-proper is identical.

The flow is assumed to be steady, two-dimensional on surfaces of revolution, nonviscous, and irrotational. The process readily gives solutions for subsonic, supersonic, or mixed-flow conditions. It is to be stressed again, however, that the solutions are channel solutions, and are realistic only in situations where a shock-free flow is possible. Hence, for

Contributed by the Gas Turbine Division of THE AMERICAN SOCIETY OF MECHANICAL ENGINEERS and presented at the 27th International Gas Turbine Conference and Exhibit, London, England, April 18–22, 1982. Manuscript received at ASME Headquarters December 7, 1981. Paper No. 82-GT-121.

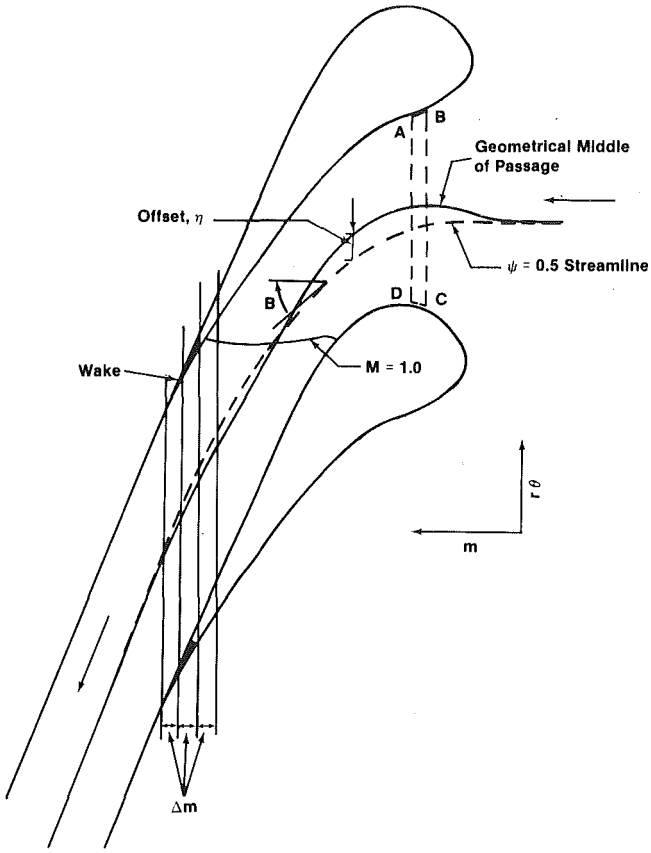

Fig. 1 Schematic of geometry

example, particularly for supersonic compressor cascades, the results must be treated with caution. No real cascade with supersonic inlet can be free of bow-shocks and not all supersonic solutions for a diffusing passage can be started.

Theory

The basic assumption of the process is that any flow quantity, Q, (pressure, velocity, etc.) can be expressed by a fourth-order TAYLOR series in θ, the circumferential direction. Thus,

$$Q(\theta) = Q + \frac{\partial Q}{\partial \theta}\delta\theta + \frac{1}{2}\frac{\partial^2 Q}{\partial \theta^2}\delta\theta^2 + \frac{1}{6}\frac{\partial^3 Q}{\partial \theta^3}\delta\theta^3 + \frac{1}{24}\frac{\partial^4 Q}{\partial \theta^4}\delta\theta^4 \quad (1)$$

Q is the value of the quantity on the $\psi = 0.5$ streamline of the passage (see Fig. 1) and the expansion is presumed, at any station, to originate from this locus. The location of the $\psi = 0.5$ streamline (which must be iteratively established) is referenced to the geometrical middle of the passage by a distance, η, which is called the offset. It is not a necessary condition, but it has been assumed for computational simplicity, that Δm, the distance between the circumferentially oriented computing stations, is constant.

For any solution, it is assumed that the radius ($r = r(m)$), the streamtube thickness ($b = b(m)$), and the blade circumferential thickness ($t = t(m)$) are known. The rotational speed (if any) is prescribed. Conditions sufficient to define the flow and the upstream angle are assumed given; the downstream average angular momentum is a prescribed condition. Upstream total pressure and enthalpy (or rothalpy) are given quantities; a total pressure loss as a function of m can be prescribed.

With one important exception, the imposed conditions listed above are sufficient to define a unique blade shape. The final condition arises directly from the application of the moment of momentum theorem to a control volume such as ABCD of Fig. 1. It is readily shown that

$$p_p - p_s = \frac{1}{br} \cdot \frac{F}{N} \cdot \frac{d\overline{rV_\theta}}{dm} \quad (2)$$

where the LHS is the pressure difference between the pressure surface and the suction surface at any m-location, F is the total streamtube flow, N is the number of blades in the cascade, and $\overline{rV\theta}$ is the average angular momentum at any m-defined computing station. The imposition, as a function of m, of a number proportional to the surface static pressure difference is sufficient completely to define the problem, since the prescribed downstream angular momentum is the required constant of integration of equation (2).

One other simple geometrical relation is useful to recognize at this point. It is

$$\tan\beta_p - \tan\beta_s = \frac{2\pi r}{N}\frac{d\lambda}{dm} \quad (3)$$

where β_p and β_s are, respectively, pressure surface and suction surface angles at any m-location, and λ is the percent circumferential blade blockage at any station.

It is evident that the specification of $p_p - p_s = \lambda = 0$ in the upstream and downstream region is equivalent to the imposition of periodicity.

The continuity equation for a stream surface of revolution is

$$\frac{\partial b\rho W_\theta}{\partial \theta} + \frac{\partial b\rho r Vm}{\partial m} = 0 \quad (4)$$

Nomenclature

a = velocity of sound
b = normal streamtube thickness
l = chord length
m = meridional distance, $m = \sqrt{z^2 + r^2}$
p = static pressure
r = radius
t = blade circumferential thickness
z = axial distance
F = flow
N = number of blades
S = distance along streamline
V_θ = θ-component of velocity (absolute)
$\overline{rV_\theta}$ = flow weighted average angular momentum
V_m = meridional component of velocity ($Vm = \sqrt{Vr^2 + Vz^2}$
V_r = radial component of velocity
V_z = axial component of velocity
W = relative velocity
W_θ = tangential component of relative velocity ($W\theta = V\theta\tau - \bar{\omega}r$)
β = angle relative to meridional direction
γ = specific heat ratio
δ = differential distance
Δ = discrete difference
η = offset (defined by equation (16))
λ = circumferential blockage due to blade thickness
ψ = streamfunction ($0 \leq \psi \leq 1.0$)
θ = circumferential angle
ρ = density
$\bar{\omega}$ = angular velocity
ϕ = $\sin^{-1}(dr/dm)$

Subscripts

s = suction surface
p = pressure surface
m = value of $\psi = 0.5$ streamsurface, $\bar{m} = (\psi = 0.5)$
i = current station

Using the relationship

$$W\frac{d}{ds}=V_m\frac{d}{dm}=V_m\frac{\partial}{\partial m}+\frac{W_\theta}{r}\frac{\partial}{\partial\theta} \tag{5}$$

Equation (4) becomes

$$\frac{\partial W_\theta}{\partial\theta}-\tan\beta\frac{\partial V_m}{\partial\theta}=-\frac{1}{b\rho}\frac{d(b\rho rV_m)}{dm}=C \tag{6}$$

The θ-component of momentum, assuming irrotationality, is simply

$$\frac{\partial Vm}{\partial\theta}-\frac{\partial rV_\theta}{\partial m}=0 \tag{7}$$

Since $V_\theta=W_\theta+\bar{\omega}r$ (and, using equation (5)) this becomes:

$$\frac{\partial V_m}{\partial\theta}+\tan\beta\frac{\partial W_\theta}{\partial\theta}=\frac{drV_\theta}{dm}=D \tag{8}$$

Treated as simultaneous equations, equations (6) and (8) can be solved for θ-derivatives of V_m and W_θ in terms of C and D, the two m-derivatives on the RHS.

One should also note that

$$\frac{C}{V_m}=\frac{\partial\tan\beta}{\partial\theta} \tag{9}$$

and (using the state equation, the energy equation and a $p-\rho$ relation),

$$V_mD=\frac{1}{2}\frac{\partial W^2}{\partial\theta}=-a^2\left(\frac{1}{\rho}\frac{\partial\rho}{\partial\theta}\right)=-\frac{a^2}{\gamma}\left(\frac{1}{p}\frac{\partial p}{\partial\theta}\right) \tag{10}$$

where a is the local speed of sound.

Second-order derivatives of, p, ρ, tan β, and the velocity components can be obtained by further differentiation, keeping in mind the meaning of d/dm as expressed in equation (5).

Thus, we have expressions for first- and second-order terms of equation (1) for all necessary fluid properties, all as functions of m-derivatives of $b\rho rV_m$ and rV_θ. These are discretized as

$$\frac{dQ}{dm}=\frac{Q_{i+1}-Q_{i-1}}{2m}$$

and

$$\frac{d^2Q}{dm^2}=\frac{Q_{i+1}-2Q_i+Q_{i+1}}{m^2}$$

The values of $b\rho rV_m$ and rV_θ (i.e., of Q) used in any one iterative loop are those which have been computed to pertain on the $\psi=0.5$ streamline in the previous loop.

Although it is necessary to track θ-derivatives for all the flow properties, the basic expansions are done in tan β and the static pressure. If these two quantities are known across the channel, everything else is implicitly known.

What is needed, therefore, are four additional boundary conditions to determine

$$\frac{\partial^3\tan\beta}{\partial\theta^3},\frac{\partial^4\tan\beta}{\partial\theta^4},\frac{\partial^3p}{\partial\theta^3},\text{ and }\frac{\partial^4p}{\partial\theta^4}$$

As stated above, the first- and second-order terms are available from direct differentiation of $\psi=0.5$ streamline quantities. We consider first the tan β expansion.

If it is assumed for any iteration that the offset, η, and (tan $\beta)_{\psi=0.5}=$tan β_m are available from the previous iteration, a second simple geometric relationship can be written, i.e.,

$$\tan\beta_p+\tan\beta_s=2\left(\tan\beta_m-r\frac{d\eta}{dm}\right) \tag{11}$$

Equations (3) and (11) can be solved simultaneously for tan β_p and tan β_s. Expressing these in a TAYLOR series gives two equations which can be solved for $\partial^3\tan\beta/\partial\theta^3$ and $\partial^4\tan\beta/\partial\theta^4$. It is to be noted that the $d\lambda/dm$-term of equation (3) comes directly from the input specification of $t=t(m)$, the blade circumferential thickness.

To deal with the third- and fourth-order terms in pressure is somewhat more difficult. One relationship which can be directly applied is equation (2). If the LHS is expressed as a TAYLOR series, we immediately have one expression in the third- and fourth-order terms (the first and second are presumed already known) as a function of the input m-derivative of the average angular momentum. We need a second relation.

A number of options, involving combinations of the momentum and continuity equation are available. The choice was made to stay with the momentum equation. Considered as a point function, the m-component can be written:

$$-\frac{1}{\rho}\frac{dp}{dm}=-W\frac{dV_m}{ds}+\frac{\tan\beta}{r\rho}\frac{\partial p}{\partial\theta}-\sin\phi\left(\frac{W_\theta^2}{r}+2\bar{\omega}W_\theta+\bar{\omega}r^2\right) \tag{12}$$

where $\sin\phi=dr/dm$ and equation (5) has been used to replace $\partial p/\partial m$ by dp/dm. This also introduces the $\partial p/\partial\theta$-term. The θ-component of momentum is

$$-\frac{1}{r\rho}\frac{\partial p}{\partial\theta}=\frac{dW_\theta}{ds}+\frac{W_\theta V_r}{r}+2\bar{\omega}V_r=WV_m\frac{d\tan\beta}{ds}+W\tan\beta\frac{dVm}{ds}+\frac{W_\theta V_r}{r}+2\bar{\omega}V_r \tag{13}$$

Eliminating dV_m/ds between equations (12) and (13) and noting that $d/ds=\cos\beta d/dm$ (i.e., equation (5)) one gets

$$\frac{1}{\rho W^2\cos^2\beta}\left(\frac{1}{r\cos^2\beta}\frac{\partial p}{\partial\theta}-\tan\beta\frac{dp}{dm}+A\right)=-\frac{d\tan\beta}{dm} \tag{14}$$

where

$$A=\frac{\rho\sin\phi}{\cos\beta}\left(\frac{W^2\sin\beta}{r}+2\bar{\omega}W+\bar{\omega}^2r\sin\beta\right)$$

which is operative only for cascades with a radius change.

Equation (14) can be expressed as a difference between $d\tan\beta/dm$ values on the pressure and suction surface to give

$$\left[\frac{\frac{1}{r\cos^2\beta}\frac{\partial p}{\partial\theta}-\tan\beta\frac{dp}{dm}+A}{\rho W^2\cos^2\beta}\right]_P-\left[\frac{\frac{1}{r\cos^2\beta}\frac{\partial p}{\partial\theta}-\tan\beta\frac{dp}{dm}+A}{\rho W^2\cos^2\beta}\right]_S=-\frac{2\pi r}{N}\left[\frac{d^2\lambda}{dm^2}+\frac{\sin\phi}{r}\frac{d\lambda}{dm}\right] \tag{15}$$

where the RHS is simply the m-derivative of equation (3).

Equations (15) and (2) are solved simultaneously. The β-angles are already available (as described above). The remaining θ-dependent terms (ρ, W and $\partial p/\partial\theta$) are expressed by appropriate TAYLOR series expansions in pressure, using the identities noted in equation (10) and higher-order equivalents. The dp/dm-terms are updated after each loop or in an interior iterative loop, called a pass, which is described below.

The process is algebraically messy to describe. Set up in a proper coding sequence, however, it does not involve serious computational problems.

The third- and fourth-order terms for all other quantities

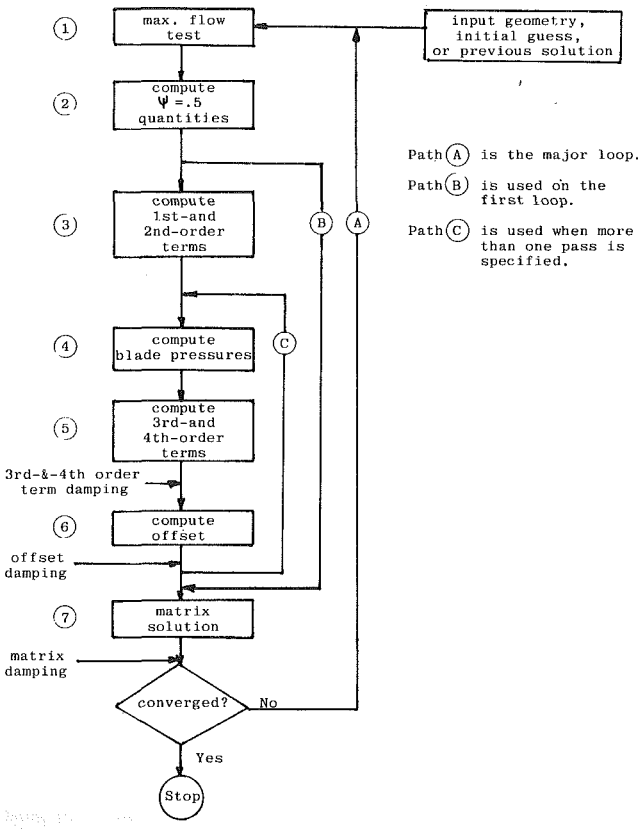

Fig. 2 TAYLOR overall block diagram

are obtained by matching these quantities at the boundaries with those obtained by expanding p and $\tan\beta$.

Both ρ and Vm are now known from pressure surface to suction surface. The offset can be updated by applying the relation:

$$\int_{-\Delta\theta-\eta}^{0} \rho V_m d\theta = 0.5 \int_{-\Delta\theta-\eta}^{\Delta\theta-\eta} \rho V_m d\theta \tag{16}$$

where $\Delta\theta$ is one-half the passage pitch distance. Equation (16) is solved iteratively for η. Thus, the η-value which divides the flow equally is established.

It remains, finally, to update the values of $b\rho rV_m$ and $rV\theta$ on the $\psi=0.5$ streamline. For simplicity in writing, we call $(b\rho rVm)_{\psi=0.5}=M$ and $(rV\theta)_{\psi=0.5}=T$. The total flow, F, and the average station angular momentum, $\overline{rV_\theta}$, are input values at each station. Two additional relations must be satisfied:

$$F=\int_{\theta_p}^{\theta_s} b\rho rV_m d\theta \tag{17}$$

$$\overline{rV_\theta}=\int_{\theta_p}^{\theta_s} (b\rho rV_m)(rV_\theta)d\theta \Big/ \int_{\theta_p}^{\theta_s} b\rho rV_m d\theta \tag{18}$$

Equations (17) and (18) can be rewritten by expanding in a TAYLOR series and integrating each term individually (as is also done in the solution of the offset equation, equation (16)). Thus,

$$F=M+\frac{1}{2}\frac{\partial M}{\partial\theta}(\theta s^2-\theta p^2)+\frac{1}{6}\frac{\partial^2 M}{\partial\theta^2}(\theta s^3-\theta p^3)+Rc \tag{19}$$

$$(\overline{rV_\theta})F=MT+\frac{1}{2}\frac{\partial MT}{\partial\theta}(\theta s^2-\theta p^2)+\frac{1}{6}\frac{\partial^2 MT}{\partial\theta^2}(\theta s^3-\theta p^3)+Rm \tag{20}$$

where Rc and Rm are residuals corresponding to third- and fourth-order integrations, which are held at values of the previous loop.

Since equations (19) and (20) will not in general be satisfied, the $\psi=0.5$ values of M and T must be corrected. A simple correction based on current θ-derivatives at any one station proves unstable. Conditions at stations upstream and downstream of the current station must be also be recognized.

In a fashion identical to that described above to obtain first- and second-order θ-derivatives of pressure, velocity, etc., one can get first- and second-order derivatives of M and T. Thus, for example, for the $\partial M/\partial\theta$-term of equation (19)

$$\frac{\partial M}{\partial\theta}=f\left(\frac{dM}{dm},\frac{dT}{dm}\right) \tag{21}$$

This comes directly from combining the momentum and continuity equations (equations (6) and (9)). If the m-derivatives are discretized, equation (21) becomes

$$\frac{\partial M}{\partial\theta}=a(M)_{i-1}+b(M)_i+c(M)_{i+1}+d(T)_{i-1}+e(T)_i+f(T)_{i+1} \tag{22}$$

A similar operation is performed on $\partial^2 M/\partial\theta^2$, $\partial MT/\partial\theta$ and $\partial^2 MT/\partial\theta^2$. Equations (19) and (20) can then be written as:

$$F_i=a_i^1(M)_{i-1}+b_i^1(M)_i+c_i^1(M)_{i+1}+d_i^1(T)_{i-1}+e_i^1(T)_i+f_i^1(T)_{i+1}+R_i^1 \tag{23}$$

$$(\overline{rV_\theta})F_i=a_i^2(M)_{i-1}+b_i^2(M)_i+c_i^2(M)_{i+1}+d_i^2(T)_{i-1}+e_i^2(T)_i+f_i^2(T)_{i+1}+R_i^2 \tag{24}$$

The coefficient terms, $a-f$, and R^1 and R^2 are treated as constants at any one station.

By applying equations (23) and (24) at each station, two matrix equations can be assembled

$$\underline{B}_1\bar{M}+\underline{C}_1\bar{T}=\bar{D}_1$$
$$\underline{B}_2\bar{M}+\underline{C}_2\bar{T}=\bar{D}_2$$

Matrices $\underline{B}_2$ and $\underline{C}_1$ can be singular and should not, therefore, be inverted. The following solution procedure is used:

(*i*) Invert $\underline{C}_2$
(*ii*) Express $\bar{T}=\underline{C}_2^{-1}(\bar{D}_2-\underline{B}_2\bar{M})$
(*iii*) Solve $(\underline{B}_1-\underline{C}_1\underline{C}_2^{-1}\underline{B}_2)\bar{M}=\bar{D}_1-\underline{C}_1\underline{C}_2^{-1}\bar{D}_2$
(*iv*) Use $\bar{M}$ in (*ii*) and solve for $\bar{T}$

Figure 2 is the overall block diagram of the computing process. At the start of any iterative loop, the updated "input" quantities are tested to determine whether the prescribed flow exceeds the maximum possible (Block (1)). This step has not been described above, since it is not integral to the overall solution. If the flow at some station exceeds the maximum, an error message is printed out and the process continues, using the maximum flow. For solutions containing a throat, it is not uncommon to get such messages in the earlier part of the solution process.

In Block (2) the $\psi=0.5$ quantities are updated, using the values of rV_θ derived from the previous loop matrix solution. For the first loop, $\overline{rV_\theta}$ is assumed to pertain on the $\psi=0.5$ streamline, which is itself assumed to be at the geometrical middle of the passage (i.e., $\eta=0$).

For each loop, (Path A), a prescribed number of passes, (Path C), is made. This is an interior iteration which updates the blade surface dp/dm-terms of equation (15). For the first loop, Path B is used to get directly to the matrix solution for an initial update on the rV_θ quantities.

Five damping coefficients are imposed and are operative at the points shown in Fig. 2. It has been established (by trial) that fixed, particular, values of damping on the third- and

fourth-order terms, and on the offset, appear optimal for all types of cascades. For supersonic cases, however, it appears expedient to damp heavily on the matrix solution for about five loops, and then release it. Provisions for doing this readily are built into the process.

It is not difficult to understand why heavy matrix damping is necessary for the early passes of transonic situations. Figure 1 is schematic, but it does indicate the locus of the $\psi = 0.5$ streamline (with respect to the geometric middle of the passage) for a turbine nozzle with supersonic discharge.

In the upstream subsonic region the $\psi = 0.5$ streamline moves toward the suction surface. It moves toward the pressure surface in the downstream supersonic region, crossing the middle of the passage at the throat. The coefficients $a - f$ of equations (23) and (24) implicitly are functions of $1 - M^2$ and change sign as the throat is passed. In their present derivation, however, they were treated as weak functions of ρ and ρ-derivatives, which are the terms which will introduce $1 - M^2$. The terms containing ρ, in the present process, are updated only on the succeeding loop. Thus, for a transonic situation, the process has not received a message on the initial loops indicating whether it is subsonic or supersonic.

It was anticipated that a more complete derivation of the coefficients of equations (23) and (24), or even a resort to upwind differencing in the discretization process, might be necessary; a simple use of heavy matrix damping in the early loop appears, however, to be sufficient.

Examples and Comparisons

The remaining portion of the paper will deal with examples of the use of the technique. The earlier cases to be presented use the process in one fashion; the later cases in another.

The TAYLOR series process will generate a unique blade and passage shape if it is given simply the Δp-difference (or a number proportional to it) and the blade thickness at each m-station (along with upstream and downstream boundary conditions, streamtube thickness and radius). If, therefore, one has available an analytic solution, or an experimental solution for a cascade for which $\Delta p = \Delta p(m)$ and $t = t(m)$ is known, the input of these values should, to the extent that the process is numerically valid, result in the proper blade shape and the proper individual suction surface and pressure surface pressure distributions.

Three cases of this type are presented: two are comparisons with analytic solutions and one is with an experimental solution. The results obtained are consistently good, but not perfect. It is unclear whether the discrepancies that exist are attributable to errors which creep into the process of graphically transforming data of solutions presented as functions of chord distance or surface length to that required by the TAYLOR series, i.e, as a function of m-distance, or whether the discrepancies are attributable to inherent deficiencies of the TAYLOR series process. Questions regarding the basic data validity multiply the indeterminancy in the case involving comparison with experimental data.

The second way to check the process is to use the TAYLOR series technique to generate a blade shape, and then to ask other direct, or analysis, computing techniques (such as streamline curvature, time-marching, etc.) whether they agree with the flow field and surface velocity distribution predicted by the TAYLOR series approach. The remaining cases have been treated in this fashion, along with a number of interest for which no check has been yet made.

Gostelow [5] used the potential flow technique of Merchant and Collar to produce a profile (very similar to the British C-4 profile), and a surface pressure distribution, which has become a standard test case. Figure 3 shows a comparison

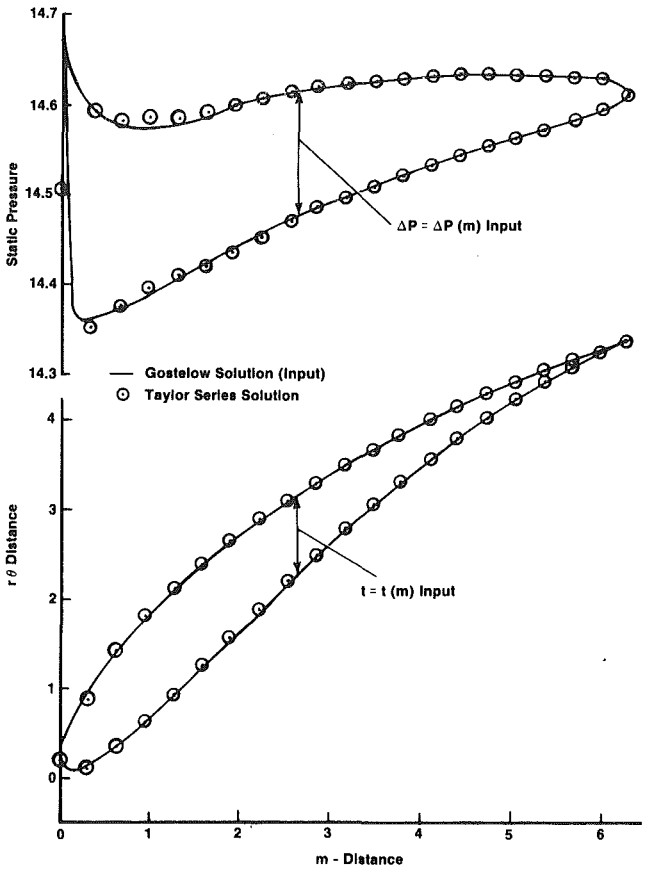

Fig. 3 TAYLOR series approximation to Gostelow profile [5]

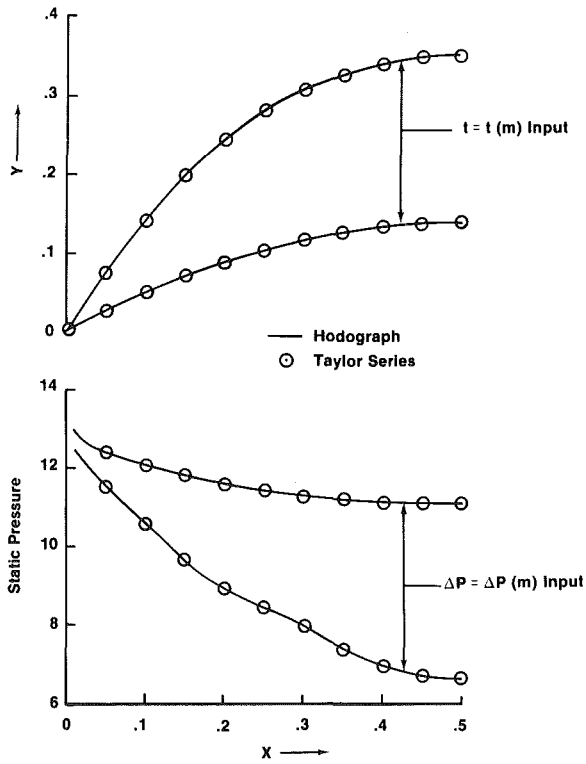

Fig. 4 TAYLOR series approximation to Hobson hodograph impulse cascade No. 2 (6): shape and surface pressure distributions

between the Gostelow solution and that obtained with the TAYLOR series technique. It is as good, if not better, than

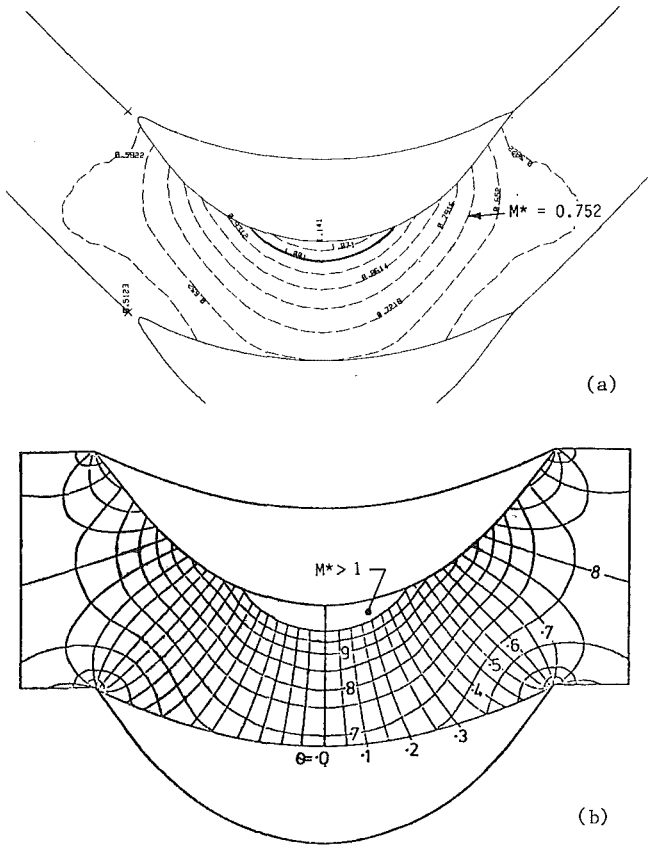

Fig. 5 TAYLOR series approximation to Hobson hodograph impulse cascade No. 2 (6): Mach number contours

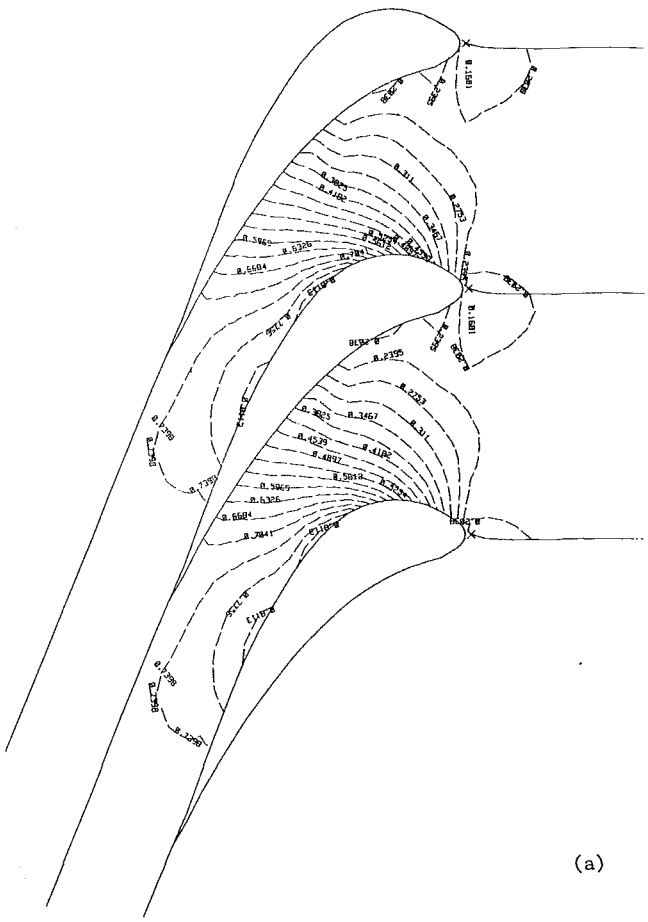

most other comparison techniques presented by Gostelow in [5].

Hobson [6] reported two hodograph solutions of completely symmetric impulse turbine profiles, one of low solidity ($\sigma = 0.988$) and one of higher solidity ($\sigma = 1.902$). The TAYLOR series process was not able to handle the low solidity case. It broke down at the leading and trailing edges of the profile; one can deduce (if the Hobson solution itself is valid) that the wide spacing and steep leading edge loading at a relatively high incident Mach number imply a velocity and an angle distribution across the passage which requires a still higher order power series. The higher solidity hodograph solution was readily reproduced by the TAYLOR series process. Figure 4 shows (the solid lines) the hodograph shape and pressure distribution compared with the shape and pressure distribution the TAYLOR series process generated from input Δp values and thickness values (i.e., the values from the hodograph solution).

Figure 5(*a*) shows Mach number contours generated by the TAYLOR series process for the second Hobson profile; Fig. 5(*b*) shows critical Mach number profiles reproduced from [6]. It is quite evident that the TAYLOR series process is recognizing what the Hobson hodograph solution is saying. Only at the very leading and trailing edges can some discrepancy be noted. It is also of interest that, while the Gostelow solution was incompressible, the Hobson profile has a suction surface peak Mach number of 1.145.

The two comparisons with analytic solutions appear to lend some credance to claims that the fourth-order TAYLOR series representation of cross-channel properties can be reasonably representative of analytic real life. The following comparison with experimental data is not so clean, but is nearly as good.

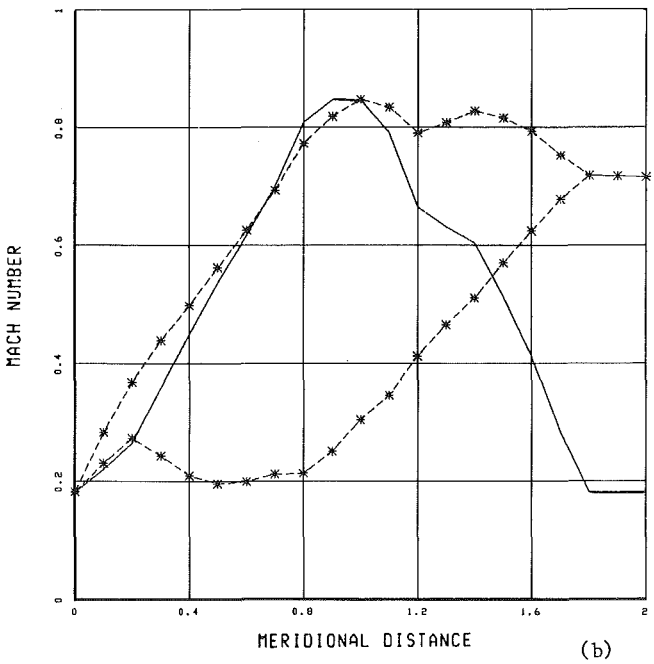

Fig. 6 Mid-span section of NASA TN D-3751 nozzle (7) – TAYLOR solution

Figures 6(*a*) and 6(*b*) show an example of the normal graphics output of the present program. The case shown is the mid-span turbine nozzle section reported in [7] for an inlet Mach number of 0.212; it is subsonic throughout. Figure 6(*a*) shows the profile generated by the TAYLOR series process, in

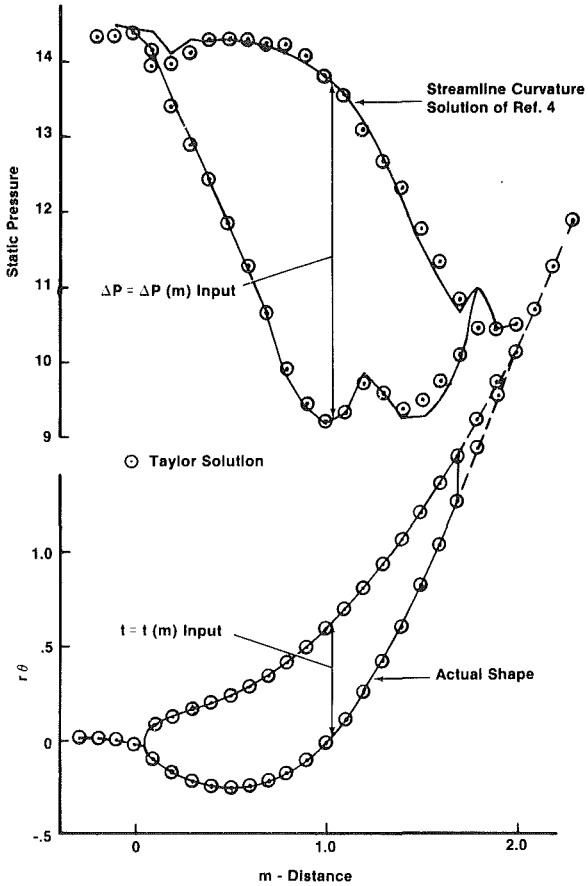

Fig. 7 Comparison of experimental shape and surface pressure distribution of [7] nozzle with that deduced by TAYLOR

this case with Mach number contours; Fig. 6(*b*) shows surface Mach number versus meridional distance. The solid line (without a scale) represents the input pressure surface/suction surface pressure difference.

The same case had been used once before (by one of the present authors) as a check against the streamline curvature blade-to-blade procedure reported in [4]. In the present instance, the $\Delta p = \Delta p(m)$ values of the previous streamline curvature solution (along with blade thickness, $t = t(m)$) were input into the TAYLOR process simply because it was easier to do so, and the streamline curvature approach gave an excellent comparison with the experimental data [4]. The TAYLOR process is quite close in surface pressure distribution, as shown in the upper portion of Fig. 7; the lower portion of Fig. 7 shows the TAYLOR deduction of the blade shape as compared with the actual blade shape.

It is evident that the results are respectable. It should be kept in mind, however, that a rather large element of chance must exist for this case. The experimental cascade was run as the mid-span section of a full-span annular cascade. Reference [7] contains no mention of streamtube thickness (it could not be measured), nor is the loss reported. The TAYLOR run of Figs. 6 and 7 was made with constant streamtube thickness and no loss, which cannot have been the actual situation. Even more to the point, the experimental surface critical Mach number reported in [7] was given to very small scale as a function of blade surface distance. The graphical conversion of the data into the form needed is a somewhat dubious operation. It is evident, however, that the TAYLOR series process does appear to recognize what it is being asked to address.

The remaining cases to be discussed are those generated by

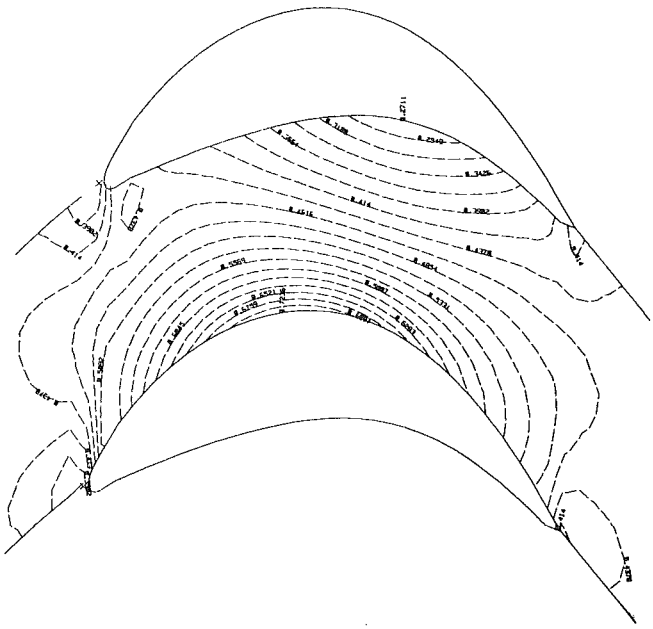

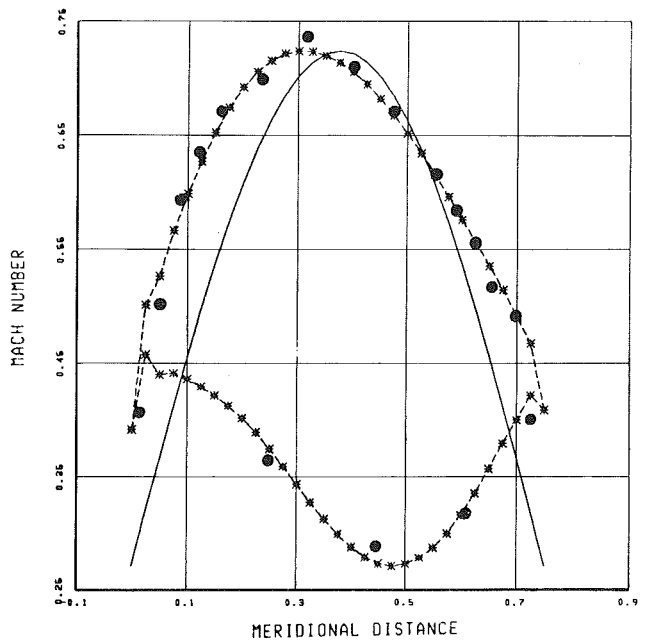

Fig. 8(*b*) Comparison of TAYLOR and XCASC surface Mach number distribution for rotor of Fig. 8(*a*)

the TAYLOR series process for arbitrarily chosen input of $drV\theta/dm$, thickness, and upstream and downstream boundary conditions. The cascade shapes resulting are then checked by other analysis techniques in order to arrive at some measure of the believability of the TAYLOR series process. It is well to stress that none of the cases to be discussed are, of themselves, necessarily practically interesting. This was not the intent. At least a few to be presented, in fact, are patently unrealistic.

Figure 8(*a*) shows the shape (with Mach number contours) of an impulse-like low-pressure turbine rotor blade generated by the TAYLOR series process. It is subsonic throughout. The thickness distribution is prescribed by a skewed sine wave distribution that requires four numbers as input; the drV_θ/dm input ($\Delta p = \Delta p(m)$) is a symmetrical half-sine wave requiring

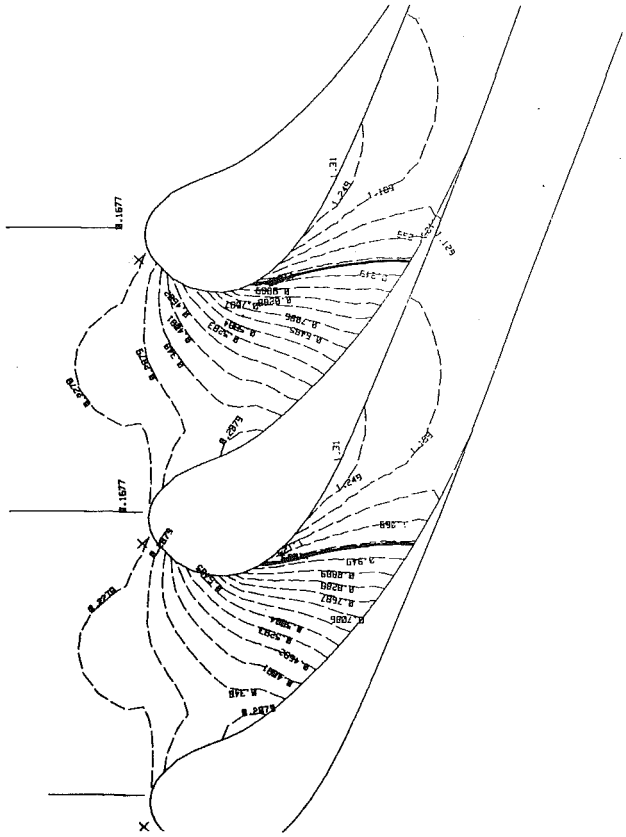

Fig. 9(*a*) Supersonic discharge turbine nozzle generated by TAYLOR

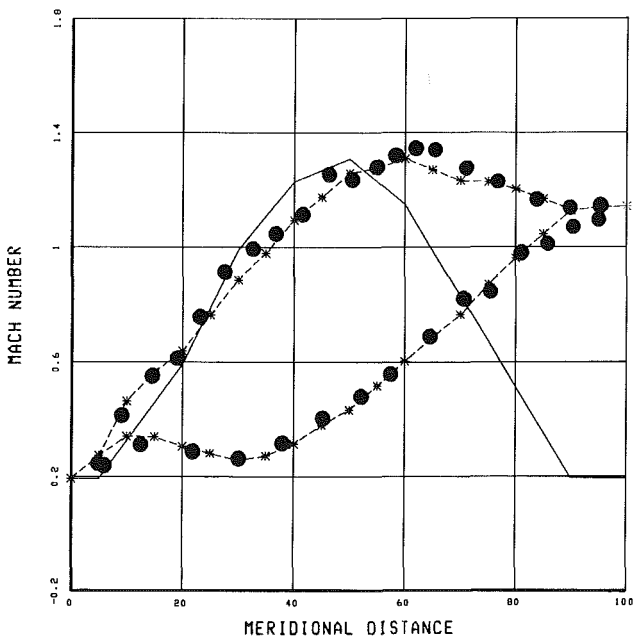

Fig. 9(*b*) Comparison of TAYLOR and XCASC surface Mach number distribution for nozzle of Fig. 9(*a*)

two input numbers. The streamtube thickness is constant and no losses are assumed in this case. Figure 8(*b*) shows the surface Mach number distribution predicted by the TAYLOR series process.

The surface coordinates generated were input in a blade-to-blade program called XCASC, which is a streamline curvature procedure.

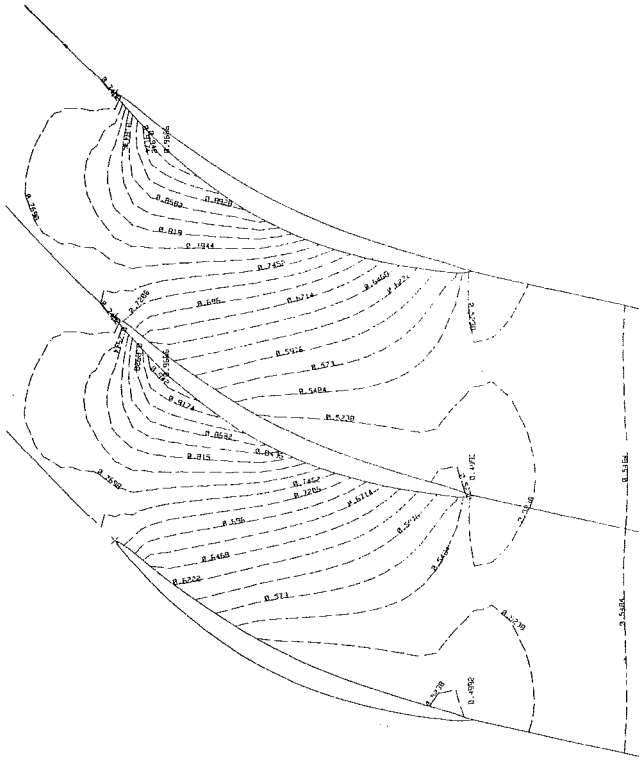

Fig. 10(*a*) Compressor rotor section generated by TAYLOR

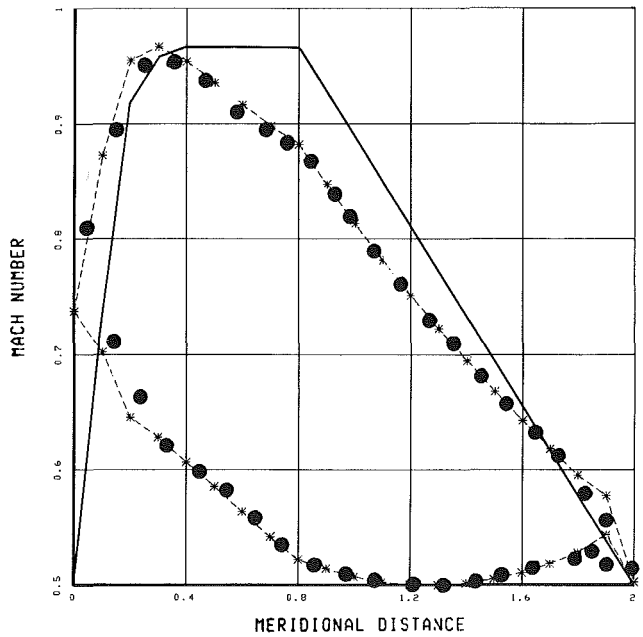

Fig. 10(*b*) Comparison of TAYLOR and CASC80 surface Mach number distribution for rotor section of Fig. 10(*a*)

Superimposed on Fig. 8(*b*), the solid circles show that XCASC thinks the surface Mach number distribution to be, compared with that of the TAYLOR series process. It is, again, not a perfect check, but it is not bad.

Figure 9(*a*) shows a turbine nozzle generated by the TAYLOR process. It was specified to have $M_1 = 0.212$ and $M_2 = 1.15$, with a $dr\overline{V_\theta}/dm$ distribution shown by the solid (unscaled) curve on Fig. 9(*b*). The dotted curve on Fig. 9(*b*) is the surface Mach number distribution as computed by the TAYLOR process. The throat is indicated by the heavy

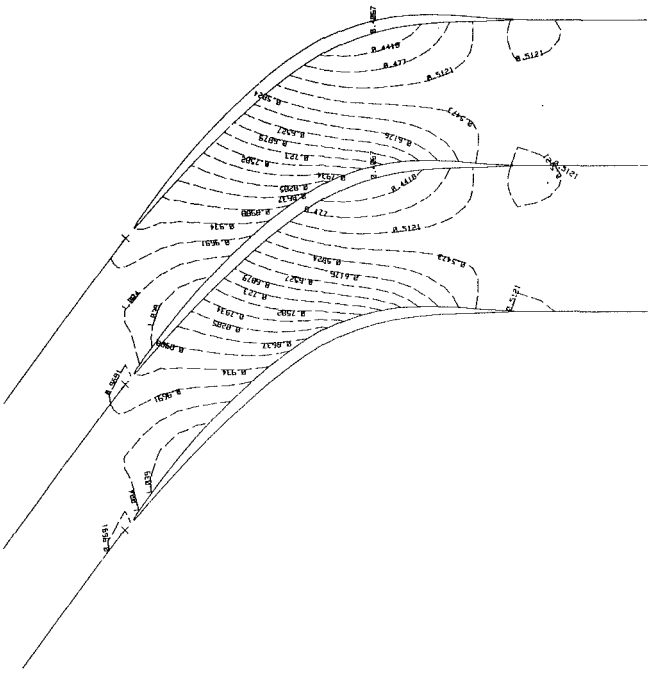

Fig. 11(*a*) Compressor stator hub section generated by TAYLOR

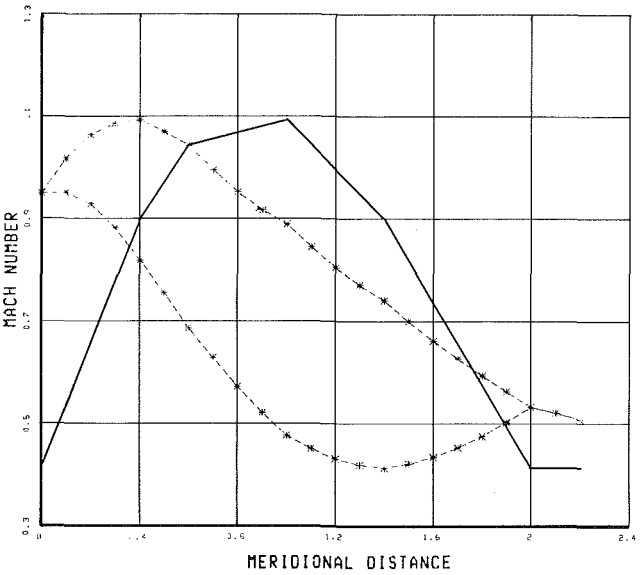

Fig. 11(*b*) TAYLOR-predicted surface Mach number for stator hub of Fig. 11(*a*)

contour on Fig. 9(*a*). The solid circles superimposed on Fig. 9(*b*) result from an XCASC run with the cascade generated by TAYLOR. Again, the check is encouraging.

Figure 10(*a*) shows a TAYLOR-generated compressor rotor section. If it were run with no preswirl, its isentropic pressure ratio would be 1.34/1. In this instance, the input $dr\overline{V_\theta}/dm$ was set so that the blade was loaded toward the leading edge. The objective was to accomplish this without exceeding unity Mach number on the suction surface.

The check program in this instance is called CASC80, which is an updated time-share version of a streamline curvature solution. Figure 10(*b*), once again, shows (solid circles) the CASC80 surface Mach number solution for the profile generated by TAYLOR. Again, the comparison with the TAYLOR solution is quite acceptable.

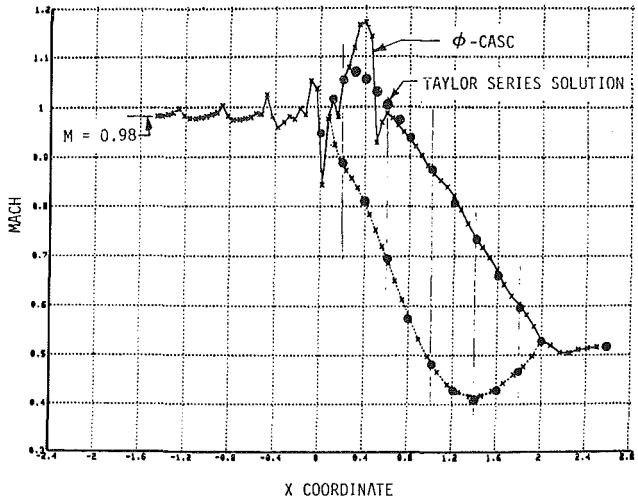

Fig. 12 TAYLOR and φCASC Mach number comparison for stator hub of Fig. 11(*a*)

The next case is a rather interesting one. Figures 11(*a*) and 11(*b*) are, again, reproductions of the standard TAYLOR graphics, i.e., the shape with Mach number contours and (for Fig. 11(*b*)) the surface Mach number distribution. This example is generally representative of the hub section of a stator operating behind a low radius ratio high-pressure ratio fan stage.

The inlet relative Mach number is 0.98 and the cascade does 55 deg of turning. The TAYLOR-predicted peak suction surface Mach number is 1.07. TAYLOR (since it cannot do otherwise) says it is shock-free.

Figure 12 is an analysis of the Taylor-generated blade shape by another program called φCASC, which uses a velocity potential correction technique. φCASC clearly shows a shock to exist on the suction surface in the same region in which TAYLOR predicts a shock-free supersonic bubble. Downstream of this point, the suction surface predictions of the two programs are in excellent agreement, as they are on the pressure surface.

It is speculated – and this is strictly speculation at this point, since no proof exists – that the discrepancy in the region of the supersonic bubble is attributable to geometry variations. A recent paper [8] puts stress on the fact that very slight changes in profile shape often are the difference between shock-free and nonshock-free solutions. φCASC does an internal smoothing of the data it is given and, thus, changes the geometry (i.e., surface curvatures) slightly. The other possible reason for the discrepancy stems from the totally different approach of the two programs; small differences would be accentuated in regions where A^*/A is close to 1.0. The extreme sensitivity of "shock-free" solutions to very small geometry variations, noted in other instances also, does cause the practical designer to wonder about the extent to which he may trust them.

The final case for which comparative analysis results will be presented is shown (i.e., blade shape and Mach number contours) on Fig. 13(*a*). It is a TAYLOR-generated compressor rotor tip section. The TAYLOR program input was set up so that $\beta_1 = \beta_2 = 65$ deg. The inlet Mach number is 1.5. Because of anticipated limitations of analysis programs available for comparison, the case has no loss and a constant streamtube thickness. As a consequence of this choice, the downstream Mach number ($M_2 = 0.65$) had to be accepted. As can be seen on Fig. 13(*b*), the resulting deceleration across the cascade is quite unrealistic. It does, however, make for a rather clean and simple test case for analysis techniques

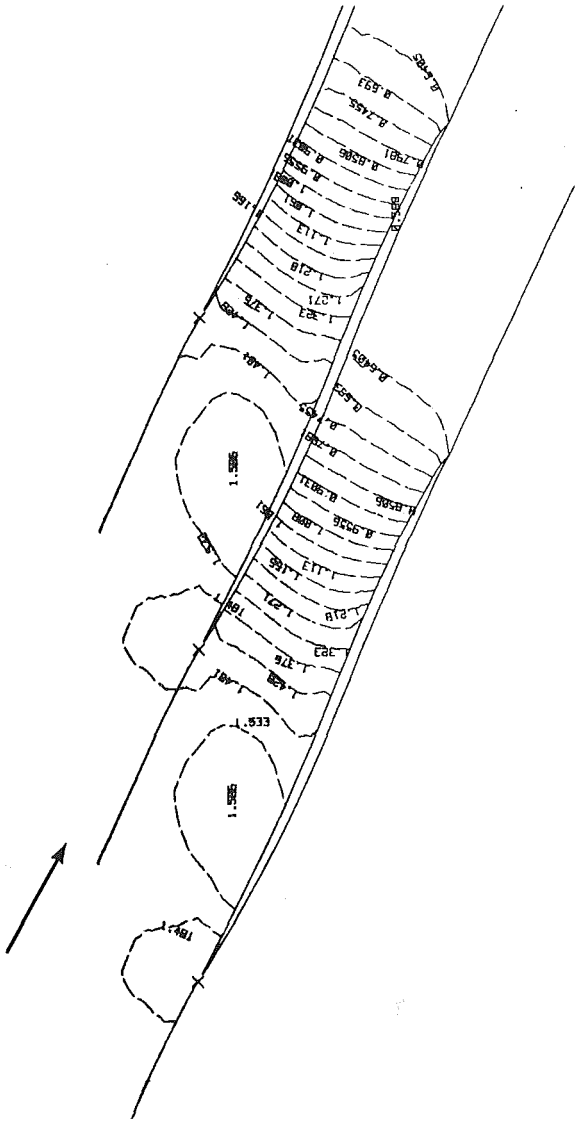

Fig. 13(*a*) TAYLOR-generated $M_1 = 1.5$ compressor tip section

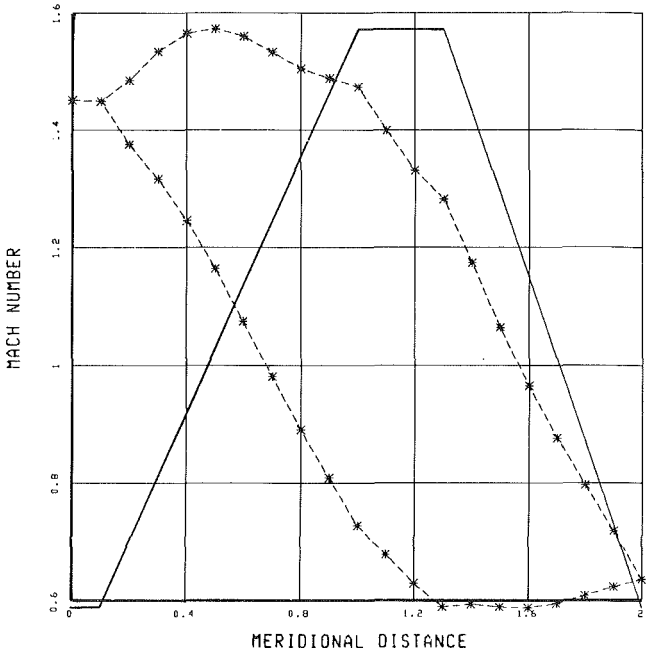

Fig. 13(*b*) Taylor-predicted surface Mach number distribution for compressor tip of Fig. 13(*a*)

which, also, do not object to unrealistic deceleration rates. As is evident from Fig. 13(*b*), the TAYLOR series solution does purport to be shock-free. This means, among other things, that TAYLOR treated the leading edge as cusped. Figure 13(*a*) clearly shows, as stated earlier, that the TAYLOR series process is a passage solution; in this case there is an easily discernable convergent-divergent channel.

Figure 14 shows the result of a check analysis solution using a time-marching program [9] for 600 time-steps (more were not asked for because the result was anticipated). This is clearly a case of an unstarted cascade.

The time-marching program used was an early version of the Denton code. Both Denton and others have since markedly improved the process in terms of avoidance of nonconservation satisfaction adjacent to profile surfaces. A time-marching technique, however, is not unrealistic when used to assess the starting capability of a supersonic compressor cascade. The cascade of Fig. 13(*a*) did not pass the test; there is a high probability that no cascade with supersonic inlet designed by a shock-free approach such as that described here can be realistic. A similar result (not shown) was obtained with a compressor cascade designed by TAYLOR for an inlet Mach number of 1.2.

Fig. 14 Mach number contour plot of time-marching solution for compressor tip of Fig. 13(*a*)

The geometry of the cascade of Fig. 13(*a*) was checked with a method of characteristics program referred to in [10]. Once again, the TAYLOR-generated profile failed the test, badly

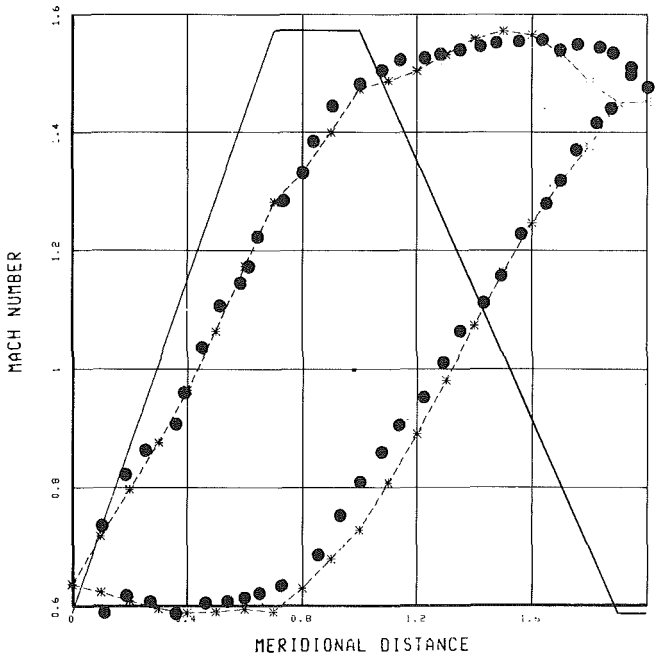

Fig. 15 Time-marching versus TAYLOR prediction of surface Mach number for compressor tip of Fig. 13(*a*) (run as expanding cascade)

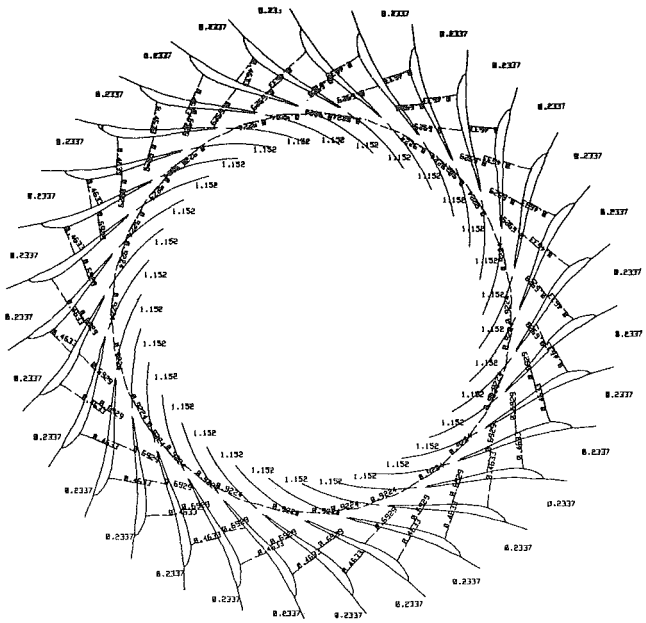

Fig. 16(*a*) TAYLOR-generated centrifugal compressor diffuser; $M_1 = 0.98$

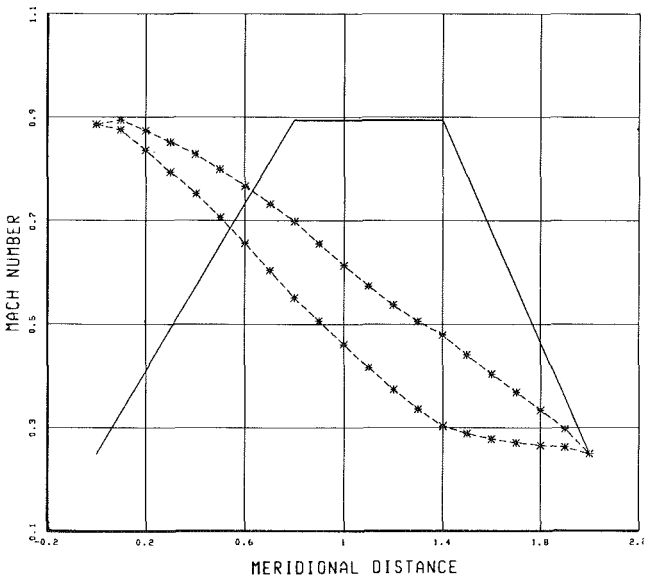

Fig. 16(*b*) Surface Mach number for diffuser of Fig. 16(*a*)

enough that there appears no point in reproducing the MOC graphics. The MOC solutions indicated a reasonably strong shock originating at the upper compression surface near the leading edge. The computed unique incidence angle was 1.5 deg lower than that implied by the TAYLOR solution.

The TAYLOR cascade of Fig. 13(*a*) was subjected to one final test. It, as stated above, was generated initially as a compressor cascade. The inviscid TAYLOR process is equally willing to run it backward as turbine cascade. The resultant TAYLOR solution was a cascade with incident Mach number of 0.65 and a leaving Mach number of 1.5. The shape generated was (to the third decimal place) the mirror image of that of Fig. 13(*a*).

Expanding cascades do not have starting problems. The geometry of the TAYLOR-generated expanding cascade was run on the Denton program; it encountered no difficulty and converged in 865 time-steps. The results, superimposed (the solid circles) on the TAYLOR-generated surface Mach number graphics, is shown on Fig. 15. The check is certainly not a perfect one, but it seems reasonably evident that both programs were recognizing the same geometry. The time-marching code shows no sign of shocks.

A careful inspection of the Denton Pass output shows that it does not conserve entropy adjacent to profile surfaces; there are regions where it loses as much entropy as it gains in other regions. It is believed that this is the primary reason for the differences in solutions observable on Fig. 15.

What has been presented are the facts currently available regarding the applicability of the TAYLOR process to supersonic compressor cascades. It is clearly evident that the shapes generated do not have adequate starting margin. The picture is not so clear with regard to the lack of correspondence with the method of characteristics solution. The MOC program, like all others, assumes that the upstream region contains only left running waves, and that all disturbances upstream of the first captured wave will have been cancelled at the far upstream boundary of the system, i.e., at "upstream infinity." For the TAYLOR solution, however, the upstream boundary at which uniform Mach number and angle pertain was prescribed to be one-half meridional chord length ahead of the cascade leading edge. In this regard, the solutions were certainly not equivalent.

The situation described here obviously warrants further discussion. Since the present objective is to present a TAYLOR series design technique only, further discussion of its applicability – or nonapplicability – to supersonic compressor cascades will be deferred.

All of the cases discussed so far have been for axial cascades. Figure 16(*a*) shows a vaned centrifugal compressor radial diffuser generated by TAYLOR with an inlet angle of 70 deg and an inlet relative Mach number of 0.98. The discharge Mach number was set to 0.25 and the discharge angle to 45 deg; these conditions were controlled in the TAYLOR process by properly setting the diffuser streamtube thickness convergence. Figure 16(*b*) shows the surface Mach number distribution which results when the $d\overline{rV\theta}/dm$ input was the simple four-point distribution shown by the solid line

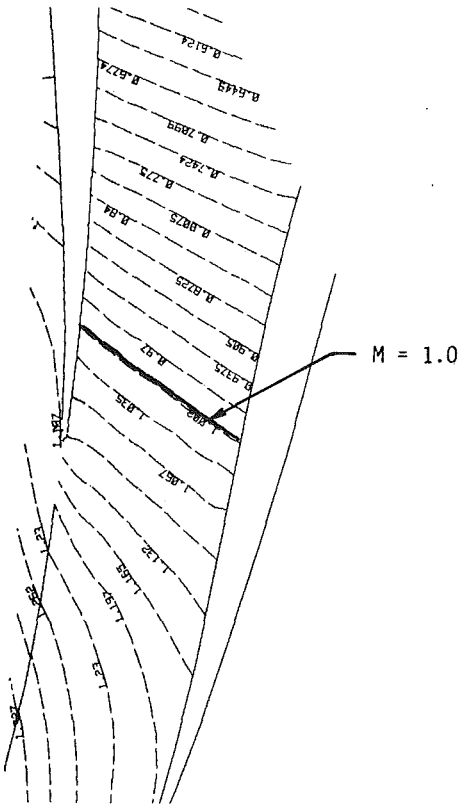

Fig. 17 TAYLOR-generated centrifugal compressor diffuser; $M_1 = 1.2$

in Fig. 16(*b*). There is no substantiating analysis for the case; it shows only that the process works for radial as well as axial configurations.

Figure 17 shows a leading edge blow-up of one passage of a diffuser with an inlet Mach number of 1.2. The sonic line has been darkened.

Conclusions

It is to be stressed once again that the objective of the present effort was to devise a conceptually simple (albeit, as it turned out, not an algebraically simple), easy to use, preliminary design technique which fit readily into the structure of an existing quasi-three-dimensional turbomachine design system. It is believed that that objective has been realized. For the predominant number of cascade types which occur in multistage axial compressors and turbines (i.e., subsonic with reasonable solidity), the process readily appears to produce results which may well be considerably better than first approximations.

The process of testing the limits of validity of the procedure naturally led to trying it on cascade types for which even the best analysis techniques sometimes have difficulties. A number of these cases have been presented as examples. In all of these, with the possible exception of the supersonic compressor cascade, the process appears to work creditably.

There are many, as yet, unresolved questions. Two, in particular, deserve attention, since they have not been stressed above.

First, the apparent inconsistency between the MOC treatment of the entrance region of supersonic compressor cascades, and that of TAYLOR, has been stressed. The same questions can be raised in regard to the downstream region of a turbine with supersonic discharge.

The other area where the TAYLOR process has difficulties is in the leading edge region of cascades for which the leading edge stagnation point falls downstream of the meridional plane highlight point – which is nearly always the case for low Mach number, high thickness, turbine rotor profiles. This is not a problem unique to TAYLOR, but it exists for TAYLOR.

In all, however, it appears to hold promise as a useful preliminary design tool.

Acknowledgments

The authors wish to acknowledge the time spent by R. D. Caney, Jr., J. S. Keith, and Dr. D. C. Prince, Jr. in helping to run the test cases presented in the latter part of the paper.

References

1 DeCuypere, R., "Solution of Two-Dimensional Mixed Flows Using a Power Series," *VKI Lecture Series 59*, Vol. 1, May 1973.

2 Giraud, F. L., "Supersonic Vortex-Source Flow Through Blade Lattices," Ph.D. thesis, Massachusetts Institute of Technology, 1950.

3 Wu, C. H., and Brown, C. A., "Theory of the Direct and Inverse Problems of Compressible Flow Past Cascades of Arbitrary Airfoils," *Journal of Aero. Sci.*, Mar. 1952.

4 Novak, R. A., and Hearsey, R. M., "A Nearly Three-Dimensional Intrablade Computing System for Turbomachinery," ASME *Journal of Fluids Engineering*, Mar. 1977.

5 Gostelow, J. P., "Potential Flow Through Cascades: A Comparison Between Exact and Approximate Solutions," ARC CP807, Nov. 1963.

6 Hobson, D. E., "Shock-free Transonic Flow in Turbomachinery Cascades," Cambridge University, Turbo/TR65, 1974.

7 Whitney, W. J., et al., "Cold-Air Investigation of a Turbine for High-Temperature Engine Application: I, Turbine Design and Overall Stator Performance," NASA TN D-3751, Jan. 1967.

8 Dulikravich, D. S., "Shockless Design and Analysis of Transonic Blade Shapes," AIAA-81-1237, 1981.

9 Denton, J. D., "A Time-Marching Method for Two-and-Three-Dimensional Blade-to-Blade Flows," ARC R and M 3775, 1975.

10 Prince, D. C., Jr., "Three-Dimensional Shock-Structure for Transonic/Supersonic Compressor Rotors," *Journal of Aircraft*, Jan. 1980.

Effect of Crossflows on the Discharge Coefficient of Film Cooling Holes

N. Hay

D. Lampard

S. Benmansour

Department of Mechanical Engineering,
University of Nottingham,
United Kingdom

The strongest flow parameter governing the film cooling effectiveness provided by a row of holes is the blowing rate. Precise setting of the blowing rate at the design stage requires accurate data for the discharge coefficient of the holes. The effects of crossflow on the discharge coefficient have received scant attention in published work to date. In the present work, the discharge coefficient of single rows of holes has been measured in a specially constructed isothermal rig over a wide range of geometric and flow conditions. Mainstream and coolant Mach numbers have been varied independently over the range 0 to 0.4 for pressure ratios in the range 0 to 2. Cooling hole length to diameter ratios were varied between 2 and 6, and inclinations of 30, 60, and 90 deg were used. The results show that the influence of crossflow is strong and complex, particularly with regard to that on the coolant side. A large range of data is presented sufficient to permit the discharge coefficient to be inferred for many cases of practical importance. Suggestions are also made for a promising theoretical approach to this problem.

Introduction

Film cooling is the standard method of cooling the stator and rotor blades in aeroengine gas turbines and the method has recently been applied also to land-based gas turbine plants [1]. The advantages of blade cooling are well known. It allows an increase in the turbine entry temperature reflecting in higher power output and efficiency. The penalty is a loss of output as the coolant, which could be 5 percent or more of the total flow, is not heated in the combustion chamber and does less work in the turbine by dint of the lower temperature and of bypassing one or more rotors. It is thus obvious that the coolant flow should be kept to the minimum that will achieve the required cooling performance.

Many parameters govern film cooling performance, but the most pertinent is the "blowing parameter," $\rho_c u_c / \rho_\infty u_\infty$, a nondimensionalised parameter reflecting the mass flow emerging from the cooling hole. This parameter determines the "effectiveness," $T_\infty - T_{aw} / T_\infty - T_c$, downstream of the hole which reflects in the metal surface temperature. For best performance, the blowing parameter should be in the region of about 1.0. But whatever is the desired value of the blowing parameter, exceeding this value means excessive usage of coolant and hence unnecessary loss of performance for the plant, and falling short of it could mean local hot spots and hence a shorter blade life. Knowledge of the discharge coefficient, *Cd*, of film cooling holes is vital in sizing film cooling holes at the design stage so that the requisite amount of coolant flow for the desired effectiveness is obtained in any given situation. The discharge coefficient is by no means invariant and depends both on the local geometry and the flow conditions upstream and downstream of the hole. Data on *Cd* for film cooling holes is sparse in the literature. The only work of substance is that of Rohde et al. [2], which examines, among other parameters, the effect of coolant crossflow. No data are available on the combined effects of mainstream and coolant crossflows. The work reported here was undertaken to provide a more extensive data base.

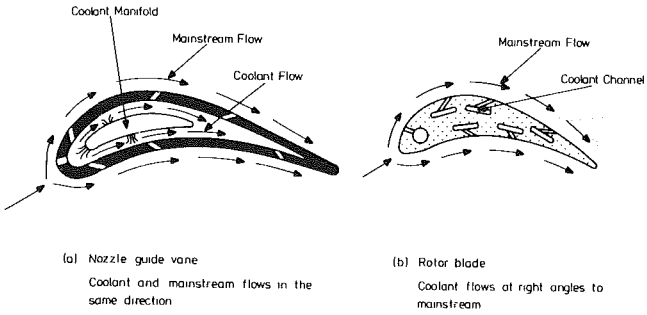

Fig. 1 Flow configurations in cooled turbine blades

Parameters That Affect *Cd*

Three flow geometries can be identified in relation to film cooling holes. In the nozzle guide vane, the coolant is usually impinged on the back of the blade skin and flows from the nose region back towards the trailing edge (Fig. 1(*a*)). Thus, the flows on the mainstream and coolant sides of the film cooling holes are parallel and in the same direction. In the nose region, there is substantial curvature of the surface but very low crossflow on the coolant side. Data on this situation is available. Along the flank of the nozzle guide vane the curvature is slight, but there is substantial coolant crossflow. This geometry can be represented by holes in a flat plate with coolant and mainstream flows on either side. This is the first geometry that was covered in this investigation and will be referred to as the "parallel configuration."

In the rotor blade (Fig. 1(*b*)) the cooling channels run

Contributed by the Gas Turbine Division of THE AMERICAN SOCIETY OF MECHANICAL ENGINEERS and presented at the 27th International Gas Turbine Conference and Exhibit, London, England, April 18-22, 1982. Manuscript received at ASME Headquarters December 11, 1981. Paper No. 82-GT-147.

radially outward and feed film cooling holes all along their length. In this situation the mainstream and coolant on either side of a hole flow at right angle to each other. This is the second geometry that was simulated again for the flank region of the blade. This geometry will be referred to as the "perpendicular configuration."

Within each flow geometry, the hole geometry introduces further parameters. These include the hole inclination, α, the hold L/D ratio, cross-sectional shape and rounding at entry and exit. Blade production techniques usually result in round holes with sharp edges. Hence attention was focused on the effects of inclination and L/D only.

Flow conditions form the last set of parameters which could affect Cd. These include the pressure ratio across the hole, the Reynolds number within the hole, the crossflow Mach number on the mainstream side, M_∞, and the crossflow Mach number on the coolant side M_c. Typical ranges for the geometrical flow parameters arising in various gas turbine designs appear in Table 1.

Experimental Apparatus

The layout of the test rig used is shown in Fig. 2 and details of the working section in Fig. 3. Referring to Fig. 2, the working fluid was room temperature air. The supply was split into two streams: the mainstream and the coolant stream. The flow and pressure could be controlled separately in each stream. Four holes were located in the sample plate separating the two streams (Fig. 3). The hole size of 3.5 mm was chosen such that the hole Reynolds number was within the range encountered in practice.

Instrumentation was provided to measure the static and stagnation pressure and the stagnation temperature in each stream. The flow rate through the cooling holes was obtained from calibrated orifice meters. Special precautions were taken to ensure high accuracy: (*a*) in the absence of crossflow in one or other stream the coolant flow was measured directly with an orifice meter in line with that stream; (*b*) when both streams had crossflows the coolant flow was obtained by difference between the flows upstream and downstream of the coolant channel. To ensure accuracy in this situation, conditions were set such that the coolant flow was at least 10 percent of the total crossflow. Additionally, a subsidiary calibration experiment was run in which a range of readings of the upstream and downstream orifices were taken without mainstream crossflow thus allowing a direct measurement of the coolant flow to be made using an orifice meter in the downstream leg of the mainstream line. A chart was thus produced relating the coolant flow and the upstream and downstream orifice meter readings. This chart gave the coolant flow rate in the actual tests with mainstream crossflow more accurately in some cases than the difference method.

For the case when the main and coolant streams are at right angles (i.e. rotor blade simulation), the sample plate was made in the form of a cross as shown in Fig. 4. The rig and instrumentation were otherwise identical.

Test Program

The test program comprised tests for the parallel and perpendicular configurations. Table 2 shows the range of parameters covered.

The effect of the number of holes was shown to be negligible in both the parallel and perpendicular configurations. Four holes were used in order to increase the coolant flow and thereby obtain high accuracy.

In the parallel tests, L/D was taken as a parameter, but it was soon apparent that for the range of L/D of interest (2–10) it had hardly any effect on Cd. This parameter was therefore dropped in the subsequent perpendicular tests which were done at one value of $L/D = 6$.

The effect of the angle of inclination α was found to be sizeable for changes of α from 90 to 30 deg. In the first test series results for $\alpha = 60$ deg were also obtained and fell between the 30 and 90 deg results, as would be expected. The

Table 1 Typical film cooling hole parameters

Reynolds numbers	
main feed holes	$0.8\text{–}1.5 \times 10^5$
leading edge passage up to	$.65 \times 10^5$
trailing edge passage up to	$.5 \times 10^5$
trailing edge holes	$.6 \times 10^5$
Mach numbers	
mainstream at hole exit (M_∞)	0–1.1
coolant crossflow (M_c)	0–0.4
Pressure ratio across the hole	1–2
Hole inclination (α)	30–90 deg
Hole L/D	2–10
Minimum hole diameter	0.2 mm

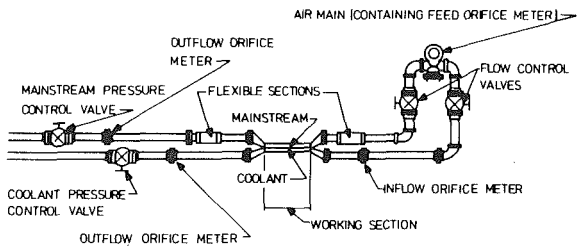

Fig. 2 Layout of the test rig

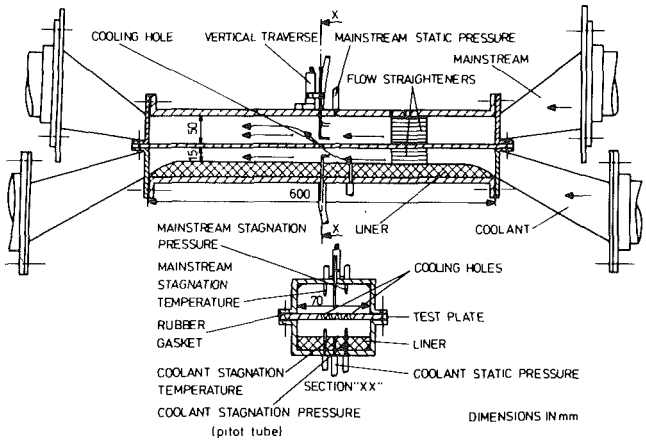

Fig. 3 Details of the working section for parallel flows

Nomenclature

Cd = discharge coefficient = $\dfrac{\text{actual flow}}{\text{ideal flow}}$

d = hole diameter
L = length of hole
M = Mach number
p = pressure
p^+ = stagnation pressure
Re = Reynolds number
S = hole spacing
T = temperature
u = velocity
α = angle of hole axis with mainstream flow direction
η = effectiveness
ρ = density

Subscripts

aw = adiabatic wall
c = coolant
d = discharge
j = jet at exit from the hole
∞ = mainstream

Table 2 Details of test parameters for parallel and perpendicular flow configurations

Flow configuration \ Parameters	Geometric parameters				Flow parameters			
	D mm	L/D	S/D	α deg	M_c	M_∞	$\mathrm{Re}\times 10^{-4}$	p_c^+/p_∞
Coolant flow parallel to mainstream flow	3.5	2	2.5	30 60 90	0 – 0.4	0 – 0.5	1 – 10	1 – 2
	3.5	6	2.5	30 90	0 – 0.4	0 – 0.5	1 – 10	1 – 2
Coolant flow perpendicular to mainstream flow	3.5	6	2.5	30 90	0 – 0.4	0 – 0.5	1 – 10	1 – 2

D = Hole diameter
L/D = length: diameter ratio
S/D = spacing: diameter ratio
α = inclination of holes
M_c = coolant Mach number
M_∞ = mainstream Mach number
Re = Reynolds number of holes
p_c^+/p_∞ = pressure ratio

Table 3 Estimates of accuracy of *Cd* values

Mach numbers		Range of pressure ratio		
		$1.01<p_c^+/p_\infty<1.2$	$1.2<p_c^+/p_\infty<1.5$	$1.5<p_c^+/p_\infty<2.0$
$M_\infty=0.3$	$M_c=0.0$	8–3.5%	3.5–1.5%	1.5%
	$M_c=0.1$	7–3.5%	3.5–1.5%	1.5%
	$M_c=0.3$	6.5–3.5%	3.5–1.5%	1.5%
$0<M_\infty<0.5$ $M_c=0$		≃6%	≃2.5%	≃1.5%
$0<M_c<0.4$ $M_\infty=0$		≃6%	≃2.5%	≃1.5%

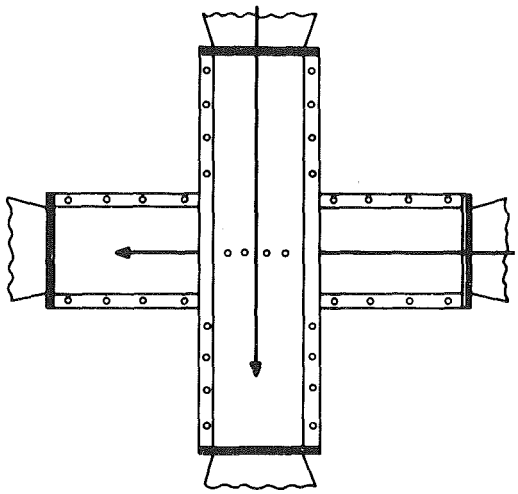

Fig. 4 Cross configuration of the working section for flows at right angles

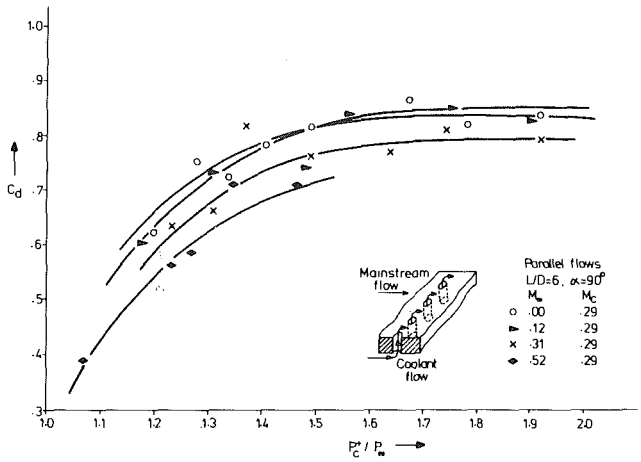

Fig. 5 Effect of the mainstream Mach number on *Cd* at $M_c = 0.3$

differences were not so large as to warrant full program coverage for $\alpha = 60$ deg. Hence subsequent tests were limited to 90 and 30 deg only.

The ranges of M_∞ and M_c were set by the capacity of the air supply (2 kg/s) to the values shown in Table 2.

The range of pressure ratios was taken whenever possible to just beyond the sonic condition within the hole.

It was pointed out earlier that particular attention was paid to accuracy. With the precautions and calibrations adopted, the uncertainty in *Cd* at representative pressure ratios and operating conditions is typically as indicated in Table 3. In the majority of cases the accuracy is better than 4 percent.

Results

In the definition of *Cd* as the ratio of the actual flow to the ideal flow, the calculation of the ideal flow was based on the coolant stagnation pressure and mainstream static pressure.

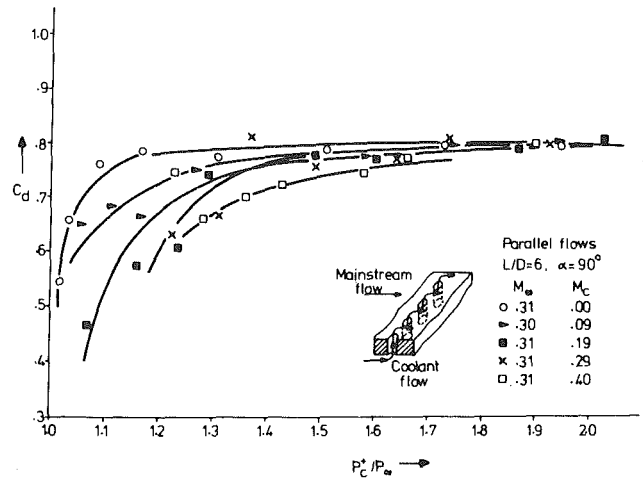

Fig. 6 Effect of the coolant Mach number on *Cd* at $M_\infty = 0.3$

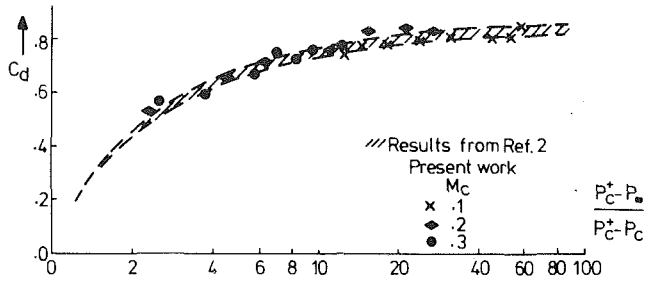

Fig. 7 Comparison with other workers' results

This takes into account the dynamic head of the flow approaching the hole which could be substantial at the higher coolant crossflow Mach numbers. The results are presented as a function of the ratio p_c^+/p_∞ as the main parameter, rather than the ratio of the dynamic head in the hole and in the crossflow stream, $(p_c^+ - p_j)/(p_c^+ - p_c)$ as used in reference [2]. As there could be crossflows on both sides of the hole in this investigation, it is difficult to use the latter approach.

A representative cross section of the results will now be presented and discussed. A more detailed account may be found in [3].

Parallel configuration, $\alpha = 90$ deg. Typical results for this geometry are shown in Figs. 5 and 6. It is seen that Cd increases with p_c^+/p_∞ up to $p_c^+/p_\infty \simeq 1.6$. Beyond this value Cd is substantially constant. This trend persists throughout the results, the plateau being reached at a lower p_c^+/p_∞ value the lower value of M_c. The effect of M_∞ was generally found to be a weak decrease in Cd, intensifying with increasing M_c. The effect of M_c itself on Cd is a more pronounced decrease as shown in Fig. 6.

This geometry, with zero mainstream crossflow has been covered by the tests of reference [2], and a direct comparison of the results is possible. This is shown in Fig. 7, where the results from this investigation have been superimposed onto the appropriate plot from [2]. The agreement is seen to be good both in the trend and value of Cd. Similar levels of agreement were obtained in comparisons with results from [4], with crossflow on the mainstream but not the coolant side. Thus the validity of all three sets of results is confirmed as well as that of the additional results given here for crossflow on both sides of the film cooling hole.

Parallel configuration, $\alpha = 30$ deg. The effect of M_∞ on Cd is weaker for $\alpha = 30$ deg than for $\alpha = 90$ deg. The effect of M_c is, however, opposite to the $\alpha = 90$ deg trend in that Cd now increases with M_c as shown in Fig. 8. This is explained by a form of contribution from the dynamic head of the coolant flow. It would be interesting to know at what angle this change in trend occurs, an avenue worth exploring in the future.

Carpet plots for high pressure ratio. It was pointed out earlier that Cd tends to be independent of p_c^+/p_∞ for p_c^+/p_∞ greater than 1.6. For these high-pressure ratios, the variation of Cd with M_∞ and M_c can be presented as a carpet plot as shown in Fig. 9 for $\alpha = 90$ deg and Fig. 10 for $\alpha = 30$ deg. The weak effect of M_∞ is easily seen. The stronger effect of M_c is equally well brought out in these plots decreasing Cd when $\alpha = 90$ deg and increasing it when $\alpha = 30$ deg.

Perpendicular configuration. Fig. 11 shows typical results for $\alpha = 90$ deg. The trends are similar to the parallel flow configuration tests but the curves level off to a slightly lower value of Cd. The effect of M_c is also similar.

For $\alpha = 30$ deg (Fig. 12), the effect of M_c is to decrease and not increase Cd as in the parallel tests. The angle of inclination in the perpendicular configuration is no longer in the direction of the coolant crossflow but at 90 deg to it. A trend

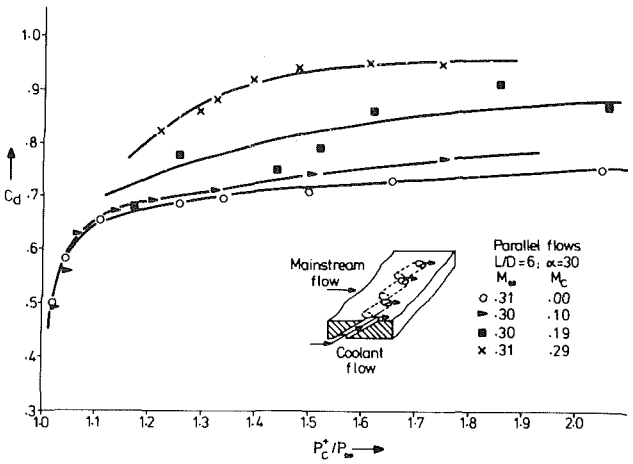

Fig. 8 Effect of the coolant Mach number Cd at $M_\infty = .3$

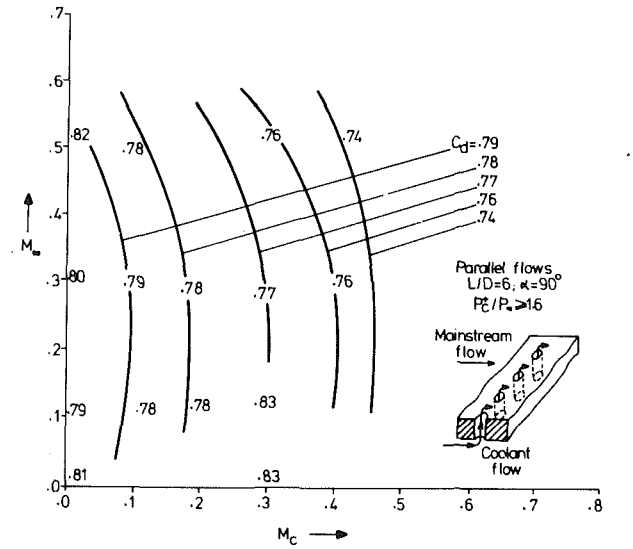

Fig. 9 Contours of constant discharge coefficient for $p_c^+/p_\infty \geq 1.6$

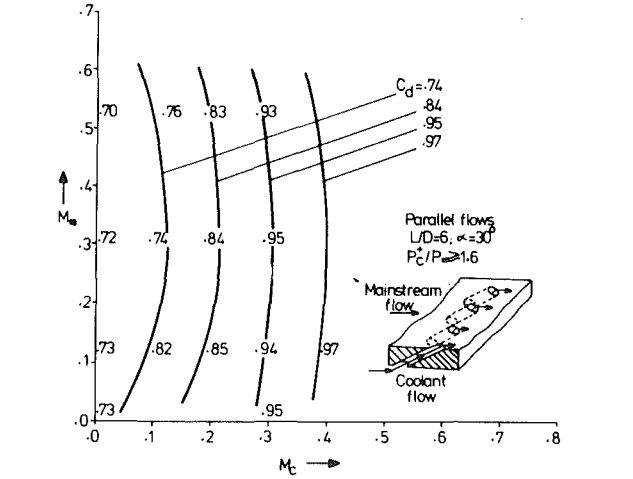

Fig. 10 Contours of constant discharge coefficient for $p_c^+/p_\infty \geq 1.6$

similar to the 90 deg hole is therefore to be expected (compare with Fig. 6).

For high values of p_c^+/p_∞ when Cd becomes substantially constant, carpet plots can be generated as before for this flow configuration. These are shown in Fig. 13 for $\alpha = 90$ deg and in Fig. 14 for $\alpha = 30$ deg. The variation with M_c leads to a decrease in Cd for both angles.

Summary and trend of results. Table 4 gives a summary

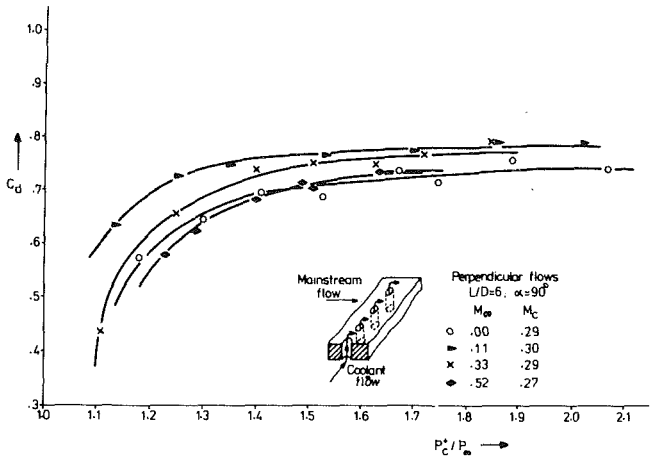

Fig. 11 Effect of the mainstream Mach number on Cd at $M_\infty = .3$

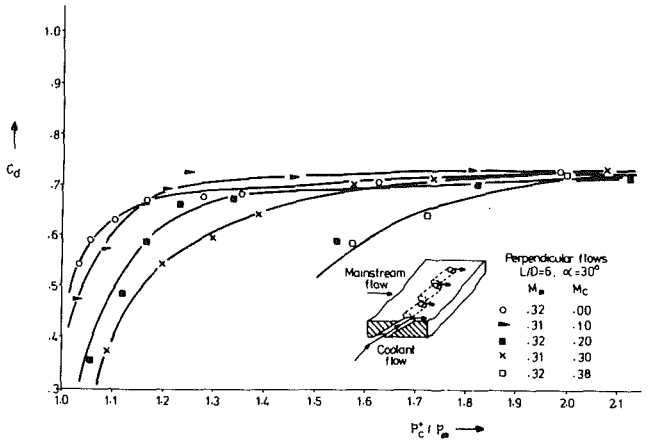

Fig. 12 Effect of the coolant Mach number on Cd at $M_\infty = .3$

of the results and their trends for the lower and higher ranges of pressure ratio. It is obvious that large variations in Cd can occur from one set of conditions to another and Cd is very much smaller at low pressure ratio. The pressure side of the blade is one location where the pressure ratio is low and particular care should be exercised in choosing the values of Cd for this location.

Discussion

In the absence of crossflow on the coolant and mainstream sides, the flow throught a 90 deg hole reduces to that of a long orifice. The flow in long orifices has had extensive coverage [5] and is well understood. For $L/D > 2$, the flow reattaches to the walls of the orifice and fills the cross-sectional area. The discharge coefficient reflects the pressure losses due to entry and the frictional losses in the length of the orifice. For high Re, Cd becomes constant at a value ranging between 0.8 and 0.74 depending on L/D. The results obtained in this work in the absence of crossflow tie in very well with the results for long orifices. In this situation the approach flow is essentially along the axis of the hole.

When crossflow on the coolant side is introduced the approach flow direction becomes perpendicular to the hole axis. The stream tube entering the holes has to turn through 90 deg and this engenders additional losses. Also, depending on the pressure ratio, the stream tube will not fill the cross-sectional area of the hole without additional expansion. This is equivalent to a reduction in the cross-sectional area of the jet entering the hole and reflects in the drop of Cd with decreasing pressure ratio shown in the results.

When the crossflow is on the downstream side of the orifice

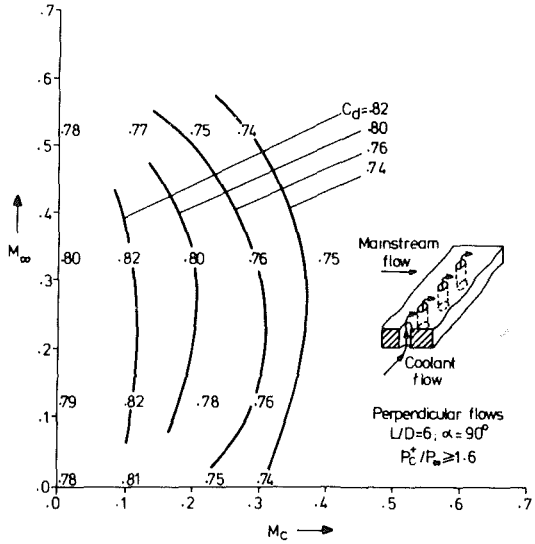

Fig. 13 Contours of constant discharge coefficient for $p_c^+/p_\infty \geq 1.6$

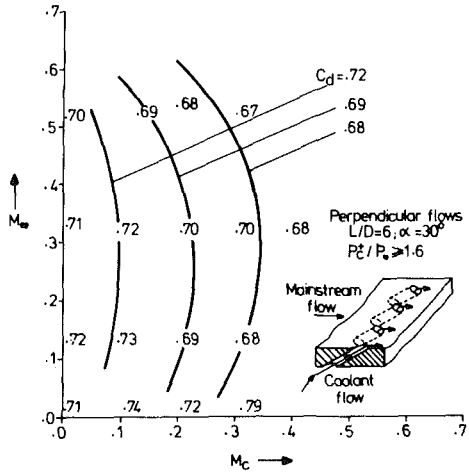

Fig. 14 Contours of constant discharge coefficient for $p_c^+/p_\infty > 1.6$

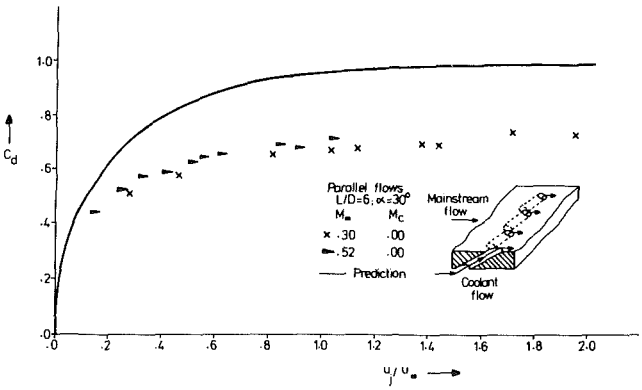

Fig. 15 Comparison of the prediction of Cd with experimental results

the issuing jet is "pinched" by the crossflow, again leading to a reduction in effective cross section and the noted decrease in Cd. This effect has been analysed by Rogers and Hersh [6], who proposed the "lid model" approach in which the stream surface separating the flow out of, or into, the orifice is modeled by a hinged, weightless lid. Their analysis is limited to 90 deg injection for incompressible flow with crossflow on either the mainstream side or the coolant side and to small "lid" opening angles, implying a small ratio of orifice flow velocity to crossflow velocity, u_j/u_∞. The approach has been

Table 4 Summary and trend of results for both flow configurations

	Main parameters affecting Cd $L/D=6$	Parallel flow configuration		Perpendicular flow configuration	
		$\alpha=90$ deg	$\alpha=30$ deg	$\alpha=90$ deg	$\alpha=30$ deg
p_c^+/p_∞	p_c^+/p_∞ 1.05 increases 1.4	Cd increases by about 50%	Cd increases by about 50%	Cd increases by about 60%	Cd increases by about 60%
	p_c^+/p_∞ 1.4 increases 2.0	Cd is approximately constant in the range 0.75 to 0.85	Cd is approximately constant $\simeq 0.72$ for $M_c=0$	Cd is approximately constant in the range 0.7 to 0.8	Cd is constant in the range 0.7 to 0.75
M_∞ 0 increases 0.5	$1.05<p_c^+/p_\infty<1.4$	Cd decreases by about 15% from 0.80	Cd decreases by about 10%	Cd decreases by about 20% from 0.80	Cd decreases by about 25% from 0.72
	$p_c^+/p_\infty>1.4$	Cd constant $\simeq 0.80$	Cd constant $\simeq 0.72$ for $M_c=0.0$ $\simeq 0.95$ for $M_c=0.3$	Cd decreases by about 5% from 0.78	Cd constant $\simeq 0.72$
M_c 0 increases 0.4	$1.05<p_c^+/p_\infty<1.5$	Cd decreases by about 20% from 0.80	Cd increases by about 30% in all the ranges of pressure ratio	Cd decreases by about 23% from 0.80	Cd decreases by about 25% from 0.72
	$p_c^+/p_\infty>1.5$	Cd decreases by about 6% from 0.80		Cd decreases by about 6% from 0.80	Cd decreases by about 5% from 0.72

extended by the present authors [3] for angled injection with crossflow on the mainstream side only. A first attempt (Fig. 15) shows that the trend is being predicted, though the absolute values are about 20 percent too high. The model shows promise and has a potential for further development, particularly in respect of the inlet or coolant side of the orifice, where the opening of the lid with increasing M_c may provide a satisfactory explanation of the large increase in Cd with M_c for the parallel flow configuration.

When crossflows exists on both the upstream and downstream sides of the hole it is likely that one or other end will be controlling. The present results show that for the geometries of interest in film cooling the inlet side is controlling, at least within the ranges of M_c and M_∞ covered. It is possible that control will transfer to the downstream side at higher values of M_∞.

The purpose of this discussion has been to highlight the complexity of the flow situation in these innocent looking geometries. The need for predictive methods seems essential in view of the wide range of values that Cd can assume. The explicit "jet in crossflow" methods of approach seem a long way off still, as they are not yet able to predict reliably the flow downstream of the jet and what is required here is the interaction between three domains of flow. The "lid model" appears to have the potential for providing interim results until more exact methods are perfected.

Conclusions

1 Further data on Cd for film cooling holes has been obtained and presented, in particular, data with crossflows on both the coolant and mainstream sides.

2 For the simpler situation of crossflow on one side only, the data agree well with earlier published results.

3 At low values of p_c^+/p_∞, Cd is a strong function of pressure ratio, increasing with it.

4 As p_c^+/p_∞ increases, Cd reaches a plateau. The value of p_c^+/p_∞ at which this plateau is reached varies with M_c and M_∞. In nearly all cases, for $p_c^+/p_\infty \geq 1.6$ the plateau will have been reached.

5 The values of Cd in the plateau region range between 0.7 and 0.8, except for parallel flow $\alpha=30$ deg, and high M_c, when the value of Cd increases to 0.97.

6 No analytical model exists for the prediction of Cd in the film cooling situation. The lid model has been extended to parallel flow with inclined holes with moderate success in the absence of coolant crossflow. Attempts to extend it to deal with coolant crossflow could, if successful, prove to be very fruitful.

Acknowledgments

The work described in this paper was done in the Department of Mechanical Engineering, University of Nottingham over the past five years in liaison with Rolls Royce Ltd. Our thanks go to the Rolls Royce personnel for many useful discussions and suggestions. Part of the work was done as final year B.Sc. projects and we are indebted to our past students, Messrs. G. S. Brember [7], B. V. Mellor [8] and C. T. Cornfield [9] for their contributions. Finally, one of the authors (S. Benmansour) worked on this project while on a scholarship from the Algerian Government to whom he would like to express his gratitude.

References

1 "BBC 120 and 210 MW Gas Turbines," *Diesel and Gas Turbine Worldwide*, Mar. 1981.

2 Rohde, J. E., Richard, T., and Metger, G. W., "Discharge Coefficients for Thick Plate Orifices with Approach Flow Perpendicular and Inclined to Orifice Axis," *NASA* TDN-5467, Oct. 1969.

3 Benmansour, S., "Discharge Coefficient of Film Cooling Holes," M. Phil. thesis, University of Nottingham, 1981.

4 Smith, M. R., Jones, T. V., and Schultz, D. L., "Film Cooling Effectiveness from Rows of Holes Under Simulated Gas Turbine Conditions," *Oxford University Engineering Laboratory* Report 1070/73.

5 Lichtarowicz, A., Duggins, R. K., and Markland, E., "Discharge Coefficients for Incompressible Non-cavitating Flow Through Long Orifices," *Journal of Mechanical Engineering Science*, Vol. 7, No. 2, 1965, pp. 210–219.

6 Rogers, T. and Hersh, A. S., "The Effect of Grazing Flow on the Steady State Resistance of Square-edged Orifices," AIAA 2nd Aero-Acoustics Conference, Mar. 1975, Paper No. 75-493.

7 Brember, G. S., "Fluid Flow into Film Cooling Holes," B.Sc. thesis, University of Nottingham, 1976.

8 Mellor, B. V., "Discharge Coefficient of Film Cooling Holes," B.Sc. thesis, University of Nottingham, 1978.

9 Cornfield, C. T., "Discharge Coefficient of Film Cooling Holes," B.Sc. thesis, University of Nottingham, 1979.

Tuning of Turbine Blades: A Theoretical Approach

P. Gudmundson
Brown Boveri Research Center,
CH-5405 Baden, Switzerland

A perturbation method is described which predicts the changes in eigenfrequencies resulting from geometrical changes of a structure. This dependence is represented by dimensionless functions, one for each eigenfrequency, which vary over the surface of the structure. The functions are presented for each eigenfrequency as isoline plots. An easily estimated integration of these functions allows one to predict a geometrical change which results in a desired change in the resonance frequencies. The method was applied to a turbine blade and a rectangular beam. For the turbine blade isoline plots are presented for the first five eigenfrequencies. Eigenfrequency changes up to 8 percent were modeled accurately.

Introduction

In this paper a method is presented which relates geometrical changes to eigenfrequency changes of a structure. This method is general and based on perturbation theory. It is therefore applicable to every calculation method which can compute eigenfrequencies and eigenmodes. In this paper the method is tested and compared with Montoya's calculations [11]. The method can as well be applied to a finite element calculation.

A typical example of a structure where the resonance frequencies are of importance is a turbine blade. Much effort has been made to develop accurate prediction methods for the eigenfrequencies of turbine blades. If one or more of the eigenfrequencies are close to an exciting frequency it might be necessary to change the geometry of the blade so that the risk for resonance excitation is minimized. This change can be made on an already produced blade or in the design stage of a new turbine blade. In the first case only a removal of material can be considered, whereas in the second case an addition of material is possible. The question that then arises, is where and how much the geometry of the blade should be changed to achieve the desired changes in the resonance frequencies. The present method makes it possible to easily and quickly determine the necessary geometrical change.

The perturbation method has been tested on two different geometries, a rectangular beam and a turbine blade. The results from the perturbation method have been compared to Montoya's calculations [11] with good agreement.

Theoretical Basis

Different forms of the perturbation theory have, for a long time, been applied to various fields in theoretical physics. The first application of the theory to perturbations of the boundary geometry in eigenvalue problems was made by Brillouin [1]. The problem of resonance frequency changes in turbine blades due to changes in geometry can be seen as a special case of this application. Brillouin [1] and later Wasserman [2, 3], Cabrera [4], and Saito [5] transformed the disturbed geometry to the undisturbed geometry. Using this method they could obtain a problem of perturbations in the differential operator and boundary conditions instead of the boundary geometry. Alternatively, Feshbach [6] transformed the differential equation, with the help of a Green's function, to an integral equation. He could with this integral equation obtain iterative formulas for the disturbed eigenvalues and eigenmodes. Jones [7] has studied the effects of perturbations in mass and stiffness of a discrete vibrating system.

These different approaches however give the same result in different forms for the first-order approximation to the disturbed eigenvalues, and in most cases, it is the first-order approximation which is of importance.

Cawley [8] has applied the first-order perturbation theory to the prediction of defect location from measurements of resonance frequencies. Stetson [9] describes a method to obtain an optimum design by using holographic measurements and the perturbation theory. In [10] he discusses the inversion of the first-order perturbation theory.

Below, the first-order approximation to the disturbed resonance frequency will be described. The resulting formula is put in an easy form and the result is valid for a linear elastic material.

The material is assumed to be linear elastic

$$\sigma_{ij} = C_{ijk1}\ \epsilon_{k1} = \left(\sum_{k=1}^{3} \sum_{l=1}^{3} C_{ijk1}\ \epsilon_{k1} \right) \tag{1}$$

$$C_{ijkl} = C_{klij} \tag{2}$$

$$\epsilon_{kl} = \frac{1}{2} \left(u_{k,l} + u_{l,k} \right) \tag{3}$$

The equations of motion for the resonance frequency calculation take the following form for the undisturbed geometry, Fig. (1).

$$\sigma^n_{ij,j} + \rho \omega_n^2 u_i^n = 0 \qquad \text{in } V \tag{4}$$

$$\sigma^n_{ij}\ n_j = 0 \qquad \text{on } C_T \tag{5}$$

$$u_i^n = 0 \qquad \text{on } C_U \tag{6}$$

Contributed by the Gas Turbine Division of THE AMERICAN SOCIETY OF MECHANICAL ENGINEERS and presented at the 27th International Gas Turbine Conference and Exhibit, London, England, April 18–22, 1982. Manuscript received at ASME Headquarters December 11, 1981. Paper No. 82-GT-148.

In equation (4) a comma denotes a differentiation with respect to x_j.

The solutions to equation (4–6) are the undisturbed eigenfrequencies and eigenmodes.

$\omega_n/2\pi$ = nth resonance frequency
u_i^n = nth eigenmode

For the disturbed problem, equation (4) is not changed but the geometry of the boundary is changed, as is shown in Fig. (1).

$$\sigma_{ij,j}'^{n} + \omega_n'^{2} u_i'^{n} = 0 \quad \text{in } V' \quad (7)$$

$$\sigma_{ij}'^{n} n_j' = 0 \quad \text{on } C_T' \quad (8)$$

$$u_i'^{n} = 0 \quad \text{on } C_U' \quad (9)$$

If the change in geometry is small compared to the dimensions of the structure, one can assume that the disturbed eigenmodes do not differ much from the undisturbed eigenmodes.

Thus:

$$u_i'^{n} = u_i^n + w_i^n \qquad (10)$$
$$\sigma_{ij}'^{n} = \sigma_{ij}^n(u_k^n) + \sigma_{ij}(w_k^n)$$

$$|w_i^n|_{\max} << |u_i^n|_{\max}, |\sigma_{ij}(w_k^n)|_{\max} << |\sigma_{ij}^n(u_k^n)|_{\max} \quad (11)$$

Equation (4–10) are then the equations and boundary conditions for the disturbed eigenfrequency ω_n' and the correction w_i^n.

$$\sigma_{ij,j}(w_k^n) + \omega_n'^{2} w_i^n + \rho(\omega_n'^{2} - \omega_n^2) u_i^n = 0 \quad \text{in } V' \quad (12)$$

$$\sigma_{ij}(w_k^n) n_j' = -\sigma_{ij}^n(u_k^n) n_j' \quad \text{on } C_T' \quad (13)$$

$$w_i^n = -u_i^n \quad \text{on } C_U' \quad (14)$$

From equation (12–14) and equation (11), the restrictions on the geometrical changes can be deduced.

$$d/l << 1 \quad (15)$$

$$|n_i - n_i'| << 1 \quad (16)$$

d = largest distance between the disturbed and undisturbed geometry
l = typical length of the structure
$n_i - n_i'$ = difference in normal vector between the disturbed and undisturbed geometry

Although condition (16) is not as obvious as condition (15), it is just as important. The normal vector condition implies that small concentrated cuts in material, such as cracks, cannot be included in the present analysis; the geometry change must both be small and smooth.

By multiplying equation (12) with u_i^n and integrating over the volume, V', it is possible to calculate the disturbed resonance frequency.

$$\int_{V'} \sigma_{ij,j}(w_k^n) u_i^n dV + \int_{V'} \omega_n'^{2} w_i^n u_i^n \, dV + \int_{V'} \rho(\omega_n'^{2} - \omega_n^2) u_i^n u_i^n \, dV = 0 \quad (17)$$

Equation (17) can be rewritten by using the Gaussian theorem and equation (1, 2, 4, 13–16). These operations result in

$$-\int_{C_T'} \sigma_{ij}^n(u_k^n) n_j u_i^n dS + \int_{C_U'} \sigma_{ij}^n(u_k^n) n_j u_i^n \, dS + \left(\frac{\omega_n'^{2}}{\omega_n^2} - 1\right) \int_{V'} \omega_n^2 \rho u_i^n u_i^n \, dV = 0 \quad (18)$$

In equation (18) the unknown correction, w_i^n, does not appear. It was eliminated by the use of equation (13) and (14) and the conditions (15) and (16). The unknown eigenfrequency, ω_n', can now be expressed as a function of the known undisturbed eigenfrequency and eigenmode. A rewriting of the surface integrals in equation (18), with the use of the Gaussian theorem, gives the following expression for ω_n'

$$\omega_n'^{2} = \omega_n^2 \left(1 - \frac{1}{W_o^n} \int_{\Delta V_T} (W_n - T_n) dV + \frac{1}{W_o^n} \int_{\Delta V_U} (W_n - T_n) dV\right) \quad (19)$$

ΔV_T = volume between C_T and C_T'
ΔV_U = volume between C_U and C_U'

$$W_o^n = \frac{1}{2} \int_V \sigma_{ij}^n(u_k^n) \epsilon_{ij}^n(u_k^n) dV = \frac{1}{2} \int_V \rho \omega_n^2 u_i^n u_i^n dV \quad (20)$$

$$W_n = \frac{1}{2} \sigma_{ij}^n(u_k^n) \epsilon_{ij}^n(u_k^n) \quad (21)$$

Nomenclature

A = amplitude of the vibrations of the rectangular beam
b = width of the rectangular beam
C_{ijkl} = components of elastic stiffness
C_T = part of the undisturbed boundary where the tractions are zero
C_T' = part of the disturbed boundary where the tractions are zero
C_U = part of the undisturbed boundary where the displacements are zero
C_U' = part of the disturbed boundary where the displacements are zero
E = Young's modulus
I_z = axial moment of inertia
l = length of the rectangular beam
n_j = outward normal vector of the undisturbed boundary
n_j' = outward normal vector of the disturbed boundary
q = distance between the undisturbed and the disturbed boundary
S = cross sectional area of the rectangular beam
T_n = kinetic energy per unit volume
u_k = displacement vector
u_k^n = nth undisturbed eigenmode
$u_k'^{n}$ = nth disturbed eigenmode
V = volume of the undisturbed structure
V' = volume of the disturbed structure
w_i^n = correction to the n-th undisturbed eigenmode ($w_i^n = u_i^n - u_i'^{n}$)
W_o^n = total strain energy in the n-th eigenmode
W_n = strain energy per unit volume
x = coordinate along the beam-axis
y,z = distance from the neutral layer in the rectangular beam
ϵ_{ij} = strain tensor
λ_n = nondimensional eigenvalue for the rectangular beam
υ_n = nth eigenfrequency
ρ = density
σ_{ij} = stress tensor
σ_{ij}^n = stress tensor for the n-th undisturbed eigenmode
$\sigma_{ij}'^{n}$ = stress tensor for the n-th disturbed eigenmode
ω_n = nth undisturbed circular eigenfrequency
ω_n' = nth disturbed circular eigenfrequency

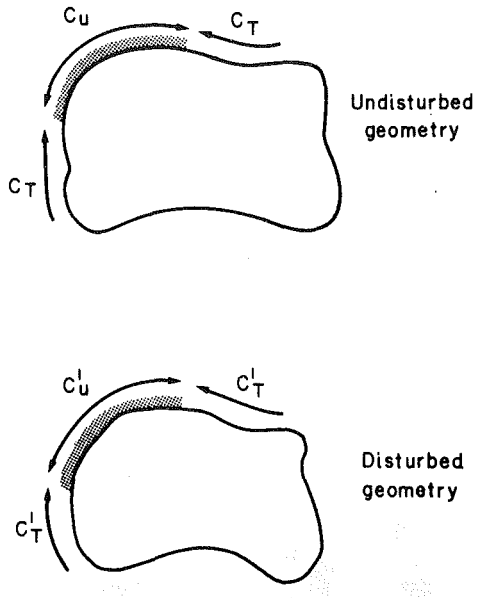

Fig. 1 Geometrical definition of the perturbation problem

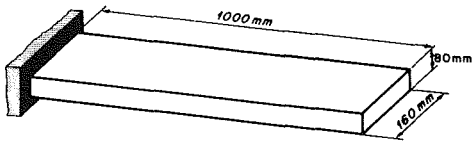

Fig. 2 Geometry of the rectangular beam

$$T_n = \frac{1}{2}\rho\omega_n^2 u_i^n u_i^n \tag{22}$$

If $q\ (x_i)$ is the distance between the undisturbed and disturbed geometry, then $dV \cong qdS$.

$$\omega_n'^2 = \omega_n^2\left[1 - \frac{1}{W_o^n}\int_{C_T} q(x_i)\,(W_n - T_n)\,dS + \frac{1}{W_o^n}\int_{C_U} q(x_i)\,(W_n - T_n)\,dS\right] \tag{23}$$

Until now, we have dealt with a removal of material, but it can be shown that equation (23) also works for an addition of material.

$q > 0$ = removal of material
$q < 0$ = addition of material

At last we can rewrite equation (23) once again to its final form.

$$\omega_n'^2 = \omega_n^2\left(1 - \int_{C_T} f_n(x_i)\,\frac{qdS}{V} + \int_{C_U} f_n(x_i)\,\frac{qdS}{V}\right) \tag{24}$$

where

$$f_n(x_i) = (W_n - T_n)/(W_o^n/V) \tag{25}$$

With equation (24) it is now possible to predict the resonance frequency changes due to arbitrary geometry changes. The dimensionless functions, $f_n(x_i)$, describe completely the effects of disturbances in geometry. Isoline plots of the functions, $f_n(x_i)$, give a very good picture of the qualitative behaviour of the resonance frequencies due to changes in geometry. If a quantitative result is desired, the integrations in equation (24) have to be carried out.

The influence of tolerances on the eigenfrequencies can easily be studied. In areas where the magnitudes of the functions, $f_n(x_i)$, are large the eigenfrequencies are sensitive to geometrical deviations. Thus, it is possible to designate certain areas where it is important to keep the tolerances low and other areas where the tolerances can be larger without changing the eigenfrequencies.

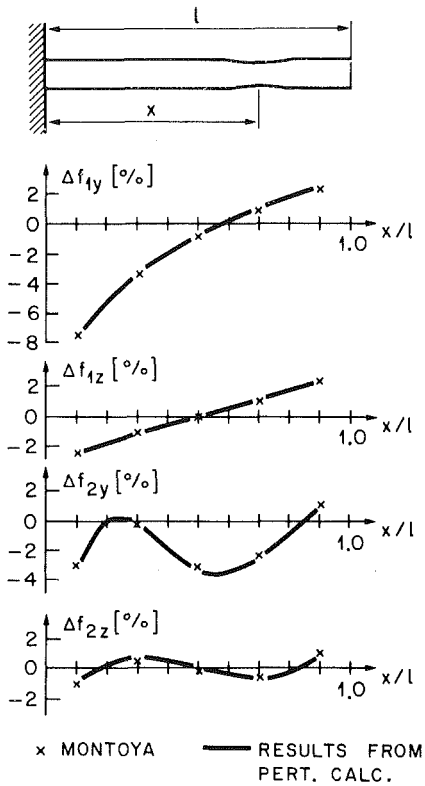

Fig. 3 Comparison between the perturbation method and Montoya calculations [11] for removal of material from the rectangular beam

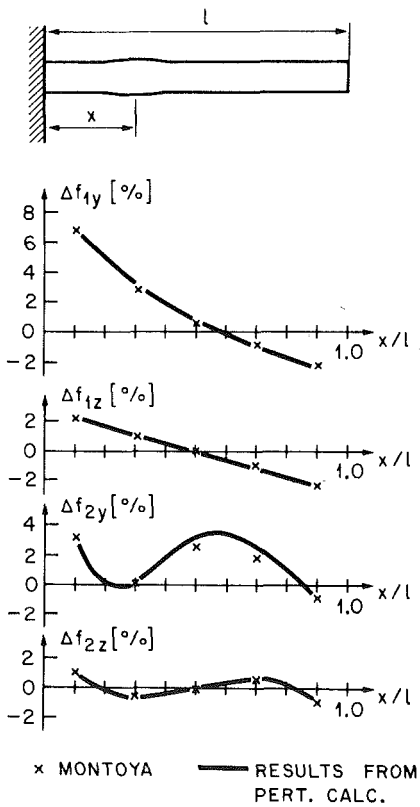

Fig. 4 Comparison between the perturbation method and Montoya calculations [11] for an addition of material to the rectangular beam

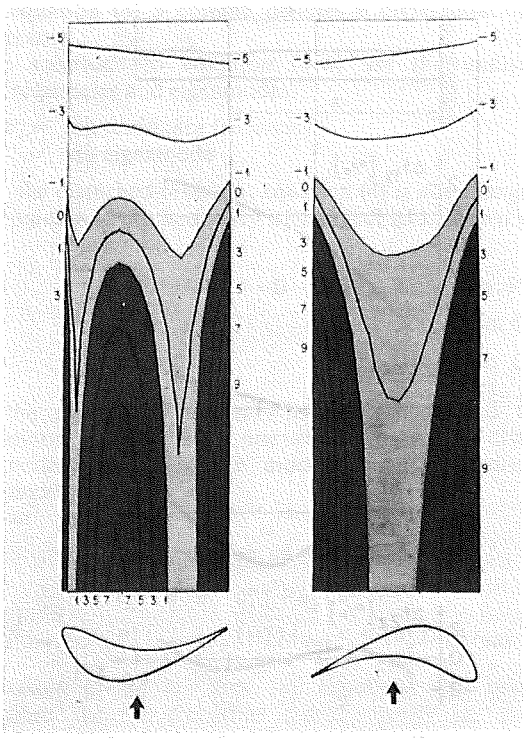

Fig. 5 Isolineplot of f_1 (S), υ_1 = 180.55 Hz

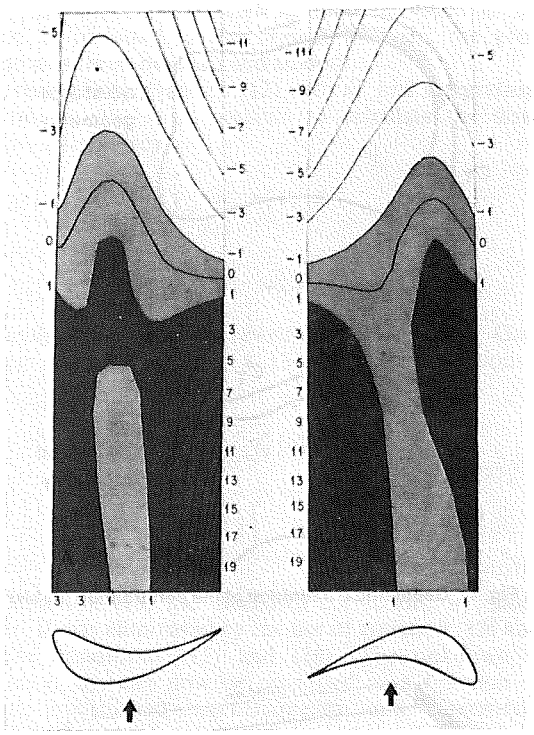

Fig. 6 Isolineplot of f_2 (S), υ_2 = 579.07 Hz

All the information which is available from $f_n(x_i)$ is easy to obtain since $f_n(x_i)$ is calculated solely from the eigenfunction and the eigenfrequency.

The Rectangular Beam

Many types of turbine blades can at least for their lower modes of vibration be treated with the beam-theory. A rectangular beam was choosen to test the accuracy of the present method. This geometry should in principle show the same dynamic behaviour as a turbine blade. An advantage of the simple geometry is that the analytical solutions are easily obtainable. The geometry of the beam is shown in Fig. 2. The beam was calculated with the Bernouilli-Euler beam theory and it was assumed to be fixed at one end. If the beam axis coincides with the x-axis and the beam vibrates in the y-direction, the strain energy per unit volume, the kinetic energy per unit volume, the total strain energy, and the eigenfrequencies can be expressed as

$$W_n = \frac{1}{2} A^2 E \frac{\lambda_n^4}{l^4} y^2 g_n^2\left(\frac{x}{l}\right) \tag{26}$$

$$T_n = \frac{1}{2} A^2 E \frac{\lambda_n^4}{l^4} \frac{I_z}{S} h_n^2\left(\frac{x}{l}\right) \tag{27}$$

$$W_o^n = \frac{1}{2} A^2 E \frac{\lambda_n^4}{l^4} I_z \cdot l \tag{28}$$

$$\upsilon_n = \frac{1}{2\pi} \frac{\lambda_n^2}{l^2} \sqrt{\frac{EI_z}{\rho S}} \tag{29}$$

$$g_n\left(\frac{x}{l}\right) = \left[\cosh\left(\lambda_n \frac{x}{l}\right) + \cos\left(\lambda_n \frac{x}{l}\right) - k_n\left(\sinh\left(\lambda_n \frac{x}{l}\right) + \sin\left(\lambda_n \frac{x}{l}\right)\right)\right]$$

$$h_n\left(\frac{x}{l}\right) = \left[\cosh\left(\lambda_n \frac{x}{l}\right) - \cos\left(\lambda_n \frac{x}{l}\right) - k_n\left(\sinh\left(\lambda_n \frac{x}{l}\right) - \sin\left(\lambda_n \frac{x}{l}\right)\right)\right]$$

$$k_n = \frac{\cosh(\lambda_n) + \cos(\lambda_n)}{\sinh(\lambda_n) + \sin(\lambda_n)}$$

The functions $f_n(x_i)$, according to equation (25), give the frequency sensitivity due to arbitrary geometry changes of the surface of a structure. With equation (26–28), $f_n(x_i)$ for the rectangular beam can be computed.

$$f_n(x_i) = (W_n - T_n)/(W_o^n/V) = 12\left(\frac{y}{h}\right)^2 g_n^2\left(\frac{x}{l}\right) - h_n^2\left(\frac{x}{l}\right) \tag{30}$$

If is is assumed that the geometry of the fixation, in other words, C_u, is unchanged only the first integral in equation (24) has to be considered. Substitution of equation (30) in equation (24) gives the new eigenfrequencies of the rectangular beam.

$$\omega_n'^2 = \omega_n^2\left[1 - \int_{C_T}\left[12\left(\frac{y}{h}\right)^2 g_n^2\left(\frac{x}{l}\right) - h_n^2\left(\frac{x}{l}\right)\right] \cdot \frac{q(S)\, dS}{bhl}\right] \tag{31}$$

Equation (30) and (31) are valid for vibrations in the y-direction. For vibrations in the z-direction, (y/h) in equation (30, 31) is changed to (z/b).

To check the accuracy of equation (31) different geometry changes were made and the frequencies predicted by equation (31) were compared to Montoya's calculations [11] with the disturbed geometry.

A parabolic change in geometry was considered.

$$q(x,y,z) = \begin{cases} \pm \dfrac{h}{16}\left(1 - \left(\dfrac{x - x_o}{l/10}\right)^2\right) & (x,y,z) \in S_o \\ 0 & (x,y,z) \notin S_o \end{cases} \tag{32}$$

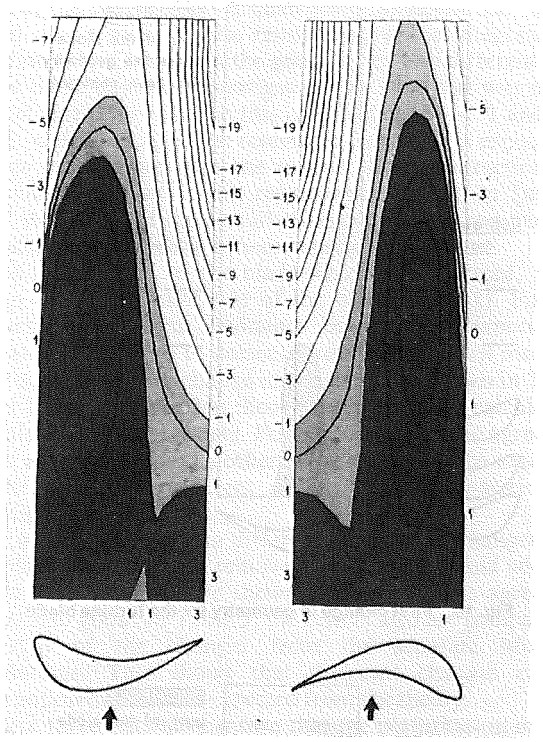

Fig. 7 Isolineplot of f_3 (S), ν_3 = 785.41 Hz

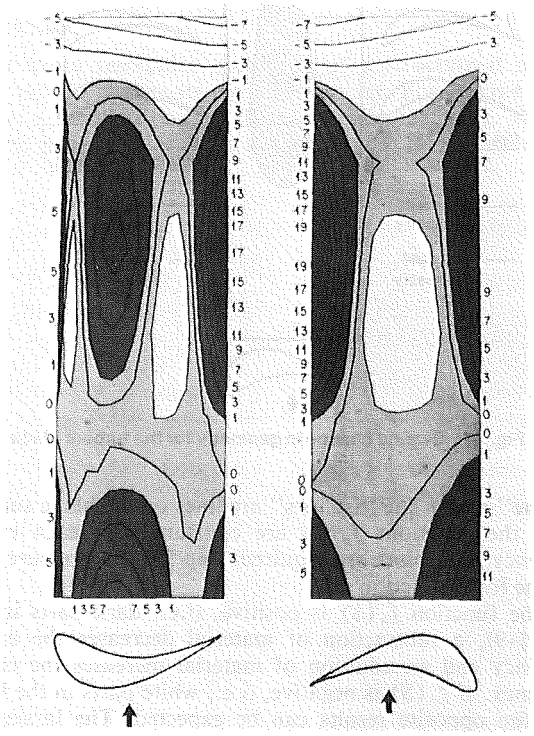

Fig. 8 Isolineplot of f_4 (S), ν_4 = 891.32 Hz

where

$$S_o: \begin{cases} x_o - l/10 \le x \le x_o + l/10 \\ y = \pm h/2 \\ -b/2 \le z \le b/2 \end{cases} \tag{33}$$

A + sign for $q(x,y,z)$ in equation (32) corresponds to a removal of material and a − sign to an addition of material.

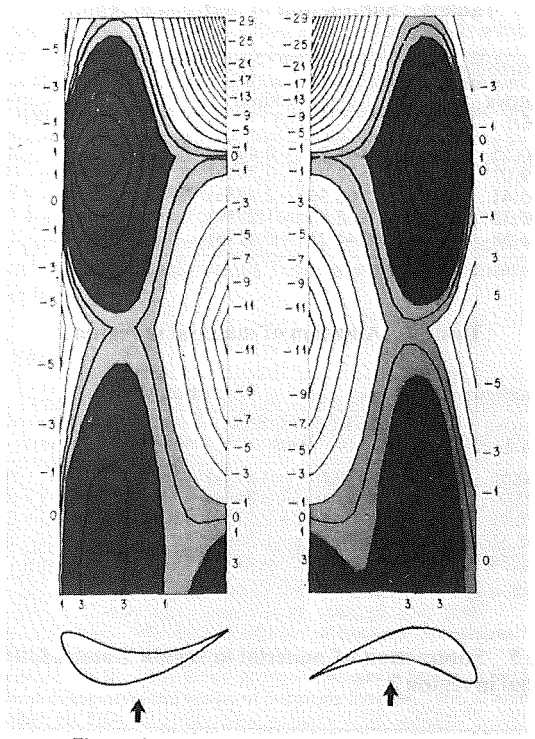

Fig. 9 Isolineplot of f_5 (S), ν_5 = 1751.58 Hz

Table 1 Subtraction of material in region 1

Undisturbed	Disturbed geometry	
Montoya [Hz]	Pert. method [Hz]	Montoya [Hz]
180.55	176.55 (−2.22%)	176.63 (−2.17%)
579.07	577.99 (−0.19%)	577.60 (−0.25%)
785.41	779.36 (−0.77%)	779.30 (−0.78%)
891.32	880.49 (−1.22%)	881.18 (−1.14%)
1751.58	1732.40 (−1.10%)	1732.04 (−1.12%)

Table 2 Addition of material in region 1

Undisturbed	Disturbed geometry	
Montoya [Hz]	Pert. method [Hz]	Montoya [Hz]
180.55	184.46 (+2.17%)	184.69 (+2.29%)
579.07	580.15 (+0.19%)	580.45 (+0.24%)
785.41	791.42 (+0.77%)	791.15 (+0.73%)
891.32	902.02 (+1.20%)	902.55 (+1.26%)
1751.58	1770.55 (+1.08%)	1770.41 (+1.08%)

By changing x_o, different geometry changes were generated. For a removal of material according to equation (32), the new eigenfrequencies in the y- and z-directions can be expressed, using equation (31), by

$$\omega'^2_{ny} = \omega^2_{ny}\left[1 - \int_{x_o/l-0.1}^{x_o/l+0.1}\left[3\, g_n^2\left(\frac{x}{l}\right) - h_n^2\left(\frac{x}{l}\right)\right]\cdot\frac{1}{8}\cdot\left[1-\left(\frac{x-x_o}{l/10}\right)^2\right]d\left(\frac{x}{l}\right)\right] \tag{34}$$

$$\omega'^2_{nz} = \omega^2_{nz}\left[1 - \int_{x_o/l-0.1}^{x_o/l+0.1}\left[g_n^2\left(\frac{x}{l}\right) - h_n^2\left(\frac{x}{l}\right)\right]\cdot\frac{1}{8}\cdot\left[1-\left(\frac{x-x_o}{l/10}\right)^2\right]d\left(\frac{x}{l}\right)\right] \tag{35}$$

Table 3 Subtraction of material in region 2

Undisturbed	Disturbed geometry	
Montoya [Hz]	Pert. method [Hz]	Montoya [Hz]
180.55	181.29 (+0.41%)	181.32 (+0.43%)
579.07	577.08 (−0.34%)	574.59 (−0.77%)
785.41	766.36 (−2.43%)	767.96 (−2.22%)
891.32	902.80 (+1.29%)	904.23 (+1.45%)
1751.58	1744.23 (−0.42%)	1733.89 (−1.01%)

Table 4 Addition of material in region 2

Undisturbed	Disturbed geometry	
Montoya [Hz]	Pert. method [Hz]	Montoya [Hz]
180.55	179.81 (−0.41%)	179.86 (−0.38%)
579.07	581.05 (+0.34%)	581.95 (+0.50%)
785.41	804.01 (+2.37%)	802.18 (+2.14%)
891.32	879.69 (−1.30%)	881.97 (−1.05%)
1751.58	1758.90 (+0.42%)	1769.56 (+1.03%)

Table 5 Subtraction of material in region 1 and addition of material in region 2

Undis-turbed	Disturbed geometry		Sum of separate Montoya-calcula-tion
Montoya [Hz]	Pert. method [Hz]	Montoya [Hz]	
180.55	175.80 (−2.63%)	175.93 (−2.56%)	−2.55%
579.07	579.98 (+0.16%)	580.60 (+0.26%)	+0.25%
785.41	798.10 (+1.62%)	794.90 (+1.21%)	+1.36%
891.32	868.71 (−2.54%)	872.23 (−2.14%)	−2.19%
1751.58	1739.80 (−0.67%)	1750.98 (−0.03%)	−0.09%

If, instead, an addition of material is considered, the sign before the integrals in equation (34, 35) is changed.

Equation (34, 35) were numerically evaluated for x_o/l-values between 0.1 and 0.9 for both removal and addition of material. These results were compared to Montoya's calculations [11] for x_o/l = 0.1, 0.3, 0.5, 0.7, 0.9. In Figs. 3 and 4 the comparisons are shown. Δf_{ny} and Δf_{nz} in Figs. 3 and 4 express the percentage change of the eigenfrequencies in y- and z-direction, respectively.

The comparison shows that the present method works very well in this case. Eigenfrequency changes up to 8 percent were modeled accurately.

Application to a Turbine Blade

The perturbation theory has also been applied to a turbine blade. The length of the blade was 400 mm, the chord 115 mm, and the pretwist 14 deg.

The five first resonance frequencies were calculated with the Montoya program [11]. The blade was assumed to be fixed at its root.

υ_1 =	180.55 Hz	first bending
υ_2 =	579.07 Hz	first edge-wise bending, strongly coupled to torsion
υ_3 =	785.41 Hz	first torsion
υ_4 =	891.32 Hz	second bending
υ_5 =	1751.58 Hz	second torsion

The functions $f_n(S)$ (equation (25)), which describe arbitrary geometry changes, were calculated from the eigenmodes and eigenfrequencies of the blade. These are presented in Figs. 5-9 for the first five eigenfrequencies in terms of

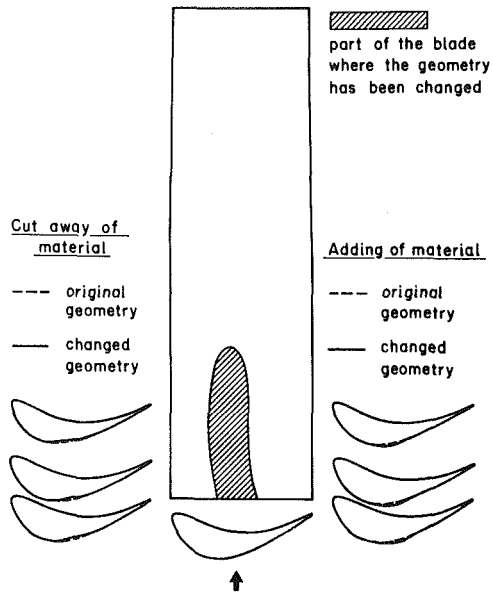

Fig. 10 First change in geometry for the turbine blade

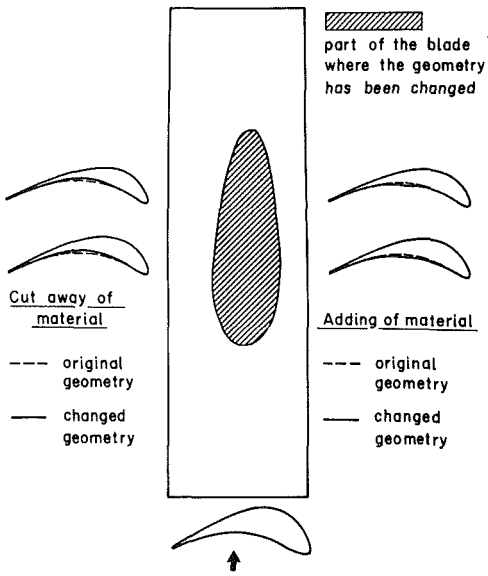

Fig. 11 Second change in geometry for the turbine blade

"isoline" plots. The "isolines" are lines on the blade surface where the functions $f_n(S)$ are constant. For each eigenfrequency, two plots are required: one for the pressure side and one for the suction side.

If the function $f_n(S)$ is positive, (i.e., dark parts in the Figs. 5-9), a subtraction of material decreases the eigenfrequency and an addition of material increases the eigenfrequency. If $f_n(S)$ is negative, (i.e., white parts in the Figs. 5-9), the opposite results can be expected. The larger the magnitude of $f_n(S)$, the bigger the frequency changes that result.

Figures 5-9 relate geometry changes to changes in resonance frequencies. This information enables a prediction to be made of how and where to tune the turbine blade to achieve desired eigenfrequency changes. Furthermore, they also provide useful information concerning tolerances, in particular where the tolerances are of primary importance regarding spread in eigenfrequencies. Where the magnitude of $f_n(S)$ is high, the tolerances give the largest spread in frequency.

From the isoline plots a qualitative prediction can be obtained, but a more precise result requires the integration in equation (24). Changes in the geometry of two different parts of the blade has been investigated. The first part was on the suction side (Fig. 10). For this case $0 < f_2(S) < 1$ and $2 < f_1(S) < 8$. Thus, the first resonance frequency is expected to change much more than the second. Both subtraction and addition of material in this region were studied. In Tables 1 and 2 the results of the perturbation method are compared to the calculations with the Montoya program [11].

The second part of the blade which was changed, was a region on the pressure side of the blade (Fig. 11). For this geometry, the fourth resonance frequency is expected to increase but the third to decrease from a removal of material. The results from this change in geometry are shown in Tables 3 and 4. The perturbation theory and Montoya's calculations [11] also agree for this case. For modes 2 and 5 the agreement is not as good as for the other modes. This can be explained by the lack of insufficient accuracy in the numerical integration.

As a final test, the two different geometrical changes were combined. Material was removed from region 1 and added in region 2. The results are shown in Table 5. The agreement here is also good. In Table 5, the results also are compared to the sum of the changes from the separate Montoya calculations. This shows that different changes can be superimposed, as is also expected from the theory.

These three tests have shown that the perturbation method works very well on a turbine blade. The discrepancies to Montoya can be explained by insufficient numerical integration.

Discussion

To avoid resonance excitation of a structure it may be necessary to change its eigenfrequencies. For turbine blades this is generally done by changing their geometry. Material can be ground away from a blade, but it is not self evident where and how much of the material which should be removed. In this paper a method is described with which it is possible to predict the necessary geometrical changes to achieve desired changes in the resonance frequencies. The limitation of this method is that these changes should be small compared to the original geometry of the structure. If large frequency changes are desired it is believed that a step by step procedure should be used.

The data necessary for this method are eigenfrequencies, eigenmodes and geometry of the unchanged structure. All these quantities usually result from a normal calculation of the eigenfrequencies.

References

1 Brillouin, L., "Perturbations by Boundary Deformation as a Problem of Proper Values," *Comp. rend*, Vol. 204, 1937, pp. 1863–1865.

2 Wasserman, G. D., "On the Theory of Boundary Perturbations," *Phil. Mag.*, Vol. 37, 1946, pp. 563–571.

3 Wasserman, G. D., "On Perturbation Problems Associated With Finite Boundaries," *Proceedings Cambridge, Phil. Society*, Vol. 44, 1947, pp. 251–262.

4 Cabrera, N., "Perturbation of Boundary Conditions," *Cahiers Phys.*, Vol. 31, 1948, pp. 24–62.

5 Saito, T., "The Perturbation Method due to Small Change in Shape of the Boundary," *J. Phys. Soc. Japan*, Vol. 15, 1960, pp. 2069–2080.

6 Feschbach, H., "On the Perturbation of Boundary Conditions," *Phys. Rev.*, Vol. 65, 1944, pp. 307–318.

7 Jones, R. P. N., "The Effect of Small Changes in Mass and Stiffness on the Natural Frequencies and Modes of Vibrating Systems," *Int. J. Mech. Sci.*, Vol. 1, 1960, pp. 350–355.

8 Cawley, P., and Adams, R. D., "Location of Defects in Structures from Measurements of Natural Frequencies," *J. of Strain Anal.*, Vol. 14, No. 2, April 1979, pp. 49–57.

9 Stetson, K. A., "Perturbation Method of Structural Design Relevant to Holographic Vibration Analysis," *AIAA Journal*, Vol. 13, No. 4, 1975, pp. 457–459.

10 Stetson, K. A., and Palma, G. E., "Inversion of First-Order Perturbation Theory and Its Application to Structural Design," *AIAA Journal*, Vol. 14, No. 4, 1976, pp. 454–460.

11 Montoya, J., "Gekoppelte Biege- und Torsionsschwingungen einer stark verwundenen rotierenden Schaufel," *Brown Boveri Mitteilungen*, Band 53, Nr. 3, 1966, pp. 216–229.

The Use of Optimization Techniques to Design-Controlled Diffusion Compressor Blading

N. L. Sanger
National Aeronautics and Space Administration,
Lewis Research Center,
Cleveland, Ohio 44135
Mem. ASME

A method is presented for automating compressor blade design using numerical optimization and is applied to the design of a controlled diffusion stator blade row. A general purpose optimization procedure is employed, which is based on conjugate directions for locally unconstrained problems and on feasible directions for locally constrained problems. Coupled to the optimizer is an analysis package consisting of three analysis programs which calculate blade geometry, inviscid flow, and blade surface boundary layers. The optimization concepts are briefly discussed. Selection of design of a two-dimensional blade section is discussed, and design results are presented.

Introduction

Throughout the history of compressor technology, blade shapes have been specified by geometric families or classes. For the most part, these families have been derived from early wing shapes and improved by empiricism, or have been directly specified from simple geometric shapes such as circular arcs and parabolas.

During the past decade, computational methods for the calculation of flow through compressor blade rows have advanced substantially, as have computer speeds. With these advances has come the capability to rapidly design and analyze flow over arbitrary blade shapes. Indeed, at the present time, these analysis methods are being synthesized into computer-aided design systems. In most cases these systems are "manual," i.e., nonautomated. Because of the great flexibility in choice of blade shape, the design process can become quite cumbersome and repetitive unless automated in some fashion. One of the most attractive methods for automating the design process is numerical optimization. Much progress has been made recently in bringing the technique to bear on engineering problems, particularly in the field of aeronautics [1]. Of the many numerical optimization algorithms in existence, the one used in [1] and described in [2] with its control program [3] is sufficiently general and user-oriented to be of particular interest. It is used in the work reported herein, and is coupled to analysis programs which calculated blade shape, the inviscid flow field, and the boundary layer for a two-dimensional blade section.

With the advent of arbitrary blade shapes, the concept of controlling velocity diffusion (and consequently boundary layer growth) on the suction surface has received increasing attention. In the transonic flow regime, such blading has generally been referred to as "supercritical blading" since the local supersonic flow is controlled as well as the boundary layer growth. In the subsonic regime the blading is often simply referred to as "controlled diffusion." Methods of analysis have generally been inverse, in which a velocity distribition of a general Stratford type [4] is prescribed at the outset, and a blade shape derived from it [5, 6].

The problem addressed in the present work is the redesign of a high-subsonic stator blade row utilizing a controlled diffusion blade shape. The analytical methods are direct rather than inverse. A blade shape is initially prescribed and aerodynamic performance calculated. Perturbations on the blade shape are effected and aerodynamic performance recalculated until specified conditions are met. The resulting velocity distributions over the suction surface of the blade are also of the general Stratford type, but in this case are controlled by constraints imposed on the geometric and aerodynamic parameters.

The subject stator row uses the same flow path and velocity triangles as the first stage stator of the NASA Two-Stage Fan [7]. The original design was highly successful, showing a first stage peak adiabatic efficiency if 87.0 percent, and a remarkably low radial distribution of loss across the stator. Consequently, significant improvement in performance with controlled diffusion blading cannot be expected, nor is that the purpose of the present work. The principal objective of the work presented herein is to develop and demonstrate the feasibility of an automated design procedure based on numerical optimization. Experimental evaluation of the resulting design is planned for both a single-stage environment and a two-dimensional cascade (midspan blade section).

Analysis Methods

Blade Section Geometry. The blade section geometry is generated by a polynomial element program. This program has been extracted from the NASA Design Program which is a

Contributed by the Gas Turbine Division of THE AMERICAN SOCIETY OF MECHANICAL ENGINEERS and presented at the 27th International Gas Turbine Conference and Exhibit, London, England, April 18-22, 1982. Manuscript received at ASME Headquarters December 11, 1982. Paper No. 82-GT-149.

streamline curvature design procedure [8]. Blade section nomenclature is presented in Fig. 1. The meanline of the blade is described by two polynomial segments, each of which can be specified by up to a quartic polynomial. The polynomial is a fit of local mean-line blade angle against mean-line distance. The fraction of chord from the leading edge at which the two polynomial segments join is referred to as the transition location, T. The polynomials may be fitted beginning from the transition location and fitting toward the leading edge and trailing edge, respectively, or they may be fitted beginning at the leading and trailing edges and fitting toward the transition location. In this report, fitting from transition location toward leading and trailing edges for each segment is the mode of operation. Note that s_1 and s_2 are both positive in this mode.

The expression for blade angle distribution is given by equation (1).

Front segment.

$$\kappa_1 = \kappa_t + AC1 \times s_1 + BC1 \times s_1^2 + CC1 \times s_1^3 + DC1 \times s_1^4 \quad (1a)$$

Rear segment

$$\kappa_2 = \kappa_t + AC2 \times s_2 + BC2 \times s_2^2 + CC2 \times s_2^3 + DC2 \times s_2^4 \quad (1b)$$

A typical distribution of blade angle is shown in Fig. 2(*a*). The blade angle at the transition location is designated as *KTC*. When fitting from the transition location, the fit is effected from *KTC* to the blade angle at inlet, *KICR* (front segment), and from *KTC* to the blade angle at outlet, *KOCR* (rear segment). Noted on the figure is a parameter calculated internally by the program, *KCS*, which is the blade angle midway between the transition location and the trailing edge. This parameter will be of importance in later discussion.

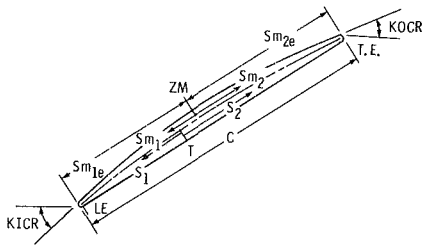

Fig. 1 Blade geometry nomenclature

The distribution of blade thickness about the mean-line is also specified by two polynomials, both of which may be quartics. The thickness is added symmetrically on either side of the meanline. The fit is made from the maximum thickness location toward the leading and trailing edges for front and rear segments respectively. The leading edge and trailing edge may be specified as circles or ellipses. Circles only were used in this design. The equations for thickness distribution are given as equation (2). Instead of being linear, the first term is of square root form, which enables simulation of 65-series blades, if desired.

Front segment:

$$t_1 = \frac{TMX}{2} + AT1 \times \left(\sqrt{s_{m1e} - s_{m1}} - \sqrt{s_{m1e}} + \frac{s_{m1}}{\sqrt{s_{m1e}}} - BT1 \times s_{m1}^2 - CT1 \times s_{m1}^3 - DT1 \times s_{m1}^4 \right) \quad (2a)$$

Nomenclature

$AC1, BC1, CC1, DC1, AC2, BC2, CC2, DC2$ = polynomial coefficients for blade angle distribution expression

$AT1, BT1, CT1, DT1, AT2, BT2, CT2, DT2$ = polynomial coefficients for blade thickness distribution expression

C = chord

$F(\bar{X})$ = objective function

$G_j(\bar{X})$ = constraint functions

H_i = incompressible form factor

$H_{i,\text{crit}}$ = critical value of incompressible form factor at which turbulent boundary layer separates. $H_{i,\text{crit}} = 2.0$ in this study

$L.E.$ = leading edge of blade

KCS = angle with respect to meridional direction of blade mean line midway between transition location and trailing edge

$KICR$ = angle with respect to meridional direction of blade mean line at leading edge

$KOCR$ = angle with respect to meridional direction of blade mean line at trailing edge

KTC = angle with respect to meridional direction of blade mean line at transition location

$\bar{S}$ = search direction

s_1 = along mean line, front segment

s_2 = distance from transition location along mean line, rear segment

s_{m1} = distance from maximum thickness location along mean line, front segment

s_{m1e} = distance from maximum thickness location to blade leading edge along mean line

s_{m2} = distance from maximum thickness location along mean line, rear segment

s_{m2e} = distance from maximum thickness location to blade trailing edge along mean line

T = distance from leading edge to intersection of two polynomial segments describing mean line/chord

t_1, t_2 = thickness of blade, front and rear segments respectively

TMX = maximum thickness/chord

$T.E.$ = trailing edge

U = stream function

V = surface velocity

$\bar{X}$ = vector of design variables

$XCHORD$ = meridional projection of blade chord

ZM = distance from leading edge to maximum thickness location/chord

α^* = move parameter

κ = blade angle

Subscripts

1 = front segment

2 = rear segment

m = number of constraints

n = number of design variables

ps = pressure surface

ss = suction surface

t = transition

Rear segment:

$$t_2 = \frac{TMX}{2} + AT2 \times \left(\sqrt{s_{m2e} - s_{m2}} - \sqrt{s_{m2e}} + \frac{s_{m2}}{2\sqrt{s_{m2e}}} \right. \\ \left. - BT2 \times s_{m2}^2 - CT2 \times s_{m2}^3 - DT2 \times s_{m2}^4 \right. \quad (2b)$$

Potential Flow Solution. The potential flow about the blade section in the two-dimensional, blade-to-blade plane is calculated by the method developed by Katsanis, TSONIC [9]. The program solves the stream function equation by finite difference techniques for the subsonic, compressible flow regime. It is necessary to specify as input the fluid properties, inlet total temperature and density, weight flow, blade geometry, inlet and outlet flow angle, finite difference mesh, and a meridional distribution of streamtube height and total pressure loss. In the design presented herein, a linear distribution of streamtube height and estimated total loss was utilized.

Because the nature of the equations dictates that the solution be of a boundary value type, the outlet flow angle must be specified on the downstream boundary. This effectively sets the Kutta condition. Since this condition is related to one of the constraints chosen for the optimization process, its discussion will be reserved until later.

Boundary Layer Calculations. Blade surface boundary layers were calculated using the program developed by McNally [10]. In addition to the surface velocities, required input includes upstream flow condition, fluid properties, and blade surface geometry. Among the output provided by the program are the conventional boundary layer thicknesses, form factors, wall friction coefficient, and momentum thickness Reynolds number.

The program uses integral methods to solve the two-dimensional compressible laminar and turbulent boundary layer equations in an arbitrary pressure gradient. Cohen and Reshotko's method [11] is used for the laminar boundary layer, transition is predicted by the Schlicting-Ulrich-Granville method [12], and Sasman and Cresci's method [13] is used for the turbulent boundary layer.

A boundary layer which is initially laminar may proceed through normal transition to a turbulent boundary layer, or it may undergo some form of laminar separation before becoming turbulent. To provide flexibility for analyzing this behavior, several program options are available to the user. The calculations may proceed from a laminar boundary layer through transition to turbulent calculations. However, if laminar separation is predicted before transition, the turbulent calculations may be started by specifying a factor by which the last calculated value of momentum thickness is multiplied (this value is commonly chosen to be 1.0 to satisfy conservation of momentum). This new momentum thickness and a value for form factor based on the last calculated momentum thickness Reynolds number are used as initial values for the turbulent calculations.

Optimization Program. The optimization algorithm in Fortran code is known as CONMIN, and is reported in [2]. A general purpose control program known as COPES is coupled to the algorithm [3].

The general mathematical representation of a numerical optimization problem is stated as

$$\begin{array}{lll} \text{Minimize} & OBJ = F(\bar{X}) & \\ \text{subject to} & G_j(\bar{X}) < 0. & j = 1,m \\ & X_i^l < X_i < X_i^u & i = 1,n \end{array} \quad (3)$$

$\bar{X}$ is a vector consisting of the design variables. X_i^l and X_i^u are the lower and upper bounds on the design variables and are referred to as side constraints. *OBJ* is the objective function. If the designer wishes to maximize a function, *OBJ* may be defined as the negative of the function. $G_j(\bar{X})$ set the constraint functions which the design must satisfy. When $G_j(\bar{X}) < 0$, it is said to be inactive; when $G_j(\bar{X}) > 0$, it is violated. When it is within a tolerance band about zero, it is active. $F(\bar{X})$ and $G_j(\bar{X})$ may be implicit or explicit functions of the design variables $\bar{X}$, but must be continuous. (Note: this should be carefully considered when formulating these functions when they are calculated from finite difference solutions or at discrete stations.)

An initial design vector, $\bar{X}$, is specified by the user. It may be feasible or infeasible, i.e., if it satisfies the inequalities of equation (3), it is feasible. If a feasible initial design can be found, it is usually more efficient to begin with it, at least for the types of problems discussed herein. An iteration process is then begun which follows the recursive relationship

$$\bar{X}^{q+1} = \bar{X}^q + \alpha^* \bar{S}^q \quad (4)$$

q is the iteration number; the vector $\bar{S}$ is the search direction in the n-dimensional space; and the scalar α^* (move parameter) defines the distance of travel in direction, $\bar{S}$, and is found by interpolation.

The search direction, $\bar{S}$, is initially obtained by moving in the direction of steepest descent (negative gradient of the objective function) without violating constraints. The procedure is then repeated using a conjugate direction algorithm in determining a new search direction. Whenever a constraint is encountered, a new search direction is found using Zoutendijk's Method of Feasible Directions. An optimum has been achieved when no search direction can be found which will further reduce the objective function without violating a constraint.

Optimization of Stator Blade Section

Formulation of a specific optimization problem involves choice of an objective function (the quantity to be optimized), choice of constraints, and choice of design variables. In the present design problem, optimization of a two-dimensional stator blade section was performed at the 90 percent span from tip section. This location represented the most difficult design problem as measured by blade loading requirements.

Results of preliminary calculations of an initial blade shape which meets the specified velocity triangles at the 90 percent span location are shown in Figs. 2–4. Figure 2 shows the distribution of blade angle and blade thickness along the mean-line, and the corresponding blade shape. Figure 3 is the surface velocity distribution corresponding to the blade shown in Fig. 2. And Fig. 4 represents the incompressible form factor distribution along the suction surface obtained form the boundary layer calculations.

The initial blade design was essentially an arbitrary choice. The blade angle distribution and thickness distribution plots were determined by running the blade geometry program in a graphics mode. In this mode, the distributions can be generated by curvefitting through points which are input by the user. The process is therefore intuitive, and guided by experience. The only restriction to the process is the desirability, with regard to optimization theory, that the design be feasible. Note that for the initial design selected, the turbulent boundary layer separates at 64 percent of chord.

A properly designed controlled diffusion blade should experience no suction surface boundary layer separation. This criterion is incorporated into the objective function. The following penalty function type of objective function proved to be the most successful

$$OBJ = \text{FORMAX} - \text{XSEPOX} \quad (5)$$

FORMAX is the maximum incompressible form factor (H_i) occuring over the rear portion of the blade, and XSEPOX is

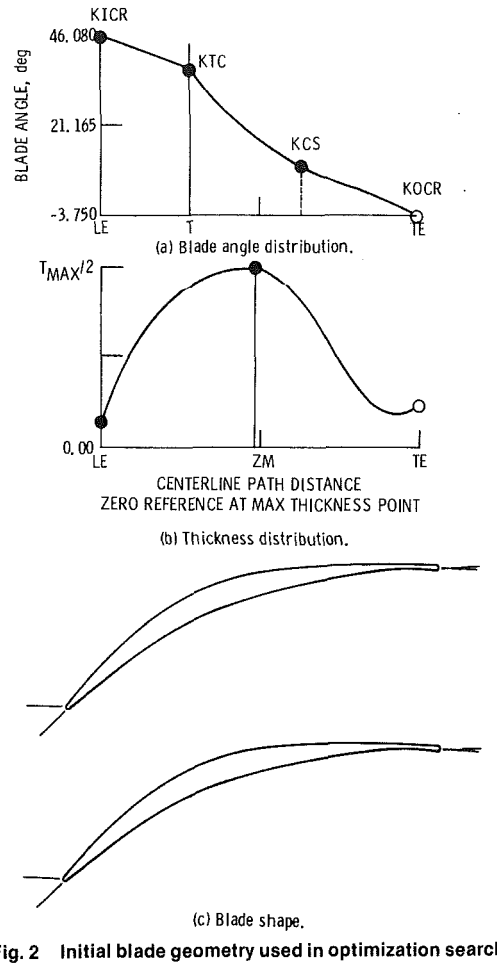

Fig. 2 Initial blade geometry used in optimization search

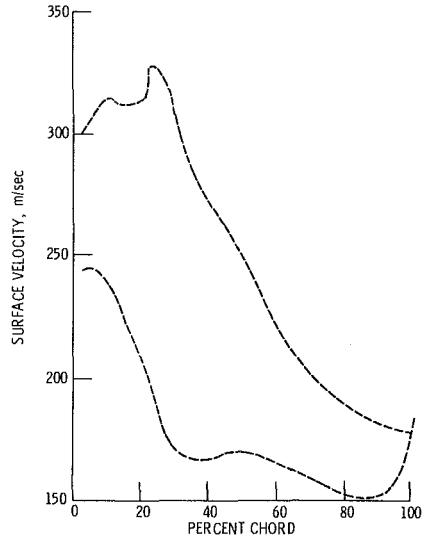

Fig. 3 Initial surface velocity distribution

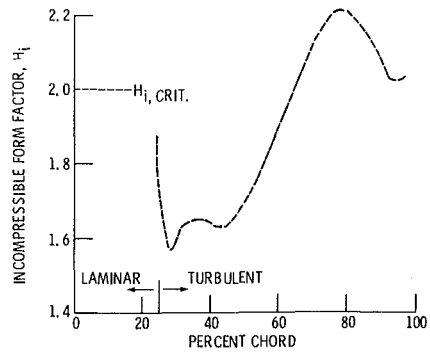

Fig. 4 Initial design-suction surface turbulent boundary layer form factor distribution

the separation location of the turbulent boundary layer expressed as a proportion of chord length.

OBJ was minimized. Reducing FORMAX acts to increase the separation location, XSEPOX. Simultaneously reducing FORMAX and increasing XSEPOX acts to reduce OBJ.

Design Variables. Nine design variables have been selected, all of which describe the geometry of the blade. These variables are:

T, transition location of two mean-line polynomials;

ZM, maximum thickness location;

KOCR, the exit blade mean-line angle (deg.);

*AC*1,*BC*1, first two coefficients of front segment mean-line polynomial;

*AC*2,*BC*2,*CC*2,*DC*2, all four coefficients of rear segment mean-line polynomial.

The velocity triangles are fixed for the blade section, thus fixing the loading or overall velocity diffusion across the blade row. By allowing *KOCR* to vary, the blade camber angle is allowed to change. The trailing edge or Kutta-type condition is controlled through a constraint described below.

Incidence angle is not allowed to vary. It is fixed at the value used in the original design [7] simply as a designer's preference. If it should become desirable or necessary to allow incidence angle to vary, it can easily be incorporated by including *KICR* as a design variable, and retaining the same velocity triangle information.

Although the maximum thickness location, *ZM*, is allowed to vary, the coefficients of the blade thickness polynomial are held fixed at the values used in the preliminary (initial) blade shape, strictly as a designer's choice.

Each of the above variables is allowed to vary within user-selected limits. The upper and lower bounds for each are listed below, and in optimization theory are referred to as side constraints. The side constraint values are chosen as a result of experience. Beyond certain values, a realistic blade shape will not result. In addition, certain extreme combinations of variables may cause convergence problems in the geometry program, and so are best avoided.

	Lower bound	Upper bound
Transition loc./chord, *T*	.20	.40
Max thickness loc./chord, *ZM*	.35	.55
Outlet blade angle, *KOCR*	−10.	−2.
All coefficients	1.E−15	1.E+15

Constraints. Five constriant functions are specified, all being implicit functions of the design variables. Two constraints are variables calculated internally to the geometry program and control the blade angle distribution. By controlling the blade angle distribution, a controlled diffusion type shape to the surface velocity distribution can be insured. The constraints are represented in Fig. 2(*a*), and are *KTC* and *KCS*, which were previously described. They were allowed to vary between the following bounds

	Lower bound	Upper bound
KTC	32.0	46.08
KCS	− 4.0	11.05

The remaining constraints are calculated in the inviscid flow program [9] and are described with reference to a surface velocity distribution. Since TSONIC is principally a subsonic calculation procedure, the maximum surface velocity on the suction surface is constrained to the subsonic flow regime. A search procedure locates the maximum suction surface velocity. This is nondimensionalized by the inlet freestream velocity and the ratio is defined as the constraint. The upper bound was set to be equivalent to Mach 1 condition. The lower bound is set equal to an arbitrary, small number.

Because no boundary layer calculations are made on the pressure surface of the blade, a constraint is applied to control the velocity diffusion on the pressure surface. Preliminary calculations were made of typical blade shapes, and a pressure surface velocity diffusion (V, max/V,min) of 1.65 was deemed to be a sufficiently safe upper bound. Subsequent to the optimization calculation, the pressure surface boundary layer of the optimized blade is also calculated to verify that it was truly free from separation. The lower bound of this constraint is set equal to an arbitrary, small number.

The final constraint is chosen to set the trailing edge condition, the condition equivalent to a Kutta condition. This is also equivalent to setting deviation angle. In the present work, outlet flow angle is fixed, so whatever value is taken on by blade outlet angle, *KOCR*, sets deviation angle. Experience with some of the conventional families of blades, supplemented with detailed analyses, permitted guidelines to be set for estimating deviation for those blade families [14]. But such experience is lacking for controlled diffusion blading, which is arbitrary in shape. For conventional blading, setting the deviation angle such that the suction surface and pressure surface velocity distributions close inside the trailing edge at perhaps 85 to 90 percent of chord, was one possible means for accounting for the effects of a rounded trailing edge and boundary layer separation over the rear portion of the suction surface. For controlled diffusion blading, the object is to have no boundary layer separation. If this is accomplished, the deviation angle would be expected to be small, and there would be justification for allowing the suction surface and pressure surface velocities to close at the trailing edge, rather then closing earlier.

The constraint is defined as a nondimensional difference between velocities on the suction and pressure surfaces at the trailing edge mesh line, and is expressed:

$$\frac{(V_{ss} - V_{ps})_{T.E.}}{15.24} \tag{6}$$

The denominator, 15.24, was chosen to scale the constraint to about order one. Upper bound was set at zero and lower bound at −1.25. The velocity difference at the trailing edge could vary between an upper bound of zero and a lower bound of −19.0 m/sec, thus permitting some closing inside the trailing edge.

Modifications of Analysis Programs

An important requirement of the optimization method is that the objective and constraint functions be continuous functions of the design variables. This necessitated certain modifications of the analysis programs.

Modification of Inviscid Code. Experience with the TSONIC code has shown that calculations in the trailing edge region can be quite sensitive for some configurations.

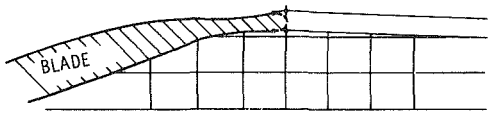

(a) Construction of effective wake.

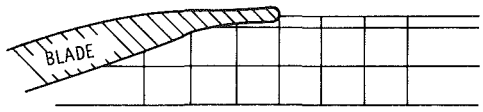

(b) Original trailing edge model (ref. 9).

Fig. 5 Mass flow injection model: TSONIC program

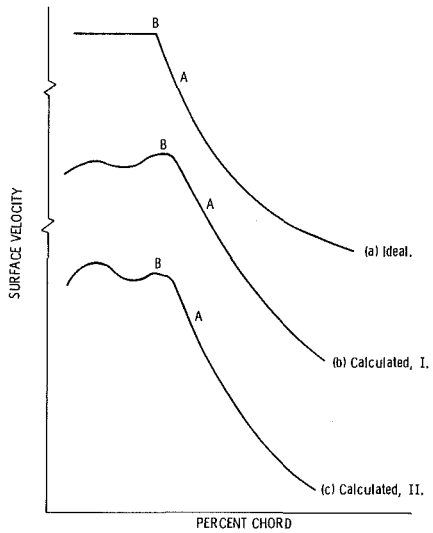

Fig. 6 Representation of ideal and calculated suction surface velocities

Orientation of the blade, trailing edge radius, and grid intersection points can affect surface velocity calculations at or near the trailing edge station, sometimes resulting in spurious behavior. Inaccurate trailing edge velocities will produce incorrect gradients of the trailing edge constraint described above, and possibly give misleading violations of that constraint.

The means used to avoid or reduce this tendency is to incorporate a mass injection model at the trailing edge [15]. In this model, tangents are formed at the intersection of the trailing edge circle with the blade surface, and extended to the vertical grid line with forms a tangent with the trailing edge circle (Fig. 5). The "wake" is then extended downstream with an orientation determined by the downstream whirl boundary condition. Experience has shown this modeling to reduce the sensitivity of the surface velocity calculations in the trailing edge region.

Modifications of Boundary Layer Code. There is presently no agreement concerning the initial state of a boundary layer on a compressor stator blade in the real flow environment. Some observors have measured laminar boundary layers, while others contend that due to high inlet turbulence and unsteady effects, a laminar boundary layer cannot persist. For the purposes of this study, the question is somewhat academic. An optimization design process can be developed for either case. In the present work the existence of a laminar boundary layer is assumed, which poses the more difficult optimization problem.

The location of laminar separation and turbulent reat-

tachment is of crucial importance to the optimization search process. The suction surface velocity distribution provided as input to the boundary layer calculation might ideally appear as represented in Fig. 6(*a*). In reality it might appear as in Figs. 6(*b*) and (*c*), due to the interrelationship of geometric variables such as blade stagger, solidity, camber distribution, thickness distribution, transition location, and maximum thickness location. Boundary layer calculations are initiated with a laminar boundary layer, which would usually persist to point A. Laminar separation, rather than normal transition, occurs there in all cases because of the steep adverse pressure gradient. Conservation of momentum is assumed through the laminar separation region, with the turbulent boundary layer reattached at the next calculating station. Turbulent separation is assumed to occur when the incompressible form factor reached a critical value.

As originally modeled, point A (Fig. 6) is identified as the station at which skin friction becomes negative. Any sensitivity to design variables can cause a discontinuous jump in point A location. This effect carries through to directly influence turbulent boundary layer separation location and the objective function. To establish a consistent and conservative criterion, the following procedure was coded. Using Lagrangian interpolation, three additional points are placed between each station in the high gradient region of the velocity versus distance array. A search procedure is begun from the trailing edge region, and locates the maximum velocity at the beginning of the high gradient region, point B in Fig. 6. Laminar separation and turbulent reattachment is effected at point B.

In addition to the modifications discussed above, several modifications were required relating to turbulent boundary layer separation. A separation criterion common to compressor blade analyses which use integral boundary layer methods is the incompressible form factor, H_i. Values of 1.8 to 2.6 have been proposed and used in the past (e.g., von Doenhoff and Tetervin, [16]). A value of 2.0 is somewhat conservative and, in the experience of the author, has proven to be useful. The program was modified to use 2.0 as the critical incompressible form factor.

In normal operation, when a form factor at a given station exceeds 2.0, separation is assumed to have occurred at that station. If calculation stations are 5 percent of chord apart, separation location becomes a discontinuous function, changing with distance in 5 percent jumps. To correct this, linear interpolation is used between stations to obtain the percent chord location corresponding to $H_i = 2.0$.

Because of the relation between blade angle distribution and thickness distribution, the incompressible form factor quite often resembles Fig. 7. A maximum form factor can be observed at *C*. A more conventional form factor distribution is also depicted in Fig. 7, where the maximum value is identified as D. A search procedure was added to locate the maximum form factor, FORMAX, which is one term in the objective function.

It was observed that allowing turbulent reattachment at a momentum thickness equivalent to momentum thickness at laminar separation often resulted in initial turbulent momentum thickness Reynolds numbers less than 320, the minimum value experimentally observed for a turbulent boundary layer [17]. Therefore, as a final modification, the code was altered to provide a minimum thickness equivalent to a Reynolds number of 320.

Design Results

The optimization history is shown in Fig. 8. Most improvement occurred in the first two iterations. At the end of two iterations a blade has been found with no boundary layer separation (XSEPOX = 1.0). Reduction of the objective function for subsequent iterations involved reduction of FORMAX only, since XSEPOX remained 1.0. All improvement beyond iteration 2 provided more safety margin from the theoretical separation condition. CPU time on an IBM 370/3033 for the eight iterations was 49.48 minutes. A total of 85 calls on the analysis programs were made.

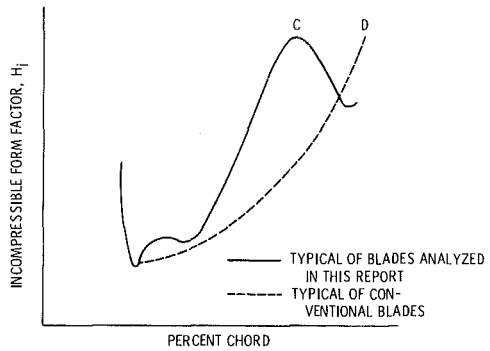

Fig. 7 Turbulent incompressible form factors for different classes of blades

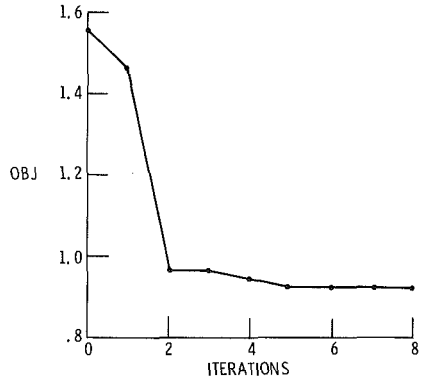

Fig. 8 Optimization history

The initial and final blade shapes, surface velocities, and suction surface boundary layer form factor are presented and compared in Figs. 9–11. The pressure surface boundary layer form factor is presented in Fig. 12.

In the course of optimization, the geometric transition location moved forward from 27.3 percent of chord to 24.1, and the level of KTC (blade angle at transition) shifted downward from 36.7 deg to 34.8 (Fig. 9). The maximum thickness location moved rearward from 48.2 percent of chord to 53.6. All polynomial coefficients describing the blade angle distribution were altered, as would be expected, since they were design variables. The polynomial coefficients describing the thickness distribution were not altered, since they were not design variables. However, since the maximum thickness location itself changed, the actual distribution of thickness was altered, as is evident from Fig. 9(*b*). If difficulties in achieving a satisfactory design had been experienced, the polynomial coefficients for thickness distribution could have been added as additional design variables, but at the cost of increased computing time. Outlet blade angle, *KOCR*, changed little during the process. Large excursions in *KOCR* were prevented because it is closely related to the trailing edge constraint (equation (6)).

The changes effected in the surface velocities by the optimization procedure (Fig. 10) are a bit more dramatic in appearance than are the geometry changes. The peak velocity on the suction surface was reduced, as was the large velocity diffusion over the front portion of the pressure surface. The unconventional waviness of the pressure surface velocity is

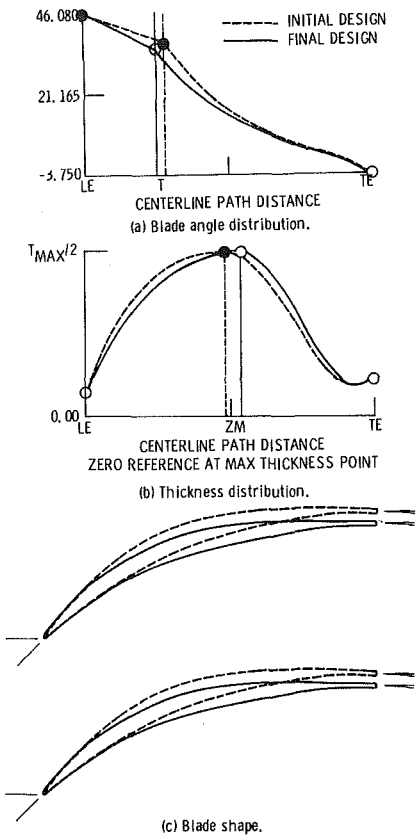

Fig. 9 Comparisons of initial and final blade designs

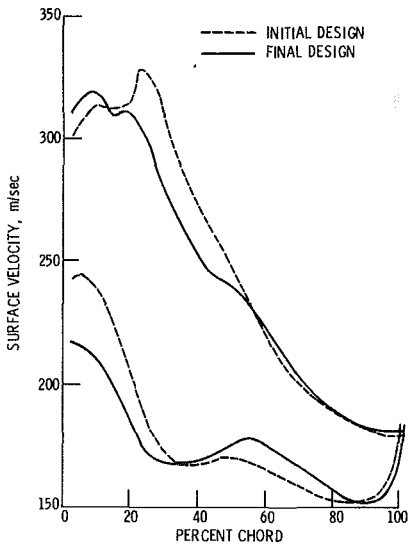

Fig. 10 Comparison of initial and final blade surface velocity distributions

due to the aft location of the maximum thickness. Fitting the thickness distribution through this maximum thickness location, in combination with the forward transition location, results in a region of reversed curvature on the pressure surface near the maximum thickness location, and is evident on Fig. 9(*c*). The effect on the flow carries across the channel and appears as a small wave on the suction surface as well. Aside from the dubious aesthetic appearance, no adverse aerodynamic effects can be attributed to this behavior. The calculated boundary layers appear well-behaved, with the maximum incompressible form factor on the suction surface being 1.924, and on the pressure surface 1.780.

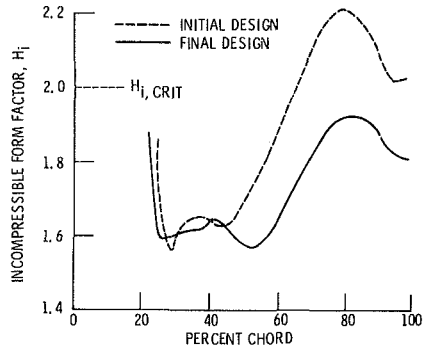

Fig. 11 Comparison of initial and final suction surface turbulent boundary layer incompressible form factor

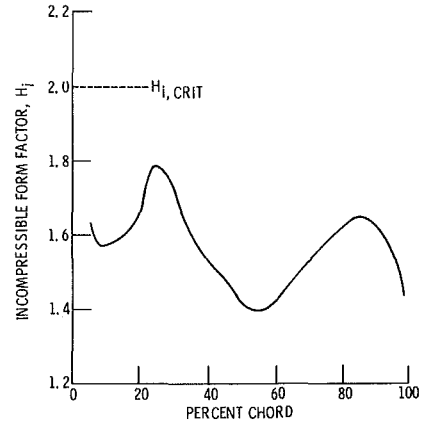

Fig. 12 Final blade design turbulent boundary layer incompressible form factor, pressure surface.

In completing the design of the stator, only one other blade section was optimized, the hub section at the inner endwall. This blade element will be in the wall boundary layer, so that true two-dimensional flow is not expected to exist. Resulting transition location and maximum thickness location were not greatly different from the values found at the 90 percent span location. Blade angle polynomial coefficients different from those obtained at 90 percent span were obtained. However, for reasons relating to the blade stacking procedure, which will be described below, the polynomial coefficients obtained at the 90 percent span location were used also at the 100 percent span. The resulting two-dimensional calculations for the blade with these coefficients indicated no boundary layer separation.

All other blade sections were specified based on the optimized design obtained at the 90 percent span section. Each of these blade sections, which lie on streamlines, is then radially stacked. Fabrication coordinates are interpolated at several planes parallel to the axis of rotation of the compressor. In principle, each of the blade sections on the six chosen streamlines utilized could be designed by optimization. This could and probably would result in six different sets of transition location, maximum thickness location, and blade angle polynomial coefficients. The fabrication coordinates are generated by a design point streamline curvature code. As input to this code, a radial curvefit of each of the polynomial coefficients must be provided. Transition location and maximum thickness location for each blade section are input directly. The blade coordinates on each streamline section are then generated. Finally, coordinates at the horizontal fabrication planes are obtained by interpolation, based on a cubic fit of the blade coordinates at the four streamlines most closely straddling the desired fabrication plane.

Because of the curvefitting at various stages of this process,

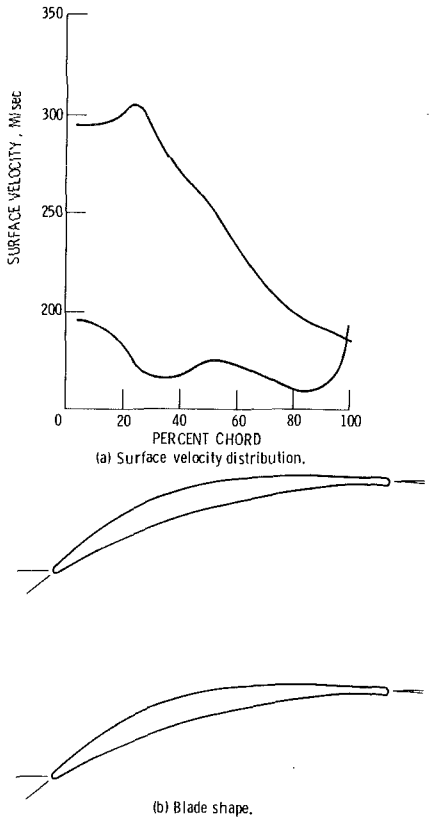

Fig. 13 Surface velocity distribution and blade shape, final blade, 50 percent span from tip

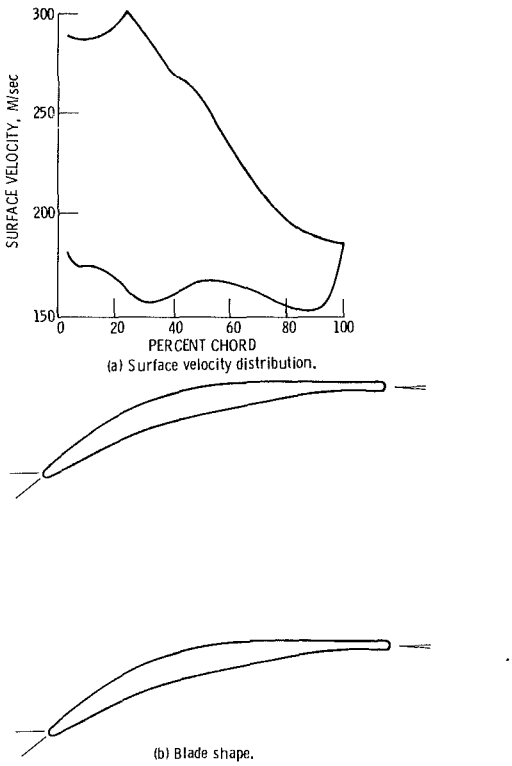

Fig. 14 Surface velocity distribution and blade shape, final blade, 10 percent span from tip

prudence suggests avoiding the possibility of large radial variations in the design parameters. Therefore, a constant radial distribution of each parameter was sought, with one exception. Maximum thickness location was arbitrarily moved forward to 47 percent of chord for all sections between the tip and 70 percent of span from tip. Although it was not necessary to do this, the effect was to relieve the reversed curvature condition on the pressure surface. The transition location and all polynomial coefficients were maintained at the same values obtained for the optimized 90 percent span section. At the 100 percent span section, transition and maximum thickness locations found from optimization at that section were used (0.26 and 0.52, respectively), and blade angle polynomial coefficients equivalent to those at 90 percent span were used. Thus, neither the polynomial coefficients for blade angle nor maximum thickness varied radially. Transition location was constant from tip to 90 percent span, and differed only slightly at 100 percent span. Maximum thickness location was constant from the tip to 70 percent span at 0.47, moved rearward to 0.53 at 90 percent span, and slightly forward to 0.52 at 100 percent span. The exit blade angle, *KOCR*, varied only slightly from tip to hub in a range from -3.7 to -4.0. Since design exit flow angle is zero deg for all sections, the negative value of *KOCR* represents deviation angle. If, indeed, the boundary layer does not separate from the blade as theoretically predicted, the deviation angles of about 4 deg may be more realistic than they appear to be. The blade geometry and surface velocity distributions for the blade sections at midspan and 10 percent span from tip are shown in Figs. 13 and 14.

Summary and Concluding Remarks

A method has been presented for automated compressor blade design using numerical optimization techniques. The method was applied to the design of a controlled-diffusion stator blade row. Three analysis programs were coupled to the numerical optimization program: a blade geometry generation program which uses polynomial representation for blade angle and thickness distributions, a compressible, inviscid flow program, and an integral boundary layer program. Seven of the nine design variables were related to blade angle distribution, another located the maximum thickness of the blade, and the last controlled camber and deviation angles. Two constraint functions operated in the geometry program to produce shapes with controlled diffusion velocity distributions. Constraint functions applied in the flow analysis programs limited suction surface velocities to the subsonic regime, limited the velocity diffusion on the pressure surface, and set the trailing edge condition for inviscid calculations. The objective function, which was minimized, was of a penalty function form, and effectively produced a blade whose suction surface turbulent boundary layer did not separate.

The optimization procedure for the subject blade section required eight major iterations involving 85 calls on the geometry/aerodynamic analysis programs. Total CPU time on an IBM 370/3033 computer was 49.48 minutes.

When using the numerical optimization procedure, it was essential that the gradients of the constraint and objective functions be smooth and accurate. Therefore, some modifications of the analysis programs were necessary to ensure that these functions were continuous.

The design problem, as formulated here, produce a blade shape which satisfied the design criteria, while holding the polynomial coefficients describing thickness distribution, the value of maximum thickness, and the incidence angle constant. The method thus still offers great flexibility for adaptation to more demanding design requirements.

References

1 Vanderplaats, G. N., "The Computer for Design and Optimization," *Computing and Applied Mechanics*, AMD, Vol. 18, New York, 1976, pp. 25-48.

2 Vanderplaats, G. N., "CONMIN a Fortran Program for Constrained Function Minimization, User's Manual," NASA TM X-62282, 1973.

3 Vanderplaats, G. N., "COPES a Fortran Control Program for Engineering Synthesis," Naval Post-graduate School, 1980.

4 Stratford, B. S., "The Prediction of Separation of the Turbulent Boundary Layer," *Journal of Fluid Mechanics*, Vol. 5, pt. 1, Jan. 1959, pp. 1–16.

5 Papailiou, K. D., "Boundary Layer Optimization for the Design of High Turning Axial Flow Compressor Blades," ASME Paper No. 70-GT-88, 1970.

6 Stephens, H. E., "Application of Supercritical Airfoil Technology to Compressor Cascades: Comparison of Theoretical and Experimental Results," AIAA Paper No. 78-1138, July 1978.

7 Urasek, D. C., Gorrell, W. T., and Cunnan, W. S., "Performance of Two-Stage Fan Having Low-Aspect-Ratio, First-Stage Rotor Blading," NASA TP-1493, Aug. 1979.

8 Crouse, J. E., and Gorrell, W. T., "Computer Program for Aerodynamic and Blading Design for Multistage Axial-Flow Compressors." proposed NASA TP.

9 Katsanis, T., "Fortran Program for Calculating Transonic Velocities on a Blade-To-Blade Stream Surface of a Turbomachine," NASA TN D-5427, 1969.

10 McNally, W. D., "Fortran Program for Calculating Compressible Laminar and Turbulent Boundary Layers in Arbitrary Pressure Gradients," NASA TN D-5681, 1970.

11 Cohen, C. B., and Reshotko, E., "The Compressible Laminar Boundary Layer with Heat Transfer and Arbitrary Pressure Gradient," NACA TR-1294, 1956.

12 Schlicting, H., "Origin of Turbulence II," *Boundary-Layer Theory*, 7th ed., McGraw-Hill, New York, 1979, pp. 489–554.

13 Sasman, P. K., and Cresci, R. J., "Compressible Turbulent Boundary Layer with Pressure Gradient and Heat Transfer," *AIAA Journal*, Vol. 4, No. 1, Jan. 1966, pp. 19–25.

14 Sanger, N. L., "Two-Dimensional Analytical and Experimental Performance Comparison for a Compressor Stator Section with D-Factor of 0.47," NASA TN D-7425, Oct. 1973.

15 Katsanis, T., unpublished addendum to reference [9].

16 Von Doenhoff, A. E., and Tetervin, N., "Determination of General Relations for the Behavior of Turbulent Boundary Layers," NACA wartime report L-382, 1943.

17 Preston, J. H., "The Minimum Reynolds Number for a Turbulent Boundary Layer and the Selection of a Transition Device," *Journal of Fluid Mechanics*, Vol. 3, pt. 4, Jan. 1958, pp. 373–384.

Convective Heat Transfer in a Rotating Cylindrical Cavity

J. M. Owen
School of Engineering and Applied Sciences,
University of Sussex, England

H. S. Onur
Makina Mühendisliği Bölümü,
Karadeniz Üniversitesi,
Trabzon, Turkey

In order to gain an understanding of the conditions inside air-cooled, gas-turbine rotors, flow visualization, laser-doppler anemometry, and heat-transfer measurements have been made in a rotating cavity with either an axial throughflow or a radial outflow of coolant. For the axial throughflow tests, a correlation has been obtained for the mean Nusselt number in terms of the cavity gap ratio, the axial Reynolds number, and rotational Grashof number. For the radial outflow tests, velocity measurements are in good agreement with solutions of the linear (laminar and turbulent) Ekman layer equations, and flow visualization has revealed the destabilizing effect of buoyancy forces on the flow structure. The mean Nusselt numbers have been correlated, for the radial outflow case, over a wide range of gap ratios, coolant flow rates, rotational Reynolds numbers, and Grashof numbers. As well as the three (forced convection) regimes established from previous experiments, a fourth (free convection) regime has been identified.

Introduction

In order to estimate the thermal growth and fatigue life of turbine and compressor disks, the gas turbine designer needs to calculate the temperatures of these disks. In a real engine the disk geometry is complicated, but the essential features of two important cases are shown in Fig. 1. Figure 1(*a*), a rotating cylindrical cavity with axial throughflow, is a simplified representation of two corotating compressor disks where cooling air passes axially through a central hole (or annulus, if a central shaft is present). Figure 1(*b*), a rotating cavity with radial outflow, represents two air-cooled corotating turbine disks.

Both cases were studied by Owen and Bilimoria [1], who measured Nusselt numbers on the heated downstream disk of the cavity. For the axial throughflow case, the flow structure is illustrated in Fig. 1(*a*) where the central jet creates secondary recirculating flow in the cavity. The structure of this flow depends on the gap ratio, G ($G \equiv s/b$, s being the axial gap between disks of radius b), the axial Reynolds number, Re_z ($\mathrm{Re}_z \equiv 2\bar{W}a/\nu$, $\bar{W}$ being the bulk mean axial velocity in the inlet pipe, a the inlet radius, and ν the kinematic viscosity), the rotational Reynolds number, Re_ϕ ($\mathrm{Re}_\phi \equiv \Omega b^2/\nu$, Ω being the angular speed) and the Rossby number, ϵ ($\epsilon \equiv \bar{W}/\Omega a = \frac{1}{2} b^2 \mathrm{Re}_z / a^2 \mathrm{Re}_\phi$). For the tests of Owen and Bilimoria, where $0.13 \leq G \leq 0.4$, it was found that, at certain values of the Rossby number, the Nusselt number could change dramatically. These changes were attributed to spiral vortex breakdown, where the central axial jet precessed, or whirled, about the axis and affected the flow structure inside the cavity. In a separate study on a smaller isothermal rig with $G = 0.53$, Owen and Pincombe [2] found that this turbulent spiral vortex breakdown occurred for $21 < \epsilon < 100$. Although forms of vortex breakdown persisted for $\epsilon < 21$, the effects were less dramatic; and it was found that the size of the recirculation flow zone tended to reduce with decreasing Rossby number leaving the outer part of the cavity in solid-body rotation.

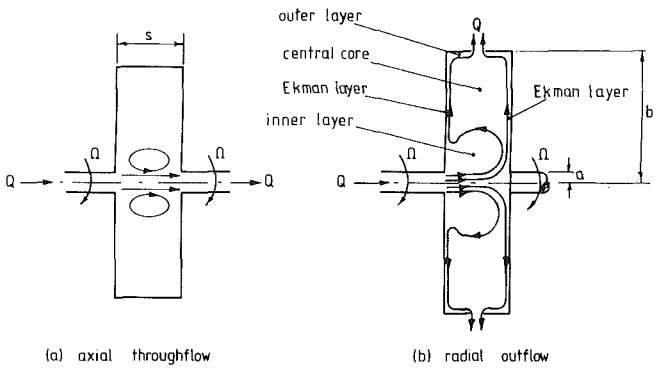

Fig. 1 Schematic representation of a rotating cylindrical cavity

Figure 1(*b*) provides a simplified representation of the flow structure in a rotating cavity with radial outflow. The inner layer distributes flow from the source into two Ekman layers, and the outer layer redistributes the flow into the sink; the interior core rotates, but the axial and radial components of velocity in the core are zero. Hide [3] analyzed the isothermal laminar case for a uniform radial source and sink, and Owen and Pincombe [4] obtained velocity measurements for the radial inlet case of Hide as well as for the axial inlet case shown in Fig. 1(*b*). For isothermal laminar flow in a cavity with $G = 0.267$, the measurements suggested that the flow in the Ekman layers became turbulent for $\mathrm{Re}_r \gtrsim 200$ (where $\mathrm{Re}_r \equiv Q/2\pi\nu r$, Q being the volumetric flow rate and r the radial distance from the center of the cavity).

For turbulent radial outflow in a heated cavity, Owen and Bilimoria found that the mean Nusselt numbers showed three distinct regimes. In regime I, at low rotational speeds and high

Contributed by the Gas Turbine Division of The American Society of Mechanical Engineers and presented at the 27th International Gas Turbine Conference and Exhibit, London, England, April 18–22, 1982. Manuscript received at ASME Headquarters December 11, 1981. Paper No. 82-GT-151.

flow rates, the Nusselt number was virtually independent of rotational speed; in regime II, at higher rotational speeds, the Nusselt number increased with both speed and flow rate; in regime III, at the highest rotational speeds tested ($Re_\phi > 10^6$), the effect of rotational speed was again weak.

In this paper, the work of Owen and Bilimoria is extended. For the axial throughflow case, tests are conducted using a "restricted outlet" where the bore of the outlet tube is reduced to model more closely the geometry of a stack of compressor disks; and, for the radial outflow case, tests are conducted over a wider range of flow rates. For both cases, in order to provide data for the designer, correlations of the mean Nusselt numbers are obtained.

2 Experimental Method

2.1 The Experimental Assembly. As the rotating rig used in these experiments was a modified version of that described in [1], only the main features and modifications are described below.

The cylindrical cavity comprised two 12.5-mm thick stainless-steel disks and a peripheral 1.5-mm thick paxolin shroud. The disks had an outer diameter of 762 mm, and each disk was connected to a central rotating tube which had a bore of 76 mm. The spacing between the disks was variable up to a maximum of 203 mm. The two disks were connected by a central drive-shaft of 25-mm dia, and the whole assembly could be rotated up to 2750 rev/min by a thyristor-controlled d-c motor.

Air could be fed into the cavity through the center of one disk (the upstream disk) and could generate either an axial throughflow or a radial outflow. For the axial throughflow case, the air left through the center of the second (downstream) disk; for the radial outflow case, a perforated shroud was used and the outlet tube from the downstream disk was sealed. For the outflow tests, the shroud had thirty holes, of 28.6-mm dia, spaced at 12 deg angular intervals on the midaxial plane ($z/s = 0.5$).

The cooling air was supplied from a centrifugal fan and cooled to ambient temperature by a heat exchanger. The flow rate was measured either by a venturimeter or (for flow rates below 0.02 m^3/s) by a rotameter. Although the flow meters had been calibrated to an accuracy of approximately 3 percent, leakage between stationary and rotating components in the rig could cause significant errors.

The disks were instrumented with ten 0.13-mm dia chromel-constantan thermocouples embedded at 34 mm radial intervals on each face. Signals from the thermocoules on each disk were brought out through two silver/silver graphite slip ring units, and the voltages were measured by a digital voltmeter (resolution 10μV) and recorded by a data logger. The outer face of the downstream disk was heated up to 100°C by radiation from thirty 750-W electric firebar elements; the elements, which were stationary, were equispaced tangentially over the outer 180 mm of the disk.

In order to determine the effects of different inlet conditions and cavity geometries on the flow and heat transfer, a number of modifications were made to the basic rig. For some axial throughflow tests, an aluminium honeycomb (with 3-mm effective hole diameter and 77-mm long) flow straightener was inserted in the inlet tube immediately upstream of the upstream disk. In order to simulate the reduced hub diameter of a compressor stack, some axial throughflow tests were conducted with the inside diameter of the downstream disk reduced from 76 to 61 mm.

Details of the flow visualization and laser doppler anenometry, which was used to determine the flow structure, are given by Owen and Pincombe [5].

2.2 Analysis of Heat Transfer Data. As the method of analysis has been described elsewhere (see [1]), only the essential features are presented below.

At each test condition, twenty successive readings of the complete set of surface thermocouple e.m.f.s were recorded. From these, the mean temperature and standard deviation (typically 0.1°C) for each thermocouple location was calculated. The mean temperatures were fitted, by a cubic spline, to provide boundary conditions for Laplace's equation, where

$$\frac{1}{r}\frac{\partial}{\partial r}\left(r\frac{\partial T}{\partial r}\right)+\frac{\partial^2 T}{\partial z^2}=0 \tag{1}$$

At $r = a$ and $r = b$, the "one-dimensional assumption" that

$$\frac{1}{r}\frac{\partial}{\partial r}\left(r\frac{\partial T}{\partial r}\right)=-\frac{\partial^2 T}{\partial z^2}=0 \tag{2}$$

was made.

From the numerical solution of Laplace's equation, the heat flux, q, on the inner surface of the heated disk was found from a second-order, backward-difference formula. The local Nusselt number, Nu, was then calculated from

Nomenclature

a = inner radius of cavity
b = outer radius of cavity
c = constant
C_w = dimensionless coolant flow rate, $Q/\nu b$
G = gap ratio of cavity, s/b
Gr = Grashof number, $\beta\Delta T\Omega^2 b^4/\nu^2$
k = thermal conductivity
Nu = local Nusselt number, $qr/k(T_s - T_{ref})$
$\bar{Nu}$ = mean Nusselt number, $\bar{q}b/k(\bar{T}_s - T_{ref})$
Q = volumetric coolant flow rate
$q,\bar{q}$ = local, radially-weighted average heat flux
r = radius
Re_r = radial Reynolds number, $C_w/2\pi(r/b)$
Re_z = axial Reynolds number, $2\bar{W}a/\nu$ ($Re_z = 2bC_w/\pi a$)
Re_ϕ = rotational Reynolds number, $\Omega b^2/\nu$
s = axial width of cavity
$T_I, T_{ref}, T_S, \bar{T}_S$ = temperature of: coolant at inlet; reference; disk surface (local); disk surface (mean)
V_ϕ = tangential component of velocity referred to a stationary frame
$\bar{W}$ = bulk-average axial velocity in inlet pipe, $Q/\pi a^2$
Z = dimensionless parameter
β = volume expansion coefficient
ΔT = difference between maximum disk temperature and coolant temperature
ϵ = Rossby number, $\bar{W}/\Omega a$ ($\epsilon = \frac{1}{2}b^2 Re_z/a^2 Re_\phi$)
ν = kinematic viscosity
Ω = angular speed of cavity

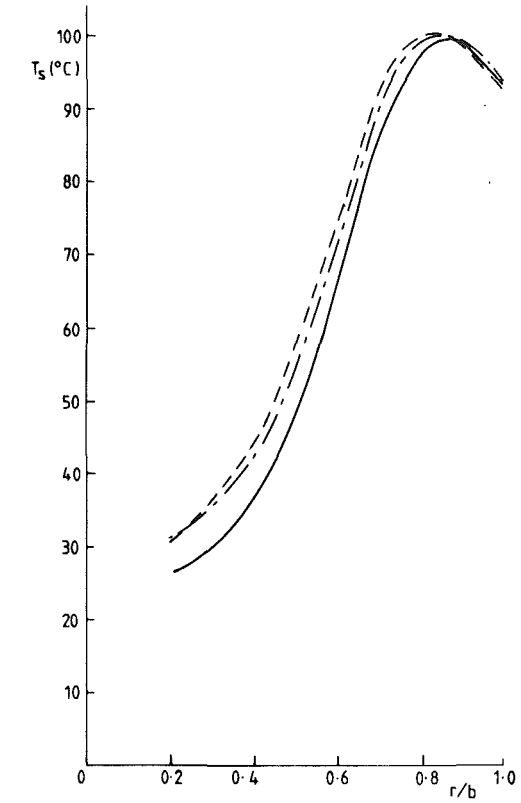

Fig. 2 Typical radial temperature profiles on the coolant-side face of the downstream disk for $G = 0.4$, $Re_z = 0.18 \times 10^5$; ---- $Re_\phi = 0.21 \times 10^5$; ·—— $Re_\phi = 10^5$; —— $Re_\phi = 2.5 \times 10^5$

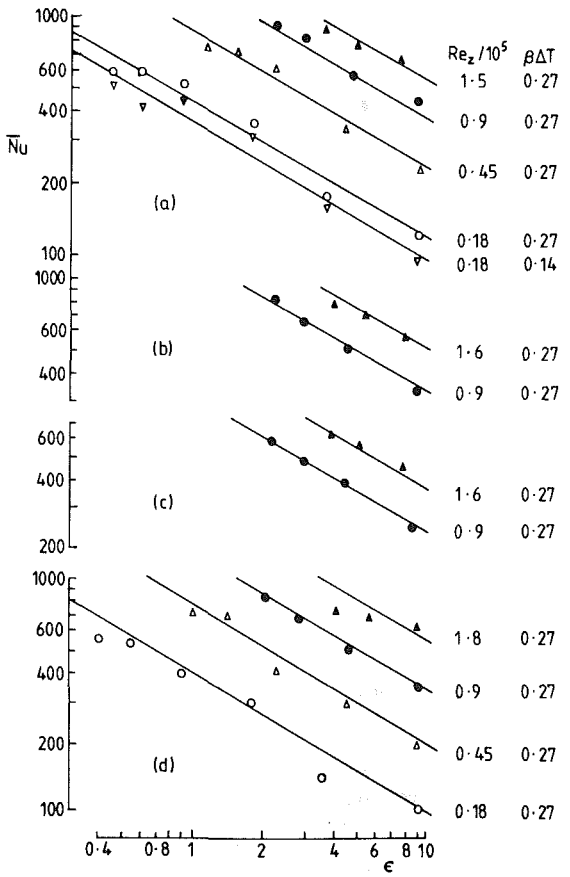

Fig. 3 Mean Nusselt number versus Rossby number for the downstream disk of a rotating cavity with an axial throughflow of coolant —— (equation 5) (*a*) $G = 0.4$, restricted; (*b*) $G = 0.267$, restricted; (*c*) $G = 0.133$, restricted; (*d*) $G = 0.267$, unrestricted

$$Nu = qr/k(T_s - T_{ref}) \quad (3)$$

where T_s is the local surface temperature and T_{ref} is a reference temperature. For the axial throughflow and radial outflow tests, T_{ref} was taken as the coolant inlet temperature, T_I; for the case of zero flow rate, T_{ref} was taken as the radially weighted average temperature of the inner surface of the unheated disk.

The mean Nusselt number was calculated from

$$\bar{Nu} = \bar{q}\, b/k(\bar{T}_s - T_{ref}) \quad (4)$$

where the overbar signifies the radially weighted average value.

It was shown by Owen [6] that small errors in surface temperature measurement can create large errors in heat flux computed from the numerical solution of Fourier's equation. Onur [7] used a similar method of analysis to estimate the errors caused for the numerical solution of Laplace's equation. Two main sources of temperature error were considered: electrical noise on the thermocouple readings, and distortion of the temperature field owing to the presence of the thermocouple. For the noise, the standard deviation of the twenty readings were used to calculate the 95 percent confidence interval for the time-averaged temperature; the distortion error was estimated from Turner's [8] results. The resulting errors in the computed Nusselt numbers depended largely on the magnitude of the Nusselt numbers. For a range of tests, it was found that the bias caused by distortion was approximately double the uncertainty caused by noise, and the combined effect could cause errors of 13 percent in the calculated mean Nusselt numbers. These errors in $\bar{Nu}$, which are usually much greater than the probable errors in the "independent dimensionless parameters" (G, C_w, Re_ϕ), can be bounded but cannot be removed.

3 The Axial Throughflow Tests

3.1 Flow Visualization. The radiant heaters produced temperature profiles, on the inner (coolant-side) face of the heated (downstream) disk of the cavity, similar to those shown in Fig. 2. Although the maximum temperature could be controlled, it always occurred at a radial location of $r/b \simeq 0.8$.

Optical measurements had previously been made by Owen and Pincombe [2] on a half-scale isothermal version of the present rig (but without the central drive-shaft) with a gap ratio of $G = 0.53$. For turbulent flow, flow visualization (using a smoke generator and slit illumination) revealed a toroidal vortex that decreased in size with increasing rotational speed. Also, for Rossby numbers in the range $21 \lesssim \epsilon \lesssim 100$, a dramatic spiral vortex breakdown (termed mode I*a* breakdown) was observed.

For the maximum gap ratio of the present rig, $G = 0.4$, flow visualization was conducted by replacing the paxolin shroud by a transparent polycarbonate shroud and using similar optical techniques to those employed by Owen and Pincombe. Under isothermal conditions, the flow structure was similar to that referred to above, and spiral vortex breakdown was observed for $23 \lesssim \epsilon \lesssim 50$. Flow visualization was more difficult under heated conditions, but for a maximum disk temperature of 50°C no change in the vortex breakdown was observed. The above tests were made with and without a flow straightener in the inlet, but no tests were conducted with a restriction in the outlet. Owing to the limited optical access, flow visualization was found to be unsatisfactory at smaller gap ratios.

3.2 Heat Transfer. For heat transfer in a rotating cavity, Bilimoria [9] had been unable to obtain any clear trends (apart from results at $G = 0.267$) from his measured Nusselt numbers. In the current program, a number of these tests

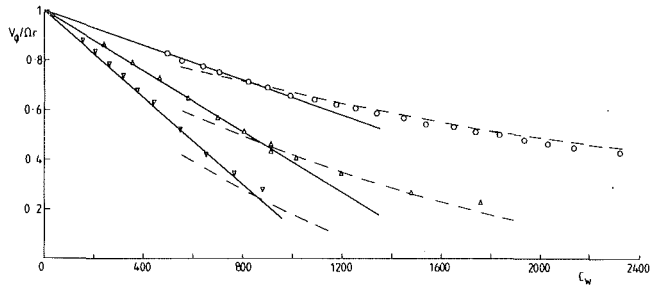

Fig. 4 The effect of flow rate on the tangential velocity in the central core for $r/b = 0.767$: ▽ $Re_\phi = 10^5$; △ $Re_\phi = 2 \times 10^5$; ○ $Re_\phi = 6 \times 10^5$ —— equation (8) ---- equation (10)

were repeated, for $G = 0.133$, 0.267, and 0.4, $Re_z = 0.18$ and 9×10^5, $2.3 \times 10^4 \leq Re_\phi \leq 2 \times 10^6$ with the flow straightener placed in the inlet. This was found to make no significant difference to the measured Nusselt numbers.

In addition to the above experiments, a number of heat transfer tests were conducted without the flow straightener but with a restricted outlet (as described in section 2.1). This was found to make a significant difference to the measured Nusselt numbers at $G = 0.133$ and 0.4 but not to those at $G = 0.267$. It was observed that at high rotational speeds (or, more precisely, at the smaller values of Rossby number), the mean Nusselt numbers now exhibited clear trends.

For $\epsilon \gtrsim 10$, in the restricted flow tests, no clear patterns could be seen; for $\epsilon \lesssim 10$ (where, according to Owen and Pincombe, vortex breakdown is confined to a central core that decreases in size with decreasing Rossby number), it emerged that $\bar{Nu} \propto \epsilon^{-0.6}$. Most of the tests were conducted with the maximum disk temperature at 100°C, but, at the higher rotational speeds, heater power limitations made this temperature impossible to achieve. To test the effect of temperature level on the results, a number of runs were made at $G = 0.4$ with the maximum temperature maintained at 60°C. Although accuracy was lower for these lower temperature tests, it was apparent that buoyancy effects were significant.

A correlation of the mean Nusselt numbers was obtained for $0.133 \leq G \leq 0.4$, $0.18 \times 10^5 \leq Re_z \leq 1.6 \times 10^5$, $0.4 \leq \epsilon \leq 10$ and $0.14 \leq \beta\Delta T \leq 0.27$ (where ΔT is the maximum temperature difference between the disk and the coolant inlet temperature, and β is the volume expansion coefficient). From a multiple regression analysis of 38 data points, the correlation coefficient was 0.981 and the correlation was obtained in the form

$$\bar{Nu} = 0.57\, G^{0.38} Re_z^{0.77} \epsilon^{-0.61} (\beta\Delta T)^{0.32} \tag{5}$$

As shown in Fig. 3, equation (5) not only fits the restricted outlet results with reasonable accuracy but also approximates the unrestricted outlet results of Bilimoria (which were not included in the correlation) for $G = 0.267$.

For a rapidly rotating cavity, it is appropriate to base a Grashof number, Gr, on the centripetal acceleration rather than on gravitational acceleration. It is convenient to define the Grashof number as

$$Gr \equiv \frac{\Omega^2 b^4 \beta\Delta T}{\nu^2} = Re_\phi^2 \beta\Delta T \tag{6}$$

that is

$$Gr \propto \epsilon^{-2} \beta\Delta T$$

If the Grashof number is used to correlate the data, the correlation becomes

$$\bar{Nu} = 0.050\, G^{0.38} Re_z^{0.15} Gr^{0.31} \tag{7}$$

and the correlation coefficient is unchanged at 0.981. It should be stressed that the above correlation is only valid for $0.133 \leq G \leq 0.4$, $1.8 \times 10^4 \leq Re_z \leq 1.6 \times 10^5$, and $9 \times 10^8 \leq Gr \leq 7 \times 10^{11}$.

At sufficiently small values of Re_z, it is to be expected that heat transfer will be caused by free convection alone; and, under these conditions, equation (7) will be inappropriate. In the above mixed convection regime, the axial throughflow acts as heat sink and removes much of the heat transferred into the cavity by the hot disk; in the free convection mode, heat can only be removed through the unheated disk and the shroud. The subject of free convection will be discussed further in section 4.2.

4 The Radial Outflow Tests

4.1 Flow Visualization. Some appreciation of the isothermal laminar flow structure inside a rotating cavity with a radial outflow of fluid can be gained by referring to Fig. 1(*b*). The inner layer has a substructure of its own: the flow enters axially, attaches to the downstream disk and moves radially outward as a wall jet; at the outer edge of the inner layer, some of this flow is released and is entrained into the boundary layer on the upstream disk. Outside the inner layer, the flow is equaly divided into the two Ekman layers, between which is a central core of fluid where axial and radial components of velocity are zero. The flow leaves the cavity via a relatively thin outer layer on the shroud.

From the linear theory of laminar flow in Ekman layers, see Hide [3], the tangential component of velocity in the central core is given by

$$\frac{V_\phi}{\Omega r} = 1 - \frac{1}{2\pi} \frac{C_w}{Re_\phi^{1/2}} \left(\frac{b}{r} \right)^2 \tag{8}$$

From this equation, V_ϕ is zero when

$$r/b = c\, C_w^{1/2} Re_\phi^{-1/4} \tag{9}$$

where $c = 0.399$. Owen and Pincombe [4] suggested that equation (9), with $c = 0.44$, provides a reasonable correlation for the radial extent of the inner layer. For sufficiently large values of C_w, or small values of Re_ϕ, the inner layer grows to meet the outer layer, and Ekman layer flows cannot exist.

Owen and Pincombe also observed that, at a critical value of Re_r ($Re_r = C_w/2\pi(r/b)$), "finger-like disturbances" appeared on the Ekman layers and propagated axially across the central core. For $Re_r \gtrsim 200$, measured values of the tangential component of velocity departed significantly from the linear laminar theory, and this was attributed to the onset of turbulent flow. These "finger-like disturbances," and the flow structure described above, were also observed in the current series of tests.

In the present tests, which were conducted with $G = 0.133$, laser doppler anenometry was used to measure the tangential component of velocity in the central core, and the results were compared with equation (8), for laminar flow, and solutions of the linear integral momentum equations (see Owen and Rogers [10]) for turbulent flow. The isothermal turbulent flow solution is

$$\frac{V_\phi}{\Omega r} = 1 - \frac{2.22\, C_w^{5/8}}{Re_\phi^{1/2}} \left(\frac{b}{r} \right)^{13/8} \tag{10}$$

and it is interesting to note that equations (8) and (10) are equal when $Re_r = 180$. For $C_w \leq 2400$ and $Re \leq 10^6$, measurements obtained by J. R. Pincombe (see Onur [7]) were in good agreement with equations (8) and (10). Figure 4 shows results obtained at $r/b = 0.767$ for a range of C_w at three different values of Re_ϕ, and the laminar to turbulent transition at $C_w \simeq 860$ ($Re_r \simeq 180$) can be clearly seen.

Equation (10) implies that V_ϕ is negative for

$$r/b < 1.63\, C_w^{5/13} Re_\phi^{-4/13} \tag{11}$$

but negative values of V_ϕ were never observed. In fact, as was the case in laminar flow, it appeared that the inner layer extended to the radius where the velocity in the central core

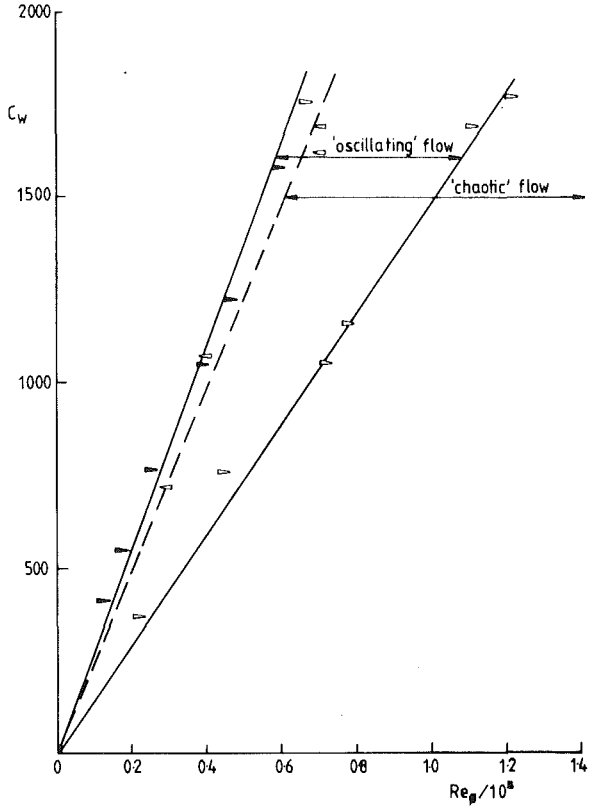

Fig. 5 The delineation of "oscillating" and "chaotic" flow by flow visualisation ($\beta\Delta T = 0.27$):
▶ The start of oscillations (Re_ϕ increasing)
▷ The start of chaotic flow (Re_ϕ increasing)
◁ The end of chaotic flow and the start of oscillating flow (Re_ϕ decreasing)

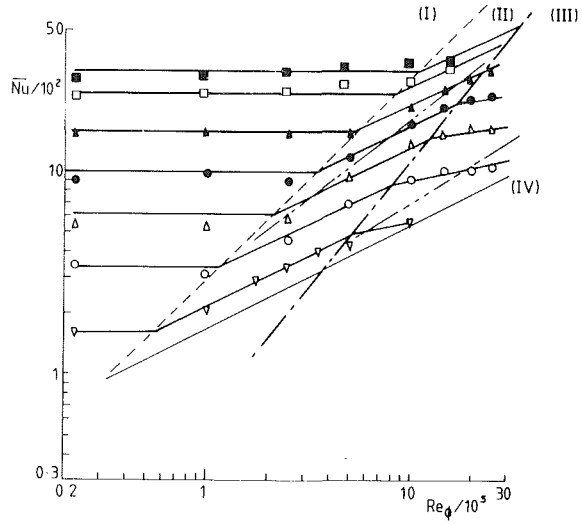

Fig. 6 Mean Nusselt numbers for radial outflow at $G = 0.4$ (downstream disk heated T 0.27)

Symbol	▽	○	△	●	▲	□	■
$C_w/10^4$	0.09	0.28	0.71	1.4	2.8	5.4	7.9

—— equation (14), ---- equation (15*a*), — — — equation (15*b*) — — — — equation (12), — — — — — equation (13)

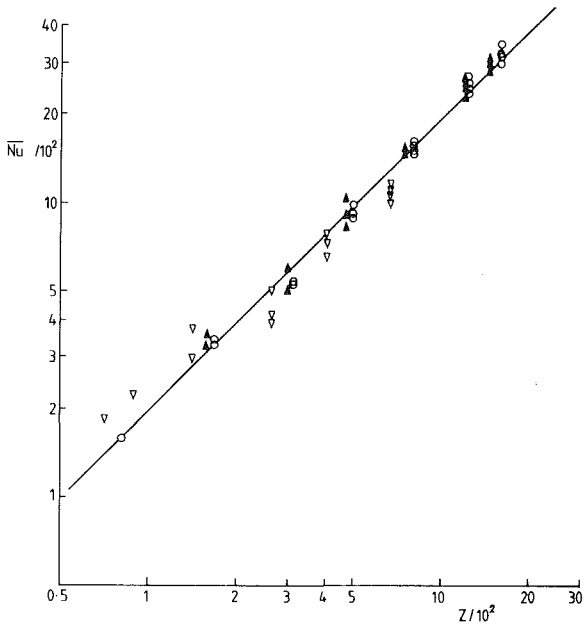

Fig. 7 The variation of mean Nusselt numbers with $Z(Z \equiv C_w^{2/3} G^{1/6})$ in regime I for radial outflow: ○ $G = 0.4$, ▲ $G = 0.267$, ▽ $G = 0.133$, —— equation (14*a*)

was approximately zero. Using this criterion in equation (10), the limiting case for the central core to appear is when V_ϕ is zero and $r/b = 1$, that is, when

$$Re_\phi = 4.93\ C_w^{5/4} \tag{12}$$

For Reynolds number below this value, the inner and outer layers would be expected to merge and turbulent Ekman layer flow could not occur. It should be emphasized, however, that equation (12) is based on the solutions of the linear turbulent integral momentum equations; for small values of $V_\phi/\Omega r$, nonlinear effects are likely to be significant.

Flow visualization was also conducted with the downstream disk heated to a maximum temperature of 100°C ($\beta\Delta T \simeq 0.27$). At a "critical speed," after the Ekman layers had become well established, the inner layer began to oscillate with a frequency approximately 70 percent of the cavity rotational frequency. At a higher "second critical speed," the flow structure became "chaotic" (when viewed by the naked eye) and smoke appeared to fill the entire cavity making further flow visualization impossible. Photographs taken during this "chaotic" condition revealed that the flow had broken down into a number of cells of alternate Ekman layer and non-Ekman layer flow: the "chaotic" appearance was created by a superposition of these alternating images. There was some evidence to suggest that radial inflow occurred, on the heated disk, during chaotic flow; this, it was believed, was caused by the dominance of buoyancy forces, and signaled the onset of free convection.

The "oscillating" and "chaotic" modes were not observed in isothermal flow; and, in order to establish the condition under which these modes appeared when the downstream disk was heated, a separate series of flow visualization tests was conducted. For a fixed flow rate, in the range $350 < C_w <$ 1750, the rotational speed was increased until the "oscillating," then the "chaotic," mode occurred, and Fig. 5 shows the results obtained for $\beta\Delta T \simeq 0.27$. It was found that the oscillating mode started at $Re_\phi/C_w \simeq 350$, and the chaotic mode at $Re_\phi/C_w \simeq 640$; however, once established the speed had to be reduced significantly before the chaotic flow disappeared. From tests with $\beta\Delta T \simeq 0.14$, it was found that oscillating flow was delayed until $Re_\phi/C_w \simeq 450$. It was, therefore, presumed that these buoyancy-induced effects were associated with the Grashof number ($Gr = \beta\Delta T\, Re_\phi^2$); and the oscillating and chaotic modes wer considered to occur when

$$Gr^{1/2}/C_w = C \tag{13}$$

where $C \simeq 180$ for oscillating flow and $C \simeq 330$ for chaotic flow. As is suggested in Section 4.2, equation (13) can be used to estimate the onset of free convection.

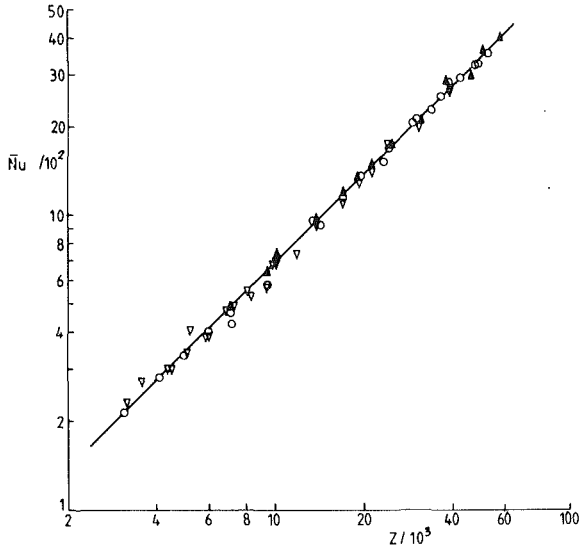

Fig. 8 The variation of mean Nusselt number with $Z(Z \equiv C_w^{1/3}\mathrm{Re}_\phi^{1/2})$ in regime II for radial outflow: ○ $G = 0.4$, ▲ $G = 0.267$, ▽ $G = 0.133$ —— equation (14*b*)

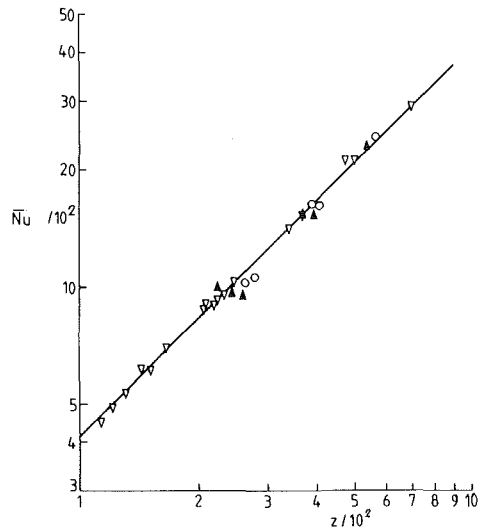

Fig. 9 The variation of mean Nusselt number with $Z(Z \equiv C_w^{1/2}\mathrm{Re}_\phi^{1/9}G^{1/9})$ in regime III for radial outflow: ○ $G = 0.4$, ▲ $G = 0.267$, ▽ $G = 0.133$ —— equation (14*c*)

4.2 Heat Transfer. At the lower rotational speeds, heat transfer would be expected to be controlled by flow in the inner layer; at the higher speeds, the flow in the Ekman layers and the effects of buoyancy would be expected to dominate. In fact, four regimes of heat transfer were identified, and the mean Nusselt numbers for the heated downstream disk are shown in Fig. 6 for $G = 0.4$; similar results were obtained for $G = 0.133$ and 0.267. Owing to the leakage, which was mentioned in section 2, there is doubt about the accuracy of the results for $C_w = 940$ (particularly at the lower values of the mean Nusselt number, where the low flux levels make accurate computation difficult). Three of these regimes were formerly identified by Owen and Bilimoria [1], but the fourth (which is believed to be a free convection regime) had not been previously observed.

Mean Nusselt numbers in each of these regimes were correlated using a multiple regression analysis (see Onur [7]), and the results are given below.

Regime I:

$$\bar{\mathrm{Nu}} = 1.94\, G^{1/6} C_w^{2/3} \tag{14a}$$

Regime II:

$$\bar{\mathrm{Nu}} = 0.07\, C_w^{1/3} \mathrm{Re}_\phi^{1/2} \tag{14b}$$

Regime III:

$$\bar{\mathrm{Nu}} = 4.11\, G^{1/9} C_w^{1/2} \mathrm{Re}_\phi^{1/9} \tag{14c}$$

Regime IV:

$$\bar{\mathrm{Nu}} = 0.707\, \mathrm{Gr}^{0.256} G^{0.1} \tag{14d}$$

For regimes I, II and III, correlations were based on results for $\beta\Delta T \simeq 0.27$, $G = 0.133$, 0.267, and 0.400, $970 \le C_w \le 79{,}000$ and $2 \times 10^4 \le \mathrm{Re}_\phi \le 2.2 \times 10^6$. For regime IV, the correlations were based on results for $G = 0.133$ and 0.400, $C_w \le 1500$, $10^9 \le \mathrm{Gr} \le 1.3 \times 10^{12}$. The number of data points used to correlate regimes I, II, III and IV were 55, 62, 30, and 41, respectively, and the correlation coefficients were 0.986, 0.998, 0.996 and 0.963, respectively. It should again be pointed out that, owing to leakage, flow measurement at the smaller values of C_w was subject to errors. However, in regime IV, where the values of C_w were small, the effect of flow rate on the mean Nusselt number was very weak.

The boundary between regimes I and II was found by equating equations (14*b*) and (14*c*) to give

$$G^{-1/6} C_w^{-1/3} \mathrm{Re}_\phi^{1/2} = 28 \tag{15a}$$

Similarly, the boundary between regimes II and III was found by equating equations (14*a*) and (14*b*) to give

$$G^{-1/6} C_w^{-1/4} \mathrm{Re}_\phi^{7/12} = 450 \tag{15b}$$

It is considered that regime I, in which rotational speed has no effect on heat transfer, is attributable to the case where the inner layer fills the cavity. However, if equation (12) gives the value of Re_ϕ below which Ekman layers cannot exist, then it would appear from Fig. 6 that regime II occurs before Ekman layers are established. The start of the buoyancy-induced "chaotic flow," equation (13) with $C = 330$, is shown to occur in regime III on Fig. 6. It would seem that, as suggested in section 4.1, the "chaotic flow" is associated with velocity reversals on the heated disk and the onset of free convection. For the heat transfer tests, equation (13) can be used to estimate the onset of free convection, but the value of C was found to depend weakly on the gap ratio and on C_w. However, for the experimental range of the correlations, free convection dominates for

$$\mathrm{Gr}^{1/2}/C_w \gtrsim 530 \tag{16}$$

The correlations for regimes I to IV are illustrated in Figs. 7–10.

Just as free convection occurs at large values of Gr for radial outflow, so it should for an axial throughflow of coolant. Accordingly, a combined correlation was obtained using results from the radial outflow and axial throughflow tests. For the axial throughflow case, the results were taken from tests at $G = 0.133$, $0 \le \mathrm{Re}_z \le 0.9 \times 10^5$, $10^5 \le \mathrm{Re}_\phi \le 2.2 \times 10^6$, and $G = 0.400$, $\mathrm{Re}_z = 0$, $2.5 \times 10^5 \le \mathrm{Re}_\phi \le 2.2 \times 10^6$. For the zero flow case, the reference temperature for the axial throughflow tests was taken as the average temperature of the unheated upstream disk (which, for tests with $\mathrm{Re}_z > 0$, was not significantly different to the coolant inlet temperature).

For 70 experimental results, the combined correlation was

$$\bar{\mathrm{Nu}} = 0.267\, \mathrm{Gr}^{0.286} \tag{17}$$

and the correlation coefficient was 0.956. Equation (17) and the associated experimental results are shown in Fig. 11. It is interesting to observe that equation (17) lies between the accepted laminar ($\bar{\mathrm{Nu}} = 0.59\,(\mathrm{GrPr})^{1/4}$) and turbulent ($\bar{\mathrm{Nu}} = 0.13\,(\mathrm{GrPr})^{1/3}$) correlations for free convection from a vertical plate (see McAdams [11]) if the disk radius is used for the linear dimension and $\Omega^2 b$ is used in place of the gravitational acceleration.

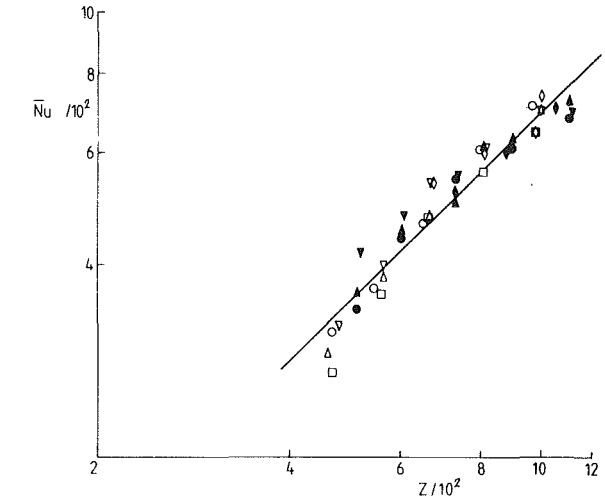

Fig. 10 The variation of mean Nusselt nubmers with $Z(Z \equiv Gr^{0.256}G^{0.1})$ in regime (IV) for radial outflow:
$G = 0.133$ ○ □ △ ▽ ◇
$G = 0.4$ ● ▲ ▼ ◆
C_w 0 110 390 710 940
—— equation (14*d*)

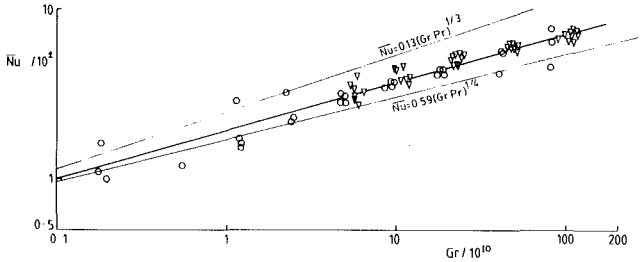

Fig. 11 The variation of mean Nusselt numbers with Grashof number in regime IV for radial outflow and axial throughflow: ○ axial throughflow, ▽ radial outflow, —— equation (17)

It should be pointed out that during the free convection experiments the temperature and flow rate were often unsteady, and the regime IV results tend to be less reliable (as suggested by the lower correlation coefficient) than those in the other regimes. As regime IV is of great practical significance, it is hoped that future theoretical and experimental work will enable more precise correlations to be made for free convection in a rotating cavity.

5 Conclusions

Flow visualization, laser doppler anemometry and heat transfer measurements have been made in a rotating cavity with either an axial throughflow or a radial outflow of coolant.

For the axial throughflow tests, flow visualization has revealed the presence of spiral vortex breakdown; and as found in earlier isothermal tests (see [2]), the occurrence and scale of this breakdown depends on the Rossby number. For small Rossby numbers, where the effects of vortex breakdown are reduced, the mean Nusselt number, $\bar{Nu}$, of the heated downstream disk of the cavity was correlated in terms of the gap ratio, G, the axial Reynolds number, Re_z, and the rotational Grashof number, Gr. For $0.133 \leq G \leq 0.4$, $1.8 \times 10^4 \leq Re_z \leq 1.6 \times 10^5$, $9 \times 10^8 \leq Gr \leq 7 \times 10^{11}$, the mean Nusselt number was correlated by $\bar{Nu} = 0.050\, G^{0.38}\, Re_z^{0.15}\, Gr^{0.31}$.

For the radial outflow tests, flow visualization was used to study the "classic structure," where Ekman layers form on the disks and a central core of inviscid fluid occurs between the Ekman layers and the inner and outer (source and sink) layers. Under isothermal conditions, measurements of the tangential component of velocity inside the central core were in good agreement with the solutions of the linear Ekman layer equations for both laminar and turbulent flow. For a constant flow rate, and with the downstream disk heated, it was observed that, when the rotational speed was increased past a critical point the inner layer began to oscillate, and at higher speeds the "classic structure" broke down into a "chaotic" flow. The occurrence of this behaviour depended on the dimensionless flow rate, C_w, and the rotational Grashof number, Gr. The "oscillating" and "chaotic" behaviour (which started at $Gr^{1/2}/C_w \simeq 180$ and 330, respectively) was believed to signal the onset of free convection.

For the three (forced convection) regimes of heat transfer identified by Owen and Bilimoria [1], for a rotating cavity with a radial outflow of coolant, correlations were obtained for the mean Nusselt number. The correlations were obtained for $0.133 \leq G \leq 0.4$, $970 \leq C_w \leq 79{,}000$ and $2 \times 10^4 \leq Re_\phi \leq 2.2 \times 10^6$. In addition, a fourth (free convection) regime was identified for $Gr^{1/2}/C_w \gtrsim 530$ (after the appearance of the "oscillating" and "chaotic" flow referred to above). For this regime, the mean Nusselt numbers for the radial outflow case, with $10^9 \leq Gr \leq 1.3 \times 10^{12}$, (together with some results for the axial throughflow case) were correlated by

$$\bar{Nu} = 0.267\, Gr^{0.286}$$

Acknowledgments

The authors wish to thank Rolls Royce Limited for funding the work described in this paper, and are grateful to Mr. J. R. Pincombe for providing the LDA measurements.

References

1 Owen, J. M., and Bilimoria, E. D., "Heat Transfer in Rotating Cylindrical Cavities," *J. Mech. Engng. Sci.*, Vol. 19, 1977, p. 175.

2 Owen, J. M., and Pincombe, J. R., "Vortex Breakdown in a Rotating Cylindrical Cavity," *Journal of Fluid Mechanics*, Vol. 90, 1979, p. 109.

3 Hide, R., "On Source-Sink Flows in a Rotating Fluid," *Journal of Fluid Mechanics*, Vol. 32, 1968, p. 737.

4 Owen, J. M., and Pincombe, J. R., "Velocity Measurements Inside a Rotating Cylindrical Cavity With Radial Outflow of Fluid," *Journal of Fluid Mechanics*, Vol. 99, 1980, p. 111.

5 Owen, J. M., and Pincombe, J. R., "The Use of Optical Techniques in the Interpretation of Heat Transfer Measurements," AGARD-CP-281, 1980, Paper No. 15.

6 Owen, J. M., "On the Computation of Heat Transfer Coefficients From Imperfect Temperature Measurements," *J. Mech. Engng. Sci.*, Vol. 21, 1979, p. 323.

7 Onur, H. S., "Convective Heat Transfer in Rotating Cavities," D. Phil. thesis, Sussex University, 1980.

8 Turner, A. B., "Heat Transfer Instrumentation," AGARD-CP-73, 1970, Paper No. 5.

9 Bilimoria, E. D., "Heat Transfer in Rotating Cylindrical Cavities," D. Phil. thesis, Sussex University, 1977.

10 Owen, J. M., and Rogers, R. H., "Solution of the Integral Momentum Equations for an Ekman Layer in a Heated Rotating Cavity," pt. 1, Report No. 80/TFMRC/15, 1980, School of Engineering and Applied Sciences, Sussex University.

11 McAdams, W. H., *Heat Transmission*, 3rd ed., McGraw-Hill, New York, 1954.

Time-Marching Analysis of Steady Transonic Flow in Turbomachinery Cascades Using the Hopscotch Method

R. A. Delaney
Research Scientist, Analytical Mechanics,
Detroit Diesel Allison Division,
General Motors Corporation,
Indianapolis, Ind. 46206

A rapid, time-marching, numerical scheme based on the hopscotch method is presented for solution of steady, two-dimensional, transonic flow in turbomachinery cascades. The scheme is applied to the strong-conservation form of the unsteady Euler equations written in arbitrary curvilinear coordinates. Cascade solutions are obtained on an orthogonal, body-centered coordinate system. Numerical solution results for two turbine cascades are presented and compared with experimental data to demonstrate the accuracy and computational efficiency of the analysis method.

Introduction

Local Mach number levels in the compressor and turbine components of advanced-technology gas turbine engines have been driven well into the supersonic regime; as a result, the effect of shock waves on aerodynamic performance has become an important turbomachinery design consideration. In order to assess this effect, improved transonic flow cascade analysis methods must be developed. To be effective design tools, these improved methods must be accurate, stable, and computationally efficient. Additionally, they must be capable of treating the broad range of airfoil geometries and flow conditions encountered in modern turbomachines.

The available transonic flow analysis methods can be categorized according to governing equation type as time-dependent, Navier-Stokes equation solvers [1–4], time-dependent, Euler equation solvers [5–10], and full-potential equation solvers [11–13]. Of these methods, the time-dependent, Euler equation solvers are the only methods which currently satisfy all of the established criteria. Although the unsteady Navier-Stokes solvers are considered the ultimate methods in terms of analysis capability, they require excessive computing time and, therefore, cannot be considered for the routine turbomachinery design and analysis tasks. Full-potential equation solvers, on the other hand, are very rapid, but they are limited to low supersonic Mach numbers as a result of the inherent irrotational flow assumption.

There are two basic numerical solution techniques currently in use for the time-dependent Euler equations. The first is the class of explicit methods. The finite difference method of MacCormack [5] and the finite area method of McDonald [7] fall under this general classification. Both of these methods have been applied with some success to transonic cascade flows [6–10]. In general, explicit methods are easily implemented, but they suffer from long computational times due to the time-step-limiting CFL stability criterion.

The second basic class of methods used to solve the unsteady Euler equations is the implicit method. Recently, Steger [1] employed the implicit approximate-factorization scheme, originally developed by Beam and Warming [3], to solve a steady transonic flow in a compressor cascade. The often-expressed advantage of implicit schemes over the explicit schemes is that they are unconditionally stable regardless of the size of the time increment; therefore, fewer time steps are required to converge the solutions. Steger did not realize this advantage, as he reports a large number of time steps (3000) were needed to obtain his steady-state results.

In addition to these basic methods, there exists a family of hopscotch methods aimed at combining the positive features of both the explicit and implicit schemes. Scala and Gordon [14] first proposed these mixed-type schemes for solution of the time-dependent, Navier-Stokes equations. The basic concept underlying these methods is to combine explicit and implicit finite-difference formulas at alternate points in the computational mesh. Gourlay [15] first gave a formal analysis of the hopscotch process, applied to elliptic and parabolic partial differential equations. Later, Gourlay and Morris [16] studied the application of the hopscotch method to hyperbolic systems. They determined that the hopscotch version of the Lax scheme [17] is computationally explicit, possesses optimal pseudoviscosity damping characteristics, and has a substantial computational speed advantage over other explicit methods.

In this paper, a two-dimensional version of the hopscotch-Lax method is applied to the unsteady Euler equations written in strong conservation form in arbitrary curvilinear coor-

Contributed by the Gas Turbine Division of THE AMERICAN SOCIETY OF MECHANICAL ENGINEERS and presented at the 27th International Gas Turbine Conference and Exhibit, London, England, April 18-22, 1982. Manuscript received at ASME Headquarters December 14, 1981. Paper No. 82-GT-152.

dinates. The numerical method is applied to the computation of transonic turbomachinery cascade flows on the body-centered coordinate system developed by Adamczyk [18]. Finally, numerical solution results are presented for two turbine cascades and compared with experimental data to demonstrate the accuracy and computational efficiency of the analysis method.

Governing Equations

The strong conservation form of the unsteady, two-dimensional Euler equations in Cartesian coordinates can be written in nondimensional variables as

$$\frac{\partial E}{\partial t}+\frac{\partial F}{\partial x}+\frac{\partial G}{\partial y}=0 \tag{1}$$

where

$$E=\begin{bmatrix}\rho\\ \rho u\\ \rho v\\ \rho e_o\end{bmatrix},\ F=\begin{bmatrix}\rho u\\ \rho u^2+p\\ \rho uv\\ u(\rho e_o+p)\end{bmatrix},\ G=\begin{bmatrix}\rho v\\ \rho uv\\ \rho v^2+p\\ v(\rho e_o+p)\end{bmatrix}$$

and where ρ is the density, p is the pressure, u and v are the velocity components in the x- and y-directions, respectively, and e_o is the total internal energy. The definition of e_o gives the additional relation

$$e_o=\frac{p}{(\gamma-1)\rho}+\frac{1}{2}(u^2+v^2) \tag{2}$$

where γ is the ratio of specific heats.

For the steady flow problem of interest, the full energy equation is eliminated in favor of the steady state adiabatic flow relation

$$h_o=\frac{\gamma p}{(\gamma-1)\rho}+\frac{1}{2}(u^2+v^2)=\text{constant} \tag{3}$$

where h_o is the total enthalpy. Veuillot [9] and Ni [10] have used this simplification, and it leads to a substantial reduction in the computational effort required to converge the solution.

For the numerical solution of the Euler equations, it is desirable first to rewrite the equations in an arbitrary cuvilinear coordinate system. If

$$\xi=\xi(x,y) \tag{4}$$

$$\eta=\eta(x,y) \tag{5}$$

represent the general transformation equations from the

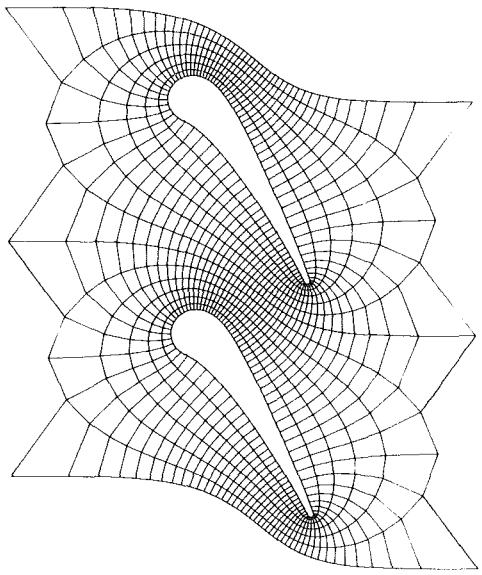

Fig. 1 Airfoil geometry and coordinate system for low-solidity turbine vane cascade

Cartesian coordinates to the curvilinear coordinates, ξ, η, then the system of equations – equation (1) with the energy equation omitted – can be rewritten in strong conservation form – see Steger [2] – as

$$\frac{\partial E'}{\partial t}+\frac{\partial F'}{\partial \xi}+\frac{\partial G'}{\partial \eta}=0 \tag{6}$$

where

$$E'=\frac{1}{J}\begin{bmatrix}\rho\\ \rho u\\ \rho v\end{bmatrix},\ F'=\frac{1}{J}\begin{bmatrix}\rho U\\ \rho uU+\xi_x p\\ \rho vU+\xi_y p\end{bmatrix},\ G'=\frac{1}{J}\begin{bmatrix}\rho V\\ \rho uV+\eta_x p\\ \rho vV+\eta_y p\end{bmatrix}$$

with

$$U=\xi_x u+\xi_y v$$

$$V=\eta_x u+\eta_y v$$

$$J=\xi_x\eta_y-\xi_y\eta_x=\frac{1}{x_\xi y_\eta-x_\eta y_\xi}$$

where U and V are the contravariant velocity components in the ξ and η directions, respectively, and J is the Jacobian of the transformation. The metrics ξ_x, ξ_y, η_x, η_y, appearing in

Nomenclature

C = airfoil chord
C_x = projection of C onto x-axis
CFL = Courant-Friedrichs-Lewy
CPU = Central Processor Unit
e_o = total internal energy
h_o = total enthalpy
i, j, n = grid point indices in x, y, and t coordinates, respectively
J = Jacobian of coordinate transformation
N_ξ, N_η = maximum grid indices in ξ and η coordinate directions, respectively
p = static pressure
p_o = total pressure
t = time
U, V = contravariant velocity components in ξ and η coordinate directions, respectively
u, v = velocity components in x and y coordinate directions, respectively
x, y = Cartesian coordinates
α_ξ, α_η = damping coefficients in ξ and η coordinates, respectively
γ = ratio of specific heats
ξ, η = curvilinear coordinates (rectangular coordinates in computational plane)
ρ = static density
ρ_o = total density

Subscripts

x, y = derivatives in x and y coordinates, respectively
ξ, η = derivatives in ξ and η coordinates, respectively
1 = uniform upstream condition
$'$ = normalized variable

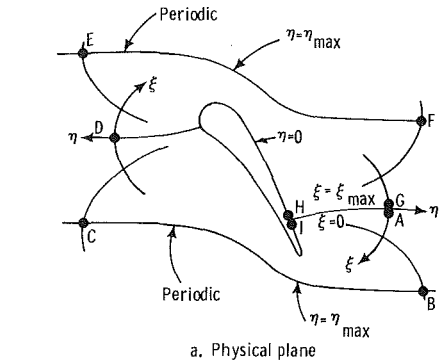

a. Physical plane

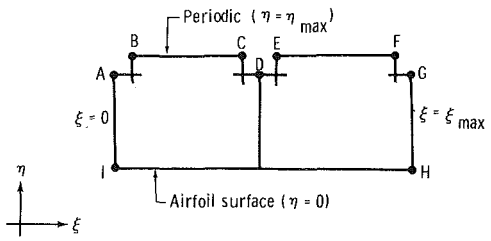

b. Computational plane

Fig. 2 Schematic of mapping from physical plane to computational plane for "0-type" grid

the above relations, are obtained from the derivatives x_ξ, x_η, y_ξ, and y_η using the identities

$$\xi_x = Jy_\eta,\ \xi_y = -Jx_\eta,\ \eta_x = -Jy_\xi,\ \eta_y = Jx_\xi$$

These transformation equations are applicable to any arbitrary curvilinear coordinate system for which the Jacobian is nonsingular.

Coordinate System

The coordinate system used for the cascade analysis is a body-conforming, "0-type," orthogonal construction, shown in Fig. 1 for a turbine vane. The coordinate generation scheme, recently developed by Adamczyk [18], has the attractive features of providing automatic mesh clustering in regions of high airfoil surface curvature and producing periodic grids for ease of enforcing the cascade periodic-flow requirement.

Adamczyk uses a hybrid approach for the coordinate system construction. Briefly, the grid point distributions along the airfoil surface and outer periodic boundaries, shown in Fig. 2, are determined first using an electrostatic analog describing the potential field around an infinite cascade. The interior-node coordinates are then determined by solving the set of Laplace equations

$$x_{\xi\xi} + x_{\eta\eta} = 0 \tag{7}$$

$$y_{\xi\xi} + y_{\eta\eta} = 0 \tag{8}$$

This system of elliptic partial differential equations is solved in the rectangular computational plane (see Fig. 2) using standard successive overrelaxation techniques.

Once the coordinate system is constructed, the coordinate derivatives x_ξ, x_η, y_ξ, y_η, needed for determination of the metrics ξ_x, ξ_y, η_x, η_y, can be obtained by simply taking finite differences of the known x, y coordinates in the rectangular computational plane. However, as Steger [2] and Hindman [19] note, certain requirements must be met when forming these derivatives in order to minimize geometrically induced errors. The first requirement is to satisfy the grid conservation law which states that the differencing procedure (backward, forward, or centered) used to form the derivatives must be identical to that used to approximate the spatial derivatives in the governing system of equations, equation (6). It is a simple matter to show that if this requirement is not met for the case of uniform flow, the solution algorithm will not reproduce the known uniform conditions. The additional obvious constraint on the coordinate derivatives is that the difference representations should be good approximations to the exact derivatives.

Numerical Solution Algorithm

A modified version of the hopscotch-Lax scheme developed by Gourlay and Morris [16] is used to solve the system of Euler equations. The hopscotch algorithm is a two-sweep scheme employing central differences for the spatial derivatives and forward and backward differences for the time derivatives. Applied to the system of Euler equations, equation (6) (with primes omitted), the algorithm is expressed as

(first sweep, $i+j+n$ even)

$$E_{i,1}^{n+1} = E_{i,j}^n - \frac{\Delta t}{2\Delta\xi}(F_{i+1,j}^n - F_{i-1,j}^n) - \frac{\Delta t}{2\Delta\eta}(G_{i,j+1}^n - G_{i,j-1}^n) + \alpha_\xi(E_{i+1,j}^n - 2E_{i,j}^n + E_{i-1,j}^n) + \alpha_\eta(E_{i,j+1}^n - 2E_{i,j}^n + E_{i,j-1}^n) \tag{9}$$

(second sweep, $i+j+n$ odd)

$$E_{i,j}^{n+1} = E_{i,j}^n - \frac{\Delta t}{2\Delta\xi}(F_{i+1,j}^{n+1} - F_{i-1,j}^{n+1}) - \frac{\Delta t}{2\Delta\eta}(G_{i,j+1}^{n+1} - G_{i,j-1}^{n+1}) + \alpha_\xi(E_{i+1,j}^{n+1} - 2E_{i,j}^{n+1} + E_{i-1,j}^{n+1}) + \alpha_\eta(E_{i,j+1}^{n+1} - 2E_{i,j}^{n+1} + E_{i,j-1}^{n+1}) \tag{10}$$

where $\xi = i\Delta\xi$, $\eta = j\Delta\eta$, and $t = n\Delta t$ and where the last two terms are added second-order damping terms (artificial viscous damping), needed to stabilize the solution in regions of large gradients. Consistent with the grid conservation law, the metrics used in forming the F and G flux terms are evaluated using central differences.

Gourlay and Morris [16] found through repetitive application of this two-sweep process that the first sweep is equivalent to a simple linear extrapolation in time of the dependent variables, i.e.,

$$E_{i,j}^{n+1} = 2E_{i,j}^n - E_{i,j}^{n-1} \tag{11}$$

This simplification results in nearly a twofold increase in the computational speed of the algorithm. Note that the three time level process indicated in equation (11) requires only two time level computer storage since $E_{i,j}^{n-1}$ can be overwritten with $E_{i,j}^{n+1}$.

A linear stability analysis of the hopscotch algorithm – see Gourlay and Morris [16] – shows it to be stable for all positive values of the damping coefficients ($\alpha_\xi \geq 0$, $\alpha_\eta \geq 0$) with all Δt satisfying the CFL stability criterion,

$$\Delta t \leq \left\{ \frac{1}{\Delta\xi}\left[\left(\frac{\gamma+1}{2\gamma}\right)|U| + \sqrt{\left(\frac{\gamma-1}{2\gamma}\right)^2 U^2 + (\xi_x^2 + \xi_y^2)\frac{p}{\rho}}\right] + \frac{1}{\Delta\eta}\left[\left(\frac{\gamma+1}{2\gamma}\right)|V| + \sqrt{\left(\frac{\gamma-1}{2\gamma}\right)^2 V^2 + (\eta_x^2 + \eta_y^2)\frac{p}{\rho}}\right]\right\}^{-1} \tag{12}$$

This freedom of choice in the magnitude of α_ξ and α_η is in

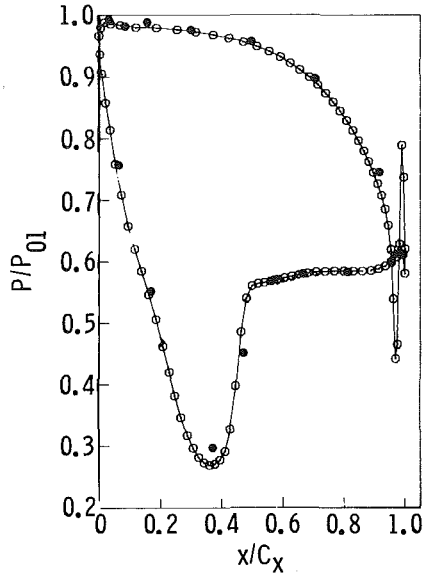

Fig. 3 Airfoil surface static pressure distributions for low-solidity turbine vane cascade: M_2 = 0.85 (• – experimental data, ○ – numerical solution)

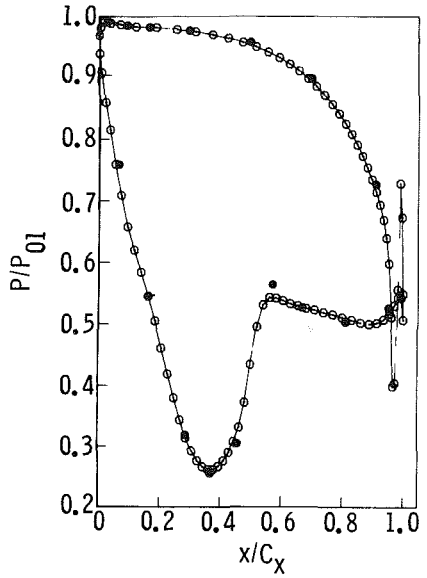

Fig. 4 Airfoil surface static pressure distributions for low-solidity turbine vane cascade: M_2 = 0.95 (• – experimental data, ○ – numerical solution)

marked contrast to the original Lax scheme [17], which has an upper stability bound on the magnitude of the damping coefficients. The independence of the damping coefficients and the time increment permits an arbitrary variation in the amount of damping introduced during the computation without limiting the allowable time increment.

The hopscotch algorithm is first-order time accurate, which is sufficient for the present application where only the steady-state solution is of interest. Second-order spatial accuracy is ensured if the damping coefficients α_ξ, α_η, appearing in equation (10), are at most of order $\Delta\xi$, $\Delta\eta$, respectively. Suitable forms for these coefficients, meeting this criterion in most of the flow field, have been found to be

$$\alpha_\xi = \alpha'_\xi + 0.5\,|p^{n+1}_{i+1,j} - 2p^n_{i,j} + p^{n+1}_{i-1,j}\,|/p^n_{i,j} \tag{13}$$

$$\alpha_\eta = \alpha'_\eta + 0.5\,|p^{n+1}_{i,j+1} - 2p^n_{i,j} + p^{n+1}_{i,j-1}\,|/p^n_{i,j} \tag{14}$$

where

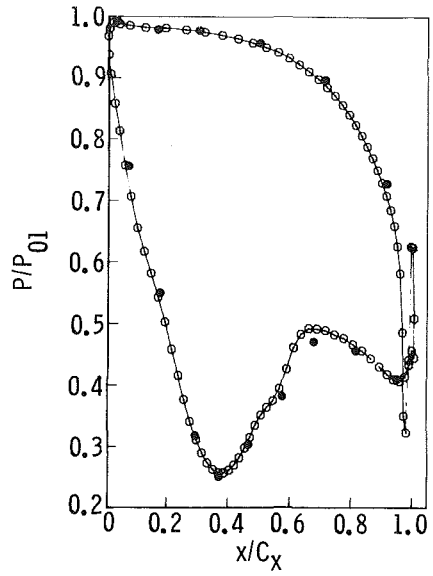

Fig. 5 Airfoil surface static pressure distributions for low-solidity turbine vane cascade: M_2 = 1.05 (• – experimental data, ○ – numerical solution)

$$0 \le \alpha'_\xi \le \frac{1}{N_\xi}$$

$$0 \le \alpha'_\eta \le \frac{1}{N_\eta}$$

and where N_ξ and N_η are the maximum grid indices in the ξ and η directions, respectively. The terms proportional to the second derivatives of pressure in equations (13) and (14) yield product fourth-order smoothing terms when applied to equation (10). Product fourth-order smoothing is useful for damping high-frequency oscillations – see Hung and MacCormack [20] – and, in the present cascade application, is especially useful for stabilizing the solution in the high-gradient airfoil trailing-edge region. Typically, the product fourth-order terms are of significant magnitude only at the trailing edge where large truncation errors have already adversely affected the accuracy of the solution.

Boundary Conditions

The boundary conditions for the cascade analysis include those imposed at the airfoil surface (H-I in Fig. 2), the inlet boundary points (C, D, E in Fig. 2), and the exit boundary points (A, B, F, G in Fig. 2). The periodic boundary points along $\eta = \eta_{max}$ (E-F, B-C) and $\xi = 0$, $\xi = \xi_{max}$ (A-I, G-H) in Fig. 2 are treated as regular interior nodes by periodically extrapolating the data outside the solution space.

The tangent flow condition, $V = 0$, along the airfoil surface, $\eta = 0$ in Fig. 2, is imposed using a special adaptation of the full two-sweep version of the interior point algorithm. Central differences in η in equations (9) and (10) are replaced with three-point one-sided differences evaluated at the n-time level in both the first and second sweeps. Also, the damping term in η is removed. Following the solution of the difference equations, the tangent flow condition is enforced by projecting the calculated velocity onto the airfoil surface and ignoring the normal component. Using the definitions of the contravariant velocity components, the projected velocity components, u, v, are obtained by solving the set of equations

$$\xi_x u + \xi_y v = U \tag{15}$$

$$\eta_x u + \eta_y v = 0 \tag{16}$$

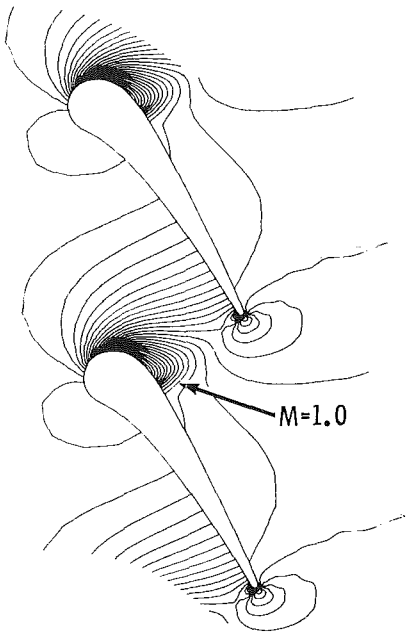

Fig. 6 Calculated static pressure contours for low-solidity turbine vane cascade: $M_2 = 0.85$

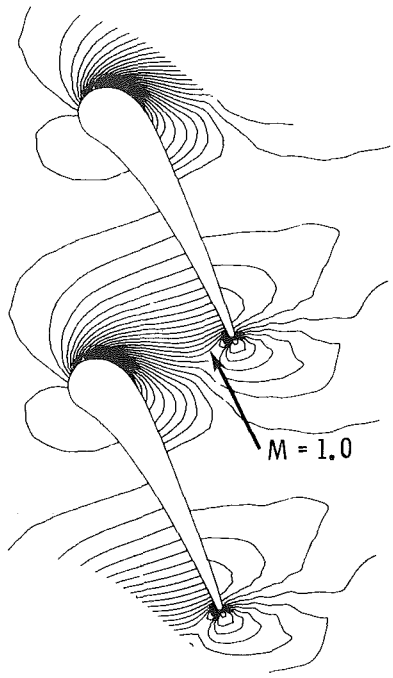

Fig. 8 Calculated static pressure contours for low-solidity turbine vane cascade: $M_2 = 1.05$

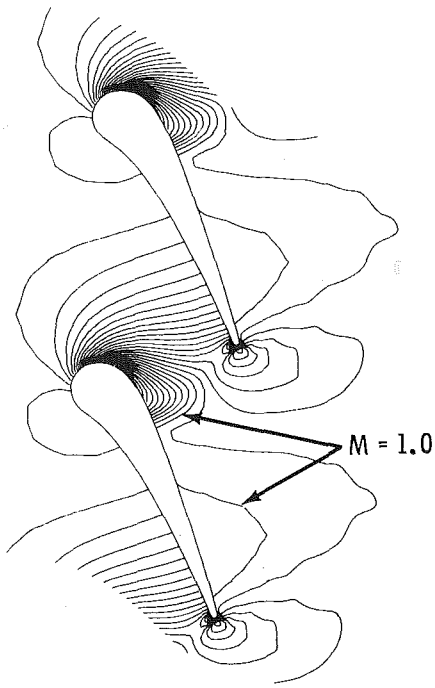

Fig. 7 Calculated static pressure contours for low-solidity turbine vane cascade: $M_2 = 0.95$

where U is determined from the solution of the difference equations.

The inlet and exit boundary conditions are imposed using a reference plane method of characteristics. The development of the characteristic relations is a lengthy procedure and, therefore, is not presented. Cline [21] gives a parallel development of the characteristic relations for isentropic flow.

The boundary conditions fixed at the inlet boundary points (C, D, E in Fig. 2) are the inlet total pressure and density and the v velocity component or the flow angle. At the exit boundary points (A, B, F, G in Fig. 2) the static pressure is specified. For this set of boundary conditions, it is convenient to normalize the dependent variables, as follows

$$p' = p/p_{o1},\ \rho' = \rho/\rho_{o1},$$
$$u' = u/(p_{o1}/\rho_{o1})^{1/2},$$
$$v' = v/(p_{o1}/\rho_{o1})^{1/2}$$

where p_{o1} and ρ_{o1} are the inlet total pressure and density, respectively.

Results

Numerical solution results for two turbine cascades are presented and compared with experimental data. Both example solutions were started from uniform stagnated flow conditions ($u' = 0, v' = 0, p' = 1.0, \rho' = 1.0$) and with the inlet flow angle and exit static pressure set to the desired steady-state values. In each case, the damping coefficients were both set equal to min. $(1/N_\xi, 1/N_\eta) = 1/N_\xi$. The solution at each point in the field was advanced at the maximum allowable CFL time increment given by equation (12). The transient solutions were assumed to be converged when the maximum relative change in static pressure between time steps, $|p^{n+1}_{i,j} - p^n_{i,j}|/p^n_{i,j}$, was less than 1×10^{-5}.

Low-Solidity Turbine Vane Cascade. The first example solution is for the low-solidity turbine vane cascade shown in Fig. 1. Hylton [22] recently tested the vane over a range of solidities, setting angles, and expansion ratios. Airfoil static pressure measurements were made for each configuration and aerodynamic condition.

Figures 3, 4, and 5 present calculated and experimental airfoil surface static pressure distributions for one cascade configuration for a range of expansion ratios corresponding to ideal exit Mach numbers of 0.85, 0.95, and 1.05, respectively. Excellent agreement between the solution results and the experimental data is indicated over the entire airfoil surface.

Presented in Figs. 6, 7, and 8 are calculated static pressure contour plots for each expansion ratio. These results show the

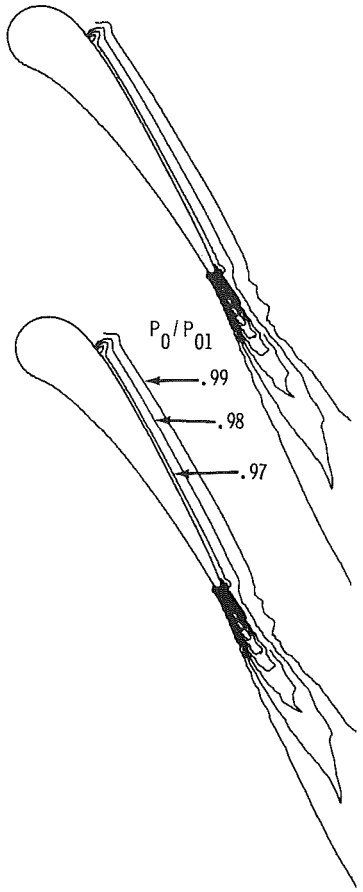

Fig. 9 Calculated normalized total pressure contours for low-solidity turbine vane

diverse flow conditions encountered as the exit pressure is varied in the transonic regime. For the highest exit pressure case ($M_2 = 0.85$), a supersonic bubble terminating in a strong normal shock is evident on the suction surface near the throat. As the exit pressure is reduced ($M_2 = 0.95$), the extent of the supersonic bubble increases and another one is formed downstream of the throat. Finally, at the lowest exit pressure ($M_2 = 1.05$) a single sonic line extends across the entire passage, indicating a fully choked condition. The demonstrated capability to accurately predict these complex flow conditions is attributed to the combined features of the excellent leading-edge resolution provided by the body-centered coordinate system and the shock-capturing capability of the numerical solution method. The leading-edge resolution capability is especially important in view of the rapid acceleration indicated in that region.

A contour plot of normalized total pressure, p_o/p_{o1}, is presented in Fig. 9 for the solution corresponding to $M_2 = 0.85$. The position of the shock wave on the vane suction surface near the throat is evident from the rapid decrease in total pressure in the streamwise direction at that location. The total pressure contours downstream of the shock follow the streamline direction, as they should for an inviscid rotational flow. The indicated low total pressure region downstream of the trailing edge is a result of inaccurate resolution and heavy damping of the solution in that high-gradient region. This increased damping is automatically introduced via equations (13) and (14) and is needed to stabilize the solution at the trailing edge.

The presented results were obtained on the 91 × 7 grid shown in Fig. 1. The sequence of solutions was from the lowest to the highest expansion ratio, with the preceding

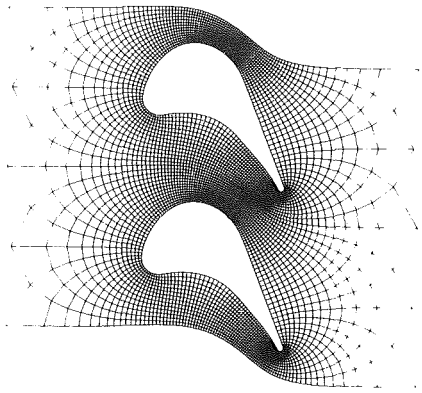

Fig. 10 Airfoil geometry and coordinate system for high-turning turbine blade cascade

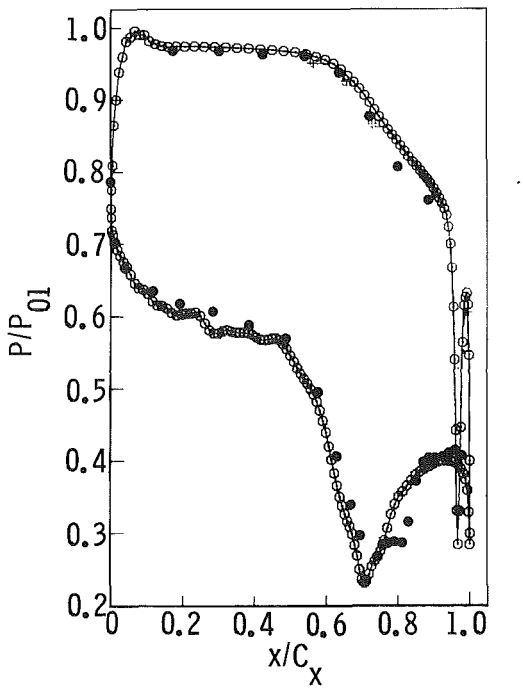

Fig. 11 Airfoil surface static pressure distributions for high-turning turbine blade cascade: $M_2 = 1.15$ (• -- experimental data, ○ – numerical solution)

solution used as initial data. The lowest expansion ratio solution ($M_2 = 0.85$) was obtained using stagnated initial conditions and took 1500 time steps and 1.3 min CPU time to converge on an IBM 370/3033 computer. The other solutions required 1000 time-steps and 0.9 min CPU time. The grid generator required approximately 30 CPU seconds on the same computer.

High-Turning Turbine Blade Cascade. Graham and Kost [23] recently conducted an experimental investigation of high-turning, coolable turbine blading to study the effects of shock-boundary layer interaction on aerodynamic performance. In that investigation, conducted at DFVLR, blade surface static pressure measurements were made on two different airfoils (denoted RA and RB) with 128 deg of turning. The data were taken over a series of expansion ratios corresponding to exit Mach numbers from 0.7 to 1.4.

Figure 11 presents the calculated and measured blade surface static pressure distributions for airfoil RB (see Fig. 10) for $M_2 = 1.15$. Good agreement between the distributions is shown over most of the airfoil surface. The discrepancy at $x/C_x = 0.8$ on the suction surface is attributed to shock-boundary layer interaction effects. The Schlieren photograph

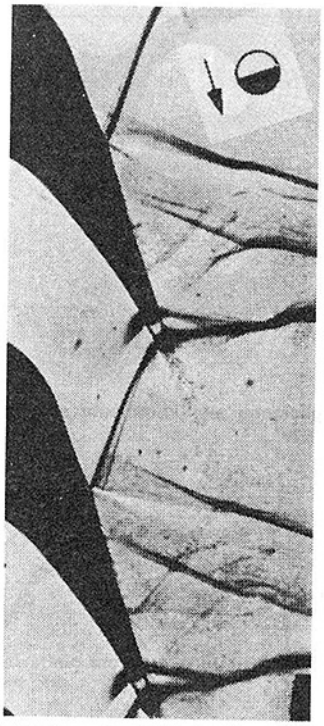

Fig. 12 Schlieren photograph of high-turning turbine blade cascade: $M_2 = 1.15$ (from reference [23])

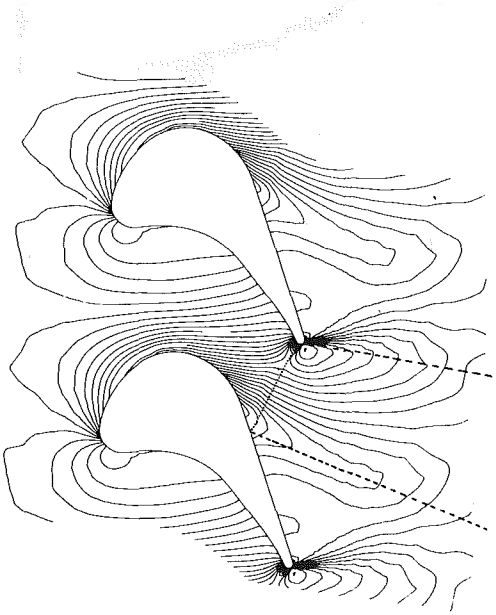

Fig. 13 Calculated static pressure contours for high-turning turbine blade cascade: $M_2 = 1.15$ (– – – shock waves)

presented in Fig. 12 shows a local separation of the suction surface boundary layer at the point of impingement of the trailing edge shock. Also, the experimental data in Fig. 11 show a plateau in the pressure distribution at the shock impingement point, indicative of separation, followed by an abrupt increase to the calculated inviscid solution level near the reattachment point. Outside this local region, the inviscid results are in close agreement with the experimental data.

A contour plot of the calculated static pressure field, presented in Fig. 13, shows the salient features of this flow field. The leading edge stagnation point is on the pressure surface of the airfoil and lies within the last contour plotted near the leading edge. Also, the sonic line is highly curved, typical of high-turning airfoils; and it extends across the entire passage, indicating a fully choked condition. Finally, abrupt changes in the slope of the contours indicate the trailing-edge shock structure.

A two-step procedure was used to obtain the calculated results in this case. First, a solution was obtained on a coarse 91×8 grid comprising every other line in the 181×15 grid shown in Fig. 10. The results were then interpolated onto the fine grid, and the solution was converged again. The coarse grid solution required 1500 time steps and 1.5 min CPU time to converge. The fine grid solution took an additional 1000 time steps and 3.8 min CPU time.

Conclusions

A hopscotch numerical scheme has been presented for solution of the time-dependent Euler equations with application to steady, two-dimensional transonic flows in turbomachinery cascades. The method is computationally explicit, possesses optimal pseudoviscosity damping characteristics, and has a substantial computational speed advantage over other explicit methods. The numerical method has been generalized to arbitrary curvilinear coordinates and applied to a body-centered coordinate system for solution of cascade flows. Numerical solution results for transonic turbine cascade flows have been presented and compared with experimental data to demonstrate the accuracy and computational efficiency of the analysis method.

For simplicity, the presentation of the numerical method was restricted to planar, two-dimensional cascade flows. The method, however, can be applied to blade-to-blade flows on stream surfaces of revolution in turbomachinery blade rows. Also, the hopscotch algorithm is directly extendible to three spatial dimensions for solution of full three-dimensional blade passage flows.

Acknowledgments

The author expresses his thanks to Detroit Diesel Allison for permission to publish this paper. The author is indebted to Dr. John Adamczyk of the Computational Fluid Dynamics Branch at NASA Lewis Research Center for his assistance in applying the grid generation code.

References

1 Steger, J. L., Pulliam, T. H., and Chima, R. V., "An Implicit Finite-Difference Scheme for Inviscid and Viscous Cascade Flow," AIAA Paper 80-1427, 1980.

2 Steger, J. L., "Implicit Finite-Difference Simulation of Flow About Arbitrary Two-Dimensional Geometries," *AIAA Journal*, Vol. 16, No. 4, July 1978, pp. 679–686.

3 Beam, R., and Warming, R. F., "An Implicit Factored Scheme for the Compressible Navier-Stokes Equations," AIAA Paper 77-645, June 1977.

4 Briley, W. R., and McDonald, H., "Solution of the Multidimensional Compressible Navier-Stokes Equations by a Generalized Implicit Method," *Journal of Computational Physics*, Vol. 24, No. 4, Aug. 1977, pp. 372–397.

5 MacCormack, R. W., "The Effects of Viscosity in Hypervelocity Impact Cratering," AIAA Paper 69-345, May 1969.

6 Gopalakrishnan, S., and Bozzola, R., "Computation of Shocked Flows in Compressor Cascades," ASME Paper 72-GT-31, 1972.

7 McDonald, P. W., "The Computation of Transonic Flow Through Two-Dimensional Gas Turbine Cascades," ASME Paper 72-GT-31, 1972.

8 Erdos, J. I., Alzner, E., and McNally, W., "Numerical Solution of Periodic Transonic Flow Through a Fan Stage," *AIAA Journal*, Vol. 15, No. 11, Nov. 1977, pp. 1559–1568.

9 Veuillot, J. P., "Calculation of the Quasi-Three-Dimensional Flow in a Turbomachine Blade Row," ASME Paper 76-GT-56, 1976.

10 Ni, R. H., "A Multiple Grid Scheme for Solving the Euler Equations," AIAA Paper 81-1025, June 1981.

11 Ives, D. C., and Liutermoza, J. F., "Second-Order Accurate Calculation

of Transonic Flow Over Turbomachinery Cascades," AIAA Paper 78-1149, 1978.

12 Holst, T. L., "A Fast, Conservative Algorithm for Solving the Transonic Full-Potential Equation," *AIAA Journal*, Vol. 18, No. 12, Dec. 1980, pp. 1431-1439.

13 Jameson, A., "Numerical Computation of Transonic Flows with Shock Waves," *Symposium Transonicum II*, Springer-Verlag, Berlin, Heidelberg, New York, 1975.

14 Scala, S. M., and Gordon, P., "Solution of the Time-Dependent Navier-Stokes Equations for Flow Around a Circular Cylinder," *AIAA Journal*, Vol. 6, No. 5, May 1968, pp. 815-822.

15 Gourlay, A. R., "Hopscotch: A Fast Second-Order Partial Differential Equation Solver," *Journal Inst. Maths. Applics.*, Vol. 6, No. 4, Dec. 1970, pp. 375-390.

16 Gourlay, A. R., and Morris, J. L., "Hopscotch Difference Methods for Nonlinear Hyperbolic Systems," *IBM Journal Res. and Develop.*, Vol. 16, No. 4, July 1972, pp. 349-353.

17 Lax, P. D., "Weak Solutions of Nonlinear Hyperbolic Equations and their Numerical Computation," *Communications on Pure and Applied Mathematics*, Vol. 7, 1954, pp. 159-193.

18 Adamczyk, J. J., "An Electrostatic Analog for Generating Cascade Grids," in NASA Conference Publication 2166: *Numerical Grid Generation Techniques*, Oct. 1980, pp. 129-142.

19 Hindman, R. G., "Geometrically Induced Errors and Their Relationship to the Form of the Governing Equations and the Treatment of Generalized Mappings," AIAA Paper 81-1008, June 1981.

20 Hung, C. M., and MacCormack, R. W., "Numerical Solutions of Supersonic and Hypersonic Laminar Compression Corner Flows," *AIAA Journal*, Vol. 14, No. 4, April 1976, pp. 475-481.

21 Cline, M. C., "NAP: A Computer Program for the Computation of Two-Dimensional, Time-Dependent, Inviscid Nozzle Flow," Los Alamos National Laboratory Report LA-5984, Jan. 1977.

22 Hylton, L. D., unpublished data for the low-solidity turbine vane cascade, Detroit Diesel Allison Division, General Motors Corporation, 1981.

23 Graham, C. G., and Kost, F. H., "Shock-Boundary Layer Interaction on High Turning Transonic Turbine Cascade," ASME Paper 79-GT-37, 1979.

The Influence of Tip Clearance, Stage Loading, and Wall Roughness on Compressor Casing Boundary Layer Development

J. L. Bettner
Research Scientist,
Detroit Diesel Allison,
Division General Motors Corporation,
Indianapolis, Ind. 46206

C. Elrod
Aerospace Engineer,
Technology Branch,
Turbine Engine Division,
Aeropropulsion Laboratory,
Wright Patterson AFB,
Dayton, Ohio

An experimental program was conducted in a highly loaded, single-stage, low-speed research compressor that featured variations in blade tip clearances, shroud wall roughness, and stage loading levels. The results showed that tip clearances and stage loading levels exerted a very strong influence on casing boundary layer growth. Shroud wall roughness not only showed some effect on casing boundary layer development, but also influenced stage stall margin. The results point out the need to understand the basic flow processes that occur if realistic mathematical models are to be developed so that casing boundary layer development and its influence on compressor stage performance can be accurately predicted.

Introduction

As advanced, lightweight, high-pressure compressors continue to be developed, endwall flow fields play an increasingly important part in determining compressor performance. The three-dimensional, viscous flow effects on smooth endwalls contribute substantially to the loss levels of advanced, high-pressure, highly loaded stages. With the additional requirement of having the least possible end clearance for good performance, abradable tip coatings come into play as they are needed for safe operational running. The desirable characteristics of compressor rotor tip track, abradable coatings are that they must abrade away without causing significant damage to the blade and not smear in the event contact takes place with the rotor tips. They should be very erosion resistant, nonporous, and structurally sound in high-temperature environments. Unfortunately, coating materials possessing all of these desirable characteristics are not available, and the ones employed in modern engines are generally both rough and/or somewhat porous. If improved performance is to be attained from future compressor design, then the impact of rough and porous endwalls and tip clearance for all compressor operating conditions must be understood and predictable.

To achieve these goals, the Air Force has contracted with Detroit Diesel Allison (DDA), Division of General Motors Corporation, to conduct an analytical/experimental program aimed at developing a system that will predict the effects of compressor casing wall roughness and porosity and blade tip clearance on stage efficiency. This paper presents some of the key experimental results of that program.

Contributed by the Gas Turbine Division of THE AMERICAN SOCIETY OF MECHANICAL ENGINEERS and presented at the 27th International Gas Turbine Conference and Exhibit, London, England, April 18–22, 1982. Manuscript received at ASME Headquarters December 14, 1981. Paper No. 82-GT-153.

Experimental Program

The experimental program was conducted in the DDA Low-Speed Compressor (LSC) Facility, and its objective was to provide very detailed endwall boundary layer measurements through the compressor stage for various wall conditions of roughness, porosity, and tip clearance on the blade tip section endwall at several compressor operating conditions. These experimental data provided a basic understanding of shroud flow fields and aided in the development of a three-dimensional, turbulent compressible casing endwall boundary layer shroud flow prediciton method.

Experimental Equipment.

Test Rig. The low-speed compressor flow path and mechanical arrangement are presented in Fig. 1. Blading and flow path of the zero inlet swirl, 184 ft/s (56 m/s) tip speed compressor, were designed to reflect realistic aerodynamic values of blockage, blade loading and loss levels, and tip clearance, along with realistic geometric design parameters that are typical of aft stages of modern multistage compressors. Also, the Reynolds number at the compressor inlet is

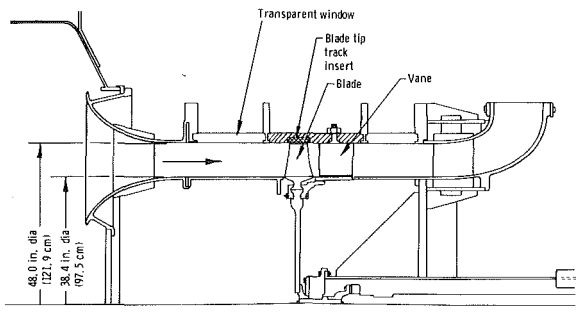

Fig. 1 Low-speed compressor flow path

Table 1 Airfoil mean section mechanical and aerodynamic characteristics

	Rotor	Stator
Type of airfoil	65 series	65 series
Chord, C-in. (m)	4.489 (0.1140)	5.089 (0.1293)
Solidity, $\sigma = C/S$	1.435	1.516
Camber, ϕ—deg	20.42	48.57
Aspect ratio, $AR = L/C$	1.046	0.943
Leading edge radius/C	0.0044	0.0049
Trailing edge radius/C	0.0028	0.0030
Inlet angle, β_1—deg	59.38	37.84
Exit angle, β_2—deg	42.41	0.00
Loss coefficient, $\bar{\omega}$	0.043	0.056
Diffusion factor, D_f	0.449	0.410

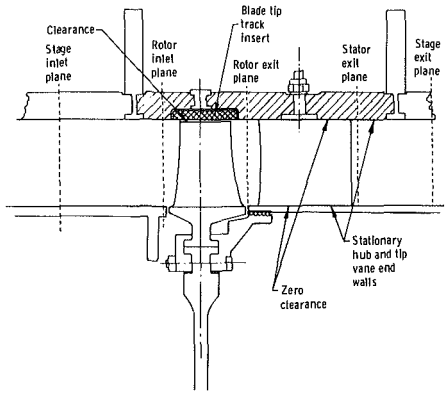

Fig. 2 Low-speed compressor stage showing shroud wall insert and instrumentation planes

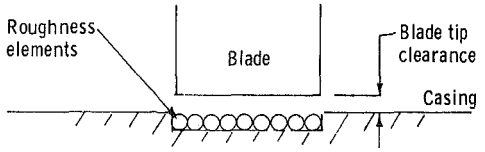

Fig. 3 Shroud endwall geometry

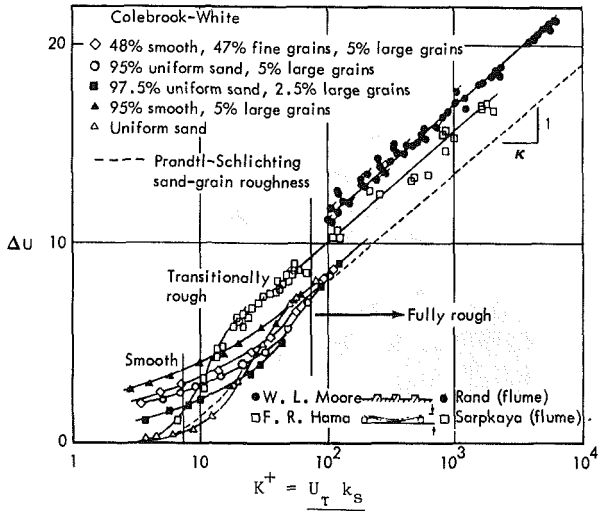

Fig. 4 Reynolds number, veolocity, roughness correlation

typical of modern compressors. The blading and flow path are physically large enough to allow high-quality, detailed, endwall boundary layer measurements to be made over the entire endwall without having to resort to extreme miniaturization.

Table 1 summarizes the compressor design with mean section aerodynamic and geometric design values.

Blade track insert sections were fabricated with three different sizes of roughness elements that were bonded to the surface and positioned in the casing as illustrated in Fig. 2. The insert was machined back to accept the various diameter roughness elements, as shown in Fig. 3, so that there would not be a step discontinuity in clearance over the blade tip.

The roughness elements employed were uniform glass spheres whose diameters (k_s) were 0.020 in., 0.030 in., and 0.080 in. (5.08×10^{-4} m, 7.62×10^{-4} m, and 20.32×10^{-4} m). These values of k_s produced roughness Reynolds numbers, K^+

$$K^+ = \frac{U_\tau k_s}{\nu} \tag{1}$$

which ranged from about 100 to 400. This allowed experiments to be conducted in the transitionally rough to fully rough zones as shown in the Clauser plot of Fig. 4 [1]. Figure 5 shows the 0.080 in. (20.32×10^{-4} m) dia element rough wall configuration positioned in the rotor tip track.

Instrumentation. Steady-state instrumentation consisted of multiple element total pressure rakes distributed circumferentially around the annulus at the stage inlet and exit plenum, boundary layer rakes on the hub and tip walls at the rotor inlet and stator exit, multiple element total temperature rakes at the stator exit, and static pressure taps distributed around the annulus on the hub and tip walls and axially

Nomenclature

AR = aspect ratio
C = chord, in. (m)
cl = tip clearance, in. (m)
D_f = diffusion factor
H = boundary layer shape factor
K^+ = roughness Reynolds number
k_s = roughness element height, in. (m)
L = airfoil length, in. (m)
ler = leading edge radius, in. (m)
N_c = corrected speed, rpm
n = normal coordinate
P_T = total pressure, psia (kPa)
R_c = total pressure ratio
S = spacing, in. (m)
s = streamwise coordinate
SM = stall margin
ter = trailing edge radius, in. (m)
U = velocity, ft/sec (m/s)
U_τ = friction velocity, $\sqrt{\tau_w/\rho}$, ft/sec (m/s)
W_c = corrected flow rate, lb/sec (kg/s)
x = axial coordinate
y = radial coordinate
z = tangential coordinate
β_1 = inlet air angle, deg
β_2 = exit air angle, deg
δ^* = displacement thickness, in. (m)
θ = momentum thickness
ν = kinematic viscosity, ft^2/sec (stoke)
ρ = density, lbm/ft^3 (kg/m^3)
τ = shear stress, lb/in.^{2} (kg/m^2)
$\bar{\omega}$ = loss coefficient

Subscripts

n = normal direction
s = streamwise direction
x = axial direction
z = tangential direction
nn = momentum in normal direction
ss = momentum in streamwise direction
xx = momentum in axial direction
zz = momentum in tangential direction
se = edge of streamwise boundary layer
xe = edge of axial boundary layer
ze = edge of tangential boundary layer

Table 2 Test configuration identification

Test configuration	Blade tip clearance, % span	Shroud roughness element size, in.	Shroud roughness element size, m
I	1.48	smooth	smooth
II (porous)			
III	1.44	0.080	20.32×10^{-3}
IV	1.30	0.030	7.62×10^{-3}
V	1.13	0.020	5.08×10^{-3}
VI	2.96	smooth	smooth
VII (porous)			
VIII	2.81	0.080	20.32×10^{-3}
IX	2.77	0.030	7.62×10^{-3}

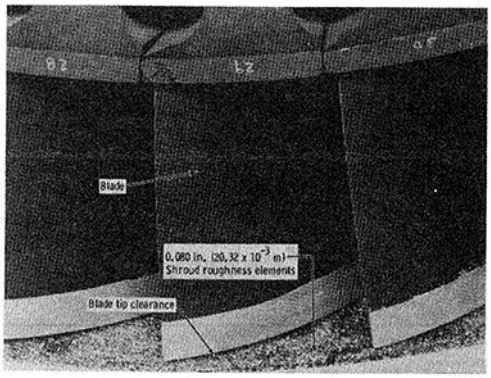

Fig. 5 Low-speed compressor stage showing 0.080 in. roughness elements installed in blade tip shroud wall

through the stage. In addition, 45 static pressure taps were arranged on the tip wall of one stator passage to allow mapping of the vane tip static pressure distribution. The stage inlet total temperature was measured in the plenum chamber located upstream of the flow path annulus. All of the pressure instrumentation was connected to six 48-channel Scanivalves, interfaced wtih a Digitic Scanner and driven by a Hewlett-Packard model 2117F computer. Differential (0–1.0 psid [0–6.894 kPa]) Druck pressure transducers were employed in the Scanivalves. A dead-weight system provided reference pressures of 0.0, 0.5, and 1.0 psia (0.0, 3.447, and 6.894 kPa) to the Scanivalve transducers.

Radial-circumferential hot wire anemometer surveys were performed in the exit planes of the rotor and stator. In addition, radial surveys were performed at three axial locations along a midflow streamline inside the stator passage. Streamwise velocity and air angle were determined by positioning the probe at a fixed axial, circumferential, and radial location, and then by yawing the probe until the output voltages of the two hot wires were the same value. DISA constant temperature hot wire anemometry equipment was used. The outputs were linearized and compensated for temperature differences that existed between the velocity calibration jet air stream and the rig flow field environment.

Blade tip clearances were measured by a Dynamic Data Capacitance clearance probe. The probe was flush-mounted in the tip track, and it measured the variation in length of each passing blade and determined an average tip clearance.

Test Configurations. The test configurations featured variations in (*i*) casing wall roughness in the blade tip track and (*ii*) balde tip clearance. Two other configurations, which featured porous tip endwalls, were investigated, but those results are not included in this paper. Blade tip clearance was varied by machining material from the blade tip section. Table 2 presents a summary of the tip clearance and shroud-roughness element size of the test configurations. All stage configurations were operated at various conditions of corrected speed, pressure rate, and flow rate.

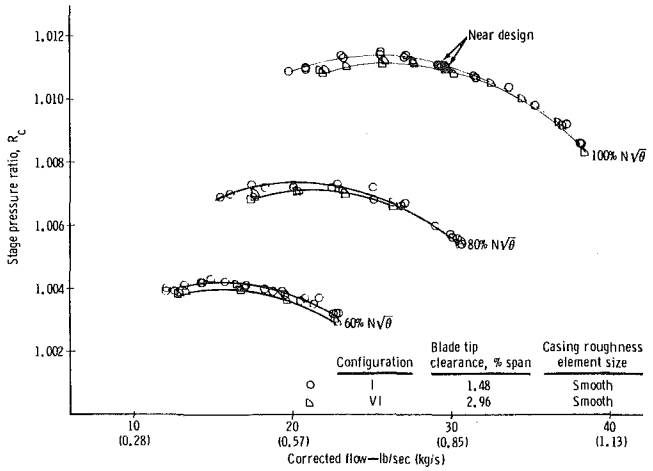

Fig. 6 Effect of tip clearance on stage performance

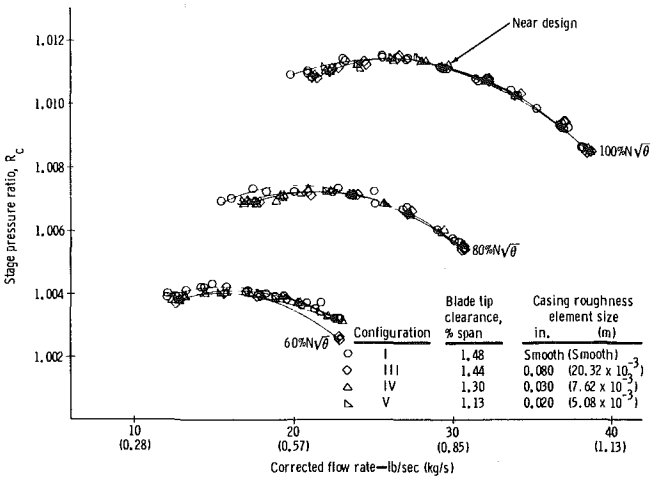

Fig. 7 Effect of shroud roughness on "smaller" tip clearance configuration

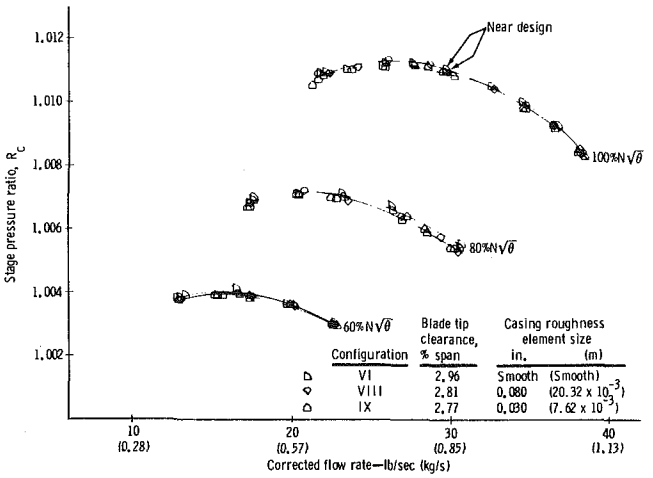

Fig. 8 Effect of shroud roughness on "larger" tip clearance configuration

Experimental Results.

Overall Stage Performance. Figures 6, 7, and 8 illustrate the effects of clearance and shroud wall roughness on the stage pressure-flow characteristics. Figure 6 shows that not only is the near-design point performance reduced, but also the stall margin defined as

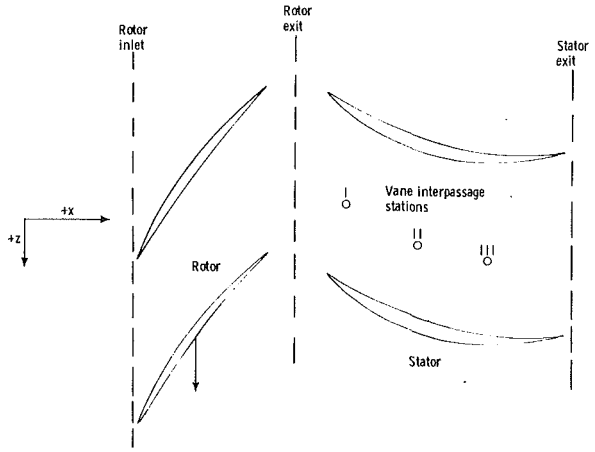

Fig. 9 Stage instrumentation stations

$$SM = \left[\frac{\left(\frac{R_c}{W_c}\right)_{sp}}{\left(\frac{R_c}{W_c}\right)_{op}} - 1 \right]_{N_c = C} \quad (2)$$

was reduced by about 12 1/2 percent as the tip clearance was increased from 1.48 to 2.96 percent of blade span.

The effect of shroud wall roughness on the smaller tip clearance stage configuration is presented in Fig. 7. At the near-design point setting, there was no discernible effect of roughness on the pressure-flow characteristics; however, there was about a 6 1/2 to 7 1/2 percent reduction in stall margin as the shroud wall roughness was increased. Figure 8 shows the effect of roughness on the larger tip clearance configurations. It is particularly interesting to note here that at the near-design setting conditions the pressure-flow characteristics were essentially the same, but the stall margin was actually increased by 2-4 percent as the shroud roughness size was substantially increased. Perhaps the shroud wall roughness elements act as turbulent eddy generators, which promote mixing in the clearance space and improve the clearance flow field conditions for configurations with very large blade tip clearances.

Detailed Boundary Layer Surveys.

Typical Profile Development. Radial-circumferential hot wire surveys were performed at several stage operating conditions for each of the various shroud wall configurations. Figure 9 presents tip section airfoil profile shapes showing measurement planes before and aft of the airfoils. Also shown is the location of the three-vane interpassage hot wire surveys. Figure 10 illustrates the coordinate system employed in the data analysis and the decomposition of a general boundary layer profile into its principal components. The two coordinate systems are (*i*) the *x-z* system (axial-tangential) and (*ii*) the intrinsic *s-n* (streamwise and its normal) system.

An example of the development of streamwise and transverse (normal) velocity profiles on the casing endwall through the compressor stage is shown in Fig. 11. The stage arrangement featured configuration I (1.48 percent span tip clearance with a smooth wall) operating at near-design conditions. The streamwise velocity profile is shown to be fairly well represented by a turbulent 1/7 power profile description as the flow progresses through the stator. However, the transverse (normal) component enters the vane with a parabolic-type of profile oriented in the direction toward the pressure surface (increased incidence) at the vane leading edge. Once inside the passage, the normal component

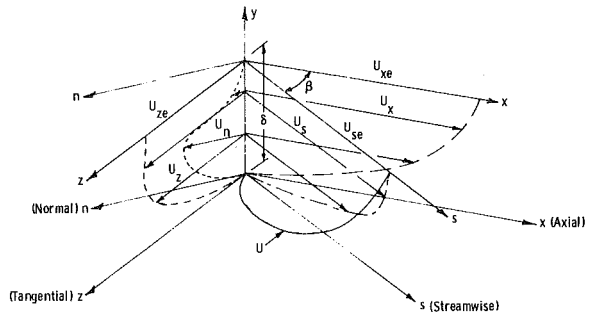

Fig. 10 Coordinate system and representative endwall velocity profile

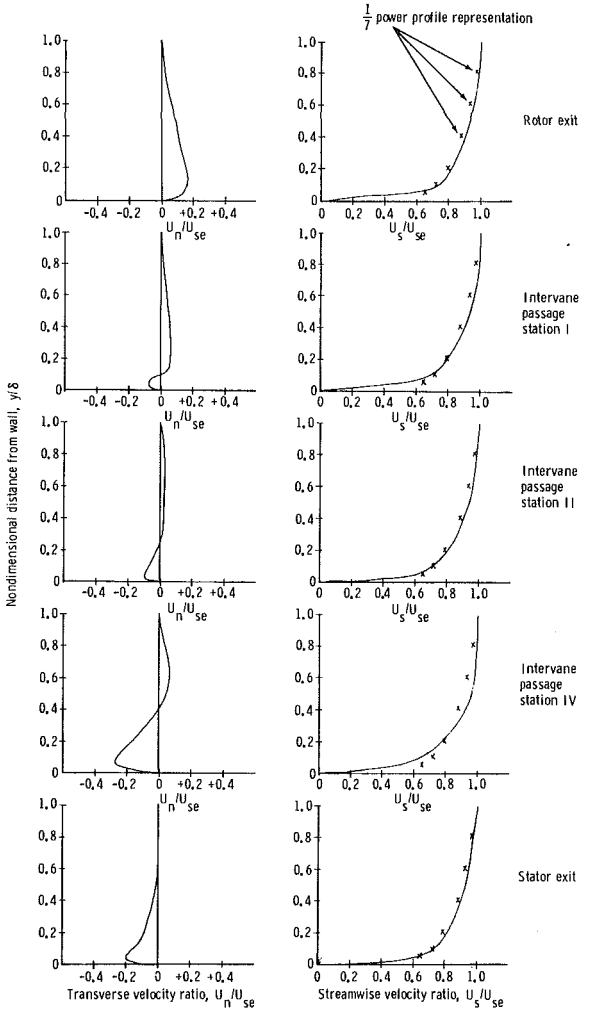

Fig. 11 Development of streamwise and transverse velocity profile through configuration I at near design operating conditions

reacts to the vane-to-vane circumferential pressure gradient, swings past the streamwise direction, developing complicated S-shaped profiles, and finally exits from the stator passage with a parabolic-type profile oriented in the direction of the suction surface. From these results, it appears that a parabolic-type representation of the transverse velocity components may be satisfactory in the inlet and exit planes but not in the interior of a stator passage.

Definition of Boundary Layer Parameters. Based on the coordinate system defined in Fig. 10, the following boundary layer parameters were defined

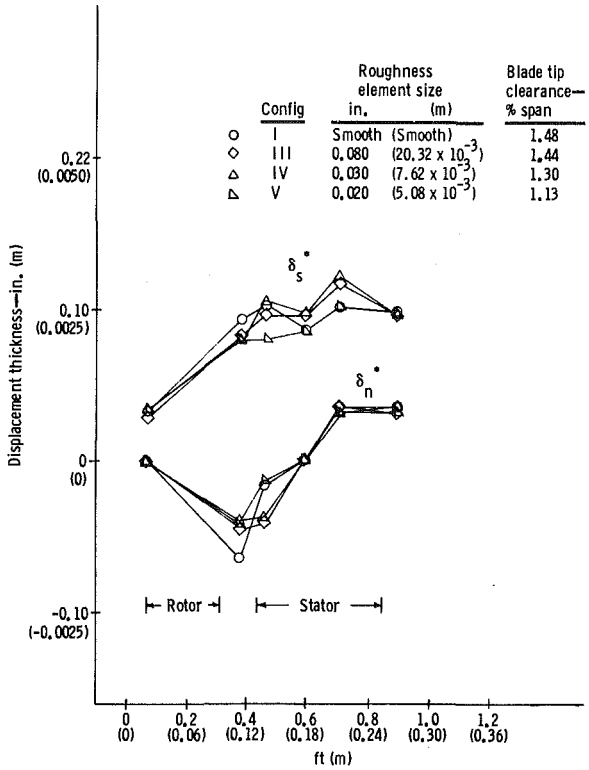

Fig. 12 Axial variation of streamwise and normal displacement thickness with shroud roughness (small clearance configurations)

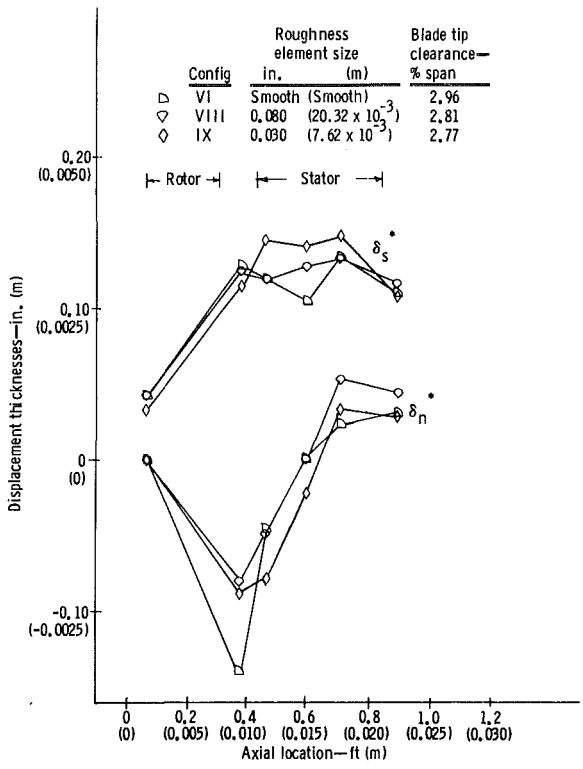

Fig. 13 Axial variation of streamwise and normal displacement thickness with shroud roughness (large clearance configurations)

Displacement thickness in:

$$\delta_s^* = \int_0^\delta \left(1 - \frac{U_s}{U_{se}}\right) dy \qquad s \text{ direction} \qquad (3)$$

$$\delta_n^* = -\int_0^\delta \left(\frac{U_n}{U_{se}}\right) dy \qquad n \text{ direction} \qquad (4)$$

$$\delta_x^* = \int_0^\delta \left(1 - \frac{U_x}{U_{xe}}\right) dy \qquad x \text{ direction} \qquad (5)$$

$$\delta_z^* = \int_0^\delta \left(1 - \frac{U_z}{U_{ze}}\right) dy \qquad z \text{ direction} \qquad (6)$$

Momentum thickness in:

$$\theta_{ss} = \int_0^\delta \left(1 - \frac{U_s}{U_{se}}\right) \frac{U_s}{U_{se}} dy \qquad s \text{ direction} \qquad (7)$$

$$\theta_{nn} = -\int_0^\delta \frac{U_n^2}{U_{se}^2} dy \qquad n \text{ direction} \qquad (8)$$

$$\theta_{xx} = \int_0^\delta \left(1 - \frac{U_x}{U_{xe}}\right) \frac{U_x}{U_{xe}} dy \qquad x \text{ direction} \qquad (9)$$

$$\theta_{zz} = \int_0^\delta \left(1 - \frac{U_z}{U_{ze}}\right) \frac{U_z}{U_{ze}} dy \qquad z \text{ direction} \qquad (10)$$

Streamwise velocity profiles at each measurement station were examined to define the edge of the boundary layer and free stream angle. Directional component profiles were constructed and the various integral parameters were determined. Values of the various integral parameters, along with measured velocities and air angles, were substituted into coordinate identities [2]. For example, the identities for displacement thicknesses were

$$U_{xe}\delta_x^* = U_{se}\{\text{Cos } \beta\, \delta_s^* - \text{Sin } \beta\, \delta_n^*\} \qquad (11)$$

$$U_{ze}\delta_z^* = U_{se}\{\text{Sin } \beta\, \delta_s^* + \text{Cos } \beta\, \delta_n^*\} \qquad (12)$$

The identities were satisfied for several configurations at each measurement station, demonstrating that the computed values of the component parameters were correct.

Variation of Streamwise and Normal Displacement Thicknesses. Figure 11 demonstrated how the streamwise and transverse (normal) velocity profiles behaved as the flow moved through the stator passage. Those results showed that the transverse boundary layer developed complicated S-shaped profiles and changed direction as it proceeded through the vane passage. Streamwise and normal displacement thickness calculations were performed on all of the measured boundary layer profiles. Figures 12 and 13 present, respectively, the axial distribution of those thicknesses for the 1.48 and 2.96 percent span tip clearance configurations. Those figures first show that the normal displacement thicknesses all initially had negative values, but became progressively more positive as the flow proceeded through the vane passage. This is a qualitative means of illustrating the secondary flow moves from the vane pressure surface at the inlet station toward the vane suction surface in the exit region. Comparison of Fig. 12 with Fig. 13 shows that the larger blade tip clearance configurations result in larger amounts of secondary flow (i.e., larger negative values of δ_n^*) impinging on the leading edge pressure surface of the vane.

The effects of several different realistic mechanical and aerodynamic operating circumstances on the behavior of some boundary layer parameters will be demonstrated in the remainder of the paper. These results show that all of those effects influence the development of the casing wall boundary layer, some to a much greater extent than others. If a reliable compressor casing wall boundary layer prediction scheme is to be developed, then these effects must be well understood. The first of these to be considered will be the influence of blade tip clearance on streamwise boundary layer parameters.

Effect of Blade Tip Clearance.

The effects of blade tip clearance on streamwise boundary layer parameters are presented in Fig. 14. Results for three values of tip clearance are shown in the figure:

- Configuration I—1.48 percent span
- Configuration VI—2.96 percent span
- Reference [3]—0.63 percent span

Work was performed [3] in the LSC with the same hardware (but with smaller tip clearance) as that used in the experiments of the present investigations.

Figure 14 shows a substantial increase in both δ_s^* and θ_{ss} across the rotor, with the increase being progressively larger with increased tip clearance. Furthermore, the distribution of parameters across the stator tip varied inversely, from a slight increase in δ_s^* and θ_{ss} with the smallest blade tip clearance configuration, to a decrease with the largest tip clearance configuration.

The absolute freestream velocity distribution in the tip region is one of acceleration across the rotor and deceleration across the stator. It is interesting to note that only the very small tip clearance (0.63 percent span) configuration produced an increase in δ_s^* and θ_{ss} across the stator (which is what would be expected in a decelerating flow field). It would appear that at the larger clearance values, the clearance flow and, possibly, the formation of the clearance flow vortex exert the controlling influence on the casing endwall boundary layer development.

Figure 15 presents further evidence of the extent to which the rotor tip clearance flow vortex penetrates into the flow field. These data [4, 5] were the results of hot wire experiments designed to determine the longitudinal and transverse fluctuating velocity components impressed on a stator by a moving upstream blade row. These results show that a 0.6 percent span tip clearance, the vortex is barely evident at a distance of 6.3 percent span from the tip wall. When the clearance was increased to 1.48 percent span, the vortex was still evident to a distance of at least 10.4 percent span from the wall. With 2.96 percent tip clearance [5], the influence of the vortex was just barely evident at 24.8 percent span from the tip wall. It is suggested that the large clearance flow vortex formation offsets the existence of the favorable pressure gradient through the rotor, resulting in a progressively thicker boundary layer at the exit of the rotor with increased rotor tip clearance.

As the flow proceeds through the stator [5], the location of the vortex moves circumferentially with respect to the blade wake. This tip clearance vortex motion may promote mixing in the stator tip region, resulting in a retarded boundary layer development.

Effect of Stage Loading. Figure 16 shows the impact of stage loading on the configuration I arrangement as the compressor was operated from open throttle to near stall. These results clearly demonstrate the effect of acceleration through the rotor on the boundary layer parameter development. At constant speed, the tip region rotor-exit absolute velocity level does not change substantially, but the rotor-inlet absolute velocity is reduced considerably as the compressor loads from open throttle to near stall. Therefore, the flow is progressively accelerated in the tip region absolute frame of reference as the stage loads toward stall. Apparently, the favorable pressure gradient at the near-stall operating point was sufficient to dominate the tip clearance effects (described in the previous section) and resulted in a reduction in boundary layer parameters across the rotor with a subsequent increase across the stator.

Effect of Shroud Wall Roughness. The effects of shroud wall roughness on boundary layer development are illustrated

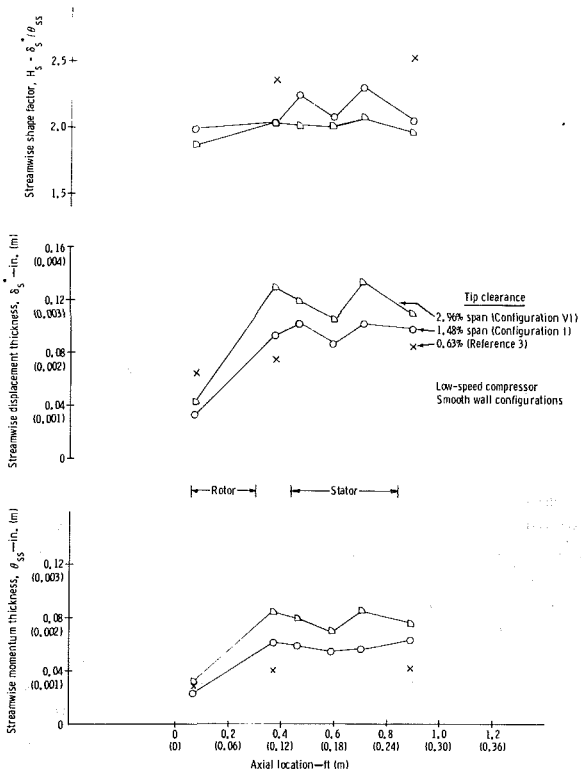

Fig. 14 Effect of blade tip clearance on streamwise boundary layer parameters

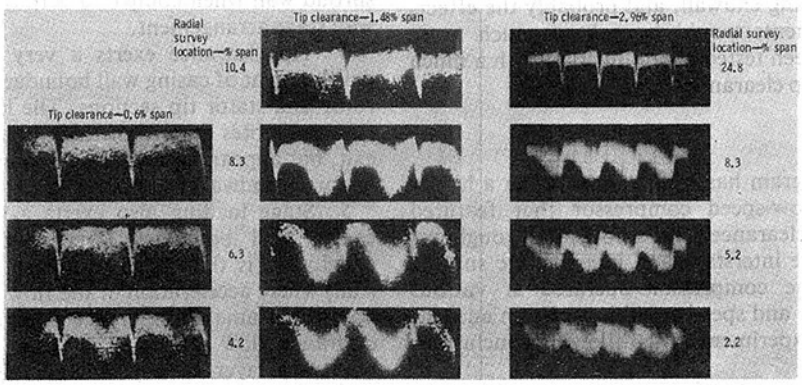

Fig. 15 Hot wire signals showing vortex development in near tip region of the rotor exit plane

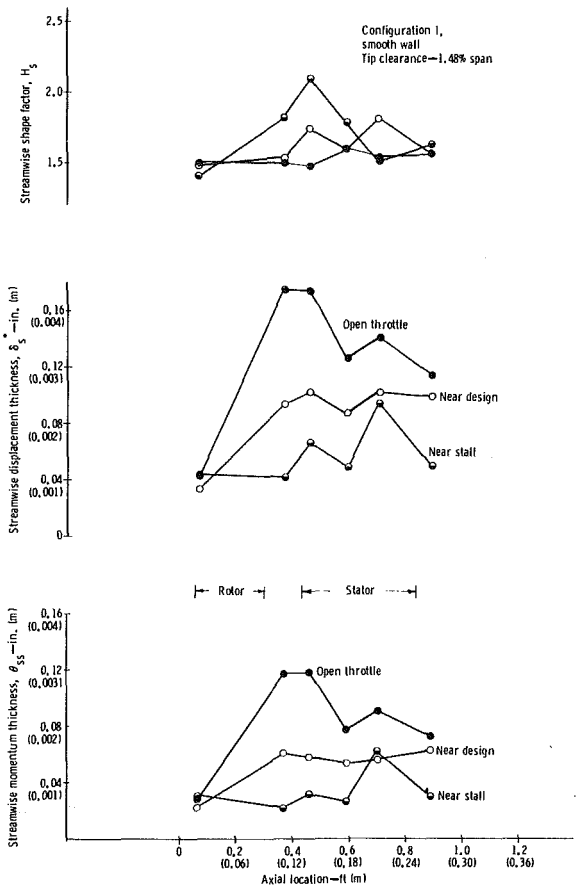

Fig. 16 Effect of stage loading on streamwise boundary layer parameters

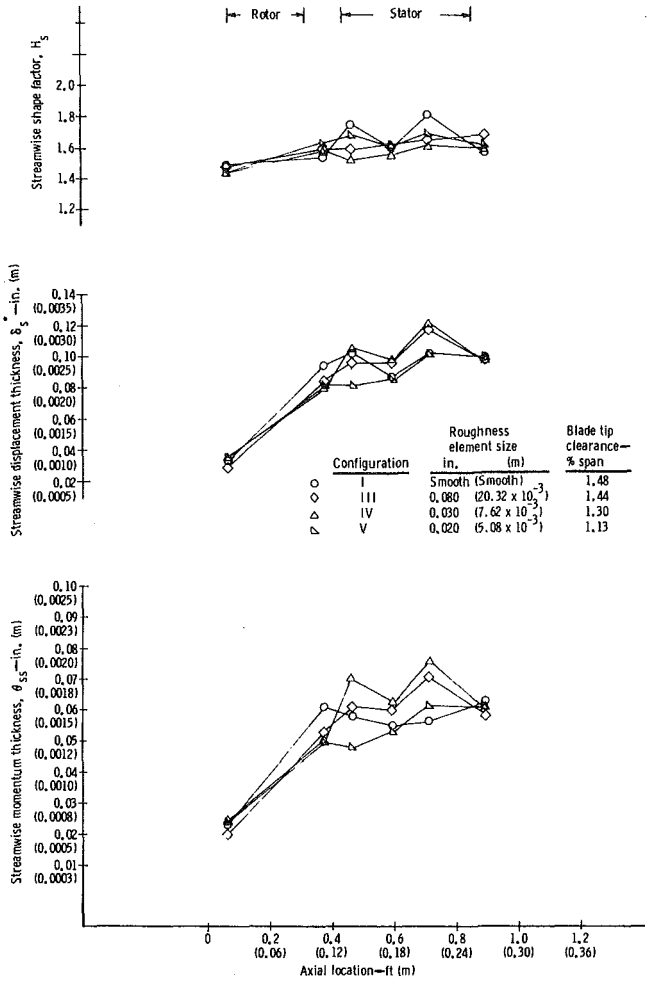

Fig. 17 Effect of shroud roughness on boundary layer development of the smaller tip clearance configurations

in Figs. 17 and 18 for, respectively, the small and large tip clearance configurations. Those results show, in general, a slight reduction in boundary layer growth across the rotor for the rougher endwalls. This may be due to a turbulent mixing between the flow over the roughness elements and the blade tip clearance flow.

As far as the complete stage is concerned, the roughest endwall configurations produeced the largest increase in boundary layer growth when compared with their individual rotor inlet displacement and momentum thickness values. The stage configurations with the smaller values of roughness element size demonstrated about the same increase in boundary layer growth across the whole stage as did the smooth wall configuration. Again, it is suggested that the large clearance flows tend to dominate the boundary layer development on the casing endwall, and probably the effects of the roughness elements would have been much more pronounced had they been tested in conjunction with a much smaller value of blade tip clearance.

Conclusions

An experimental program has been conducted in a highly loaded, single-stage, low-speed compressor that featured variations in blade tip clearances and shroud wall roughness levels. Detailed hot wire interstage and interpassage surveys were performed as the compressor operated at various pressure ratios and flow and speed conditions. From analysis of the results of those experiments, the following conclusions are drawn:

1 An increase in blade tip clearance from 1.48 to 2.96 percent blade span for the smooth casing wall configuration resulted in a deterioration of near-design performance and a 12 1/2 percent reduction in stage stall margin.

2 Variation in shroud roughness (which ranged from transitionally rough to fully rough Reynolds number zones) showed no discernible impact on the stage pressure-flow characteristic; however, a 6 1/2–7 1/2 percent reduction in stall margin was observed for rough wall, smaller, tip-clearance configurations when compared with the smooth wall at about the same tip clearance.

3 For the larger tip clearance configuration, a slight improvement in stall margin was observed with the roughened shroud wall when compared with the large clearance smooth wall stage arrangement.

4 Tip clearance exerts a very strong influence on the development of casing wall boundary layers, both through the rotor and stator tip sections. The large, tip-clearance vortex flow promotes growth of thick boundary layers at the rotor exit, but appears to discourage boundary layer growth on the stator tip endwall.

5 Stage loading also exerts a very strong influence on casing wall boundary layer development. The principal conclusion is that stage operating conditions exist (toward stall) where acceleration of the flow across the rotor tip in the absolute frame of reference is large enough to offset the clearance flow effects. The result is a comparatively thin boundary layer at the rotor exit. This layer then seems to respond to the adverse pressure gradient across the stator, producing a thicker boundary layer at the stator exit.

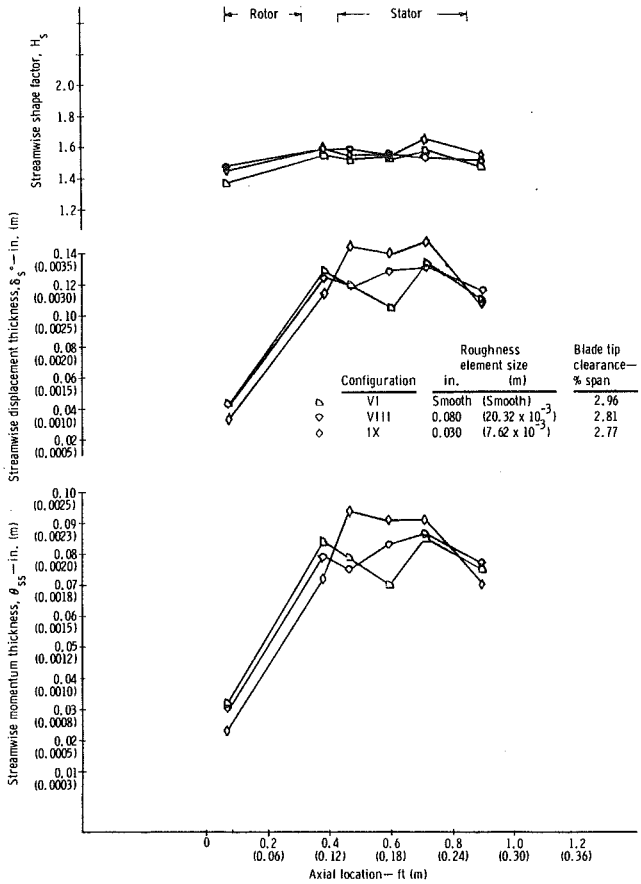

Fig. 18 Effect of shroud roughness on boundary layer development of the larger tip clearance configurations

6 The effects of rotor tip shroud roughness showed a slight reduction in boundary layer growth across the rotor. However, when the whole stage was considered, the ratio of the stator exit-to-rotor inlet boundary layer thickness values was slightly higher for the roughest endwall configurations. The effects of shroud wall roughness would probably have been more evident had the stage been operated with smaller values of tip clearance.

7 The values of test variables employed in this experiment were typical, in terms of percent span tip clearance, shroud coating roughness Reynolds number, and absolute acceleration across the blade tip section that would be found in aft stages of full-size compressors. The experimental results reported herein point out the sensitivity of casing wall boundary layer development to those important mechanical and aerodynamic design variables. The results demonstrate the need to understand the basic flow processes and interactions that occur if realistic mathematical models are to be developed so that casing boundary layer development and its influence on compressor stage performance can be accurately predicted.

References

1 Clauser, F. H., *Advances in Applied Mechanics Journal*, Vol. 4, 1956, pp. 1–51.

2 Daneshyar, M., "Annulus Wall Boundary Layers in Turbomachines," Ph.D. thesis, St. John's College, Cambridge, Jan. 1974.

3 Bettner, J. L., "Summary of Tests in the DDA Low-Speed Compressor Facility," DDA EDR 10911, Nov. 1981.

4 Fleeter, S., Jay, R. L., and Bennett, W. A., "The Effect of Rotor-Stator Axial Spacing on the Time Variant Aerodynamic Response of a Compressor Stator," DDA EDR 9379, Dec. 1977.

5 Jay, R. L., and Bettner, J. L., "Aerodynamically Induced Vibration," DDA EDR 10840, Sept. 1981.

A Computational Geometry for the Blades and Internal Flow Channels of Centrifugal Compressors

M. V. Casey
Head, Radial Compressor Development Group,
Turbocompressor Department,
Thermal Turbomachinery Division,
Sulzer-Escher Wyss Ltd.,
Zurich, Switzerland

A new computational geometry for the blades and flow passages of centrifugal compressors is described and examples of its use in the design of industrial compressors are given. The method makes use of Bernstein-Bezier polynomial patches to define the geometrical shape of the flow channels. This has the following main advantages: the surfaces are defined by analytic functions which allow systematic and controlled variation of the shape and give continuous derivatives up to any required order: and the parametric form of the equations allows the blade and channel coordinates to be very simply obtained at any number of points and in any suitable distribution for use in subsequent aerodynamic and stress calculations and for manufacture. The method is particularly suitable for incorporation into a computer-aided design procedure.

Introduction

The design of centrifugal compressor impellers usually assumes two distinct stages. A preliminary design, making use of one-dimensional flow analysis based on previous experience, is sketched out to specify the inlet and outlet blade angles and the "skeletal" dimensions (such as inlet and outlet diameters, axial length, and impeller tip outlet width). This is followed by a detailed design in which the complete blade and channel geometry is specified and then subsequently refined by means of successive aerodynamic and stress analyses.

During the detailed design stage the designer repeatedly adjusts the shape of the blades and flow channels until he finds a suitable geometry that combines acceptable aerodynamic performance with low stress levels and is economic to manufacture. This process of continual refinement of the shape can be expensive, tedious, and time-consuming, since at each stage the geometrical data for the necessary aerodynamic or stress analysis must be prepared. The task is greatly simplified when a simple flexible system of geometry definition for the components of a compressor is available.

The definition of compressor geometry is especially complicated for industrial centrifugal compressors, where three different types of impeller are to be found (Fig. 1):

- High flow coefficient impellers ($\Phi > 0.1$) with three-dimensional twisted blade surfaces, axial inlet flow, and a radial leading edge (similar to modern supercharger impellers)
- Intermediate flow coefficient impellers ($0.1 > \Phi > 0.04$) with three-dimensional twisted blade surfaces, radial inlet flow, and an inclined leading edge
- Low flow coefficient impellers ($\Phi < 0.04$) with two-dimensional curved blades, comprised of purely axial elements, radial inlet flow and an axial leading edge

It is the purpose of this paper to describe a method of computational geometry that has proved extremely useful for the definition of component geometry in industrial centrifugal compressors. The method can be used to specify each of the impeller types mentioned above and, in addition, is capable of defining the complete flow passage through the compressor. For example, the geometry of the hub and shroud contours, including inlet, diffusor, crossover channel and return channel, as well as all of the vaned cascades of the compressor, such as inlet guide vanes, diffusor vanes and return channel de-swirl vanes, can be defined using the present method.

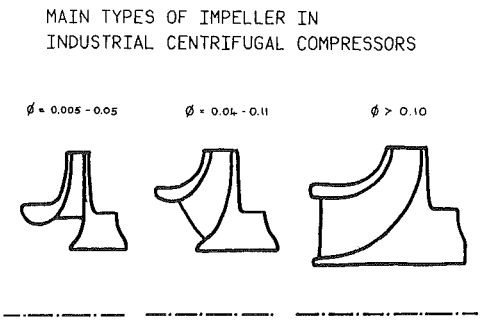

Fig. 1 Sketch of main types of impeller in industrial centrifugal compressors

Contributed by the Gas Turbine Division of THE AMERICAN SOCIETY OF MECHANICAL ENGINEERS and presented at the 27th International Gas Turbine Conference and Exhibit, London, England, April 18-22, 1982. Manuscript received at ASME Headquarters December 14, 1981. Paper No. 82-GT-155.

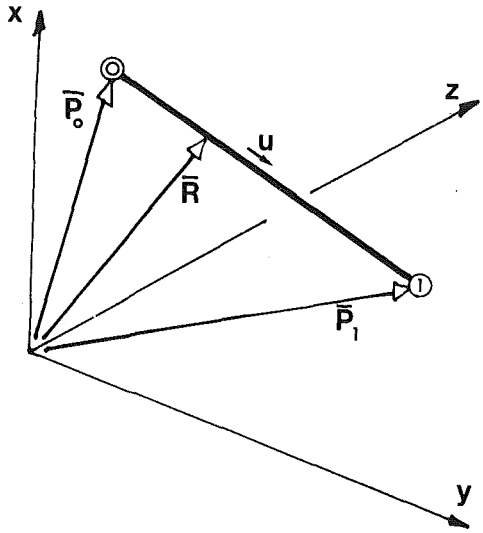

Fig. 2(*a*) Example of Bezier curve, degree 1

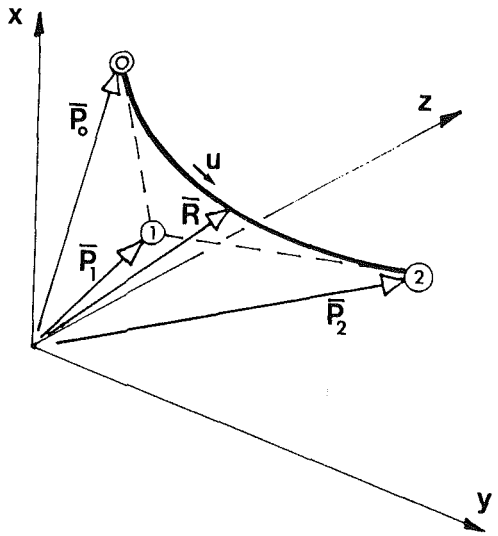

Fig. 2(*b*) Example of Bezier curve, degree 2

Geometry Definition Methods

Several methods for the definition of the shape of impeller blades have been previously published. These are briefly reviewed below.

An early choice of many designers for the definition of impeller geometry was conic sections (for example, circular arc, ellipse, etc.), for both the hub and shroud contours and the impeller blades. A general description of the blade surface geometry using conic sections is, for example,

$$r\vartheta = ar^2 + 2brz + cz^2 + 2dr + 2ez + f \tag{1}$$

where the parameters a,b,c,d,e, and f determine the inlet and outlet angles and the blade curvature. Examples of elliptical bladed impellers which fall into this class are quoted by Moore [1] and by Eckardt [2]. An alternative procedure was suggested by Whitfield, Atkey, and Wallace [3]. This made use of Lamé ovals of the general form

$$\left\{\frac{\varphi + a}{b}\right\}^e + \left\{\frac{z + c}{d}\right\}^f = 1 \tag{2}$$

where φ is either r or ϑ to define the blade surface shape. A more complex equation was suggested by Krain [4], who proposed the following formula to define the mean blade surface for "through flow" calculations

$$\vartheta = (a + be^{-r} + c(\pi/2 - \tan^{-1}(r)).$$
$$(1 + e\tan^{-1}(z) + f\tanh(z) + g\sinh(z)) \tag{3}$$

All of these methods allow considerable freedom of shape through adjustment of the parameters a,b,c, etc., but are clearly unsuitable for a general method.

An early general method was described by Jansen and Kirschner [5]. The blade shape was specified by straight-line elements from hub to shroud which were distributed from the inlet to the outlet of the impeller to provide a specified blade aerodynamic loading or a specified blade camber angle (β) distribution. No equations, however, were developed for the blade surface. Smith and Merryweather [6] and Came [7] described a similar computer-aided design method in which the impeller blade is represented by a system of three-dimensional analytic equations, following the method of Coons [8] for surface geometry definition. Fister and Eikelmann [9] described another method that was also based on the interpolation formulae of Coons [8].

These last two methods are quite similar to the procedure adopted here. The fundamental difference in the present work, however, is that the interpolation formulae due to Bezier [10] are used. The methods of both Coons and Bezier fall into a new class of geometries that have been recently developed for numerical controlled machining and manufacturing. Both methods are given in some detail by Faux and Pratt [11]. The particularly elegant technique developed by Bezier has been adopted in the present work for the following reasons:

- The definition of the geometry of any surface is relatively simple.

Nomenclature

a,b,c,d,e,f,g = parameters in various equations
$B_k^n(u)$ = Bernstein Polynomial
D_2 = impeller tip diameter (m)
j,k = indices
m = meridional distance (m)
$\dot{m}$ = mass flow rate (kg/s)
n = degree of Bernstein Polynomial
n = number of Bezier patches
$\bar{P}_k$ = vector of point P_k
r = radius (m)
$\bar{R}$ = vector of point R
s = camberline distance (m)
u,v = parameters to define Bezier patches
U_2 = impeller tip speed (m/s)
x,y,z = rectangular Cartesian coordinates
r,ϑ,z = cylindrical coordinates
β = blade camber angle (deg)
δ = blade thickness (m)
ϵ = meridional pitch angle (deg)
Φ = flow coefficient ($\Phi = \dot{m}/\rho U_2 D_2^2$)
ρ = inlet total density (kg/m^3)

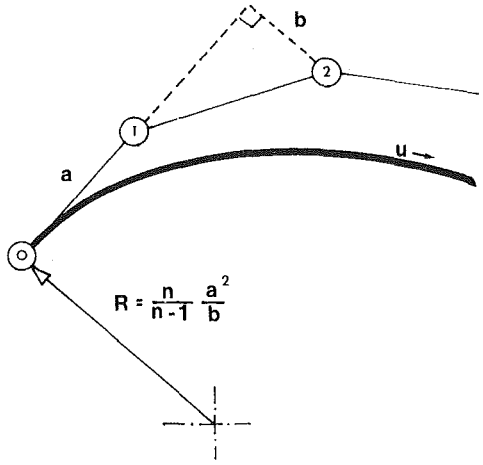

Fig. 3(*a*) Properties of Bezier curves, radius of curvature end point

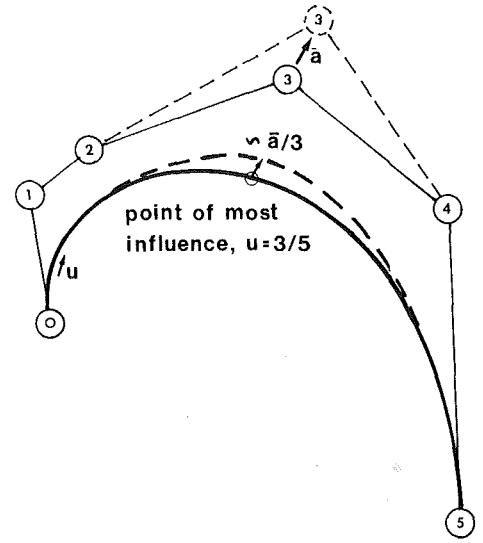

Fig. 3(*b*) Properties of Bezier curves, point of most influence

• Both the flow passages and the blade surfaces can be defined by equations of the same type.

• The shapes produced are general enough to be used in the design of new compressors and in approximation of the geometry of existing ones.

• The defining equations are particularly suitable for incorporation into a computer-aided design (CAD) procedure for compressors.

• The surfaces are defined by algebraic functions which allow systematic and controlled variation of the shape and which provide continuous derivatives up to any required degree.

• The parametric form of the equations allows the coordinate geometry of blades and flow passages to be very simply obtained at any number of points and in any suitable distribution for aerodynamic and stress calculations and for manufacture.

A brief and simple description of the method follows.

Bernstein-Bezier Surfaces

Bezier Curves. A Bezier curve is a parametric representation of a space curve. The curve is specified by the coordinates of a series of points in space of which only the first and last lie on the curve they define. The points are known as the polygon points of the curve, and the figure constructed by connecting these polygon points with straight lines is known as the Bezier polygon of the curve.

The simplest example is a Bezier curve of degree 1 which can be written as

$$\bar{R} = (1-u)\bar{P}_0 + u\bar{P}_1 \tag{4}$$

where R is a vector of a point on the curve with coordinates (x,y,z), and $\bar{P}_0$ and $\bar{P}_1$ are vectors of the polygon points 0 and 1 with coordinates (x_0, y_0, z_0) and (x_1, y_1, z_1), u is a parameter that is constrained to vary from 0 to 1 along the curve. Note that when $u = 0$, $\bar{R} = \bar{P}_0$ and when $u = 1$, $\bar{R} = \bar{P}_1$. For values of u between 0 and 1, the vector $\bar{R}$ describes a straight line from point 0 to point 1, as shown in Fig. 2(*a*). The Bezier curve of degree 2 requires three polygon points to define it and can be written as follows

$$\bar{R} = (1-u)^2\bar{P}_0 + 2u(1-u)\bar{P}_1 + u^2\bar{P}_2 \tag{5}$$

An example is given in Fig. 2(*b*). It can be seen that the second polygon point, P_1, does not lie on the curve, but that the tangents to the curve at the starting point ($u = 0$) and end point ($u = 1$) are in the direction of this point.

The Bezier curve of degree 3 requires four polygon points to define it and can be written as follows

$$\bar{R} = (1-u)^3\bar{P}_0 + 3u(1-u)^2\bar{P}_1 + 3u^2(1-u)\bar{P}_2 + u^3\bar{P}_3 \tag{6}$$

From the form of these equations it can be seen that the Bezier curve is, in some sense, the weighted average of the polygon points defining the curve. The weighting functions are the Bernstein polynomials $B_k^n(u)$ where

$$B_k^n(u) = \binom{n}{k} u^k (1-u)^{n-k} \tag{7}$$

The general form of the Bezier polynomial of degree n is given by

$$\bar{R} = (1-u)^n\bar{P}_0 + n(1-u)^{n-1}u\bar{P}_1 + \frac{n(n-1)}{2}(1-u)^{n-2}u^2\bar{P}_2 + \ldots + \binom{n}{k}u^k(1-u)^{n-k}\bar{P}_k + u^n\bar{P}_n = \sum_{k=0}^{n}\bar{P}_k B_k^n(u) \tag{8}$$

Some important properties of Bezier curves are listed below, without proof:

(*a*) Degree of polynomial. A polynomial of degree n is defined by $n + 1$ points in space.

(*b*) Tangents at end points of curve. The tangent at the beginning ($u = 0$) of a Bezier polynomial is in the direction of the second polygon point. Similarly, at the end point ($u = 1$), the tangent is in the direction of the last but one point. This can be easily proved by differentiating equation (8) with respect to u and setting $u = 0$ or 1.

(*c*) Second derivatives at end point. The second derivative of the curve at the end points depends only on the first three points P_0, P_1, and P_2. The radius of curvature at the end point is given by the construction shown in Fig. 3(*a*). This simple construction can be used to ensure that a polynomial will have a certain radius of curvature at its ends. For example, if a curve is needed which has zero curvature at the end then the first three points must form a straight line ($b = 0$ in Fig. 3(*a*)).

(*d*) Points of most influence. If the point, P_k, of an nth degree Bezier polynomial is moved by a vector, $\bar{a}$, then this movement has most influence at the point on the curve, where $u = k/n$. The point of most influence moves by approximately $\bar{a}/3$. This is demonstrated in Fig. 3(*b*). This

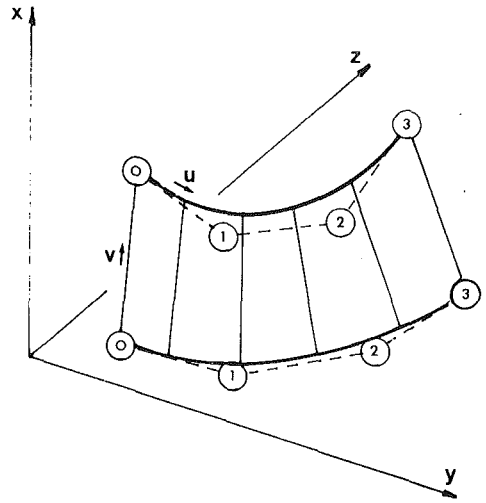

Fig. 4(*a*) Examples of Bezier surfaces, a cubic linear patch

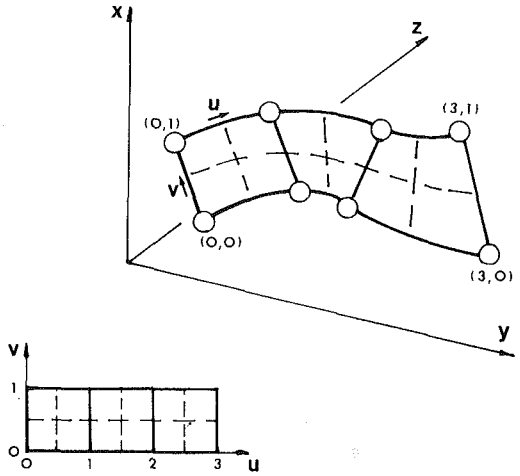

Fig. 4(*b*) Examples of Bezier surfaces, a string of patches

property can be used to produce controlled modifications to the shape of the curve.

(*e*) Increasing the degree of a Bezier curve. It is usually possible to obtain a Bezier curve of low degree that gives approximately the required shape. Sometimes, however, it may be necessary to increase the degree of the curve in order to obtain more freedom of shape. The degree, n, of a curve can be increased in the first instance without changing the shape by following some elementary geometrical rules (see Forrest [12]. This enables the degree of a curve to be systematically increased until it can represent the appropriate shape.

(*f*) Derivative with respect to u. The following identities can be used to calculate the derivatives with respect to u

$$\frac{d}{du}\{B_k^n(u)\} = n\{B_{k-}^{n-}\}(u) - B_k^{n-1}(u)\} \tag{9}$$

where

$$B_{-1}^{n-1}(u) = 0 \quad \text{and} \quad B_n^{n-1}(u) = 0$$

Bezier Surface. A simple three-dimensional curved surface can be defined by a series of straight lines joining points of constant, u, of two adjacent Bezier curves, as shown in Fig. 4(*a*). A second parameter, v, can be introduced which varies from 0 to 1 as one proceeds along the straight lines between the two curves. Thus any point on this surface can be referred to by the parametric coordinates (u,v). The three-dimensional surface (x,y,z) is mapped onto a two-dimensional plane (u,v) by the equations

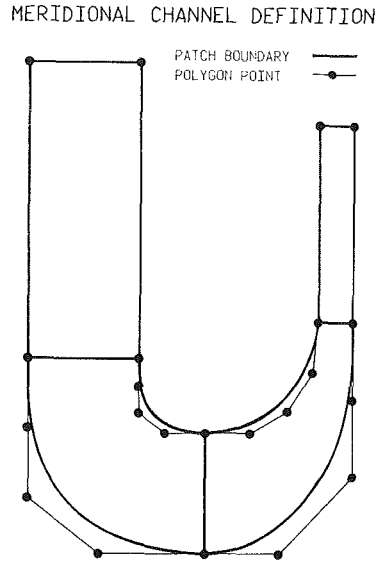

Fig. 5 Definition of meridional channel by means of Bezier surfaces

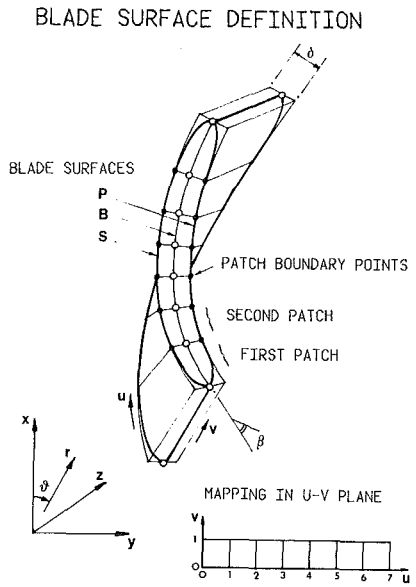

Fig. 6 Definition of blade surfaces

$$\bar{R}(x,y,z) = \bar{R}(u,v) = \sum_{k=0}^{n} \{(1-v)\bar{P}_k^0 + (v)\bar{P}_k^1\} B_k^n(u) \tag{10}$$

where $\bar{P}_k^0$ are the vectors of the polygon points along the $v = 0$ curve and the $\bar{P}_k^1$ are those along the $v = 1$ curve.

In the present method, it is only possible to construct surfaces which are linear in the v-direction. Such surfaces are considered to be aerodynamically acceptable and clearly greatly simplify the manufacture of the surface.

Bezier Patches. The segment of the surface shown in fig. 4(*a*) is known as a cubic-linear patch as it is third degree in the u-direction and first degree in the v-direction. More complicated surfaces can be obtaned by increasing the degree of the Bezier curves in the u-direction, or, alternatively by connecting several curved patches together. An example of a surface comprising three patches and its mapping onto the (u,v) plane is shown in Fig. 4(*b*).

The curves u = constant and v = constant can be mapped onto the surface to form a net, as shown in Fig. 4(*b*). Thus the parametric representation of the surface provides a simple method of referring to any point on the curved surface.

Implementation of Bezier Patches to Describe Geometry of a Compressor

The Meridional Channel (M). The meridional channel is defined by a string of Bezier patches in the $x-z$-plane, thus giving a plane surface that is a meridional section through the compressor. The mathematical rotation of this plane surface around the z-axis defines the internal flow channel of the compressor. The blades are defined separately, and there is no distinction between moving and stationary parts of the channel.

A representation of a meridional channel defined in this way is shown in Fig. 5. The channel includes an inlet section, an impeller section, and a diffusor section. It comprises four patches and the polygon points of these patches are shown. The consecutive patches are of degree 1,4,4, and 1. The line v = 0 represents the hub side contour, and the line v = 1 represents the shroud side contour.

The meridional channel can be specified by expressly defining the polygon points themselves. This procedure is, however, rather inconvenient, and in the present method various subprograms are used to determine the polygon points from data that is more readily available to the designer. For example, the channel shown in Fig. 5 has been specified with the following data:

(*a*) Radii of patch corner defining points
(*b*) Axial spacing between patch corner defining points, that is inlet and outlet channel widths, axial length of inlet, and axial length of impeller section
(*c*) Additional data to position the internal polygon points of each patch, in general expressed as fractions of the length of the sides of the polygon, so that the shape of the shape of the channel walls can be simply adjusted

Various subprograms have been developed for different types of compressor channels. These subprograms are usually written to provide:

(*a*) Continuity of derivatives across patch boundaries
(*b*) Sufficient free parameters that the designer can readily specify the "skeletal" dimensions of the channel and easily change the shape of the curved portions of the channel

The use of these subprograms allows the designer to specify the hub and shroud contours as one of a family of related shapes.

Blade Surfaces (B, S and P). The method of this paper can be used to define all the vaned cascades of a compressor, that is, inlet guide vanes, impeller vanes, diffusor vanes and return channel deswirl vanes. For each vane three separate strings of patches are used to define three blade surfaces, as in the method of Smith and Merryweather [6].

The first surface, known as the blade camber surface (B), is the three-dimensional equivalent of the two-dimensional camber line used in the traditional aerofoil design methods. The other surfaces are the suction surface (S) and the pressure surface (P) of the vane. These are spaced equal distances on either side of the camber surface, as shown in Fig. 6.

In the present method the three blade surfaces (B, S, and P) can be defined as single patches of high polynomial degree or as strings of patches of lower degree. Each surface must, however, have the same number of patches of the same degree, and the variation of the parameters (u, v) on adjacent points must be the same. With this formulation only one coordinate value of the parametric variables (u, v) refers to equivalent points on these three surfaces.

The most convenient method for determining the polygon points of the blade is by means of a subprogram which calculates the polygon points from data provided by the designer, such as blade camber angle (β) and thickness (δ) distributions. Various subprograms have been developed which, in general, utilize the following procedure:

(*a*) A meridional channel (M) is defined within which the blade is to be specified.
(*b*) The position of the blade within the channel M is defined by specifying four values of parameter u corresponding to the leading and trailing edge on the hub and shroud.
(*c*) The distribution of camber line angle (β) is specified as a function of the meridional distance (m) along the hub and shroud. The shape of the camber line along the hub and shroud is then calculated by integration along the meridional channel.

$$\vartheta = \int \frac{\tan \beta}{r}\, dm \tag{11}$$

(*d*) The blade thickness distribution (δ) is specified as a function of the meridional distance (m) along the hub and shroud. The suction and pressure surfaces are placed an equal distance either side of the camber line to give the required thickness distribution.
(*e*) The blade shape along the hub and shroud contours is fully specified by the operations *a*, *b*, *c*, and *d*, outlined above, but the coordinates of the Bezier patches for this shape have yet to be found. The first step is to select a certain spacing of the patch boundary points along the hub and shroud contours. The patch boundaries can, for example, be spaced equidistant along the blade surface or equidistant along the projection of the blade surface onto the meridional channel. The choice of position for patch boundary points influences the final shape of the blade as it determines the orientation of the straight line elements from hub to shroud. Having selected the required number of patches and the required patch distribution along the blade, the polygon points at the junctions between the patches are then suitably interpolated.
(*f*) It now remains to calculate the position of the internal polygon points within each patch, such that the shape produced is a close approximation to that specified by operations *a*, *b*, *c*, and *d* above. Experience has shown that sufficient accuracy is obtained if each patch is chosen to be of degree 3 in the u-direction, giving rise to cubic-linear patches that resemble the patch shown in Fig. 4(*a*). For each cubic-linear patch there are four internal polygon points so that if the surface has n patches there are $4n$ points whose coordinates must be determined. Conditions of continuity of slope and curvature across n-1 patch junctions provide $4(n\text{-}1)$ equations for the unknown points. The remaining four equations are obtained by the specification of the blade angles at the leading and trailing edges on the hub and shroud. This algebraic problem is exactly equivalent to fitting parametric cubic splines through the patch corner defining points on the hub and shroud, and is explained in detail in the Appendix.
(*g*) In order to improve the aerodynamics of the blade a final modification to the end patches at the leading and trailing edges may be made in order to produce rounded shapes, much in the same way suggested by Smith and Merryweather [6].

This procedure produces blade shapes that are defined by means of a string of cubic-linear patches for each of the blade surfaces (B, S, and P). The cubic curves lie in streamwise direction, and the straight line elements lie roughly normal to

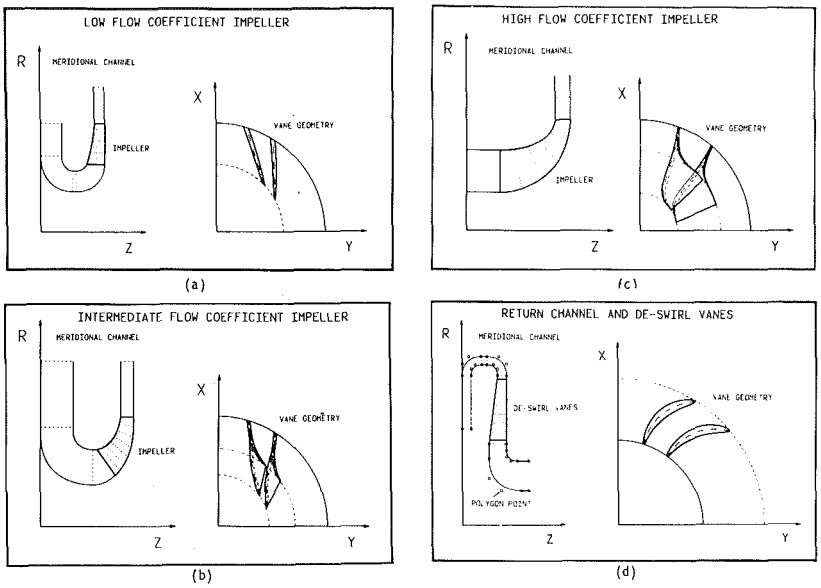

Fig. 7 Examples of channels and blades defined by the present method (a) low flow coefficient impeller, (b) intermediate flow coefficient impeller, (c) high flow coefficient impeller, (d) return channel and deswirl vanes

the stream lines from hub to shroud. The generated blade shapes are restricted to having trapezoidal thickness distributions, i.e., constant taper along any line element between hub and shroud. The orientation of the straight line blade elements can be controlled to give rise to the following blade surfaces:

(*a*) An arbitrary blade surface in which the elements have no particular preferred orientation, but lie roughly normal to the channel walls

(*b*) An axial element blade surface in which all blade elements are straight lines in the axial directions

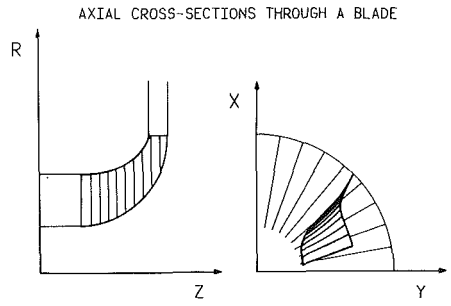

Fig. 8 Axial cross-sections through an impeller blade

Examples of Use

Definition of Compressor Geometry. Impellers and blades of almost any geometrical form can be defined by this method. Some examples of impellers for high, intermediate and low flow coefficients are shown in Fig. 7(*a*), 7(*b*), and 7(*c*), respectively. A further example of the flexibility, is shown in Fig. 7(*d*), which represents a return channel and deswirl vane. In each of these diagrams the patch boundaries are shown, and in Fig. 7(*d*) the channel polygon points are also given. Typical computer run times for these problems are of the order 1–3 s on an IBM 3033 computer, depending on the amount of output and the number of plots.

Blade Sections. The use of analytic equations for the blade definition makes geometrical operations, such as rotation or intersection with a specified plane, relatively straightforward. An example is shown in Fig. 8, where cross sections of a blade with planes normal to the axis are delineated. In this example, the sections through the blade are very nearly radial lines, which produces low bending stresses at the blade root. If these lines were not radial, the designer might wish to modify the blade by introducing a rake angle at the trailing edge or by changing the blade angle distribution along the hub or shroud.

Automatic Net Generation for Flow and Stress Calculations. The great advantage of using a parametric description for all of the surfaces is that the coordinates of points on the surface can then be very simply obtained by specifying the values of the parametric coordinates (u, v). By this means the geometric data of the channel walls and blade surfaces can be generated at any number of points and in any suitable distribution for subsequent aerodynamic and stress calculations or for manufacture.

Any point on a Bezier surface can be referred to by its appropriate (u,v) coordinate. Normally, however, the coordinates of many points on the surface are required and it would be extremely tedious to have to specify all of the individual u, v coordinates. In the present method, this problem is solved by using supplementary parameters to set up an array of points in the u, v plane at which the geometrical details are to be calculated. An example is shown in Fig. 9, where the blade and channel parametric coordinates (u, v) are specified to set up a suitable grid for a streamline curvature "throughflow" calculation. A further example is given in Fig. 10, where a grid for a three-dimensional stress calculation is generated.

This aspect of the method has proved extremely useful in the computer-aided procedure, since the interface between the geometry definition and the subsequent aerodynamic or stress calculations can be made extremely general. The differing distributions of coordinate data needed by different flow and stress programs can be very simply obtained. The net generation method has shown itself to be extremely well adapted for flow calculations, as it automatically produces a grid of "body-fitted" coordinates.

Standarization of Impellers. In the standarization of industrial centrifugal compressor, it is often the case that a

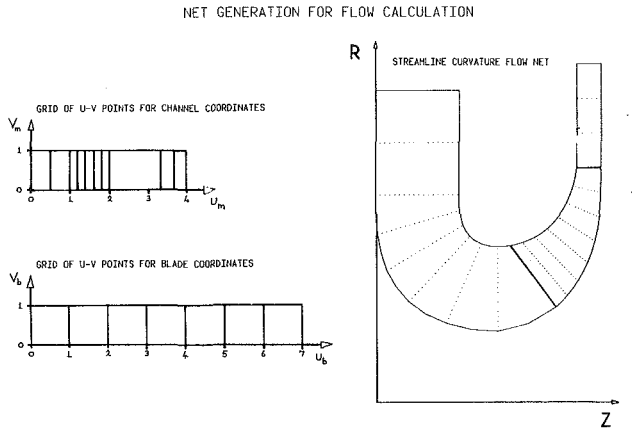

Fig. 9 Automatic net generation for streamline curvature flow calculation

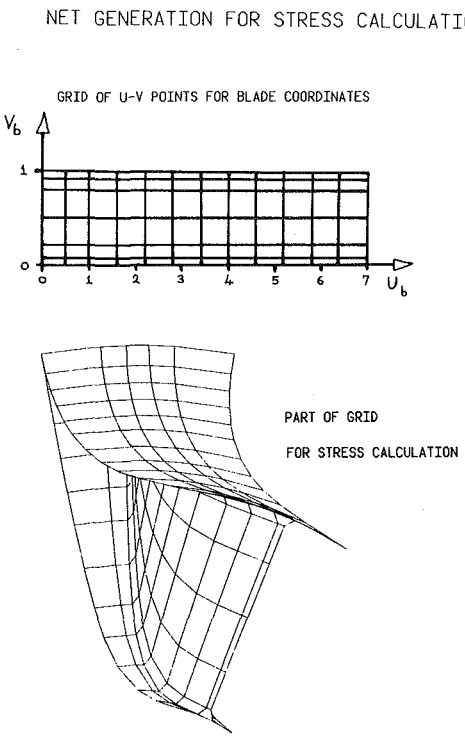

Fig. 10 Automatic net generation for a finite element stress calculation

particular blade shape is used in combination with different meridional channels in order to adapt the blade to different aerodynamic conditions. The original blade may be modified by removing (or adding) a section on the shroud side (shroud-cut) or a section on the hub side (hub-cut). The present formulation allows this standardization to be carried out in the following way:

(*a*) The impeller blade surfaces (B, S, and P) are originally defined to lie within a meridional channel (M′).

(*b*) A new meridional channel (M) is then defined which may be narrower or wider than the original channel (M′).

(*c*) The new flow channel between the blades is then redefined by the intersection of the new meridional surface (M) with the blade surfaces (B, S, and P).

(*d*) The net of u, v-coordinates that refers to the blade surfaces (u_b, v_b) is then suitably modified so that the values are truly confined to that part of the blade within the flow channel. The use of algebraic equations makes the mathematics of the rotation and intersection relatively simple.

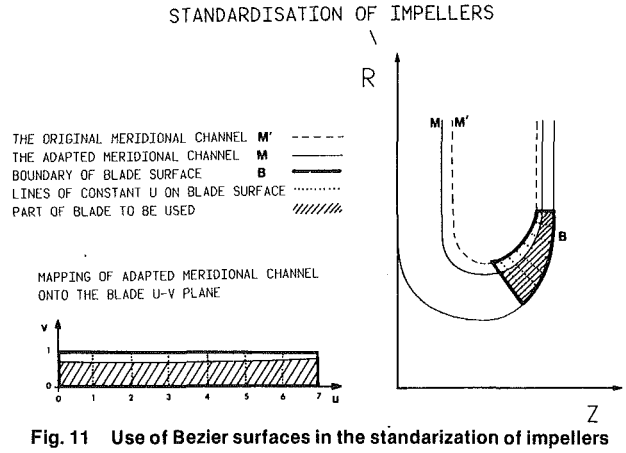

Fig. 11 Use of Bezier surfaces in the standarization of impellers

The definition of the blade surface is extrapolated linearly outside the range $0 < v < 1$, if the new meridional channel (M) is wider than the blade in question.

An example of this procedure is given in Fig. 11.

Manufacture of Impellers. The use of equations to define the shape of impeller blades enables the coordinates required for manufacture to be easily generated. The impeller can then be machined by any conventional method. This method of geometry description is particularly well adapted for manufacture by a five-axis numerically controlled milling machine. The straight line generators of the blade surface focus approximately on a common point and are nearly normal to the hub wall and this allows the impeller to be flank milled on a numerically controlled machine.

Concluding Remarks

An extremely flexible computational geometry for the shape definition of various components in centrifugal compressors has been put forward. In addition to its use in the definition of impeller geometry, the method can be used to define the complete flow passages in a compressor. The method has been including in a computer-aided design system and offers the following advantages over earlier methods:

- Blade and flow channels of almost any required shape can be designed.
- The coordinate data for flow or stress calculations or for manufacture can be readily obtained.

By using this method the designer is able to get a better "feel" for the geometry during the design process, he spends less time on mundane data preparation, and he has more freedom to make full use of his creativity to design a better machine.

Acknowledgments

The author would like to thank Sulzer-Escher Wyss Brothers Ltd., Switzerland, for permission to publish this paper, and Dr. M. Engeli of Fides, Zurich, for introducing him to the theory of Bezier surfaces.

References

1 Moore, J., "Eckard's Impeller—A Ghost From Ages Past," University of Cambridge, Department of Engineering, CUED/A—Turbo TR 83, 1976.

2 Eckardt, D., "Flow Field Analysis of Radial and Backswept Centrifugal Compressor Impellers, Part. 1: Flow Measurements Using a Laser Velocimeter," ASME *Conference Publication: Performance Prediction of Centrifugal Pumps and Compressors*, Mar. 1980, New Orleans, pp. 77-86.

3 Whitfield, A., Atkey, R. C., and Wallace, F. J., "Computer Aided Design and Testing of Radial and Mixed Flow Centrifugal Impellers with Straight and Backwardswept Blades," Paper C21/78, I Mech. E., 1978.

4 Krain, H., "Beitrag zur Berechnung der quasidreidimensionalen Strömung in Radialverdichter-Laufrädern," Doctoral thesis, Technische Hochschule, Aachen, Dec. 1975.

5 Jansen, W., and Kirschner, A. M., "Impeller Blade Design Method for Centrifugal Compressors," NASA—SP 304, pt. II, 1974, pp. 537-563.

6 Smith, D. J. L., and Merryweather, H., "The Use of Analytic Surfaces for the Design of Centrifugal Impellers," *International Journal for Numerical Methods in Engineering*, Vol. 7, 1973, pp. 137-154.

7 Came, P. M., "The Development Application and Experimental Evaluation of a Design Procedure for Centrifugal Compressors," *Proc. I, Mech. Eng.*, Vol. 192, No. 5, 1978.

8 Coons, S. A., "Surfaces for Computer Aided Design of Space Forms," Report MAC-TR-41, Massachusetts Inst. of Technology, MA, U.S.A., 1967.

9 Fister, W., and Eikelmann, J., "A Procedure for the Computer Aided Construction of Radial Compressor Impellers with High Flow Coefficient," Paper 16, AGARD Conference Proceedings No. 282, Bruxelles 1980.

10 Bézier, P., *Emploi des Machines â Commande Numêrique*, Masson et Cie., Paris, 1970.

11 Faux, I.D., Pratt, M. J., *Computational Geometry for Design and Manufacture*, Ellis Horwood (John Wiley), London, 1979.

12 Forrest, A. R., "Interactive Interpolation and approximation by Bezier Polynomials," *Comp. Journal*, Vol. 15, 1972, pp. 71-79.

APPENDIX

In this appendix we illustrate some aspects of the algebra required to determine the polygon points of the blade surface Bezier patches. For the sake of clarity we describe only the equations for the x-coordinates of the polygon points in detail.

On both the hub and shroud of each blade surface (B, S, and P) we determine a set of $n+1$ patch corner defining points with x-coordinates, x_1, x_2 . . . . x_{n+1}. A curve in space between these points is interpolated with a cubic parametric spline of the form

$$x = a_j(1-u)^3 + b_j\, 3u(1-u)^2 + c_j\, 3u^2(1-u) + d_j\, u^3 \qquad \text{(A1)}$$

where u varies from 0 to 1 along each curve between two adjacent defining points and j taken values from 1 to n for the n intervals between the points. If we now compare equation (A1) with the Bezier curve of degree 3 as given in equation (6) we see that the two equations are identical, whereby the parameters a_j, b_j, c_j and d_j are the x-coordinates of the polygon points and j is the number of the patch.

If we differentiate equation (A1) with respect to u and apply the conditions for continuity of x, dx/du and d^2x/du^2 at the junction between patch j and patch $j+1$ we obtain the following relationships

$$\begin{aligned} a_{j+1} &= x_j \\ b_{j+1} &= 2\,d_j - c_j \\ c_{j+1} &= b_j + 4\,d_j - 4\,c_j \\ d_{j+1} &= x_{j+1} \end{aligned} \qquad \text{(A2)}$$

In addition we can also derive that at the leading edge (where $u = 0$ and $j = 1$),

$$\frac{dx}{du} = -3a_1 + 3b_1 \qquad \text{(A3)}$$

and at the trailing edge (where $u = 1$ and $j = n$),

$$\frac{dx}{du} = -3c_n + 3d_n \qquad \text{(A4)}$$

The values of parameters a_j, b_j, c_j, and d_j are fully defined by the recurrence relationship given in equation (A2), the set of defining points x_1, x_2, . . . x_{n+1} and two additional items of information. In the present method it is convenient to specify the derivatives at the leading and trailing edges as additional information, as this ensures that the inlet and outlet angles of the blading are exactly as specified. The required derivatives are determined from the known geometry of the blade by the following equations

$$\begin{aligned} \frac{dx}{du} &= \frac{ds}{du} \cdot (\sin\beta.\ \sin\vartheta + \cos\beta.\ \sin\epsilon.\ \cos\vartheta) \\ \frac{dy}{du} &= \frac{ds}{du} \cdot (-\sin\beta.\ \cos\vartheta + \cos\beta.\ \sin\epsilon.\ \sin\vartheta) \\ \frac{dz}{du} &= \frac{ds}{du} \cdot (\cos\beta.\ \cos\epsilon) \end{aligned} \qquad \text{(A5)}$$

where s is the length along the camber line of the blade, β is the blade camber angle, ϵ is the meridional pitch angle of the hub or shroud $\left(\epsilon = \tan^{-1}\left(\frac{dr}{dm}\right)\right)$ and ϑ is the circumferential coordinate.

The parameters a_j and d_j are easily obtained from equation (A2) as these are identical to the defining point coordinates, but parameters c_j and b_j must be calculated. This is done in the following way. Parameter b_1 is determined from equations (A3) and (A5). The value of c_1 is then taken as $c_1 = 0$, and the recurrence relations (A2) are successively applied at each patch junction until a value of c_n is determined. This precedure is repeated for $c_1 = 1$, and another value for c_n is established. The correct value of c_1 is then chosen by linear extrapolation such that equation (A4) gives the correct slope at impeller outlet. Equations (A2) are then applied once more to each patch successively to fully determine the polygon point coordinates.

Flow Distributions and Discharge Coefficient Effects for Jet Array Impingement With Initial Crossflow

L. W. Florschuetz
Professor.
Mem. ASME

Y. Isoda
Graduate Assistant.
Student Mem. ASME

Department of Mechanical and Energy Systems Engineering,
Arizona State University,
Tempe, Ariz. 85287

Two-dimensional arrays of circular air jets impinging on a surface parallel to the jet orifice plate are considered. The jet flow, after impingement is constrained to exit in a single direction along the channel formed by the jet orifice plate and the impingement surface. In addition to the crossflow which originates from the jets following impingement, an initial (independent) crossflow is present which approaches the array through an upstream extension of the channel. The configurations considered are intended to model the impingement cooled midchord region of gas turbine airfoils in cases where an initial crossflow is also present. Experimentally determined row-by-row streamwise distributions of the jet and crossflow velocities are presented for ratios of the initial crossflow rate to the total jet flow rate ranging from zero to unity. Comparisons are drawn between the measured flow distributions and a theoretical model which is presented. Effects of crossflow velocity and impingement surface proximity on jet hole discharge coefficients are also presented and discussed.

Introduction

Impingement with high velocity gas jets has become an established method of convectively cooling or heating surfaces in a wide variety of process and thermal control applications. Examples include cooling of gas turbine airfoils and electronic equipment, drying of paper and textiles or other thin layers or films, annealing of metals, and glass tempering operations.

For gas turbine airfoils a significant application utilizing a two-dimensional array of jets is the cooling of the midchord region with a trailing edge discharge. The jet air, after impingement, is constrained to flow toward the rear of the airfoil along the channel formed between the orifice plate and the inner surface of the airfoil envelope. Thus, in this configuration, exhaust from the upstream jets imposes a confined crossflow on the downstream jets.

In some schemes there is an initial (independent) crossflow approaching the midchord jet array. This crossflow arises from leading edge cooling air which is subsequently ducted in the chordwise direction along the airfoil inner surface to provide additional cooling. This air, after flowing past the midchord jet array, is exhausted along with the jet air at the trailing edge.

Extensive measurements of heat transfer characteristics and flow distributions for two-dimensional impinging jet arrays intended to model those of interest in gas turbine cooling schemes with no independent crossflow (noninitial crossflow) were previously reported [1, 2, 3]. A correlation was also developed [3]. As a continuation of this investigation both heat transfer and flow distribution characteristics for jet arrays *with* an initial crossflow are being studied. This paper reports on the flow distribution studies for these arrays.

The jet arrays tested had uniform, rectangular inline hole patterns with streamwise and spanwise hole spacings expressed in jet hole diameters ($x_n/d, y_n/d$), of (5, 4); (5, 8); (10, 4); and (10, 8). Each array had ten spanwise rows of holes. The jet plate-to-impingement surface spacings (z/d) were 1-, 2-, and 3-hole diam. Most tests were conducted with a nominal mean jet Reynolds number ($\overline{Re}_j$) of 10^4. The ratio of initial crossflow rate to total jet flow rate (m_c/m_j) was set at nominal values of 0.2, 0.5, and 1.0 for each geometry with a reference test at zero initial crossflow also included.

A primary objective of the paper is to report and characterize the experimentally determined streamwise distributions of the jet flow, emphasizing the parametric effect of the initial crossflow. During the course of the tests significant inconsistencies arose for some cases with larger initial crossflow, when experimental mass balances failed to adequately check. By means of special tests it was found that these inconsistencies were due to crossflow effects on the discharge coefficients of the jet holes. Additional special tests were conducted to account for these effects. An additional objective of the paper is, therefore, to report experimental results for the effect of crossflow on the discharge coefficients of jet orifices. A final objective is to present a relatively simple predictive model for the flow distributions, which in its general form, includes effects of initial crossflow, variable discharge coefficients, and crossflow channel wall shear. Predictions based on the model are compared with the experimentally determined flow distributions.

Contributed by the Gas Turbine Division of the THE AMERICAN SOCIETY OF MECHANICAL ENGINEERS and presented at the 27th International Gas Turbine Conference and Exhibit, London, England, April 18–22, 1982. Manuscript received at ASME Headquarters December 14, 1981. Paper No. 82-GT-156.

Experimental Facility

The basic test model geometry and nomenclature are shown schematically in Fig. 1. The flow region of primary interest is that bounded by the jet exit plane and the impingement surface. The length (L) of this region is considered to extend from one-half a streamwise hole spacing ($x_n/2$) upstream of the first spanwise row of holes to the same distance downstream of the last row. The total crossflow rate approaching a given row is equivalent to the initial crossflow rate (m_c) combined with the total jet flow introduced upstream of that row.

The basic experimental facility was that originally used for a comprehensive series of noninitial crossflow tests [1, 2, 3], but set up in a modified form suitable for conducting tests with initial crossflow. A complete description of the original facility may be found in [4]. The facility was designed for conducting heat transfer tests but was also utilized for measurement of jet flow distributions. In this paper only those features relevant to flow distribution tests in the initial crossflow configuration will be described.

A cross-sectional view of the arrangement is shown in Fig. 2. There were two plenum chambers, supplied individually with laboratory compressed air, one for introducing air to the main jet plate, and one for introducing the initial crossflow air to the channel. The initial crossflow was introduced to the channel through two spanwise rows of jet holes. The main jet plates, each with ten spanwise rows of holes, were interchangeable. The plenum /jet plate assembly was mounted over the test plate unit (impingement plate) through interchangeable spacers which fixed the channel height (i.e., the jet exit plane to impingement surface spacing). The spacers also formed the upstream end surface and slide walls of the channel (side walls not apparent in Fig. 2), thus constraining the initial crossflow and the jet flow to discharge in a single direction to the laboratory environment at atmospheric pressure. Significant geometric characteristics of the configurations tested are summarized in Table 1. The array of length L = 12.7 cm with matching jet plenum (Fig. 2) was designated as size B. The jet plates are identified by the notation $B(x_n/d, y_n/d)I$ where the I designates the inline hole pattern. Reckoned from the centerline of the second (i.e., downstream) spanwise jet row of the initial crossflow plenum, the channel length available for flow development upstream of the jet array (initial crossflow development length) ranged from 16 to 95 hydraulic diameters, depending on the channel height. It may also be noted that this length was 19 times the streamwise hole spacing in the main jet array (x_n = 1.27 cm). Average jet plate discharge coefficients, to be discussed later, are also included in Table 1.

Table 1 Geometric parameters and mean discharge coefficients for jet plates tested

Jet plate $B(x_n/d, y_n/d)I$	A_o^*	d and b (cm)	N_s'	$\bar{C}_D$
B(5,4)I	0.0393	0.254	18	0.85
B(5,8)I	0.0196	0.254	9	0.80
B(10,4)I	0.0196	0.127	36	0.76
B(10,8)I	0.0098	0.127	18	0.76

Channel height, (z/d) = 1, 2, and 3
Fixed parameters:
channel width (span), w = 18.3 cm
overall channel length, 43.2 cm
initial crossflow channel length, 26.0 cm
B – size jet array and plenum length, L = 12.7 cm
downstream exit length, 4.5 cm
initial crossflow development length, 24.1 cm
number of spanwise rows of jet holes, N_c = 10
inline hole patterns

Experimental Procedures and Data Reduction

The initial crossflow rate and total jet flow rate for each test condition were measured utilizing standard square-edged orifice plates in flow metering sections upstream of the respective plenums. Plenum pressure levels were measured via static pressure taps, while plenum air temperatures were determined using copper-constantan thermocouples. All pressure measurements were made with either U-tube or single leg well-type manometers. Plenum air temperatures were nominally at ambient levels of about 300K. Plenum pressures ranged from slightly above the nominal exhaust pressure level of one atmosphere to as high as 275 kPa, depending on test conditions. The distribution of the jet flow among the individual spanwise rows of the array was determined from measurements of streamwise channel pressure profiles and jet plate discharge coefficients.

Nomenclature

A_o = total jet hole area
A_o^* = ratio of jet hole area to opposing impingement surface area (open area ratio)
b = thickness of jet plate
B = dimensionless quantity defined following equation (6)
C = dimensionless quantity defined following equation (6)
C_D = jet plate discharge coefficient
d = jet hole diameter
f = friction coefficient defined as $2\tau_w\rho/G_c^2$
G_c = crossflow mass velocity based on channel cross-sectional area
$\tilde{G}_c$ = G_c normalized by channel exit mass velocity, $G_c/[(m_c+m_j)/(z\cdot w)]$
G_j = jet mass velocity based on jet hole area
G_j^* = superficial jet mass velocity based on jet plate area
L = streamwise length of jet plate and impingement surface (Figs. 1 and 5)
m_c = initial (independent) crossflow rate
m_j = total jet flow rate
M = initial crossflow-to-total jet flow ratio, m_c/m_j
N_c = number of spanwise rows of holes in streamwise direction
N_s' = number of jet holes across span of channel
P = channel pressure
P_o = jet plenum pressure
R = ideal gas constant
Re_c = crossflow (channel) Reynolds number, $G_c(2z)/\mu$
Re_j = jet Reynolds number, $G_j d/\mu$
T_o = jet plenum air temperature
w = width (span) of channel
x = streamwise location along jet plate or impingement surface (Figs. 1 and 5)
$\tilde{x}$ = x/L
$\tilde{x}'$ = $\tilde{x}-(1/2)(x_n/L)$
x_n = streamwise jet hole spacing
y_n = spanwise jet hole spacing
z = channel height (jet plate-to-impingement surface spacing)

Greek

ξ = function defined by equation (2)
γ = ratio of specific heats
μ = dynamic viscosity
ρ = fluid density
τ_w = channel wall shear stress

Subscripts and Superscripts

bp = refers to "break point" value of G_c/G_j
$(\bar{\ })$ = overbar refers to mean value over jet plate

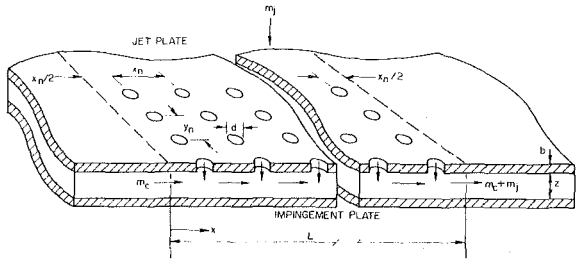

Fig. 1 Basic test model geometry and nomenclature

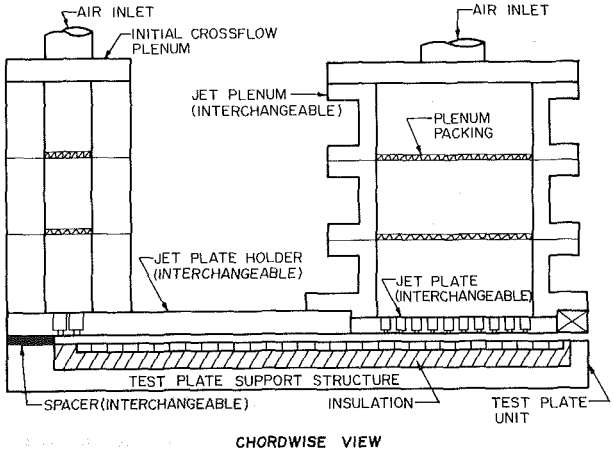

Fig. 2 Initial crossflow test unit assembly

Streamwise channel pressure traverses were accomplished with static pressure probes inserted from the open downstream end of the channel. The probes were stainless steel tubes of either 0.089 or 0.124 cm outside diameter closed at the upstream end, with a single orifice of 0.0254 cm in the tube sidewall located 0.32 cm from the end. For a given run the tube was positioned along one lower corner of the channel and pressed against the channel side wall and bottom by slightly bowing the tube. This positioning provided support of the tube, thus preventing vibration and possible whipping in the presence of a strong channel flow. It may be noted that each channel side wall location, hence the nominal probe position, was at a plane of symmetry midway between streamwise hole row centerlines. For most traverses the orifice was positioned facing upward toward the jet plate, with readings made opposite each spanwise jet row location. For some traverses readings were also made midway between spanwise jet rows. And in some instances, traverses were repeated with the orifice positioned facing downward toward the impingement surface, or toward the channel sidewall. These, as well as prior similar results [5], showed that the pressure measurements were not normally very sensitive to the orifice orientation and that the profiles were rather smooth in traversing from positions between jet rows to positions immediately opposite jet rows. This indicated that dynamic presssure effects were normally of minor significance.

Discharge coefficients for each jet plate were determined from separate tests conducted with the plenum/jet plate assembly removed from the impingement plate and discharging directly to the laboratory environment at atmospheric pressure. Discharge coefficients were defined in the standard manner as the ratio of the actual to the ideal flow rate, where the latter was calculated assuming one-dimensional isentropic perfect gas flow, using measured values of plenum pressure, plenum temperature, and atmospheric pressure. The defining equation is

$$G_j = C_D P_o (P/P_o)^{1/\gamma} \cdot \{2\gamma(\gamma-1)^{-1}(RT_o)^{-1}[1-(P/P_o)^{(\gamma-1)/\gamma}]\}^{1/2} \quad (1)$$

where $G_j = m_j/A_o$. The actual flow rate (m_j) was determined via the standard orifice in the flow metering section upstream of the plenum. A discharge coefficient determined as described above is an average value over all holes in the jet plate. While discharge coefficients for individual holes were not determined, each jet plate was checked for flow uniformity with very satisfactory results as detailed in [4]. Discharge coefficients for each jet plate were measured over a nominal range of jet Reynolds numbers from 2.5×10^3 to 5×10^4. The values were found to be essentially independent of Re_j over this range [4]. The values summarized in Table 1 are mean values over the range.

The jet mass velocity for each spanwise row of holes was calculated based on equation (1) using the channel pressure measured at the row location and $C_D = \bar{C}_D$ for the particular jet plate (Table 1). The sum of the flow rates over all ten rows was then compared with the standard orifice measurement of the total jet flow rate. These mass balances ordinarily closed to within a few percent. However, for tests with the smaller channel heights and larger initial crossflow rates, significant discrepancies up to 42 percent were observed. The discrepancies were thought to be due to crossflow and impingement surface proximity effects on the discharge coefficients.

Several special tests were then conducted to determine the effect of crossflow and impingement surface proximity on the discharge coefficients. These tests were performed with the plenum jet plate assembly mounted over the impingement plate as in standard flow distribution tests, but with the last nine spanwise rows taped over, leaving only the upstream row open. This permitted the jet flow rate through the single open row to be measured directly at the standard orifice flow metering section upstream of the jet plenum. A crossflow rate was also orifice-metered and then introduced through the initial crossflow plenum as in the standard flow distribution tests. The channel pressure at the open row location was measured with the static pressure probe, using the same technique as described above for the channel pressure traverses. In this way, discharge coefficients were determined as a function of crossflow-to-jet velocity ratio (G_c/G_j) and impingement surface proximity (z/d). The use of these results in the reduction of the flow distribution data greatly improved the mass balances (flow rate closures) in those cases where significant discrepancies had existed. The detailed results of the special tests for the crossflow effect on discharge coefficients are presented in the next section.

Effect of Crossflow on Discharge Coefficients

Special tests were conducted as just described using the $B(5, 4)I$ jet plate at $z/d = 1$, 2 and 3 and the $B(5, 8)I$ jet plate at $z/d = 1$. The jet flow rate was set to give a jet Reynolds number of 10^4. The crossflow was then varied to give a range of G_c/G_j. The results are plotted in Fig. 3. For the larger values of G_c/G_j, the jet Reynolds numbers were set at less than 10^4 in order not to exceed the available compressed air supply for the crossflow rate. For these cases the specific Re_j values are noted in the Figure adjacent to the appropriate data points. The composite uncertainly for these C_D values was estimated by the method of Kline and McClintock [6] to be ± 3 percent.

The behavior indicated is that C_D remains essentially constant for G_c/G_j, ranging from zero to a value somewhat less than unity. The data in this range is in close agreement with the individual jet plate average values previously determined in the absence of both a crossflow and an impingement surface (Table 1). Beyond this range, C_D decreases

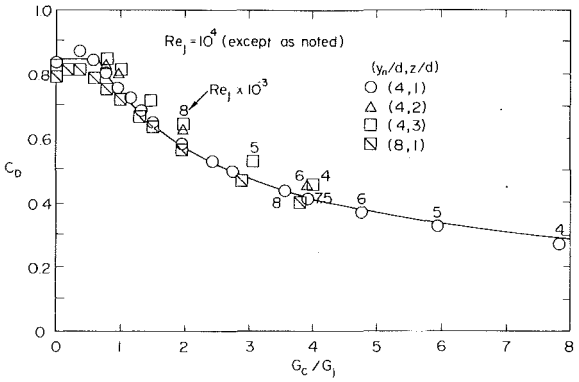

Fig. 3 Effect of confined crossflow on jet orifice discharge coefficients

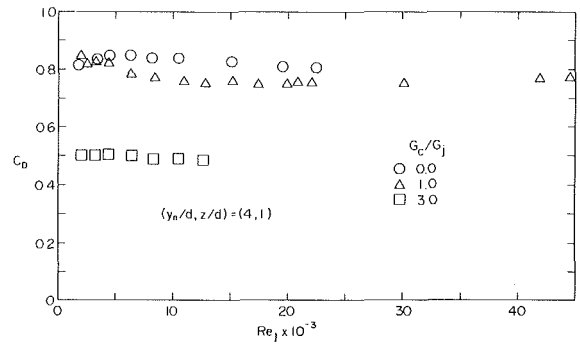

Fig. 4 Effect of jet Reynolds number on jet orifice discharge coefficients for several values of cross-to-jet velocity ratio

significantly in a smooth monotonic fashion, and values for $z/d = 2$ and 3 are somewhat larger than values for $z/d = 1$.

To examine the sensitivity of C_D on Re_j in the presence of a confined crossflow, a second set of special tests was conducted using the upstream row of holes of the $B(5, 4)I$ jet plate with $z/d = 1$. The value of G_c/G_j was maintained constant at several different values. At each value C_D was determined over a range of Re_j. The results (Fig. 4) indicate that for $G_c/G_j = 0$, C_D is not very sensitive to Re_j, which is consistent with the prior test results made with the full jet plate in the absence of both a crossflow and an impingement surface. For the finite values of G_c/G_j, a similar conclusion may be drawn, though for $G_c/G_j = 1$ some small dependence is noticeable as Re_j drops below about 5×10^3. Nevertheless, deviations from a mean value over the Re_j range are no larger than a few percent.

Labeling the value of G_c/G_j at which C_D begins to decrease as the "break point" (*bp*) value the observed behavior may be summarized as follows: (*i*) for $0 \le G_c/G_j \le (G_c/G_j)_{bp}$, C_D may be considered constant (i.e., independent of G_c/G_j and z/d) and equal to $\bar{C}_D$, (*ii*) for $G_c/G_j > (G_c/G_j)_{bp}$, C_D depends primarily on G_c/G_j and secondarily on z/d, and (*iii*) for practical purposes C_D may be considered independent of Re_j.

In order to make use of these results in the reduction of the flow distribution data, algebraic representations of C_D versus G_c/G_j were developed. These are summarized in Table 2. The function $\xi(G_c/G_j)$ appearing in Table 2 is defined by

$$\xi(G_c/G_j) = \frac{1.06}{(G_c/G_j + 0.806)^{0.602}} \tag{2}$$

This represents a nonlinear least squares curve fit to the C_D data points for $G_c/G_j > (G_c/G_j)_{bp}$ obtained using the $B(5, 4)I$ jet plate with $z/d = 1$ (open circles in Fig. 3). The coefficients of ξ shown in Table 2 for the (5, 4) plate at $z/d = 2$ and 3 (1.08 and 1.11, respectively) are the best fit constant multipliers of ξ based on the $z/d = 2$ and 3 data, respectively. The equation for intermediate G_c/G_j values for the (5, 8, 1) case is a best fit straight line constrained to be tangent to the ξ function at $G_c/G_j = 1.5$. For clarity, only the curve for the (5, 4, 1) case is shown in Fig. 3.

Table 2 Algebraic representations for dependence of discharge coefficients on the crossflow parameter (G_c/G_j)

Configuration	Equation	Range of G_c/G_j
$B(5,4,1)I$	$C_D = 0.85$	0 to 0.63
	$C_D = \xi(G_c/G_j)$	>0.63
$B(5,4,2)I$	$C_D = 0.85$	0 to 0.83
	$C_D = 1.08\xi(G_c/G_j)$	>0.83
$B(5,4,3)I$	$C_D = 0.85$	0 to 0.90
	$C_D = 1.11\xi(G_c/G_j)$	>0.90
$B(5,8,1)I$	$C_D = 0.80$	0 to 0.54
	$C_D = -0.169(G_c/G_j) + 0.893$	0.54 to 1.5
	$C_D = \xi(G_c/G_j)$	>1.5
$B(10,4,1)I$ and $B(10,8,1)I$	$C_D = 0.76$	0 to 0.54
	$C_D = -0.128(G_c/G_j) + 0.825$	0.54 to 1.8
	$C_D = \xi(G_c/G_j)$	>1.8

Note: The function $\xi(G_c/G_j)$ is defined by equation (2).

Since the (10, 4) and (10, 8) jet plates were not used in conducting the special C_D tests, the representation summarized in Table 2 for the (10, 4, 1) and (10, 8, 1) configurations was inferred from the results for the (5, 4, 1) and (5, 8, 1) cases. The "break point" was set at the same value as existed for the (5, 8, 1) case. As in the prior cases, C_D for G_c/G_j below the "break point" was set equal to $\bar{C}_D$ from Table 1. For the largest values of G_c/G_j, the ξ function was used, with a linear function joining the "break point" with the ξ function.

In a prior study by Damerow et al. [7], no significant effect of a confined crossflow on jet orifice discharge coefficients was found. Since in that study the maximum value of G_c/G_j was only about 0.8, the conclusion reached is quite consistent with the present results. For angled film cooling holes, Meitner and Hippensteele [8] found a significant effect of the mainstream flow on the coolant injection rate for coolant to mainstream momentum flux ratios less than about 0.4.

Flow Distribution Model

In a previous paper [3], a simple one-dimensional, incompressible flow distribution model was found to be adequate for predicting flow distributions for the array geometries considered here, under noninitial crossflow conditions. The model was developed by assuming the discrete hole array to be replaced by a surface over which the injection is continuously distributed. It also included the assumptions of constant discharge coefficient and negligible effect of channel wall shear. A similar approach was used by Dyban et al. [9] for arrays with no initial crossflow, including some attempt at accounting for channel friction effects. Martin [10] applied a similar model for a geometry in which the injected flow was in fact continuous in the streamwise direction; i.e., an array of slot nozzles in which the outlet flow was constrained to exit parallel to the slots.

The basic model developed in [3] is here extended to include the presence of an initial crossflow. For some of the geometries considered the effect of crossflow on the discharge coefficient and the effect of wall shear were found to be significant when an initial crossflow was present. The model is therefore extended to include these effects as well.

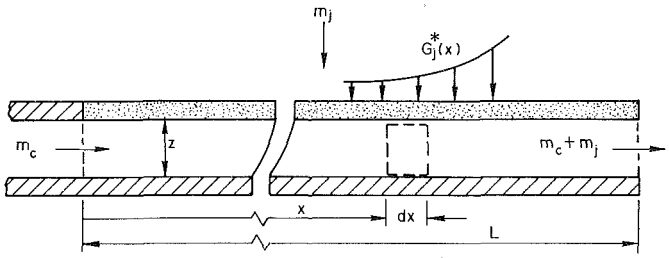

Fig. 5(*a*) Continuous injection model with initial crossflow

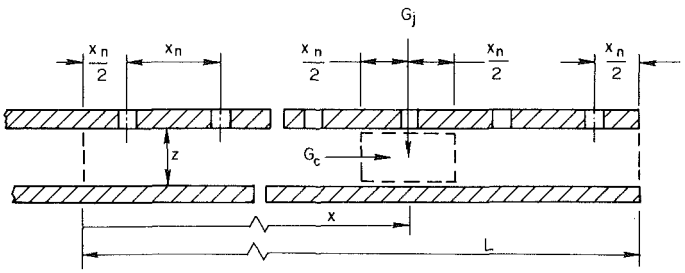

Fig. 5(*b*) Discrete hole injection model

Consider the continuous injection model illustrated in Fig. 5(*a*). The continuously distributed injection velocity G_j^* is related to the jet velocity G_j (Fig. 5(*b*)) through the open area ratio, $G_j^* = G_j A_o^*$. The distributed injection velocity may then be written in terms of the discrete hole discharge coefficient as

$$G_j^* = A_o^* C_D [2\rho(P_o - P)]^{1/2} \tag{3}$$

where, in general, we consider

$$C_D = C_D(G_c/G_j)$$

A force-momentum balance on the control volume indicated in Fig. 5(*a*) results in

$$dP = -\frac{2G_c dG_c}{\rho} - \frac{2\tau_w dx}{z} \tag{4}$$

A mass balance leads to

$$G_j^* = \frac{z dG_c}{dx} \tag{5}$$

For constant P_o, the elimination of G_j^* and P from equations (3), (4), and (5) in favor of G_c yields in dimensionless form

$$\frac{d^2\tilde{G}_c}{d\tilde{x}^2} = \frac{B^2\tilde{G}_c[1 + f(L/2z)\tilde{G}_c/(d\tilde{G}_c/d\tilde{x})] + C(d\tilde{G}_c/d\tilde{x})}{1 + C\tilde{G}_c/(d\tilde{G}_c/d\tilde{x})} \tag{6}$$

where

$$B = \sqrt{2} A_o^* C_D L/z$$

and

$$C = \frac{A_o^* L}{z} \cdot \frac{1}{C_D} \cdot \frac{dC_D}{d(G_c/G_j)}$$

In the presence of an initial crossflow the boundary conditions are $G_c = m_c/(z \cdot w)$ at $x = 0$ and $G_c = (m_c + m_j)/(z \cdot w)$ at $x = L$ or in dimensionless form

$$\tilde{G}_c = M/(1+M) \quad \text{at} \quad \tilde{x} = 0 \tag{7a}$$

$$\tilde{G}_c = 1 \quad \text{at} \quad \tilde{x} = 1 \tag{7b}$$

Equation (6) is nonlinear and must be solved numerically for the general case. Numerical solutions will be presented shortly. However, for the important and useful special case where C_D is constant and wall shear is negligible ($f = 0$) the equation is linear and closed form solutions may be easily written.

Closed Form Solutions For Constant C_D, $f = 0$. For constant C_D and $f = 0$, the solution to equation (6) for $\tilde{G}_c$, with boundary conditions (7*a*) and (7*b*), may be conveniently written in terms of hyperbolic trigonometric functions. The corresponding continuous injection velocity, G_j^*, may then be written in closed form with the aid of equation (5). This result is then utilized to evaluate the discrete hole array jet velocity distribution by assuming that the value of G_j for a given spanwise row of holes is that corresponding to $G_j^*(x)$ with x evaluated at the centerline of the row. The final result for the jet velocity distribution is

$$\frac{G_j}{\bar{G}_j} = B\frac{(1+M)\cosh B\tilde{x} - M\cosh B(1-\tilde{x})}{\sinh B} \tag{8}$$

The crossflow parameter of interest is the crossflow velocity approaching a given spanwise jet row relative to the jet velocity of the row. This may be satisfactorily approximated utilizing G_c from the continuous injection model evaluated one-half a hole spacing upstream of the given row (Fig. 5(*b*)), divided by G_j from equation (8). This operation results in

$$\frac{G_c}{G_j} = \frac{1}{\sqrt{2}C_D}\frac{(1+M)\sinh B\tilde{x}' + M\sinh B(1-\tilde{x}')}{(1+M)\cosh B\tilde{x} - M\cosh B(1-\tilde{x})} \tag{9}$$

where $\tilde{x}' = \tilde{x} - (1/2)(x_n/L)$.

Numerical Solutions. For conditions under which C_D is dependent on G_c/G_j or the wall shear term is included, or both, equation (6) must be solved numerically. C_D was evaluated as a function of G_c/G_j using the appropriate equation from Table 2. Note that G_c/G_j may be written in the form

$$\frac{G_c}{G_j} = \frac{A_o^* L}{z} \cdot \frac{\tilde{G}_c}{(d\tilde{G}_c/d\tilde{x})} \tag{10}$$

with the aid of equation (5) and the relation $G_j^* = G_j A_o^*$. Thus, C_D may be considered as a function of $\tilde{G}_c$ and $d\tilde{G}_c/d\tilde{x}$.

For the complex flow conditions encountered in these jet array geometries a general accurate model for the friction factor is not available. However, in order to assess the significance of wall shear effects the friction factor was approximated according to standard representations for fully developed flow in smooth ducts of constant cross section [11]:

$$f = \begin{cases} 24/\mathrm{Re}_c & \mathrm{Re}_c < 2\times 10^3 \\ 0.079/\mathrm{Re}_c^{0.25} & 2\times 10^3 < \mathrm{Re}_c < 3\times 10^4 \\ 0.046/\mathrm{Re}_c^{0.20} & \mathrm{Re}_c > 3\times 10^4 \end{cases} \tag{11}$$

For use in equation (6), the crossflow channel Reynolds number appearing in these friction factor expressions may be replaced by

$$\mathrm{Re}_c = 2\tilde{G}_c\overline{\mathrm{Re}}_j(1+M)A_o^*(L/d) \tag{12}$$

To proceed with the numerical solution of equation (6) with boundary conditions (7*a*) and (7*b*) it is necessary to specify the geometrical parameters, the flow ratio, M, and the mean jet Reynolds number, $\overline{\mathrm{Re}}_j$. Then, taking into account equations (10), (11), and (12), equation (6) is of the form

$$d^2\tilde{G}_c/d\tilde{x}^2 = fcn(\tilde{x}, \tilde{G}_c, d\tilde{G}_c/d\tilde{x})$$

Solutions were obtained by the shooting method using a fourth order Runge-Kutta integration scheme. Results for $G_j/\bar{G}_j$ and G_c/G_j were then obtained using the same approach as outlined above for the special case of constant C_D and $f = 0$. These results are presented in graphical form in the next section.

Results and Discussion

Experimental flow distribution results for seven different configurations are presented in Figs. 6–12, with one con-

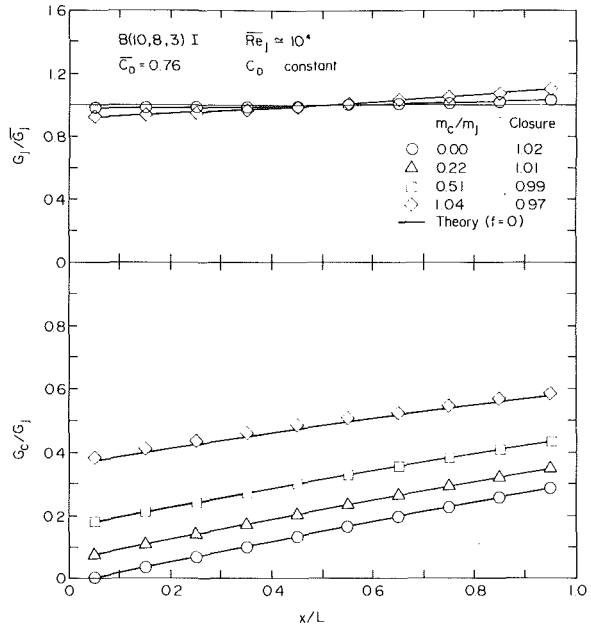

Fig. 6 Effect of initial crossflow on jet array flow distribution for *B*(10, 8, 3) *I* geometry – experimental data compared with predictive model

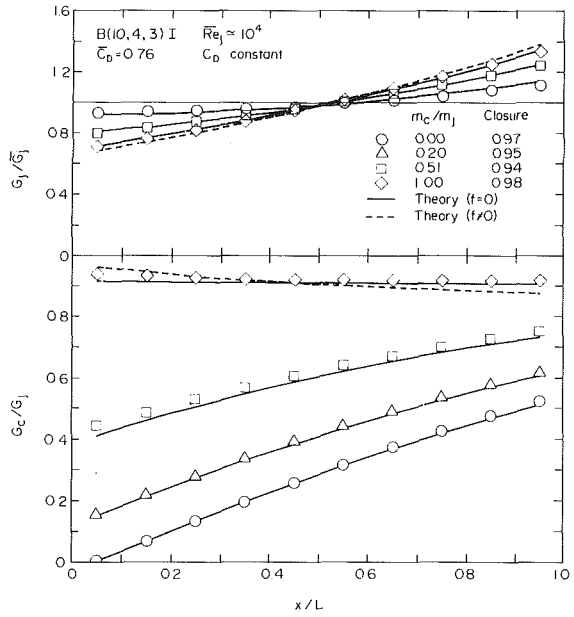

Fig. 8 Effect of initial crossflow on jet array flow distribution for *B*(10, 4, 3)*I* geometry – experimental data compared with predictive model

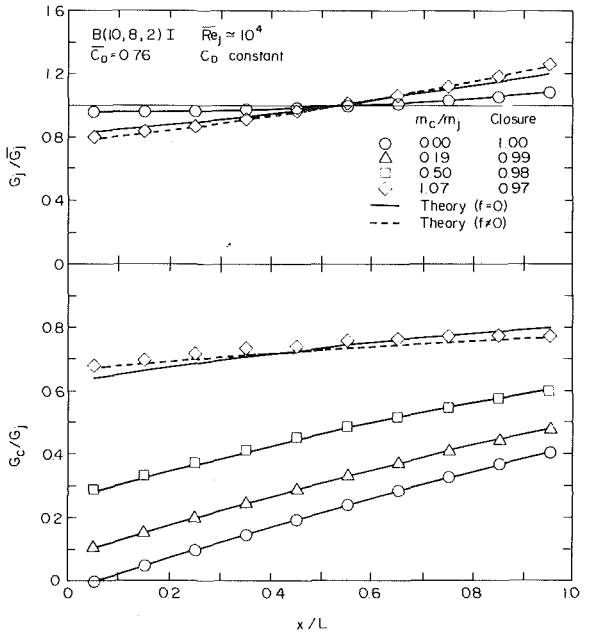

Fig. 7 Effect of initial crossflow on jet array flow distribution for *B*(10, 8, 2)*I* geometry – experimental data compared with predictive model

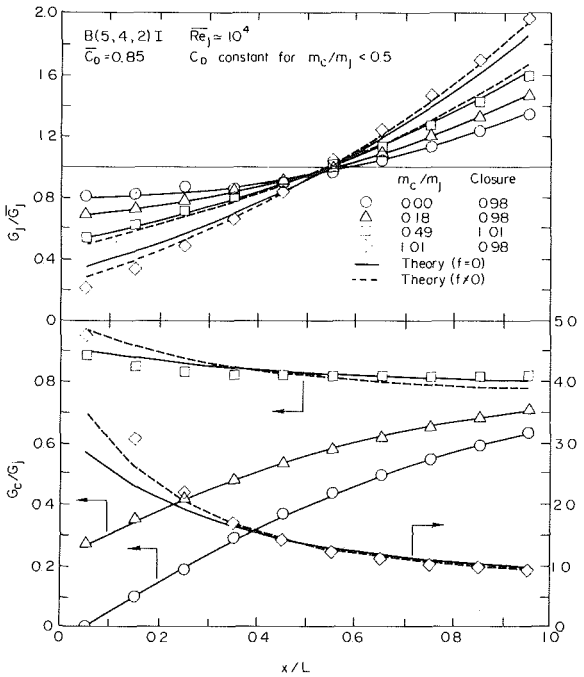

Fig. 9 Effect of initial crossflow on jet array flow distribution for *B*(5, 4, 2)*I* geometry – experimental data compared with predictive model

figuration represented by each figure. Both the jet flow distribution ($G_j/\bar{G}_j$) and the cross-to-jet velocity ratio (G_c/G_j) are shown in each figure for nominal values of $M = m_c/m_j$ at zero, 0.2, 0.5, and 1.0. However, in some instances the data for intermediate values of M is omitted for clarity. The closure obtained for the experimental mass balance in each case is listed in the figures. This closure value is the ratio of the sum of the individual spanwise row jet flow rates to the total jet flow rate measured by the standard orifice. The data points for $G_j/\bar{G}_j$ were determined using $\bar{G}_j$ based on the sum of the individual row flow rates. This approach tends to compensate for any small bias which may have been present in the individual row measurements. The uncertainty associated with these data points was estimated by the method of [6] to be ±2 percent. The uncertainty for the G_c/G_j data points ranges from about ±2 percent for downstream rows, smaller values of m_c/m_j, and larger values of $(y_n/d)(z/d)$ to about ±4 percent for upstream rows, larger m_c/m_j, and smaller $(y_n/d)(z/d)$.

The solid curves in each figure are based on the theoretical model with $f = 0$ (i.e., neglecting wall shear effects). For those cases where G_c/G_j did not exceed $(G_c/G_j)_{bp}$, C_D was constant and the solid curves are represented by the closed form solutions (8) and (9). These cases are indicated in the figures by the notation "C_D constant." Where C_D depended on G_c/G_j, indicated by the notation "C_D variable," the solid curves represent numerical solutions. Numerical solutions including the effect of wall shear ($f \neq 0$) are shown by dashed curves for those cases where the effect is noticeable relative to the corresponding $f = 0$ case.

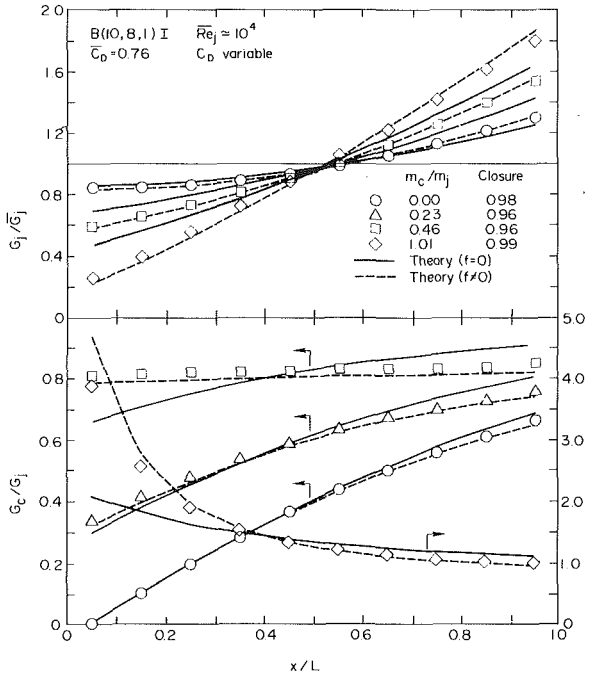

Fig. 10 Effect of initial crossflow on jet array flow distribution for *B*(10, 8, 1)/ geometry – experimental data compared with predictive model

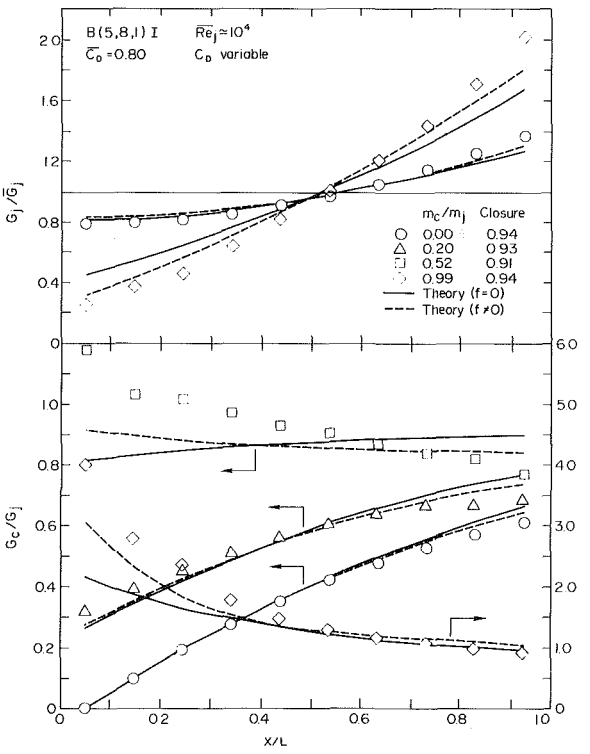

Fig. 11 Effect of initial crossflow on jet array flow distribution for *B*(5, 8, 1)/ geometry – experimental data compared with predictive model

Consider first Figs. 6, 7, and 8. These are geometries with $x_n/d = 10$, and values of the product $(y_n/d)(z/d)$ equal to or greater than 12. For the (10, 8, 3) case (Fig. 6), the jet flow distribution remains nearly uniform with a nearly uniform linear increase in G_c/G_j even for $m_c/m_j = 1$. As $(y_n/d)(z/d)$ decreases (Figs. 7 and 8) and m_c/m_j increases, the flow distribution becomes more nonuniform. G_c/G_j continues to increase in a nearly linear fashion, but at $m_c/m_j = 1$ the

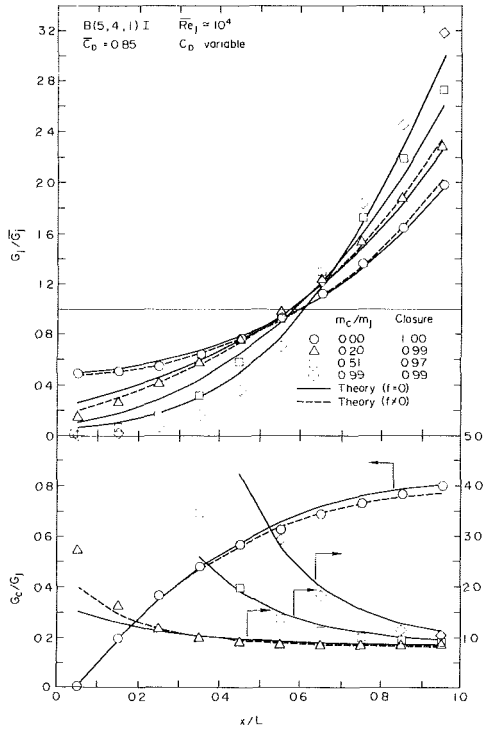

Fig. 12 Effect of initial crossflow on jet array flow distribution for *B*(5, 4, 1)/ geometry – experimental data compared with predictive model

initial crossflow has become large enough to cause G_c/G_j to be almost uniform for the (10, 4, 3) case (Fig. 8). The predictions show the effects of wall shear just beginning to appear for (10,8,2) and (10,4,3) at $m_c/m_j = 1$. Test results with $x_n/d = 5$ (not shown here) were essentially the same as those for $x_n/d = 10$. The theoretical predictions were also identical, except for an even smaller effect of wall shear. The composite uncertainty of these predictions due to uncertainties in the input parameters, again based on the method of [6], is ±2 percent for $G_j/\bar{G}_j$ and ±4 percent for G_c/G_j. In light of these uncertainties and the previously noted data point uncertainties, verification of the predictions by the data is excellent.

Consider next Figs. 9–12. These geometries all have $(y_n/d)(z/d)$ equal to or less than eight, and all have $z/d = 1$, except the (5,4,2) case (Fig. 9). The flow distributions all become much more highly nonuniform with increasing m_c/m_j than for the previous cases considered. The cross-to-jet velocity ratio varies, in general, in a nonlinear fashion and in all cases changes from an increasing to a decreasing function of streamwise location as m_c/m_j goes from zero to unity. For the (5,4,2) and (10,8,1) cases (Figs. 9 and 10) this transition occurs for a nominal value m_c/m_j of 0.5, while for the (5,8,1) case (Fig. 11) it occurs between 0.2 and 0.5, and for the (5,4,1) case (Fig. 12) it occurs before m_c/m_j has reached 0.2.

For all of these cases (Figs. 9–12), except (5,4,2) for $m_c/m_j < 0.5$, G_c/G_j reached values greater than the "break point" values at which C_D began to decrease (see Fig. 3 and Table 2). However, the effect is minor for $m_c/m_j = 0$ and becomes significant more or less rapidly with increasing m_c/m_j, depending on the particular geometry. With increasing m_c/m_j, G_c/G_j greatly exceeds unity at the upstream locations, and for the (5,4,1) case (Fig. 12) with $m_c/m_j = 0.5$ and 1, the jet flow at the first upstream row is essentially zero.

The effect of wall shear for the cases of Figs. 9–12 also becomes much more significant than for the previous cases. However, the effect is still minor with no initial crossflow present. Where the theory curves show little or no effect of

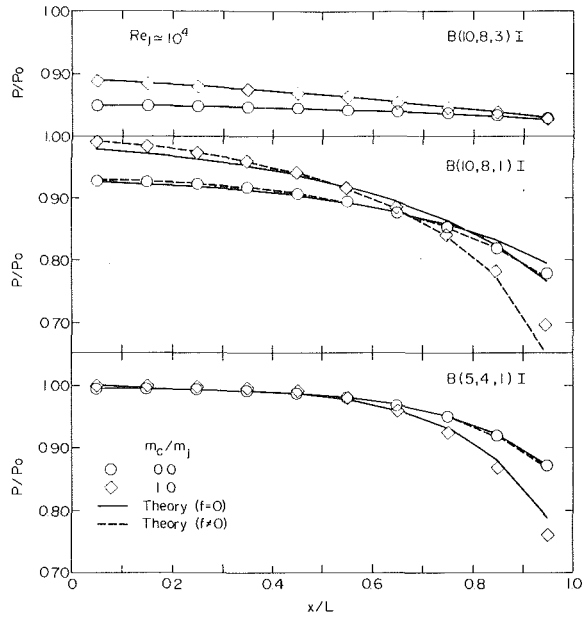

Fig. 13 Channel pressure profiles compared with predictive model

friction, they are again quite consistent with the data. Where the theory shows a significant friction effect, the prediction including this effect generally agrees more closely with the data; and considering the complexity of developing a more precise accounting of wall shear effects for these flow fields, the agreement is quite satisfactory. The results with friction are particularly good for the (10,8,1) case (Fig. 10). For (5,8,1) (Fig. 11) the magnitude of the friction effect appears to be somewhat underpredicted. This may be due to the smaller streamwise flow development length between spanwise rows for this case, which is just one-half that for the (10,8,1) case. Recall that the predictive model for the friction factor, equation (11), was written assuming a fully developed flow. It may also be noted, however, that the mass balance closures were, unfortunately, not quite as good for (5,8,1) as they were for (10,8,1).

For the cases with $(y_n/d)(z/d) \leq 8$ (Figs. 9–12), the composite uncertainty of the predictions due to uncertainties in the input parameters is the same as previously noted for $(y_n/d)(z/d) \geq 12$ (Figs. 6–8), except for the first several upstream rows at the larger m_c/m_j, where the composite uncertainty is larger. For example, at the first row for $(y_n/d)(z/d) = 8$ (Figs. 9, 10, and 11), with $m_c/m_j = 1.0$, it is ± 12 percent for $G_j/\bar{G}_j$ and, ± 16 percent for G_c/G_j. At the first row for $(y_n/d)(z/d) = 4$ (Fig. 12), with $m_c/m_j = 0.2$, it is ± 18 percent for $G_j/\bar{G}_j$ and ± 22 percent for G_c/G_j. For these conditions, the largest discrepancies between the predicted curves and the data points are also observed for the first row or two, the agreement, in general, quickly improving downstream. The discrepancies may be due to uncertainties, or to an inadequate friction factor model, or both.

Finally, it should be noted that predictive curves with friction are not indicated for (5,4,1) (Fig. 12) for $m_c/m_j = 0.5$ and 1. Because of singularities arising during iterations involved in the numerical solution technique these predictive results were not obtained. However, the position of the $G_j/\bar{G}_j$ curves for f = 0 (Fig. 12) relative to the data points fits the pattern shown by the results for the smaller initial crossflow ratios for which predictive curves with the friction effect are shown. In any event, this (5,4,1) geometry with any significant crossflow is not a good candidate for practical application since the jet flow rates at the upstream rows of holes are essentially nullified by the crossflow.

The measured pressure distributions corresponding to several of the cases for which flow distributions have been presented are shown in Fig. 13. These are typical and span the range from the most nearly uniform to the most nonuniform pressure distributions. The theoretical curves shown were computed from equation (1) using as input the solutions for $G_j/\bar{G}_j$ from the flow distribution model. This approach results in quite satisfactory predictions for the pressure distributions and therefore also for the overall pressure drop from the jet plenum to the jet array exit section.

Concluding Remarks

Experimentally determined flow distributions for jet arrays with ten spanwise rows of holes in the presence of an initial crossflow have been presented. These flow distributions range from uniform to highly nonuniform depending on the geometric parameters and the ratio of initial crossflow to jet flow. For crossflow-to-jet velocity ratios greater than a value somewhat less than unity, jet orifice discharge coefficients do not remain constant but decrease significantly, and show a secondary dependence on z/d. However, for the full range of geometric parameters covered the crossflow-to-jet velocity ratios never become large enough for this discharge coefficient effect to be very significant when there is no initial crossflow present. In addition, the effect is not significant in the presence of initial crossflow rates at least as high as the total jet flow rate, as long as the geometric parameter $(y_n/d)(z/d)$ is equal to or greater than 12. As this parameter decreases, cross-to-jet velocity ratios become large enough to affect the discharge coefficients but only for initial crossflow to total jet flow ratios above a certain value. This value decreases as the parameter $(y_n/d)(z/d)$ decreases.

Predictions based on a relatively simple one-dimensional model in which effects of channel wall shear were first excluded, then included, show that this effect becomes significant for essentially the same conditions that the variable discharge coefficient effect does. The model, with constant C_D and f = 0, results in closed from solutions. These are in excellent agreement with the data. Otherwise, numerical solutions are required. These, too, are consistent with the data but the agreement is not as good in some cases, the primary reason presumably being the lack of an adequately precise friction factor model for these complex flows. However, the cases where variable discharge coefficient and wall shear effects tend to be of more than minor significance are primarily those with narrow channel heights of $z/d = 1$. These cases may also have somewhat lesser significance in terms of immediate practical application. Additional details regarding the work reported herein, including complete graphical and tabular presentation of all reduced data, may be found in [12].

Acknowledgment

The support of the National Aeronautics and Space Administration, Lewis Research Center is hereby gratefully acknowledged.

References

1 Metzger, D. E., Florschuetz, L. W., Takeuchi, D. I., Behee, R. D., and Berry, R. A., "Heat Transfer Characteristics for Inline and Staggered Arrays of Circular Jets with Crossflow of Spent Air," ASME *Journal of Heat Transfer*, Vol. 101, 1979, pp. 526–531.

2 Florschuetz, L. W., Berry, R. A., and Metzger, D. E., "Periodic Streamwise Variations of Heat Transfer Coefficients for Inline and Staggered Arrays of Circular Jets with Crossflow of Spent Air," ASME *Journal of Heat Transfer*, Vol. 102, 1980, pp. 132–137.

3 Florschuetz, L. W., Truman, C. R., and Metzger, D. E., "Streamwise

Flow and Heat Transfer Distributions for Jet Array Impingement with Crossflow," ASME *Journal of Heat Transfer*, Vol. 103, 1981, pp. 337–342.

4 Florschuetz, L. W., Metzger, D. E., Takeuchi, D. I., and Berry, R. A., "Multiple Jet Impingement Heat Transfer Characteristics—Experimental Investigation of Inline and Staggered Arrays with Crossflow," NASA Contractor Report 3217, Mechanical Engineering Department, Arizona State University, Tempe, January 1980.

5 Florschuetz, L. W., Metzger, D. E., and Truman, C. R., "Jet Array Impingement with Crossflow—Correlation of Streamwise Resolved Flow and Heat Transfer Distributions," NASA Contractor Report 3373, Department of Mechanical Engineering, Arizona State University, Tempe, January 1981.

6 Kline, S. J., and McClintock, F., "Describing Uncertainties in Single Sample Experiments," *Mechanical Engineering*, Vol. 75, 1953, pp. 3–8.

7 Damerow, W. P., Murtaugh, J. C., and Burggraf, F., "Experimental and Analytical Investigation of the Coolant Flow Characteristics in Cooled Turbine Airfoils," NASA Contractor Report 120883, General Electric Company, Cincinnati, Ohio, June 1972.

8 Meitner, P. L., and Hippensteele, S. A., "Experimental Flow Coefficients of a Full-Coverage Film-Cooled Turbine Vane Chamber," NASA TP-1036, Sept. 1977.

9 Dyban, E. P., Mazur, A. I., and Golovanov, V. P., "Heat Transfer and Hydrodynamics of an Array of Round Impinging Jets with One-Sided Exhaust of the Spent Air," *International Journal of Heat and Mass Transfer*, Vol. 23, 1980, pp. 667–676.

10 Martin, H., "Heat and Mass Transfer Between Impinging Gas Jets and Solid Surfaces," *Advances in Heat Transfer*, Vol. 13, Academic Press, New York, 1977, pp. 1–60.

11 Kays, W. M., *Convective Heat and Mass Transfer*, ch. 6, McGraw-Hill, New York, 1966.

12 Florschuetz, L. W., et al, "Jet Array Impingement Flow Distributions and Heat Transfer Characteristics—Effects of Initial Crossflow and Nonuniform Array Geometry," NASA Contractor Report 3630, Department of Mechanical and Aerospace Engineering, Arizona State University, Tempe, Ariz., Nov. 1982.

S. L. K. Wittig
Professor.
Mem. ASME

L. Dörr
Dipl.-Ing.

S. Kim
Dr.-Ing.

Lehrstuhl und Institut für Thermische Strömungsmaschinen, Universität Karlsruhe (T.H.), 7500 Karlsruhe 1, West Germany

Scaling Effects on Leakage Losses in Labyrinth Seals

The accurate prediction of leakage losses through labyrinth seals in gas turbine engines depends largely on exact measurements. As tolerance effects are important, scaled-up models are used for experimental analysis. Application to real size engine conditions is of predominant importance. Measurements in a newly developed test section over wide pressure ranges with geometrically similar straight-through seal models of different scale indicate that the flow coefficient is not independent of scale. In a first attempt to clarify these questions, the results obtained from various models were correlated using Fanno-line analysis with dimensionless integral friction coefficients. The results obtained reveal the necessity for simultaneous consideration of Reynolds and Mach-number effects as well as relatively small geometrical deviations.

Introduction

Despite considerable progress in the development of advanced techniques such as gas-film seals, labyrinths will continue to be the most widely used sealing element in jet engines as well as in stationary turbomachines. Simplicity and compact design, reliability and operational characteristics – especially high temperature resistance – are some of the major advantages.

Many attempts have been made in describing the leakage losses through labyrinth seals. Trutnovsky [1] in his comprehensive book summarizes the earlier attempts by Stodola [2], Egli [3], Jones [4], Komotori [5] and others. Jerie recognizes the importance of various geometrical parameters for straight-through labyrinth seals [6], and Martin derives the drag coefficient for isothermal, low-Mach number flow [7]. Reasonably good results are in general obtained by using these empirical or semiempirical relations. However, the new generation of jet engines, for example, with drastically reduced fuel consumption requires more accurate predictions, as the reduction of leakage losses leads directly to an improvement of the thermal efficiency of the engine and its thrust. Furthermore, compressor characteristics and pumping are dependent on the sealing with direct consequences to the maneuverability of the aircraft.

Stocker [8], therefore, in his recent studies, developed advanced labyrinth seals with reduced leakage losses through detailed aerodynamic testing. Flow visualization gave an additional insight, especially under the assumption of incompressible flow.

One major factor, however, which has been widely neglected so far is the scaling and transfer to engine conditions. Due to experimental requirements, measurements are usually made with scaled-up models. This is necessary to reduce errors in determining the geometry especially the radial clearance. With an engine clearance of 0.1 mm, for example, a deviation of 0.01 mm would lead to an error of approximately 10 percent. The question, therefore, arises on how to utilize experimental results obtained from scaled-up models for the engine design.

The present paper is a first attempt to clarify the effects of various influence parameters. Leakage losses are determined using geometrically similar, two-dimensional plane models at three different scales. Rotational effects have not been considered. An attempt is made to analyze the results using Fanno-line flow assumptions.

Experimental Conditions

The labyrinth test loop of conventional design is shown schematically in Fig. 1(*a*). Air is supplied by compressors with pressure ratios up to 4.0 and maximum flow rates of 4.5 kg/s. The inlet temperature of the settling tank is controlled by an intercooler or a heater. In designing the test section, care has been taken to achieve entrance conditions for the labyrinth similar to those under engine conditions and to avoid any geometrical deviations, i.e., expansion during pressurized operation. Heavy top and bottom plates support the labyrinth and the clearance can be altered by inserting spacer plates of predetermined width. Large side windows serve for optical diagnostics. Due to an extremely high channel width to clearance ratio of up to 900, side wall effects can be neglected.

The pressure distribution across the individual throttling knives measured on the tip of the knife and within the chambers on the inner surface is determined by a Scanivalve-controlled pressure transducer. The determination of the mass flow rate is accomplished by two parallel orifice meters. This is necessary for accurate measurements at high and low mass flows. All pressure data are stored and preprocessed by a mini-computer. Two modes of operation are possible: under regular conditions the back pressure is kept constant and the pressure ratio is altered by varying the pressure of the settling chamber. It is, however, possible to change the back pressure by throttling the exhaust flow with constant inlet total pressure. This is important for a detailed analysis of Reynolds number effects. All temperatures are determined using Ni-CrNi-thermocouples. Mass flow rates are obtained from orifice and 1/4 circle-nozzle measurements in accordance with

Contributed by the Gas Turbine Division of THE AMERICAN SOCIETY OF MECHANICAL ENGINEERS and presented at the 27th International Gas Turbine Conference and Exhibit, London, England, April 18–22, 1982. Manuscript received at ASME Headquarters December 14, 1981. Paper No. 82-GT-157.

DIN 1952 (German Standard), with calibrated orifice and 1/4 circle nozzle for high and low flow rates, respectively. Reproducibility was found for all measurements. Here, the most critical parameters were always the accurate determination of the clearance and the mass flow rate at low pressure ratios.

Experimental Results and Analysis

Conventional straight-through seal configurations were used to evaluate the influence of the scale on the loss parameters. Figure 1(*b*) illustrates the geometrical configuration. It should be mentioned, however, that absolute dimensions are not of major interest in this analysis as we are primarily concerned with scaling effects, i.e., dimensionless parameters describing the flow.

The number of effective knives was varied from one to nine with the majority of measurements with three and five-knife seals. Various flow parameters have been used in the literature for the analysis and description of labyrinth seal losses. Stocker [8], for example, evaluates the flow parameter

$$\phi = \frac{\dot{m}\sqrt{T_0}}{p_0 A} \tag{1}$$

as a function of the overall pressure ratio $\pi = p_0/p_\infty$ with $\phi = f(\pi, n, \text{Geometry})$.

Other definitions have been introduced: The flow parameter $\bar{\phi}$ discussed by Jones [4], for example, is frequently used for reference purposes. Here

$$\bar{\phi} = f(\pi, n, t/s)$$

with

$$\dot{m} = A\bar{\phi}\sqrt{p_0 \rho_0} \tag{3}$$

It is interesting to note that using Stocker's [8] and Jones's [4] data, dynamic similarity is not considered in transferring the data to, for example, high-altitude conditions and larger/smaller scale prototype engines. This, however, is of primary interest in the present study.

The dimensionless mass flow parameter used in the present analysis is defined as:

$$c_D = \frac{\dot{m}}{\dot{m}_{\text{ideal}}} \tag{4}$$

where $\dot{m}_{\text{ideal}}$ is calculated in the usual way:

$$\dot{m}_{\text{ideal}} = \frac{Q_{\text{ideal}} p_0 A}{\sqrt{T_0}} \tag{5}$$

with

$$Q_{\text{ideal}} = \sqrt{\frac{2\kappa}{R(\kappa-1)}\left[1-\left(\frac{p_\infty}{p_0}\right)^{\frac{\kappa-1}{\kappa}}\right]}\left(\frac{p_\infty}{p_0}\right)^{1/\kappa} \tag{6}$$

for subcritical pressure ratios and

$$Q_{\text{ideal}} = Q_{\text{ideal}}\left(\frac{p_0}{p_\infty} = \left(\frac{2}{\kappa+1}\right)^{\frac{\kappa}{\kappa-1}}\right) \tag{7}$$

for supercritical values. This definition is convenient for application in the present study.

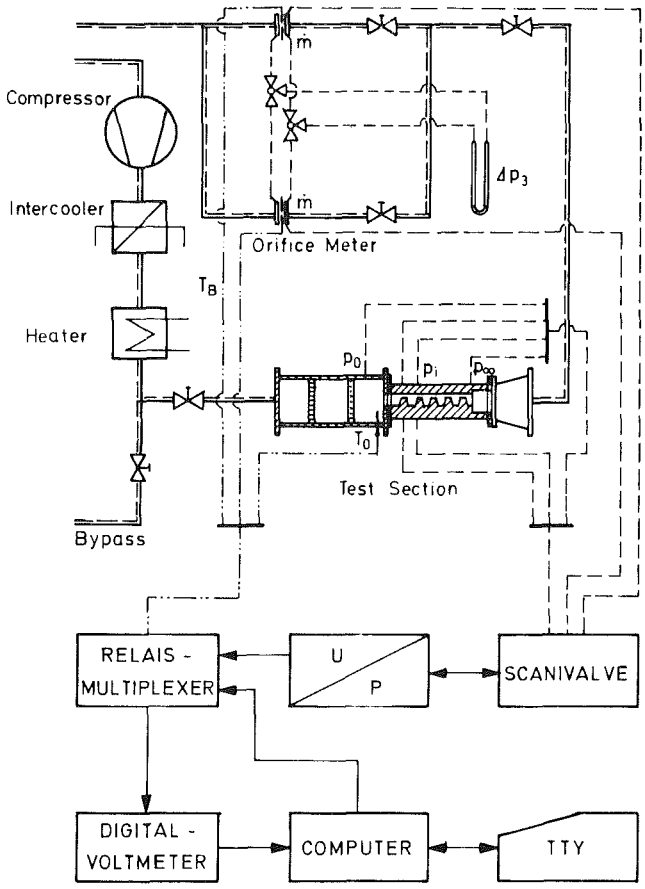

Fig. 1(*a*) Labyrinth seal test facility

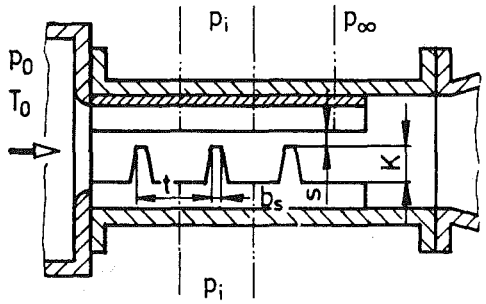

Fig. 1(*b*) Straight-through labyrinth seal: $K/t = 0.875$; $b_s/t = 0.208$ $s/t = 0.041 \div 0.208$

At a given number of throttlings, c_D was determined for a conventional straight-through labyrinth seal (see Fig. 1(*b*)) as a function of the overall pressure ratio across the test section. The pressure ratio was varied from $p_0/p_\infty = 1.02$ to 2.5. Note that the flow regimes considered are extended to relatively low Reynolds numbers – i.e., nearly incompressible flow – and include high Mach-number flow as well. Four different

Nomenclature

A = cross-sectional area, m^2
b = width of test section, m
c_D = mass flow parameter
d_h = hydraulic diameter, m
f = coefficient of friction, $\frac{\tau_w}{\rho w^2/2}$
$\dot{m}$ = mass flow rate, kg/s
$\dot{m}_{\text{ideal}}$ = ideal mass flow rate, kg/s
n = number of knives (throttlings)
p_0 = upstream pressure, N/m^2
P_∞ = downstream pressure, N/m^2
Q_{ideal} = expansion function, s $\sqrt{K}/m$
Re = Reynolds number
s = clearance, mm
T_0 = temperature at labyrinth inlet, K
t = pitch, mm
w = axial velocity over knife tip, m/s
κ = specific heat ratio
μ = dynamic viscosity, kg/sm
ν = kinematic viscosity, m^2/s
ϕ = flow parameter, s $\sqrt{K}/m$
π = pressure ratio
$\bar{\phi}$ = dimensionless flow parameter

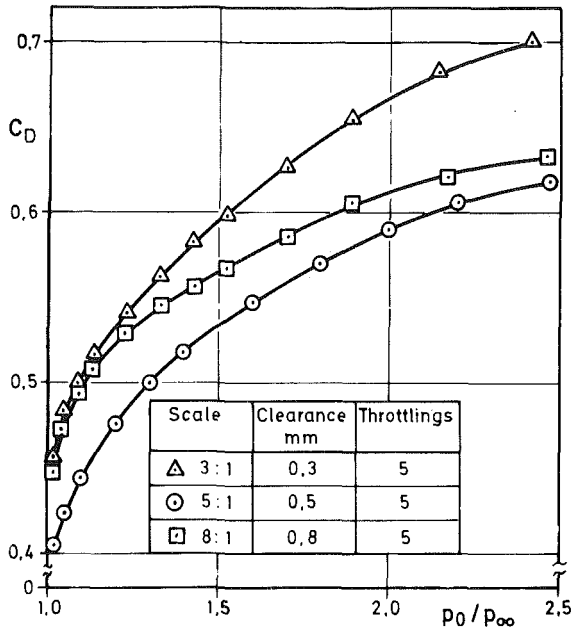

Fig. 2 Leakage losses for five-throttlings straight seal nominal clearance 0.1 mm

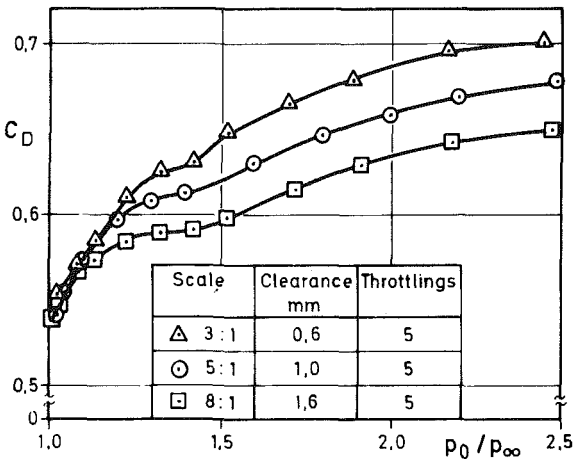

Fig. 3 Leakage losses for five-throttlings straight seal nominal clearance 0.2 mm

nominal clearances were chosen for each of the three models at scales of 3 to 1, 5 to 1, and 8 to 1 with respect to the engine prototype. Figures 2 to 5 illustrate the flow parameter for a typical labyrinth with five throttlings. Qualitatively, the results are in good agreement with available data. However, the influence of the scale is most evident for small clearances as shown in Figs. 2, 3, and 6. Deviations exceeding 10 percent are observed. With increasing nominal clearance, the difference will be not quite as high (Fig. 5). An interesting observation, however, is the reversal of the actual dependence with increasing clearance. Figure 3, for example, shows, that at constant pressure ratio and a nominal clearance of 0.2 mm c_D is higher for scale 5:1 than for 8:1, whereas the opposite is observed for 0.1 mm nominal clearance.

At a relatively large clearance, the scaling effects are drastically reduced at higher c_D-values. The highest relative leakage losses, i.e., the highest c_D parameter, is always observed for the smallest scale. This means that leakage losses under true engine conditions (i.e., scale 1:1) could be even higher. Numerous other experiments in our program confirm this observation for labyrinths with three and more throttlings (see Fig. 6). The question, therefore, arises which dominating similarity parameters are to be considered. Principally, at low pressure ratios, the Reynolds number should dominate

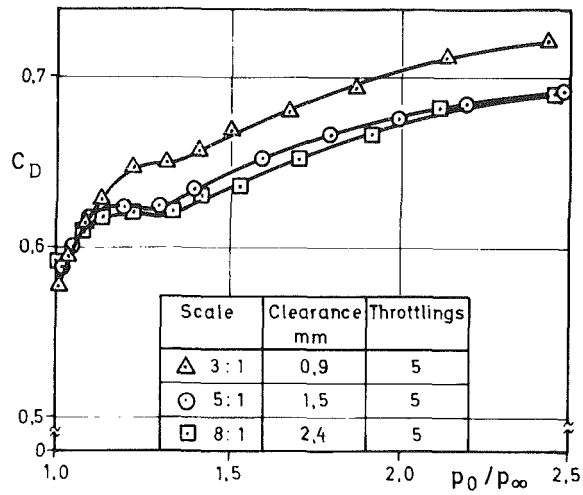

Fig. 4 Leakage losses for five-throttlings straight seal nominal clearance 0.3 mm

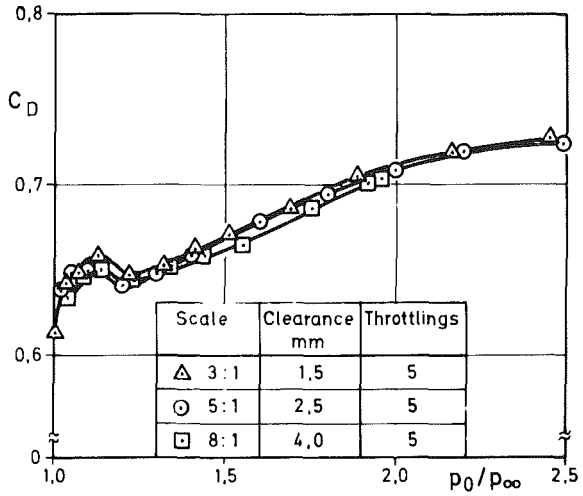

Fig. 5 Leakage losses for five-throttlings straight seal nominal clearance 0.5 mm

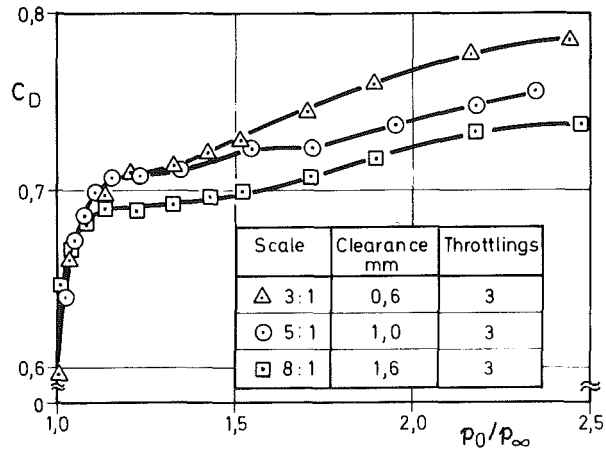

Fig. 6 Leakage losses for three-throttlings straight seal nominal clearance 0.2 mm

whereas at higher pressure ratios the compressibility effects could be of primary interest.

For clarification, Fanno-line theory was chosen for analysis as frequently suggested. Using the mass flow rate data, the Fanno-line can be calculated when the cross-sectional area and the initial flow conditions (pressure ratio) are known. The integral coefficient of friction is then readily obtained.

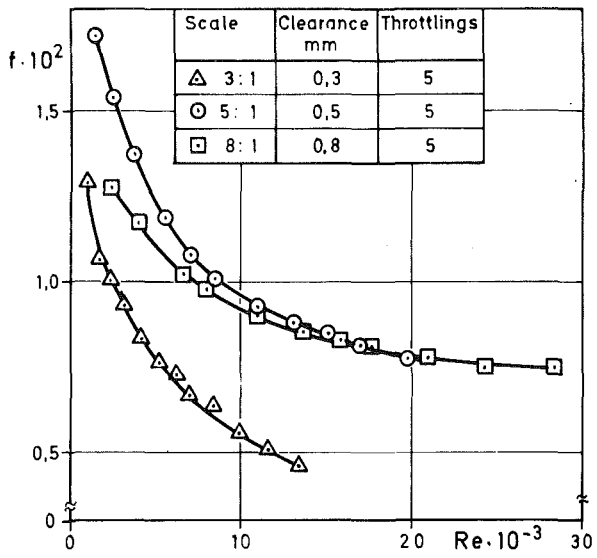

Fig. 7 Dependence of friction factor on Reynolds number for five-throttlings straight seal nominal clearance 0.1 mm

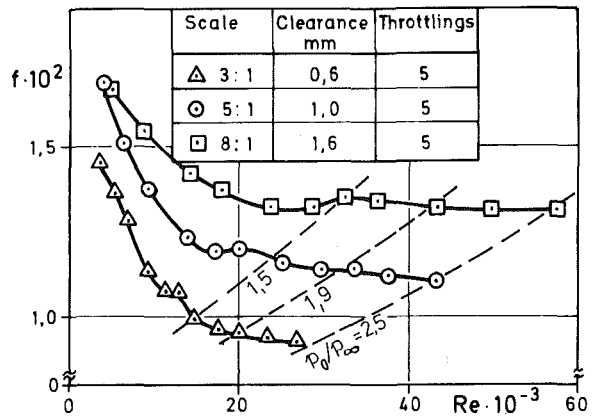

Fig. 8 Dependence of friction factor on Reynolds number for five-throttlings straight seal nominal clearance 0.2 mm

Figures 7–11 show the friction coefficient calculated from the experimental data as a function of the Reynolds number with the model scale as a parameter. Note the linear scale in plotting the experiments.

Here, the Reynolds number is defined in the usual way as

$$\mathrm{Re} = \frac{w d_h}{\nu} \simeq \frac{2\dot{m}}{\mu b} \tag{8}$$

and is readily determined from the mass flow. If the temperature change is moderate, the Reynolds number will be approximately constant across the labyrinth. Notice that the roughness parameter – i.e., the ratio of the knife pitch to knife height – is the same for all scales. Again, the influence of the scale is evident. Even at relatively low Reynolds numbers considerable deviations are observed. In contrast to conventional rough pipe flow, the friction coefficient as calculated here, therefore, is not a function of the Reynolds number and dimensionless roughness parameter only.

As demonstrated in Fig. 8, for example, the influence of the scale is important even at relatively high Mach numbers and Reynolds numbers as indicated by the constant pressure ratio lines. Typical transitional characteristics are observed for higher nominal clearances such as shown in Fig. 10. The relative changes of the friction coefficient with Reynolds number and pressure ratio (Mach number), though, are smaller for increasing clearances. This is obvious from comparing Figs. 8 and 10. Higher nominal clearances lead to

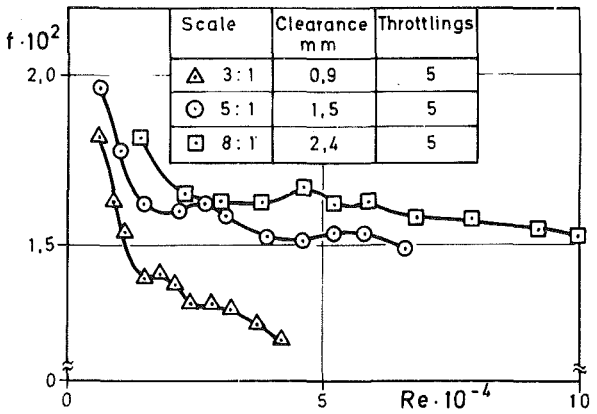

Fig. 9 Dependence of friction factor on Reynolds number for five-throttlings straight seal nominal clearance 0.3 mm

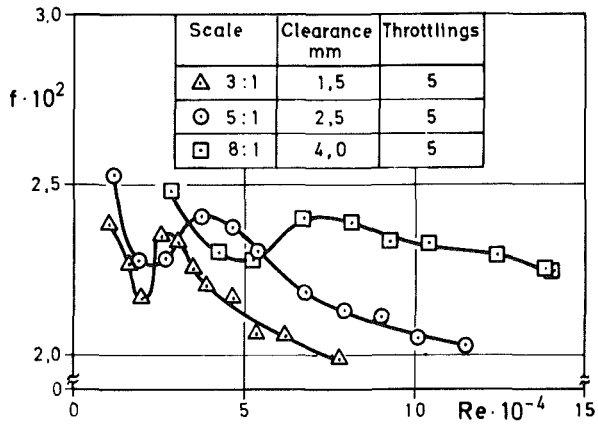

Fig. 10 Dependence of friction factor on Reynolds number for five-throttlings straight seal nominal clearance 0.5 mm

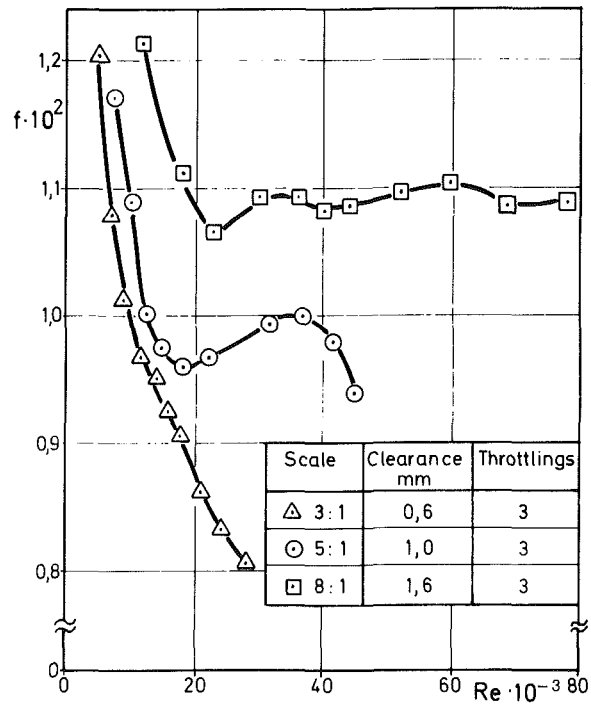

Fig. 11 Dependence of friction factor on Reynolds number for three-throttlings straight seal nominal clearance 0.2 mm

smaller pitch-to-clearance ratios used as dominant parameter by Jones [4]. Stocker's [8] and Jones's [4] data were derived from labyrinths with relatively low pitch/clearance-ratios,

whereas our measurements were made using pitch/clearance-ratios from 4.8 to 24 with the higher ratios revealing the scaling effects.

Discussion and Conclusions

Various explanations for the observed dependence of the flow coefficient and friction factor on the scale can be found. An obvious reason is the requirement of dynamic similarity. For labyrinth seals, this results in

$$c_D = g(\mathrm{Re}, p_0/p_\infty, \text{ Dimensionless Geometry}) \quad (9)$$

and

$$f = g(\mathrm{Re}, p_0/p_\infty, \text{ Dimensionless Geometry}) \quad (10)$$

when compressibility effects, i.e., larger pressure ratios, are to be considered. For different fluids, the specific heat ratio, κ, can also be of importance. In the present study, however, only air has been used. Equations (9) and (10) reveal that the Reynolds number and hence the scale will have a marked effect, especially in aircraft engine application. Relatively small clearances and high-altitude operation are conditions which yield comparatively small Reynolds numbers even when higher pressure ratios are considered. From basic analysis of conventional frictional flow, it is well known that increasing subcritical Reynolds numbers will lead to reduced frictional coefficients. The friction coefficients derived from our Fanno-line calculations, as shown in Figs. 8, 9, and 10, reveal similar characteristics. This partly explains the general increase in c_D with Reynolds number and pressure ratio. However, the inversion of the loss coefficient c_D with scale – i.e., with increasing Reynolds number – is not to be expected. The simultaneous influence of Mach number and Reynolds number which has been largely neglected in the majority of previous studies must be considered. Its importance is readily seen from Fig. 8. The present experimental analysis illustrates that, unless dynamic similarity is fulfilled, errors in the order of 10 percent or more may arise from using available data for design point calculations.

One quite obvious reason for the scaling effects can be found in small differences of the geometry due to manufacturing or operation. Although in the present study an attempt was made to secure geometric similarity, minute differences (0.01 mm, for example) of such important parameters as the radii of the labyrinth knives cannot be excluded. Small scales, for examples, could lead to relatively larger radii resulting in lower friction coefficients, i.e., higher loss parameters. This assumption, however, is not fully supported by the results as shown in Figs. 2 and 7 for small nominal clearances. Here, scale 5:1 leads to the smallest flow coefficient, whereas scale 8:1 approaches that of 3:1 for small pressure ratios and Reynolds numbers.

Finally, variations in the turbulence structure with scale could be responsible for the observed behaviour. For complete similarity, equation (9) should read

$$c_D = g(\mathrm{Re}, p_0/p_\infty, \text{ Dimensionless Geometry}, \kappa, \mathrm{Tu}) \quad (11)$$

where Tu is the intensity of turbulence under the assumption of a similar turbulence structure. The latter condition, however, is hard to achieve. A detailed analysis using two-dimensional flow field models and employing recently developed turbulence models hopefully will reveal the influence of the turbulence characteristics. Also, additional experiments extending our present measurements to wider absolute pressure ranges are necessary for clarification. Experiments as well as detailed numerical computations are planned in conjunction with heat-transfer measurements.

Acknowledgments

Thanks are due to H. Zimmermann and Dr. A. Klein of Motoren und Turbinen-Union, München, for their continuous support and helpful discussions during the progress of the work.

The work was sponsored by the Bundesministerium der Verteidigung (German MOD) under contract of the Komponentenprogramm (German Engine Development Program). The support is greatfully acknowledged.

References

1 Trutnovsky, K., ed., *Beruhrungs freie Dichtungen*, 2. Auflage, VDI-Verlag, Dusseldorf, 1964.

2 Stodola, A., ed., *Dampf- und Gas turbinen*, 5. Auflage, Springer-Verlag, Berlin, 1922.

3 Egli, A., "The Leakage of Steam Through Labyrinth Seals," *Trans. ASME*, Vol. 57, 1935, pp. 115–122.

4 Jones, J. S., Communication to Kearton, W. J. and Keh, T. H., "Leakage of Air Through Labyrinth Glands of Staggered Type," *Proceedings of the Institution of Mechanical Engineers*, Vol. 166, 1952, pp. 189–195.

5 Komotori, K., "Probleme bei Labyrinth-Stopfbuchsen," *Proceedings of the Fujihara Memorial Faculty of Engineering*, Keio University, Vol. 14, No. 54, 1961, pp. 1–48.

6 Jerie, J., "Flow Through Straight Through Labyrinth Seals," *Proceeding of the Seventh International Congress for Applied Mechanics*, Vol. 2, Part 1, 1948, pp. 70–82.

7 Martin, P., "Beitrag zur Durchflussberechnung von Spaltdichtungen," Dissertation, TH Karlsruhe, 1967.

8 Stocker, H. L., "Determining and Improving Labyrinth Seal Performance in Current and Advanced High Performance Gas Turbines," *AGARD-CP-237*, 1978, reference 13.

M. E. Ward
Mem. ASME

A. G. Metcalfe
Mem. ASME
Solar Turbines Incorporated,
San Diego, Calif. 92101

S. J. Dapkunas
Department of Energy,
Washington, D.C.

Ceramic Tube Heat Exchanger Technology Development for Indirect-Fired Gas Turbine Cycle

Technology for pressurized, high-temperature, ceramic-tube heat exchangers is being established by materials evaluation, design, and fabrication studies followed by rig tests. Candidate ceramic materials have been surveyed for strength, environmental reactions with coal ash, and other design properties. Design and fabrication studies of joining methods were responsible for selection of the chosen heat exchanger configuration. A full-length, twenty eight-tube, 4.56 m (15 ft), ceramic-tube heat exchanger with an 11.43-cm (4.5 in.)-dia ceramic header has been successfully tested with a 1232°C (2250°F) outlet temperature at 689 kPa (100 psi). Hot side gas temperature during this test was 1370°C (2500°F). This module has been operated for approximately 125 hrs including operation with a pulverized coal combustor.

Introduction

Modern, high-efficiency, gas turbine engines have been designed to operate on clean fuels that do not cause corrosion, fouling, or erosion of the hot turbine section. The range of fuels has been extended to a very limited extent by careful control or neutralization of potential corrosive agents such as sodium and vanadium. Economic factors are forcing examination of lower grade fuels, as illustrated in Table 1.

Table 1 Composite cost of energy in dollar per million Btu for United States (*Energy User News*, March 9, 1981)

Fuel	March 1981	March 1980	% increase
Electricity	14.40	12.48	15
Gasoline	12.63	10.32	22
Distillate oil	8.83	7.01	26
Residual oil	5.87	4.60	28
Coal	1.42	1.36	5

Noteworthy is the more rapid rise in costs of petroleum-based energy than electricity and coal; the need to broaden the range of fuels used in the gas turbine is clear.

Earlier attempts to direct-fire a gas turbine with coal were terminated in the early 1960s because of the erosion and fouling that occurred. More recent work on direct firing has been through the PFBC, where the coal is burnt in a fluidized bed with limestone to fix the sulfur to meet environmental requirements [1]. Two factors limit the acceptibility of this solution. The first is that the outlet gas temperature is limited to 954°C (1750°F) by factors such as clinkering in the bed and sulfur capture efficiencies. The second is uncertainty that conventional cleaning by multiple cyclones will maintain adequate cleanliness on a continuous basis. All tests run to date have involved some cool-down of the PFBC off-gases resulting from duct losses which in turn required partial reheating by a "clean" fuel such as natural gas or diesel oil. Further, there appears to be evidence that a PFBC will be more effective in very large sizes (e.g., larger than 70 MW).

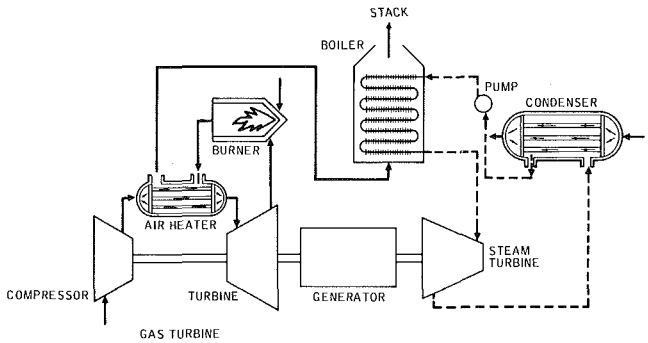

Fig. 1 Indirect exhaust coal-fired combined cycle

An alternate approach to firing a gas turbine with dirty fuels is indirect firing. Figure 1 shows a schematic of such a system. The gas turbine's compressor discharge air is passed through one or more tubular heat exchangers fired externally by a coal combustor. The system includes heat recovery from the exhaust by a waste heat boiler and steam turbine using a once-through cycle demonstrated at Solar Turbines Incorporated (Solar). Particular importance is attached to the operation of the "gas" turbine on clean air. Analyses suggest that at least a 28°C (50°F) higher inlet temperature may be possible by avoidance of the combustion pattern factor and avoidance of accelerated corrosion or fouling. After expansion through the turbine, the warm air is then used to supply the combustion air to the coal combustor. It is evident that this clean and warm air (~427°C (~800°F) could be used for other purposes if desired. Figure 2 shows some of these alternatives.

Requirements of Indirect-Fired System. An indirect-fired

Contributed by the Gas Turbine Division of THE AMERICAN SOCIETY OF MECHANICAL ENGINEERS and presented at the 27th International Gas Turbine Conference and Exhibit, London, England, April 18–22, 1982, Manuscript received at ASME Headquarters December 14, 1981. Paper No. 82-GT-158.

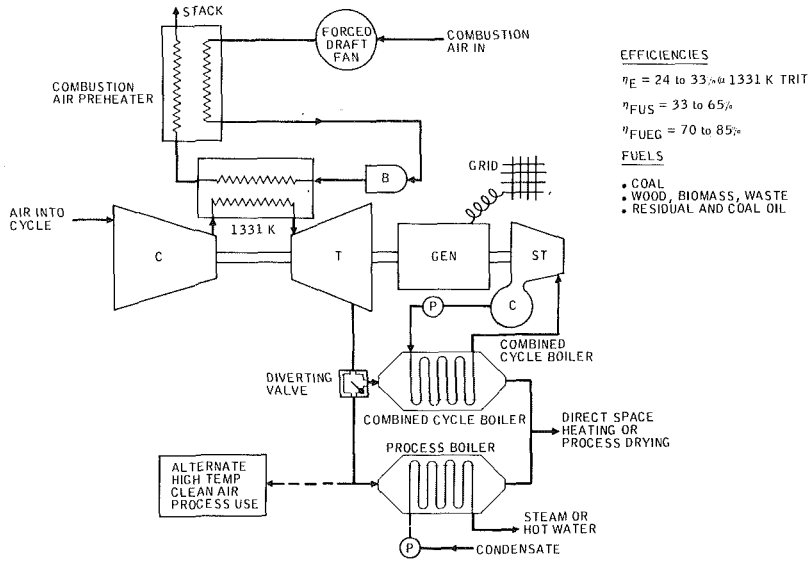

Fig. 2 Separately fired cogeneration systems

gas turbine requires development and matching of a large number of components. These components would include manifolds, trim combustors, coal burners, and controls. When the problem areas were examined by a critical path type of analysis it was concluded that the heat exchanger to heat high-pressure air from 1300°F up to the turbine inlet temperature was the critical barrier to the system. It was further concluded that work on other components should not be started until a heat exchanger module had been operated to simulate the high-pressure, high-temperature service conditions expected in an indirectly coal-fired, open-cycle gas turbine. A tubular ceramic heat exchanger was selected as most likely to meet the range of requirements expected for a coal-fired unit.

Current Status of the Technology Development

The present effort to expand the technology base needed to design and fabricate a pressurized ceramic heat exchanger suitable for use in an indirectly coal-fired, open-cycle gas turbine began in January 1977 with funding support from the Department of Energy. This effort is currently continuing with support from both the Department of Energy [2] and the Electric Power Research Institute (EPRI). The objectives of this work are to identify and develop the necessary technologies for the construction of a pressurized, high-temperature, ceramic, heat exchanger module. This module was operated for approximately 10 hrs in 1980 with outlet temperatures up to 1232°C (2250°F) at 689 kPa (100 psi) discharge pressure. Subsequently, a longer duration run extended this testing to 125 hrs. Future plans include operation with a pulverized coal combustor in November 1981. The technology development includes work in material strength characterization, compatibility of ceramics with environments created by coal combustion, the development of ceramic joining technology, and design methodology studies. This work will conclude the first phase of the development of a ceramic heat exchanger for an indirectly fired, open-cycle gas turbine.

Key Problems. Heat up, shutdowns, and quick thermal transients found in gas turbine operation are recognized to be a key problem for large heat exchangers and ceramic components. Coal combustion with its potential fouling and slagging problems, together with the impracticality of many cleaning methods used in boilers was the second key problem. A common solution to both of these key problems was found to lie in the axial combustion gas flow paths selected for the

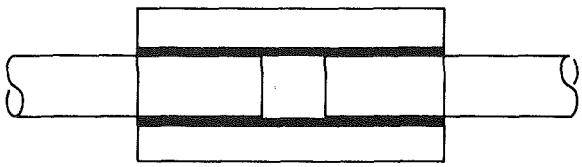

Fig. 3 Sketch of relaxing tube joint

exchanger. This solution was supplemented by methods to limit peak stresses that develop in critical ceramic components. The methods examined were relaxing glass ceramic joints and individually piloted tubes. Adaptations of these approaches were analyzed and reviewed in order to match the design with fabrication capabilities and material limitations.

Material Strength Screening Tests. Three ceramic materials were selected as primary candidates for the heat exchanger module tubes (alpha-sintered silicon carbide, Carborundum; reaction sintered silicon carbide, NC 430, Norton; Super KT silicon carbide, Carborundum). Radial compression tests were completed over a temperature range from ambient extending up to 1371°C (2500°F). None of the ceramics tested has sufficient strength to be used without thermal expansion provisions between the ceramic tubes themselves and between the ceramic components and the heat exchanger's metal shell [strengths above 138 MPa (20 ksi) are required].

Additionally, all of the materials were tested and found to be impermeable to air at 689 kPa (100 psi) and temperatures up to 870°C (1600°F).

Coal Environment/Materials Interaction. Interaction with coal was studied for NC 430 SiC, alpha-sintered SiC, and Super KT SiC specimens at two temperature regimes (air temperature from 1400 to 1315°C with material temperature from 1260 to 1040°C; and air temperature from 1250 to 1095°C with material temperature from 1090 to 980°C). Specimens were examined after a 1000 hr test in a low velocity environmental test chamber. Contaminants in this test were 6.16E-04 (gm/m^3 gas) of Homer City flyash, 5.72E-04 (gm/m^3 gas) of sea salt. Ceramic material from a 100 hr V_2O_5 contaminant test was also evaluated. Contaminant levels of V_2O_5 were 4.35E-04 (gm/m^3 gas). For comparisons, ceramic material in the as-received condition was also examined.

A selection of material test specimens from the environmental tests were examined to determine changes in geometry and microstructure, and identify reaction products. Metallographic examination and scanning electron mi-

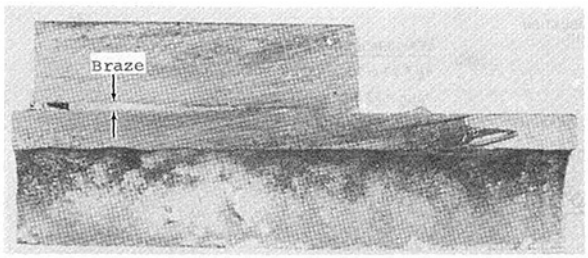

Fig. 4 Sectional permanent joint

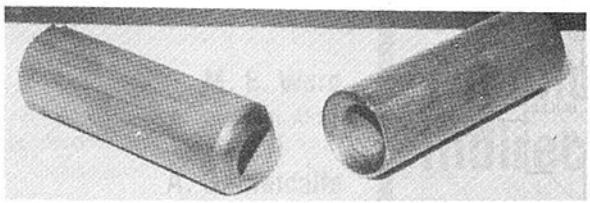

Fig. 5 Spherical compression joint

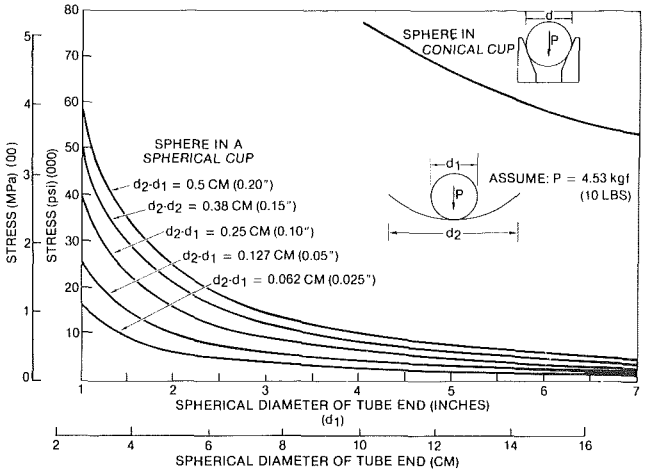

Fig. 6 Effect of relative spherical dimensions on Hertzian contact stresses

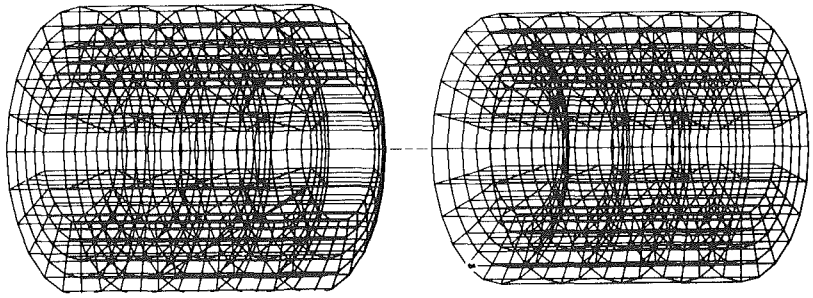

Fig. 7 Finite element stress model of a spherical compression joint

croscopy with dispersive X-ray capability were used for the analysis.

After the 1000 hr test, the test specimens experiencing higher temperatures, exhibited a glassy deposit indicative of melting of the contaminants. The deposit on the test specimens subjected to the lower temperature regime still retained characteristics of the flyash particles. Both NC 430 and Super KT SiC exhibited no significant change in structure and minor dimensional change after the 1000 hrs exposure. Significant material removal occurred on the alpha-sintered SiC material (approximately 20 mm or 20 percent of tube wall thickness). For all ceramic materials, maximum attack occurred at the leading edge (test specimens were tubular segments tested with the environment flow perpendicular to the tube's axis) and was characterized by uniform thinning of the structure. Preferential attack of free silicon was not observed. Energy dispersive X-ray analysis did not reveal any reaction products or elemental concentration gradients which would account for the loss of material. The probable cause of material removal is accelerated oxidation due to the impingement of contaminants which act to fracture, dissolve and wash away the normally pure silica protective layer that forms on the carbide. The accelerated thinning of the alpha-sintered material compared with Super KT and NC 430 SiC under these test conditions indicated that the molten contaminants are more reactive in contact with the alpha-sintered material. A possible explanation is that the sintering aid in the alpha-sintered material acts to decrease the viscosity of the molten ash, thus allowing more rapid dissolution of the oxide.

No structural or dimensional changes were observed for any of the ceramic materials after the 100 hr test with V_2O_5 contaminant.

Joining Technology. A number of glasses and joint designs were tested using the relaxing joint concept. This concept addresses the problem of use of a brittle material where large, thermally induced relative material expansions are common. The relaxing joint concept consists of joining two ceramic tubes to a ceramic sleeve with a glass filler (see Fig. 3). With proper design of the joint, relative movement between the two tubes under controlled thermal conditions can be accomplished without deterioration of the heat exchanger's permeability.

Through the improvement in manufacturing capabilities, a dense glass filled joint was fabricated. This joint was tested for 100 hrs at 704°C (1300°F) and 689 kPa (100 psia) internal pressures without significant leakage occurring in the glass joint.

Gas tight permanent joints (i.e., nonrelaxing shown in Fig. 4) were constructed and have successfully completed 50 hrs endurance tests at pressure and temperature. This was accomplished through the development of an alloy which allows the brazing together of two ceramic materials.

A ceramic to metal spherical compression joint was designed and tested at 704°C (1300°F) with an internal gas pressure of 551 kPa (80 psig) and end load of 20 kgm (44 lbs) for 25 hrs without leakage. Also, ceramic to ceramic spherical joints shown in Fig. 5 were constructed and tested.

The spherical joints that were fabricated and tested underwent extensive analysis. Practical conditions require that the design avoid loading at the edge of either part of the seat. This requires that the radius of the receptor seat be slightly larger than the tube end. Figure 6 shows how the Hertzian stress level rises as the seat diameter becomes progressively larger than the tube and for various tube end diameters. The Hertzian contact area diminishes as the difference in diameter increases until the minimum "line" contact is reached with a spherical-ended tube in a conical receptor. The stress rises as this contact area decreases as shown by Fig. 6. Several spherical joints were made and compression tested. The results indicate that the spherical joints being considered for this project are more than adequate (failure loads for the 2.54-

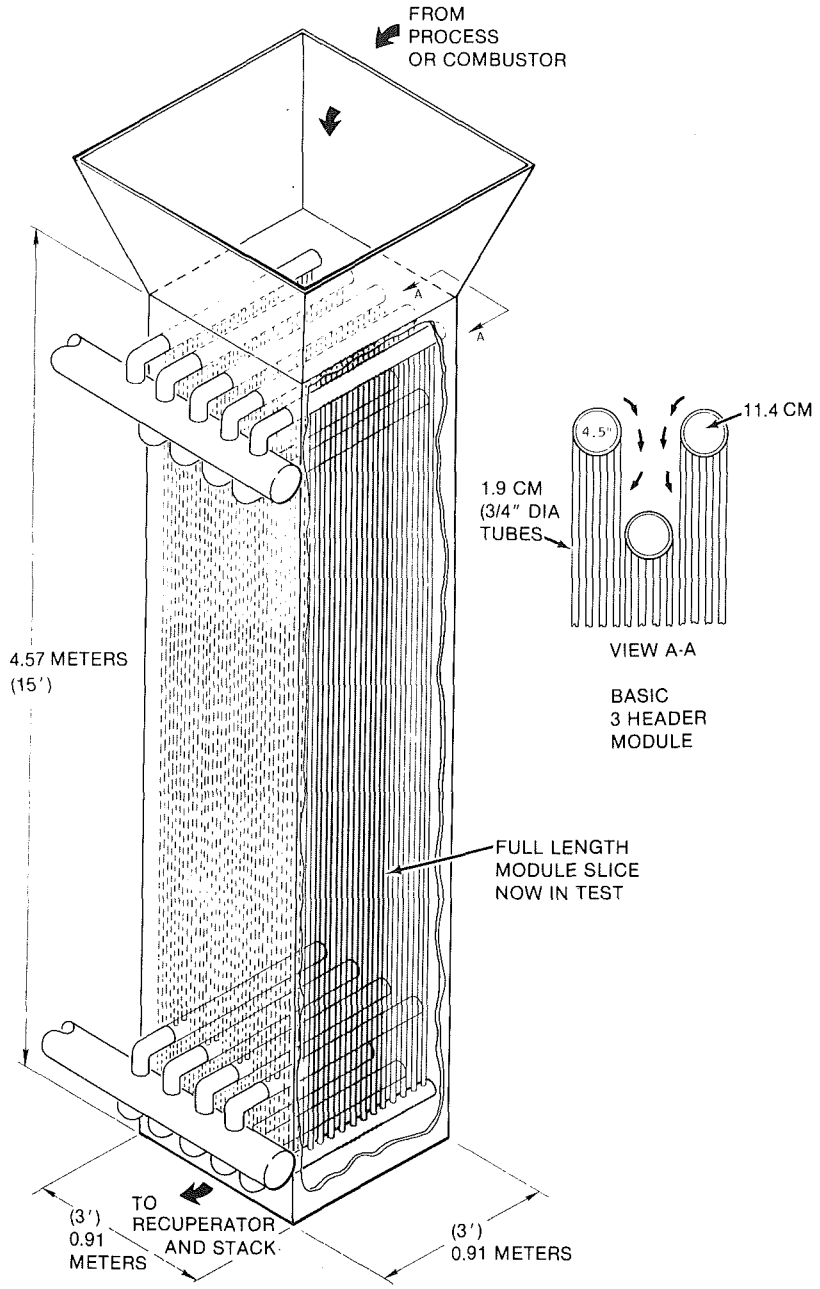

Fig. 8 Axial counterflow heat exchanger concept

cm (1-in.) radius joint was approximately 11,778 kgm (26,000 lbs). One of the design requirements for the full-size, ceramic heat exchanger is a maximum load on spherical joints not exceeding 22.6 kgm (50 lbs). A finite element stress model, shown in Fig. 7, was constructed of a spherical joint. The results from the computer analysis for the failed spherical joint test specimens indicate that failure was shear. These failure stresses averaged 172,250 kPa (25,00 psi).

Heat Exchanger Full Size Module. Design and construction of an axial counter flow shell and tube, heat-exchanger module was completed. The following reasons are considered primary in choosing the vertical, axial-flow heat exchanger rather than a crossflow horizontal tube design:

- Minimizes circumferential thermal gradients and strain caused by cross flow
- Eliminates internal air baffles; therefore, tube to baffle friction joints
- Reduces bending stress in ceramic tubes caused by tube weight over a long horizontal span

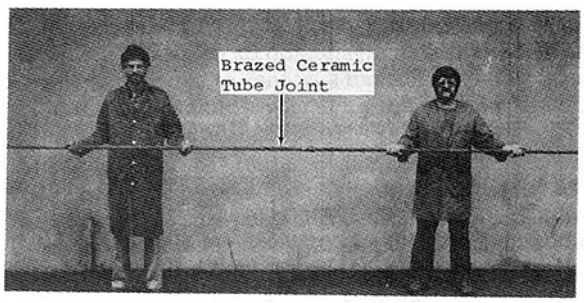

Fig. 9 4.57-m (15-ft) ceramic tube

- Has potential of reducing flyash accumulations due to lower catch efficiency and self-washing flow
- Minimizes large ceramic tube temperature variations between tubes connected to the same header

Figure 8 illustrates the primary design advanced in this program.

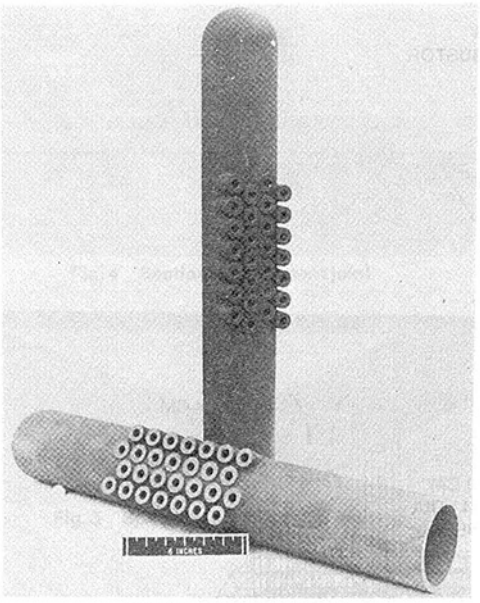

Fig. 10 Ceramic header

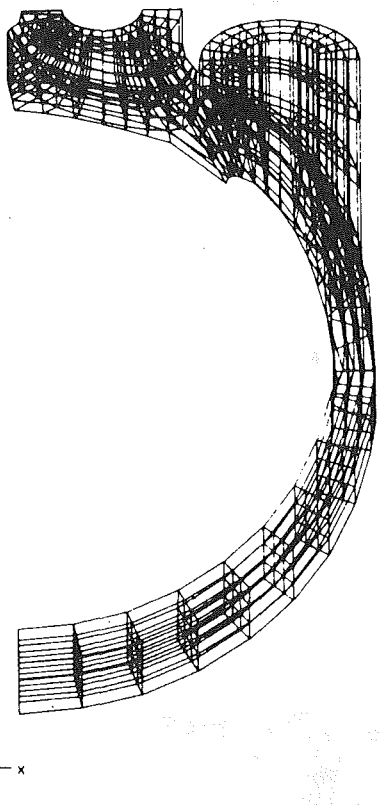

Fig. 11 Finite element model of ceramic header joint

The heat exchanger module utilizes 4.57-m (15-ft) long, 2.54-cm (1-in.) o.d., 0.635-cm (1/4-in.) wall silicon carbide ceramic-tubes (Fig. 9) spaced 0.635 cm (1/4 in.) apart in a triangular matrix. A metal header with bellows was designed into the heat exchanger's cold end. A silicon carbide ceramic header was used at the module's hot end (Fig. 10).

The 11.4-cm (4.5-in.) SiC ceramic header underwent a finite-element stress analysis in order to determine the stress concentrations in the fillet area at the header-tube intersection (finite-element model shown in Fig. 11). The results indicate that the maximum tensile stress, 41,340 kPa (6,000 psi), in the header will occur in the fillet area for the conditions expected during transient operation. This stress, when combined with

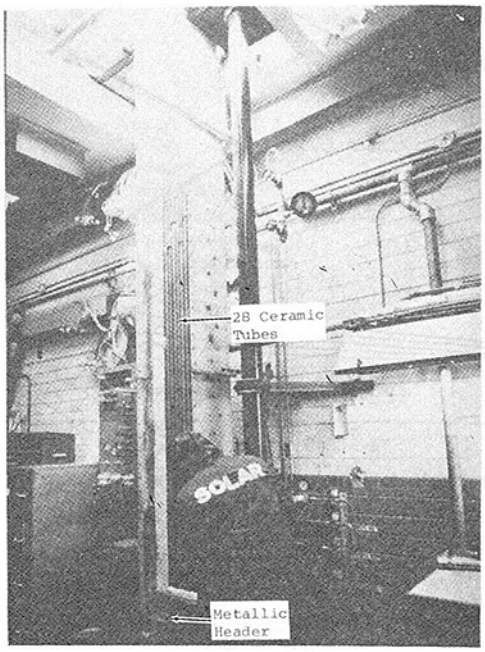

Fig. 12 28-tube NC-430 SiC ceramic heat exchanger

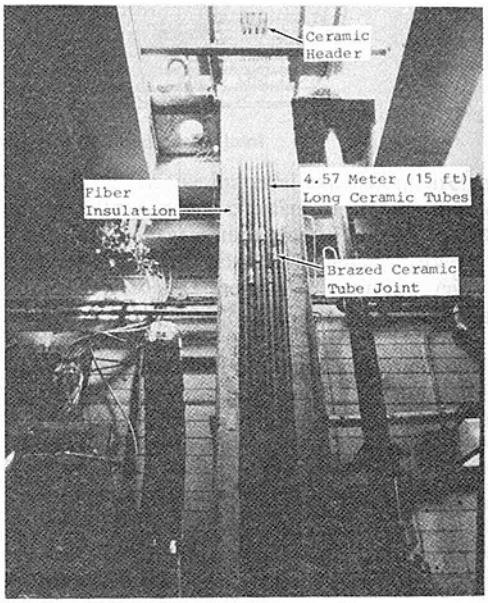

Fig. 13 28-tube NC-430 SiC ceramic heat exchanger with a NC-430 SiC ceramic header

others in the ceramic components, gives a calculated probability of success of 99.999912.

In the heat exchanger module, tube-to-tube differential expansions were relieved by incorporating a superalloy bellows for each tube into the metal header at the heat exchanger's cold end. The assembly of the module was accomplished by providing a spherical compression joint between the ceramic tubes and the ceramic header and the ceramic tubes and the metal header. The spherical joint required that the ceramic tubes be kept in compression to insure a gas-tight seal between the tubes and headers. This system offers a significant advantage, which is the ability to assemble the heat exchanger module and replacing ceramic tubes or headers by simply untensioning the floating header, removing and replacing the desired components and then repositioning the floating header. These features obviously facilitate field repair.

The test module is shown in Figs. 12 and 13. Ten hrs of

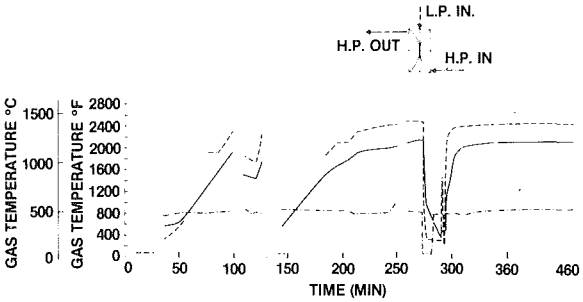

Fig. 14 Initial module tests

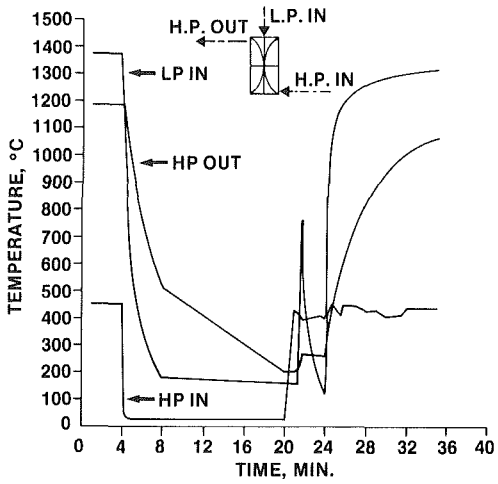

Fig. 15 Thermal transient plot

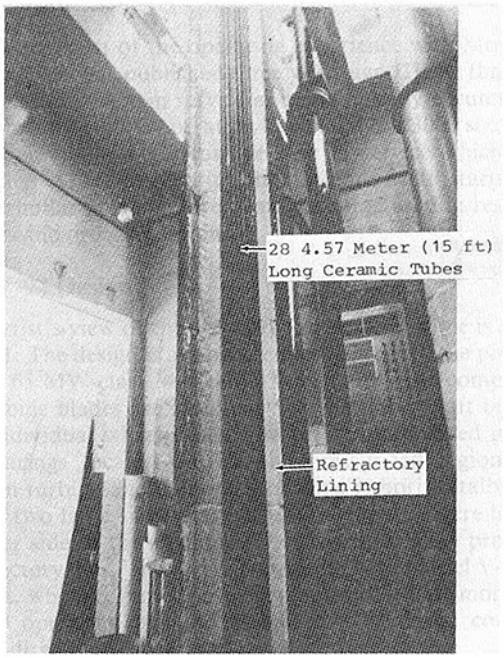

Fig. 16 New test facility

operation with internal pressure of 689 kPa (100 psi), and oil firing up to 1371°C (2500°F) was successfully completed in 1980. The testing included seven starts and shutdowns and one instrumented thermal cycle. The thermal cycle consisted of a severe shutdown from maximum operating conditions (1371°C firing temperature and 1204°C tube side outlet temperature). Cool down rates of 556°C per min were recorded. A plot of the testing showing firing, inlet, and outlet temperatures is presented in Fig. 14 and 15.

The full-size, ceramic heat exchanger was moved to a new

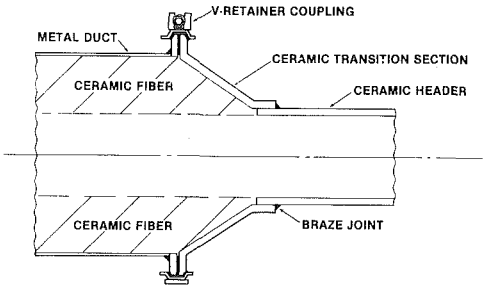

Fig. 17 Header-to-duct transition

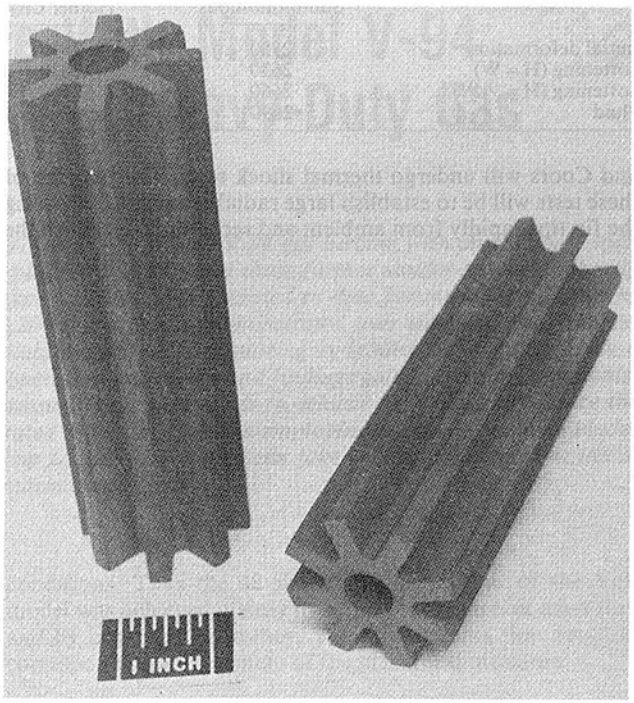

Fig. 18 Axial finned tube (Norton Co.)

test facility (see Fig. 16). A new outer shell was constructed with a refractory lining (Kaocrete 32-C) in order to survive the environments resulting from coal firing the heat exchanger. The 4.57 m (15 ft) long ceramic tube spherical seats were refurbished. The tubes were installed in the new shell and readied for endurance testing. This ceramic, heat exchanger module has successfully completed 125 hrs of running at temperature and pressure. The ceramic, heat exchanger was fired up to 1370°C (2500 on the shell side and achieved tube side temperatures of 1232°C (2250°F) at 689 kPa (100 psi). A SiC ceramic transition section, diagramatically shown in Fig. 17, has been ordered to connect a metallic internally insulated duct to the SiC ceramic header. This will be incorporated into the full size ceramic heat exchanger.

After the endurance testing of the heat exchanger module on No. 2 oil, the ceramic heat exchanger will be fired using Solar's pulverized coal burner. The coal that will be utilized is a Colorado sub-bituminous with properties shown in Table 2 and 3. These tests will be run at specific firing temperatures (selected in reference to the coal slagging temperature) in order to evaluate the fouling potential of this particular ceramic heat-exchanger design (i.e., axial counterflow). These tests are scheduled for October 1981.

Ceramic tubes from three suppliers will be tested in order to determine their respective "f" and "j" factors used in heat-transfer and pressure-drop calculations procedures. These tests are scheduled for August 1981. Along with these bench tests, axial finned tubes supplied from Norton (see Fig. 18)

Table 2 Colorado sub-bituminus coal

Proximate analysis		Ultimate analysis	
% Moisture	6.37	% Carbon	68.07
% Ash	7.05	% Hydrogen	5.53
% Volatile	35.45	% Nitrogen	1.35
% Fixed carbon	51.13	% Oxygen	17.48
		% Ash	7.05
		% Sulfur	0.52
Total	100.00	Total	100.00

Table 3 Ash fusion temperatures, °F

	Colorado Sub-bituminous	Homer City
Initial deformation	2550	2590
Softening (H = W)	2630	2630
Softening (H = ½W)	2660	2660
Fluid	2690	2700

and Coors will undergo thermal shock tests. The purpose of these tests will be to establish large radial gradients by heating the fin tips rapidly from ambient and secondly to establish the entire test specimen temperature at 1315°C (2400°F) and then rapidly cooling the tube's internal surface. These tests will aslo be completed in August 1981. The Norton finned tubes are slip-cast while the Coors tubes are vertically extruded and fired.

Conclusion

At the conclusion of our present contract with DOE and EPRI, Solar feels that with the technology that we have acquired since the early 1970's in the use of structural ceramics, we would be in a position to enter into a ceramic heat exchanger prototype development project ending with the field testing of a pressurized full size modularized ceramic heat exchanger in an environment suitable for siliconized silicon carbide materials.

References

1 Moskowitz, S., Weth, G., and Leon, A., "Development of a Coal-Fired Pressurized Bed for Combined Cycle Power Generation," ASME Paper 80-GT-189, presented in New Orleans, La., Mar. 1980.

2 Ward, M. E., Solomon, N. G., Gulden, M. E., and Smeltzer, C. E., "Development of A Ceramic Tube Heat Exchanger With Relaxing Joint," Final Report, June 1980 for DOE Contract EF-77-C-01-2565.

Operating and Maintenance Experience With Model V-94 100/135 MW Heavy-Duty Gas Turbines

B. Deblon
Department Manager,
Gas Turbine Mechanics
and Aerodynamics.

H. Maghon
Division General Manager,
Gas Turbine Technology.

Kraftwerk Union AG,
Muelheim/Ruhr, West Germany

Towards the end of 1974, the first Model V-94 gas turbine with an ISO base-load rating of 91 NW was placed in service and three further similar machines shortly thereafter. The prototype unit has been operated to date for more than 21,000 hr and started up over 3,200 times. It has demonstrated over the past few years excellent operating availability, as well as starting reliability. The paper gives a detailed report of the operating experience and findings gained from the overhauls. It also describes the measures that were taken to achieve high reliability. Since the end of 1979 three uprated V-94 gas turbines employing air-cooled turbine blades with a unit output of up to 125 MW have been taken into operation. The initial experience with these machines is discussed.

Introduction

The first report of the operating experience with Model V-94 gas turbine was published three years ago [1]. At that time four such units were in service and had already accumulated approximately 10,000 operating hrs and about 3000 starts. At present, seven V-94 gas turbines are in service which have aggregated 31,000 operating hours and 6200 starts. Six further similar machines are being manufactured in response to orders and order intentions.

Basic V-94 Design

An artist's view of the V-94 prototype gas turbine is shown in Fig. 1. The design is almost identical to that of the previous smaller 65 MW-class Model V-93 machines. The compressor and turbine blades are mounted on a common shaft built up from individual wheel disks. The rotor is supported in only two bearings located outside the pressurized region. The common turbine and compressor casing is horizontally split, and the two large silo-type combustion chambers are located on either side of the machine. The flame tubes are protected by refractory tiles. The earlier experience with Model V-93 gas turbines, which together have accumulated to date more than 800,000 operating hrs and almost 35,000 starts, could be applied directly to the larger Model V-94 machines.

The salient data for the V-94 and V-93 gas turbines are listed in Table 1.

Although the V-94 model was designed from the beginning for a turbine inlet temperature around 1000°C, the first V-94 machines were built for the same temperature as that of the V-93 gas turbines at the time, namely 850°C under base-load conditions. Thus the 42 percent higher output of the V-94 model was achieved mainly by 40 percent higher air mass flow and by improved efficiency. This higher mass flow required corresponding enlargement of the machine dimensions.

First V-94 Gas Turbine Plant

The first Model V-94 gas turbine was installed at the end of 1974 in the Munich Freimann municipal heating power plant.

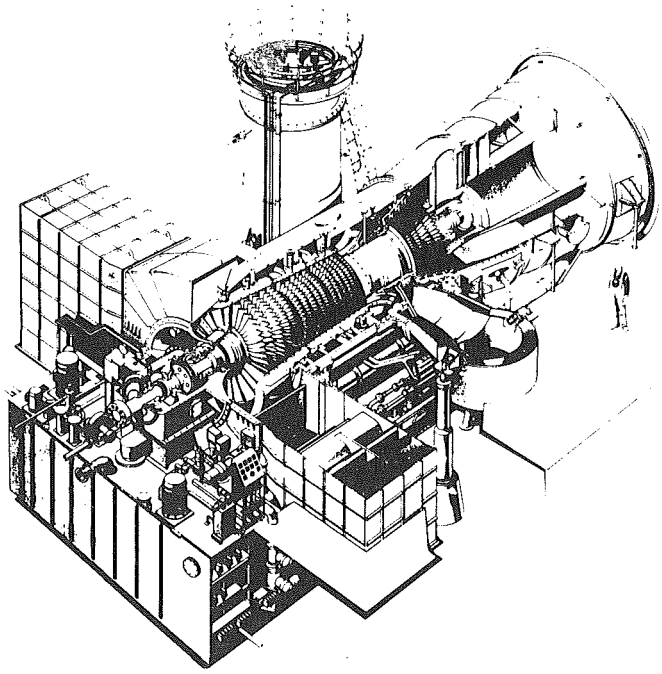

Fig. 1 Type V-94.0 gas turbine

Contributed by the Gas Turbine Division of THE AMERICAN SOCIETY OF MECHANICAL ENGINEERS and presented at the 27th International Gas Turbine Conference and Exhibit, London, England, April 18–22, 1982. Manuscript received at ASME Headquarters December 14, 1981. Paper No. 82-GT-159.

Table 1 Model V-94 and V-93 gas turbine rated base-load performance data and dimensions

	V-94	V-93
Air mass flow, kg/s	482	343
Turbine inlet temperature, °C	850	850
Power output, MW	91.2	64.2
Bearing span, mm	8500	7800
Distance between the combustion chamber centers, mm	8280	7150

Although all the extensive operating experience with the V-93 gas turbines was utilized in designing the V-94 model, a comprehensivive test program was carried out in the Freimann station to test the reliability of the unit under actual operating conditions. Three further V-94 machines were installed in 1974/75 for peak-load generation in power plants in Vienna [2], Stuttgart and Munich (Freimann 2). One of these installations is photographed in Fig. 2.

The first gas turbine in Munich Freimann [3, 4] operates with heat recovery to produce hot water for district heating purposes. It normally runs for about 4,500 hr per year and is started up two or three times a day. The second machine in the Freimann station, however, is operated primarily to meet peak-load demands for only about 500 hr per year. The unit is started with its own generator in order to attain the required fast start-up times. The automated starting and loading procedures are shown in the Fig. 3 diagram.

As can be seen from Fig. 3, full speed is reached within 2 min. The loading commences with a 15-MW step following synchronization and is continued linearly up to about 95 percent of base load at a normal rate of 8.5 MW/min or at a fast rate of 23 MW/min when the output is needed more rapidly. This means that 95 percent output can be attained normally within 10 min. or within 5 min. if there is a more urgent load demand. Loading above this 95 percent value can be accomplished at the more gradual rate of 3 MW/min. The starting, loading and unloading procedures are optimized in order to minimize the thermal stresses and resultant fatigue accumulation of the hot turbine parts. With this mode of operation, the Freimann 1 gas turbine has been run more than 21,000 hr and started up over 3200 times. The systematically evaluated operating statistics of this unit since 1977, when an extensive test program and some corrective work were completed, are depicted in Fig. 4. It shows that, except for 1978, the machine was available for operation more than 97 percent of the time. However, any comparison of "availability" between different gas turbines and modes of operation is difficult because the total outage time depends on the basic application, load demand, owner's policy in regard to stocking spare parts, productivity and training of the operating personnel, along with numerous other factors not directly related to the quality of the equipment.

The real significance lies in the forced-outage time and starting reliability. It can also be seen in Fig. 4 that over the last four years of operation the gas turbine had a forced-outage factor of well below 2 percent and started 99.2 percent of the times successfully when called upon to do so. These values are remarkably good considering the high utilization (service factor of about 50 percent) and the high start-up frequency (two or three times a day). The low availability in 1978 was due to a major overhaul. The reason why this overhaul took so long is that all the components were examined much more intensively than is normally done because this was the first V-94 gas turbine which had accumulated such a large number of operating hours and so many starts.

During this overhaul the attachment of the inner shroud at

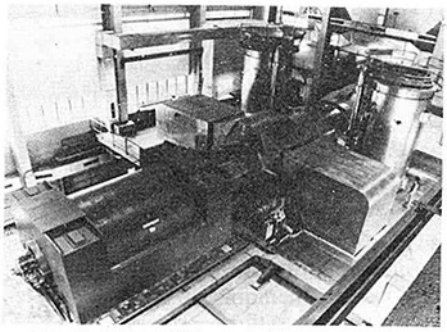

Fig. 2 Model V-94 gas turbine installation

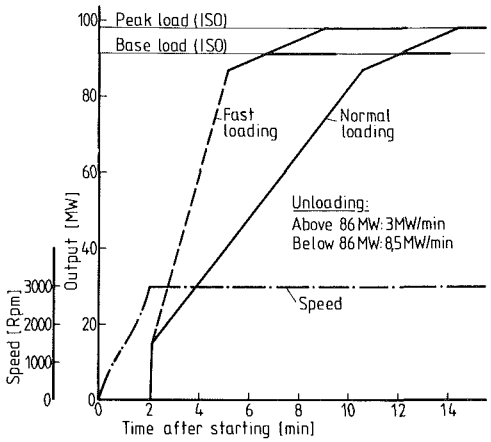

Fig. 3 Automated starting and loading gradients of the Freimann 1 gas turbine

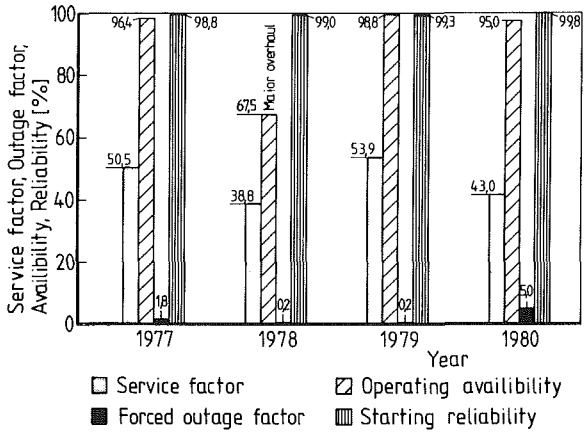

Fig. 4 Operating factors of the Freimann 1 gas turbine

the compressor stator blades was found to be damaged. As shown in Fig. 5, the inner shroud is attached to each stator blade by a blade hook. Although the operating forces on the blade hooks are very low, nevertheless several hooks were found with cracks. In one case a hook part had broken off from the attachment and damaged several blades in the downstream stages. Analysis confirmed that the fatigue cracks were caused by the stress concentrations at the sharp hook corners despite the low operating forces. This was rectified by rounding the sharp corners of the blade hooks.

The vibration behavior of the rotor had also to be improved. As shown in Fig. 6, the steady-state vibration amplitudes were normally less than 5 microns. During start-up, however, they rose and reached a maximum of 30 microns about 10 min. after the gas turbine had attained synchronous speed and fell again within the following 30 min. to the normal low steady-state level.

Measurements indicated that the vibration increase was caused by temporarily disturbed rotor balance. The cause for

this transient unbalance was found during the overhaul to lie in inadequate sealing of the front rotor disks in the compressor. As can be seen in Fig. 7, the disk rims of the front rotor wheels are sealed with rubber rings. The grooves for the rubber rings in the Freimann 1 gas turbine were found to be eccentric. This eccentricity resulted in some of the rings being squeezed which led to unsymmetrical leakage of the warm air out of the rotor, producing thermal bowing of the shaft during the warm-up period whenever the gas turbine was started up. This deficiency was overcome by sealing the front rotor disks with additional metallic bushings at the inner diameter of the disks. Since the machine was returned to service, no more unusual temporary vibration rises have occurred [5]. A second major overhaul of the Freimann 1 gas turbine was carried out at the beginning of 1981 after 20,000 operating hrs and 3100 starts. No defects were found when the opportunity was taken to recheck the attachment of the inner shroud to the compressor stator blades with particular care.

Particularly noteworthy was the excellent condition of the more critical turbine parts, such as the turbine blading and the combustion chambers. No defects were revealed when the turbine blades were subjected to the usual very careful crack-testing procedures. Furthermore, no repairs even to the combustors, including the flame tubes with their ceramic tiles, as well as the hot-gas ducts and liners were necessary. This remarkable durability demonstrated once again the many benefits of the large silo-type combustor design. One of the main advantages is that the temperature profile of the hot gas entering the turbine is quite uniform, far more so than is the case with can-type or annular combustion systems. Also highly advantageous is that the flame zone does not have a line of sight to the turbine first-stage vanes which eliminates the radiational heat load and substantially reduces the possibility of vane cracking due to excessive thermal stress [6, 7].

Maintenance Philosophy

Orginally the maintenance cycle for V-94 gas turbines called for a one-week inspection after every 8000 hr of operation and a major overhaul at 16,000-hr intervals. Meanwhile this recommendation has been changed for both Model V-93 and V-94 gas turbines. A major overhaul is now recommended after every 20,000 hr of operation and a two-day inspection after every 4000 hr instead of the one-week inspection after 8000 hr. This change in maintenance intervals has the advantage of reducing the scheduled maintenance factor from 6.3 to 5 percent on the basis of the major overhaul requiring five weeks. It is also better to check the hot turbine parts more frequently between major overhauls because incipient defects, such as thermal cracks, fatigue cracks, or wear between the transition pieces in the hot-gas ducts, can be found more readily before they can grow in the course of time to a serious extent and result in heavy and consequently expensive damage to the turbine blading. The large-size combustor design yields another benefit: a man-hole access in the transition duct enables direct inspection of all the hot-gas regions, an accurate evaluation of the findings and easy repair possibilities without the need of dismantling any additional parts.

All operating events affecting the life of machine components are weighted to form an equivalent operating time for the purpose of determining the inspection and overhaul intervals. This equivalent operating time is calculated by the equation:

$$t_{eq} = a_1 n_1 + a_2 n_2 + \sum^{n_3} t_3 + b_1 t_1 + b_2 t_2$$

where:

t_{eq} = equivalent operating time
n_1 = number of starts

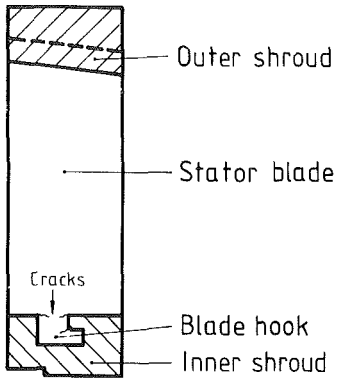

Fig. 5 Compressor stator blade ring assembly

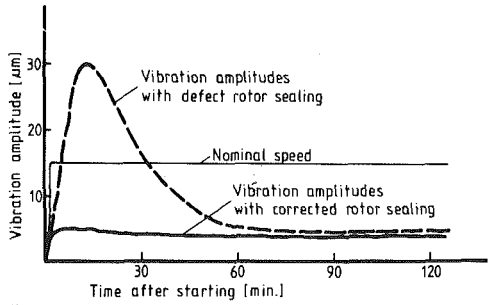

Fig. 6 Bearing vibrations of the Freimann 1 gas turbine

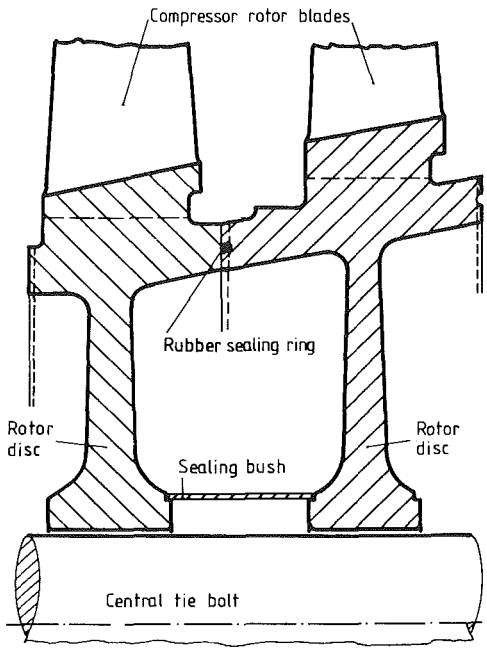

Fig. 7 Compressor rotor sealing design

a_1 = 10 (weighting factor for each start)
n_2 = number of fast loading procedures
a_2 = 10 (weighting factor for fast loading)
t_3 = equivalent operating hours for rapid temperature changes, e.g., due to step load changes or load rejections (see Fig. 8)
n_3 = number of rapid temperature changes
t_1 = operating hours with output up to base-load rating
b_1 = 1 (weighting factor for base-load duty)
t_2 = operating hours with output between base and peak-load ratings
b_2 = 4 (weighting factor for peak-load duty)

The inspections can be done by either the gas turbine manufacturer or the customer. In the latter case the manufacturer's instructions with specific details on where and

how to check should be followed. The authors' company has requested customers to furnish monthly reports on all outage times and faulty starts. These reports allow the manufacturer to analyze this important information and consequently to help the customer to make his equipment increasingly more reliable, thus enhancing the operation availability of the gas turbine equipment.

Advanced V-94 Machines

The turbine inlet temperature could be raised up to 970°C (ISO definition) by cooling the turbine first-stage blades, thus increasing the power output in the base-load mode up to 121 MW. A cooling technique was selected for the vanes which had already proved itself successfully in the previous smaller V-93 gas turbines [8]. In addition, two cooled vanes were installed for factory testing purposes in the first two stages of the Freimann 1 prototype turbine, where they were left to gain prolonged field operating experience with them. These vanes were subjected during each of the many starts of Freimann 1 to the same stress cycles as in the case of the uprated V-94 machines. This is because the highest thermal stresses occur during start-up, and the starting procedure is the same for both types of V-94 machines. Thus, all the operating experience from the model prototype could be directly transferred to the uprated Type V-94.1 machines.

With regard to the combustion chambers and hot-gas liners, Type V-94.1 machines are also equipped with the elbow-shaped silo-type combustors that proved so successful in conjunction with the V-93 gas turbines. Figure 9 shows the difference in configuration between the two combustor designs. By adopting the elbow shape a concentric air flow could be achieved between the inner and outer shells, so that despite the higher hot-gas temperature the metal temperature did not become higher than in the first V-94 machines with a lower hot-gas temperature. All the other components were retained without alteration.

Before the first uprated Type V-94.1 machine was installed in a power plant, it was tested in the Berlin gas turbine test facility under all possible operating conditions. This KWU test facility is equipped with a 120 MW water brake so the machine could be tested up to full load. Following the KWU philosophy of testing each newly designed component before it is released for service, a great deal of measurements were taken during the test runs, e.g., vibratory stresses of the compressor and turbine blades, casing temperatures, hot-gas temperature distributions, and various thermodynamic data [9–11]. Considerable effort was expended in measuring the cooled-blade temperatures. As expected, the vane temperatures did not differ from those in the V-93 gas turbines. Special attention was paid to the rotating-blade temperatures because it is very difficult to calculate these metal temperatures exactly due to the effect of rotation on the cooling-air flow inside the blades. As can be seen from Fig. 10, the measured and calculated values were highly consistent. It should be noted that with unchanged cooling-air mass flow the allowable metal temperature would only be reached with a turbine inlet temperature increase of approximately 100°C above the present level. This represents a sizeable margin in power output and efficiency.

Two Type V-94.1 machines were installed in the South Munich GUD (Gas und Dampf) combined-cycle power plant [12]. The exhaust gases of both turbines raised steam in unfired boilers for a 70-MW steam turbine. A portion of the heat energy is used for district heating purposes. This plant has underrated conditions (4°C/980°C/954 mbar) and at maximum machine ratings without any steam being used for external heating systems a total power output of 310 MW and an overall efficiency of 42 percent. It has been in operation since the beginning of 1980. The mode of operation is similar

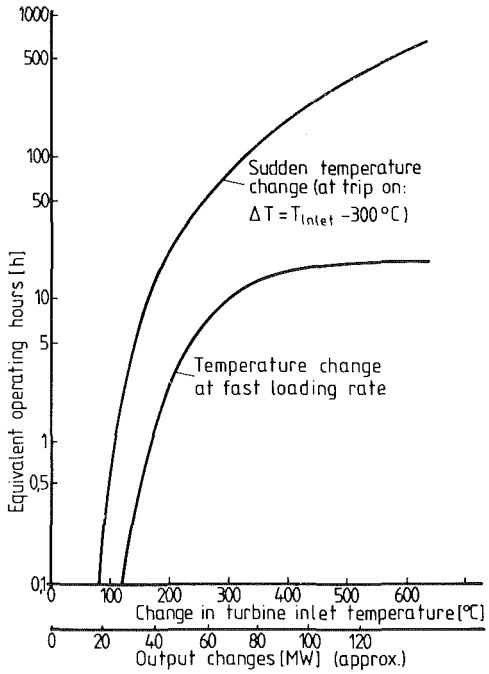

Fig. 8 Equivalent operating hours for rapid changes in turbine inlet temperature

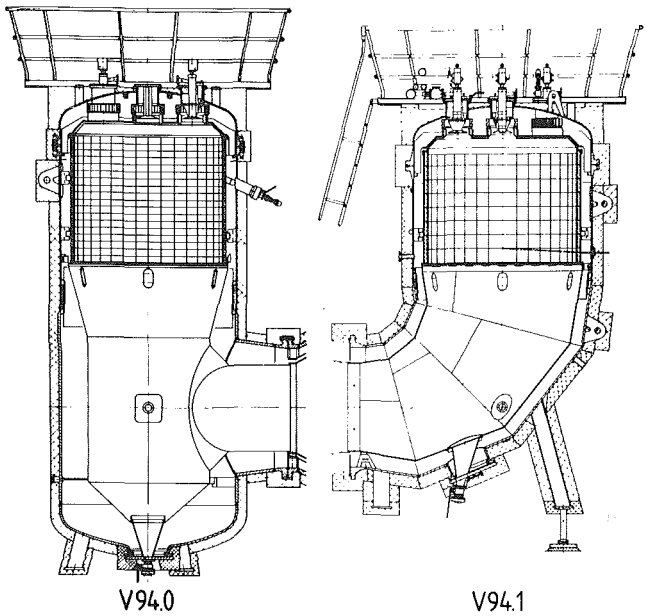

Fig. 9 Comparison of the configurations of the Type V-94.0 and V-94.1 gas turbine combustion chambers

to that of the Freimann 1 unit. To date the South Munich gas turbines have accumulated a total of about 2000 service hrs and 400 starts. They have demonstrated the same excellent availability and reliability as the predecessor V-94 gas turbines in the Munich Freimann station.

A further step in the development of the Model V-94 gas turbine resulted in the V-94.2 type which was dictated more by economic than technical considerations. A self-supporting casing was provided to facilitate transportation and installation of the factory-assembled gas turbines in power stations without the need for a base frame. This design resulted in a correspondingly smaller overall height, lower transportation cost, shorter assembly time and sufficiently greater space for maintenance within the building.

A comparison of Fig. 11 with Fig. 1 reveals that the design goals were achieved mainly by adopting the following modifications:

- Relocation of the air intake duct to the front of the compressor bearing
- Common supports for the rotor and casing instead of two separate ones at different levels
- Insertion of the first stationary blade rows of the compressor in the outer casing
- Reduction of the transportation weight from 217 to 195 metric tons
- Maximum outer dimensions within most railway profile limitations

This means that for the most part only the casings were modified, whereas the decisively important internals, such as the rotor and blading, remained practically unchanged [13].

Additional power output and efficiency increases were gained by improving the flow at the compressor inlet and turbine exhaust. At a baseload turbine inlet temperature of 970°C the power output and efficiency are 125 MW and 32.7 percent, respectively. The first such uprated V-94 gas turbine was tested up to full load in the KWU test facility in Berlin. It was installed in the Walheim power plant early in 1981. No problems were encountered since it was released for commercial service later in the same year.

Further Trends

The considerable performance margins, which were confirmed by the extensive factory test measurements, as well as by the later operating experience, allow further uprating of the V-94 model by increasing the turbine inlet temperature up to above 1000°C. This will result in an output increase, as well as in an efficiency improvement. The turbine inlet temperature can be increased mainly by intensifying the cooling of the existing turbine blades by means of larger cooling-air mass flows. In addition, the second-stage rotor blades would also have to be cooled by the same technique which has already proved itself successfully in the Model V-93 gas turbines. These modifications will not affect the high operating reliability record of the Model V-94 gas turbines. This is because the blade surface metal temperature will be maintained below 850°C, as in the case of all Model V-93 and V-94 gas turbines in operation, to prevent high-temperature oxidation of the blade materials that can occur above 850°C.

Conclusion

The latest Model V-94 gas turbines offer electric utilities highly available and reliable machines with high efficiency, long durability and low maintenance costs. They are equally suited to peak-load generation, as well as to combind-cycle power plants for base-load generation. Experience has demonstrated that they are capable of utilizing a large variety of fuels which is especially important in view of the ongoing development of coal gasification.

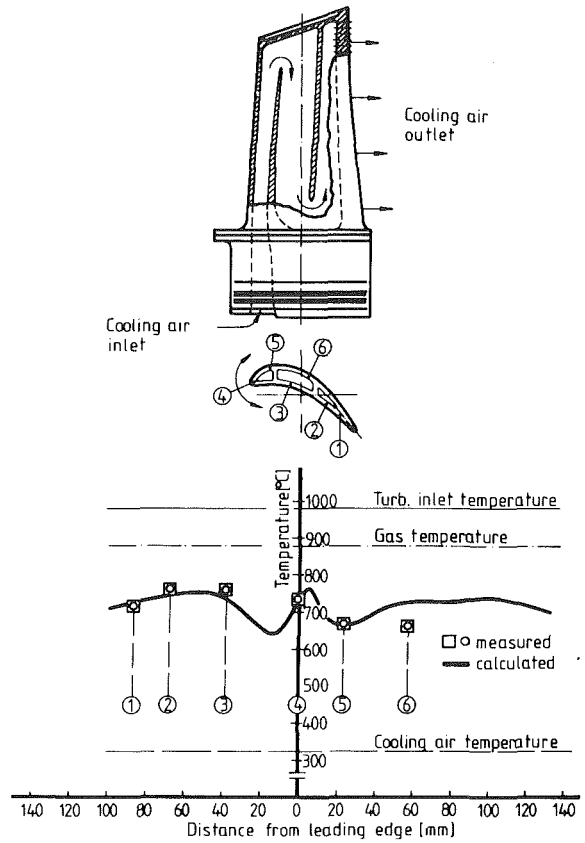

Fig. 10 Model V-94 turbine first-stage air-cooled rotor blade temperature distribution

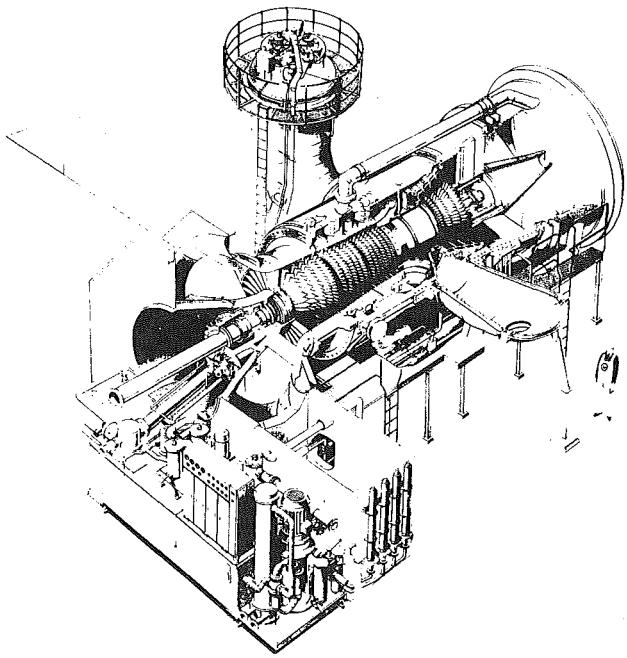

Fig. 11 Type V-94.2 gas turbine

References

1 Maghon, H., "Betriebserfahrungen mit grossen KWU-Gasturbinen," *VGB Kraftwerkstechnik,* 58, Vol. 5, May 1978, pp. 323–330.

2 Kastl, H., "Das 80/100 MW Gasturbinenkraftwerk der Wiener Stadtwerke-Elektrizitäts-werke Österreich," *Z. Elektro-Wirtschaft* 30, No. 4, 1977, pp. 140–148.

3 Maikranz, F., "Das Heizkraftwerk Freimann der Stradtwerke München-Elektrizitätswerke," *Energie und Technik,* Vol. 10, 1971, pp. 369–372.

4 Schäch, R., "Der Einsatz von Gasturbinen in Heizkraftwerken, gezeigt am Beispiel des Heizkraftwerkes Munchen-Freimann," *Energie-wirtschaftliche Tagesfragen,* 25, Vol. 8, 1975, pp. 368–374.

5 Schmoch, O., and Deblon, B., "Experience with Large Heavy-Duty Gas Turbine Rotors," ASME Paper 81-GT-181.

6 Lienert, A., and Schmoch, O., "Design Philosophy of the KWU Silo Combustors," ASME Paper 82-GT-57.

7 Grevstad, P. E., Smith, M. J., and Duncan, R. L., "A Baseload Gas Turbine to Meet Utility Requirements for Reliability and Availability," ASME Paper 81-GT-127.

8 Deblon, B., "Full Load Tests of the 80-MW Gas Turbine V 93.2 Using a Water Brake," ASME Paper 78-GT-68.

9 Goebel, K., and Becker, B., "Works Load Tests Fix Tighter Performance Guarantees," *Energy International,* Vol. 15, No. 6, June 1978, pp. 29–31.

10 Bals, H., Biniaris, S., and Rochel, U., "Full Load Testing of Gas Turbines up to 120 MW," CIMAC Paper GT 21, 1979.

11 Becker, B., "Erprobung einer neuen Leistungs-klasse für Gasturbinen mit Grundlast über 100 MW," *Motortechnische Zeitschrift,* 40, No. 5, 1979, pp. 247–249.

12 "Kombinierte Gas-Dampfturbinenanlage für Heizkraftwerk Munchen Süd," KMU Publication, March 1978, Order No. KWU 427.

13 Schmoch, O., "Development of a Single Shaft 114/125 MW Gas Turbine for the 50 Hz Range," CIMAC Paper GT 13, 1979.

H. D. Joslyn
Research Engineer.

R. P. Dring
Manager.

Gas Turbine Technology,
United Technologies Research Center,
East Hartford, Conn. 06108

O. P. Sharma
Project Engineer,
Commercial Products Division,
Pratt & Whitney Aircraft

Unsteady Three-Dimensional Turbine Aerodynamics

High response aerodynamic measurements were made in a large-scale, axial, flow turbine model to study the unsteadiness and three dimensionality of the flow. High response velocity vector and total pressure data were acquired. A comparison was made of the results of phase lock averaging both raw and reduced data (voltages and velocities). The velocity vector measurements showed that there were strong radial flows present as well as significant periodic changes in the flow field due to relative rotor and vane positions. Random, periodic, and total unsteadiness levels were computed from the instantaneous and phase-lock-averaged velocity data. Time-averaged data were compared with an inviscid two-dimensional calculation. A comparison was also made of time-averaged total pressure measurements obtained from high-response and low-response (steady-state) probes.

Introduction

Turbomachinery flow fields are highly unsteady, three-dimensional and spatially nonuniform. These characteristics make them extremely difficult to model analytically. As a result, much of the insight into the complex physical mechanisms that govern turbomachinery aerodynamics has come from a broad range of experimental studies that have been carried out by numerous investigators employing steady-state and high response instrumentation. Much of this work was done in linear cascades and has resulted in a number of excellent flow studies that include those by Langston et al. [1], Sjolander [2], and Machal and Sieverding [3]. However, the cascade is unsuitable for studying mechanisms of interest to the turbine designer which are related to the unsteady, three-dimensional, spatially nonuniform aerodynamic flow fields that occur in an actual turbomachine environment.

Three-dimensional flow mechanisms are of considerable concern to the turbine designer since the assumption of strip theory is the basis of many design systems and the degree to which it is violated can impact many aspects of turbine design. In particular, the prediction of spanwise performance can be greatly complicated by the radial redistribution of total pressure (loss) and total temperature in turbomachinery flows. Using rotating steady-state instrumentation, Dring and Joslyn [4] have demonstrated that the spanwise migration of high loss fluid in a turbine rotor flow field can be considerably different than what would be expected based upon cascade flow studies. In addition to the three-dimensional flow effects, the turbine designer must contend with unsteadiness. Unsteadiness (due to periodic and random velocity fluctuations) in the flow is known to significantly affect heat transfer rates [5, 6] as well as airfoil boundary layer behavior (7). Bayley and Priddy [5], for example, have shown that free stream turbulence intensity, as well as the frequency of the periodic free stream velocity fluctuations, dramatically influence convective heat transfer to turbine blading. The work of Evans [7] demonstrated that the boundary layer on a stator airfoil periodically alternated between a laminar and turbulent profile due to the unsteadiness introduced into the flow by the upstream row of rotor airfoils.

At the present time, while there are various studies dealing with unsteady, three-dimensional compressor aerodynamics (e.g., [8–11]), there is only limited high response aerodynamic data available for turbine stages. In one study, Hunter [12] employed steady-state and high-response instrumentation to study endwall boundary layer flows in a large-scale, lightly loaded, single-stage turbine model. In this study, using a technique similar to that of Whitfield [13], a single element hot film probe was rotated to three successive positions at each measurement location, and the output voltage was phase-lock averaged [14]. This averaging technique enhances the periodic time-dependent flow information, while the random unsteadiness is suppressed. The results from this study showed the presence of strong secondary flows at the high turning turbine rotor hub section. Also, the results showed that the flow pattern at the turbine rotor exit was found to be influenced by the rotor/stator axial spacing and the relative circumferential position of interacting blade rows.

The present program was formulated to provide a contribution to the limited body of high-response (time-dependent) turbine aerodynamic data. In particular, the program was formulated to meet the following objectives: (*i*) the validity of processing three-element, hot film data by phase-lock-averaging linearized anemometer voltages prior to converting to velocity components was to be investigated. This was motivated by the fact that it is far less expensive to reduce phase-lock-averaged (PLA) voltages to velocity than to phase-lock-average velocity components reduced on a revolution by revolution basis. (*ii*) The temporal and spatial influences of a moving blade row on the three-dimensional nature of the flow field properties (speed, yaw, and pitch) of upstream and downstream airfoil rows were to be measured.

Contributed by the Gas Turbine Division of THE AMERICAN SOCIETY OF MECHANICAL ENGINEERS and presented at the 27th International Gas Turbine Conference and Exhibit, London, England, April 18–22, 1982. Manuscript received at ASME Headquarters December 14, 1981. Paper No. 82-GT-161.

(*iii*) Time-averaged values of velocity, air angle, and total pressures were to be determined and compared with other redundant measurements and a theoretical prediction. (*iv*) The relative magnitude of the random and periodic contributions to the total unsteadiness in the turbine flow field were to be quantified. (*v*) Finally, the impact on accuracy of using pneumatic (steady-state) probes in the unsteady flow field of a large scale turbine model were to be quantified by comparison with results from a high-response pneumatic probe.

Experimental Facility and Instrumentation

The experimental program was conducted in the United Technologies Research Center's 5 ft (1.52 m) diameter Large Scale Rotating Rig (LSRR). A one and one-half stage axial flow turbine model consisting of 22 first vanes, 28 first blades and 28 second vanes having an 0.8 hub/tip ratio was used in this experiment. The model airfoils all have aspect ratios of approximately 1.0 and axial chords of approximately five times engine scale. At typical running conditions, the axial flow velocity in the test section is 75 f/s (23 m/s) and the rotor speed is 410 rpm. Airfoil Reynolds numbers are approximately 5.6×10^5, which is typical of high-pressure turbine airfoils. The absolute and relative flow angles and the airfoils (Table 1) that produce them are also typical of current high pressure turbine stages.

A cross section of the turbine model flow path and flow angle sign conventions are shown in Fig. 1. High-response and steady-state traverse data were obtained at stations 1, 2 and 3. The rig inlet flow (C_x) was based upon the static pressure at station 0. The probes were mounted in a traverse device located external to the rig. They entered the flow path through sealed slots in the casing. The probes could be traversed circumferentially over two airfoil pitches and radially from hub to tip. The probes could also be rotated in yaw to optimize hot film probe yaw angle sensitivity. Two types of three-element hot film probes were used in this program to measure the instantaneous flow velocity. A standard Thermo Systems Inc. (TSI) "X"-array (Model 1295-U-20) probe, calibrated from +25 deg to −25 deg in yaw and from +5 deg to −15 deg in pitch, was used at station 1. At stations 2 and 3, a 45 deg conical TSI (Model 1294-CL-20) probe was used. It was calibrated from +25 deg to −25 deg in yaw and from +20 deg to −15 deg in pitch. Both probes were calibrated over a range from 30 to 110°F (−1.1 to 43.3°C) in ambient temperature, over a range of velocities from 50 to 200 f/s (15.2 to 60.9 m/s) and were powered by TSI (Model 1050) anemometers. The anemometers were connected to TSI (Model 1052) linearizes which provided an output voltage (0-10 V) to the data acquisition system. Temperature calibration of the hot films was essential since the LSRR test facility employs ambient air drawn from out-of-doors. In this connection, a single 0.002 in. dia thermocouple sensor was attached to the hot film probes and the flow temperature was measured so that the appropriate correction could be applied

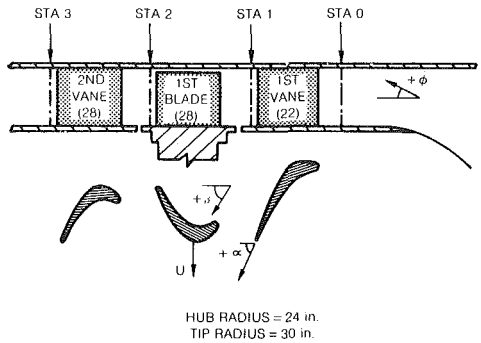

Fig. 1 Model geometry

Nomenclature

b_x = airfoil axial chord
c = absolute flow speed
$\bar{c}$ = time-averaged PLA flow speed
$\tilde{\hat{c}}$ = phase-lock-averaged (PLA) absolute flow velocity
$\hat{c}$ = absolute flow velocity
c_s = streamwise component of absolute velocity
c_n = normal component of absolute velocity
c_r = radial component of absolute velocity
C_P = pressure coefficient: $(P_{T_o} - P)/\frac{1}{2}\rho U m^2$
C_{PT} = total pressure coefficient: $(P_{T_o} - P_T)/\frac{1}{2}\rho U M^2$
h = streamtube height
i = incidence angle
n = number of blade passing periods
P = static pressure
P_T = total pressure: $(P + \frac{1}{2}\rho c^2)$
q = dynamic pressure
r = radius
St = Strouhal number
t = normalized time: $(T - T_o)$/rotor passing period
t_b = rotor passing period
T = time
T_o = reference time
U_m = wheel speed at midspan
w = relative flow speed
$\hat{w}$ = relative velocity
x = axial distance
α = absolute flow angle (yaw)
β = relative flow angle (yaw)
ϕ = pitch angle
ρ = density
τ = airfoil pitch
θ = circumferential position
θ_τ = normalized circumferential position: (θ/first vane pitch)
$\sqrt{\bar{U}_T^2}$ = total unsteadiness
$\sqrt{\bar{U}_P^2}$ = periodic unsteadiness
$\sqrt{\bar{U}_r^2}$ = random unsteadiness

Subscripts

0 = first vane inlet
1 = first vane exit
1B = first blade (rotor)
1V = first vane
2 = rotor exit
3 = second vane exit
k = revolution number
o = steady state
P = periodic
r = radial
s = streamwise direction
P = pressure surface
S = suction surface

Superscripts

$\hat{}$ = vector
$\sim$ = phase-lock averaged
$-$ = time averaged
$'$ = random

during data reduction. A more detailed description of the hot film calibration and reduction procedure is presented in [15].

High-response total pressure traverse data were obtained using a Kulite (Model XSC-093-5) semiconductor transducer installed in a standard United Sensors Kiel probe (USC-KBC-12). The response time for this device was adequate for the present application since from shock tube tests the response of the probe was found to be 8 KHz (approximately 42 times blade passing frequency). This probe was calibrated for temperature and velocity changes over the same range as the hot film probes. The probe incorporated the same flow temperature measurement thermocouple in its design. Steady-state pneumatic traverse data were obtained with a United Sensor KBC-12 Kiel probe. Calibration of both total pressure probes showed them to indicate the true total pressure from +50 deg to −50 deg in pitch or yaw relative to their centerline axes.

The radial, circumferential, and yaw positioning of all probes as well as data acquisition (and some data reduction) was accomplished by a dedicated on-line minicomputer (Perkin Elmer 8/16E). A schematic diagram of the system configured for high response, phase-lock-averaged (PLA) data acquisition is shown in Fig. 2. The system is capable of simultaneously acquiring up to four channels of high-response data. The recording of the linearized hot film output voltages and thermocouple voltage was initiated once every rotor revolution by a reference signal generated by an optical photosensor (Optron Model OPB 253) focused on a reference rotor blade tip. For the present program, data were acquired at 300 rotor positions (over three consecutive rotor pitches) and averaged over 100 revolutions. "Quick look" PLA velocities, pressures, and temperatures were obtained on-line via the Perkin Elmer 8/16E mini-computer in order to monitor any drift in probe calibration or instrumentation malfunction. At each of typically 1000 radial/circumferential locations in a traverse plane, 30,000 pieces of information (300 per revolution over 100 revolutions) were acquired for each sensor (120,000 for the three-element hot film probe with thermocouple sensor). All instantaneous raw digitized data (voltages) were stored on magnetic tape for a detailed off-line analysis.

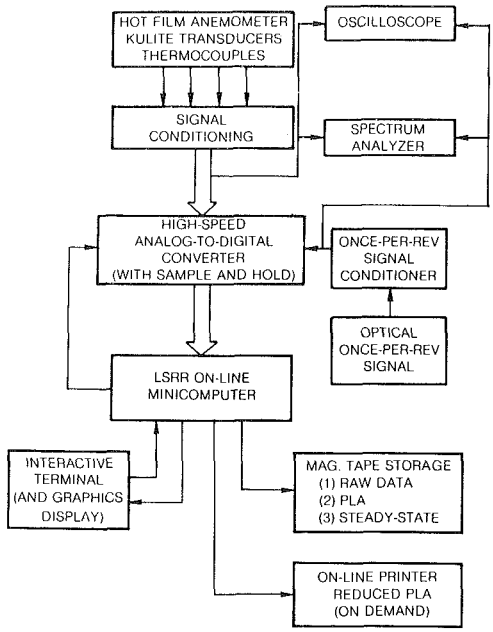

Fig. 2 PLA data system

Data Reduction

Although the pressure/voltage calibration of the high-response Kiel probe was linear, the 100 revolutions of voltage data were reduced to total pressure data and then phase-lock averaged to obtain the periodically time varying pressure at each radial/circumferential location in the traverse planes. The data were reduced in this manner to be consistent with the hot film reduction described below. A time-averaged total pressure coefficient, C_{PT}, was subsequently computed for data analysis.

The practice commonly found in the open literature for hot film data reduction has been to phase-lock average the output voltages and to subsequently convert the averaged voltages to velocity. This approach is valid only if the calibration relating velocity magnitude and orientation is linear with hot film sensor output voltage. Also, unless additional signal processing is done, random unsteadiness (turbulence) information is lost with the above approach. The results of the three-element hot film probe calibration, described in [15], showed that the variation in velocity magnitude (speed) was nearly linear with the square root of the sum of the squares of the linearized hot film voltages from the three sensors. Velocity vector orientation, and hence flow angles (yaw and pitch) were correlated with a calibration parameter based upon flow speed and the linearized voltage output of each hot film sensor. The resulting correlation was a trigonometric function that varied nearly linearly over a limited range of yaw and pitch angles (approximately ±10 deg about the probe and centerline axis). Since one of the objectives of the present program was to determine random and periodic unsteadiness levels, the raw digitized voltage data were reduced to aerodynamic quantities (velocity and flow angles) in each rotor revolution on an instant by instant basis and then phase-lock averaged. For each rotor revolution, the instantaneous velocity was obtained and was defined in terms of its streamwise component, radial component, and a component normal to the streamwise and radial components. Each velocity component was defined to consist of a steady, periodic and random part. For the kth revolution ($k=1$ to 100), the instantaneous velocity was expressed as follows

$$\hat{c}_k(t) = c_{s_k}(t)\hat{s} + c_{n_k}(t)\hat{n} + c_{r_k}(t)\hat{r}$$

where

$$c_{s_k}(t) = c_{s_o} + c_{s_p} + c'_{s_k}$$
$$c_{n_k}(t) = c_{n_o} + c_{n_p} + c'_{n_k}$$
$$c_{r_k}(t) = c_{r_o} + c_{r_p} + c'_{r_k}$$

Since

$$\sum_{k=1}^{100} c's_k = 0,$$
$$\sum_{k=1}^{100} c'n_k = 0,$$

and

$$\sum_{k=1}^{100} c'r_k = 0$$

averaging over 100 revolutions resulted in the PLA velocity, i.e., the sum of the steady and periodic components:

$$\bar{\hat{c}}(t) = \frac{1}{100}\sum_{k=1}^{100}\hat{c}_k(t) =$$
$$(c_{s_o} + c_{s_p})\hat{s} + (c_{n_o} + c_{n_p})\hat{n} + (c_{r_o} + c_{r_p})\hat{r}$$

A timewise integration over an integral number of rotor blade

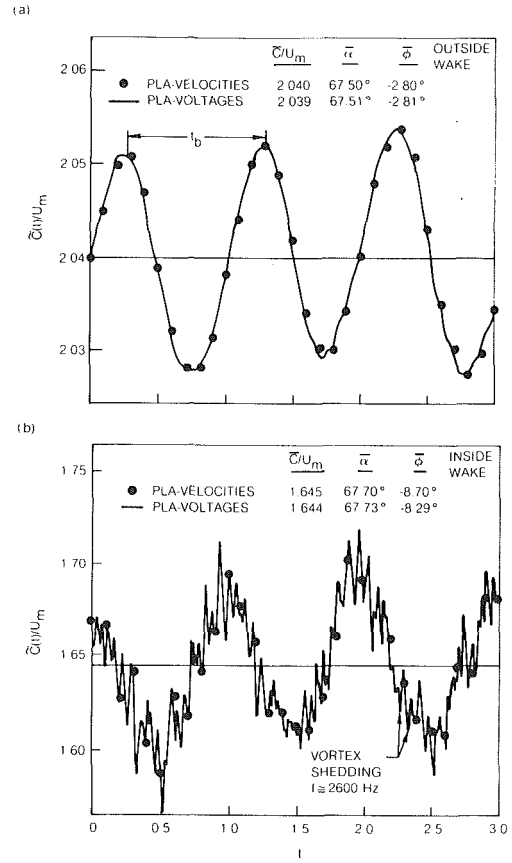

Fig. 3 PLA reduction comparison at first vane exit (station 1)

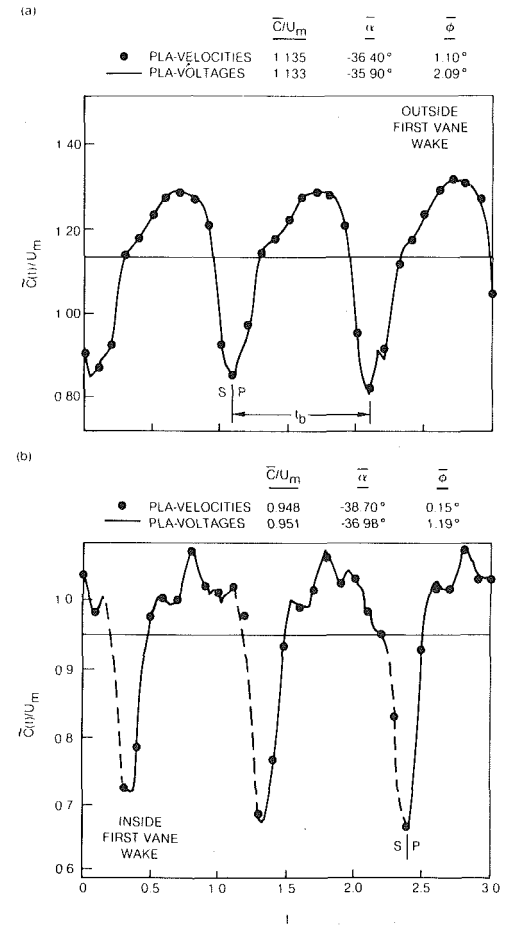

Fig. 4 PLA reduction comparison at rotor exit (station 2)

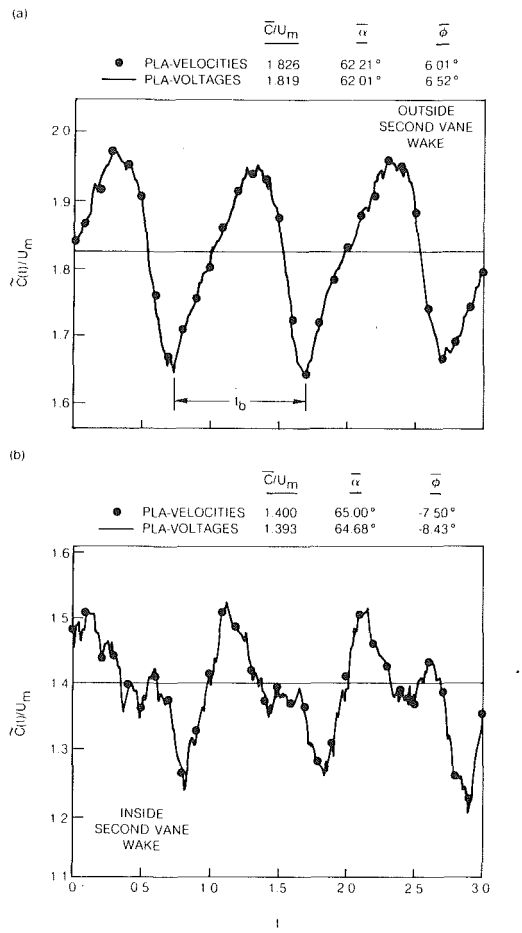

Fig. 5 PLA reduction comparison at second vane exit (station 3)

passing periods ($n=3$) provided the time-averaged (steady-state) velocity

$$\bar{\tilde{c}} = \frac{1}{nt_b}\int_o^{nt_b} \tilde{c}(t)\,dt = c_{s_o}\hat{s} + c_{n_o}\hat{n} + c_{r_o}\hat{r}$$

since

$$\frac{1}{nt_b}\int_o^{nt_b} c_{s_p}\,dt = 0,$$

$$\frac{1}{nt_b}\int_o^{nt_b} c_{n_p}\,dt = 0,$$

and

$$\frac{1}{nt_b}\int_o^{nt_b} c_{r_p}\,dt = 0$$

The resultant time-averaged speed is therefore

$$c = \sqrt{{c_{s_o}}^2 + {c_{n_o}}^2 + {c_{r_o}}^2}$$

All reduced hot film velocity data presented in this discussion were nondimensionalized by U_m, the rotor speed at midspan. The PLA and time-averaged flow angles were computed by summing the reduced instantaneous flow angles and then time averaging the resulting PLA results over an integral number of rotor passing periods. With all the data acquired and reduced in this manner, it was possible to examine the steady and unsteady aerodynamics in the turbine model in terms of both periodic fluctuations (due to blade row interaction) and random fluctuations (due to turbulence). Due to the large amount of data acquired, only the results obtained at or near

midspan have been examined in detail and are presented in this paper.

PLA Results

Strictly speaking, unless the calibration/reduction scheme is linear over the range of instantaneous yaw and pitch in the actual flow field, hot film data should be reduced to velocity and flow angles and the results phase-lock averaged. For applications in which only the PLA velocity and flow angles are required and for which the calibration is linear, a significant reduction in computational time can be achieved by digitizing only the phase-lock-averaged hot film voltages and then applying the calibration. For the present case a reduction by a factor of 100 could have been achieved. To explore this possibility and to assess the influence of the nonlinearity in the yaw and pitch calibration, a comparison of the two averaging techniques (phase-lock averaging raw voltages versus phase-lock averaging reduced flow properties) was made at or near midspan locations both inside and outside airfoil wakes for each traverse plane. The results for the flow speed as a function of time (rotor position) are presented in Figs. 3 and 4, and 5. Data reduced by phase-lock averaging voltages are the solid lines, while the data based on phase-lock averaging velocities are the solid symbols. The point by point agreement between the two approaches is seen to be excellent. The time averaged speed, $\bar{c}$, obtained at station 1, and 12.6 percent of axial chord downstream of the first vane trailing edge (Fig. 3(*a*)) in the inviscid flow between first vane wakes at station 1, agreed to within 0.01 percent. The corresponding time-averaged yaw and pitch angles agreed to within 0.01 deg, respectively. Inside the first vane wake the agreement of the two techniques is also seen to be excellent (Fig. 3(*b*). The difference in the time-averaged speed was 0.02 percent, while the corresponding time-averaged yaw and pitch angles agreed to within 0.03 and 0.41 deg, respectively.

From the data presented in Fig. 3, the root-mean-square (RMS) of the variation in the periodic speed about the average was ± 0.20 and ± 0.91 percent, respectively, for these locations outside and inside the first vane wake. At the location outside the first vane wake, the yaw and pitch angles varied ± 0.35 deg and ± 0.5 deg, respectively, about the time-averaged values. Inside the first vane wake, the yaw and pitch variations were both ± 0.75 deg about the time-averaged values. Both inside and outside of the first vane wake the upstream influence of the rotor potential field on the first vane exit flow field was found to be very small at this rotor-stator and axial spacing. This observation is consistent with the high-response stator pressure and hot film measurements of [16] and with the unsteadiness results discussed below.

In both the instantaneous and PLA data, the effect of the trailing edge Karman vortex street could be seen in the first vane wake data (Fig. 3(*b*)). A measured shedding frequency of 2600 Hz was found to correspond to a Strouhal number [17] of 0.21 based upon the first vane trailing edge diameter. The effect of the vortex shedding was also observed in the high-response total pressure data.

The corresponding results at station 2 (9.5 percent of axial chord downstream of the rotor trailing edge) are shown in Fig. 4. The results are presented for data acquired at a radial location slightly inboard of midspan ($r = 26.70$ in.). Based upon relative frame total pressure transverse data [4] it was believed that the flow was more nearly two dimensional at this radial location than at midspan. In the region outside of the convected first vane wakes (Fig. 4(*a*)), the time-averaged speed obtained from the two PLA techniques agreed to within 0.16 percent. The time averaged yaw and pitch angles agreed to within 0.5 and 0.99 deg, respectively. In the convected first vane wake region both techniques agreed to within 0.28 percent in flow speed. The station 2 data in the convected first vane wake region was not usable in subsequent analyses since for some of the time the outward radial flow angles exceeded the hot film probe acceptance angle of +20 deg in pitch. This region is indicated by the dashed line in Fig. 4(*b*). The largest rotor wake angles ($\phi > 20$ deg) occurred when the rotor interacted with the first vane wake.

Based upon the concept of slip velocity [18] and the results of [16], the first vane wake would be expected to impact and be accumulated on the rotor suction surface. From the rotor wake flow pitch angle data corresponding to the flow speed data of Fig. 4(*b*), it was observed that the pitch angles exceed the probe acceptance angle of +20 deg only on the suction side of the rotor blade wake. Flow visualization studies using an ammonia ozalid technique [4] indicated that on a time-averaged basis, the flow on the rotor suction surface at midspan, near the trailing edge, has relatively little radial component. Thus, it would appear that the periodic rotor first vane wake interaction results in significant periodic radial outward flows on the rotor blade suction surface which on a time averaged basis are nearly zero. The pitch angle data corresponding to Fig. 4(*a*) was relatively symmetric about the rotor wake centerline with a maximum pitch angle of +15 deg. Since the radial static pressure gradient is relatively small downstream of the rotor, and since the traverse plane was 9.5 percent axial chord downstream of the rotor trailing edge (1.5 trailing edge diameters), this radially outward flow is probably the result of wake fluid being centrifuged in the rotor blade trailing edge near wake region.

At the locations outside of the convected first vane wakes (Fig. 4(*a*)) where the pitch angles did not exceed the probe acceptance angle, the RMS of the variation in periodic speed and about the time-averaged, $\bar{c}$, was ± 6.4 percent. The maximum variation was ± 20 percent about the time-averaged speed. The corresponding variations in yaw and pitch angle about the time-averaged values were ± 14.5 and ± 10.0 deg, respectively.

At station 3, 10.0 percent of axial chord downstream of the second vane trailing edge, the agreement between the two averaging procedures was also found to be excellent (Fig. 5). The time-averaged velocities obtained outside the second vane wake (Fig. 5(*a*) agreed to within 0.4 percent. The corresponding yaw and pitch angles agreed to within 0.2 and 0.5 deg, respectively. Inside the second vane wake (Fig. 5(*b*), the agreement of the two techniques is also seen to be excellent. The difference in the time averaged speed was 0.50, while time averaged yaw and pitch angles agreed to within 0.32 and 0.93 deg, respectively.

The high degree of periodic unsteadiness due to the rotor is very evident in the data both outside and inside the second vane wake. Outside the wake, the RMS of the periodic speed about the time averaged speed, $\bar{c}$, is ± 2.6 percent, while the maximum to minimum variation is ± 8.6 percent. The maximum to minimum variations in yaw and pitch angle about their respective time-averaged values are ± 5.4 and ± 4.0 deg respectively. Inside the second vane wake, the RMS of the periodic speed about the time average, $\bar{c}$, is ± 7.9 percent. The yaw and pitch angles varied ± 4.3 and ± 7.0 deg, respectively, about their time-averaged values. From the digitized instantaneous data, a trailing edge vortex shedding frequency of 2645 Hz was determined to be consistent with a Strouhal number of 0.21 [17] based upon the second vane trailing edge diameter.

From the results presented in Figs. 3, 4, and 5, it was evident that phase-lock averaging of linearized hot film voltages prior to reduction to aerodynamic properties yields nearly the same results as phase-lock averaging of the reduced aerodynamic properties on a revolution by revolution basis, provided that the calibration/reduction scheme is linear over the range of instantaneous speed and flow angles. The PLA

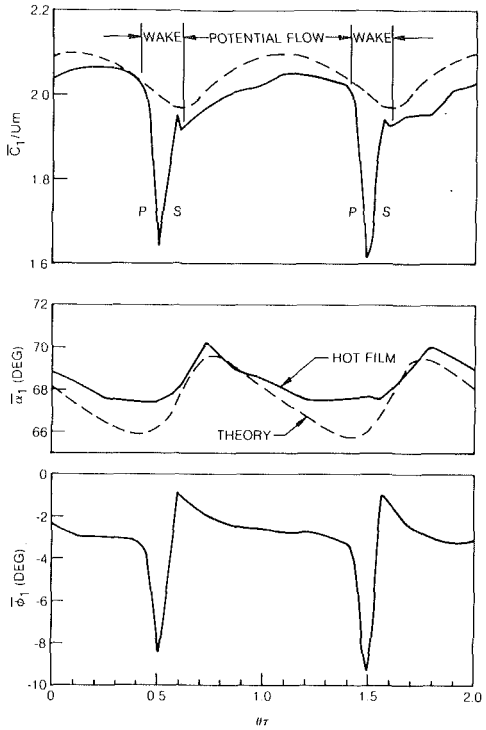

Fig. 6 Gapwise variation of time-averaged absolute flow properties (station 1)

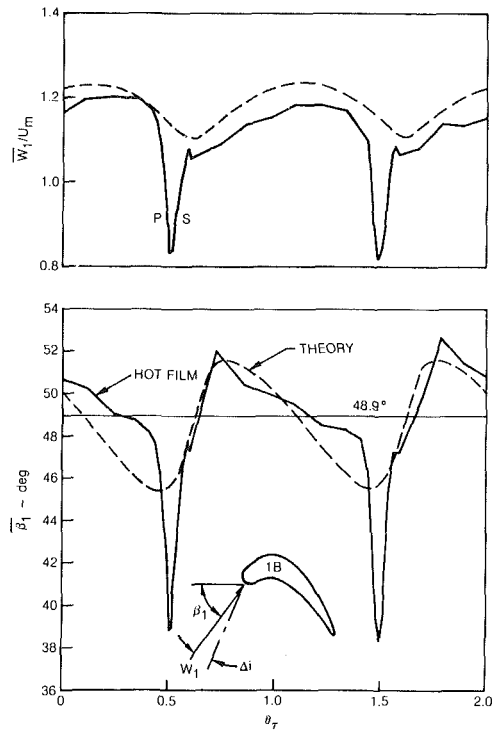

Fig. 7 Gapwise variation of time-averaged relative flow properties (station 1)

hot film data reduced at each traverse plane shows that the flow in the turbine is three dimensional and changes periodically at rotor passing frequency. The largest variations in flow speed, yaw, and pitch angle occur downstream of the rotor (station 2) and the second vane (station 3). The PLA data also shows that for a rotor/first vane axial spacing of $\Delta x/b_x = 0.65$, the rotor potential field has relatively little affect on the first vane exit flow. However, the interaction of the first vane wake with the rotor results in large periodic radial outflows on the suction side of the rotor wake ($\phi > 20$ deg). At a rotor/second vane axial spacing of 0.57, the periodic interaction of the rotor wake with the second vane results in significant periodic variations in the second vane exit flow field.

Spatial Variation of Time-Averaged Hot Film Data

At each radial/circumferential location in each of the traverse planes the time-averaged flow properties were computed. The resulting circumferential variations in non-dimensional speed, absolute yaw, and pitch angles at the first vane exit (station 1) at midspan are presented in Fig. 6. Also shown are the speed and yaw angles obtained from a two-dimensional inviscid potential flow calculation [19].

The total pressure loss input to the calculation was based on the measured loss and the stream tube contraction was based on a design throughflow analysis. To obtain the analytical results presented in Fig. 6, the exit angle in the calculation was varied until the computed first vane surface pressure distribution at midspan matched measured surface pressure data [16]. The circumferential extent of the potential flow region shown in the measured hot film data was determined from the high-response total pressure results. Between the wakes, the results from the calculation closely agreed with the time-averaged PLA speed and yaw data even though the calculation procedure does not explicitly account for viscous (wake blockage) effects. Since the measurement plane was close coupled to the first vane trailing edge ($\Delta x/b_x = 0.126$), significant vane to vane potential flow effects are seen in both the measured PLA data and the potential flow calculation. The decrease in speed near the suction side of the first vane wake is a potential flow effect as is the 2 deg increase in pitch angle. The circumferential RMS variation in speed as measured by the hot film probe is ±2.0 percent of the gap averaged value. The corresponding circumferential variations in yaw and pitch angles are ± 1.4 and ± 5.2 deg, respectively.

The absolute frame velocity measurements acquired at station 1 (Fig. 6) were converted to the relative frame of reference and the resulting absolute frame circumferential variation in relative speed and yaw are presented in Fig. 7. This spatial variation in the absolute frame corresponds with a temporal (timewise) variation that would be seen by an observer moving with the rotor. The results of the stator potential flow calculation (Fig. 6) are also shown in Fig. 7 in terms of relative speed and yaw. Calculated potential flow variations in speed and yaw are ± 6.4 percent and ± 2.5 deg respectively, about the corresponding gap-averaged values at station 1. In contrast to the relatively small potential flow variation in relative speed and yaw, the measured hot film data, which includes viscous effects, shows a speed defect of 30 percent and an effective incidence angle variation from −10 deg in the first vane wake to +3 deg in the region between wakes. It should be pointed out that due to the decay of the potential flow and wake variations with axial distance, the defect and incidence variations at the rotor inlet (65 percent of axial chord downstream of the vane) would be less than shown at this upstream location. At the rotor leading edge plane the calculated potential flow variations decay to less than ± 0.25 percent in speed and ± 0.2 deg in yaw. It is interesting to note, however, that the gap-averaged rotor inlet angle, β_1, deduced from rotor surface pressure measurements [16] agreed to within 1 deg of the gap-averaged hot film data in Fig. 7.

The time-averaged spatially varying results obtained in the absolute frame downstream of the rotor (station 2) are shown in Fig. 8. The convected first vane wakes are seen in the flow

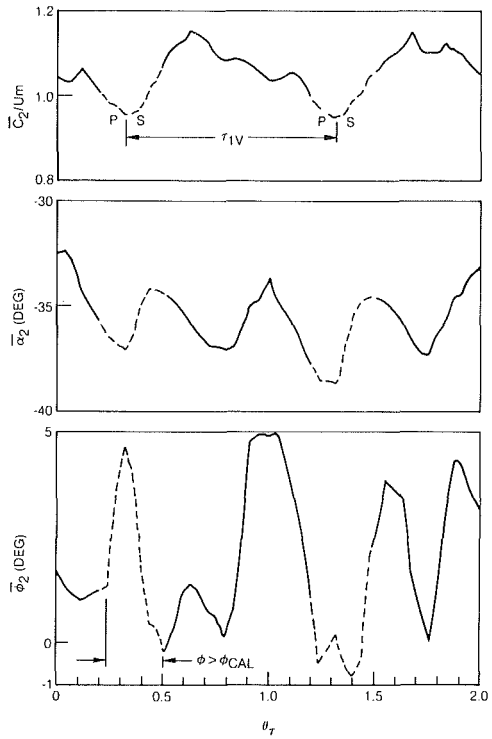

Fig. 8 Gapwise variation of time-averaged absolute flow properties (station 2)

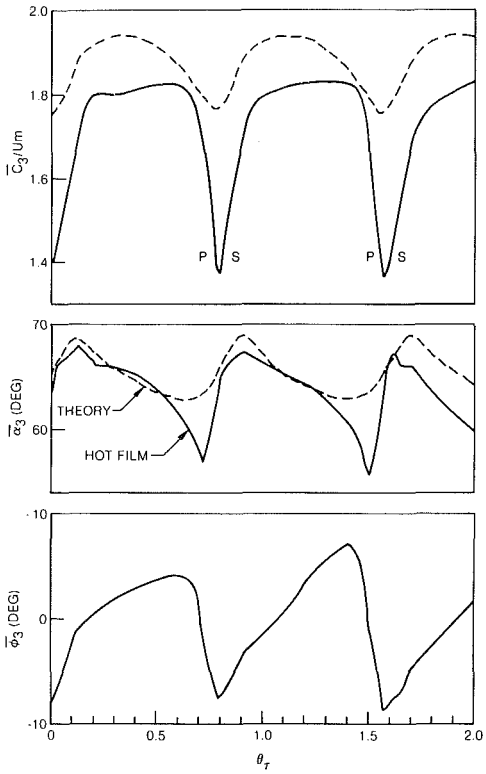

Fig. 9 Gapwise variation of time-averaged absolute flow properties (station 3)

field as low velocity regions. As stated previously, the data acquired in the region containing the convected first vane wakes were not usable for subsequent quantitative analyses, since the pitch angle there generally exceeded the hot film probe acceptance angle and accurate solutions to the calibration equations were not obtainable. These regions are shown by the dashed line in Fig. 8.

In regions where solutions were obtained (as shown by the solid lines) the time-averaged pitch angle varied from near 0 to 5 deg radially outward. The corresponding yaw angles varied from -32.5 to -37.3 deg. Although the accuracy of the data shown by the dashed lines is in question, the data presented does give an indication of the spatial nonuniformities in the time-averaged flow properties at the rotor exit. These nonuniformities are due to the convected first vane wakes and would affect the inlet conditions to the second vane.

The spatial variations in the time-averaged speed, yaw, and pitch angles measured downstream of the second vane (station 3) are shown in Fig. 9. The measured wake defect is 25.7 percent of the maximum freestream speed. The measured yaw and pitch angles vary from 54.8 to 68.0 deg and from -9.2 to $+6.5$ deg, respectively. Since the traverse plane is close coupled to the second vane trailing edge ($x/b_x = 0.10$),significant variations due to potential flow effects would be expected. That this is the case is shown in Fig. 9 by the results of a two-dimensional potential flow calculation [19] which predicted a speed variation of ± 4.7 percent about the gap-averaged speed and a yaw angle variation from 63 to 69 deg. The potential flow solution was obtained by varying the second vane inlet and exit angles (α_2 and α_3) until the best match of the calculated and measured vane surface pressure distribution was obtained. As with the first vane, a measured second vane total pressure loss was used as input to the calculation along with an exit static pressure based on a free vortex interpolation between measured hub and tip values. The streamtube contraction was based on a design through flow analysis. Although the potential flow calculation and yaw angle variation agrees closely with the time-averaged hot film data, the speed results do not agree as well as the results obtained for the first vane data where the inlet flow was more nearly two dimensional and was not complicated by three dimensional, spatially and temporally varying inlet conditions.

Unsteadiness

In flows where the flow direction is unknown or the turbulence is high, treating fluctuations in speed as velocity fluctuations, as done by Evans [20] for a basically two-dimensional flow, can lead to significant errors in the determination of unsteadiness levels in the flow field. In the present study, the periodic, random, and total unsteadiness levels at each circumferential measurement location were determined by including the unsteadiness in all three velocity components through the following relations

$$\bar{U}_P^2 = \frac{1}{nt_b}\int_o^{nt_b} [\tilde{\hat{c}}(t) - \tilde{\bar{c}}]^2 dt/\bar{c}^2$$

$$= \frac{1}{nt_b}\int_o^{nt_b} [c_{s_p}{}^2 + c_{n_p}{}^2 + c_{r_p}{}^2] dt/\bar{c}^2$$

$$\bar{U}_r^2 = \frac{1}{nt_b}\int_o^{nt_b} \frac{1}{100}\sum_{k=1}^{100} [\hat{c}_k(t) - \tilde{\hat{c}}(t)]^2 dt/\bar{c}^2$$

$$= \frac{1}{nt_b}\int_o^{nt_b} \frac{1}{100}\sum_{k=1}^{100} [c_s'^2 + c_n'^2 + c_r'^2] dt/\bar{c}^2$$

$$\bar{U}_T^2 = \bar{U}_P^2 + \bar{U}_r^2$$

The normalizing speed, $\bar{c}$, used in the above relations was the time-averaged value determined from each location.

The results for the first vane exit (station 1) are presented in Fig. 10. The total unsteadiness is not shown since it is only

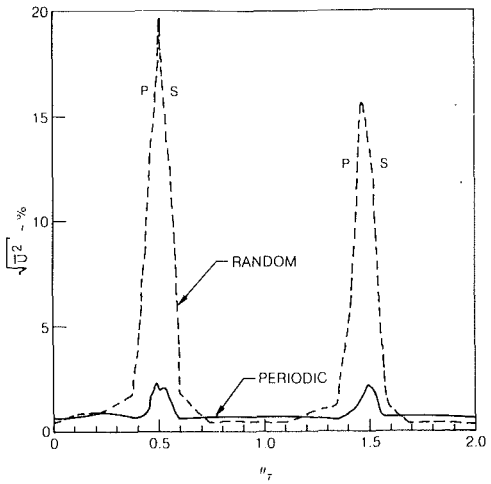

Fig. 10 Unsteadiness at first vane exit (station 1)

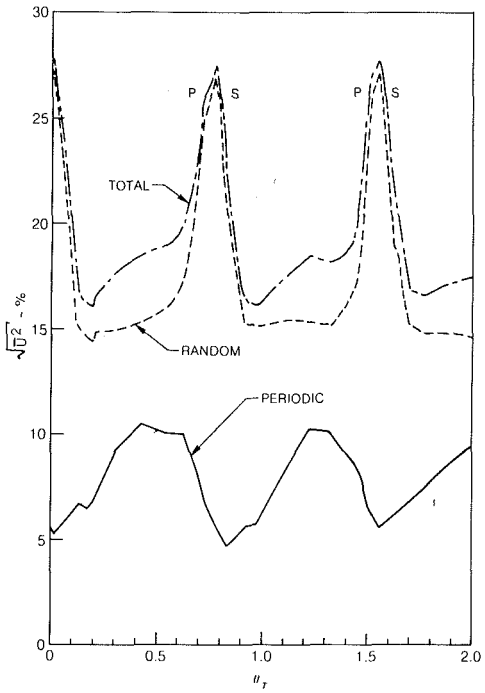

Fig. 11 Unsteadiness at second vane exit (station 3)

slightly greater than the random unsteadiness. The results are typical of what would be expected from a cascade with low inlet freestream turbulence. Between the first vane wakes the maximum total unsteadiness level was typically less than 1.0 percent. The periodic and random components were 0.5 and 0.75 percent, respectively. The maximum total unsteadiness of 18.7 percent occurred on the wake centerline where the periodic and random levels were 1.9 and 18.6 percent, respectively. From the periodic unsteadiness data presented in Fig. 10, it is evident that the rotor has a relatively small impact on the first vane exit flow field at this rotor-vane axial spacing ($\Delta x/b_x = 0.65$).

Relative to an observer moving at rotor wheel speed at this traverse plane, the circumferential variation in random unsteadiness (Fig. 10) would be seen as a temporal variation. In addition, a periodic unsteadiness of 10 percent would be seen due to the temporal variation of the relative velocity flow field (Fig. 7). Therefore, as the observer moved through the first vane exit flow field (station 1), the total unsteadiness would be seen to vary from nearly 10.0 percent to a maximum of 21

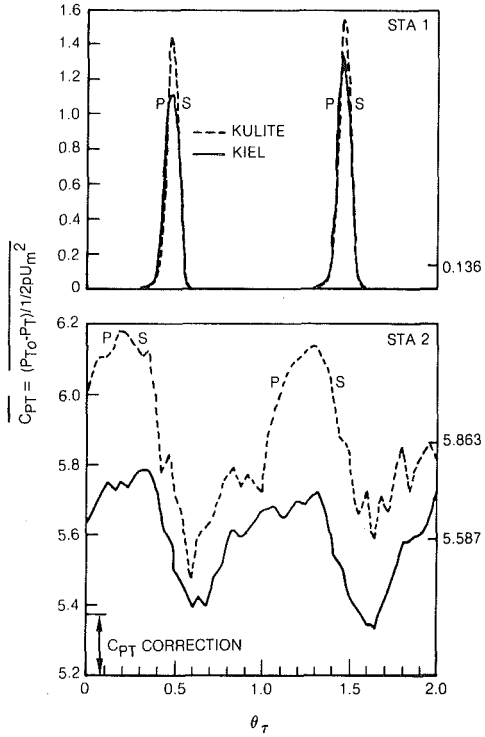

Fig. 12 Time-averaged total pressure comparison

percent. The total unsteadiness at the rotor leading edge ($x/b_x = 0.65$) would be somewhat less than this due to the decay of the first vane potential field, wake defect and random turbulence.

Since the flow exceeded the hot film probe acceptance angle in pitch at station 2, unsteadiness effects downstream of the rotor blade could not be examined.

The results obtained downstream of the second vane (station 3) are shown in Fig. 11. The maximum total, random, and periodic unsteadiness levels are 28, 27, and 5 percent, respectively, in the wake. Outside the wake they are 18, 15, and 10 percent, respectively. The random unsteadiness distribution varies from a minimum of nearly 15 percent between the second vane wakes to a maximum of 27 percent on the wake centerline. This would be expected from a cascade with high inlet turbulence.

In contrast to the results obtained downstream of the first vane (station 1), on a gap-averaged basis the periodic unsteadiness due to the rotor at station 3 is approximately ten times greater than at station 1 (8 percent versus 0.8 percent). Across the second vane gap, the periodic unsteadiness decreases from a maximum of nearly 10 percent near the pressure side of the second vane wake to a minimum of 5 percent near the suction side. The mechanisms producing this effect are not presently understood, but for this rotor-vane axial spacing ($\Delta x/b_x = 0.57$) they are probably related to the viscous interaction of the rotor wake with the second vane and are not potential flow effects. Due to the periodic unsteadiness, the total unsteadiness is nearly 4 percent greater than the random unsteadiness.

Total Pressure Measurements

The time-averaged total pressure data obtained from phase-lock averaging the digitized, instantaneous, high-response Kulite/Kiel probe pressure transducer voltage output at midspan at traverse planes 1 and 2 are shown in Fig. 12. The total pressures are referenced to the turbine inlet total pressure (P_{T_O}) measured at station 0 and are nondimensionalized by a dynamic head, based upon rotor wheel

Table 1 Airfoil geometry and nominal operating conditions, $(C_x/U) = 0.78$

Airfoil	First vane	Rotor blade	Second vane
Number	22	28	28
B_x (ins.)	5.93	6.34	6.45
(τ/B_x)	1.30	0.96	0.96
Span (in.)	6.00	6.00	6.00
(Span/B_x)	1.01	0.95	0.93
Inlet flow angle (deg.)	0.0	50.0	−39.2
Exit flow angle (deg.)	67.5	−64.5	65.0
Re (B_x,$\bar{C}_1$, $\bar{W}_2$ or $\bar{C}_3$)	5.9×10^5	5.5×10^5	5.2×10^5

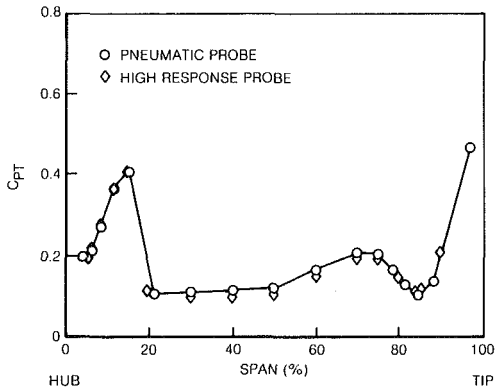

Fig. 13 Comparison of pneumatic and high-response total pressure probe data at the first vane exit

speed at midspan ($\frac{1}{2}\rho U_m{}^2$). Also shown for comparison are the results obtained with a standard United Sensors KBC-12 pneumatic (steady-state) Kiel probe which, because of a difference in probe configuration, was located typically 6 percent of axial chord further downstream than the high-response probe at both measurement planes.

During calibration, it was determined that the high-response transducer had long-term, random zero shifts which, although small relative to the transducer specifications, were large in the present application ($\Delta C_{PT} \approx 0.2$). For this reason, it was necessary for the data at station 1 to be shifted so that the time-averaged total pressure coefficient, C_{PT}, was zero in the inviscid regions between the first vane wakes. A shift of the same magnitude was arbitrarily applied to the data at station 2.

The results obtained at station 1 with the high-response Kulite/Kiel probe and the pneumatic probes are in excellent agreement (after zero shift). At station 1 the circumferentially averaged total pressure coefficients differ by 3.0 percent. The greatest difference in the total pressure measured by the two probes was found to be downstream of the rotor at station 2 ($\Delta C_{PT} = 4.9$ percent). At this station, the circumferential variation measured by the two probes is similar; however, the high-response probe consistently indicated a lower total pressure (high-pressure coefficient) than the pneumatic probe. Since both probe tips were geometrically identical and since the flow probably did not exceed the ± 50 deg acceptance angle of either probe, the difference is probably due to a combination of the probes being at slightly different axial locations, the respone time characteristics of the two probe/transducer systems, and the zero shift in the high response transducer.

The first vane exit (station 1) spanwise distribution of gap-averaged total pressure coefficient obtained from the pneumatic and high-response probe data are shown in Fig. 13. In general, the agreement between the two sets of data is good. The high loss region near the hub is probably due to endwall passage vortex system and the general tendency of low total pressure fluid to move radially inward toward the hub in this high swirl environment. In the tip region, the high loss is likely due to the endwall passage vortex system which is more spread out in the spanwise direction. This is also due to the radial pressure gradient causing low total pressure fluid to migrate toward the hub.

Conclusions

An extensive series of high-response velocity and total pressure measurements have been made downstream of each airfoil row of a large scale 1½ stage turbine. In general, the data examined at or near midspan indicate the highly unsteady and three-dimensional nature of the flow in this typical turbine configuration. Specific conclusions about the results are summarized as follows.

Experimental Techniques. A major savings in the expense of data reduction may be realized by phase-lock averaging raw linearized anemometer voltages instead of velocity components. This approach is, however, accurate only if the reduction from voltages to velocity components is close to linear.

The high-response and steady-state total pressure data for the first vane exit were in excellent agreement after the high-response transducer was corrected for a zero shift. Comparisons downstream of the rotor blade showed good agreement as to wake shape but the difficulty with zero shift casts doubts on any absolute comparison.

Flow Structure. Downstream of the first vane the unsteadiness was weak due to the relatively large rotor-vane axial gap. There was, however, considerable radial flow in the vane wake at midspan toward the hub due to the high swirl at this station.

The nature of the rotor midspan wake changed markedly as the rotor periodically interacted with the first vane wakes. The pitch angle on the suction surface side of the rotor wake increased to very high levels as the vane wakes periodically impacted on the rotor suction surface.

The flow downstream of the second vane (at midspan) had a high degree of random and periodic unsteadiness due to the upstream vane and blade. In addition, there were strong gapwise variations of the pitch angle.

The results presented are for the midspan where three-dimensional effects would be expected to be minimal. Generally speaking, however, the high degree of unsteadiness and three dimensionality shown by the data are beyond the scope of current analytical design systems. There is little doubt that these mechanisms are having a significant impact on the levels and spanwise distributions of airfoil loss and heat load and on the interpretation of rotating rig data.

Acknowledgment

The hot film and pneumatic traverse data reported herein were acquired under funding from Pratt & Whitney Aircraft Commercial Products Division. The remainder of the data were acquired under UTRC Corporate funding.

The authors are indebted to many people for the successful completion of this program and in particular to Mr. Tom Butler and Mr. Joel Wagner for help in probe calibration and data reduction, to Mr. John Kostic for help in acquiring the data, and to Ms. Diane Rodimon for reducing the data.

References

1 Langston, L. S., Nice, M. L., and Hooper, R. M., "Three-Dimensional Flow Within a Turbine Cascade Passage," ASME Paper No. 76-GT-50, 1976.

2 Sjolander, S. A., "The Endwall Boundary Layer in an Annular Cascade of Turbine Nozzle Guide Vanes," Carleton University Msc thesis, 1975.

3 Marchal, P., and Sieverding, C. H., "Secondary Flows Within Turbomachinery Bladings," *Secondary Flows in Turbomachines*, AGRAD, 1977.

4 Dring, R. P., and Joslyn, H. D., "Measurements of Turbine Rotor Blade Flows," ASME JOURNAL OF ENGINEERING FOR POWER, Vol. 103, No. 2, Apr. 1981.

5 Bayley, F. J., and Priddy, W. J., "Effects of Free Stream Turbulence Intensity and Frequency on Heat Transfer to Turbine Blading," ASMe Paper No. 80-GT-79, Mar. 1981.

6 Blair, M. F., "Influence of Free Stream Turbulence on Turbulent Boundary Layer Heat Transfer and Mean Profile Development, Part I—Experimental Data, Part II—Analysis of Results," submitted to ASME *Journal of Heat Transfer*.

7 Evans, R. L., "Boundary Layer Development on an Axial-Flow Compressor Stator Blade," ASME JOURNAL OF ENGINEERING FOR POWER, Apr. 1978, Vol. 100, n. 2, pp. 287–293.

8 Wagner, J. H., and Okiishi, T. H., "Analysis of Multistage, Axial Flow Turbomachine Wake Production, Transport and Interaction," ISU-ERI Report 78173, Dec. 1977.

9 Hirsch, C., and Kool, P., "Measurements of the Three-Dimensional Flow Field Behind an Axial Compressor Stage," ASME JOURNAL OF ENGINEERING FOR POWER, Apr. 1977, pp. 168–180.

10 Raj, R., and Lakshminarayana, B., "Three-Dimensional Characteristics of Turbulent Wakes Behind Rotors for Axial Flow Turbomachines," ASME JOURNAL OF ENGINEERING FOR POWER, Apr. 1976, pp. 218–228.

11 Thompkins, W. T., and Kerrebrock, J. L., "Exit Flow from a Transonic Compressor Rotor," Massachusetts Institute of Technology, Gas Turbine Lab., Report No. 123, Sept. 1975.

12 Hunter, I. H., "Endwall Boundary Layer Flows and Losses in an Axial Turbine Stage, presented at ASME Gas Turbine Conference, Houston, TX, Mar. 1981.

13 Whitfield, C. E., Kelly, J. C., and Barry, B., "A Three-Dimensional Analysis of Rotor Wakes," *Aeronautical Quarterly*, Nov. 1972, pp. 285–300.

14 Gostelow, J. P., "A New Approach to the Experimental Study of Turbomachinery Flow Phenomena," ASME Paper 76-GT-47, 1976.

15 Butler, T. L., and Wagner, J. H., "An Improved Method for Calibration and Use of a Three-Sensor Hot Wire Anemometer in Turbomachinery Flows," to be presented at the AIAA 20th Aerospace Conference, Orlando, Fla., Jan. 11–14, 1982.

16 Dring, R. P., Joslyn, H. D., Hardin, L. W., and Wagner, J. H., "Turbine Rotor-Stator Interaction," ASME Paper to be presented at 1982 Gas Turbine Conference, Wembly, England, Apr. 1982.

17 Schlichting, H., *Boundary Layer Theory*, 6th ed., McGraw-Hill, 1968.

18 Kerrebrock, J. L., and Mikolajczak, A. A., "Intra-Stator Transport of Rotor Wakes and Its Effects on Compressor Performance," ASME JOURNAL OF ENGINEERING FOR POWER, Oct. 1970, p. 359.

19 Caspar, J. R., Hobbs, D. E., and Davis, R. L., "Calculation of Two-Dimensional Potential Cascade Flow Using Finite Area Methods," *AIAA Journal*, Vol. 18, No. 1, Jan. 1980, pp. 103–109.

20 Evans, R. L., "Turbulence and Unsteadiness Measurements Downstream of a Moving Blade Row," ASME Paper No. 74-GT-73, Mar. 1974.

A. V. Srinivasan
Manager, Applied Mechanics Research.

D. G. Cutts
Research Engineer.

United Technologies Research Center,
East Hartford, Conn. 06108

Dry Friction Damping Mechanisms in Engine Blades

In the context of jet engines, significant vibration damping due to dry friction can occur at (a) shroud interfaces of fans and (b) the platform of turbine blades fitted with "platform dampers." Analytical and experimental studies in regard to this important source of nonaerodynamic damping of blade vibration are presented in this paper. Comparisons between results from analytical models and laboratory test data are made and discussed.

1 Introduction

Vibration induced fatigue failure of blades is of continuing concern to the designer of aircraft engines. The emphasis on improved engine performance under the necessary constraints of minimum weight and satisfactory life requires that vibration levels be kept low. Further, certain important design considerations require a thorough understanding of the structural dynamic characteristics of blades. These design considerations include (*i*) blade life prediction methods which use vibration amplitudes in their calculations, (*ii*) allowable frequency margins which need to be justified on the basis of the intensity of resonant stresses computed at low integral orders, and (*iii*) accurate prediction of susceptibility to aeroelastic instabilities. The analytical techniques used in flutter and resonant stress prediction rely on accurate determination of modal characteristics of blades. These characteristics include not only the natural frequencies and mode shapes *but also* damping available in each mode. Contributions to damping in a vibrating blade arise from aerodynamic sources as well as nonaerodynamic sources. The latter include contributions from material damping, friction damping due to rubbing at interrupted interfaces (shroud to shroud, root to disk), and friction damping due to an external device such as a turbine blade platform-type damper.

Under a NASA-sponsored program, (NASA C. R. 165406), single blades and blade-like components were analyzed and tested to obtain the contribution from each mechanism of damping. The components included a part-span-shrouded fan blade, a high-pressure turbine blade, a bladelike titanium twisted plate, uniform cantilever beams of titanium, and strips of composite material. In addition, small titanium specimens were used in rub tests aimed at determining the nature of dry friction characteristics at an interface. In the interest of space, this paper will present the results of studies pertaining only to dry friction damping mechanisms leading to damping at shrouds and platform dampers.

The analytical approaches for estimating friction damping can be broadly classified as follows: (*i*) macroslip approach and (*ii*) microslip approach. In the macroslip approach, the entire interface is assumed to be either slipping or stuck. The friction mechanism is either replaced by an equivalent linear viscous model or assumed to be governed by some form of Coulomb's law of dry friction. The effect of friction damping is obtained by determining the forced response of the component. The analysis involved is relatively straightforward and the justification for widespread use of this approach is its effectiveness at predicting the actual response. However, there is some question as to the validity of the macroslip approach when the interface has a large area and is subjected to a nonuniform load distribution. In the microslip approach, a relatively detailed analysis of the stress distribution at the interface is carried out, typically via a finite element procedure. The extent of local slip, not necessarily throughout the interface, between pairs of contacting points is determined by applying Coulomb's law of friction to the normal and tangential stresses. A detailed knowledge of interface slip dynamics can be obtained from this approach. However, the computational effort needed to modify, iteratively, the interface stress distribution subsequent to local slipping can make the microslip approach unacceptable in a practical application.

In the context of jet engine blades, the macroslip approach was found to be suitable for modeling the friction mechanism and was therefore adopted in this investigation.

The considerations governing the experimental phase of the investigation included the design of fixtures, method of blade excitation, and measurement of damping. Fixtures were designed such that their participation during vibration is minimal. The excitation was chosen to be sinusoidally varying displacement at blade root provided by an electrodynamic shaker. Estimates of damping were made by measuring either (*a*) the attenuation of resonant vibration or (*b*) decay of vibratory motion obtained upon abrupt termination of excitation when the blade attained its peak response at resonance.

2 Damping Due to Rubbing at Shroud Interfaces

In the case of part-span-shrouded fan blades, untwisting of the blades under centrifugal pull brings neighboring blades into contact at the shrouds. Major parameters which control the nature and extent of friction damping at the shroud to shroud interface are: centrifugal loading, roughness of

Contributed by the Gas Turbine Division of THE AMERICAN SOCIETY OF MECHANICAL ENGINEERS and presented at the 27th International Gas Turbine Conference and Exhibit, London, England, April 18-22, 1982. Manuscript received at ASME Headquarters December 14, 1981. Paper No. 82-GT-162.

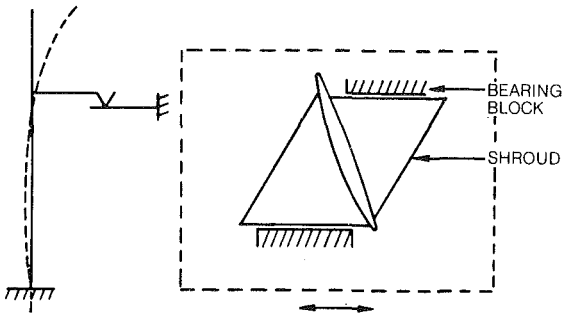

Fig. 1 Schematic of shroud rubbing

surfaces, level of external excitation, shroud location on the blade, blade geometry and shroud geometry. Studies which address the specific problem of shroud damping can be found in [1–5]. Presented in this section are the results of analysis and testing of a part-span shrouded fan blade with rubbing at its shroud faces.

Forced Response of a Fan Blade With Rubbing at the Shrouds. Schematics of a part-span-shrouded fan blade, and shroud rubbing surfaces are shown in Fig. 1. The following assumptions are made:

1 Friction damping is of macroslip-type and governed by Coulomb's law of dry friction.

2 Friction damping does not drastically alter blade resonant frequency and mode shape, so that attention can be focused on a single chosen mode of vibration.

3 Shrouds are infinitely rigid and shroud load is uniformly distributed over the rubbing surfaces.

4 Slipping motion is resisted by the static stiffness of the blade below the shrouds.

Under the assumptions made, the equations of motion can be written as (see Fig. 2)

$$\bar{m}\ddot{\bar{x}}_1 + \bar{k}(\bar{x}_1 - \bar{x}_2) + \bar{c}\dot{\bar{x}}_1 = \bar{P}\cos\bar{\omega}\bar{t},$$
$$\beta\bar{k}\bar{x}_2 + 2\mu\bar{N}\,\mathrm{sgn}\,(\dot{\bar{x}}_2) - \bar{k}(x_1 - x_2) = 0 \qquad (1)$$

where overbars denote dimensional quantities: m, k, and c, are modal quantities; x_1 is the blade tip deflection; x_2 denotes the slip at the shroud; P is the excitation amplitude; ω is the excitation frequency; μ is the coefficient of friction; and N is the normal load. The quantity βk is the static stiffness of the blade below the shrouds and resists the slipping motion. It is convenient to nondimensionalize the equations of motion by introducing the following quantities

$$x_1 = \bar{x}_1/\bar{x}_0, x_2 = \bar{x}_2/\bar{x}_0, \bar{\omega}_0^2 = \bar{k}/\bar{m}_1, \omega = \bar{\omega}/\bar{\omega}_0, t = \bar{t}\bar{\omega}_0,$$
$$\zeta = \bar{c}/2\bar{m}_1\bar{\omega}_0, F = 2\mu\bar{N}/\bar{k}\bar{x}_0, p = \bar{P}/\bar{k}\bar{x}_0 \qquad (2)$$

where $\bar{x}_0$ is some characteristic length. Assuming a solution of the form

$$x_1 = a\cos(\omega t + \phi - \delta),$$
$$x_2 = b\cos(\omega t + \phi), \qquad (3)$$
$$\mathrm{sgn}(\dot{x}_2) \approx -(4/\pi)\sin(\omega t + \phi)$$

leads to a set of algebraic equations

$$\eta\alpha_1 + (1-\omega^2)\alpha_2 - Q_2 = \cos\phi,$$
$$(\omega^2 - 1)\alpha_1 + \eta\alpha_2 - \eta Q_2 = -\sin\phi,$$
$$(1+\beta)Q_2 - \alpha_2 = 0$$
$$G + \alpha_1 = 0 \qquad (4)$$

where

$$\eta = 2\zeta\omega, Q_2 = b/p, G = 4F/\pi p,$$
$$\alpha_1 = (a/p)\sin\delta, \alpha_2 = (\alpha/p)\cos\delta \qquad (5)$$

The last two equations of Eq. (4) yield

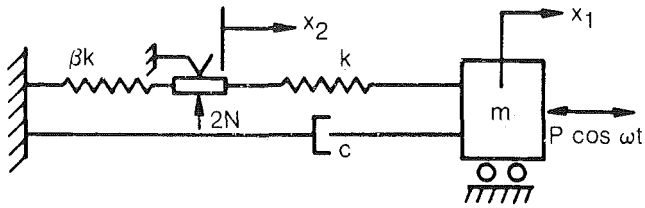

Fig. 2 Analytical model for shroud rubbing

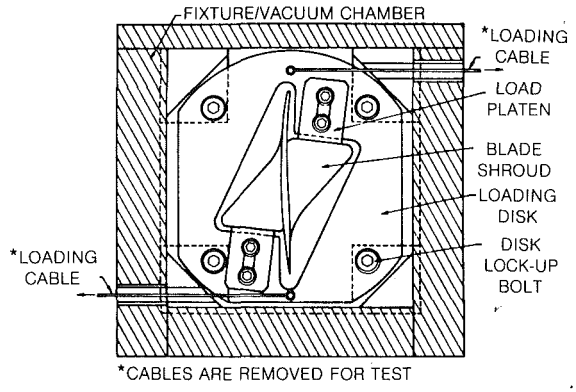

Fig. 3 Shroud loading device for investigation of fan blade shroud damping mechanism

$$\alpha_1 = -G, \alpha_2 = (1+\beta)Q_2 \qquad (6)$$

so that,

$$Q_1 a/p = (\alpha_1^2 + \alpha_2^2)^{1/2} \text{ and } \tan\delta = \alpha_1/\alpha_2 \qquad (7)$$

Substitution of equation (6) into the first two equations of equation (4) leads to

$$\tan\phi = [\eta(1-\beta)Q_2 + (1-\omega^2)G]/[(\beta + \beta\omega^2 + \omega^2)Q_2 - \eta G] \qquad (8)$$

and after some algebra, a quadratic equation, the solution of which yields

$$Q_2 = -C_2 G + [(C_2 G)^2 - C_1(C_3 G^2 - C_4)]^{1/2}, \qquad (9)$$

where

$$c_1 = (\omega^2 + \beta\omega^2 - \beta) + \eta^2(1+\beta)^2, \qquad c_2 = \eta/c_1$$
$$c_3 = [(1-\omega^2)^2 + \eta^2]/c_1, \qquad c_4 = 1/c_1$$

It is noted that Q_1 is a measure of the blade response and Q_2 a measure of the slip amplitude at the shroud interface. From equation (8) the condition for slip to occur; i.e., $Q_2 > 0$, is

$$(c_3 G^2 - c_4) < 0; \qquad G < [(1-\omega^2)^2 + \eta^2]\}^{1/2} \qquad (10)$$

If the excitation is applied at the base of the blade, as was done for tests performed in this program, the analysis follows along similar lines to the one given above, the only modifications being redefinition of the nondimensional excitation amplitude,

$$p = \bar{p}/x_0, \quad \text{and} \quad c_4 = \omega^4/c_1$$

where $\bar{p}$ is the displacement amplitude of the base excitation.

The influence of friction at the shrouds can be expressed as a loss factor, defined as

$$\eta_f = \frac{1}{2\pi}\frac{D}{U} \qquad (11)$$

where D is the energy dissipated per cycle of vibration and U is the peak strain energy in the blade. The two energies are given by

$$D = 8\mu\bar{N}\bar{x}_2, \qquad U = \frac{1}{2}\bar{k}\bar{x}_1^2 \qquad (12)$$

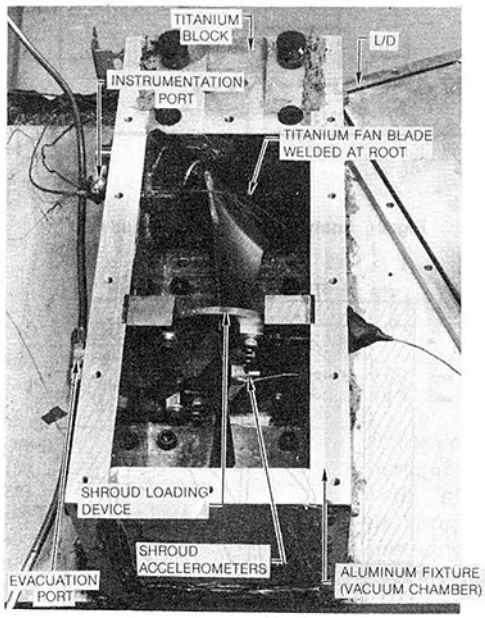

Fig. 4 Test set-up for shroud damping investigation

so that, in terms of dimensionless quantities

$$\eta_f = GQ_2/Q_1^2 \tag{13}$$

and total loss factor for the blade is,

$$\eta_b = \eta_0 + \eta_f \tag{14}$$

where η_0 accounts for damping from sources other than friction, such as, material hysteresis and air damping.

For the damping levels expected in the problem being studied, maximum response occurs when the excitation frequency is near the natural frequency (i.e., $\omega \approx 1$) so that a good approximation to the maximum response is obtained by simply setting $\omega = 1$ in the solution. The blade tip deflection can be related to the blade stress by specifying a baseline or reference condition where the blade vibration characteristics are fully known. If the baseline tip deflection of the blade is chosen as the characteristic length, $\bar{x}_0$, used for non-dimensionalization in equation (2), it can be shown that

$$\sigma = a\sigma_0,$$

where σ_0 is the blade stress in the baseline condition and σ is the blade stress at any other condition. In the present study, the condition of no friction at the shroud interfaces is chosen as the baseline condition so that the baseline blade stress is the same as the modal blade stress.

The analysis presented above enables the calculation of maximum response of a single blade subjected to excitation at its base and whose shrouds rub in rigid surfaces under a given normal load. The fan blade used in these tests was welded at its root to a massive block and provided with a means for applying a static normal load on the shroud surfaces. The whole assembly was mounted in a vacuum chamber and subjected to harmonic excitation. The shroud normal loads and input acceleration levels were varied and the strain response at the ASMT (Above-Shroud-Maximum-Thickness) position was monitored. Damping levels were estimated from transient response curves resulting from abrupt cut off of input signals.

The loading platens (Fig. 3), which were used to apply normal loads on the shrouds, have a rectangular rubbing surface designed to mate with the curved perimeter of the shroud interface. The platens were made of titanium alloy 8-1-1 and hardfaced with tungsten carbide to be compatible with the surface treatment on the shroud interfaces. The loading disk holding the load platens (Fig. 4) was positioned around the blade so that the platens rested on the shroud surfaces. A cable and weight system was used to impose a normal load on the shrouds. The cables were positioned 11.4-cm apart on the loading disk. Upon reaching the required torque (and hence, the required normal load on the shroud interfaces), the disk was locked in position and the cables were removed. Complete air tightness was achieved by capping the access holes on the fixture. The above setup assured constant shroud loading through the series of tests.

Actual flexural and torsional stiffness of the blade at the shroud location were measured (see table below) and were used in the design of the shroud loading mechanism and subsequently in the analytical calculations.

Table 1 Table of measured blade flexural and torsional stiffness

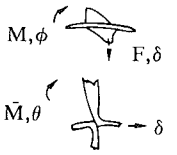

Stiffness coefficient	Measured value
K_{F_δ}	114,000 N/m
K_{M_ϕ}	743 Nm/rad
K_{M_δ}	5694 Nm/m
K_{M_θ}	412 Nm/rad

M, $\bar{M}$, applied moments: F, applied force
θ, ϕ, angular displacement: δ, linear displacement

Test results. The response plot for tip flapwise acceleration during a frequency sweep is shown in Fig. 5. This was performed at a relatively low applied torque (5.2 Nm) and so the boundary conditions at the shroud interface represented neither a fully locked nor a freely slipping condition. In fact, during tests at this low normal load on the shrouds, a rattling type of motion was observed at the shroud location. This resulted in a number of peaks occuring as a result of the inherently nonlinear nature of the constraint forces at the shroud interfaces. However, within the range of frequencies swept, the observed modes included three predominantly above-shroud modes. Because of the low shroud load, these modes occurred at 260 Hz (bending), 475 Hz (second bending) and 880 Hz (torsion). Decay tests were performed from which the damping levels in each of these modes were measured. Upon increasing the applied torque, it was noted that the number of nonlinear responses diminished. Also, the three above-shroud modes manifested themselves (see Fig. 6) at 278 Hz (bending), 1110 Hz (torsion) and 1440 Hz (second bending). It was also noted that the response included some participation from the "free" blade bending mode at 93 Hz.

Subsequent testing was focused only on the "above-shroud-bending" and the "above-shroud-torsion" modes. These tests were performed with a reduced pressure of 16 torr inside the chamber. Two methods of obtaining the responses to various input levels were used. The frist was to employ a slow frequency sweep at constant input level for a given shroud load. The frequency range was just large enough to at least include the half power points. The sweep rate was chosen to be low enough not to distort the response curve at the existing modal damping levels. A characteristic of these curves was a flat peak over a significant bandwidth around the resonance, as shown in Fig. 7. The second method was to tune the frequency to obtain the maximum response for a given mode. After the maximum strain value had been recorded, the input was abruptly cut off and the decay curve recorded on the peak level recorder. It was noted that this latter method produced maximum blade responses which were approximately 12% higher than those obtained by using the sweep method. The higher results were used for comparison with analysis and are tabulated in Table 2. Shroud acceleration data obtained for certain test points are also given in Table 2. The loss factor for

Table 2
Summary of shrouded blade response test data[a]

Shroud normal load N	Input accel. g(pk)	Excit. period ms	ASMT stress MPa(pk)	Loss factor η	Shroud O.O.P.[b] acceleration g unfilt[d]	Shroud O.O.P.[b] acceleration g filt.	Shroud I.P.[c] acceleration, g unfilt	Shroud I.P.[c] acceleration, g filt.
				First flap mode results				
150	0.5	3.566	41	.0034	2.5	2.5	1.8	1.2
	1.0	3.574	54	.0038	2.9	2.9	2.7	1.8
	2.0	3.589	59	.0056	3.6	3.6		
	3.0	3.589	60	.0054				
	4.0	3.579	63	.0053				
300	0.5	3.563	61	.0024	3.8	3.8	1.7	1.6
	1.0	3.566	103	.0023	7.2	7.0	2.1	1.7
	2.0	3.574	124	.0036	8.8	8.8	4.0	3.2
	3.0	3.575	128	.0044	9.6	9.1	5.2	2.6
	4.0	3.580	134	.0036	10.0	7.6	9.0	3.6
500	0.25	3.558	39	.0031				
	0.5	3.551	56	.0026	4.0	4.0		
	0.5	3.558	60	.0024			1.5	1.4
	1.0	3.556	102	.0027	6.8	6.8		
	1.0	3.559	124	.0022				
	2.0	3.560	154	.0034	12.0	11.0		
	2.0	3.564	163	.0031			4.7	3.1
	3.0	3.562	178	.0031	13.0	11.0		
	3.1	3.566	182	.0034			8.2	
	4.0	3.565	186	.0031	14.0	14.0		
	4.0	3.565	195	.0032				
				First torsion mode results				
150	0.5	0.8932	5.5	.00052	2.6	2.1	2.0	1.8
	1.0	0.8940	9.2		3.8	3.6	3.0	2.7
	2.0	0.8944	12.0	.00080	5.6	5.0	1.3	0.9
300	0.5	0.8932	6.1	.00058	3.4	3.4	0.9	0.8
	1.0	0.8935	11.0	.00055	5.8	5.2	2.4	1.2
	2.0	0.8933	15.0	.00075	4.0	3.6	3.0	1.3
	3.0	0.8940	20.0	.00082	14.0	9.9	9.9	3.5
500	0.5	0.8910	7.7	.00040	4.4	3.8	1.5	1.4
	1.0	0.8912	13.0	.00045	6.2	6.2	1.9	1.7
	2.0	0.8918	17.0	.00059	8.4	8.4	3.8	3.0
	3.0	0.8924	23.0	.00074		11.0	3.2	3.1
	4.0	0.8933	28.0	.00084	14.0	13.0	3.2	1.8

Notes: [a]Slope of decay taken between the 1 and 4dB points
[b]O.O.P = out of plane (normal to shroud plane)
[c]I.P. = in plane (along shroud interface)
[d]Low pass filter

each test point was determined from the decay curves and was obtained from the mean slope between 1 dB and 4 dB points down from the maximum value. A sampling of the decay curves obtained for mode 1 is shown in Figs. 8 and 9. Figure 8 shows how the decay pattern changes as the input level is increased for a given shroud load, and Fig. 9 shows the manner in which the decaying signal changes with shroud load and input level. Figures 10 and 11 give the ASMT stress as a function of shroud normal load for modes 1 and 2.

After testing, the platens were removed and their rubbing surfaces examined. As can be seen in Fig. 12, most of the wear took place at the outer corners of the surfaces. This occurred even though initially the surfaces were true and tight against the entire length. It is likely that initially some of the new hardfacing may have quickly worn off allowing the load to move outward and concentrate on a small area since the loading device was not able to automatically adjust to the new contact condition. The distance between these contact points was 5.08 cm. However, the fact that the shroud load acted on a vary narrow region enabled its value to be determined from the applied torque.

Discussion of Results. In this section, a comparison of the numerical results from analysis and testing of a part-span-shrouded fan blade with rubbing at the shroud faces is presented. Preliminary vibration tests provided some insight into the dynamics of shrouds during vibration; for example, the mode shape, and the out-of-plane motion of shrouds observed suggested that the second bending mode of the blade with shrouds unrestrained is the appropriate mode of vibration to model. Therefore, the modal stiffness and modal stress from this mode normalized to unit tip displacement were used in the analysis. Values of parameters used in computation are as follows:

Coefficient of friction, μ	0.3, 0.35
Nonfriction damping loss factor, η_0	0.0005
Frequency (test)	280 Hz
Static stiffness of blade below shrouds	113.8 kN/m (650 lb/in.)
Modal stiffness, k	79.5 kN/m (425 lb/in.)
Modal stress, ASMT (Above-Shroud-Max.-Thickness)	1003 MPa (1.464 E + 6 psi)
Stiffness ratio, β	1.44

The following observations are made upon a close examination of Figs. 5–12:

1 The modes of interest correspond to those in which the motion is essentially above the shroud (see Figs. 5 and 6).

2 The stress amplitude at slip resonance (see flat top in Fig. 7) is proportional to shroud load (N) and excitation level (g). Off resonance, however, the stress amplitude is proportional to excitation level only. An increase in shroud load at a given g level, increases the frequency and response amplitude at which macroslipping would begin. For a given shroud load, an increased g level hastens the slipping action and leads to a wider bandwidth of frequencies in which damping can be

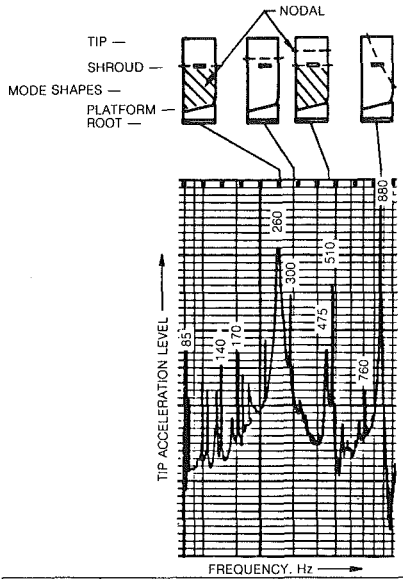

FREQUENCY, Hz	RESPONSE DESCRIPTION
85	NONLINEAR — MODIFIED FIRST FREE BLADE BENDING MODE
140	NONLINEAR RESPONSE
170	NONLINEAR RESPONSE
260	ABOVE SHROUD BLADE BENDING (FLAP) MODE ($\eta = 0.003$)
300	NONLINEAR — MODIFIED SECOND FREE BLADE BENDING MODE
475	ABOVE SHROUD BLADE SECOND BENDING MODE ($\eta = 0.003$)
510	NONLINEAR RESPONSE
760	NONLINEAR RESPONSE
880	ABOVE SHROUD BLADE TORSION ($\eta = 0.001$)

Fig. 5 Fan blade response characteristics from a 2*g* level exploratory sweep – shrouds loaded with 102N

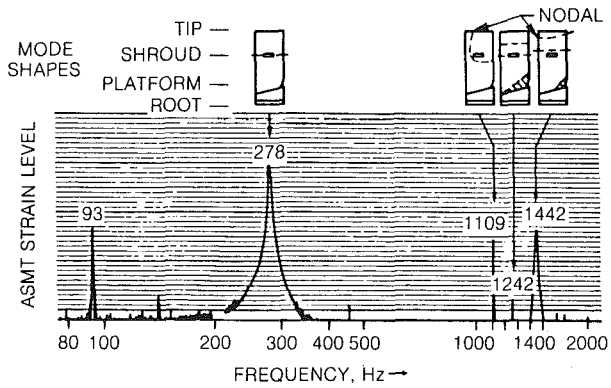

FREQUENCY, Hz	RESPONSE DESCRIPTION
93	NONLINEAR — MODIFIED FIRST FREE BLADE BENDING MODE
278	ABOVE SHROUD BLADE BENDING (FLAP) MODE
1109	ABOVE SHROUD BLADE TORSION
1242	NONLINEAR — MODIFIED SECOND BENDING MODE
1442	ABOVE SHROUD SECOND BENDING MODE

Fig. 6 Fan blade response characteristics from a 2*g* level exploratory sweep – shrouds loaded with 150 N

effective. At a given frequency and *g* level, an increase in shroud load leads to an increase in stress level.

3 Reference to Figs. 8 and 9 suggests that slipping increases with *g* levels as indicated by the progressively steeper slopes at the start of the decay. However, the decay curves superpose at lower stress levels indicating damping levels which are essentially independent of initial conditions.

4 Reference to Fig. 10 suggests that, for a given shroud

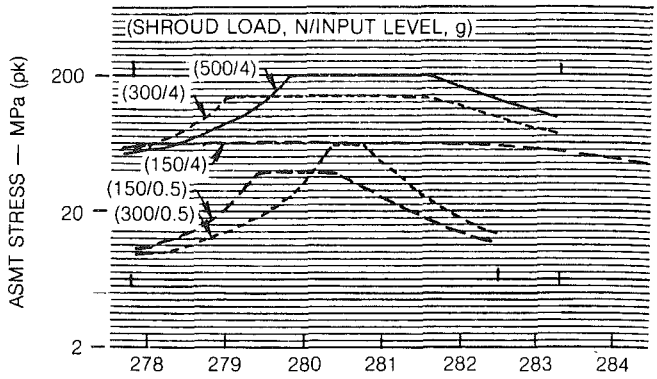

Fig. 7 First flap mode response to a slow frequency sweep at constant input acceleration levels

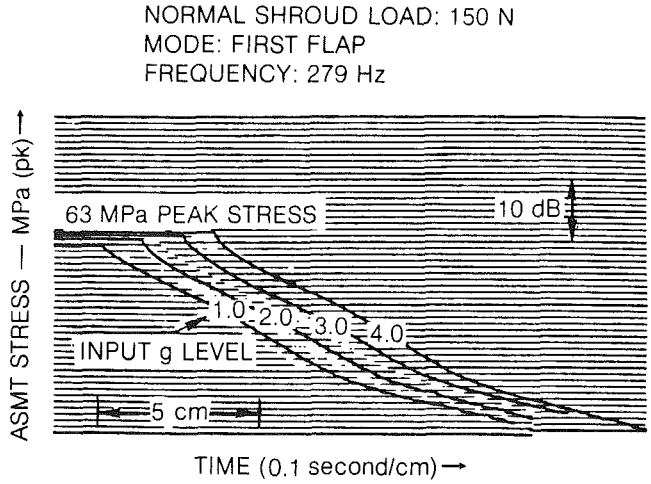

Fig. 8 Damping due to rubbing at shroud for a typical fan blade – variation of response decay with initial stress

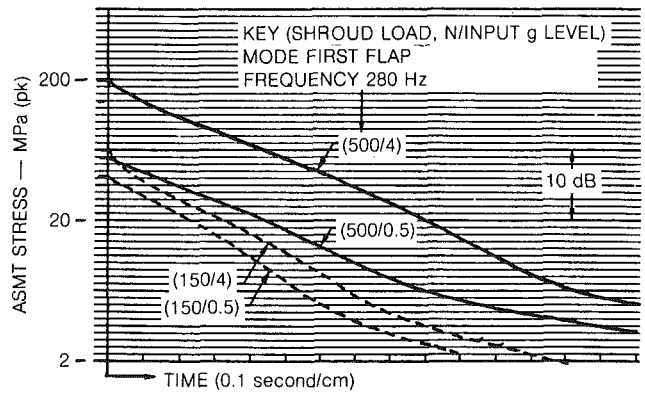

Fig. 9 Damping due to rubbing at shroud for a typical fan blade – variation of response decay with shroud load and initial stress

normal load, the balde stress approaches a constant asymptotic value with increase in excitation level, i.e., distinct macroslip conditions. The analysis predicts an abrupt transition, at low *g* levels, from a region of no friction damping to the macroslip region. The test results indicate a smoother transition at about 1 g for 150 N, about 2 g for 300 N, and about 3 g for 400 N; the smoothness of the transition indicating a region for partial microslip conditions.

Analysis suggests that blade stresses are sensitive to the coefficient of friction; the higher the coefficient of friction, the higher the stresses at which transition to macroslip occurs. The ability of the analytical model to predict blade stress appears to improve with reduction in shroud normal load

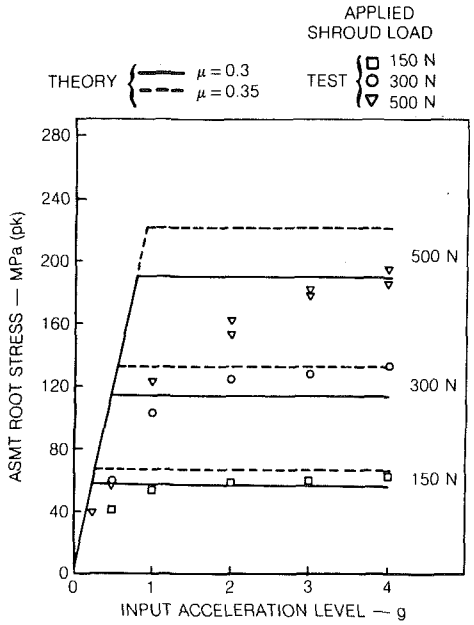

Fig. 10 Shroud damping effects on blade response (first flap mode ~ 280 Hz)

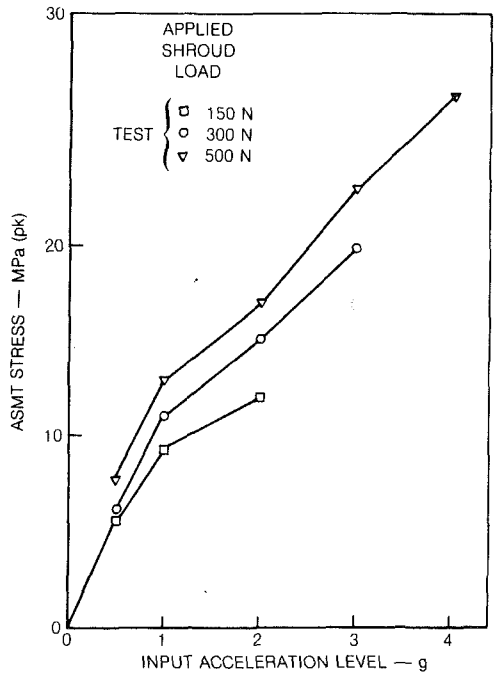

Fig. 11 Blade response in the above-shroud-torsion mode

and/or increase in excitation level, i.e., conditions representing macroslip motion.

Measurements made in the "above-shroud-torsion" mode indicate damping levels substantially lower than those in the "above-shroud-bending" mode. The vibratory motion in the torsion mode causes a slipping motion (rotational) that is different from that caused in a bending mode (translational). In the tests performed, the rubbing action at the interfaces in the torsion mode may have been microscopic as no trend to reach a constant stress level could be observed as g levels increased up to 4 g (compare Figs. 10 and 11). It would appear that in these tests, dry friction damping was more effective in the bending mode than in the torsion mode. This is most likely due to the restraint against torsional motion in the present setup being different from that offered by neighboring blades in an assembly. The wear pattern shown in Fig. 12 suggests

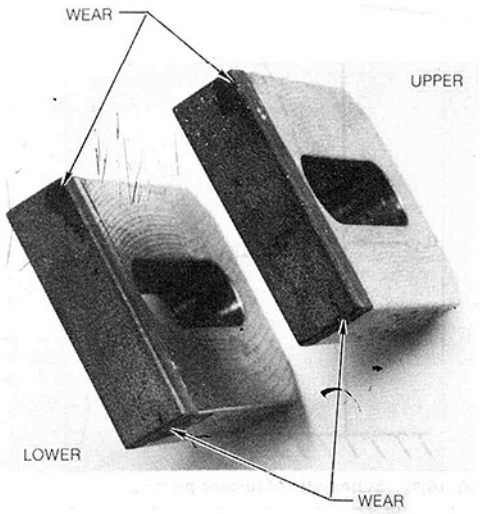

Fig. 12 Wear areas on shroud load platens

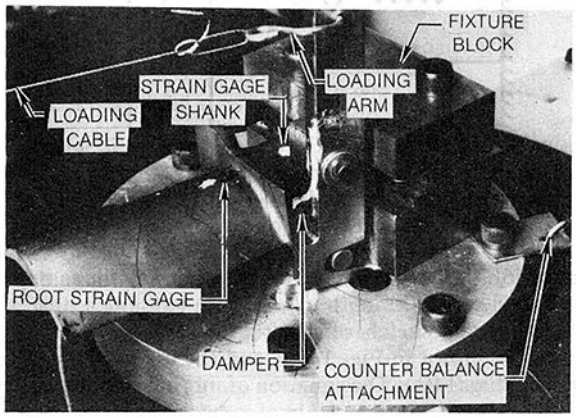

Fig. 13 Turbine blade/platform damper vibration test set-up

that the shroud contact during vibration occurs over a very narrow region and even this minimal contact is sufficient to cause changes in mode shapes as well as to provide adequate damping.

3 Damping due to Platform-Dampers

Platform-type dampers are frequently used in gas turbine blade design to dissipate energy through friction generated at the interface between the damper and blade platform. The type of damper considered in this program is the so-called blade-to-ground damper (see Fig. 13). During engine operation, centrifugal forces bring one end of the damper into contact with the blade platform, the other end being attached to a relatively static component such as disk cover plate. Major parameters which control the extent of friction damping at the damper to platform interface are: contact load, roughness of surfaces, level of external excitation, location of platform on the blade and stiffness of the damper. Studies which address the specific problems of damping at a blade platform can be found in [6–8]. Presented in this section are the results of analysis and testing of a turbine blade subjected to friction damping at its platform.

Forced Response of a Turbine Blade With a Platform Damper. The assumptions in regard to the nature of friction damping are the same as those made in the shroud rubbing studies. Generic models which can be used to analyze blade-to-ground type of platform dampers can be found in [9, 10]. The analytical approach used in this section closely follows

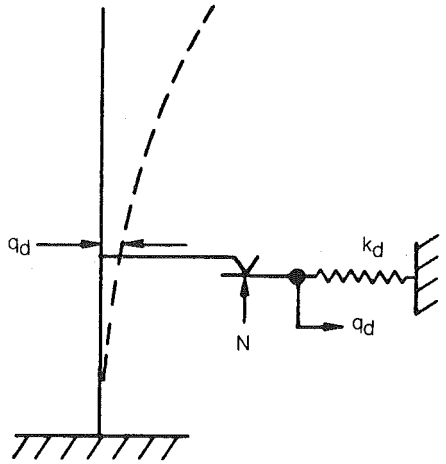

Fig. 14(*a*) Schematic of turbine blade and platform damper

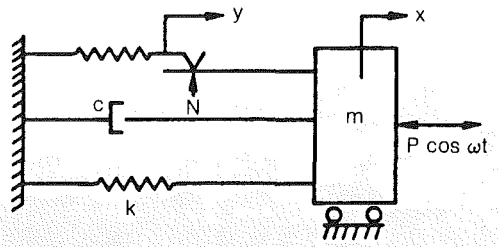

Fig. 14(*b*) Analytical model for platform damping

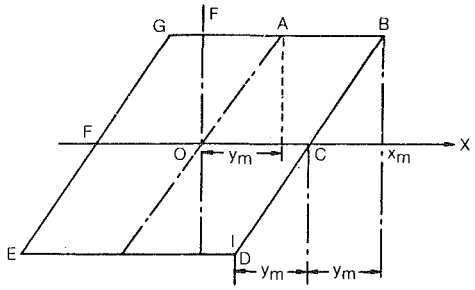

Fig. 15(*a*) Damper force versus blade displacement at platform

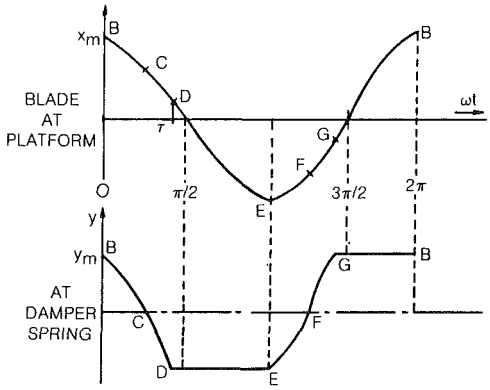

Fig. 15(*b*) Blade and damper spring displacements over one cycle of vibration

that of [6], the generic model being essentially the same as the one in [10].

A schematic sketch of a turbine blade with a platform damper is shown in Fig. 14(*a*), and the associated analytical model in Fig. 14(*b*). The equation of motion can be written as

$$\bar{m}\ddot{\bar{x}} + \bar{k}\bar{x} + \bar{c}\dot{\bar{x}} = \bar{P}\cos\bar{\omega}\bar{t} - \phi_d \bar{F}_a \tag{15}$$

where overbars denote dimensional quantities, m, k, and c are modal quantities, P is the excitation amplitude, ω is the excitation frequency, x is the blade tip displacement, ϕ_d is the modal displacement at the platform, and F_d is the force due to the damper.

Denoting the blade displacement at the platform by q_d, the damper spring displacement by $\hat{q}_d$, and introducing

$$q_d = \phi_a x, \qquad \hat{q}_d = \phi_d y \tag{16}$$

it can be shown that

$$F_d = \phi_d k_d \begin{cases} \bar{x} + \bar{y}_m - \bar{x}_m, & 0 < \bar{\omega}\bar{t} < \tau \\ -\bar{y}_m, & \tau < \bar{\omega}\bar{t} < \pi \end{cases} \tag{17}$$

$$\bar{y}(\bar{t}) = -\bar{y}(\bar{t}+\pi),\ \cos\tau = 1 - (2\bar{y}_m/\bar{x}_m), \bar{y}_m = \mu\bar{N}/\phi_d\bar{k}_o, \tag{18}$$

where subscript m denotes peak value, N is the damper normal load, and μ is the coefficient of friction.

The damper force is a discontinuous function of time, and is shown in Fig. 15(*a*) as a function of the blade displacement at the platform. Figure 15(*b*) shows the blade displacement at the platform and the damper spring displacement over one cycle of vibration. It is noted that the slip amplitude at the damper to platform interface is $(x_m - y_m)$.

It is convenient to nondimensionalize equations (15–18) by introducing

$$x = \bar{x}/\bar{x}_o, a = \bar{x}_m/\bar{x}_0, y = y/\bar{x}_0, b = \bar{y}_m/\bar{x}_0, \bar{\omega}_0^2 = \bar{k}/\bar{m}, \omega = \bar{\omega}/\bar{\omega}_0,$$
$$t = \bar{t}\bar{\omega}_0, \epsilon = \phi^2{}_d\bar{k}_d, \zeta = \bar{c}/2\bar{m}\bar{\omega}_0, p = \bar{P}/\bar{k}\bar{x}_0 \tag{19}$$

where $\bar{x}_o$ is some characteristic length. The result is

$$\ddot{x} + x + 2\zeta\dot{x} = p\cos\omega t - \epsilon y,$$
$$y = \begin{cases} x + b - a, & 0 < \omega t < \tau \\ -b, & \tau < \omega t < j \end{cases} \tag{20}$$

$$y(t) = -y(t+\pi),\ \cos\tau = 1 - (2b/a), b = \mu\bar{N}/\phi_d\bar{k}_d\bar{x}_0 \tag{21}$$

From the equations developed above, two limiting cases can be identified as follows: damper free (no contact with the platform), $\tau = 0$, $b = 0$, and damper stuck (no slip at the platform), $\tau = \pi, b = a$.

Due to the nonlinear (discontinuous) nature of the function, y, the solution of equation (20) is obtained by using the method of averaging, a perturbation method [11]. The essence of the method is the assumption that, if the nonlinearity is small (i.e., ϵ is small), then the amplitude and phase of the response may be treated as constants *within a cycle of vibration*. A solution is sought in the form

$$x = a(t)\cos[t + \theta(t)] = a\cos\gamma \tag{22}$$

where the amplitude and phase are assumed to be functions of time. Application of the method of averaging transforms equation (20) to a set of first-order differential equations,

$$\dot{a} = (1/2\pi)[-2\pi\zeta a - \epsilon a\sin^2\tau - \pi p\sin(\gamma - \omega t)],$$
$$\dot{\theta} = (1/2\pi a)[a\tau - (a/2)\sin 2\tau - \pi p\cos(\gamma - \omega t)], \tag{23}$$

where the case of near resonance, i.e., $\omega \approx 1$, has been assumed.

Equations (2.9) yield the steady-state response as a set of nonlinear algebraic equations,

$$-2\zeta a + R(\epsilon, a, \tau) = p\sin\psi,$$
$$-2\delta a + S(\epsilon, a, \tau) = p\cos\psi, \tag{24}$$

where

$$\psi = \gamma - \omega t, \qquad \delta = \omega - 1, \tag{25}$$

$$R = -(\epsilon a/\pi)\sin^2\tau, \qquad S = (\epsilon a/2\pi)(2\tau - \sin 2\tau). \tag{26}$$

Though Eqs. (24) are nonlinear equations, due to their special structure, it is possible to calculate the maximum response by some algebraic manipulations; see Ref. 10. Some of the steps are outlined below.

Squaring and adding Eqs. (24) yields a quadratic equation for δ, the solution of which is

$$\delta = (1/2a)\{S \pm [p^2 - (R - 2\zeta a)^2]^{1/2}\}. \tag{27}$$

Since δ is a frequency parameter, the maximum response occurs when δ has a double root, that is

$$p^2 - (R - 2\zeta a)^2 = 0. \tag{28}$$

By using the definitions for τ and R given by Equations (18) and (25), respectively, it can be shown that Eq. (28) leads to a quadratic equation for the maximum amplitude. The final results are

$$Q_m = (\tfrac{1}{2}\pi\eta_0)\{(\pi - 4\epsilon G) + [(\pi - 4\epsilon G)^2 + 16\epsilon\pi\eta_0 G^2]^{1/2}\} \tag{29}$$

$$\omega_m = 1 + (\epsilon/4\pi)(2\tau_m - \sin\tau_m); \tau_m = \cos^{-1}[1 - (2G/Q_m)] \tag{30}$$

where Q_m is the maximum response and ω_m is the frequency at which the maximum occurs, and

$$Q_m = a/p, \qquad G = b/p, \qquad \eta_0 = 2\zeta.$$

Further, it is seen from Eq. (29) that Q_m is a function of η_0, ϵ, and G which in turn is a function of the normal load on the platform; see Eq. (21). The optimum value of damper normal load can be determined by minimizing Eq. (29) with respect to G; that is

$$\frac{dQ_m}{dG} = 0,$$

which leads to

$$G^* = \pi/[2(\epsilon + \pi\eta_0)], \tag{31}$$

where G^* is the optimum value. The associated optimum response and frequency can be shown to be

$$Q_m^* = 2G^*, \omega^* = 1 + (\epsilon/4) \tag{32}$$

The analysis and solution developed above is applicable to the case of direct excitation of the blade. If the excitation is applied at the base of the blade, as was done for tests performed in this program, the analysis follows along similar lines to the one given above, the only modification being a redefinition of the nondimensional excitation amplitude

$$p = \bar{p}/\bar{x}_0$$

where $\bar{p}$ is the displacement amplitude of the base excitation.

The energy dissipated per cycle of vibration, D, is

$$D = 4\mu\bar{N}\phi|\bar{x}_m - \bar{y}_m| \tag{33}$$

and the peak strain energy, U, is

$$U = \frac{1}{2}\bar{k}\bar{x}_m^2$$

so that in terms of dimensionless quantities

$$\eta_f = (4\epsilon/\pi)G(Q_m - G)/Q_m^2 \tag{34}$$

and total loss factor for the blade is

$$\eta_b = \eta_0 + \eta_f \tag{35}$$

where as before, η_0 accounts for damping from sources other than friction, such as, material hysteresis and air damping.

The blade tip deflection can be related to the blade stress by specifying a baseline or reference condition where the blade characteristics are fully known. If the baseline tip deflection of the blade can be chosen as the characteristic length $\bar{x}_0$ used for nondimensionalization in equation (19), then it can be shown that

$$\sigma = a\sigma_0,$$

where σ_0 is the blade stress in the baseline condition, and σ is the blade stress at any other condition. In the present study, the damper free condition (no contact between damper and platform) is chosen as the baseline condition.

It was found from tests in the damper free condition that the blade shank stress is a nonlinear function of the base excitation level (see Fig. 16). In other words, damping due to sources other than platform friction, η_0, is a function of the excitation level. It can be shown that

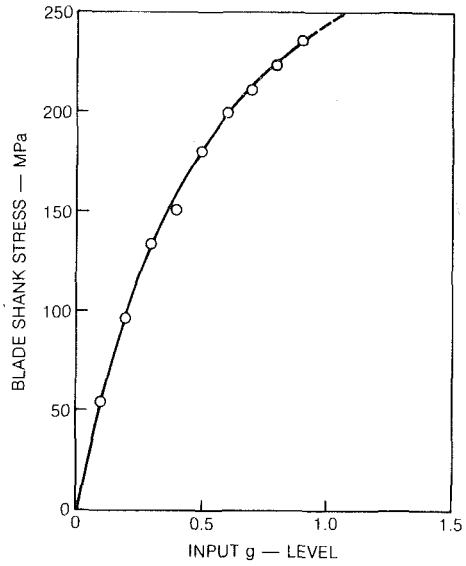

Fig. 16 Baseline conditions for turbine blade

$$\eta_0 = \bar{p}\sigma_m/\sigma_0 \tag{36}$$

where σ_m is the modal stress.

Platform Damping Tests. The analysis shown above enables the calculation of the forced response of a platform damped blade in terms of the modal quantities of the structure, the normal load applied through the damper, the stiffness of the damper, and the frictional characteristics of the rubbing interface. In order to verify the analysis, a turbine blade with a suitable platform configuration was chosen for the test program and a means was devised to provide damping at the platform.

In an operating engine, centrifugal forces acting on the damper provide the contact load between the damper and the blade platform. In this test series, the contact load was applied and controlled by a lever and weight mechanism as shown in Fig. 13. The blade was rigidly clamped in a steel fixture and excitation was provided at the root by a powerful electrodynamic shaker. This method was chosen so that sufficiently high input force was available to overcome the large damping forces expected and to obtain realistically high stresses in the shank of the blade. The modal response of the blade was measured using strain gages located at the blade root on the shank and at the airfoil root on the centerline through the shank.

The test method chosen was to apply a selected damper load and excite the blade sinusoidally at a given input level in the vicinity of the blade's first mode frequency. The frequency was then tuned to produce the maximum blade response.

Since the level of damping produced by the platform damper far exceeds the contributions from other sources, the tests were performed in air. The test piece was a second stage high pressure turbine blade having a three teeth fir tree root configuration and a platform located at approximately 27.7 percent blade span as measured from the shank root. The platform had a generous trailing edge overhang which was convenient for accommodating the damper. The blade material was a nickel chromium high temperature alloy.

The damper was a rectangular prism integral with, and cantilevered from, a T416 stainless steel loading arm. The free end was arranged to rub on the underside of the platform, with the load vector normal to the platform and damper end face surfaces. Two dampers were made, both with a length of 10.1 mm and thickness of 3.2 mm. Their depth measurements were 7.6 mm and 4.2 mm, giving nominal stiffnesses at the free ends of 10.3 and 48.6 MN/m, respectively. The area of

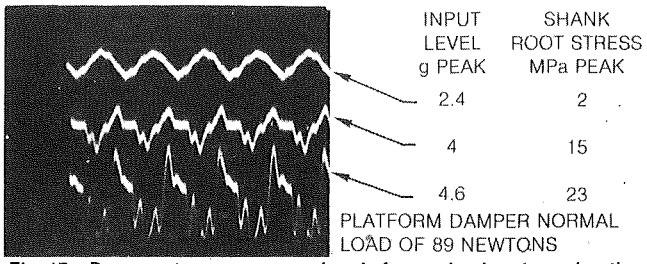

Fig. 17 Damper stress response signals for varying input acceleration levels

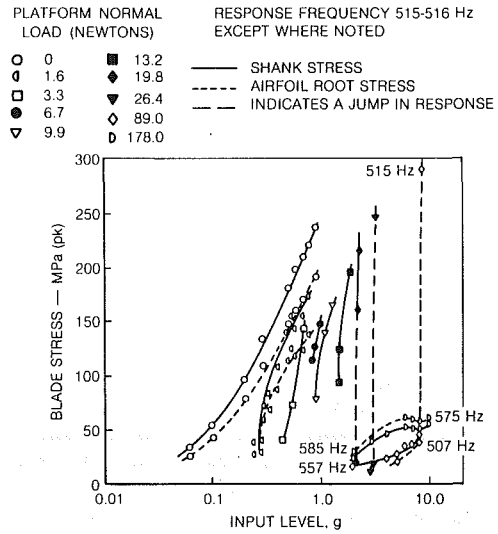

Fig. 18 Platform damping test results (large damper)

the rubbing surface was made the same for both dampers, i.e., 2 mm × 2 mm. The damper and loading arms were heat treated to HRC 41 to match the hardness of the blade. The basic fixturing requirements were that the blade be held rigidly at its root so that damping at root is negligible and that it provides a means of applying a damper load up to 900N on the blade platform with no free motion in the damping mechanism. The fixture used is shown in Fig. 13 and comprises a two piece clamp bolted to an adapter base plate mounted on the shaker. The clamp has steps machined in its upper and lower pieces, which contact the peaks of the two outer lobes of the blade root fir tree. Four 3/8 in. bolts, each torqued to 48 Nm, allowed the blade to be tightly gripped between the two clamp blocks. The loading arm of the damper mechanism was pivoted on a pin mounted in the lower clamp block. The pivot was designed to be self adjusting and no free play was possible. The mechanical advantage of the loading mechanism was 4:1, with the lever loaded horizontally at the top using a cable pulley and hanging weight system. A counterbalance was attached to the base plate to prevent lateral loading of the shaker armature.

Testing and Results. Prior to vibration testing, the stiffness of the small damper was estimated with the loading arm mounted on the fixture by statically loading the damper tip and measuring the tip displacement using a dial indicator. The measured stiffness was 5.5 MN/m.

During early exploratory vibration testing, the strain gage on the large damper was monitored. An example of the traces obtained is shown in Fig. 17. It may be noted that at a constant normal load of 89N on the platform, the damper strain gage response changes from nearly sinusoidal to one with a much more complex wave form as the excitation level is increased from 2.4 *g* pk. At 15 MPa shank stress, the signal

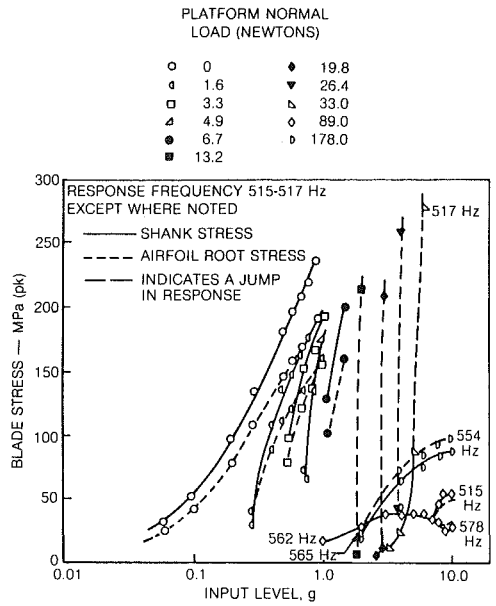

Fig. 19 Platform damping test results (small damper)

clearly shows periods of slipping and loss of contact with the platform. At this point, acoustical noise was emitted from the blade. At 4.6 *g* pk input level, the signal distortion is more pronounced and the noise level is increased.

Final testing consisted of setting the platform damper load and input acceleration level and exciting the blade in the vicinity of its fundamental (first flap) mode. It was found that there was a threshold of both frequency and input (*g*) level below which the blade showed no significant response. Once the threshold is crossed, the blade vibration would continue even with reduction in input level back into the threshold region. Thus, this region could not be clearly defined but every effort was made to obtain these threshold results in a consistent manner. For the highest levels of platform load (> 50N) the resonant response frequency varied significantly from that of the fundamental mode of the lightly loaded blade. This required an increase in the range of test frequencies to include any other resonant modes. Plots showing the variation of blade stresses with input level for the range of platform normal loads are given in Figs. 18 and 19. It should be noted in Figs. 18 and 19 that the faired curves used to connect the test points are to aid in identification of the various load cases and *do not* represent theoretical results. On Fig. 20, the shank stress is shown plotted against the applied platform normal load for input values of 0.5 g, 0.7 *g*, and 1.0 g. Test and theoretical values are shown for comparison.

Discussion of Results. In this section, a comparison of the numerical results from analysis and testing of a turbine blade with a blade-to-ground platform damper is presented. Values of the parameters used in computation are as follows:

Coefficient of friction	0.15, 0.3
Frequency (test)	515 Hz
Damper stiffness, k_d	5472 kN/m (31250 lb/in.)
Modal stiffness, k	245 kN/m (1400 lb/in.)
Modal displacement at platform, ϕ_d	0.12
Modal shank stress, σ_m	2293 MPa (3.348 E + 5 psi)
Base line conditions	see Fig. 16

The modal information is for the first mode and normalized to unit tip displacement of the blade.

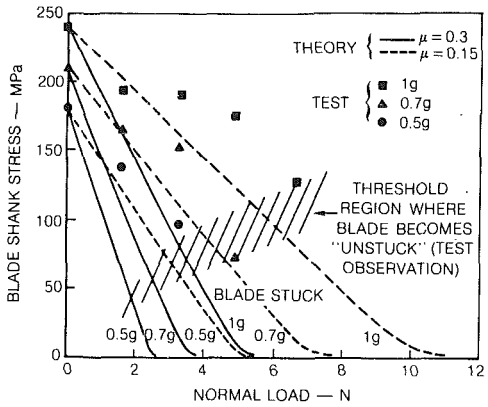

Fig. 20 Turbine blade platform damping characteristics (small damper)

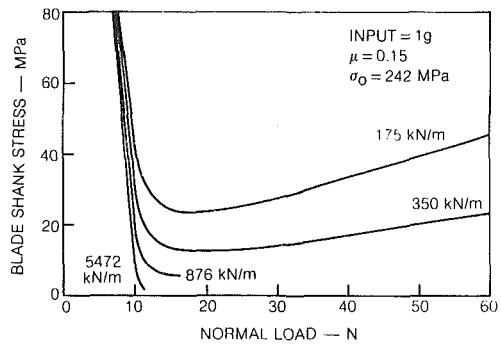

Fig. 21 Influence of damper stiffness on platform damping

Figure 20 shows the theoretical and test results of blade shank stress as a function of normal load for three base excitation levels and two values of friction coefficient. For the theoretical results shown, the change in resonant frequency is less than 1 percent of the baseline frequency. From Fig. 20, the following observations can be made:

1 The theoretical results for the case of $\mu = 0.15$ are in general agreement with the test results.

2 Higher excitation levels and/or lower values of friction coefficient imply lower rates of stress attenuation.

3 For the relatively high stiffness of the damper used in the present program, the rate of stress attenuation is essentially linear.

The analytical prediction of the influence of damper stiffness on the response characteristics is shown in Fig. 21, where the blade shank stress is plotted as a function of normal load, for a given excitation level and for four values of damper stiffnesses. For all the results shown in Fig. 21, the change in resonant frequency is less than 1 percent of the baseline frequency. It can be seen that for smaller values of damper stiffness, there is an optimum normal load where the stress is a minimum. For normal loads higher than the optimum, there is a gradual increase in shank stress.

Devices such as the platform damper belong to a class of inherently nonlinear damping mechanisms similar to those of shroud damping. As in the case of shroud damping, the vibration characteristics depend on the nature and extent of contact between the damper and the blade platform, as well as the excitation level imposed on the system. The traces shown in Fig. 17 are a clear indication of the changes taking place at the contact region; a nearly sinusoidal response changing to one which emitted audible noise.

Examination of Figs. 18 and 19 suggest that until a certain combination of g levels and normal loads are attained, the blade response would be practially not measurable. Upon reaching those levels at which the inertial loads just exceed "stiction" the response of the blade is dependent on the magnitude of the normal load. If the latter is "high," the response mode may correspond to a "stuck damper" condition as is evident from slightly higher frequencies measured. If the g levels continued to increase, then a condition in which the damper breaks contact may be reached. Under these conditions, the blade "plunges" into a lower mode resulting in the jumps in stress as shown in Figs. 18 and 19. Further examination of these figures reveals that the airfoil stresses which begin by being lower than those measured on the shank become higher for the "larger" loads and higher input levels. This is a clear indication of a change in mode shape which points to the need to include more than a single mode in the mathematical model.

A damper design must take into account both stiffness and effective mass of the damper since certain combinations of these properties govern its performance. Heavy dampers, i.e., those that operate with high normal loads, tend to minimize slip damping, but detune the blade, moving the position of maximum stress and changing the resonant frequency. High damper stiffness tends to maximize slip damping in a given mode but may result in a smaller range of operating speeds within which the damper is effective.

Acknowledgment

The permission granted by NASA LeRC to publish this research work is gratefully acknowledged. Also, it is a pleasure to acknowledge the assistance provided by Dr. S. Sridhar in the analytical phases of this program.

References

1 Bielawa, R. L., "An Analytical Study of the Energy Dissipation of Turbomachinery Bladed-Disk Assemblies Due to Inter-Shroud Segment Rubbing," ASME Paper No. 77-DET-73, Sept. 1977.

2 Srinivasan, A. V., Lionberger, S. R., and Brown, K. W., "Dynamic Analysis of an Assembly of Shrouded Blades Using Component Modes," ASME JOURNAL OF MECHANICAL DESIGN, Vol. 100, No. 3, 1978, pp. 520-527.

3 Earles, S. W. E., and Williams, E. J., "A Linearized Analysis for Frictionally Damped Systems," *Journal of Sound an Vibration*, Vol. 24, 1972, pp. 445-458.

4 Williams, E. J., and Earles, S. W. E., "Optimization of the Response of Frictionally Damped Beam Type Structures with Reference to Gas Turbine Compressor Blading," ASME *Journal of Engineering for Industry*, May 1974, pp. 471-476.

5 Rimkunas, D. A., and Frye, H. M., "Investigation of Fan Blade Shroud Mechanical Damping," Report Number FR-11065, Wright-Patterson Air Force Base, Aero Propulsion Lab., 1979.

6 Griffin, J. H., "Friction Damping of Resonant Stresses in Gas Turbine Engine Airfoils," ASME Paper Number 79-GT-109, Mar. 1979.

7 Allen, R. E., and Sidenstick, J. E., "Turbine Blade Technology—Present and Future," ASME Paper Number 80-C2 Aero-10, Aug. 1980.

8 Dickerson, E. O., "Turbine Blade Structural Dynamic Analysis," AIAA Paper No. 80-0782.

9 Levithan, E. S., "Forced Oscillation of a Spring-Mass System Having Combined Coulomb and Viscous Damping," *Jour. Acoustical Society of America*, Vol. 32, No. 10, 1960, pp. 1265-1269.

10 Caughey, T. L., "Sinusoidal Excitation of a System with Bilinear Hysteresis," ASME *Journal of Applied Mechanics*, Vol. 27, Dec. 1960, pp. 640-643.

11 Nayfeh, A. H., *Perturbation Methods*, Wiley Interscience, ch. 5, 1973.

F. Sisto
Professor.
Mem. ASME

A. Chang
Professor.
Mem. ASME

M. Sutcu
Research Assistant.

Department of Mechanical Engineering,
Stevens Institute of Technology,
Hoboken, N.J. 07030

The Influence of Coriolis Forces on Gyroscopic Motion of Spinning Blades

Turbomachine blades on spinning and precessing rotors experience gyroscopically induced instabilities and forcing. With vehicle-mounted turbomachines, either constant or harmonic precession occurs, depending on vehicle or mount motion. Responses of uniform cantilever beams at arbitrary stagger, subjected to the noted rotor motion, are predicted in both self-excited and forced-excitation modes taking into account Coriolis acceleration.

Introduction

The spinning rotors in aircraft engines are often subjected to precession of the rotor spin axis. The precessional motion may be introduced by rapid yaw, pull-up, or nose-over maneuvers. Flight through severe atmosphere turbulence, taxiing over rough runways, and hard landings are other potential sources of precessional motions of the engine axis. Two types of precessional velocity were investigated in two previous papers: a constant angular velocity [1], a harmonic angular velocity changing with time [2]. In both papers, it was shown that the dynamic motion of a typical turbofan or compressor blade on a spinning rotor that is subjected simultaneously to precession of the rotor spin axis can become unstable under certain conditions. The stability of the motion can be represented in a diagram very similar to the Strutt diagram for Mathieu's equation.

There are many factors that influence the dynamic motion of a spinning blade. Some fo these factors are not very significant. For example, the rotor may be considered entirely rigid; to abandon this assumption would unduly complicate the analysis without introducing any concomitant aid to understanding or accuracy. Other factors neglected in this paper for convenience are: the acceleration of the center of the rotor, blade to blade interaction, aerodynamic forces, and the effect of blade pretwist. Some of these can be important in the study of blade motion. The effect of pretwist and aerodynamic forces will be presented in a coming paper.

It is assumed in the present study that the rotor spin velocity and angular precessional velocity are constant. Furthermore, the precessional velocity is considered to be orders of magnitude smaller than the rotor spin velocity. Beam theory forms the basis for the analysis of the blade since the type of failure being investigated would be expected to occur with high aspect ratio blades of low hub/tip ratio.

The main purpose of the present paper is to study the nonlinear effect of the Coriolis acceleration. The dynamical equation of motion employed has time dependence in the coefficients of the differential equations; hence a form of self-excitation or instability may be expected in certain regions of the governing parameters. There are forcing terms on the right hand side of the dynamic equation so that away from the regions of instability the blade will have forced response. This phenomenon is also discussed in this paper.

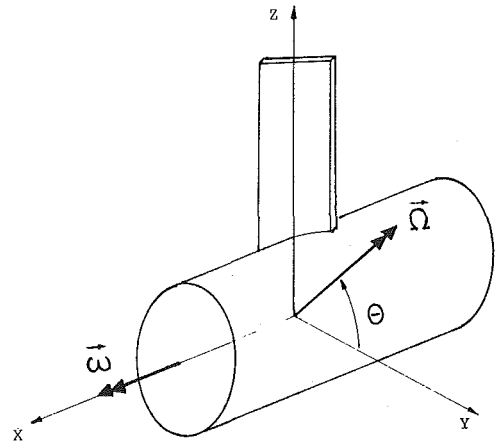

Fig. 1 Coordinate system of spinning rotor with space-fixed precession

There are many numerical schemes available to deal with this class of dynamic governing equation. With modern computers, the computational effort is usually manageable. However, numerical solution is often of less value to the designer. In the sequel the results of parameter studies are presented in charts where stable and unstable regions are easily recognizable, and the effect of governing parameters may be delineated in broad terms. Forced response results, on the other hand, may be expressed in terms of simple approximate formulas.

Governing Equation

The general class of problems dealt with in this paper is governed by similar equations of motion which have been derived in two other papers [1, 2]. The derivation is given here briefly for the sake of completeness.

Contributed by the Gas Turbine Division of THE AMERICAN SOCIETY OF MECHANICAL ENGINEERS and presented at the 27th International Gas Turbine Conference and Exhibit, London, England, April 18-22, 1982. Manuscript received at ASME Headquarters December 14, 1981. Paper No. 82-GT-163.

It is assumed that the precessional velocity vector $\vec{\Omega}$ is space fixed and the origin of the rotor fixed xyz coordinate system (see Fig. 1) is a fixed inertial point.

The angular velocity of the rotor is

$$\vec{\omega} = \omega i + \Omega(\cos\theta j + \sin\theta k) \tag{1a}$$

where $\theta = -\omega t$ and ω is the magnitude of the rotor spin velocity. The position vector of a displaced point on the beam can be given as

$$\vec{r} = (x+s_x)i + (y+s_y)j + (z+s_z)k \tag{1b}$$

where s_x, s_y, and s_z are the centroidal displacement components of an arbitrary beam cross section. The displacement s_z includes only the foreshortening effect [3] and is given as

$$s_z = -\frac{1}{2}\int_R^z \left[\left(\frac{\partial s_x}{\partial z}\right)^2 + \left(\frac{\partial s_y}{\partial z}\right)^2\right] dz \tag{1c}$$

With equations (1*a*) and (1*b*), the velocity of a point on the beam and the kinetic energy expression for the moving blade can be derived. In the derivation, the rotating blade was considered as a beam with a thin rectangular cross section, and only the bending vibration perpendicular to the major axis was considered. In order to employ only one degree of freedom to simulate the beam vibration, it was assumed that the blade deflection is distributed according to

$$u^*(z,t) = \bar{u}(t)\left(1 - \cos\frac{\pi z}{2L}\right) \tag{1d}$$

Employing the kinetic energy expression based on beam tip velocity in the deformed state and the standard potential energy of a beam the motion of the beam tip, $\bar{u}$, including the influence of Coriolis acceleration, can be derived from Lagrange's equation. The result is

$$\begin{aligned}\frac{d^2\bar{u}}{d\theta^2} &+ [a_0 + \epsilon^2 a_1 + \epsilon q_1\cos\theta + \epsilon^2 q_2\cos 2\theta]\bar{u} \\ &- \epsilon q_3 \sin\theta \bar{u}^2 + q_4\left[-\bar{u}^3 + 2\bar{u}^2\frac{d^2\bar{u}}{d\theta^2} + 2\bar{u}\left(\frac{d\bar{u}}{d\theta}\right)^2\right] \\ &= \epsilon^2 F\sin 2\theta + 2\epsilon F\cot\beta\sin\theta\end{aligned} \tag{2}$$

where the quantities a_0, a_1, q_1, q_2, q_3, q_4, and F are all dependent on blade parameters as follows:

$$\begin{aligned}\theta &= -\omega t \text{ (dimensionless time)} \\ \epsilon &= \Omega/\omega << 1 \text{ (typically about 0.001)} \\ a_0 &= \frac{13.42\,EI}{mL^3\omega^2} - \sin^2\beta + 1.2619 + 1.6173\,R/L \\ a_1 &= -0.369 + 0.5\sin^2\beta + 0.809\,R/L \\ q_1 &= \sin 2\beta \\ q_2 &= 0.631 + 0.5\sin^2\beta + 0.809\,R/L \\ q_3 &= (1.094\cos\beta)/L\end{aligned}$$

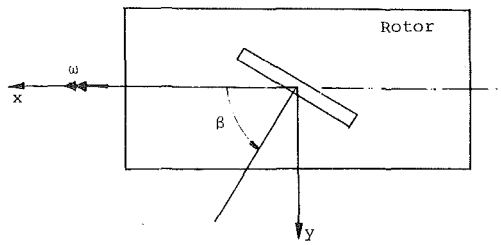

Fig. 2 Blade setting angle β

$$\begin{aligned}q_4 &= 0.608/L^2 \\ F &= -L\sin\beta\,(0.5921 + 0.8011\,R/L)\end{aligned} \tag{3}$$

The blade parameters are setting angle (stagger), β, blade length, L, rotor radius, R, mass of blade, m, section modulus, EI. ω is the rotor spin velocity where as Ω is the magnitude of the space fixed precessional velocity.

The parameters given in equation (3) are for uniform blades. If the blade is tapered these parameters have different expressions and they reflect taper effects. However, the equation of motion (2) retains the same form and the characteristics of the solutions presented in this paper remain general.

It should be pointed out here that the xyz coordinates used in equation (2) are rotating with the rotor angular velocity $\vec{\omega}$. Therefore, the tip deflection $\bar{u}$ is located in a moving coordinate system. This in turn produces the Coriolis term ($\epsilon q_3 \sin\theta\bar{u}^2$), which is not explicitly dependent on velocity.

Comparing the parameter q_4 to the other parameters in the differential equation (2), q_4 can be neglected for large blade length L. Since gyroscopic instability is important for relatively long turbine or fan blades, this nonlinear term will be omitted from further consideration in this paper. The effect of this term will be discussed in a future paper. For the time being it is worthwhile to mention that this term is due to higher order effects of the foreshortened axial displacement.

Studying the other terms in equation (2), Mathieu's equation will be obtained if all higher order terms (ϵ^2, $\epsilon\bar{u}^2$) are neglected. This means, in the first approximation, the stability of the blade tip motion in the rotating and precessional field is governed by the curves in a Strutt diagram. In papers [1] and [2], it was shown that additional unstable regions are generated by those terms that are multiplied by ϵ^2. However, those unstable regions are in general narrower than those associated with Mathieu's equation. The additional effect due to Coriolis acceleration term ($\epsilon q_3 \sin\theta\bar{u}^2$) is studied in detail in the present paper.

The two terms on the right hand side of equation (2) represent forcing functions. They are generated by the centrifugal acceleration of rotor rotational motion. The first term

Nomenclature

a_0 = dimensionless squared frequency
a_1 = defined in equation (3)
A_1, B_L = solution constants of u_L
A_0, B_0 = solution constants of u_0
b_0, b_1, b_2 = expansion parameters of a_0
EI = section modulus
F = coefficient of inhomogeneous term in equation (2)
L = blade length
m = mass of blade
p,q = mutually prime, small integers
q_1, q_2, q_3, q_4 = defined in equation (3)
R = rotor radius
u^* = deflection of the blade
u = tip deflection
u_L = harmonic part of $\bar{u}$
u = disturbance to u_L
u_0, u_1, u_2 = perturbation expansion of u
v_1, v_2 = numerical solutions of equation (10)
s_x, s_y, s_z = centroidal displacement
t = time
x,y,z = rotor fixed coordinate system
β = blade setting angle, defined in Fig. 2
ϵ = ratio of precession to rotor spin, Ω/β
η_1, η_2 = initial condition parameters
θ = dimensionless time
ω = rotor spin velocity
Ω = space fixed precessional velocity
ν = time coefficient

is a time function with twice the frequency of the rotor spin, i.e., the force becomes zero four times in every rotation. This force vector is in the y direction of the moving coordinate system (see Fig. 2). The second term is generated by a force vector that is in the x direction of the moving coordinate system. Both inhomogeneous terms on the right hand side of equation (2) represent components of these force vectors that cause blade bending in the $\bar{u}$ direction.

Stability Analysis

A general stability analysis of equation (2) is not possible. However certain predictions can be made about systems which have the form:

$$\frac{d^2\bar{u}}{d\theta^2} + a_0\bar{u} = \epsilon f\left(\nu\theta, \bar{u}, \frac{d\bar{u}}{d\theta}\right) \tag{4}$$

where ϵ is small and $f(\nu\theta, \bar{u}, d\bar{u}/d\theta)$ is periodic with a period 2π in the product variable $\nu\theta$. In these systems resonance occurs only if

$$\sqrt{a_0} \approx \frac{p}{q}\nu$$

where p and q are small and mutually prime integers [4]. If $\sqrt{a_0}$ is irrational and cannot be obtained by the division of two integers, the solutions to (4) are not periodic but usually bonded. Therefore, it suffices to make the stability analysis of (2) for only those $\sqrt{a_0}$ values which can be represented as a division of two mutually prime integers:

$$\sqrt{a_0} = \frac{p}{q} \tag{5}$$

Equation (2) can be written in the form of equation (4). The coefficient ϵ in this equation is the ratio of the precessional angular velocity Ω to the spin angular velocity ω. In general, this ratio is very small compared to a_0. Therefore, it can be expected that the solution of (2) is nearly harmonic. An approximate linearized differential equation can be obtained by assuming that the solution consists of two parts:

$$\bar{u} = u_L + \epsilon u \tag{6}$$

The first part u_L satisfies the equation:

$$\frac{d^2u_L}{d\theta^2} + a_0u_L = 0 \tag{7}$$

which has the solution:

$$u_L = A_L\cos\sqrt{a_0}\theta + B_L\sin\sqrt{a_0}\theta \tag{8}$$

Substituting equations (6) and (7) into equation (2), and linearizing by neglecting the $(\epsilon u)^2$ term, results in

$$\frac{d^2u}{d\theta^2} + [a_0 + \epsilon^2 a_1 + \epsilon q_1\cos\theta + \epsilon^2 q_2\cos2\theta - \epsilon 2q_3\sin\theta u_L]u = \epsilon^2 F\sin2\theta + 2\epsilon F\cot\beta\sin\theta + q_3\sin\theta u_L^2 - (\epsilon a_1 + q_1\cos\theta + \epsilon q_2\cos2\theta)u_L \tag{9}$$

The stability of the above differential equation can be studied by considering the homogeneous part only

$$\frac{d^2u}{d\theta^2} + [a_0 + \epsilon^2 a_1 + \epsilon q_1\cos\theta + \epsilon^2 q_2\cos2\theta - \epsilon 2q_3\sin\theta u_L]u = 0 \tag{10}$$

Under the condition of equation (5), the period of the coefficient of u in the differential equation (10) is $2q\pi$. Furthermore, the stability of this differential equation can be studied by means of Floquet theory.

The perturbation method of strained parameters is used to determine the periodic solutions of u. This requires the expansion of the solution $u(\theta)$ in terms of

$$u = u_0 + \epsilon u_1 + \epsilon^2 u_2 \tag{11}$$

Also, it is necessary to expand the dimensionless squared frequency in terms of ϵ

$$a_0 = b_0 + \epsilon b_1 + \epsilon^2 b_2 \tag{12}$$

Substituting equations (11) and (12) into (10) a set of differential equations are obtained

$$\frac{d^2u_0}{d\theta^2} + b_0u_0 = 0$$

$$\frac{d^2u_1}{d\theta^2} + b_0u_1 = -(b_1 + q_1\cos\theta - 2q_3\sin\theta u_L)u_0$$

$$\frac{d^2u_2}{d\theta^2} + b_0u_2 = -(b_2 + a_1 + q_2\cos2\theta)u_0 - (b_1 + q_1\cos\theta - 2q_3\sin\theta u_L)u_1 \tag{13}$$

, etc.

The differential equations (13) are solved successively and secular terms are supposed by imposing conditions on the expansion parameters b_1, b_2, etc. This is based on Floquet theory for the transition behavior between stable and unstable solutions.

The solution of the first differential equation (13) is an harmonic function

$$u_0 = A_0\cos\sqrt{b_0}\theta + B_0\sin\sqrt{b_0}\theta \tag{14}$$

with constants A_0 and B_0. Substituting this equation into the second differential equation (13),

$$\frac{d^2u_1}{d\theta^2} + b_0u_1 = -(b_1 + q_1\cos\theta - 2q_3\sin\theta u_L)u_0 \tag{15}$$

and solving this differential equation yields

$$u_1(\theta) = -\frac{A_0b_1\theta\sin\sqrt{b_0}\theta}{2\sqrt{b_0}} + \frac{B_0b_1\theta\cos\sqrt{b_0}\theta}{2\sqrt{b_0}} + A_0\left\{-\frac{q_1}{2}\left[\frac{\cos(1-\sqrt{b_0})\theta}{2\sqrt{b_0}-1} - \frac{\cos(1+\sqrt{b_0})\theta}{2\sqrt{b_0}+1}\right] + \frac{q_3A_L}{2}\left[\frac{\sin(1+2\sqrt{b_0})\theta}{-(3b_0+4\sqrt{b_0}+1)} + \frac{\sin(1-2\sqrt{b_0})\theta}{-(3b_0-4\sqrt{b_0}+1)}\right] + q_3A_L\frac{\sin\theta}{b_0-1} + \frac{q_3B_L}{2}\left[\frac{\cos(1-2\sqrt{b_0}\theta}{-(3b_0-4\sqrt{b_0}+1} + \frac{\cos(1+2\sqrt{b_0}\theta}{3b_0+4\sqrt{b_0}+1}\right]\right\} + B_0\{\ldots\ldots\} \tag{16}$$

The first two terms on the right hand side of (16) are secular terms. Additional secular terms arise when $\sqrt{b_0} = 1$, $\sqrt{b_0} = 1/2$, and $\sqrt{b_0} = 1/3$. The differential equation (15) has to be solved for these specific values of b_0 and the secular terms that arise must be elimated by imposing conditions on b_1. This is done in the neighborhood of those b_0 values which possess a singularity in the solution.

Starting with $b_0 = 1/9$, equation (15) is:

$$\frac{d^2u_1}{d\theta^2} + \frac{1}{9}u_1 = -b_1A_0\cos\frac{\theta}{3} - b_1B_0\sin\frac{\theta}{3} + \frac{1}{2}A_0A_Lq_3\sin\frac{\theta}{3} + \frac{1}{2}A_0B_Lq_3\cos\frac{\theta}{3} + \frac{1}{2}B_0A_Lq_3\cos\frac{\theta}{3} - \frac{1}{2}B_0B_Lq_3\sin\frac{\theta}{3} + \ldots \tag{17}$$

Eliminating the secular terms in (17) requires that

$$-b_1 A_0 + \frac{1}{2} B_L q_3 A_0 + \frac{1}{2} A_L q_3 B_0 = 0$$

$$-b_1 B_0 - \frac{1}{2} B_L q_3 B_0 + \frac{1}{2} A_L q_3 A_0 = 0 \tag{18}$$

Equations (18) can be written in the form

$$\begin{bmatrix} -b_1 + \frac{q_3}{2} B_L & \frac{q_3}{2} A_L \\ \frac{q_3}{2} A_L & -b_1 - \frac{q_3}{2} B_L \end{bmatrix} \begin{Bmatrix} A_0 \\ B_0 \end{Bmatrix} = \begin{Bmatrix} 0 \\ 0 \end{Bmatrix} \tag{19}$$

To obtain nontrivial solutions the determinant of the coefficient matrix must be zero. This yeilds the following equation:

$$b_1^2 - \frac{q_3^2}{4} (A_L^2 + B_L^2) = 0$$

or

$$b_1 = \pm \frac{q_3}{2} \sqrt{A_L^2 + B_L^2} \tag{20}$$

The two values of b_1 in equation (20), when inserted into equation (12), correspond to two different stability transition curves in the (a_0, ϵ) plane. These curves separate stable regions from unstable regions. For each b_1 that is obtained from (20) the corresponding ratio of A_0 to B_0 can be determined from (19)

$$\frac{A_0}{B_0} = \frac{B_L \pm \sqrt{A_L^2 + B_L^2}}{A_L} \tag{21}$$

Using these results, the second order approximation of the transition curves can be obtained by eliminating secular terms in the solution of the third differential equation in (13). For each transition curve at $a_0 = 1/9$ there are two different conditions for b_2 that have to be fulfilled in order to eliminate the secular terms. They are, respectively,

$$b_2 = -a_1 - \frac{9}{10} q_1^2 \mp \frac{9}{8} q_3^2 B_L \sqrt{A_L^2 + B_L^2} - (39A_L^2 - 33B_L^2) \frac{q_3^2}{32} \tag{22}$$

$$b_2 = -a_1 - \frac{9}{10} q_1^2 \mp \frac{9}{8} q_3^2 B_L \sqrt{A_L^2 + B_L^2} - (75B_L^2 + 3A_L^2) \frac{q_3^2}{32} \tag{23}$$

Obviously, conditions (22) and (23) cannot be satisfied simultaneously for arbitrary A_L and B_L. Examining the two expressions for b_2 in these equations, the difference is in the last term of the equations. If these terms are neglected the perturbation solution (11) will not be exactly periodic due to u_2. The prerequisites of applying Floquet theory for the transition curve will be violated. The method of strained parameters fails to determine the stability transition curves to the second and also to higher powers of ϵ. Therefore, the solution so obtained is not uniformly valid as $t \to \infty$. Other perturbation methods have been tried without much success in resolving this inconsistency. This remains a mathematical problem that may be tackled rigorously at a future time.

Fortunately, in most practical cases the ratio ϵ, of precessional speed to rotor spin is small. The numerical error resulting from omitting these inconsistent terms is negligible. In order to verify these approximated stability curves an independent numerical method was employed directly to determine the stability of the basic equation (10). This is presented in the next section.

The approximate equations (22) and (23) for b_2 and equation (20) for b_1 are inserted into (12) to obtain the equations for the two transition curves that emanate from $a_0 = 1/9$, $\epsilon = 0$.

$$a_0 = \frac{1}{9} \pm \epsilon \frac{q_3}{2} \sqrt{A_L^2 + B_L^2} - \epsilon^2 \left[a_1 + \frac{9}{10} q_1^2 \pm \frac{9}{8} q_3^2 B_L \sqrt{A_L^2 + B_L^2} \right] \tag{24}$$

The above process is repeated at other singularity points: $\epsilon = 0$ and $a_0 = 1/4$, 1, etc. The approximate transition curves at $a_0 = 1/4$ are

$$a_0 = \frac{1}{4} + \epsilon \frac{q_1}{2} + \epsilon^2 \left[-a_1 - \frac{q_1^2}{8} + \frac{q_3^2}{15} (14A_L^2 - 6B_L^2) \right] \tag{25}$$

$$a_0 = \frac{1}{4} - \epsilon \frac{q_1}{2} + \epsilon^2 \left[-a_1 - \frac{q_1^2}{8} + \frac{q_3^2}{15} (14B_L^2 - 6A_L^2) \right] \tag{26}$$

and at $a_0 = 1$ are

$$a_0 = 1 + \epsilon \frac{q_3}{2} [2B_L \pm \sqrt{A_L^2 + B_L^2}] - \epsilon^2 \left[a_2 - \frac{q_3^2}{32} (A_L^2 + B_L^2) \right] \tag{27}$$

Emanating from each singular point in the (a_0, ϵ) plane there are two transition curves. The loci of transition values separate the (a_0, ϵ) plane into regions of stability and regions of instability. It should be mentioned that these are not the only stability curves. Additional unstable regions can be derived for higher values of a_0. However, these regions of instability are usually narrow and do not have practical significance.

All of these transition curves contain A_1 and B_1 which are the initial condition constants of the basic solution u_L. The dependence of stability transition curves on the initial conditions is typical for nonlinear systems. But these transition curves do not depend on the constants A_0 and B_0 in equation (14) of the perturbed solution. This indicates that the stability curves are valid for any arbitrary initially perturbed motion.

Numerical Example

The equations for stability transition curves derived by the perturbation method contain the blade parameters β, R/L, Ω/ω, L, etc. with the initial condition constants A_L and B_L. For each of these parameters, one can construct a family of stability curves while the other parameters are held constant. In this paper we choose to demonstrate the effect of initial conditions on the stability curves for a given set of blade parameters.

Stability charts of Figs. 3, 4 and 5 are constructed for the particular set of blade parameters, $L = 25.4$ cm, $R/L = 1.384$, $\beta = 45$ deg which yields the following parameters $a_1 = 1$, $q_1 = 1$, $q_2 = 2$, and $q_3 = 0.1547$.

For this purpose, two nondimensional initial value parameters, η_1 and η_2 are defined as follows:

$$\eta_1 = \frac{A_L}{L} \tag{28}$$

$$\eta_2 = \frac{B_L}{L}$$

Note that A_L is the initial displacement, $u_L(0)$ $(\bar{u} \approx u_L)$ and B_L is proportional to the initial velocity.

Figures 3, 4, and 5 correspond to different initial displacement values, $\eta_1 = 0$, $\eta_1 = 0.05$, and $\eta_1 = 0.1$, respectively. In each figure, four pairs of transition curves are drawn for four different values of η_2: 0, 0.05, 0.1, and 0.5.

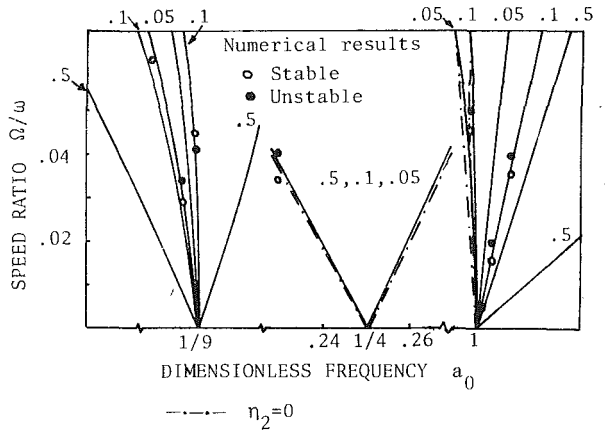

Fig. 3 Stability chart for zero initial displacement, $\eta_1 = 0$ and for different initial speed η_2

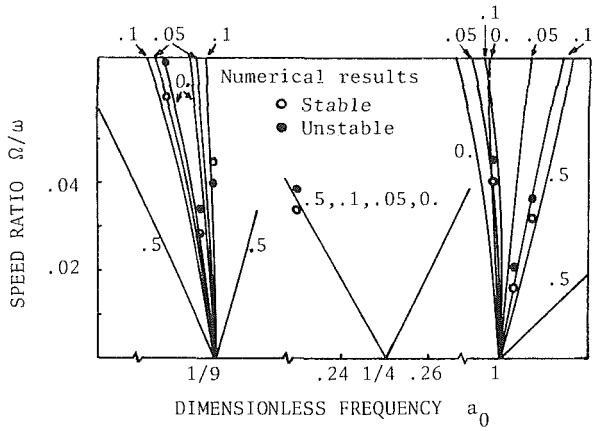

Fig. 4 Stability chart for initial displacement $\eta_1 = 0.05$ and for different initial speed η_2

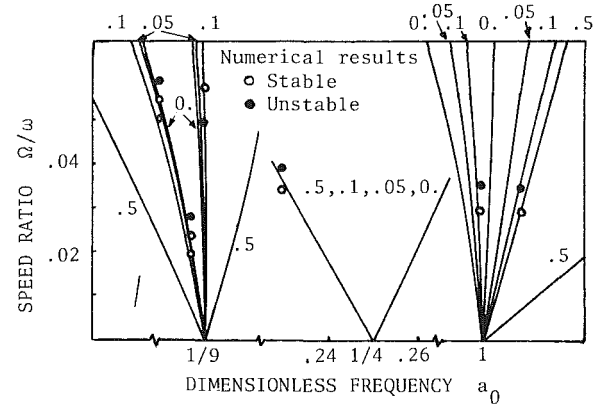

Fig. 5 Stability chart for initial displacement $\eta_1 = 0.1$ and for different initial speed η_2

Note that $\eta_2 = 0.5$ corresponds to a significant initial speed. For example, if the spin velocity is 4000 rpm the initial speed for the transition curves emanating from $a_0 = 1/4$ is 26.5 m/s.

For every pair of curves that emanates from the discrete a_0 values, the region between the transition curves correspond to (a_0, ϵ) values which give unbounded solutions of the equation of motion. Therefore, these are regions of instability. In these regions the perturbed motion, u, grows and, consequently, according to equation (6), the blade tip motion $\bar{u}$ is unstable.

In reality, after an appreciable amount of growth has taken place nonlinearity prevents further growth and stationary solutions are obtained. In the present paper these stationary amplitudes in the unstable region are assumed to be large so that catastrophic behavior is not prevented by the attainment of these stationary amplitudes.

In Fig. 3 the transition curves for $\eta_1 = \eta_2 = 0$ are of particular interest. These are stability transition curves when the nonlinear Coriolis term is not taken into consideration. It can be seen from equation (10) that if the Coriolis term is neglected the stability characteristics of the blade tip motion will not depend on initial conditions (A_L, B_L). This is expected since the stability of linear systems should be independent of initial conditions. Also, when there is no initial motions $(A_L = 0, B_L = 0)$ relative to the spinning system the Coriolis acceleration does not effect the stability regions.

An interesting effect of Coriolis acceleration is the creation of additional region of instability at $a_0 = 1/9$. This region does not exist for $\eta_2 = \eta_1 = 0$, and it widens for increased values η_1 or η_2.

Unstable regions at $a_0 = 1/9$ and at $a_0 = 1$ are quite narrow for practical initial values ($\eta_1 < 0.1$, $\eta_2 < 0.05$). These regions depend strongly on initial conditions and Coriolis effect. On the other hand, the unstable region at $a_0 = 1/4$ does not depend on the initial conditions. This region is even important when the nonlinear Coriolis term is not neglected.

Studying the three stability charts it might be concluded that for moderate initial values and low precession rates ($\epsilon << a_0$), the effect of Coriolis force on motion stability can be neglected for blades undergoing gyroscopic motion.

So far the stability of tip motion has been analyzed by the perturbation method. Because of the uncertainty in the accuracy of this method, it was decided to verify the stability charts presented in Figs. 3, 4, and 5 by numerical solutions. According to reference [5], the solutions of the equations of motion (10) are stable if:

$$|V_1(2q\pi) + V_2'(2q\pi)| < 2 \tag{29}$$

where $V_1(\theta)$ and $V_2(\theta)$ are numerical solutions of the homogeneous equation of motion (10) with the following initial conditions

$$V_1(0) = 1, \quad V_1'(0) = 0$$
$$V_2(0), \quad V_2'(0) = 1 \tag{30}$$

The predictor-corrector numerical scheme of Adams-Bashforth was used to obtain $V_1(\theta)$ and $V_2(\theta)$ for given (a_0, ϵ) values when $a_1 = 1$, $q_1 = 1$, $q = 2$, and $q_3 = 0.1547$. In all three figures, the transition curves for the initial condition $\eta_2 = 0.1$ were checked. The stable and unstable (a_0, ϵ) points are marked on the stability charts. They indicate that the stability curves obtained from the perturbation method are quite reliable.

Forced Vibrations

The equation of motion (2) indicates that the gyroscopic motion is a forced vibratory motion. From the stability analysis, it has been determined that the motion in the unstable regions of the (a_0, ϵ) plane is unbounded. This is due to the fact that the forcing function initiates vibrations which lead to parametric resonance. Hence, it is only necessary to give the forced response away from the resonance regions.

In the stable regions, the solution to the equation of motion (2) can be assumed to be

$$\bar{u} = u_L + \epsilon u \tag{31}$$

where u_L now includes the forced response

$$\frac{d^2 u_L}{d\theta^2} + a_0 u_L = \epsilon^2 F \sin 2\theta + 2\epsilon F \cot\beta \sin\theta \tag{32}$$

where F is given in equation (3) and is of $0(L)$ and u is the perturbed solution due to the right hand side of equation (4).

In the stable regions, the perturbed motion is bounded. From equation (31), the error in taking u_L equal to $\bar{u}$ is in the order of ϵ. Therefore, in the stable region, the forced response of the equation of motion (2) with error of order ϵ can be obtained from equation (32) directly.

$$\bar{u} \approx u_L = A\cos\sqrt{a_0}\theta + B\sin\sqrt{a_0}\theta + \frac{\epsilon^2 F}{a_0 - 4}\sin 2\theta + \frac{2\epsilon F}{a_0 - 1}\cot\beta\sin\theta \tag{33}$$

where

$$A = \bar{u}(0)$$

$$B = \frac{1}{\sqrt{a_0}}\left[\left.\frac{d\bar{u}}{d\theta}\right|_{\theta=0} - \frac{2\epsilon^2 F}{a_0 - 4} - \frac{2\epsilon F\cot\beta}{a_0 - 1}\right] \tag{34}$$

The peak value of (33) can be determined by summing the amplitudes of individual harmonics:

$$|\bar{u}|_{\max} = \sqrt{A^2 + B^2} + \left|\frac{\epsilon^2 F}{a_0 - 4}\right| + \left|\frac{2\epsilon F\cot\beta}{a_0 - 1}\right| \tag{35}$$

To check the validity of the solution (33), the complete equation of motion (2) is integrated directly using the predictor-corrector numerical scheme of Adams-Bashforth. Both the numerical solution and the approximate solution are plotted in Figs. 6 and 7. Figure 6 is constructed with zero initial conditions, whereas in Fig. 7 the initial values are $u(0) = 2.54$ cm, $d\bar{u}/d\theta|_{\theta=0} = 2.54$ cm, which correspond to

$$\left.\frac{d\bar{u}}{dt}\right|_{t=0} = (2.54 \times \omega)\text{cm/s}$$

The solutions of Fig. 6 and Fig. 7 correspond to a stable point in the (a_0, ϵ) plane which is $a_0 = 2$ and $\epsilon = 0.01$. The particular blade data used in Figs. 6 and 7 was the same as those used in the stability chart.

The approximate solutions of (2) in the stable region which are obtained from equation (33) are in very good agreement with direct numerical solutions of (2), as can be seen in Figs. 6 and 7. For smaller and more realistic ϵ values the accuracy of the approximate solution will be even better.

The previous discussion leads us to conclude that for practical purposes the peak value of the vibratory motion which is governed by equation (2) can be predicted from equation (35), provided the particular blade and rotary data correspond to points inside the stable region of the (a_0, ϵ) plane. It is worthwhile to note that bending moments associated with peak tip displacements in this case ($\epsilon = 0.01$) are acceptable. Therefore, the forced motion of blade under gyroscopic disturbance is generally less important than the corresponding motion stability problem.

Summary and Conclusions

The stability of the blade tip motion can be represented in a diagram very similar to the Strutt diagram for Mathieu's equation. All the unstable frequencies a_0 from solutions of the Mathieu's equation are present. However, the regions of stability characteristics are now different.

Perturbation methods, with accuracy confirmed by direct numerical integration, have shown that the inclusion of Coriolis acceleration alters the stability of blades mounted on a spinning and precessing rotor. The principal result is the creation of new regions of instability, one of which emanates from $a_0 = 1/9$ on an a_0, ϵ diagram. The parameter a_0 corresponds roughly to the square of the blade rotating natural frequency and ϵ is the shaft precession rate, both angular rates being dimensionless with respect to the rotor spin rate.

In addition to new regions of instability, it is found that the size, or extent, of some of the unstable regions become dependent upon initial conditions with large initial displacements and/or velocities not unexpectedly yielding larger unstable areas in the a_0, ϵ plane. However, there is no Coriolis effect unless there are nonzero initial conditions, and the dependence on initial condition is such that very large values of these parameters are needed to widen out appreciably what are basically very narrow regions to begin with. Hence, the important effect of Coriolis acceleration is mainly to create new regions of instability, and, in particular, at one lower blade bending frequency, rather than to increase the width of the frequency bands very appreciably where instability might be encountered.

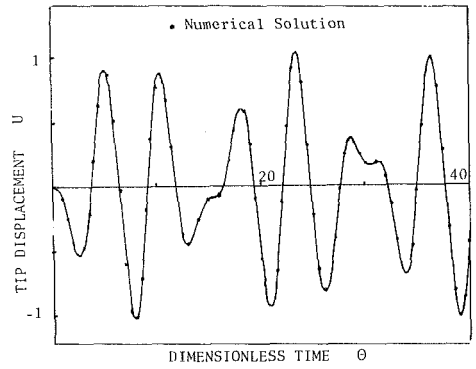

Fig. 6 Comparison of numerical and approximate solutions in the stable region with zero initial conditions

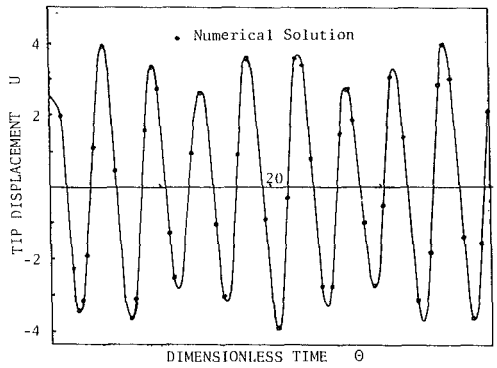

Fig. 7 Comparison of numerical and approximate solutions in the stable region when initial conditions are $u(0) = 2.54$ cm and $d\bar{u}/d\theta = 2.54$ cm

Forced response in the stable regions shows an interesting characteristic at the expected frequency of twice the frequency of spin. The cantilever blade tip deflection is proportional to the square of the ratio of precession to spin frequencies. Since the ratio is usually small, $\epsilon << 1$, the forced response will be very small as a fraction of the blade length. However, a resonant condition will obtain as $\sqrt{a_0} \to 2$, i.e., as the natural bending frequency approaches twice the spin frequency. This may provide further insight into the extreme importance attached to second engine order resonance by axial compressor and jet engine designers.

Acknowledgment

This research was sponsored by the National Aeronautics and Space Administration, Lewis Research Center under Grant NAG-3-47. The guidance provided by L. James Kiraly, NASA program manager for this contract, is gratefully acknowledged.

References

1 Sisto, F., Chang, A. T., "The Influence of Gyroscopic Forces on the Dynamic Behavior of Rotating Blades," submitted to the Fifth International Symposium on Airbreathing Engines, Feb. 16-21, 1981, Bangalore, India.

2 Sisto, F., Chang, A. T., and Sutcu, M., "Blade Excitation due to Gyroscopic Forces," *Proceedings of the IFTo MM Conference on Rotor-Dynamic Problems in Power-Plants*, Rome, Sept. 1982.

3 Vigneron, F. R., "Comment on 'Mathematical Modeling of Spinning Elastic Bodies for Modal Analysis,'" *AIAA Journal*, Vol. 13, No. 1, Jan. 1975, pp. 126-127.

4 Bogoliubov, N. N., Mitropolsky, Y. A., "Influence of Extenal Periodic Forces," *Asymptotic Methods in the Theory of Nonlinear Oscillations*, Gordon and Breach Science Publishers, New York, 1963, pp. 196-198.

5 Magnus, W. and Winkler, S., "Basic Concepts," *Hill's Equation*, Dover Edition, Dover, 1979, pp. 7-8.

Status Report—Advanced Heat Exchanger Technology for a CCGT Power Generation System

D. E. Wright

L. L. Tignac

Rockwell International, Rocketdyne Division, Canoga Park, Calif. 91304

Rocketdyne is under contract to the Department of Energy for the development of heat exchanger technology that will allow coal to be burned for power generation and cogeneration applications. This effort involves both atmospheric fluidized bed and pulverized coal combustion systems. In addition, the heat exchanger designs cover both metallic and ceramic materials for high-temperature operations. This paper reports on the laboratory and small AFB test results completed to date. It also covers the design and installation of a 6 × 6 ft atmospheric fluidized bed test facility being used to correlate and expand the knowledge gained from the initial tests. The paper concludes by showing the direction this technology is taking and outlining the steps to follow in subsequent programs.

Introduction

Between the years 1977–1980, the Department of Energy funded studies of coal-fired, closed-cycle gas turbine (CCGT) power generation systems for both central station power at 350 MWe unit sizes and cogeneration units of 10 to 50 MWe. The advantages and problems of CCGT power generation systems were explored and comparisons made between such systems and more conventional steam-based cycles. Fired heat exchanger concepts were described for application to CCGT cycles having maximum working fluid temperatures between 1460 and 2250°F. Finally, technology barriers were identified, which required solutions before the fired heat exchanger concepts would be built.

In February 1980, the Department of Energy contracted with Rocketdyne to conduct the necessary research and development that would allow the practical construction of the heat exchanger designs offered. Figure 1 shows the overall plan for the Advanced Heat Exchanger Program.

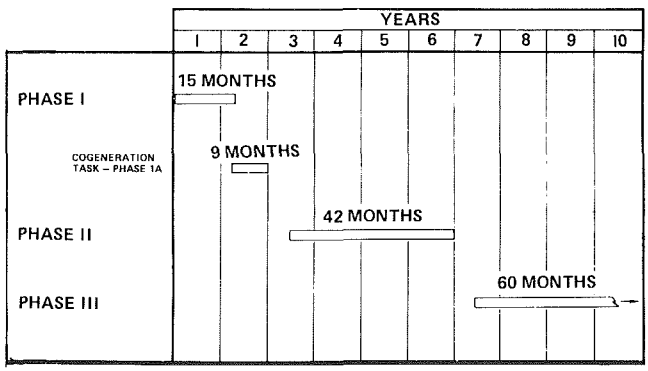

Fig. 1 Advanced heat exchanger (overall program schedule)

Current Program

Previous studies have identified four heater designs: two operating at a turbine inlet temperature of 1550°F (metal heat exchangers, one with a pulverized coal (PC) combustion system and one with a fluidized bed (FB) combustion system), and two operating at 1750°F or above turbine inlet temperatures (both requiring ceramic heat exchangers and operating with fluidized bed combustion systems). Technical issues relative to these designs were identified (Table 1).

A program for Phase 2 was designed to address the technical issues and maximize the amount of information generated for all designs that would allow a choice for building a complete operating module in a subsequent program phase. The prime issue is one of corrosion/erosion of materials versus cost for the various designs.

Work to be accomplished meant that test facilities would have to be identified or built (Table 2), test articles designed and built, test plans devised, and a study made to outline the best program for later efforts.

A philosophy evolved that said that the state-of-the-art for ceramic technology was such that during the course of this contract only basic research could be conducted to enlarge the engineering data base available for HEX design work and address the joining problems of ceramic to ceramic or ceramic to metal. About 10 percent of the effort would be devoted to ceramic technology for future designs.

Research and development work for pulverized coal systems could utilize existing pulverized coal boilers and thus minimize the need for expending a large amount of contract money for pulverized coal test facilities. The pulverized coal program was designed to conduct cold-flow modeling to understand mixing processes that govern the progress of combustion, flame stability, and dilution by recirculated

Contributed by the Gas Turbine Division of THE AMERICAN SOCIETY OF MECHANICAL ENGINEERS and presented at the 27th International Gas Turbine Conference and Exhibit, London, England, April 18-22, 1982. Manuscript received at ASME Headquarters December 14, 1981. Paper No. 82-GT-164.

Table 1 Major technical issues

Dry bottom pulverized coal

- High temperature corrosion/material cost
- Uniformity and limitation of furnace heat flux
- Minimization of working fluid, ΔP
- Hot gas side cleanliness
- Fired heater economics

Low temperature fluidized bed

- Corrosion/erosion versus material cost
- Bed/CCGT interactions—location, control, etc.
- Bed economics—sizing, no. units, Ca/S

High temperature fluidized bed

- All the metals issues of low-temperature bed
- All the bed issues of low-temperature bed
- Ceramics materials issues
- Series bed emission issues
- Series bed materials issues
- Series bed emission issues
- Series bed economic issues

Very high temperature slagging heater

- All the metals issues of dry bottom PC
- Ceramics materials issues
- Slagging combustor NOX issues

Table 2 High-temperature heat exchanger experimental facilities

	1650 F AFB	Series AFB	PC
24-in. dia. AFB*	X	X	-
18- by 18-in. AFB**	X	-	-
6- by 6-ft. AFB**	X	-	-
Ceramics**			
Corrosion/erosion	-	X	-
Ceramic/metal joint	-	X	-
Materials laboratory*	X	X	X
PC burner - EGR*			
Cold flow	-	-	X
Hot fire	-	-	X

*Battelle Columbus Laboratories
**Rockwell International

exhaust gas and to optimize the heat flux distribution in the furnace. Hot tests in a lab facility would establish the preferred mechanism for introducing exhaust gases into the combustion chamber. Corrosion/erosion tests could be conducted with selected materials in selected locations within existing boiler facilities.

The AFB program consists of three parts. Under a company-sponsored program, an 18- × 18-in. AFB test facility has been built at Rocketdyne. Work will continue with this facility, concentrating on tests which would explore upset conditions that could occur. These conditions will include such cases as plugged air inlets, loss of coolant, or slumped bed. It was reasoned that these types of tests would be better conducted with a small facility than with a more expensive, larger facility.

Battelle had a circular 24-in. AFB available from previous programs, which could be modified for use on this program. BCL's facility could be used to characterize bed operation under the operating conditions desired, and research with oxygen and corrosion probes would give use detailed AFB operating data not previously known.

A 6- × 6-ft AFB test facility is being built at Rocketdyne to capitalize on the knowledge generated by the 18- and 24-in. work and perform duration tests with the selected materials.

The pulverized coal effort is about 15 percent of the total program with the AFB work equal to 75 percent.

Program Organization

The team organized to accomplish this work is illustrated in Fig. 2.

With Rocketdyne as the prime contractor, team members include Battelle, because of their background in materials research and coal combustion, Solar, because of their experience with small gas turbines, General Electric, with their large gas turbine background and previous systems studies, General Atomics, with a background in closed cycles, Burns and Roe, with their understanding of balance of plant equipment, and Riley Stoker/Babcock Contractors, with commercial experience in building fluidized beds/boilers. This team promises to provide all the necessary expertise to meet the program objectives.

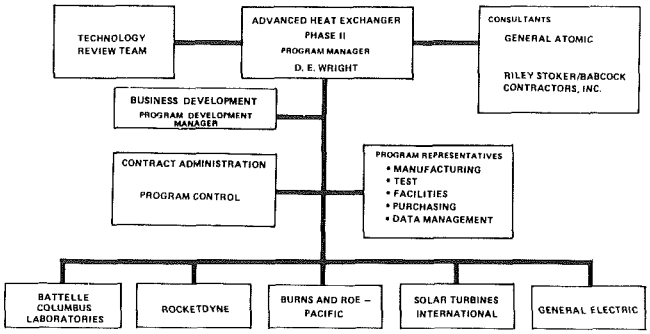

Fig. 2

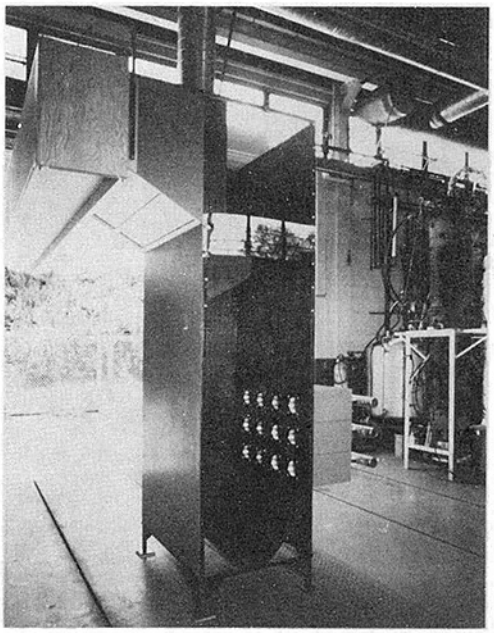

Fig. 3 Cold-flow model of front-fired furnace

Pulverized Coal-Fired Heater Program

The pulverized coal burner and furnace development program is being conducted at the Battelle Columbus Laboratory (BCL) facilities in Columbus, Ohio, to examine and refine designs for control of furnace heat flux. The primary mechanism is through the use of exhaust gas recirculation (EGR). In a commercial pulverized coal furnace designed for CCGT service, it is required to control and limit the local intensity of thermal radiation, and this is achieved by feeding cool flue gases from the convection pass exhaust back into the flame zone. This development program includes cold-flow testing of burner and furnace designs, hot-fire testing of burner designs, and exposure of metallic heater materials specimens in existing commercial boilers.

Individual cold-flow burner testing was conducted under controlled and measured conditions, in which the variables were primary air, secondary air, and recirculated flue gas (EGR), as well as burner configuration. Various methods of

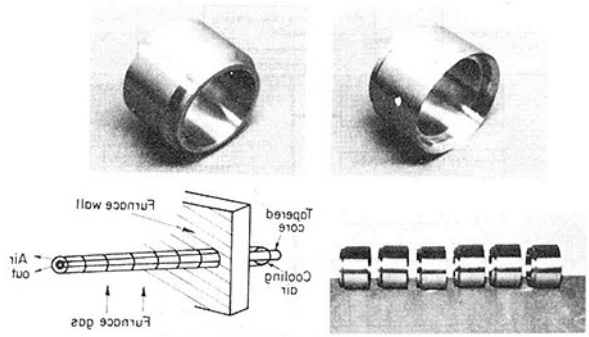

Fig. 4 Material specimen probes

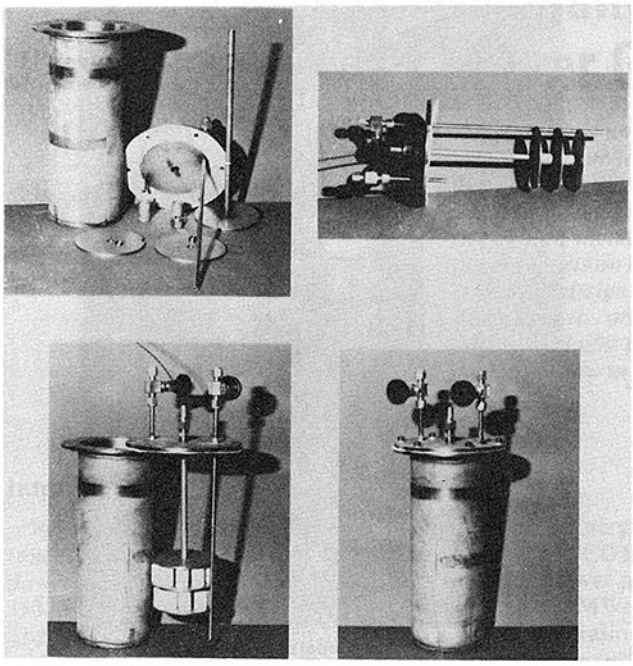

Fig. 5 Salt corrosion furnace

injecting the flue gas were experimentally evaluated, which avoided direct dilution in the stabilizing zone, and a candidate burner configuration was developed for further evaluation.

A 0.15-scale, cold-flow model of a front-fired furnace was constructed (Fig. 3), and cold-flow studies were carried out to define the degree of mixing of the fuel with combustion air, and of recirculated flue gas with combustion products. In both the furnace and burner cold-flow testing, measurements were taken to determine the degree of mixing of the various fluid streams and local velocity.

The burner configuration developed from the cold-flow program will be verified in a single-burner, hot-fire test program. This program will verify the stability of the flame, and measurements will be made of local heat fluxes.

Promising metallic heat exchanger materials will be screened by exposure in commercial boilers under actual combustion conditions. In this way, results can be obtained under actual combustion conditions and compared to laboratory test sample results. The design and construction of the material specimen probes (Fig. 4) is being completed, and selection of three sites is nearing completion.

Metallic Laboratory Program

The metals laboratory program is being conducted at Battelle Columbus facilities in conjunction with the pulverized coal field and AFB experimental unit testing. Candidate heat exchanger materials are being experimentally

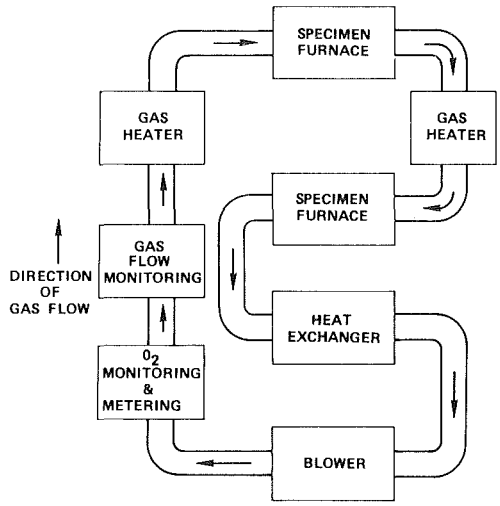

Fig. 6 Working fluids material test rig

assessed for the pulverized coal (PC) combustor, atmospheric fluidized bed (AFB) combustor, and the working fluid environments.

The pulverized coal laboratory program is investigating the corrosion behavior of metallic specimens in the presence of a deposit of flyash. Alkali-iron-trisulfate has been identified as the major corrosive species, which is molten above 1050°F and unstable above 1350°F. Hence, the corrosion studies have been divided into two distinct regimes to address the two temperature ranges and salt-type combinations. At the temperature range of 1050–1350°F, specimens were exposed up to 500 hrs to an equimolar mixture of potassium and sodium iron-trisulfate salt in especially built laboratory furnaces (Fig. 5). The exposed specimens were cathodically descaled and weight loss data determined to develop a criteria for selection of the most corrosion resistant materials. (Results are being presented in another paper at this conference). For tubes that operate in the 1400–1700°F range, these materials could also experience operation at the lower temperatures due to load changes or an outage. Therefore, specimens will be cycled between 1250 and 1650°F in the salt environment exposure. This program will consist of 25 hrs of each temperature, with exposures up to 500 hrs.

The AFB laboratory program consists of controlled tests in simulated AFB environments that are designed to facilitate the interpretation of corrosion data obtained from exposure of material specimen probes in the 24-in. dia and 6- by 6-foot fluidized bed combustors. These tests include exposure of specimens at: (*i*) steady-state oxygen partial pressure (P_0) in a gaseous environment, (*ii*) steady-state P_0 in a gaseous environment and deposits of $CaO/CaSO_4$, and (*iii*) oscillating P_0 in a gaseous environment. A primary variable will be the P_0, where the range of interest is derived from tests with the 24-in. dia AFB, and P_0 levels as low as 10^{-14} atmospheres were measured. The SO_2 partial pressure is generally controlled to correspond to the equilibrium conditions at a given P_0 level. These tests are being conducted at a (simulated bed) temperature of 1650°F with exposures up to 250 hrs.

The heat exchanger materials are also subject to attack from the working fluid of which air and helium are proposed. A special test rig was designed (Fig. 6) to simulate heat exchanger metal and gas temperatures, gas velocity, and helium to oxygen ratios. This rig is a closed-loop circuit with specimens exposed at two temperatures (1000 and 1600°F), and tests are being conducted with both air and helium, with exposures up to 1000 hrs. After exposure, the specimens will be metallurgically examined to determine the depth and type of attack, and the extent of depletion of chromium.

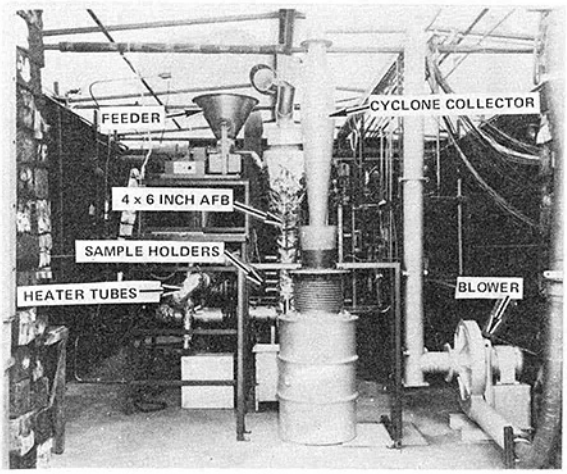

Fig. 7 4- by 6-in. AFB test facility

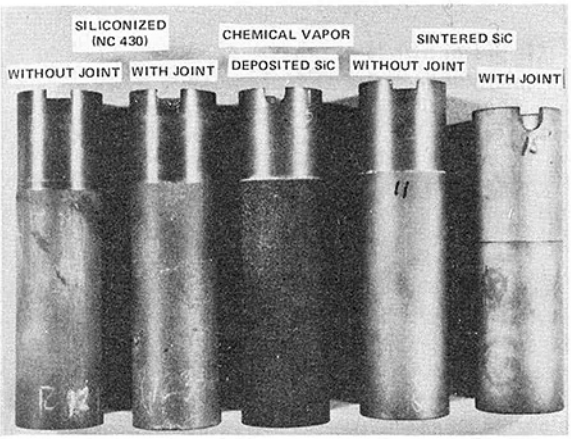

Fig. 8 Ceramic tube samples (as-fabricated condition)

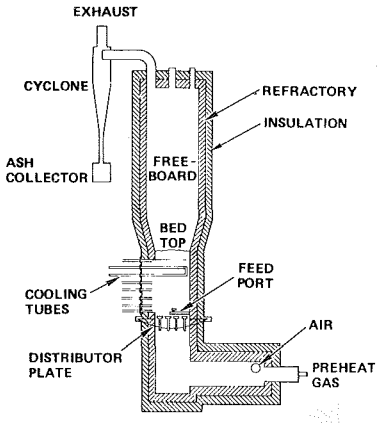

Fig. 9 Fluidized bed reactor

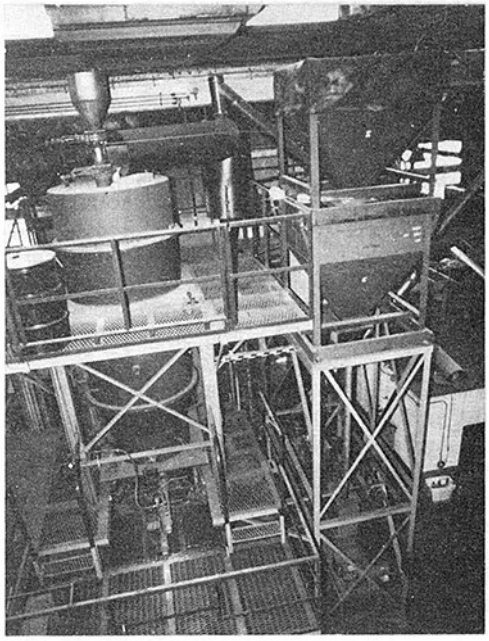

Fig. 10 24-in. fluidized bed reactor

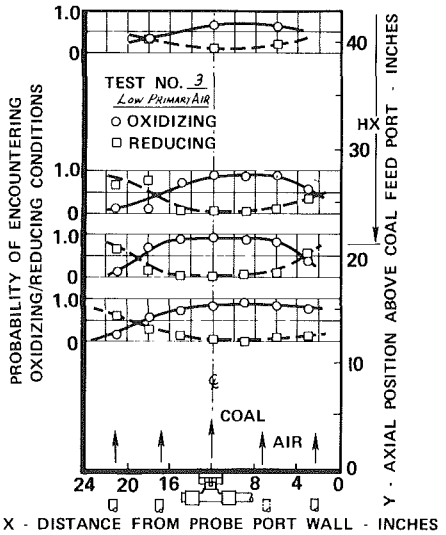

Fig. 11 Probability of encountering oxidizing/reducing conditions

Ceramics Program

Significant gains in cycle efficiency can be achieved through higher working fluid temperature (1750°F) and ceramic heat exchanger surfaces. A series of laboratory and atmospheric fluidized bed heater experiments has been designed to demonstrate the feasibility of the high-temperature series AFB-fired heater concept by showing that ceramic tube materials are durable in the AFB environment. To this end, design data on candidate silicon carbide (SiC) will be obtained. Laboratory evaluation, types and sources, of SiC will be compared in an AFB environment, and a ceramic-to-metal joint will be developed and tested. The primary experimental task includes: (*i*) exposure of ceramic specimens in a 4- by 6-in. unfired fluidized bed, (*ii*) exposure of ceramic specimens in the 24-in. dia fired AFB, and (*iii*) pressure and temperature cycle testing of ceramic-to-metal joints.

SiC is one of the most erosion resistant materials available, and the oxidation rate is negligible at 1800°F. However, it is possible that the oxidization rate could be accelerated in the AFB environment by removal of the protective layer of SiC by erosion. For example: a 4- by 6-in. fired AFB test rig was built (Fig. 7) to expose tube samples (Fig. 8) in a simulated fluidized bed environment at 1800°F. Fluidizing air was preheated to 1800°F with a bed of used bed material (Georgetown University atmospheric fluidized bed combustor), and steady-state runs were conducted at superficial velocities from 6 to 18 ft/s for 100 hrs each. The specimens were evaluated by measuring changes in weight, wall thickness, microstructure, and strength (burst tests), and these promising results indicate that SiC does not experience corrosion or erosion in the fluidized bed environment.

Other tests were conducted using strain-gaged ceramic and

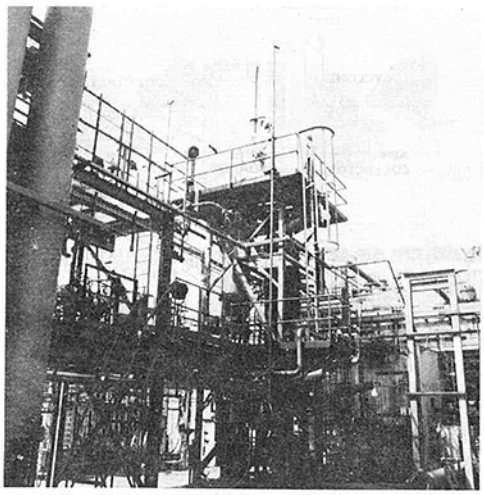

Fig. 12 18- by 18-in. AFB/CCGT experimental unit

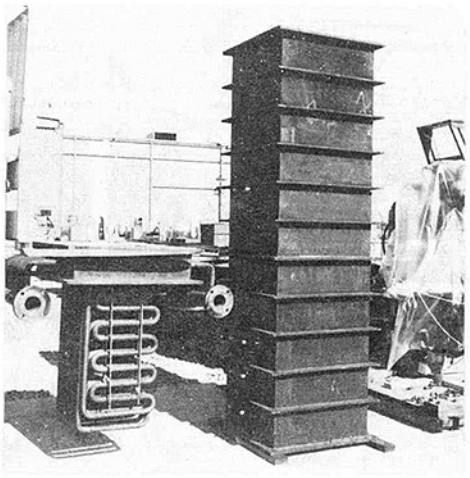

Fig. 14 18- by 18-in. AFB heat exchanger

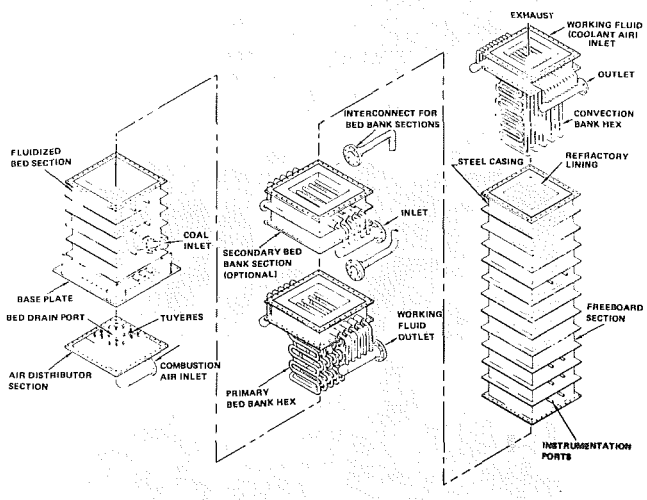

Fig. 13 18- by 18-in. AFB heat exchanger

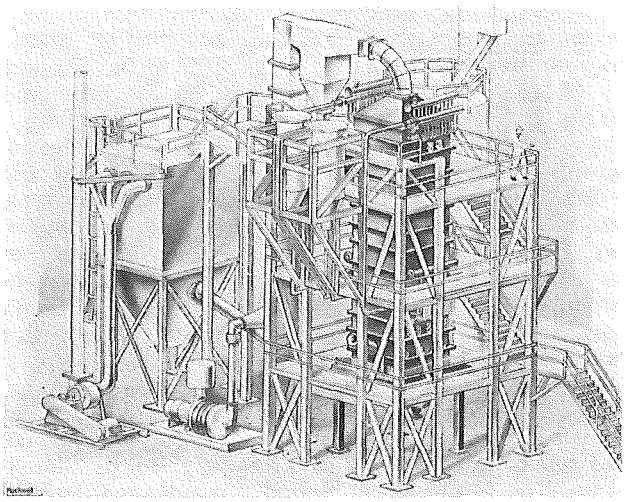

Fig. 15 6- by 6-ft closed-cycle gas turbine AFB experimental facility

metallic tubes in the 24-in. dia AFB to determine bed loads and establish design criteria for ceramic heat exchanger tubes. An upcoming series will be conducted where ceramic tube specimens will be exposed for 250 hrs in the fired 24-in. atmospheric fluidized bed. Designs are currently being developed for ceramic-to-metal joints, and candidate configurations will be fabricated and tested in a test rig that will cyclically vary the material temperatures and pressures.

Fluidized Bed Programs

The AFB programs have been organized to address two major technology areas. One area is the identification of heater materials, and design and operating practices that permit the economical and competitive design of CCGT/AFB fired heaters. The other area is the adaptation of the technology of fluidized bed combustion from steam boiler practice to the special needs of the CCGT fired heater. The three fired AFB facilities are being utilized to meet these goals. The first two facilities are currently operating (the 24-in. dia AFB and the 18- by 18-in. AFB) while the 6- by 6-ft facility is nearing completion.

24-In. Dia. AFB. This facility was an existing facility, located at Battelle Columbus Laboratory in Columbus, Ohio, which was specifically modified for this program. The unit was a 24-in. dia bed with air-cooled heat exchanger tubes to control bed temperature and a single coal feed port (Fig. 9 and 10). Since this was an existing facility, it was modified and activated early in the program to support laboratory work and to provide design information for the larger 6- by 6-ft unit. A series of programs has been designed to address the various technical issues, which are: (*i*) characterization of the CCGT fluidized bed and combustion environment, (*ii*) long-term (250 hr) exposure of metal specimens, (*iii*) simulation of the low-temperature bed of a series bed system, and (*iv*) operation of the high-temperature bed of a series bed system with exposure of ceramic tube specimens.

To date, the characterization tests have been conducted and significant data have been collected with research probes exploring combustion zones for oxidizing and reducing potentials. Physical design of coal ports and other factors affecting the operating conditions have been examined as to their relation to the combustion process and creation of "healthy" environment for the heat exchanger materials. Transverse probe data across the combustor, as shown in Fig. 11, have identified regions of oxidizing and reducing potential, and changes in the bed design and operating parameters can be directly accessed with this technique.

The work with the 24-in. facility was expanded with tests at the Babcock and Wilcox 6- by 6-ft boiler facility located at Alliance, Ohio. These tests showed a correlation in that the P_0 probes could be used to identify similar zones on combustion as previously noted, and these data are expected to be directly applicable to the CCGT 6- by 6-ft AFB facility being built at Rocketdyne.

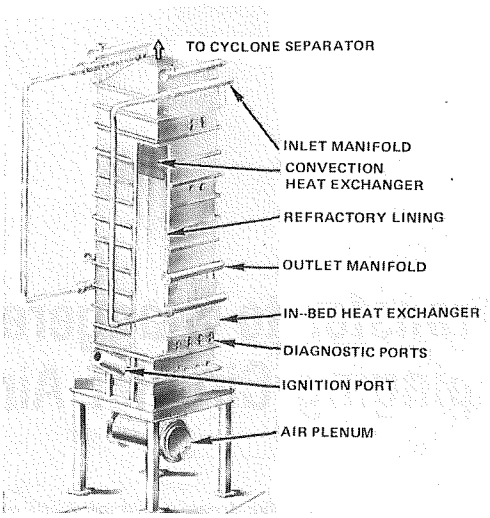

Fig. 16 6- by 6-ft AFB combustor/heat exchanger

Fig. 17 Erection of CCGT/AFB test platform

18- by 18-½n. AFB. This facility, shown in Fig. 12, was built and is being operated under company sponsorship at the Rockwell Thermodynamics Laboratory in El Segundo, Calif., to explore technology issues of the CCGT/AFB. The design features of this AFB unit are similar to the larger scale 6- by 6-ft AFB and proposed commercial design, including rectangular cross section, refractory liner with steel ribbed casing, in-bed tube bank, and convection tube bank, as shown in Figs. 13 and 14.

This facility is being used to resolve design issues of the CCGT application, such as operation of the relatively high bed and verification of the heat transfer with the high-temperature heat exchanger. This facility is also particularly suited to exploring upset conditions, such as plugged or failed tubes and loss of coolant. The philosophy is that it would be better to explore these issues with the smaller facility than the larger and more expensive 6- by 6-ft facility. To date, several tests have been conducted with bed temperatures up to 1800°F and heater output temperature of 1550°F. These tests have commissioned the facility and verified the heat transfer performance on the bed and heat exchanger with the high metal temperatures.

6- by 6-Ft AFB. This facility is located at the Rockwell Thermodynamics Laboratory in El Segundo, Calif., and facility construction began in the spring of 1981. The fired heater assembly has been completed and installed along with the auxiliary equipment. The facility (Fig. 15) has all the combustion side components typical of a commercial installation, including air heater, solids feed systems, cyclone, and baghouse, while the air working fluid is provided by the laboratory heater air system.

The system was designed to be a versatile investigation tool for exposing heater material specimens, diagnosing the combustion environment, and where practical, controlling the bed combustion environment. Where possible, auxiliary systems are typical of the commercial application. The fired heater (Fig. 16) has an in-bed and convection heat exchanger in a refractory lined setting, similar to proposed commercial designs. The heater unit has numerous access ports for specimen and diagnostic probes, and the heat exchangers have shortened loops in several locations that allow probes to be inserted into the midpoints of the heat exchangers. The specimen probes are cooled to control the specimen temperature, such that the exposure accurately simulates the condition of the candidate tube materials. Other probes are diagnostics for oxidizing and reducing zones, gas analysis, and bed loading.

The heater and its equipment have been designed for a wide range of operational capability where superficial velocity can be from 2 to 8 ft/s. Other features are capability of ash recycle, up to three times the cold feed rate and independent control of the four coal feed points. The heater has a surrounding access platform (Fig. 17), which will provide easy access to the diagnostic ports, instrumentation, and equipment.

The facility is nearing completion and commissioning and activation will begin such that the test program will be underway during the latter part of the year. The current program consists of a series of characterization tests and corrosion/erosion tests with metal specimen exposure up to 250 hrs. The facility has the capability of further long term testing, and provisions have been made for future addition of a closed-cycle working fluid loop complete with turbogenerator, recuperator, and steam/water heat exchangers.

Phase 3

It is planned that a subsequent phase of this program will include the building and testing of a complete closed-cycle system (either pulverized coal or atmospheric fluidized bed) at a 10- to 20-MWe size located at a site that represents an actual location that can use this advanced technology for power generation purposes. This prototype system is expected to demonstrate:

1 The integrity of the components and system involved
2 Through long duration tests, the survivability of the tube materials selected for the in-bed and correction heat exchanger sections of the system
3 A more efficient way to burn coal
4 The economic feasibility of the concept

In addition, we expect to continue to expand our ceramics research to lay the groundwork for future heat exchanger configurations that will offer even more efficient power generation systems.

Acknowledgment

The research and development program discussed in this paper is funded by the U.S. Department of Energy under Contract DE-AC 01-80ET15020. The program manager is Mr. Carey Kinney.

Local Heat Transfer to Staggered Arrays of Impinging Circular Air Jets

A. I. Behbahani

R. J. Goldstein

Mechanical Engineering Department,
University of Minnesota,
Minneapolis, Minn. 55455

Measurements are made of the local heat transfer from a flat plate to arrays of impinging circular air jets. Fluid from the spent jets is constrained to flow out of the system in one direction. Two different jet-to-jet spacings, 4 and 8 jet diameters, are employed. The parameters that are varied include jet-orifice-plate to impingement-surface spacing and jet Reynolds number. Local heat transfer coefficients vary periodically both in the flow direction and across the span with high values occurring in stagnation regions. Stagnation regions of individual jets as determined by local heat transfer coefficients move further in the downstream direction as the amount of crossflow due to upstream jet air increases. Local heat transfer coefficients are averaged numerically to obtain spanwise and streamwise-spanwise averaged heat transfer coefficients.

Introduction

An effective way of cooling or heating a surface is to use impinging fluid jets, often air jets. Not only are high local heat transfer coefficients attained, but by using a number of jets, the surface heat transfer distribution can be controlled. Applications of impinging jets include paper drying, tempering and cooling of glass plates, and the cooling of electronic components, flat-plate solar collectors and gas turbine components.

In many applications the jet air after impingement is constrained to exit from the system in one direction. The spent air from upstream jets imposes a crossflow on downstream jets.

Earlier studies reported measurements of the local heat transfer from single jets in a crossflow [1, 2, 3], the average heat transfer from a row of jets, [4], and the average heat transfer for an array of jets [5]. Recent measurements have been made of the variation in the mean flow direction of the heat transfer averaged across the span of a plate for various jet configurations [6, 7, 8, 9].

The present investigation was undertaken to determine the two-dimensional distribution of local heat transfer from a plate to an array of staggered circular impinging jets. All geometrical parameters are nondimensionalized using the jet diameter, D. Two jet orifice plates with different jet-to-jet spacing, $S/D=4$ and 8, were used. For each S/D, four jet-orifice to impingement-plate spacings were employed ($Y/D=2$, 3, 4, 5). The flow rate was characterized by the Reynolds number, Re_j based on the average jet velocity. Three different Reynolds numbers, Re_j = 5,000, 10,000, and 15,000 were used. The local Nusselt number is presented as a function of these parameters defined above. The local heat transfer coefficients are numerically integrated to obtain an average of Nusselt numbers across the span, $\overline{\mathrm{Nu}}$, and over the plate surface, $\bar{\bar{\mathrm{Nu}}}$ (see Fig. 2).

Experimental Apparatus and Operation Procedure

Apparatus. Only a brief description of the apparatus is given here. For further details, the reader is referred to reference [10].

Air for the jets is supplied by the building compressor. After filtration and regulation, the air is metered by a thin orifice plate and passes into the plenum chamber from which it is distributed to the individual orifices on the jet-orifice plate via vinyl and stainless steel tubes. The mass flow rate is taken to be the same for each individual jet. Based on the analysis of [9], the range of variation of the main flow from a single jet to the average jet mass flow for the extreme condition (smallest Y/D and largest mass flow) varies from 0.96 to 1.10. Figure 1 shows details of the jet-orifice plate and an injection tube. Two different jet-orifice plates, one with D = 5 mm and the other with D = 10 mm, were used. Each jet-orifice plate has 18 jets positioned in staggered arrays such that each jet is a distance, S, from its nearest neighbor with S = 40 mm. The jet-orifice plate is flush with the top of one of several frames which provide the desired jet orifice plate to impingement plate spacing. These frames form part of the walls of the test section beneath the jet-orifice plate.

The test section is 103-cm long by 20.3-cm wide with 1.9-cm thick side walls. The bottom wall (the impingement plate) is made of 0.16-cm thick textolite backed by 5-cm thick styrofoam. The heater surface consists of 18 stainless steel heating foils 0.0254-mm thick and 5-cm wide. They span the entire 24.10-cm width of the test surface and have an unheated gap of only 0.04-mm between any pair. The heat flux, q_w, during heated runs was approximately 1300 W/m^2.

Contributed by the Gas Turbine Division of THE AMERICAN SOCIETY OF MECHANICAL ENGINEERS and presented at the 27th International Gas Turbine Conference and Exhibit, London, England, April 18–22, 1982. Manuscript received at ASME Headquarters December 15, 1981. Paper No. 82-GT-211.

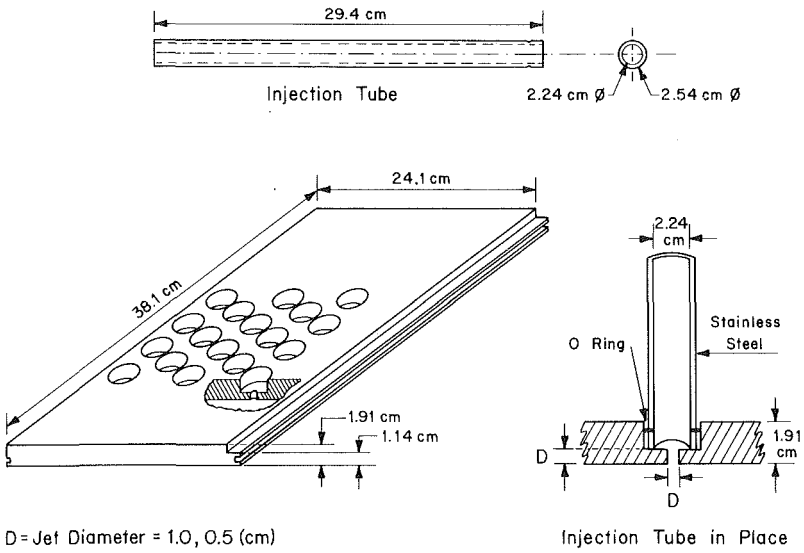

Fig. 1 Jet orifice plate

Silicon rubber cement is used to fasten the heaters to the textolite backing. One hundred twelve (112) 36-gauge iron-constantan thermocouples are embedded in the textolite plate in contact with the heating foils via copper oxide. Many thermocouples (46) are located on the centerline of the test plate. The jet orifice can be set at different lateral positions to obtain off-centerline data.

To keep a constant distance between the jets and the side walls with the lateral movement of the jet-orifice plate, two inner walls made of 0.5-cm thick masonite material are attached to the jet orifice plate via slots. These inner walls run the entire length of the test section. There is one set of inner walls for each jet orifice-to-impingement plate spacing used (see Fig. 2).

A Fluke 2240A data logger with a maximum uncertainty in reading thermocouple output of $\pm 2.4\ \mu$ volts ($\simeq 0.05°C$) and a Multiteck FM 300 acoustic coupler were employed to collect and transmit data via telephone lines to a CDC Cyber 74 computer system at the University of Minnesota.

Experimental Procedure. Measurements at different locations across the span showed symmetry about the central row of holes. Data representative of a large expanse of jets could then be taken in region $0 \le Z \le 20$ mm.

In each experimental run the flow rate is adjusted to give the desired Re_j and then, after reaching steady state, the adiabatic wall temperature (essentially the recovery temperature, $q_w = 0$) is recorded at $Z = 0$. The jet-orifice plate is then moved so that the centerline of the tunnel floor and the large number of thermocouples along it are at $Z = 5$ mm, and after steady state is reached, the next set of data is recorded. The above procedure is repeated until $Z = 20$ mm.

After all adiabatic wall temperature measurements are taken for a given set of test conditions, the jet-orifice plate is moved back to $Z = 0$ and the current through the heating foils is started. Then a procedure similar to that for the adiabatic wall measurement is followed at the same Re_j. In addition, the voltage drop across the heating foils and current are recorded at each spanwise location. This provides heat flux to each heating foil. This heat flux is corrected for lateral conduction in the X- and Z-directions due to the temperature gradient along the wall, conduction to the back of the heating wall, and radiation.

Results and Discussion

The local heat transfer is defined by

$$h = \frac{q_w}{(T_w - T_{aw})} \tag{1}$$

where q_w is the heat flux corrected for conduction to the back of the test surface, lateral conduction, and radiation. Use of $(T_w - T_{aw})$ as the driving force for heat flux in the definition

Nomenclature

D = jet diameter
h = local heat transfer coefficient, $h = q_w/(T_w - T_{aw})$
$\bar{h}$ = heat transfer coefficient averaged over area shown in Fig. 2
k = thermal conductivity of air evaluated at $(T_w + T_j)/2$
$\dot{m}_j$ = mass flow rate of an individual jet
Nu = local Nusselt number, $\mathrm{Nu} = hD/k$
$\mathrm{Nu}_{\max}$ = maximum local Nusselt number at a given Y/D and a given jet Reynolds number
$\overline{\mathrm{Nu}}$ = Nusselt number averaged across the span (Z-direction)
$\overline{\overline{\mathrm{Nu}}}$ = area-averaged Nusselt number, $(\bar{h}D/k)$
q_w = heat flux at wall determined from electrical energy input per unit area of heated surface modified for conduction and radiation effects
Re_j = jet Reynolds number, $\mathrm{Re}_j = (\rho u_j D/\mu)$
S = jet center-to-center spacing
T_j = jet static temperature
T_j° = jet total temperature
T_{aw} = local adiabatic wall temperature
T_w = local wall temperature
u_j = average jet-exit velocity, $(4\dot{m}_j/\rho\pi D^2)$
X,Z = coordinate system, see Fig. 2
Y = jet-orifice-plate -to- impingement-plate spacing

Greek Symbols

μ = viscosity of jet evaluated at T_j
ρ = density of jet evaluated at T_j

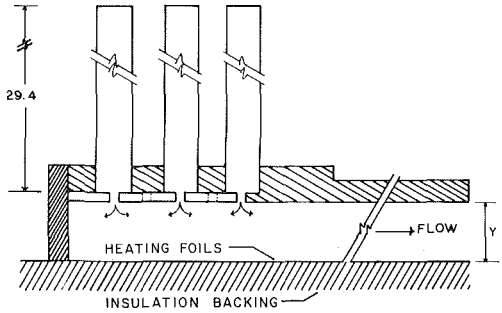

DIMENSIONS ARE IN CENTIMETERS

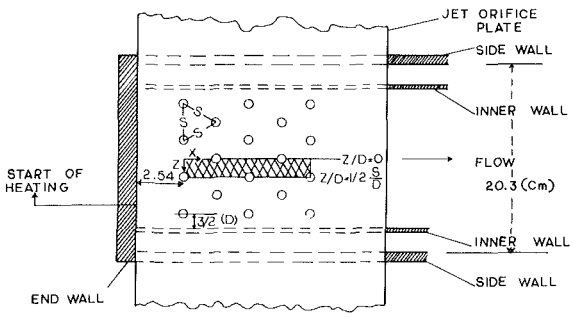

DOUBLE CROSS HATCHED AREA USED IN COMPUTATION OF AREA AVERAGE HEAT TRANSFER COEFFICIENT

GEOMETRICAL CENTER OF ROWS OF HOLES ARE AT; X = 0, 3.46, 6.93, 10.39 AND 13.86 CM.

Fig. 2 Test section and coordinate system

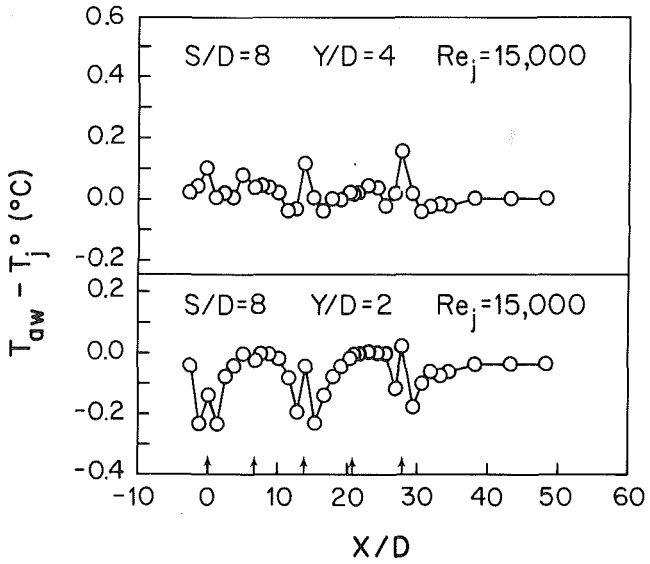

Fig. 3 Adiabatic wall temperature

of h is well established [11, 1]. Figure 3 shows the variation of T_{aw} for two sample runs. This variation in adiabatic wall temperature can be compared to the minimum value of $(T_w - T_{aw})$ of about 3°C for Re_j of 15000 and $Y/D = 2$ in the stagnation region.

The local Nusselt number, Nu, is defined by

$$\mathrm{Nu} = \frac{hD}{k} \tag{2}$$

Nu is averaged numerically over five positions across the span to give $\overline{\mathrm{Nu}}$

$$\overline{\mathrm{Nu}} = \frac{2}{S}\int_0^{S/2} \mathrm{Nu}(X,Z)\,dZ \tag{3}$$

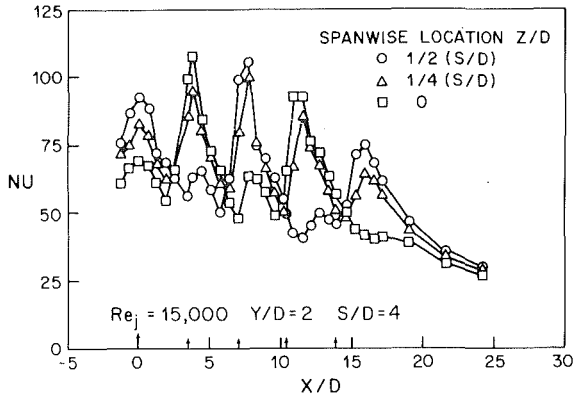

Fig. 4(a)

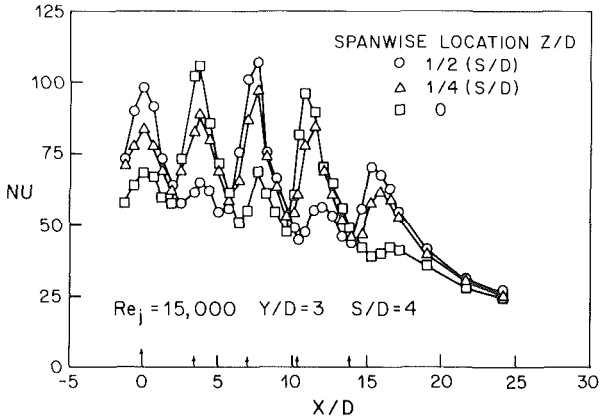

Fig. 4(b)

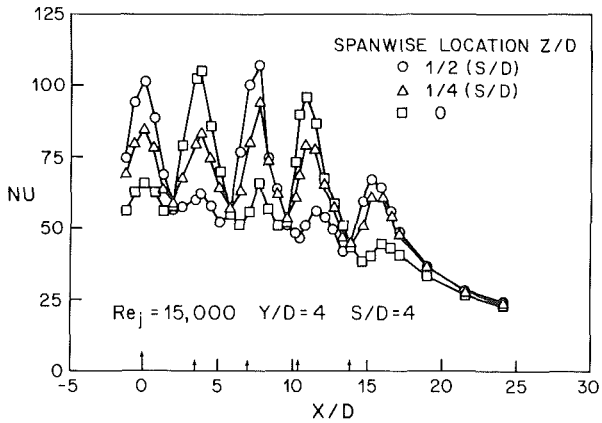

Fig. 4(c)

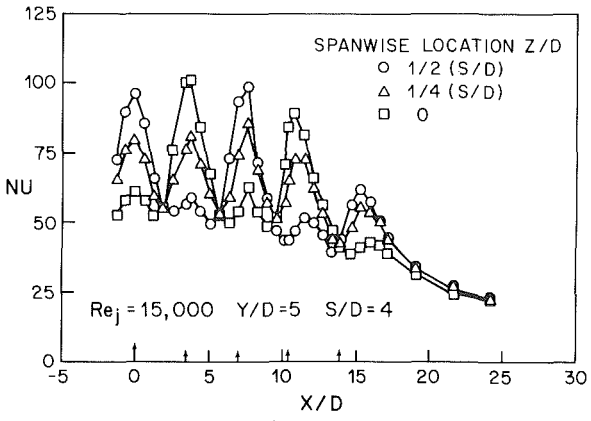

Fig. 4(d)

Fig. 4 Local Nusselt number for jet-to-jet spacing (S/D) of 4

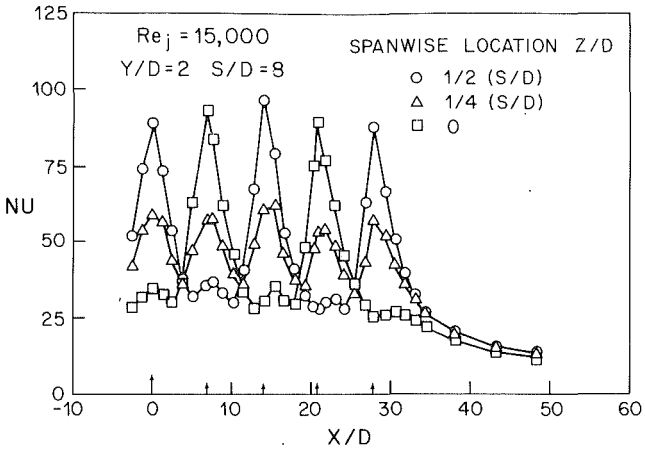

Fig. 5(a)

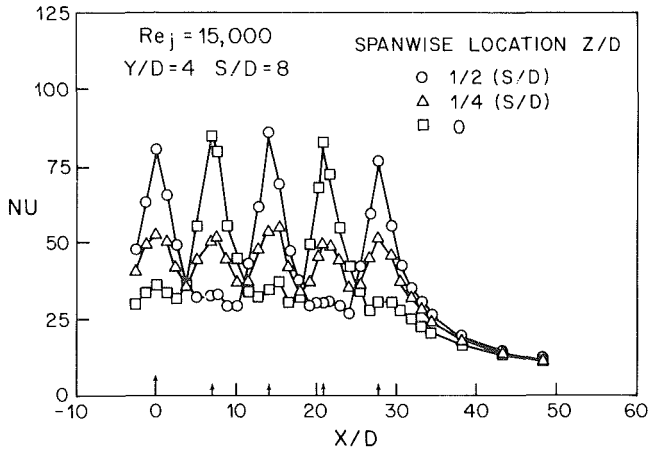

Fig. 5(c)

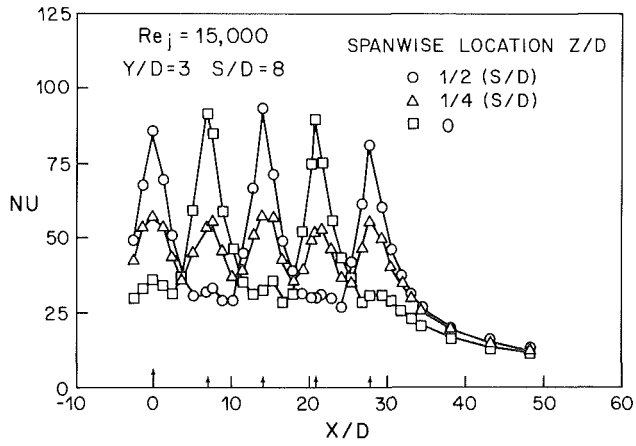

Fig. 5(b)

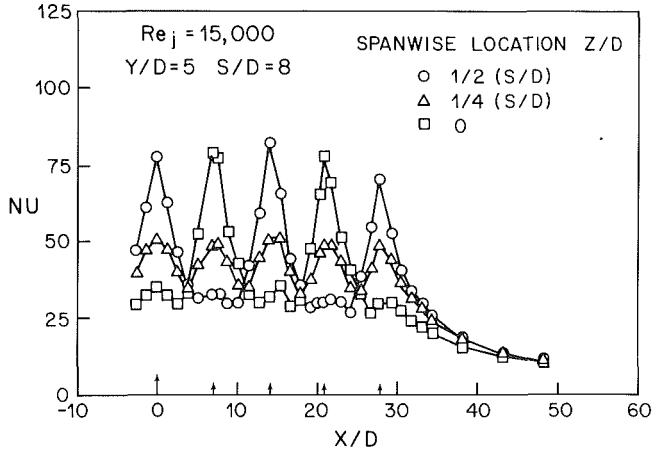

Fig. 5(d)

Fig. 5 Local Nusselt number for jet-to-jet spacing (*S/D*) of 8

The heat transfer over the plate from the first row of holes to the last row of holes is characterized by $\overline{\overline{Nu}}$ which is obtained by averaging Nu over the strip shown in Fig. 2.

Figures 4 and 5 are plots of Nu as a function of X/D for $S/D = 4$ and 8, respectively. Each figure has four graphs with each graph corresponding to a specific Y/D. Arrows on the abscissa indicate the geometrical location of the rows of jets. Each data point is from a single thermocouple along the centerline of the test plates. To conserve space, results are shown only for $Re_j = 15{,}000$.

A common feature of Figs. 4 and 5 is the periodic variation of Nu with X/D. Plots of Nu as a function of Z/D at X/D corresponding to the first row of holes and the last row of holes (Fig. 6), also show a periodic variation of Nu with Z/D. The highest values of Nu are found in the vicinity of the impingement zones of the rows of jets. Relatively high heat transfer occurs not only beneath the individual jets but at all spanwise locations beneath a row of jets (that is, at different values of Z for the X corresponding to a row of jets).

The value of Z/S corresponding to hole locations are 0 and 1/2 for alternate rows. At these Z, primary maxima occur at X locations corresponding to the stagnation regions of the rows with holes centered on these Z (i.e., every other row) and lower secondary maxima occur at X approximately half-way between these primary maxima. At Z/S of 1/4, moderate and approximately equal maxima occur at X corresponding to the stagnation flow from each row of holes. The maxima at $Z/S = 1/4$ are strongest at the smallest jet-orifice-plate-to-impingement-plate spacing, $Y/D = 2$, and they decrease as Y/D increases. This can be attributed to the high radial velocity of jets in the deflected region as the spacing Y/D is decreased. Occurence of high Nu between jets at small Y/D was also observed in a study of impingement of a single row of jets [12].

The graphs of Fig. 4 show that although the largest value of Nu_{max} occurs when $Y/D \simeq 4$ (Fig. 4(*c*)), there is little variation for the first four rows of holes until $Y/D \simeq 5$ (Fig. 4(*c*)). For impingement of a single jet, the maximum transfer coefficient was found in different investigations to be at $6 \leq Y/D \leq 7$ [11], at $Y/D = 6$ [13], and at $Y/D = 8$ [14]. For a row of jets, the maximum Nu occurs at $4 \leq Y/D \leq 6$ [12]. In a study of impingement of a single jet in the presence of crossflow [2], the maximum heat transfer coefficient occurred at $Y/D \leq 3$ for low values of the ratio of jet velocity to crossflow velocity.

The maximum Nu_{max} occurs at closer spacing, Y, with an array of jets than it does with a single jet. This difference in spacing at which the maximum Nu occurs can be understood by considering the influence of a crossflow on the turbulence in a jet. For a single jet, the arrival velocity is relatively unaltered within the so-called potential core but decreases at large spacing as a result of entrainment. The jet centerline turbulence intensity, low at small Y/D [15, 16], increases with Y/D. These two factors (lower arrival velocity and higher turbulence intensity) lead to maximum in Nu at some intermediate spacing. With multiple jet impingement, the jet centerline turbulence intensity at small Y/D is increased by mixing with the spent flow from neighboring jets, as also

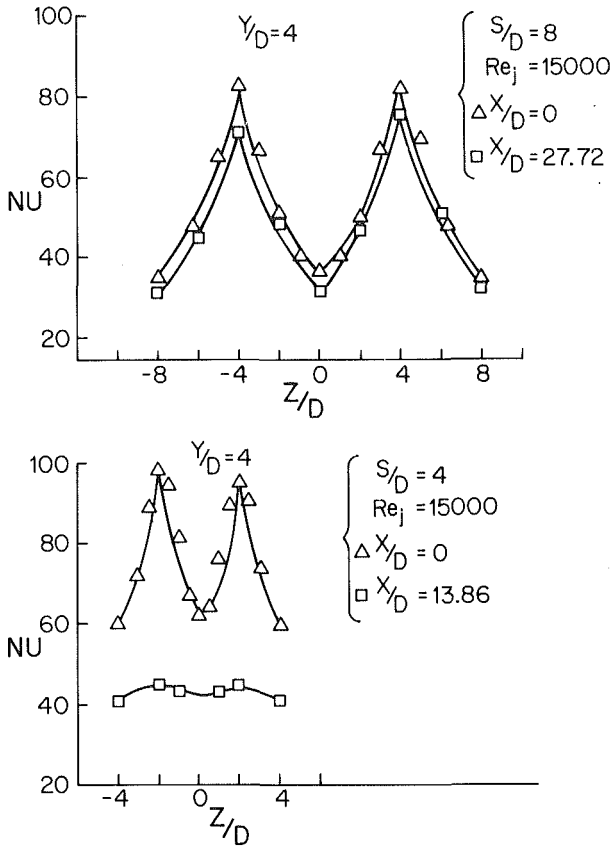

Fig. 6 Local Nusselt number across the span

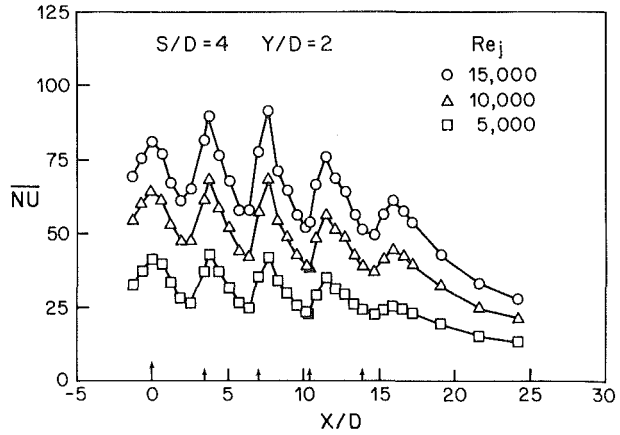

Fig. 7(a)

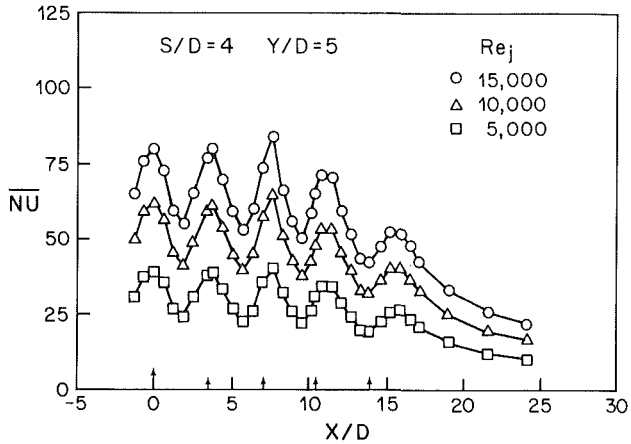

Fig. 7(b)

Fig. 7 Spanwise average Nusselt number for $S/D = 4$

occurs with a single jet in a crossflow. Then the Y value at which Nu_{max} is largest would be smaller than occurs with a single isolated jet.

The impingement positions (region of maximum Nu) for the rows of jets move further downstream as the average crossflow velocity increases. This is most evident for the fourth and fifth rows of jets. Comparing results at Re_j = 15,000 for $S/D = 4$ and $Y/D = 2$ and 5 (Fig. 4(*a*), 4(*d*)), Nu_{max} for the fifth row are moved downstream of the actual jet location by about 2.2 and 1.5 jet diameters, respectively. The higher average cross-velocity at small Y/D more than compensates for the closer spacing.

Inspection of Fig. 5 shows that the general trends of the data for $S/D = 8$ are similar to those for $S/D = 4$. Since the jet-to-jet spacing in this case is double (diameter is half) and the mass flow in a jet for the same Re_j is half that when $S/D = 4$, the heat transfer across the span between the jets is lower and the relative maxima of Nu between alternate rows of jets are lowered. For this particular spacing, the maximum Nusselt numbers for each of the different rows decrease with increasing Y/D. For this jet-orifice plate, the variations in peak Nu for different rows is not as great as for $S/D = 4$. This is attributed to the lower crossflow for $S/D = 8$. Also due to lower crossflow for $S/D = 8$, the maximum Nu are moved less in the streamwise direction. This is clear from Fig. (6) where Nu corresponding to the geometrical center of the last row of holes are closer to maximum Nu for $S/D = 8$ than $S/D = 4$.

Average Heat Transfer Coefficient. Figures 7 and 8 present heat transfer coefficients averaged across the span, $\overline{Nu}$, at two different spacings, $Y/D = 2$ and 5, and at Re_j = 5000, 10,000, and 15,000. Maximum $\overline{Nu}$ occur in the stagnation region for each row of jets. The peak $\overline{Nu}$ are moved further downstream as crossflow from the upstream jet air increases. This is most clear for the jet-orifice plate of S/D = 4 at $Y/D = 2$ (Fig. 7(*a*)), where the average crossflow velocity is the highest. Over the present range of conditions, the maximum value of $\overline{Nu}$ is almost independent of Y/D until $Y/D = 4$, after which it decreases with increased spacing.

Table 1

Y/D	a	n
2	0.0918	0.6262
3	0.0966	0.6610
4	0.10	0.6991
5	0.0954	0.7

Empirical correlation of the heat transfer coefficient averaged over the plate area, $\overline{\overline{Nu}}$, is presented in the form of

$$\overline{\overline{Nu}} = a Re_j^m (S/D)^{-n} \quad (4)$$

The exponent, m, was found from the best fit of the experimental data to be equal to 0.78, and the value of a and n are given in Table 1. Figure 9 shows this correlation in graphic form.

Although Nu is higher for a more dense array of jets (smaller S/D) at a given Re_j, a greater mass flow is present as compared to a less dense array. It is helpful to compare the heat transfer rates at the same mass flow of coolant per unit area of impingement surface, at least within the range of the present test.

Assuming a, m, and n are constant over the range of conditions of interest, equation (4) can be rewritten as

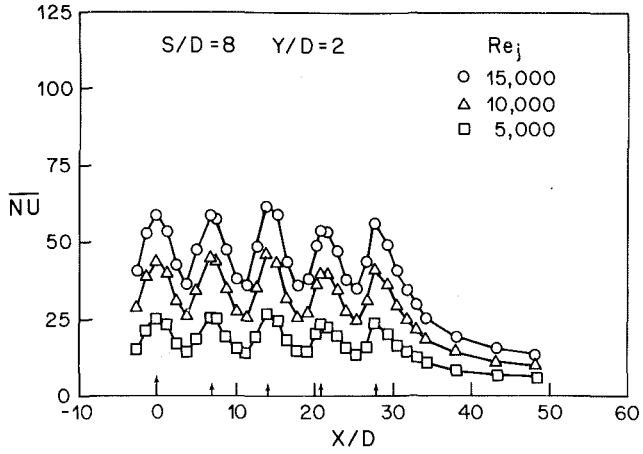

Fig. 8(a)

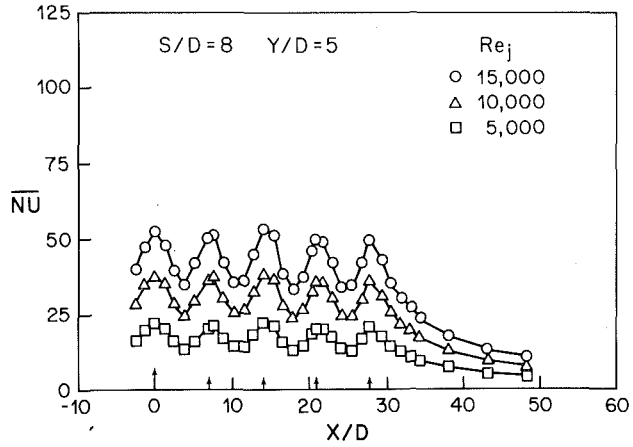

Fig. 8(b)

Fig. 8 Spanwise average Nusselt number for $S/D = 8$

$$\frac{\bar{h}D}{k} = a\left(\frac{4\dot{m}_j}{\mu\pi D}\right)^m (S/D)^{-n} \tag{5}$$

or

$$\bar{h} = \left\{\left[a\left(\frac{4}{\pi}\right)^m\right] k \left(\frac{\dot{m}_j}{\mu}\right)^m\right\} \frac{S^{-n}}{D^{1+m-n}} \tag{6}$$

Note that for a given mass flow rate per jet, $\dot{m}_j$, the heat transfer coefficient increases with decreasing S (less area to heat or cool) and with decreasing D (higher jet velocity and Re_j).

For a fixed mass flow per unit area of heat transfer surface, equivalent to a fixed value of $(2\dot{m}_j/\sqrt{3}S^2)$, consider

$$\bar{h} = \left\{\left[a\left(\frac{2\sqrt{3}}{\pi}\right)^m\right] k \left(\frac{2\dot{m}_j}{\sqrt{3}S^2}\,\frac{1}{\mu}\right)^m\right\} \frac{S^{2m-n}}{D^{1+m-n}} \tag{7}$$

With the values of m and n determined for the range of variables in the present study, the average heat transfer can be seen to increase with increasing jet-to-jet spacing (as S^{2m-n}).

Note that for constant flow rate per jet or per unit area of heat transfer plate,

$$\bar{h} \alpha D^{-(1+m-n)} \tag{8}$$

For the values of m and n obtained in the present test, this average heat transfer coefficient is approximately inversely proportional to D.

The average heat transfer coefficients measured in the present study are compared in Fig. 10(*a*) and 10(*b*) to values presented in [6]. The agreement between the two sets of data is quite good.

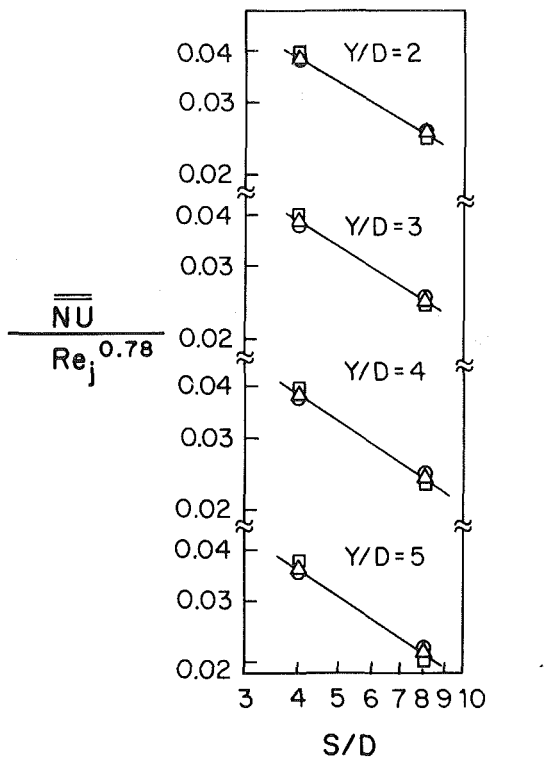

Fig. 9 Effect of *S/D* on the area-averaged Nusselt number (see equation 4 and Table 1)

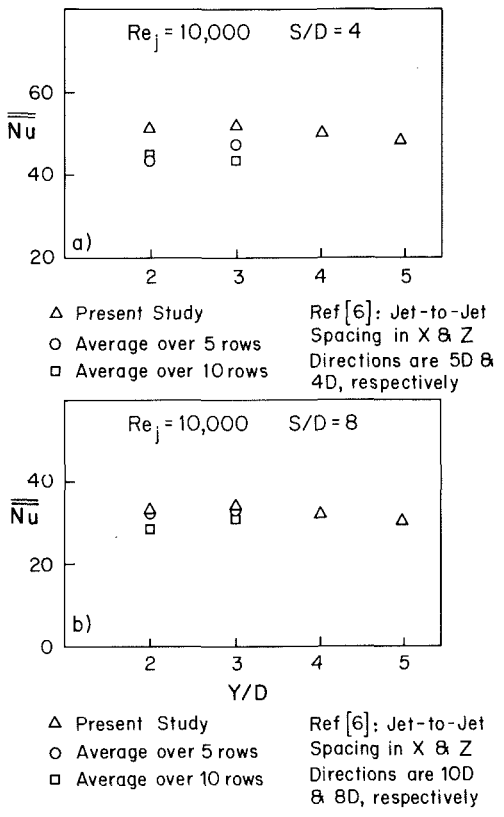

Fig. 10 Comparison of area-averaged Nusselt number

Concluding Remarks

The distribution of local Nusselt number is characterized by periodic variations in the streamwise direction as well as

across the span with peak values occurring under the jets and relative maxima of Nu between alternate rows of a staggered array of jets. The stagnation region as indicated by the relative maxima in Nusselt number are moved further in the streamwise direction as the average crossflow velocity, due to upstream jet air, increases.

The area-averaged Nusselt number has a weak dependence on jet-to-impingement plate spacing up to a value of four and then decreases at higher spacing. At a given jet Reynolds numbers, larger jet-to-jet spacing produces smaller area average Nusselt number since a larger heated area is cooled by the impinging jets. The area-averaged Nusselt number at a fixed mass flow of coolant per unit area transfer surface increases with an increase in jet-to-jet spacing. At constant jet-to-jet spacing and mass flow rate, the area averaged heat transfer coefficient is approximately inversely proportional to the jet diameter within the range of the present tests.

References

1 Bouchez, J. P., and Goldstein, R. J., "Impingement Cooling From a Circular Jet in a Crossflow," *International Journal of Heat and Mass Transfer*, Vol. 18, 1975, pp. 719–730.

2 Sparrow, E. M., Goldstein, R. J., and Rouf, M. A., "Effect of Nozzle-Surface Separation Distance on Impingement Heat Transfer for a Jet in a Crossflow," ASME *Journal of Heat Transfer*, Vol. 97, 1975, pp. 528–533.

3 Hollworth, B. R., and Bowley, W. W., "Heat Transfer Characteristics of an Impinging Jet in Crossflow," ASME Paper 75-WA/HT-100, 1975.

4 Metzger, D. E., and Korstad, R. J., "Effect of Crossflow on Impingement Heat Transfer," ASME *Journal of Engineering for Power*, Vol. 94, 1972, pp. 35–42.

5 Kercher, D. M., and Tabakoff, W., "Heat Transfer by a Square Array of Round Air Jets Impinging Perpendicular to a Flat Surface Including Effects of Spent Air," ASME *Journal of Engineering for Power*, Vol. 92, 1970, pp. 73–82.

6 Metzger, D. E., Florschuetz, L. W., Takeuchi, D. I., Behee, R. D., and Berry, R. A., "Heat Transfer Characteristic for In-Line and Staggered Arrays of Circular Jets with Crossflow of Spent Air," Gas Turbine Heat Transfer Conference, 1978, ASME Winter Annual Meeting, San Francisco, Dec. 1978, pp. 9–19.

7 Florschuetz, L. W., Berry, R. A., and Metzger, D. E., "Periodic Streamwise Variations of Heat Transfer Coefficients for In-Line and Staggered Arrays of Circular Jets with Crossflow of Spent Air," ASME Paper 79-WA/GT-11, 1979.

8 Saad, N. R., Mujumdar, A. S., Abdelmesseh, W., and Douglas, W. J. M., "Local Heat Transfer Characteristics for Staggered Arrays of Circular Impinging Jets with Crossflow of Spent Air," ASME Paper 80-HT-23.

9 Florschuetz, L. W., Truman, C. R., and Metzger, D. E., "Streamwise Flow and Heat Transfer Distributions for Jet Array Impingement with Crossflow," ASME *Journal of Heat Transfer*, Vol. 103, 1981, pp. 337–342.

10 Behbahani, A. I., "Heat Transfer to Staggered Arrays of Impinging Circular Air Jets," Ph.D. thesis, Department of Mechanical Engineering, University of Minnesota, Minneapolis, Minn., 1979.

11 Gardon, R., and Cobonpue, J., "Heat Transfer Between a Flat Plate and Jets of Air Impinging on It," *Proceedings of the 2nd International Heat Transfer Conference*, 1962, pp. 454–460.

12 Koopman, R. N., and Sparrow, E. M., "Local and Average Transfer Coefficients Due to an Impinging Row of Jets," *International Journal of Heat and Mass Transfer*, Vol. 19, 1976, pp. 673–687.

13 Tataoka, K., Komai, T., and Nakamura, G., "Enhancement Mechanics of Mass Transfer in a Turbulent Impinging Jet for High Schmidt Number," ASME Paper No. 78-HT-5.

14 Kieger, K. K., "Local and Average Heat Transfer from a Flat Surface to a Single Circular Jet of Air Impinging on It," M.S. thesis, Department of Mechanical Engineering, University of Minnesota, Minneapolis, Minn., 1981.

15 Gardon, R., and Akfirat, J. C., "The Role of Turbulence in Determining Heat Transfer Characteristics of Impinging Jets," *International Journal of Heat and Mass Transfer*, Vol. 8, 1965, pp. 1261—1272.

16 Yokobori, S., Kasagi, N., Hirata, M., Nakamaru, M., and Haramura, Y., "Characteristic Behavior of Turbulence and Transport Phenomena of the Stagnation Region of an Axisymmetrical Impinging Jet," presented at the 2nd Symposium on Turbulent Shear Flow, Imperial College, London, July 2–4, 1979.

A Theoretical Investigation of an Overhung Flexible Rotor Mounted on Uncentralized Squeeze-Film Damper Bearings and Flexible Supports

R. A. Cookson
Head of Applied Mechanics,
School of Mechanical Engineering,
Cranfield Institute of Technology,
Cranfield, Bedford, England

Xin-Hai Feng
Head of Vibration and Strength
Analytical Research Group,
Aero Gas Turbine Research Institute,
Chinese Aeronautical Establishment,
Peking, Peoples' Republic of China

Previous investigations have shown that the uncentralized type of squeeze-film damper is an effective means of reducing the transmission of unbalance forces into the supporting structure. In this theoretical study a more complex model, which includes an overhung "fan" disk and and a noncentral "turbine" disk has been employed. This model represents the conventional gas turbine somewhat closer than does the previously studied single disk system. This investigation has shown that it is possible to minimize the force transmitted into the surrounding structure by a careful selection of squeeze-film damper characteristics, although it may be found that some larger amplitudes of motion accompany the minimized transmissibility.

Introduction

Almost all of the work previously carried out on squeeze-film dampers has been limited to the case where the steady-state motion of the rotor center can be assumed to be a circular synchronous orbit around the bearing geometric center; for example, [1-3]. Concentration upon this particular model arose perhaps from the very simple modification to Reynold's equation for the case of a nonrotating journal. It was perhaps this trend which led some gas-turbine manufacturers to mount their squeeze-film dampers in parallel with a preloaded spring, usually in the form of a squirrel-cage, which located the rotor in the center of the clearance circle. Excursions of the rotor due to unbalance (say) would therefore always result in a circular motion around the clearance circle center. However, some manufacturers (in particular, Rolls-Royce Ltd.) decided to fit squeeze-film dampers without a centralizing spring. The reasons given were that they were cheaper and that they took up less space. By the same token, however, the analytical treatment of the system where the rotor center falls to the bottom of the clearance circle until unbalance lifts it off, and so brings it into action, is obviously much more complex than for the circular synchronous orbit.

Although experience indicates that squeeze-film dampers can produce smoother running engines, even under conditions far removed from critical speeds, it is surely at, or near, an engine critical speed that the full potential of the device will be realized. However, only a few previous researchers [4-6] have investigated the performance of the squeeze-film damper in conjunction with a flexible shaft system. In the same way, many previous reseachers have limited their investigations to rigid single-mass systems with emphasis on the resulting oil-film properties. Much of this work was for operating parameters which were inappropriate to industrial applications and some of it for conditions where the forces transmitted into the surrounding structure were not reduced but instead were amplified.

For the reasons outlined above, an investigation into the effectiveness of squeeze-film damper bearings was begun at Cranfield. Because it is the form used by U.K. industry, only the uncentralized type of device was considered. Initially, investigations were carried out into the effectiveness of squeeze-film damper bearings in conjunction with rigid rotors [7]. However, since most modern gas-turbines are patently not rigid systems, the research programme was quickly extended to cover the flexible shaft/rotor system. Some of the results arising from these experimental and analytical investigations are given in [8-11]. These results show that the uncentralized squeeze-film damper bearing is a truly effective means of reducing the vibratory forces transmitted into the supporting structure. Similarly it was shown that the effectiveness of the device is a function of the various characteristics, such as clearance, land-width, fluid viscosity, etc., and that these properties can be chosen in combination so as to give high (if not optimum) performance.

The flexible shaft/rotor system employed for both the theoretical and experimental investigations reported in (8-11) was a simple two-bearing device with a single rotor positioned midway between the bearings. It is the purpose of this report

Contributed by the Gas Turbine Division of THE AMERICAN SOCIETY OF MECHANICAL ENGINEERS and presented at the 27th International Gas Turbine Conference and Exhibit, London, England, April 18-22, 1982. Manuscript received at ASME Headquarters December 15, 1981. Paper No. 82-GT-218.

to describe a theoretical investigation of a shaft/rotor system which approaches somewhat closer to the conventional gas-turbine. This model includes an overhung rotor (fan disk) and a second rotor (turbine), positioned noncentrally between two squeeze-film damper bearings. Both bearings are attached to earth by means of springs intended to represent the stiffness of the supporting gas-turbine structure.

In [8–11] the vibration inhibiting properties of the squeeze-film dampers were expressed in terms of nondimensional groupings such as the bearing parameter, B, unbalance ratio, U, and speed ratio, Ω, etc. This technique is particularly useful if the overall performance of the squeeze-film damper is to be optimized and will be employed again with the present more complex model.

An experimental investigation is being carried out in parallel with the present analytical study. Naturally, the nine-mass theoretical model described in this paper is intended as a close approximation to the experimental rotor. It is intended that the experimental results will be presented in a future publication.

Theory

In practice, any real rotor system can be considered to be made up of an infinite number of constitutive parts, and hence to have an infinite number of degrees of freedom. However, since it is impractical to carry out an investigation of a system made up of an infinite, or even a large number, of component parts, it is necessary to simplify the proposed system to the point where it can be adequately modeled mathematically, whilst at the same time maintaining a sufficient degree of accuracy.

Figure 1 is a mathematical model of the test-rig which has been built in order that an experimental investigation can be carried out in parallel with this theoretical study. For the purpose of comparison with the experimental results, the asymmetric rotor system has been simplified into a lumped-mass model having nine concentrated mass stations connected by a massless elastic shaft. The mathematical model illustrated in Fig. 1 can be seen to represent a two-disk system supported by two squeeze-film damper bearings. Rotor mass m_1 represents an overhung fan, and rotor mass m_4 represents a turbine (noncentral). Masses m_2, m_3, and m_5 are lumped shaft masses, whilst masses m_6 and m_7 are partly made up of bearing journal masses and partly lumped shaft masses. Masses m_8 and m_9 represent the squeeze-film damper housing masses.

These latter masses are earthed through springs which represent the stiffness of the machine supporting structure.

For the purposes of this theoretical study, it has been assumed that only relatively small amplitudes of vibration will occur, that rotor motion in the axial direction can be assumed to be negligible, and that only the two disks, m_1 and m_4, will have an associated gyroscopic effect. In the analytical treatment of the dynamic equations produced for the above theoretical model, it has also been possible to include the effect of journal misalignment on the oil-film forces produced in a standard squeeze-film damper bearing [12].

For the shaft-supported masses m_1 to m_5 the equations of motion can be expressed in the following form.

$$\begin{bmatrix} X_j'' \\ \theta_{xj} \\ Y_j'' \\ \theta_{yj} \end{bmatrix} = \begin{bmatrix} \bar{B} & 0 \\ 0 & \bar{B} \end{bmatrix} \begin{bmatrix} -\bar{u}_j + \sum_{i=1}^{5} \bar{\alpha}_{ji} \bar{P}_{xi}^* + \sum_{i=1}^{5} \bar{\beta}_{ji} \bar{M}_{yi}^* \\ -\hat{\theta}_{xj} + \sum_{i=1}^{5} \bar{\phi}_{ji} \bar{P}_{xi}^* + \sum_{i=1}^{5} \bar{\gamma}_{ji} \bar{M}_{yi}^* \\ -\bar{v}_j + \sum_{i=1}^{5} \bar{\alpha}_{ji} \bar{P}_{yi}^* - \sum_{i=1}^{5} \bar{\beta}_{ji} \bar{M}_{xi}^* \\ -\hat{\theta}_{yj} + \sum_{i=1}^{5} \bar{\phi}_{ji} \bar{P}_{yi}^* - \sum_{i=1}^{5} \bar{\gamma}_{ji} \bar{M}_{xi}^* \end{bmatrix} \quad (1)$$

Where

$$[X_j'' \ \theta_{xj} \ Y_j'' \ \theta_{yj}]^T = [X_1'' \ X_2'' \ X_3'' \ X_4'' \ X_5'' \ \theta_{x1}'' \ \theta_{x2}' \ \theta_{x3}' \ \theta_{x4}'' \ \theta_{x5}' \ Y_1'' \ Y_2'' \ Y_3'' \ Y_4'' \ Y_5'' \ \theta_{y1}'' \ \theta_{y2}' \ \theta_{y3}' \ \theta_{y4}'' \ \theta_{y5}']^T$$

Also

Nomenclature

$A_{8,9}$ = amplitude of displacements at supports (m)
$\bar{A}$ = nondimensional mass matrix
$B_{6,7}$ = bearing parameter (dimensionless), $\{\mu R L_6^3/m_6\omega_c c_6^3\}$ or $\{\mu R L_7^3/m_7\omega_c c_7^3\}$
$\bar{B}$ = inverse of matrix $\bar{A}$
$c_{6,7}$ = radial clearance of squeeze-film damper (m)
c_{67} = ratio of damper clearances $\{c_7/c_6\}$
C_{di} = rotor station transverse damping coefficient (kg/s)
$\bar{C}_{di}$ = dimensionless damping $\{= C_{di}/m_6\omega_c\}$
$C_{\theta i}$ = rotor station angular damping coefficient (kg•m²/s)
$\bar{C}_{\theta i}$ = dimensionless angular damping $\{= C_{\theta i}/m_6 c_6^2\omega_c\}$
e_u = unbalance eccentricity (m)
F_x, F_y = oil-film forces in x- and y-directions (N)
F = resultant oil-film force (N)
$\bar{F}_x, \bar{F}_y$ = dimensionless oil-film forces, $F_{x,y}/m_6 c_6 \omega_c^2$
I_{ti} = rotor station transverse moment of inertia (kg•m²)
$\bar{I}_{ti}$ = dimensionless transverse moment of inertia, $I_{ti}/m_6 c_6^2$
I_{pi} = rotor station polar moment of inertia (kg•m²)
$\bar{I}_{pi}$ = dimensionless polar moment of inertia, $I_{pi}/m_6 c_6^2$
K_{si} = rotor station transverse stiffness (N/m)
$\bar{K}_{si}$ = dimensionless transverse stiffness $K_{si}/m_6\omega_c^2$
K_{ti} = rotor station torsional stiffness (Nm)
$\bar{K}_{ti}$ = dimensionless torsional stiffness $K_{ti}/m_6 c_6^2\omega^2$
l_i = axial distance to bearing number 6 (m)
$\bar{l}_i$ = dimensionless distance to bearing 6 $(l_i - l_6)/c_6$
$\bar{l}_{76}$ = span parameter, $(l_7 - l_6)/c_6$
m_i = rotor station mass (kg)
$\bar{M}_i$ = dimensionless mass m_i/m_6
P = force acting on disk (N)
R = journal radius (m)

$$[\bar{B}] = [D_1\bar{M}_1\Omega^2, D_2\bar{M}_2\Omega^2, D_3\bar{M}_3\Omega^2, D_4\bar{M}_4\Omega^2, D_5\bar{M}_5\Omega^2, E_1\bar{I}_{t1}\Omega^2, E_2\bar{C}_{\theta_2}\Omega, E_3\bar{C}_{\theta_3}\Omega, E_4\bar{I}_{t4}\Omega^2, E_5\bar{C}_{\theta 5}\Omega] \quad (2)$$

Where D_1, D_2, ... E_1, E_2, etc are column matrices as follows

$$D_i = [\bar{\alpha}_{1i}, \bar{\alpha}_{2i}, \bar{\alpha}_{3i}, \bar{\alpha}_{4i}, \bar{\alpha}_{5i}, \bar{\phi}_{1i}, \bar{\phi}_{2i}, \bar{\phi}_{3i}, \bar{\phi}_{4i}, \bar{\phi}_{5i}]^T$$

$$E_i = [\bar{\beta}_{1i}, \bar{\beta}_{2i}, \bar{\beta}_{3i}, \bar{\beta}_{4i}, \bar{\beta}_{5i}, \bar{\gamma}_{1i}, \bar{\gamma}_{2i}, \bar{\gamma}_{3i}, \bar{\gamma}_{4i}, \bar{\gamma}_{5i}]^T$$

Similarly the equations of motion for the bearing-related masses, m_6 to m_9, can be expressed as follows

$$X_6'' = \frac{1}{\bar{M}_6\Omega^2}\left\{\frac{1}{\bar{l}_{76}}\left[-\sum_{i=1,4}(-\bar{I}_{ti}\Omega^2\theta_{xi}'' + \bar{M}_{yi}^*) + \sum_{i=1,4}(-\bar{M}_i\Omega^2 X_i'' + \bar{P}_{xi}^*)(\bar{l}_{76} - \bar{l}_i) - \sum_{i=2,3,5}(-\bar{C}_{\theta i}\Omega\theta'_{xi} + \bar{M}_{yi}^*) + \sum_{i=2,3,5}(-\bar{M}_i\Omega^2 X_i'' + \bar{P}_{xi}^*)(\bar{l}_{76} - \bar{l}_i)\right] + \bar{F}_{x_6}\right\} \quad (3)$$

$$Y_6'' = \frac{1}{\bar{M}_6\Omega^2}\left\{\frac{1}{\bar{l}_{76}}\left[\sum_{i=1,4}(\bar{I}_{ti}\Omega^2\theta_{yi}'' + \bar{M}_{xi}^*) + \sum_{i=1,4}(-\bar{M}_i\Omega^2 Y_i'' + \bar{P}_{yi}^*)(\bar{l}_{76} - \bar{l}_i) + \sum_{i=2,3,5}(\bar{C}_{\theta i}\Omega\theta'_{yi} + \bar{M}_{xi}^*) + \sum_{i=2,3,5}(-\bar{M}_i\Omega^2 Y_i'' + \bar{P}_{yi}^*)(\bar{l}_{76} - \bar{l}_i)\right] + \bar{F}_{y_6} - \bar{W}_6\right\} \quad (4)$$

$$X_7'' = \frac{1}{\bar{M}_7\Omega^2}\left\{\frac{1}{\bar{l}_{76}}\left[\sum_{i=1,4}(-\bar{I}_{ti}\Omega^2\theta_{xi}'' + \bar{M}_{yi}^*) + \sum_{i=1,4}(-\bar{M}_i\Omega^2 X_i'' + \bar{P}_{xi}^*)\bar{l}_i + \sum_{i=2,3,5}(-\bar{C}_{\theta i}\Omega\theta'_{xi} + \bar{M}_{yi}^*) + \sum_{i=2,3,5}(-\bar{M}_i\Omega^2 X_i'' + \bar{P}_{xi}^*)\bar{l}_i\right] + \bar{F}_{x_7}\right\} \quad (5)$$

$$Y_7'' = \frac{1}{\bar{M}_7\Omega^2}\left\{\frac{1}{\bar{l}_{76}}\left[-\sum_{i=1,4}(\bar{I}_{ti}\Omega^2\theta_{yi}'' + \bar{M}_{xi}^*) + \sum_{i=1,4}(-\bar{M}_i\Omega^2 Y_i'' + \bar{P}_{yi}^*)\bar{l}_i - \sum_{i=2,3,5}(\bar{C}_{\theta i}\Omega\theta'_{yi} + \bar{M}_{xi}^*) + \sum_{i=2,3,5}(-\bar{M}_i\Omega^2 Y_i'' + \bar{P}_{yi}^*)\bar{l}_i\right] + \bar{F}_{y7} - \bar{W}_7\right\} \quad (6)$$

$$X_8'' = \frac{1}{\bar{M}_8\Omega^2}[-\bar{K}_{s8x}X_8 - \bar{F}_{x6}] \quad (7)$$

$$Y_8'' = \frac{1}{\bar{M}_8\Omega^2}[-\bar{K}_{s8y}Y_8 - \bar{F}_{y6} - \bar{W}_8] \quad (8)$$

$$X_9'' = \frac{1}{\bar{M}_9\Omega^2}[-\bar{K}_{s9x}X_9 - \bar{F}_{x7}] \quad (9)$$

$$Y_9'' = \frac{1}{\bar{M}_9\Omega^2}[-\bar{K}_{s9y}Y_9 - \bar{F}_{y7} - \bar{W}_9] \quad (10)$$

Where

Nomenclature (cont.)

TR_8, TR_9 = transmissibility at supports 8 and 9
u_i, v_i = relative deflection (m)
$\bar{u}_i, \bar{v}_i$ = dimensionless relative deflections, u_i/c_6 and v_i/c_6
U_i = dimensionless unbalance e_{ui}/c_6
$\bar{W}$ = dimensionless gravity parameter $g/c_6\omega_c^2$
x_i, y_i, z_i = body-fixed coordinate system
x_i', y_i', z_i' = body-rotated coordinate system
X_i, Y_i = dimensionless deflection parameter, x_i/c_6 and y_i/c_6
α_{ij} = influence coefficient, deflection at station i per unit force applied at station j (m/N)
$\bar{\alpha}_{ij}$ = dimensionless influence coefficient, $\alpha_{ij}m_6\omega_c^2$
β_{ij} = influence coefficient, deflection at station i per unit moment applied at station j (m/Nm)
$\bar{\beta}_{ij}$ = dimensionless influence coefficient, $\beta_{ij}m_6c_6\omega_c^2$
ϕ_{ij} = influence coefficient, slope at station i per unit force applied at station j(rad/N)
$\bar{\phi}_{ij}$ = dimensionless influence coefficient, $\phi_{ij}m_6c_6\omega_c^2$
γ_{ij} = influence coefficient, slope at station i per unit moment applied at station j (rad/Nm)
$\bar{\gamma}_{ij}$ = dimensionless influence coefficient, $\gamma_{ij}m_6c_6^2\omega_c^2$
θ, ψ, ϕ = Eulerian angles (rad)
$\hat{\theta}_x, \hat{\theta}_y$ = relative slope angles (rad)
ϕ_{oi} = phase angle at station i between unbalance vector and x-direction (rad)
ω = rotor speed (rad/s)
ω_c = first (pin-pin) critical speed (rad/s)
Ω = dimensionless speed ratio, ω/ω_c
$(')$ = $d/d(\omega t)$
$(\dot{})$ = d/dt

Subscripts

1, 2, ...9, i = station number
x, y, = x-, y-directions

$$X_1' = \frac{dX_1}{d(\omega t)} = \frac{\dot{X}_1}{\omega} \qquad X_1'' = \frac{d^2X_1}{d(\omega t)^2} = \frac{X_1''}{\omega^2} \text{ ETC}$$

The generalized force terms for $i = 1$ and 4 are defined as follows

$$\bar{P}_{xi}^* = -\bar{K}_{si}X_i - \bar{C}_{di}\Omega X_i' + \bar{M}_i U_i \Omega^2 \cos(\omega t + \phi_{oi})$$
$$\bar{P}_{yi}^* = -\bar{K}_{si}Y_i - \bar{C}_{di}\Omega Y_i' + \bar{M}_i U_i \Omega^2 \sin(\omega t + \phi_{oi}) - \bar{W}_i$$
$$\bar{M}_{xi}^* = -\bar{I}_{pi}\Omega^2\theta_{xi}' + \bar{K}_{ti}\theta_{yi} + \bar{C}_{\theta i}\Omega\theta_{yi}'$$
$$\bar{M}_{yi}^* = -\bar{I}_{pi}\Omega^2\theta_{yi}' - \bar{K}_{ti}\theta_{xi} - \bar{C}_{\theta i}\Omega\theta_{xi}'$$

And for $i = 2$, 3, and 5 the generalized force terms are given as

$$\bar{P}_{xi}^* = -\bar{K}_{si}X_i - \bar{C}_{di}\Omega X_i'$$
$$\bar{P}_{yi}^* = -\bar{K}_{si}Y_i - \bar{C}_{di}\Omega Y_i' - \bar{W}_i$$
$$\bar{M}_{xi}^* = \bar{K}_{ti}\theta_{yi}$$
$$\bar{M}_{yi}^* = -\bar{K}_{ti}\theta_{xi}$$

The determination of the fluid-film forces. F_{x6}, F_{y6}, F_{x7}, and F_{y7}, occurring at the flexible supports 8 and 9, respectively, is obviously of paramount importance for any investigation of the performance of a dynamic system which incorporates squeeze-film damper bearings. If information were available on the equivalent stiffness and damping coefficients of the squeeze-film (say in the form of the usual eight oil film force coefficients) it would be possible to derive these forces directly. Unfortunately, at the present time these coefficients are not known. However, it is possible to determine the forces from some general oil-film model (say π-film) in the manner employed in [8]. In this paper it is not intended to attempt to determine the most approximate film-model available, nor yet to create a new model. The results shown are all based upon the π-film model, although others are available within the computer programme produced for the present investigation. Also available is an analytical treatment [12] which allows for the effect of the misalignment of the rotor within the squeeze-film clearance.

In order to determine the effectiveness of the squeeze-film damper bearing in the context of the nine-mass rotor model, it is obviously desirable to define the transmissibility (that is, ratio of transmitted force to exciting force) at the two flexible supports. This is done in the following manner:

$$\text{Transmissibility at support 8} = TR_8 = \frac{K_{s8}A_8}{N_8}$$

$$\text{Transmissibility at support 9} = TR_9 = \frac{K_{s9}A_9}{N_9}$$

Where A_8, A_9 are the maximum displacements at supports 8 and 9.

$$A_8 = \sqrt{x_8^2 + y_8^2}\,|\max \qquad A_9 = \sqrt{x_9^2 + y_9^2}\,|\max$$

and N_8, N_9 are the support reaction forces for the nine-mass system *without* squeeze-film dampers at points 8 and 9, respectively. For the present case the stiffnesses of the two flexible supports K_{s8} and K_{s9} are both given the value 3.81×10^7 N/m, while the bearing masses, m_6 and m_7, are both assumed to be 7.35 kg. These values for the spring stiffnesses and bearing masses are chosen as typical of those which will be employed in the experimental rig which will be tested in a parallel investigation to the analytical study reported here. By the same token, the critical speed chosen for the present investigation is 6113 r.p.m. which is the first critical speed for the same rig.

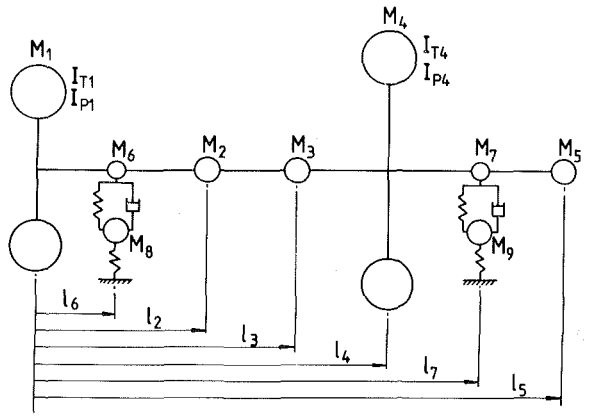

Fig. 1 Analytical model of overhung flexible rotor

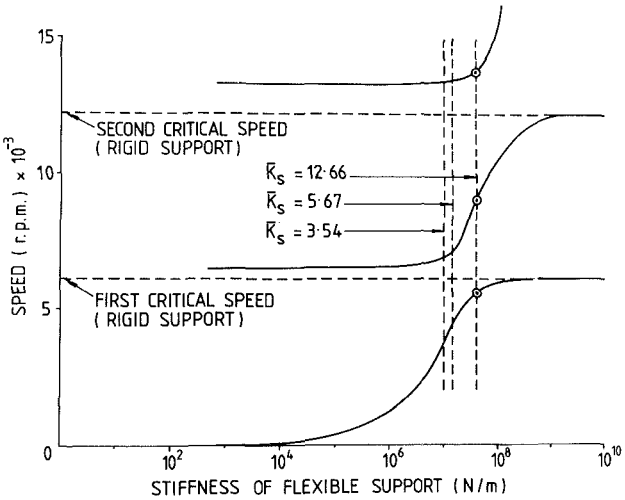

Fig. 2 Variation of critical speed with support stiffness

Analysis

The equations of motion for the nine-mass overhung rotor/shaft system have been reduced to a set of first-order differential equations (1-10) which can be numerically integrated. Any suitable integration technique could be used for the solution of the above set of equations but for the present investigation the modified Euler method and the fourth-order Runge-Kutta method were employed.

If the initial displacements and velocities are specified at starting time, t_0, for all points within the system, it is clearly possible to obtain the acceleration rates at these points and subsequently to calculate the displacements and velocities at time $t_0 + \Delta t$.

The component oil film forces, F_x and F_y, produced within the squeeze-film dampers supporting the rotor/shaft system under consideration, are written into the main computer program in a generalized form. In this way it is possible to choose any appropriate fluid-film model (e.g., Π-film) for inclusion in the analysis. Five fluid-film models are available in an associated subroutine to the main program, and are described more fully in [13]. The fifth of the five fluid-film models, referred to above, is automatically selected if the slope of the shaft at the bearing is greater than 0.5×10^{-3}. In this way it is possible to make allowance for the effect of misalignment of the shaft center-line relative to the bearing. The analytical approach employed in evaluating the effect of misalignment is described in [12].

In this type of investigation only steady-state conditions are considered, thus if some starting value of the displacement and velocity of the rotor centroid is chosen, the numerical

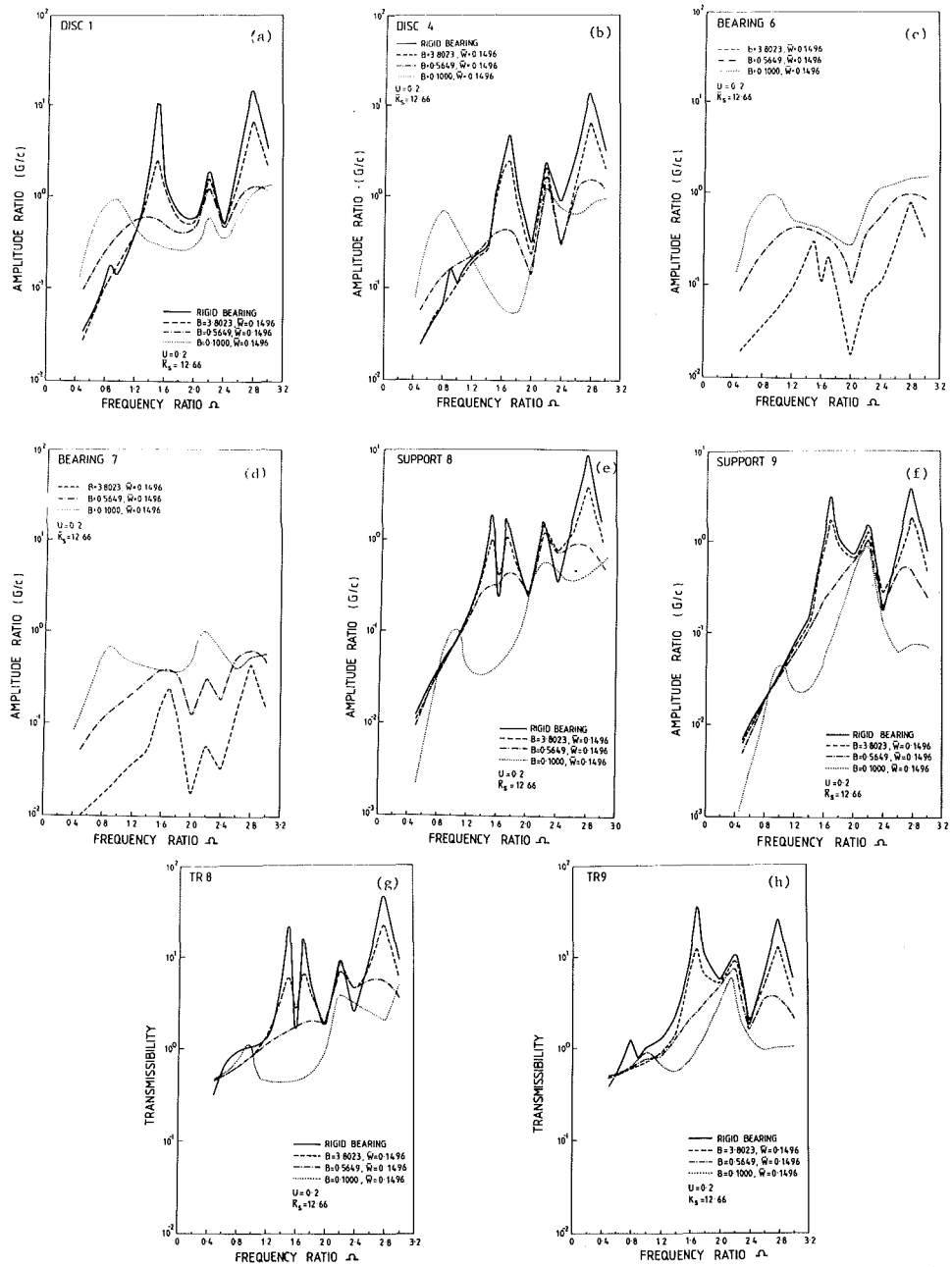

Fig. 3 Variation of amplitude ratios and transmissibilities with bearing parameter

solution is time-marched through the transient condition until a steady-state orbit is achieved. Naturally, the transient path followed by the bearing centroid depends upon the initial conditions chosen but the final steady-state orbit is unique and independent of initial conditions. The choice of time interval, or time-step, in the time-marching process is of great significance. For example, if the chosen time-step is too small then the computer costs will be excessive, similarly if the time-step is too large then the travel of the bearing centroid during one time interval will attempt to carry the orbit outside the normal squeeze-film damper clearance. Since this condition is clearly impossible the main program employed here brings the computation to a halt. In general, it has been found that smaller time-steps are required for the analysis of an asymmetric system with multi-mass points, and including gyroscopic effects, than were required for the analysis of a symmetric single-mass system [8–11]. The smallest time-step used for the present investigation was 0.0087266 radians, equivalent to 720 points for each cycle. This value for the time-step gave excellent results in a reasonable time.

In the fuller version of this report [13], results for a wide range of system nondimensional parameters are given. However, in this paper only the following parametric values have been used.

Bearing parameter, B	=	rigid bearing, 3.8023, 0.5649, 0.10
Gravity parameter, $\bar{W}$	=	0.1496
Unbalance parameter, U	=	0.2
Phase angle, ϕ_{oi}	=	Zero
Support stiffness, $\bar{K}_s$	=	12.66 ($K_s = 3.81 \times 10^7$ N/m)
Mass parameter, $\bar{M}_i$	=	$\bar{M}_1 = 1.1$, $\bar{M}_4 = 1.33$, $\bar{M}_{8,9} = 2.93$

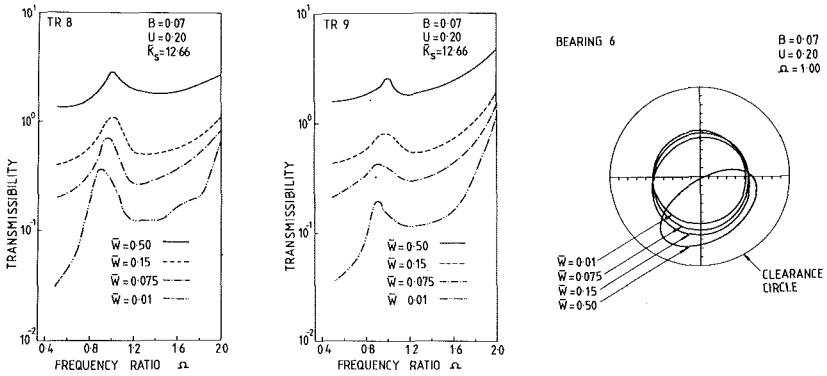

Fig. 4 Variation of transmissibilities at supports 8 and 9 and the bearing orbit at bearing 6 with gravity parameter, $\bar{W}$

Transverse damping ratio, $\bar{C}_d$ = 0.01
Angular damping ratio, $\bar{C}_\theta$ = 70.00
Speed ratio Ω from 0.5 to 3.0

Also for initial conditions within the rotor/shaft system, all initial velocities are assumed to be zero and all initial displacements are those produced by the dead-weights of the rotor.

Results

In the analytical study reported here, the dynamic response of the nine-mass model shown in Fig. 1 was determined for the range of parameters quoted earlier. However, for reasons of space, only a few of the results obtained can be included in this paper, and since the bearing parameter B has previously been shown to have the strongest influence on the effectiveness of the squeeze-film damper, it is the effect of varying this parameter which is used as an illustrative result.

Since they form a basis of comparison for the squeeze-film damper results, the critical speeds of the nine-mass model without squeeze-film dampers were determined first. These values, which were calculated by means of the technique described in [14], were obtained for a range of support stiffnesses and are shown in Fig. 2. The specific values of the critical speeds for the case where the squeeze-film dampers were not in operation and where the support stiffnesses were infinite, i.e., for the case of rigid bearings and rigid supports, the first and second critical speeds are found to be 6113 and 12221 r.p.m., respectively.

The amplitude ratios at the two disks, the two bearings, and the two supports plus the transmissibilities at the two supports have been determined for a number of system parameters. Figure 3 is one such set of results for the specific conditions of unbalance ratio $U = 0.2$, spring stiffness $K_s = 3.81 \times 10^7$ N/m, transverse damping coefficient $\bar{C}_d = 0.01$, and angular damping coefficient $\bar{C}_\theta = 70.0$. Similarly, for this particular set of results the gravity parameter $\bar{W} = 0.1496$ and the overhung and inboard masses 8.04 kg and 9.78 kg, respectively. The distance between the bearings, l_{76} was 0.54m; with this basic specification of the dynamic system a number of different values of the bearing parameter B were introduced into the squeeze-film damper subroutine and the resulting amplitude ratios and transmissibilities were determined. Only the results for $B = 3.8023$, 0.5649, 0.1, and the rigid bearing condition, are reported in this paper.

The variation of the amplitude ratio and transmissibility with gravity parameter, $\bar{W}_i$, stiffness parameter, $\bar{K}_{si}$, unbalance parameter, U_1, and mass parameter, M_i, (m_i/m_6)

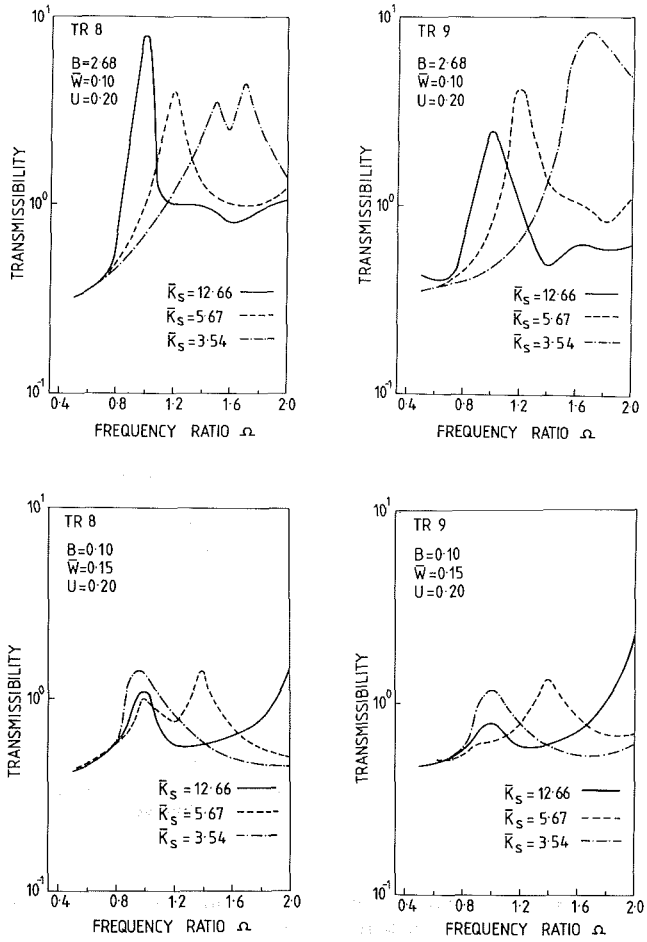

Fig. 5 Variation of transmissibilities at supports 8 and 9 with support stiffness, K_{si}, for two values of the bearing parameter, B

were also investigated and are reported fully in [13]. These results will not be reported in detail here, but Figs. 4 and 5 illustrate typical results. For example, Fig. 4 indicates the variation of the transmissibilities at supports 8 and 9 with the gravity parameter, $\bar{W}$. Figure 4 also contains a typical variation of a bearing centroid orbit (in this instance bearing 6), with the gravity parameter. Similarly, Fig. 5 shows the variation of the transmissibilites at supports 8 and 9 with stiffness parmeter, $\bar{K}_s$, for two discrete values of the bearing parameter, B (2.68 and 0.10). Other results are contained in [13] but, in brief, the following trends were observed:

(*a*) Increase in the gravity parameter, $\bar{W}$, leads to increased

transmissibility. For large $\bar{W}$ (say 0.5) the orbit shape is irregular (it has a tail), and nonsynchronous behaviour can result at high speed.

(*b*) Variation of the amplitude ratio and transmissibility with support stiffness ratio, $\bar{K}_s$ (the values 3.542, 5.676, and 12.66 were used) was significantly greater when B was large (say 2.68) than when it was small (say 0.1). Interestingly, the influence of the support stiffness on the critical speed of the nine-mass system followed the same trend. This latter result would appear to show that the engine casing stiffness will have least influence on the critical speed when the squeeze-film damper is operating most effectively in reducing the transmissibility.

(*c*) As would probably be expected, an increase in the unbalance parameter, U, leads to increased transmissibility at both supports, but the variation is nonlinear. For very small values of U, that is, for a well balanced machine, a non-synchronous instability arises. However, the associated orbit is so small that the unstable condition would probably not prove to be serious.

(*d*) A decrease in the bearing mass, m_6 (usually = 7.35 kg), increases the size of orbit at the disks and the bearings, although the size of the orbit at the supports will be reduced in some speed regions. Similarly, a reduction in the bearing mass will result in increased transmissibilities, TR_8 and TR_9, at any speed. A decrease in the bearing mass produces relatively larger disk masses ($\bar{M}_1 = m_1/m_6$ and $\bar{M}_4 = m_4/m_6$) and hence relatively larger moments of inertia which in turn tend to increase the gyroscopic effect. Thus, the (nondimensional) transmissibility will also increase.

Discussion

A comparison of Fig. 2 with Fig. 3 shows that the speed ratios at which the critical speeds occur in Fig. 3 do coincide with the critical speeds predicted from Fig. 2, for the case of support stiffness $\bar{K}_s = 3.81 \times 10^7$ N/m. It is interesting to note that the amplitude ratio for the first critical speed is much smaller than those for the second and third critical speeds.

The general impression of the diagrams, which go to make up Fig. 3, is that the amplitude ratios and transmissibilties can be reduced by the inclusion of uncentralized squeeze-film dampers in the system. In order to appreciate the full effect of varying the bearing parameter, it is necessary to inspect all of the diagrams which are shown in Fig. 3.

It would obviously be undesirable to adopt a set of parameters which, while reducing the transmissibility, gave rise to some unrealistically large amplitude of (say) a disk. However, since the object of including squeeze-film dampers in our machines is to reduce the transmission of force to the surrounding structure, it is the transmissibility graphs given in Figs. 3(*g*) and 3(*h*) which should be discussed first.

From Figs. 3(*g*) and 3(*h*) it is possible to see that transmissibility decreases with reducing values of the bearing parameter. High values of B (say 3.8023) can be seen to lead to transmissibilities close to those encountered with rigid bearings, whilst values of B around 0.1 lead to a considerable reduction in the transmissibility. Not shown in Figs. 3(*g*) and 3(*h*) are the responses for $B = 0.01$ or $B = 0.001$. Values of B as low as this led to instability over part of the speed range. This phenomenon was also reported by Kossa in reference [8].

Figures 3(*a*) and 3(*b*), which show the amplitude ratios for the two disks over a range of frequency ratios, show some interesting trends. For the inboard disk (No. 4), the effect of reducing the bearing parameter, B, is to reduce the amplitude ratio everywhere except for the low-speed range (say $\Omega < 1.2$). In this low-speed range the amplitude ratio increases with decreasing B and in so doing, appears to remove evidence of the presence of the first critical speed. For the overhung disk (No. 1) the results are very similar.

From Figs. 3(*c*) and 3(*d*) it can be seen that the movement of the squeeze-film damper journal increases with reducing bearing parameter. Hence, in the region where the squeeze-film damper bearing is most effective the journal movement is at its greatest.

From Fig. 4, it is apparent that an increase in the gravity parameter, $\bar{W}$, leads to an increase in the transmissibility. Figure 5 shows that the variation in transmissibiility with support stiffness, $\bar{K}_s$, is much greater when the bearing parameter is large (2.68) than when it is small (0.1). This would appear to indicate that the influence of the support stiffness is least when the squeeze-film damper is operating most effectively.

Conclusions

From the analytical study described above it would appear that noncentralized squeeze-film damper bearings can be very effective in reducing the transmission of unbalance forces into the structure surrounding a two-disk nine-mass simulation of a gas-turbine rotor.

Over part of the operating speed range reduced transmissibility could be accompanied by increased disk orbit. Hence, care may be required in choosing bearing parameters so as to optimize their performance from all aspects.

In general it would appear that the optimum value of the bearing parameter, B, is about 0.1. Much larger values of B lead to conditions similar to those which arise when the bearings are rigidly held, while smaller values of B appear to lead to instability. From similar considerations it has been found desirable to keep the gravity parameter, $\bar{W}$, reasonably small (about 0.05).

The influence of the support stiffness, K_s, on the vibration response of the nine-pass rotor system was found to be quite significant. It would appear that the bearing parameters and support stiffnesses should be considered in combination if the optimum performance of a squeeze-film damper bearing is to be achieved.

Acknowledgment

The authors wish to thank the Science and Engineering Council for their support of the foregoing work through Research Grant GR B48307.

References

1 White, D. C., "The Dynamics of a Rigid Rotor Supported on Squeeze-film Bearings," *Proceedings of the Conference on Vibrations of Rotating Systems*, Inst. Mech. Engrs., pp. 213-229, 1972.

2 Mohan, S., and Hahn, E. J., "Design of Squeeze-film Damper Supports for Rigid Rotors," ASME *Journal of Engineering for Industry*, Aug. 1974, pp. 976-982.

3 Gunter, E. J., Barrett, L. E., and Allaire, P. E., "Design and Application of Squeeze-film Damper for Turbomachinery Stabilization," Report No. ME-4040-122-75, University of Virginia, 1975.

4 Cunningham, R. E., "Influence of Oil Squeeze-film Damping on Steady-state Response of Flexible Rotor Operating to Supercritical Speeds," NASA Tech. Paper 1094, Dec. 1977.

5 Kirk, R. G., and Gunter, E. J., "Transient Response of Rotor-bearing Systems," ASME *Journal of Engineering for Industry*, Vol. 96, May 1974, pp. 682-693.

6 Shen, F. A., "Transient Flexible-Rotor Dynamics Analysis, Part 1—Theory," ASME *Journal of Engineering for Industry*, Vol. 94, May 1972, pp. 531-538.

7 Cookson, R. A., and Kossa, S. S., "The Effectiveness of Squeeze-Film Damper Bearings, Supporting Rigid Rotors Without a Centralising Spring," *International Journal of Mechanical Science*, Vol. 21, 1979, pp. 639-650.

8 Kossa, S. S., "Theoretical and Experimental Investigation of Uncentralised Squeeze-film Damper Bearings Supporting Flexible Rotors Without a Centralising Spring," Ph.D. thesis, Cranfield Institute of Technology, 1980.

9 Cookson, R. A., and Kossa, S. S., "The Effectiveness of Squeeze-film

Damper Bearings Supporting Flexible Rotors Without a Centralising Spring," *International Journal of Mechanical Science*, Vol. 22, May 1980, pp. 313–324.

10 Cookson, R. A., and Kossa, S. S., "Theoretical and Experimental Investigations into the Effectiveness of Squeeze-film Damper Bearings Without a Centralising Spring," Inst. of Mech. Engineers Meeting on Vibrations in Rotating Machinery, Churchill College, Cambridge, Sept. 1980.

11 Cookson, R. A. and Kossa, S. S., "The Vibration Isolating Properties of Uncentralised Squeeze-film Damper Bearings Supporting a Flexible Rotor," ASME JOURNAL OF ENGINEERING FOR POWER, Vol. 103, No. 4, Oct. 1981, pp. 781–787.

12 Cookson, R. A., and Feng, X. H., "The Effect of Journal Misalignment on the Oil-Film Forces Generated in a Squeeze-Film Damper," Paper No. 82-GT-285, presented at the 1982 ASME Gas-Turbine Conference, London, to be published in the JOURNAL OF ENGINEERING FOR POWER.

13 Cookson, R. A., and Feng, X. H., "Uncentralised Squeeze-Film Damper Bearings Applied to an Overhung Disc/Rotor System," Paper No. 33, AGARD, *Proceedings, Problems in Bearings and Lubrication*, AGARD CP-323, Ottawa, Canada, May 1982.

14 Cookson, R. A., and Feng, X. H., "A Transfer Matrix Technique for Determining the Critical Speeds of a Two-Spool Rotor System," Appl. Mechs. Report AM 69, School of Mechanical Engineering, Cranfield Institute of Technology, Bedford, U.K., 1980.

Siu Shing Tong
Graduate Student Research Assistant.

W. T. Thompkins, Jr.
Associate Professor.

Department of Aeronautics and Astronautics,
Massachusetts Institute of Technology,
Cambridge, Mass. 02139

A Design Calculation Procedure for Shock-Free or Strong Passage Shock Turbomachinery Cascades

A previously described, inviscid design technique has been substantially improved to allow the generation of either shock-free, weak-shock or low total pressure loss supersonic rotor cascade designs. Improvements have been introduced in inflow-outflow boundary conditions, imposition of geometric constraints and in shock pressure rise specifications. Calculation examples are presented for precompression type rotor designs.

Introduction

Design of transonic airfoil shapes, either isolated airfoils or airfoils in cascade, which possess specific aerodynamic characteristics, is now an extremely active research area. Many current analyses concentrate on producing shock-free airfoil designs for subsonic freestream conditions (see [1, 2,] for example). Other workers recognize that shock-free designs may not necessarily represent optimum airfoil shapes and have concentrated on full potential flow solutions, with isentropic shock waves (see [3-5]). A concise discussion of the role of constraints in such schemes is available in [6]. These results may now be applied to turbomachinery stator row and turbine design and should be quite successful.

For the rotor design problem, it is expected that optimum designs will involve both normal and oblique shock waves at high Mach number, 1.5 to 2.0, and a potential flow analysis appears inadequate. Design schemes for supersonic rotor cascades are considered in this report and in an earlier paper [7], using Euler equation flow simulations. This earlier paper demonstrated that an inverse or design calculation scheme was possible for general inviscid flow, and this paper explores the use of such inverse schemes to design supersonic inflow cascades. The scheme investigated uses an input target blade pressure distribution and attempts to determine a profile shape through a sequence of direct calculations on known trial geometries. Due to the fact that quite a number of geometric constraints, as well as the pressure distribution, must be satisfied, the final calculated blade pressure may match the target pressure only in a least-squares sense. The geometric construction technique proceeds by first assuming a trial geometry and coordinate system. Flow equations are then numerically integrated using MacCormack's time-marching method for a small number of time steps. The difference between the current blade pressure and the target wall pressure is then used to predict a geometry change which will move the computed wall pressure toward the target and the process is repeated to convergence. During the blade geometry calculations, constraints on the blade geometry, such as leading and trailing edge closure or minimum thickness, are obeyed.

Contributed by the Gas Turbine Division of THE AMERICAN SOCIETY OF MECHANICAL ENGINEERS and presented at the 27th International Gas Turbine Conference and Exhibit, London, England, April 18-22, 1982. Manuscript received at ASME Headquarters December 15, 1981. Paper No. 82-GT-220.

Flow Equations

The flow calculations presented in this paper use the strong conservation law form of the Euler equations expressed in a form suitable for use with time dependent, body-fitted coordinate systems (see [7, 8]). For two-dimensional flow, these equations written in vector form for Cartesian coordinates are

$$\partial_t \bar{q} + \partial_x \bar{F} + \partial_y \bar{G} = 0 \tag{1}$$

where

$$\bar{q} = \begin{pmatrix} \rho \\ \rho u \\ \rho v \end{pmatrix} \quad \bar{F} = \begin{pmatrix} \rho u \\ \rho u^2 + P \\ \rho uv \end{pmatrix} \quad \bar{G} = \begin{pmatrix} \rho v \\ \rho uv \\ \rho v^2 + P \end{pmatrix}$$

These equations express conservation mass and momentum. In inverse code applications where only steady-state solutions are required, the energy equation may be replaced with the assumption of isoenergetic flow, or the assumption that the stagnation enthalpy (h_0) is constant everywhere. This assumption provides a simple algebraic relation between the pressure, density, and velocity components.

$$P = \rho \frac{(\gamma - 1)}{\gamma} \left(h_0 - \frac{(u^2 + v^2)}{2} \right) \tag{2}$$

Following Viviand [8], a coordinate mapping may be defined as

$$\xi = \xi(x,y,t) \quad \eta = \eta(x,y,t) \quad t = t \tag{3}$$

where ξ and η are general mapping functions that may depend on time. Subject to such a mapping, the flow equations may be written as

$$\partial_t \hat{\bar{q}} + \partial_\xi \hat{\bar{F}} + \partial_\eta \hat{\bar{G}} = 0 \tag{4}$$

where

$$\hat{q} = \tilde{q}/J \quad J\hat{\bar{F}} = ((\partial_t \xi)\tilde{q} + (\partial_x \xi)\bar{F} + (\partial_y \xi)\bar{G})$$
$$J\hat{\bar{G}} = ((\partial_t \eta)\tilde{q} + (\partial_x \eta)\bar{F} + (\partial_y \eta)\bar{G})$$

Here J is the transformation Jacobian

$$J = (\partial_x \xi)(\partial_y \eta) - (\partial_y \xi)(\partial_x \eta) \tag{5}$$

These equations have a particularly instructive form when the contravariant velocities along coordinate lines are introduced:

Normal to the η coordinate line

$$U = \partial_t \xi + (\partial_x \xi)u + (\partial_y \xi)v \tag{6}$$

and normal to the ξ coordinate line:

$$V = \partial_t \eta + (\partial_x \eta)u + (\partial_y \eta)v \tag{7}$$

With these definitions, the flux vectors, $\hat{\bar{F}}$ and $\hat{\bar{G}}$, may be rewritten as

$$J\hat{\bar{F}} = \begin{bmatrix} \rho U \\ \rho u U + (\partial_x \xi)P \\ \rho v U + (\partial_y \xi)P \end{bmatrix}, \quad J\hat{\bar{G}} = \begin{bmatrix} \rho V \\ \rho u V + (\partial_x \eta)P \\ \rho v V + (\partial_y \eta)P \end{bmatrix} \tag{8}$$

Along the body surface, for body-fitted coordinate systems, the flow tangency boundary condition is simply expressed as $V = 0$. The wall pressure is usually found from a compatibility condition derived from the momentum equation such as

$$\partial_n P = \frac{\rho U_p^2}{R_s} \tag{9}$$

where n indicates the direction normal to the surface; U_p is the velocity parallel to the surface; R_s is the radius of curvature of the surface.

The flow equations in finite difference forms are numerically integrated using MacCormack's explicit, time-marching scheme [9], which may be written in symbolic form as

$$\hat{q}^{n+2}_{j,k} = (L_\xi L_\eta L_\eta L_\xi)\hat{q}^n_{j,k} \tag{10}$$

Here L_ξ and L_η are both multiple step operators which include finite difference operations in only one space direction. For example, L_η is defined as

$$\hat{q}^{n+1/2}_{j,k} = L_\eta \hat{q}^n_{j,k} = (L_{3\eta} L_{2\eta} L_{1\eta})\hat{q}^n_{j,k} \tag{11}$$

where

$$\hat{q}^*_{j,k} = L_{1\eta}\hat{q}^n_{j,k} = \hat{q}^n_{j,k} - \frac{\Delta t}{\Delta \eta}(\hat{\bar{G}}^n_{j,k+1} - \hat{\bar{G}}^n_{j,k})$$

$$\hat{q}^{**}_{j,k} = L_{2\eta}\hat{q}^*_{j,k} = \frac{1}{2}\left(\hat{q}^n_{j,k} + \hat{q}^*_{j,k} - \frac{\Delta t}{\Delta \eta}(\bar{G}^*_{j,k} - \bar{G}^*_{j,k-1})\right)$$

$$\hat{q}^{n+1/2}_{j,k} = L_{3\eta}\hat{q}^{**} = \left\{\hat{q}^{**}_{j,k} + \left(AV_{j,k+\frac{1}{2}}\right)(\hat{q}^{**}_{j,k+1} - \hat{q}^{**}_{j,k}) + \left(AV_{j,k-\frac{1}{2}}\right)(\bar{q}^{**}_{j,k+1}\bar{q}^{**}_{j,k})\right\}$$

L_ξ is defined in a similar fashion. Convergence is checked after each sequence of operators in equation (10).

The damping operators, $L_{3\xi}$ and $L_{3\eta}$, are required for stability of the scheme and involve coefficients, AV, which depend on the flow solution. Two forms for this coefficient were used in computational examples. These forms were

$$(AV)_{j\pm\frac{1}{2},k} = \alpha |u_{j\pm1,k} - u_{j,k}|;$$
$$(AV)_{j\pm\frac{1}{2},k} = \alpha |v_{j\pm1,k} - u_{j,k}|; \tag{12}$$

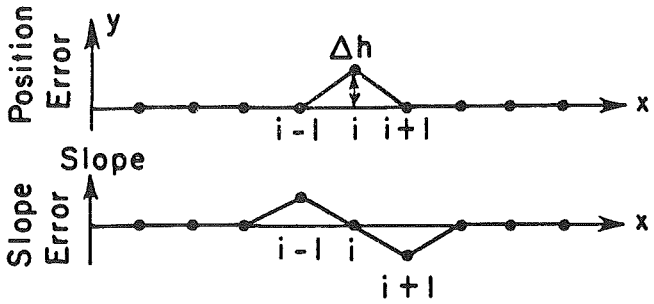

Fig. 1(a) Idealized initial geometry error

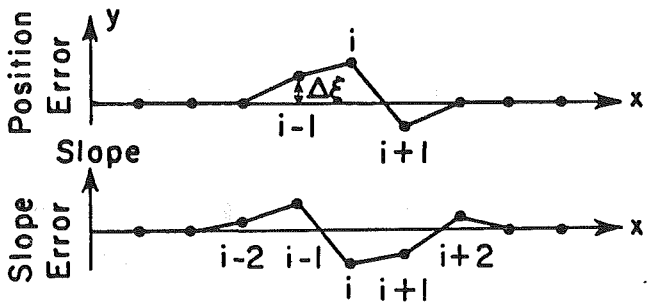

Fig. 1(b) Idealized intermediate geometry error

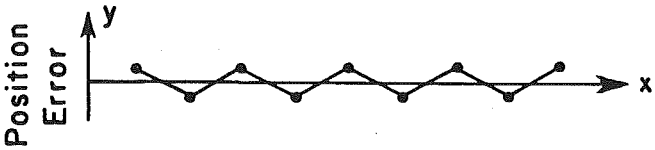

Fig. 1(c) Idealized final geometry error

or

$$(AV)_{j,k} = \alpha \frac{(P_{j+1} - 2P_j + P_{j-1})}{|P_{j+1} + 2P_j + P_{j-1}|} \tag{13}$$

where α is a constant which was chosen to be 0.25.

Geometry Construction

The wall movement algorithm is expressed in terms of a design wall momentum flux and a transient wall momentum flux. Since the solid wall boundary condition is that the contravariant velocity, V, is zero, the design wall momentum flux can be expressed in terms of the known wall pressure and the coordinate mapping coefficients which are to be determined.

$$\hat{\bar{G}}^d_w = \begin{bmatrix} \eta_x p^d \\ \eta_y p^d \end{bmatrix} j,0 \tag{14}$$

Since a trial geometry will not produce the design pressure distribution, a virtual wall momentum flux vector is formed from the predicted wall pressure and a virtual contravariant wall velocity.

$$\hat{\bar{G}}^v_w = \begin{bmatrix} \rho u^v V^v + \eta_x p \\ \rho v^v V^v + \eta_y p \end{bmatrix} n \; j,0 \tag{15}$$

where

$$V^v = \eta_x u^v + \eta_y v^v$$

V^v represents a fictitious wall velocity needed to provide a

balance between the current wall pressure amd the design wall pressure. Equations (14) and (15) can be solved for u^v and v^v as

$$v^v = \pm \frac{\eta_y{}^2}{\eta_x^2 + \eta_y{}^2} \frac{|P^d - P^n|}{\rho} \tag{16}$$

$$u^v = v^v \frac{\eta_x}{\eta_y} \tag{17}$$

Since the wall boundary condition is always $V^n_{j,0} = 0$, a correction wall velocity is calculated from

$$\bar{V}^n_{j,0} = 0 = (\eta_t + \eta_x u^v + \eta_y v^v)^n_{j,0} \tag{18}$$

or

$$(\eta_t)^n_{j,0} = -(V^v)^n_{j,0} \tag{19}$$

The correction wall velocity in the y-direction is proportional to η_t, and the signs of u^v and v^v are chosen so that an excess predicted pressure is balanced by a positive wall velocity. This virtual flux scheme is used for both supersonic and subsonic flow.

An analysis of the wall movement scheme stability shows that the predicted wall velocity must be underrelaxed in order to provide overall stability of the algorithm. Consider for example the situation shown in Fig. 1(a) where the correct wall geometry has been obtained for all but one point, j. The calculated wall slope at point j and its neighbors using central differencing is also shown in Fig. 1(a). After the next time step, if the flow is supersonic, the new wall pressure will be higher than specified at point $j-1$ and lower than specified at point $j+1$. New wall positions will be assigned as in Fig. 1(b). After the next time step, the calculated wall pressure will become lower than specified, causing the point j to move toward its correct position.

As may be seen, the assumed error at point j induces a position error at points $j-1$ and $j+1$. For the solution process to converge these induced errors must be smaller than the original position error. Referring to Fig. 1(a) and assuming small deflections, the induced error will be

$$\Delta h_i = \Delta t \omega \sqrt{\frac{\Delta P}{\rho}} < \Delta h \tag{20}$$

where ω is an under relaxation factor.

Numerical experiments showed that, counter to intuition, the relaxation factor itself should be chosen to be proportional to $(1/c)\sqrt{\Delta P/\rho}$ for best convergence rate. Choice of this relaxation parameter eliminated small geometry oscillations which retarded global convergence. We may now write equation (20) as

$$\Delta t \Omega \frac{1}{c} \frac{\Delta P}{\rho} < \Delta h \tag{21}$$

For small deflections, linearized supersonic flow analysis gives

$$\frac{\Delta P}{P} = \frac{\gamma M^2}{\sqrt{M^2 - 1}} \theta = \frac{\gamma M^2}{\sqrt{M^2 - 1}} \frac{\Delta h}{2 \Delta x} \tag{22}$$

Equation (21) becomes

$$\Delta t \Omega \frac{1}{c} \frac{\gamma M^2}{\sqrt{M^2 - 1}} \frac{\Delta h}{2 \Delta x} < \Delta h \tag{23}$$

or

$$\Omega \frac{\Delta t}{\Delta x} c \frac{1}{2} \frac{M^2}{\sqrt{M^2 - 1}} < 1 \tag{24}$$

If we set the CFL number, $(\Delta t/\Delta x)(u+c)$, equal to 1.0, we may rewrite this as

$$\Omega < 2 \frac{\sqrt{M^2 - 1}}{M^2 (M + 1)} \tag{25}$$

This analysis shows that the wall update scheme should be strongly underrelaxed in order to provide global stability when the flow is everywhere supersonic. Ω approaches zero slowly as M goes to one (for example, $\Omega < 0.19$ for $M = 1.02$) but this was not a problem in any calculation performer. A similar discrete node stability analysis for subsonic flow shows that the wall update scheme is also stable for subsonic flow. In general, it was found numerically that the best value of Ω was about 0.2 and that the wall geometry should be corrected every 4 integration time steps. In earlier work [7], it was reported that an underrelaxation parameter of 0.01 was required.

An initial geometry error will propagate in all directions symmetrically and induce an error with a wavelength to $4\Delta x$, see Fig. 1(c). These errors of wavelength $4\Delta x$ were eliminated by introducing a wall position smoothing

$$y_j = y_j + \omega_s (|y_{j+1} - y_j|(y_{j+1} - y_j) + |(y_{j-1} - y_j|(y_{j-1} - y_j)) \tag{26}$$

A value of ω_s equal to 0.2 was found to be sufficient to eliminate these errors. However, the correct geometry for arbitrary input pressure may not be as smooth as demanded by equation (26), and a real position error may be introduced. A careful balance must be maintained between smoothing out the $4\Delta x$ wavelength errors and producing a geometry which does not fit the specified pressure geometry but is as smooth as requested.

Since a blade position error is eliminated by moving neighboring wall points, the present inverse scheme is not effective at node points next to geometrically constrained points such as leading or trailing edge and maximum or minimum thickness constraint violation. The wall movement at these points will be constrained by the blade smoothing algorithm so that smooth blade shapes will be produced, but the specified wall pressure will not necessarily be achieved at these points.

Inflow-Outflow Boundary Formulation

As might be expected, we found that the overwhelming factor determining the number of iterations required for convergence of direct or inverse solutions was the physical size of the computational domain. When relatively simple, one-dimensional, inflow-outflow treatments were used, it was required to place the computational boundaries two to three chord lengths upstream of the cascade and one chord downstream in order to insure accuracy in the computed solution. Even when these boundaries were placed three chord lengths away, a spurious reflected wave was introduced at the upstream boundary by the approximate boundary condition. When using the locally one dimensional, "nonreflecting" boundary treatment described below, the computational boundary could usually be moved in to approximately 0.2 chords upstream of the cascade with an order of magnitude reduction in computer time usage.

When subsonic, inflow boundaries are encountered in Euler flow simulations, some flow quantities must be specified as boundary conditions and some must be computed as part of the flow solution. For consistency as well as accuracy, the inflow boundary formulation was manipulated so that the entering fluid stagnation pressure and temperature remained constant at all times. The fluid velocity and its derivatives were determined as part of the boundary formulation.

If the inflow boundary quantities are assumed to be periodic, the L_η operator, equation (11), may always be executed without further boundary conditions. Execution of the L_ξ operator, however, requires an inflow boundary formulation. The scheme chosen was a locally, one-dimensional method of characteristics in the x-direction. The fluid equations for an x-direction split operator are

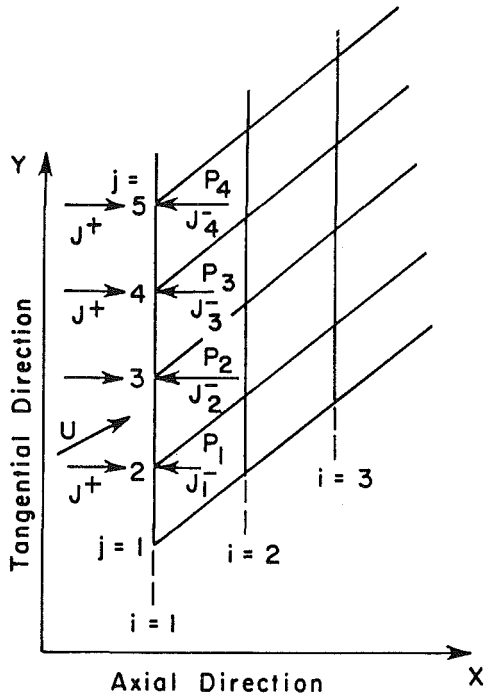

Fig. 2 Assumed locally one-dimensional characteristic wave pattern at inflow boundary

$$\partial_t(\rho) + \partial_x(\rho u) = 0 \tag{27}$$

$$\partial_t(\rho u) + \partial_x(\rho u^2 + P) = 0 \tag{28}$$

$$\partial_t(\rho v) + \partial_x(\rho u v) = 0 \tag{29}$$

If we assume that the boundary is sufficiently far upstream that any waves may be considered as isentropic "shocks" or compressions, equation (29) may be replaced by the statement that the entropy or stagnation pressure is constant in the upstream region. Equations (27) and (28) may then be rewritten in a characteristic form

$$u + \frac{2}{\gamma - 1} c = J^+ = \text{constant along} \tag{30}$$

$$\frac{dx}{dt} = u + c$$

$$u - \frac{2}{\gamma - 1} c = J^- = \text{constant along} \tag{31}$$

$$\frac{dx}{dt} = u - c$$

For the cascade simulations, the value carried by J^+ characteristic is specified, and the value carried by the J^{-1} characteristic is calculated by interpolation back to the point that a J^- characteristic intersecting the upstream boundary would originate (see Fig. 2).

If the J^+ characteristic value and an interpolation procedure for the J^- characteristic value is specified, equations (30) and (31) are two simultaneous equations for the axial velocity and the fluid speed of sound. The tangential velocity is found from the assumption of known stagnation pressure and temperature as

$$v^2 = c^2 \left(\frac{2}{\gamma - 1}\right)\left[\left(\frac{c_{\text{stag}}}{c^2}\right) - 1\right] - u^2 \tag{32}$$

where c_{stag} is the speed of sound at stagnation conditions.

It is important to note that specification of the J^+ characteristic value does not directly specify either the mass flow rate through the cascade or the average inlet flow angle. These quantities are determined through interaction of the inflow boundary, the blade entrance region geometry, and the exit static pressure of the cascade. The J^+ characteristic value may be regarded as a free parameter which may be chosen to generate an infinite variety of solutions with different mass flow rates and/or different inlet flow angles.

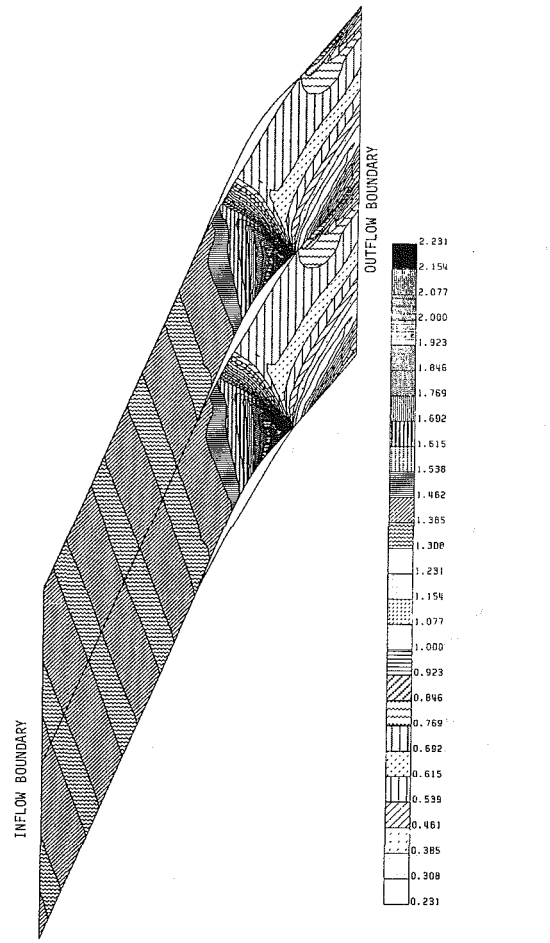

Fig. 3 MACH number contour levels for large computational domain showing periodic wave structure

Numerical experiments showed that the fluid static pressure in the downstream region became uniform within 3/4 to 1 chord length behind the blade exit plane. A similar characteristic formulation was applied at the exit boundary but with the static pressure specified rather than the J^+ characteristic value. A J^+ downstream running characteristic value was calculated by interpolation of the interior point solution and the tangential velocity calculated from a conservation of stagnation pressure condition.

The efficiency of these inflow-outflow formulations is illustrated in Figs. 3 and 4. In Fig. 3, a computation with the inflow boundary placed several chords upstream is shown in terms of a Mach number contour plot. The upstream running bow waves are clearly shown. Accuracy of the upstream solution may be checked by looking at the undisturbed waves generated on the suction surface entrance region. On such an upstream running wave path, the flow angle should always be equal to the suction surface flow angle (see Fig. 5). For this solution, the upstream flow angle is 67.94 deg and the corresponding suction surface angle is 67.98 deg. In Fig. 4, a computation with the inflow computational domain truncated 0.2 chords upstream is shown. The change in the airfoil lift from the original domain is 0.02 percent, and the upstream

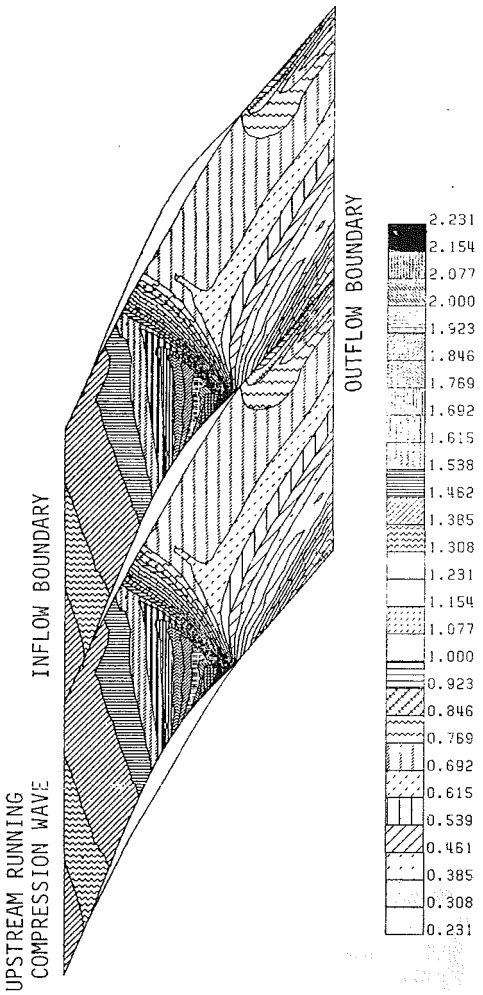

Fig. 4 MACH number contour levels for truncated computational domain

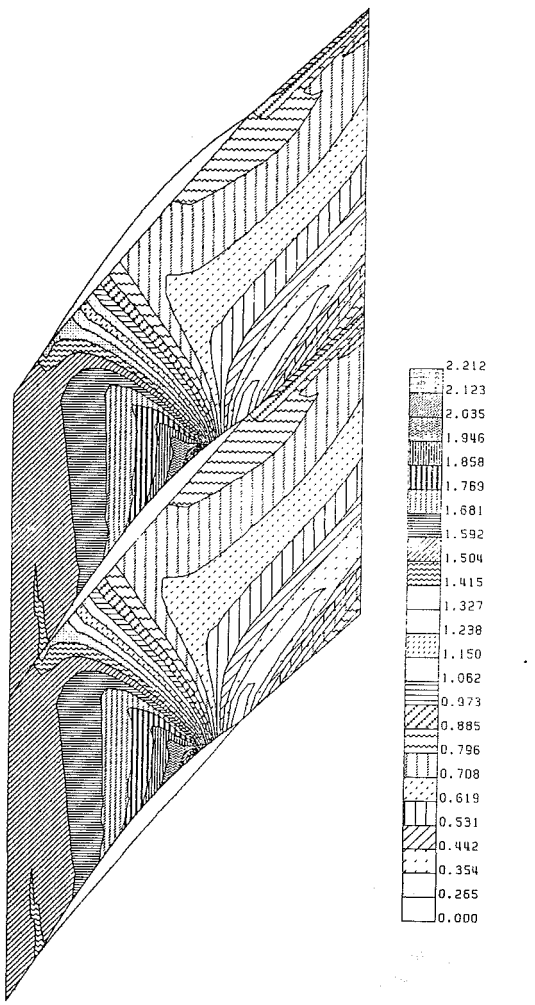

Fig. 6(*a*) MACH number contour levels for original multiple circular arc cascade

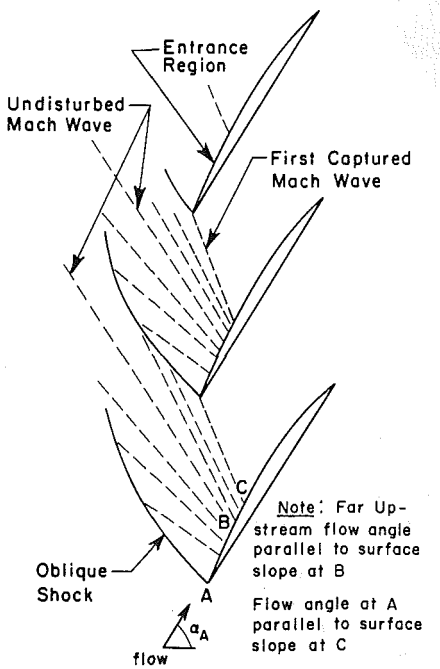

Fig. 5 Ideal upstream wave structure for a supersonic cascade with subsonic axial flow

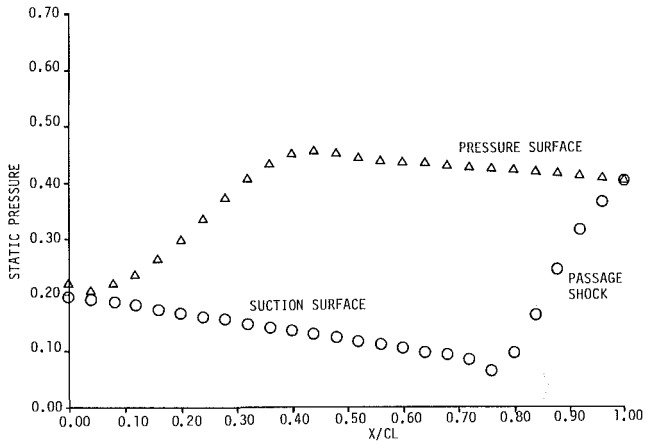

Fig. 6(*b*) Computed blade surface pressures for original multiple circular arc blade

running wave strength and flow angles are nearly identical. The number of iterations to convergence was reduced from 2000 to 400 and the computation time from 70 to 6.5 min by using the truncated domain and the maximum value of the steady-state residual

$$SSR^n = \partial_\xi \hat{\bar{F}}^n + \partial_\eta \hat{\bar{G}}^n + L_{3\xi}\hat{\bar{q}}^n = L_{3\eta}\hat{\bar{q}}^n \qquad (33)$$

at any node point is approximately 1×10^{-5}. Computation times are for a Perkin Elmer 3242 minicomputer.

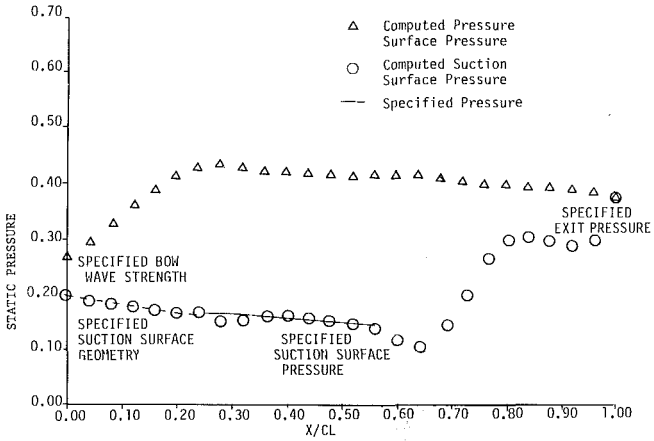

Fig. 7 Blade pressure distribution target and computed pressure for new blade shape

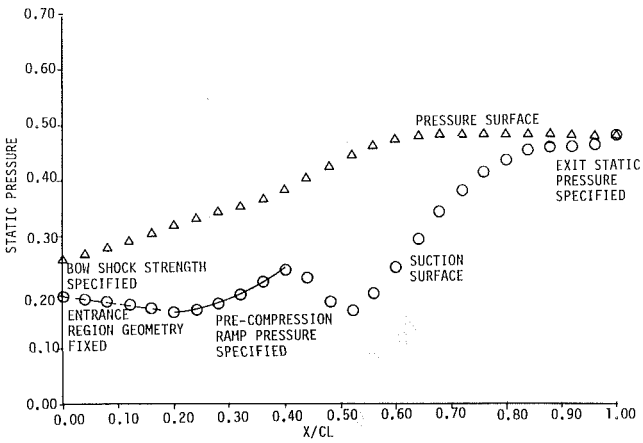

Fig. 9 Target and resultant blade pressure for precompression type design

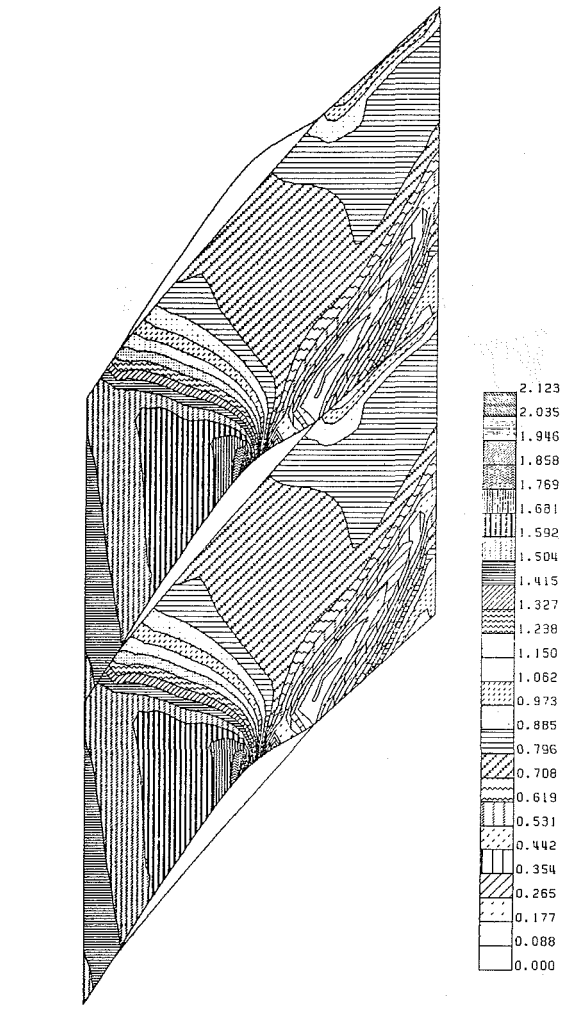

Fig. 8 MACH number contour levels for reduced stagnation pressure loss blade shape

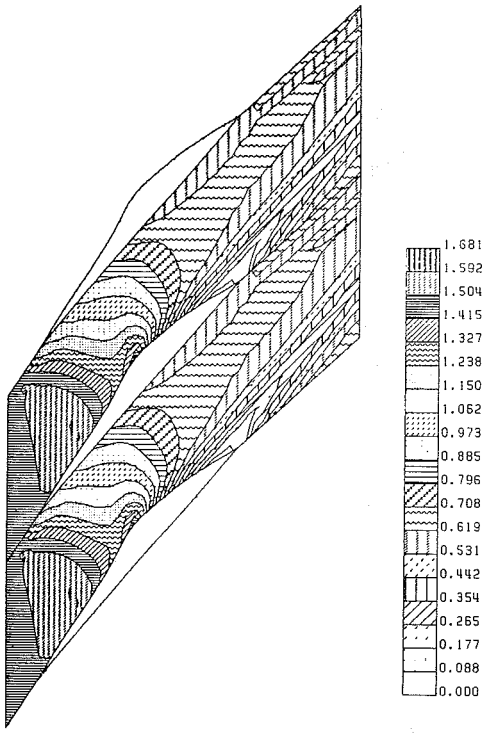

Fig. 10 MACH number contour levels for precompression type design

Trailing Edge Flow Model

These calculational examples show a distinct wake region in which a considerable but erroneous stagnation pressure loss is generated. This wake region is generated by the difference in passage shock strength on the pressure and suction surfaces. The shock stagnation pressure ratio in the pressure surface is 0.93, while the suction surface ratio is 0.68. An ideal, sharp trailing edge flow pattern should have a slip surface across which the velocity varies, but the static pressure is constant. This situation requires that the trailing edge Mach number be about 0.70 on the pressure surface side and about 0.2 on the suction surface side in order that the static pressures at the blade trailing edge match. An exact Euler flow simulation would propagate such a slip surface unchanged, but this inviscid wake tends to be quite unstable. Due to the higher stagnation pressure loss on the suction surface and the fact that the static pressures are expected to be equal, the velocity profile must have a minimum on the suction surface and an inflection point in the wake. It is well known [10] that flows with such velocity profiles are unstable.

In our numerical calculations, we generally found that the ideal flow situation did not appear, but rather, a closed, recirculating flow bubble tended to appear near the suction surface. This bubble has a strong influence on the flow solution downstream of the blade row but only a minor influence on the flow solution upstream of the passage shock

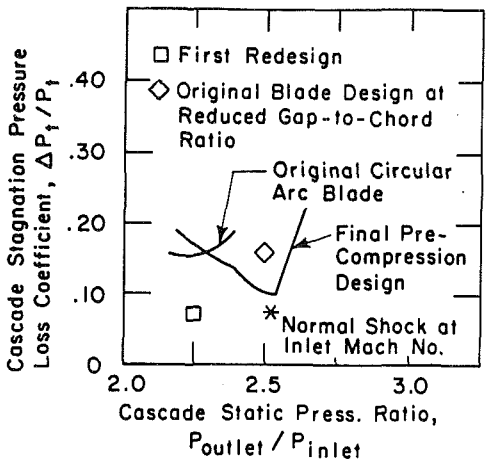

Fig. 11 Computed stagnation pressure loss coefficient for a range of row static pressure ratios

which is the primary objective of the inverse or design process.

The computed solution shown in Fig. 3 was calculated using an artificial viscosity coefficient, $AV_{j,k}$, which itself is dependent on velocity differences (see equation (12)) and the damping terms in the wake region are comparable in magnitude to those inside the passage shock. The erroneous wake stagnation pressure loss is greatly reduced when an artificial viscosity coefficient calculated from static pressure differences (see equation (13)) is used, and all remaining computational examples were computed using these artificial viscosity coefficients. It was not possible to reduce the magnitude of these damping terms to zero as this usually led to a numerical instability in the wake region. Explicit numerical schemes such as MacCormack's method have neutral stability points, in a linear sense, at stagnation points as well as sonic points.

Even though the trailing edge region flow details did not significantly influence the flow solution in front of the passage shock, the flow solution downstream of the passage shock near the suction surface and blade lift were sensitive to the artificial viscosity formulation. The major criticism of the present results is not the appearance of the recirculating region, which appears to be an inevitable result of the inviscid flow assumption, but rather the dependence of the blade lift on the form of the artificial viscosity terms. Further work, including comparisons with fully viscous flow calculations, is underway to understand the full implication of the inviscid flow model.

Computational Examples and Discussion

In order to demonstrate the efficiency of the inverse technique, a sample design problem was attempted. An initial geometry, multiple circular arc with maximum thickness of 5.4 percent, was selected, and an initial solution for an inlet Mach number of 1.52 was computed. The cascade achieved a static pressure ratio of 2.25 with a stagnation pressure loss coefficient, $\Delta P_t/P_t$, of 0.1555. The stagnation pressure loss coefficient for a normal shock at the far upstream Mach number would be 0.077. Mach number contours and blade static pressure distribution are shown in Figs. 6(*a*) and 6(*b*).

The calculated stagnation pressure loss for this cascade is twice as large as the stagnation pressure loss for a normal shock at the far upstream Mach number. This high stagnation pressure loss originates in the monotonic suction surface expansion, from Mach number 1.52 to 2.08, which is characteristic of circular arc blading. Attempts to limit this expansion require a thicker blade section, and it is difficult to design a thicker section which will pass the same mass flow rate. Thus the constraints on the design problem attempted were to pass the same mass flow rate, to have the same static pressure ratio, and to have the same gap to chord ratio. These constraints are representative to those encountered in a development or preliminary design situation.

The target pressure distribution selected is shown in Fig. 7. On the suction surface, the passage shock was moved forward and weakened. On the pressure surface, the bow shock was strengthened, and the second shock eliminated. The position of the passage shock was not specified precisely. In order to maintain the same mass flow rate, the suction surface entrance region geometry was retained. Figure 7 also shows the degree to which the target blade pressure distribution was obtained, and Fig. 8 shows the Mach number contours and blade shapes obtained. The inlet flow quantities and exit static pressure were retained. The Mach number in front of the passage shock has been reduced all across the passage with the stagnation pressure loss coefficient reduced to 0.085. This value is 55 percent of the original value and only 10 percent larger than that required by a normal shock at the upstream Mach number of 1.52. As might be expected, the maximum blade thickness increased to 10.0 from 5.4 percent.

Figures 7 and 8 are excellent examples of the influence on the overall flow solution of the trailing edge flow pattern. The slip line originates on the suction surface rather than at the trailing edge, and the passage shock near the suction surface is strong oblique rather than normal. The stagnation pressure loss at the design point is influenced by the shape of the recirculating region. The effect of the wake region is greatly reduced if the outflow static pressure is raised. The original outflow static pressure boundary condition was retained for comparison purposes, but the design point of a reduced stagnation pressure loss blade should be at a higher exit pressure.

The previous example illustrates that an existing blade shape design can be improved but does not illustrate the extent to which passage Mach number distributions may be controlled. If the requirement that the original blade gap to chord ratio be retained is eliminated, a blade design of substantially improved performance may be generated. A new target pressure is shown in Fig. 9. On the suction surface the pressure distribution is built up from the requirements that: (*a*) a weak oblique bow shock exists, (*b*) the original blade entrance region be retained (in order to retain the original inflow conditions), (*c*) the flow precompress to a Mach number of 1.3, and (*d*) the exit pressure be achieved through a strong oblique shock. The original pressure surface geometry was retained, and the gap to chord chosen such that the original inflow conditions could be retained. The design exit to inlet static pressure ratio was increased to 2.50 from 2.25.

The resulting blade shapes and Mach number contour lines are shown in Fig. 10. The stagnation pressure loss, $\Delta P_t/P_t$, has been reduced to 0.10, and the maximum Mach number reduced to 1.62. This blade design shows clearly that the inverse technique has evolved to the point that it can be used to create blade shapes with controlled Mach number distributions.

While it is not surprising that low stagnation pressure loss blades can be designed for single operating points, it appears that the present design might have good off-design performance. The original blade design had an inlet to exit static pressure rise of 2.25, but the present design can be pushed to 3.21 before the bow shock becomes normal at the passage entrance. The flow through the original blade breaks down completely at a pressure ratio of 2.4. The predicted stagnation pressure loss coefficient is plotted in Fig. 11 for several row static pressure ratios. The minimum loss of 0.10 occurs at a pressure ratio of 2.5 and good performance is maintained for

the range from 2.4 to 2.6. For reference, the performance of the original blade row is also illustrated in Fig. 11.

These computational results for a range of off-design conditions while encouraging and interesting must be considered as only preliminary since the effects of viscosity are neglected in the present analysis. Efforts are presently underway to duplicate these calculations with a fully viscous analysis and to include viscous effects in the inverse analysis. These calculations will also attempt to determine the value of the gap to chord ratio which leads to the best off-design performance.

Acknowledgments

This research was supported by Air Force Office of Scientific Research under contract number F49620-78-C-0084, supervised by J. D. Wilson.

References

1 Dulikravich, D. S., and Sabieczky, H., "Shockless Design and Analysis of Transonic Blade Shapes," AIAA Paper 81-1237, 1981.

2 Fung, K. Y., Seebass, A. R., Dickson, L. J., and Pearson, C. F., "An Effective Algorithm for Shock-Free Wing Design," AIAA Paper 81-1236, 1981.

3 Carlson, L. A., "Transonic Airfoil Analysis and Design Using Cartesian Coordinates," *Journal of Aircraft*, Vol. 13, May 1976, pp. 349–356.

4 Henne, P. A., "An Inverse Transonic Wing Design Method," AIAA Paper 80-0330, 1980.

5 Shankar, V., "A Full Potential Inverse Method Based on a Density Linearization Scheme for Wing Design," AIAA Paper 81-1234, 1981.

6 Volpe, G., and Melnik, R. E., "The Role of Constraints in the Inverse Design Problem for Transonic Airfoils," AIAA Paper 81-1233, 1981.

7 Thompkins, W. T., and Tong, S. S., "Inverse or Design Calculations for Nonpotential Flow in Turbomachine Blade Passages," ASME Paper No. 81-GT-78, to appear in JOURNAL OF ENGINEERING FOR POWER.

8 Viviand, H., "Conservation Forms of Gas Dynamic Equations," *La Recherche Aerospatiale*, No. 1, Jan. 1974, pp. 65–68.

9 MacCormack, R. W., "Computational Efficiency Achieved by Time Splitting of Finite Difference Operators," AIAA Paper 72-154, 1972.

10 Lord Rayleigh, "On the Stability of Certain Fluid Motions," *Proc. Math. Soc. London*, Vol. 11, No. 57, 1880.

The Effect of Rotor Blade Thickness and Surface Finish on the Performance of a Small Axial Flow Turbine

R. J. Roelke
National Aeronautics and Space Administration,
Lewis Research Center,
Cleveland, Ohio 44135

J. E. Haas,
Propulsion Laboratory,
AVRADCOM Research and Technology Laboratories,
Lewis Research Center,
Cleveland, Ohio 44135

An experimental investigation was conducted to determine the effect of blade profile inaccuracies and surface finish on the aerodynamic performance of a 11.15-cm tip dia turbine. The as-received cast rotor blades had a significantly thicker profile than the design intent and a fairly rough surface finish. Stage test results showed an increase of one point in efficiency by smoothing the surface finish and another three points by thinning the blade profiles to near the design profile. Most of the performance gain between the as-cast thick and the thinned rotor blades, both with the same surface finish, was attributed to reduced trailing edge losses of the recontoured blades.

Introduction

The efficiency of small (under about 15-cm tip dia) axial turbines has not equaled that demonstrated in larger machines. The chief reasons for this are Reynolds number effects and compromises made in the aerodynamic design to accommodate limitations in mechanical design and fabrication processes. A practical small turbine design will almost always have a lower blade aspect ratio, higher trailing edge blockage, and a higher rotor tip clearance than a similar large turbine. Further performance degradation may also be caused by manufacturing imperfections because it is difficult to make the blade profiles with the same precision or relative surface smoothness as large turbines. The effect of these manufacturing imperfections on the performance of a small single stage turbine is the subject of this paper.

Few reports have appeared on the effect of these manufacturing imperfections in comparison to the other causes affecting the performance of small turbines. Bammert and Sandstede [1] reported on a series of cascade tests and a four-stage turbine test where the surface roughness was changed and the blade profiles were either uniformly thinned or thickened to simulate manufacturing errors. Their results indicated dramatic changes in blade losses.

The results of the investigation described herein are an outgrowth of the automotive gas turbine technology program conducted at the NASA-Lewis Research Center. A part of that program consisted of a series of component performance tests of the compressor-drive turbine for the Department of Energy automotive gas turbine demonstrator engine. The engine and technology program are described in [2]. The turbine blading used in the subject tests consisted of duplicates of the stator and rotor castings used in the demonstrator engine. Inspection of the blading made before the start of the turbine component tests showed significant deviations from design in the profile shape and a fairly rough surface. The initial tests were made to determine the performance of the as-cast blading. After these initial tests, two subsequent turbine builds were evaluated. One build had reduced rotor blade surface roughness and in the other build the rotor blade profiles were reworked to more nearly approach the design profile.

All performance tests were conducted with air at a nominal inlet temperature of 320 K and an inlet pressure of 0.827 bars. The results reported in this paper were obtained by measuring the overall stage performance for a range of pressure ratios with the turbine operating at design speed. Rotor-exit radial surveys of angle, total pressure, and total temperature were taken at design equivalent values of speed and specific work. Results are presented in terms of efficiency and mass flow for each of the three turbine builds. Also included is the effect of the blading changes on the static pressures within the stage and the calculated changes in local efficiency based on the rotor-exit surveys. The results of the complete series of performance tests conducted with this turbine are reported in [3].

Turbine Description

The turbine used in this program was the NASA-designed compressor drive turbine for the Department of Energy automotive gas turbine demonstrator engine. A cross section of the turbine is shown in Fig. 1. Reference [4] describes the aerodynamic design of the turbine. The turbine was designed with a tip dia of 11.15 cm, stator and rotor blade heights of nominally 1.12 cm and trailing edge thicknesses of 0.038 cm for both blade rows. There were 15 stator blades and 62 rotor blades. The design trailing edge blockages were nominally 4.3 and 11.8 percent for the stator and rotor, respectively. The turbine was designed for a work factor (specific work/mean

Contributed by the Gas Turbine Division of THE AMERICAN SOCIETY OF MECHANICAL ENGINEERS and presented at the 27th International Gas Turbine Conference and Exhibit, London, England, April 18–22, 1982, Manuscript recieved at ASME Headquarters December 15, 1981. Paper No. 82-GT-222.

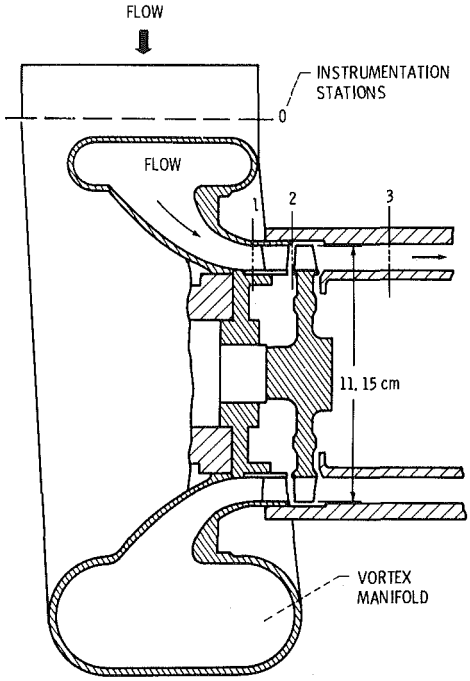

Fig. 1 Cross-sectional schematic of turbine

blade speed squared) of 2.1. The design mean section velocity diagram and blade surface velocity distributions are shown in Fig. 2. The stator exit absolute critical velocity ratio was 0.929, and the rotor exit relative critical velocity ratio was 0.818. Very little diffusion was predicted on either of the stator blade surfaces; however, moderate diffusion was predicted for both the pressure and suction surfaces of the rotor blade.

The turbine blading used for component testing were duplicates of the stator and rotor castings used in the engine. Inspection of the rotor blading before the start of the turbine testing showed significant deviations from design in the profile shape and a fairly rough surface. Figure 3 compares inspection tracings of the mean and tip sections with the design profile of two randomly selected rotor blades. Hub section tracings were not obtained because the tracing stylus was too large to fit in the small hub area. The inspection tracings show some waviness in the blade profiles and an increase in the blade thickness. Measurements made indicated local regions of the blade profiles fell outside the profile tolerance band by up to 0.05 mm. The profile tolerance was ±0.1 mm. The average trailing edge thickness based on these and other inspection tracings and the hub throat measurement was 0.053 cm resulting in a trailing edge blockage of 16.5 percent. Surface roughness measurements were made on the pressure and suction surfaces of several blades and averaged 1.35 microns.

Surface velocity distributions were not generated for the as-cast rotor blades primarily because there was no "typical" as-cast profile. The inspection traces made showed profile variations from blade to blade. Also tracings of the hub section profile could not be obtained.

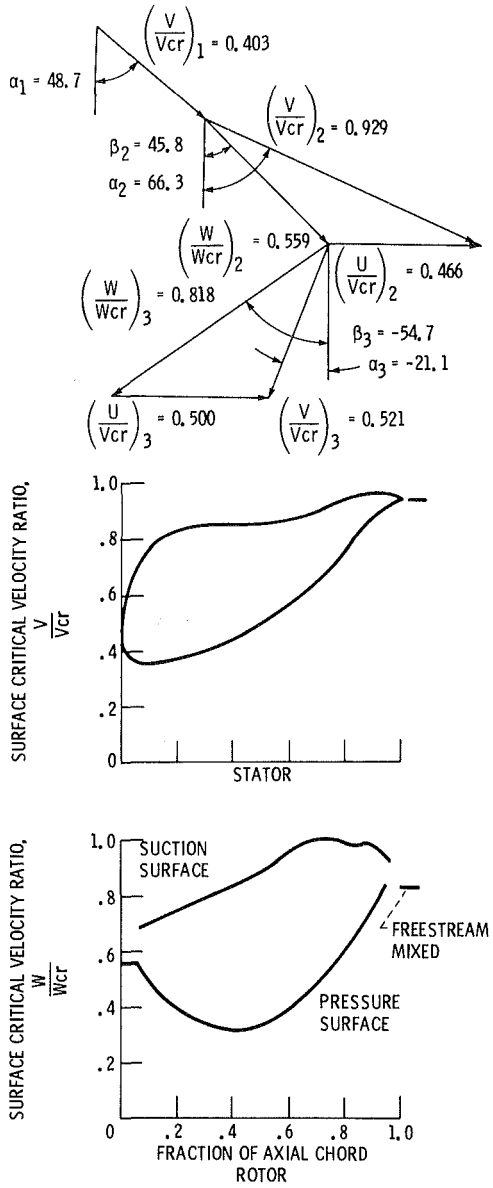

Fig. 2 Design mean section velocity diagram and blade velocity distributions

Profile tracings for the stator were not generated since the blades were cast integrally with the endwalls. However, stator throat measurements indicated that the stator flow area was undersized by 4.1 percent. The reduced flow area was caused by the size of the fillets and draft angles used in casting the stator. The as-cast stator trailing edge blockage was nominally 4.5 percent.

Turbine aerodynamic performance tests were made using the as-cast blading. After these tests were made, two modifications were made to the rotor blading. The first modification consisted of reducing the blade surface roughness. This process consisted of polishing the suction

Nomenclature

m = mass flow rate, kg/s
r = radius, m
U = blade velocity
V = absolute gas velocity, m/s
W = relative gas velocity, m/s
α = absolute gas angle measured from axial direction, deg
β = relative gas angle measured from axial direction, deg
μ = viscosity, kg/(m)(sec)

Subscripts

cr = condition corresponding to Mach number of unity
m = blade midspan
0 = station at vortex manifold inlet (Fig. 1)
1 = station at stator inlet (Fig. 1)
2 = station at stator exit (Fig. 1)
3 = station at rotor exit (Fig. 1)

surface of each of the blades (reducing the average suction surface roughness to 0.33 microns) and applying a thin coat of lacquer to the pressure surfaces. The average pressure surface roughness was 0.95 micron, resulting in an average surface roughness for the blade of 0.64 microns. Tests were then made on this configuration. The second modification consisted of electric discharge machining the rotor profiles to the design profile. The process consisted of slowly removing metal from the rotor profiles until inspection traces at the mean and tip agreed closely with the design profile. Rotor throat measurements indicated that the hub section was still thick. However, any further hub machining may have resulted in undersized profiles away from the hub, and perhaps steps in the hub endwall if the machining electrode had touched the hub. Figure 4 shows a comparison of the throat dimensions for the design, as-cast, and reworked rotor profiles. This figure shows the close agreement in the throat dimension between the design and reworked rotors, near the mean and tip sections, and the difference that remained near the hub. The average trailing edge blockage for the reworked rotor was about 13 percent. The respective suction and pressure surface roughness measurements of the reworked rotor were essentially the same as those measured after polishing and coating the as-cast rotor. Tests were then conducted using the reworked rotor blading.

Research Equipment and Procedure

The apparatus used in this investigation consisted of the research turbine, an airbrake dynamometer used to control the speed and absorb and measure the power output of the turbine, an inlet and exhaust piping system, including flow controls, and appropriate instrumentation. A schematic of the experimental equipment is shown in Fig. 5. The rotational speed of the turbine was measured with an electronic counter in conjunction with a magnetic pickup and a shaft-mounted gear. Mass flow was measured with a calibrated venturi. Turbine torque was determined by measuring the reaction torque of the airbrake which was mounted on air trunion bearings, and adding corrections for tare losses. The torque load was measured with a commercial strain-gage load cell.

The turbine instrumentation stations are shown in Figs. 1 and 6. Instrumentation at the manifold inlet (Station 0) measured wall static pressure, total pressure, and total temperature. At both the stator inlet (Station 1) and stator exit (Station 2) static pressures were measured with six taps with three each on the inner and outer walls. The inner and outer wall taps were located opposite each other at different intervals around the circumference

The rotor exit instrumentation station (Station 3) was located in a constant area exhaust duct approximately three axial chord lengths downstream of the rotor. This location was determined using a hot-wire anemometer survey probe so that the rotor exit instrumentation could be located at a position where the rotor wakes were mixed out.

At the rotor exit, static pressure, total pressure, total temperature, and flow angle were measured. The static pressure was measured with six taps, with three each on the inner and outer walls. Three self-aligning probes located around the circumference were used for measurement of total pressure, total temperature, and flow angle.

For each rotor configuration, data were obtained over a range of manifold inlet-to-rotor exit static pressure ratio at design equivalent speed. Data were obtained at nominal inlet flow conditions of 320 K and 0.827 bars. The turbine Reynolds number, $m/\mu r_m$, at these conditions was about 2.44×10^5. The rotor tip clearance was the same for all turbine configurations tested and equaled 1.7 percent of the blade length.

For each rotor configuration a rotor exit radial survey was first conducted at design equivalent values of speed and specific work. Mass averaged values of flow angle, total temperature, and total pressure were obtained for each of the

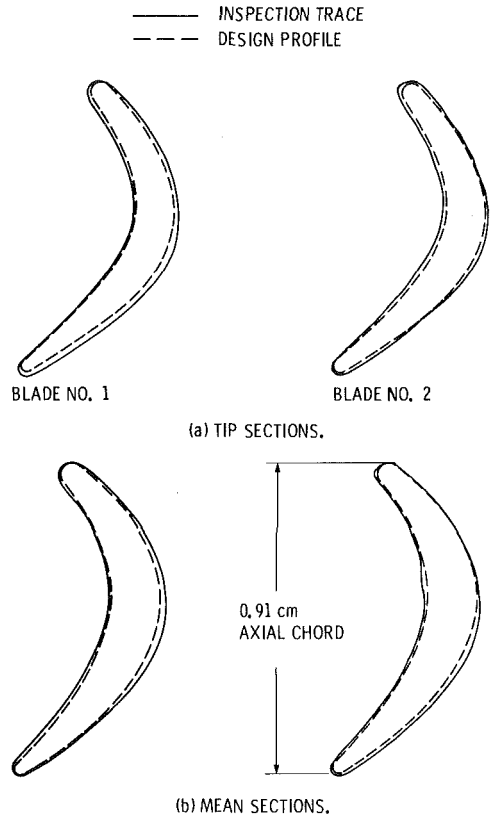

Fig. 3 Comparison of design and ar-cart rotor blade profiles

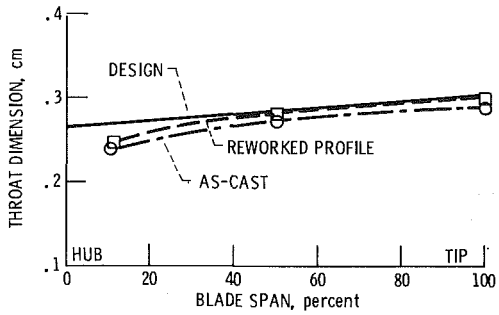

Fig. 4 Radial variation in rotor throat dimension

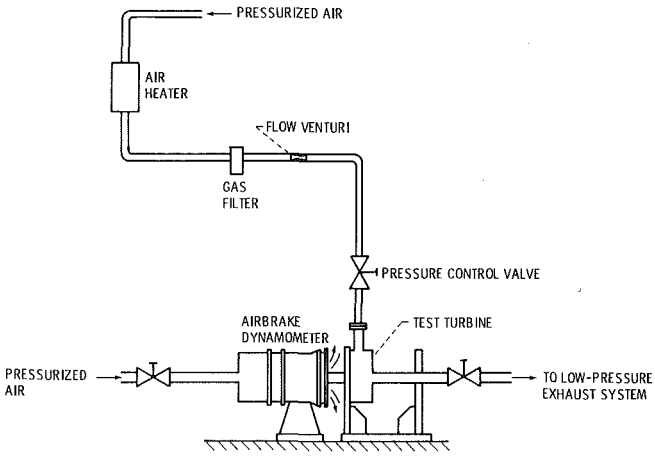

Fig. 5 Test installation schematic

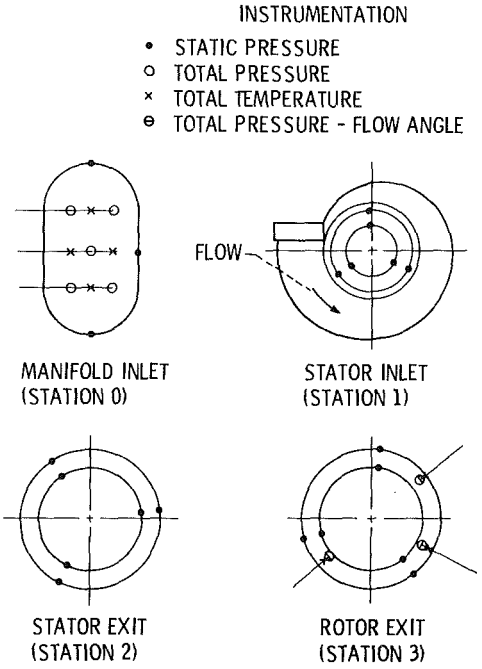

Fig. 6 Flow path instrumentation, viewed looking downstream

three survey locations. These mass-averaged values were then arithmetically averaged to obtain overall values. The survey probes were then positioned with one each near the tip, near midspan, and near the hub so that the average flow angle from these three positions would correspond closely to the overall mass-averaged value obtained from the survey. The radial positions of the survey probes, so determined, were not changed during the remainder of the testing of that rotor configuration. Performance data were then obtained over a range of turbine pressure ratio at design equivalent speed.

The turbine was rated on the basis of total efficiency. The actual work was calculated from torque, speed, and mass flow measurements. The ideal work was based on the manifold inlet-to-rotor exit total pressure ratio. The manifold inlet and rotor exit total pressures were calculated from mass flow, static pressure, total temperature, and flow angle. For the calculation of manifold inlet total pressure, the flow angle was assumed to be zero.

Results and Discussion

The variation in equivalent mass flow with stage total-pressure ratio at 100 percent of design speed is shown in Fig. 7. The turbine configuration with the as-cast rotor had the lowest mass flow. When the blade surface roughness of this rotor was reduced there was a slight increase in flow in the unchoked pressure ratio range, but the choking flow was the same as the original rotor. The highest flow was measured with the reworked profile, but the difference is small, only about 0.7 percent. The flow increase with the reworked rotor was much less than the increase in flow area of the rotor, which was 3 percent. These results indicate, that at this rotor speed, the as-cast rotor choked before the stator but with the reworked rotor installed the stator choked first and therefore controlled the stage mass flow.

The changes in stage efficiency for the three turbine builds are shown in Fig. 8. The difference in efficiency between the as-cast and reduced roughness rotor was nominally 1 point and between the as-cast and reworked profile was nominally 4 points. These differences could be expected to increase further if it were possible to thin the rotor profile near the hub and to further smooth the surface finish of the rotor and stator blades. A probable explanation for a major portion of the

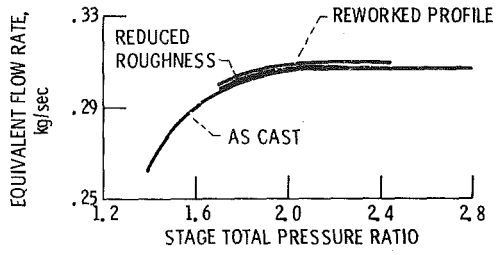

Fig. 7 Variation of equivalent mass flow with pressure ratio at design speed

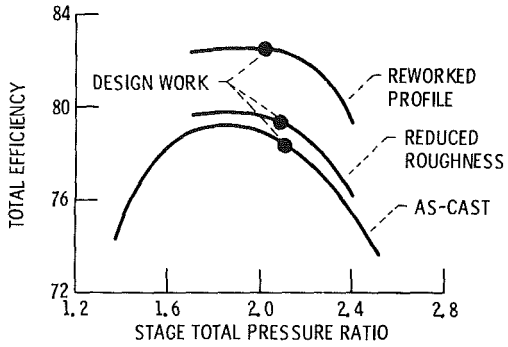

Fig. 8 Variation of efficiency with pressure ratio at design speed

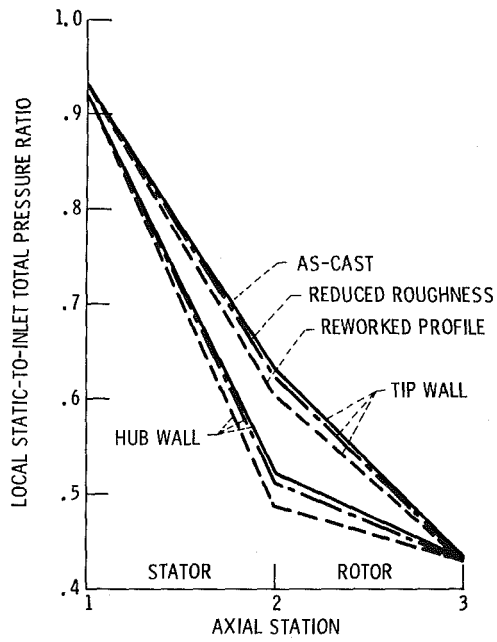

Fig. 9 Variation of static pressure with axial location at design speed and stage total pressure ratio

increase in performance of the reworked rotor configuration is the reduced trailing edge losses. An analysis of these losses is discussed later in this paper.

The changes in wall static pressure through the turbine for the design equivalent total-to-total pressure ratio of 2.01 are shown in Fig. 9. All pressures were ratioed to the inlet total pressure at Station 0. As the rotor blades were first smoothed and then thinned, the static pressure between the stator and rotor decreased slightly. This change increased the reaction across the stator and reduced it across the rotor; however, positive rotor reaction was always maintained. It was felt that the decrease in rotor reaction was not large enough to decrease either the rotor or stage efficiency.

The rotor exit radial surveys of total temperature, total pressure, and flow angle conducted at design equivalent

values of speed and specific work were used to determine radial variations in stage performance. The radial variations in turbine efficiency calculated from these survey data are shown in Fig. 10. These results show that the largest benefits of reducing the surface roughness and thinning the blade profile occurred from midspan out to the tip. This may have occurred because, as mentioned earlier, it was difficult to improve the blade surface finish and profile near the hub. With these results mass-averaged efficiencies were calculated and compared to the corresponding efficiencies shown in Fig. 8 that are based on torque measurements. In all cases the two methods of calculating the efficiencies gave values that were within 0.8 point of each other. In most comparisons the difference was only 0.1 to 0.2 point.

The rotor exit survey data together with the overall stage measurements and the results of a stator exit survey [5] were used to calculate the stage velocity diagrams for the three turbine builds at the design work condition. Selected results from those calculations are tabulated in Table 1. The velocity diagram information listed in the table shows that the flow velocities generally decreased in the rotor and increased in the stator as the rotor was first smoothed and then thinned. This agrees with the trends shown in Fig. 9. Also to be noted is that the change in flow angles was not very large. In particular, the rotor incidence did not change very much as the rotor configuration was changed. This indicates that the change in rotor incidence among the three turbine configurations was not a major factor contributing to the change in stage performance.

As mentioned earlier the as-cast blade profile was thicker than the design profile and, therefore, would have more trailing edge drag and a larger mixing loss. It was suspected that the increased trailing edge losses of the as-cast blade could account for a large portion of the performance difference between it and the reworked blade. To test this hypothesis, an estimate of the effect of the rotor trailing edge thickness on rotor performance was obtained by using the Stewart mixing model [6]. To this model was added a trailing edge drag suggested by Prust [7]. The blade surface-friction boundary layer parameters needed in the mixing equations were obtained from a boundary layer computer code, [8], using the design mean section blade surface velocities. Rotor kinetic energy loss coefficients were calculated for three values of trailing edge thickness: design, as-cast, and reworked. The trailing edge thicknesses of the as-cast and reworked blades were the averages of the hub, mean, and tip obtained from hardware measurements. The result of these calculations predicted an increase in rotor efficiency of 1.9 points due to the trailing edge difference between the as-cast and reworked blades. This change in rotor efficiency was then used in a turbine performance computer code [9] to predict the effect on the stage performance. The results of the analysis indicated an increase in stage efficiency of 2.7 points by thinning the rotor blades. The difference in efficiency

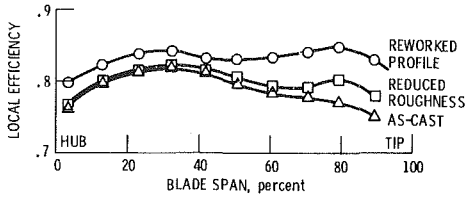

Fig. 10 Radial variation in efficiency at design speed and work

shown in Fig. 8 between the reduced roughness and reworked rotors was nominally three points. Therefore, it appears that the reduction in rotor trailing edge loss was the main reason for the performance gain.

An analysis procedure similar to that described above for the effect of blade trailing edge thickness was used to try to predict the effect of blade surface roughness. However, the results were inconclusive because of present limitations in the referenced boundary layer code to account for surface roughness changes.

A comparison was also made between the effect of blade surface roughness measured in this test program and the results reported in [1]. According to the information in the reference, a decrease in the surface roughness from 1.35 to 0.64 microns could result in an increase in stage efficiency of about 1.2 points. This predicted increase in efficiency is generally consistant with the increase measured during the test program. An increase of nominally 1 point was measured with the turbine operating at design equivalent speed and work.

Concluding Remarks

The results obtained in this experimental investigation showed that inaccuracies in the manufacture of small turbine blades can cause significant turbine performance penalties. Small dimensional deviations from design that may be acceptable in large machines must be critically examined to judge the impact in a small machine. Ultimately, analytical methods must be developed to predict these effects. For this turbine, obtaining an accurate blade profile and a smooth surface finish significantly improved its performance. Analytical predictions of these effects compared closely with the experimental results. Finally, the quality of the castings procured for this demonstrator engine program may not be indicative of what may be reasonably achieved given more time to further develop the manufacturing processes.

References

1 Bammert, K. and Sandstede, H., "Influence of Manufacturing Tolerances and Surface Roughness of Blades on the Performance of Turbines," ASME Paper No. 75-GT-35, Mar. 1975.

2 Ball, G. A., Gumaer, J. I., and Sebestyen, T. M., "The ERDA/Chrysler Upgraded Gas Turbine Engine-Objectives and Design," SAE Paper No. 760279, 1976.

3 Roelke, R. J. and Haas, J. E., "Cold-Air Performance of Compressor-

Table I Calculated stage velocity diagrams at design work factor

	Design	As-cast					Reduced roughness					Reworked				
Percent span (hub is zero)	50	5	25	50	75	95	5	25	50	75	95	5	25	50	75	95
Station 2 Absolute velocity ratio	0.929	0.945	0.899	0.869	0.841	0.808	1.000	0.970	0.873	0.863	0.752	1.002	0.937	0.923	0.897	0.792
Relative velocity ratio	.559	.632	.551	.495	.464	.450	.691	.573	.500	.487	.402	.694	.592	.553	.522	.437
Relative flow angle, deg	45.8	44.7	47.6	46.0	38.0	27.5	46.3	48.4	46.3	30.4	23.0	46.4	49.1	48.4	41.3	26.7
Rotor incidence, deg	0.1	-4.3	-0.2	0.3	-4.6	-11.5	-2.7	0.6	0.6	-3.2	-16.0	-2.6	1.3	2.7	-1.3	-12.3
Station 3 Absolute velocity ratio	0.521	0.524	0.593	0.570	0.520	0.466	0.508	0.562	0.555	0.507	0.493	0.507	0.539	0.504	0.499	0.463
Relative velocity ratio	.818	.808	.862	.845	.832	.815	.780	.830	.830	.818	.861	.773	.805	.785	.806	.841
Absolute flow angle, deg	-21.1	-27.6	-23.1	-19.2	-20.4	-22.1	-23.9	-21.6	-18.5	-18.5	-28.8	-22.7	-20.2	-17.5	-18.3	-29.6

Drive Turbine of Department of Energy Upgraded Automobile Gas Turbine Engine, II—Stage Performance," NASA TM-82818, 1982.

4 Roelke, R. J. and McLallin, K. L., "The Aerodynamic Design of a Compressor-Drive Turbine for Use in a 75 kW Automotive Engine," NASA TM X-71717, 1975.

5 Roelke, R. J. and Haas, J. E., "Cold-Air Performance of Compressor-Drive Turbine of Department of Energy Upgraded Automobile Gas Turbine Engine, I—Volute-Manifold and Stator Performance," NASA TM-81932, 1981.

6 Stewart, W. L., "Analysis of Two-Dimensional Compressible-Flow Characteristics Downstream of Turbomachine Blade Rows in Terms of Basic Boundary-Layer Characteristics," NACA TN-3515, 1955.

7 Prust, H. W., Jr., "Boundary Layer Losses," Turbine Design and Application, Vol. II, NASA SP-290, 1973, pp. 93–124.

8 McNally, W. D., "FORTRAN Program for Calculating Compressible Laminar and Turbulent Boundary Layers in Arbitrary Pressure Gradients," NASA TN D-5681, 1970.

9 Flagg, E. E., "Analytical Procedure and Computer Program for Determining The Off-Design Performance of Axial Flow Machines," NASA CR-710, 1967.

Comparison of Beam and Shell Theories for the Vibrations of Thin Turbomachinery Blades

A. W. Leissa
Professor,
Department of Engineering Mechanics,
Ohio State University,
Columbus, Ohio 43210

M. S. Ewing
Assistant Professor,
Department of Engineering Mechanics,
United States Air Force Academy

A great deal of published literature exists which analyzes the free vibrations of turbomachinery blades by means of one-dimensional beam theories. Recently, a more accurate, two-dimensional analysis method has been developed based upon shallow shell theory. The present paper summarizes the two types of theories and makes quantitative comparisons of frequencies obtained by them. Numerical results are presented for cambered and/or twisted blades of uniform thickness. Significant differences between the theories are found to occur, especially for low aspect ratio blades. The causes of these differences are discussed.

Introduction

Vibration analysis of turbomachinery blades has traditionally been carried out by means of beam theory. One can find literally hundreds of references in the literature incorporating considerations such as coupling between bending and torsion, taper, shear deformation, rotary inertia, pretwist and rotational effects into one-dimensional beam vibration analyses. For example, a recent literature survey [1] uncovered approximately 150 references dealing with *rotational* effects in beam vibration analysis. Particularly notable among the carefully developed beam theories are those presented by Carnegie [2–8], Houbolt and Brooks [9] and Montoya [10]; these incorporate most of the considerations needed in blade vibration analysis by means of beam models and are widely used.

However, beam analysis becomes inadequate for low aspect ratio blades. Most obviously, vibration modes which involve predominantly chordwise bending are completely missed. These modes become more important as blade thicknesses and aspect ratios decrease. Furthermore, another important question arises: Even for those modes obtainable from beam analysis (i.e., spanwise bending and torsion), how accurate is beam theory for low aspect ratio blades?

In recent years two-dimensional methods of blade vibration analysis have been developed. As seen in a recent survey article [11], most of these utilize finite elements and tend to require considerable computation time. However, the chordwise bending effects are accounted for and, with properly conformable finite elements, accurate results are obtainable if sufficient elements are employed.

More recently a two-dimensional method of blade analysis has evolved which does not require finite elements and is based upon shell equations [12–14]. The method assumes general forms for the three components of displacement of a cantilever shell in terms of continuous functions, and utilizes the well-known Ritz method to obtain frequencies and mode shapes. The method has been demonstrated to be computationally more efficient than finite elements [12] for the blade configurations that it can accommodate, and is well suited for parametric studies. It is also capable of providing very accurate solutions against which one-dimensional, beam model results can be compared.

The primary purpose of the present paper is to demonstrate the accuracy and limitations of blade vibration analyses which utilize one-dimensional beam theories. From the thorough literature search previously performed by the senior author, it appears that no quantitative comparisons between the one-dimensional and the more accurate two-dimensional models have been previously undertaken. Furthermore, where the results of beam analysis have been compared with experiment, it has only been for blades of relatively large aspect ratio. For this reason, the present work makes comparisons between the theories and experiment for low aspect ratios as well. Of particular importance are the effects of shear deformation, rotary inertia, and warping which should be properly dealt with by beam models, and which can become more significant for smaller aspect ratios.

In the two sections which follow, the essential descriptions of the beam theory and shell theory to be used in subsequent comparisons are laid out. Each section has its own notation, independent of each other, consistent with widespread usage in beam and shell theory and following closely the notation used in the relevant references. In subsequent sections, quantitative comparisons of vibration frequencies obtained from beam theory and shell theory are made for blades having camber and/or twist. Models are chosen for which other accurate analyses can also be found in the published literature. Finally, a concluding section summarizes the limitations of beam theory and what is needed to make it more accurate for the spanwise bending and torsional modes which it may reasonably represent.

Contributed by the Gas Turbine Division of The American Society of Mechanical Engineers and presented at the 27th International Gas Turbine Conference and Exhibit, London, England, April 18–22, 1982. Manuscript received at ASME Headquarters December 15, 1981. Paper No. 82-GT-223.

Beam Theory Description

Undoubtedly the most thorough work to develop a comprehensive set of equations representing a vibrating blade as a beam was presented in a sequence of papers by Carnegie [2–8] which appeared during the period 1957–1967. In the first work [2] potential energy functionals were derived for a twisted blade of arbitrary cross section, and variational methods were then employed to obtain static equations of equilibrium describing bending about two axes and torsion. These equations were then integrated for the case of cross sections uniform along the length subjected to either concentrated or uniformly distributed transverse static loadings, and numerical results were obtained for blades of rectangular and airfoil cross sections.

Vibrations were taken up in a subsequent paper [3]. The strain energy of elastic deformation used in the static analysis [2] was taken, i.e.,

$$V=\frac{1}{2}\int_0^l\left\{EI_{yy}\left(\frac{\partial^2 u}{\partial z^2}\right)^2+2EI_{xy}\frac{\partial^2 u}{\partial z^2}\frac{\partial^2 v}{\partial z^2}+EI_{xx}\left(\frac{\partial^2 v}{\partial z^2}\right)^2+C\left(\frac{\partial\theta}{\partial z}\right)^2\right\}dz \tag{1}$$

and the kinetic energy was written as

$$T=\frac{1}{2}\int_0^l\{\rho(\dot{u}+r_y\dot{\theta})^2+\rho(\dot{v}+r_x\dot{\theta})^2+I_c\dot{\theta}^2\}dz \tag{2}$$

where z is the longitudinal (i.e., spanwise) coordinate passing through the centers of flexure (see Fig. 1) of the cross sections; x and y are coordinates orthogonal to z; and u and v are displacements in the x-and y-directions, respectively. Figure 1 also shows an XYZ coordinate system, with Z being parallel to z and passing through the centroid of the blade cross section, and X and Y being the axes of principal moments of inertia I_{xx} and I_{yy} (more properly, the principal second moments of areas). The moments and product of inertia, I_{xx}, I_{yy}, and I_{xy}, are taken with respect to axes parallel to x and y and passing through the centroid. The angular displacement during torsional vibration is given by θ, and C is the torsional stiffness of the cross section, ρ is mass per unit length and I_c is the polar mass moment of inertia per unit length with respect to the centroid. Time derivatives in equation (2) are denoted by dots above the variables. Applying the Euler-Lagrange equations of the calculus of variations yielded the equations of motion [3]

$$\frac{\partial^2}{\partial z^2}\left\{EI_{yy}\frac{\partial^2 u}{\partial z^2}+EI_{xy}\frac{\partial^2 v}{\partial z^2}\right\}=-\rho(\ddot{u}+r_y\ddot{\theta}) \tag{3a}$$

$$\frac{\partial^2}{\partial z^2}\left\{EI_{xy}\frac{\partial^2 u}{\partial z^2}+EI_{xx}\frac{\partial^2 v}{\partial z^2}\right\}=-\rho(\ddot{v}+r_x\ddot{\theta}) \tag{3b}$$

$$\frac{\partial}{\partial z}\left(C\frac{\partial\theta}{\partial z}\right)=\rho r_y\ddot{u}+\rho r_x\ddot{v}+(\rho r_y^2+\rho r_x^2+I_c)\ddot{\theta} \tag{3c}$$

Equations (3) show clearly the coupling which exists between the three displacement variables, u, v and θ. For a general section possessing no symmetry (such as in Fig. 1), coupling is complete among the two bending displacements and the torsional displacement.

Another significant contribution of Carnegie's second paper [3] was the recognition of additional torsional stiffnesses in a cantilevered blade beyond that represented by C. In the case of a *straight* blade, the constant, C, depends upon the cross-sectional shape and the shear modulus (G), and is determined by solving the St. Venant torsion problem of classical elasticity for the given shape (see [15], chapter 10). But the St. Venant torsion problem assumes that both ends of the blade are free to warp out of their xy-planes. Clearly, the clamped end of a cantilevered blade is restrained from warping, and this constraint yields additional torsional stiffness to the blade. Carnegie [3] viewed the additional stiffness as being due to "torsion bending"—that is, the additional stiffness due to the longitudinal fibers each being bent as cantilever beams during the torsional rotations of the cross sections. For a straight blade of rectangular cross section having width, b, and depth, h, he showed that the total twisting moment at a typical location (z) is given by

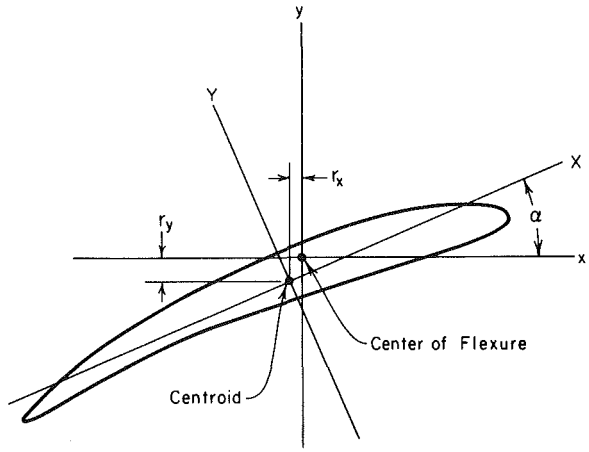

Fig. 1 Typical blade cross section, showing coordinates for beam analysis

$$M_\theta=C\frac{\partial\theta}{\partial z}-C_1\frac{\partial^3\theta}{\partial z^3} \tag{4a}$$

where $C = Gbh^3/3 = Ebh^3/6(1+\nu)$ is the St. Venant torsional stiffness constant, and

$$C_1=Eb^3h^3/144 \tag{4b}$$

Of course, the second term of equation (4) causes additional stiffening in spite of the negative sign because, at a point having $\partial\theta/\partial z$ positive, $\partial^3\theta/\partial z^3$ is typically negative. The correction factor, C_1, was shown to have little effect upon the fundamental torsional frequency of a typical, large aspect ratio blade, but to have pronounced effect upon the higher torsional frequencies ([3], Figs. 11 and 15).

The additional torsional stiffening was expounded upon further in a subsequent publication [5]. Therein Carnegie demonstrated that the torsional strain energy term (last term in equation (1)) is generalized to

$$C\left(\frac{\partial\theta}{\partial z}\right)^2-C_1\frac{\partial\theta}{\partial z}\frac{\partial^3\theta}{\partial z^3} \tag{5}$$

and that the third equation of motion (3c) has its left-hand side replaced by

$$\frac{\partial}{\partial z}\left(C\frac{\partial\theta}{\partial z}-C_1\frac{\partial^3\theta}{\partial z^3}\right) \tag{6}$$

and the order of the system of differential equations (3) is thereby raised from ten to twelve. The latter set requires the statement of six boundary conditions at each end of the blade; in particular, for the cantilever blade of length, l.

$$u=\frac{\partial u}{\partial z}=v=\frac{\partial v}{\partial z}=\theta=\frac{\partial\theta}{\partial z}=0,\ \text{at } z=0 \tag{7a}$$

$$M_x=M_y=Q_x=Q_y=\frac{\partial^2\theta}{\partial z^2}=M_\theta=0,\ \text{at } z=l \tag{7b}$$

where M_x and M_y are the bending moments about the x and y axes, Q_x and Q_y are the transverse shearing forces in the x and y directions, and M_θ is the twisting moment, given by equation (4).

In an interesting discussion of the Carnegie paper, Barr

pointed out (see [5], p. 319) that the additional torsional stiffness constant, C_1 could be obtained from the classical St. Venant torsion theory by solving for the warping function, ψ, where the longitudinal (z-direction) displacement w determines the warping, and is given by

$$w(x,y) = \psi(x,y)\,\frac{\partial\theta}{\partial z} \tag{8}$$

and the constant, C_1, is then obtained from

$$C_1 = E\int\int_A \psi^2 dxdy \tag{9}$$

As part of this reply to Barr's discussion, Carnegie also showed that the torsional strain energy term (5) can be equivalently written as

$$C\left(\frac{\partial\theta}{\partial z}\right)^2 + C_1\left(\frac{\partial^2\theta}{\partial z^2}\right)^2 \tag{10}$$

Carnegie [6] also added the effects of shear deformation and rotary inertia to the problem, following the now well-known approach first suggested by Timoshenko [16]. In considering shear deformation the changes in slope of a beam due to bending and shear must be entered into the problem independently, and the strain energy functional (1) is generalized to

$$V = \frac{1}{2}\int_0^l \left\{EI_{yy}\left(\frac{\partial\phi_x}{\partial z}\right)^2 + 2EI_{xy}\frac{\partial\phi_x}{\partial z}\frac{\partial\phi_y}{\partial z} + EI_{xx}\left(\frac{\partial\phi_y}{\partial z}\right)^2 + \frac{AG}{2k}\left[\left(\frac{\partial u}{\partial z} - \phi_x\right)^2 + \left(\frac{\partial v}{\partial z} - \phi_y\right)^2\right] + C\left(\frac{\partial\theta}{\partial z}\right)^2 + C_1\left(\frac{\partial^2\theta}{\partial z^2}\right)^2\right\} dz \tag{11}$$

where, for example, the shearing slope in the xz-plane, $\partial u/\partial z - \phi_x$, is the difference between the total slope ($\partial u/\partial z$) and the slope due to bending alone (ϕ_x). The shear rigidity also involves the blade cross sectinal area (A), and a shear stress distribution factor (k) depending upon cross-sectional shape. The kinetic energy functional is given by equation (2) with the terms reflecting the rotary inertia [7] added to the integrand:

$$\rho\left[\dot\phi_x + \frac{\partial}{\partial z}(r_y\dot\theta)\right]^2 + \rho\left[\dot\phi_y + \frac{\partial}{\partial z}(r_x\dot\theta)\right]^2 \tag{12}$$

During the foregoing theoretical development, the dynamic effects due to blade rotation while mounted on a disk were added to the problem [4], including both the stabilizing (frequency increasing) primary and the destablizing (frequency decreasing) secondary centrifugal force effects. The final, most general potential and kinetic energy functions, along with corresponding equations of motion, were summarized in a short note [7] in 1966. Experimental studies [2, 3, 17, 18] were also made, which verified most of the theoretical conclusions.

Where numerical solutions were given in the papers by Carnegie described above, they were obtained in a few cases by exact integration of the equations of motion, but more often by a somewhat crude Rayleigh method using static deflection functions to represent the mode shapes. Subsequent papers with colleagues (for example, [19–23]) served to obtain more accurate solutions by other approximate methods such as finite differences, Runge-Kutta numerical integration, Ritz-Galerkin, and an extended Holzer technique. Most of these publications are summarized in survey papers by one of the present authors [1] and Rao [24–26]. By and large, the following general comments can be made about the references containing numerical results:

1 Blades are of large aspect ratio.

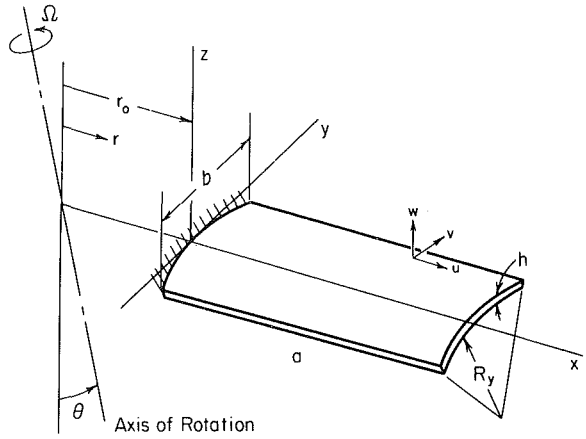

Fig. 2 Simplified model of a rotating blade

2 Airfoil cross-sectional data is not given, thereby preventing comparison by other methods.

3 The torsional warping constant, C_1, is not considered.

Houbolt and Brooks [9] and Montoya [10] also derived sets of differential equations of motion for twisted blades of arbitrary cross section. However, in both derivations neither shear deformation nor rotary inertia were included. Nor were the effects of cross-sectional warping during bending or cross-sectional warping constraint during torsion explicitly considered in either analysis.

In the present work, beam theory representations of blades will be made by means of Carnegie's equations which, as the foregoing paragraphs have indicated, appear to be the most comprehensive set thus far appearing in the published literature of blade vibrations. Although an exact solution of the twelfth-order set of differential equations of motion is possible for the cantilevered blade, the procedure is algebraically cumbersome, and a straightforward Ritz procedure will be used instead. For the free vibration problem, classical beam theory displacements, u, v, and θ, are taken as

$$\begin{aligned} u(z,t) &= U(z)\sin\omega t \\ v(z,t) &= V(z)\sin\omega t \\ \theta(z,t) &= \Theta(z)\sin\omega t \end{aligned} \tag{13}$$

where ω is the radial frequency. The functions U, V, and Θ must be chosen such that:

1 The geometric boundary conditions (7a) are exactly satisfied along the clamped edge

2 The functions form complete sets (i.e., capable of representing any set of kinematically possible displacements along the blade axis)

For the present problem a set of displacements for straightforward application is given by the algebraic polynomials

$$U(z) = \sum_{i=1}^{I} A_i z^i, V(z) = \sum_{j=1}^{J} B_j z^j, W(z) = \sum_{k=2}^{K} C_k z^k,$$

$$\Phi_x(z) = \sum_{l=1}^{L} D_l z^l, \Phi_y(z) = \sum_{m=1}^{M} E_m z^m \tag{14}$$

when shear deformation and torsional warping constraint are now included. For the classical Euler-Bernoulli theory, the functions Φ_x and Φ_y are not used, and the index k begins at one, instead of two. To apply the Ritz method, the functional $T_{\max} - V_{\max}$ is formed, where $T_{\max}$ and $V_{\max}$ are the

maximum values of kinetic energy (i.e., at maximum velocity) and potential energy (i.e., at maximum displacement). The functional is then minimized by equations of the type

$$\frac{\partial(T_{\max} - V_{\max})}{\partial A_i} = 0, (i = 1,2. \ . \ .I) \tag{15}$$

with derivatives taken with respect to each of the A_i, B_j, C_k, D_l, E_m in turn, and where V is given by equation (11) and T by equation (2) with the terms (12) added, yielding a set of $I + J + K + L + M - 1$ simultaneous linear algebraic equations in the same number of unknowns $A_i, \ . \ . \ . \ ,E_m$. For a nontrivial solution the determinant of the coefficient matrix of the equations is set equal to zero and the roots of the determinant are the eigenvalues (i.e., nondimensional frequencies). The eigenfunctions (mode shapes) are determined by backsubstitution of the eigenvalues in the usual way. The resulting frequencies are upper bounds on the exact frequencies and, if a complete set of functions such as equations (14) is used, the exact beam frequencies can be determined as accurately as desired.

Shell Theory Description

The shell analysis used in this work is based upon *shallow* shell theory. This theory contains the essential features needed, namely, bending and stretching effects coupled together, and is applicable provided the curvature and twist are relatively small. It is capable of representing variable curvature and twist and variable thickness and, for blades which are relatively thick, can be generalized to include shear deformation and rotary inertia effects. However, the present study will be limited to blades which are sufficiently thin so that the latter effects can be neglected. For shells of arbitrary curvature and twist, *deep* shell theory will typically involve nonprincipal, nonorthogonal coordinates with considerable complication in the resulting equations (see [27], p. 54) and is therefore desirable to avoid in blade analysis.

Consider the simplified model of a rotating blade shown in Fig. 2. It has a length, a, a planform width, b, (i.e., the projected width in the xy reference plane), and a thickness, h. The present study assumes a rectangular planform for the blade, although other shapes can also be treated. The blade is represented as a shallow shell having curvature $1/R_y$ in the y-direction. Twist ($1/R_{xy}$) is not shown, but can be readily accommodated in the analysis. The shell is assumed rigidly clamped at one end ($x = 0$), whereas the other three edges are completely free. Angular velocity Ω is assumed about an axis located at a hub radius, r_o, from the blade root. The blade is inclined with a stagger angle, θ, with respect to the rotation axis. Displacements are measured as in conventional shell theory by w taken normal to the shell midsurface, and u and v

Table 1 Comparison of $\omega a^2\sqrt{\rho h/D}$ between shell and beam theories for cambered blades ($b/h = 20$)

			Symmetric modes			Antisymmetric modes			
				Beam theory			Beam theory (no C_1)		Beam theory (with C_1)	
$\frac{a}{b}$	$\frac{b}{R}$	Mode No.	Shell theory	Shear def. and R.I.	Classical	Shell theory	Shear def. & R.I.	Classical	Shear def. & R.I.	Classical
5	0.1	1	3.516	3.463	3.463	33.98	32.12	32.21	33.86	33.86
		2	21.95	21.69	21.70	65.35[c]	65.08[c]	67.11[c]	65.09[c]	67.11[c]
		3	61.62	60.68	60.76	103.9	96.38	96.64	103.5	103.5
		4	127.9	118.8	119.1	179.6	160.6	161.1	178.7	178.7
	0.3	1	4.271	4.242	4.242	34.00	31.90	31.99	33.63	33.63
		2	26.43	26.56	26.58	65.36[c]	65.33[c]	67.36[c]	65.35[c]	67.38[c]
		3	73.83	74.28	74.44	104.1	95.79	96.05	102.9	102.9
		4	148.3	145.3	145.9	180.2	159.6	160.0	177.6	177.7
	0.5	1	5.454	5.513	5.514	34.02	31.46	31.55	33.17	33.17
		2	33.51	34.50	34.55	65.37[c]	65.81[c]	67.87[c]	65.86[c]	67.91[c]
		3	92.48	96.41	96.75	104.3	94.61	94.88	101.7	101.7
		4	181.3	188.4	189.6	181.1	157.5	158.0	175.5	175.5
2	0.1	1	3.545	3.461	3.463	14.81	12.85	12.85	14.74	14.74
		2	21.92	21.62	21.70	48.23	38.55	38.65	48.04	48.04
		3	61.00	60.24	60.76	57.52[c]	57.08[c]	67.11[c]	57.11[c]	67.11[c]
		4	93.28[a]	———	———	92.67	64.25	64.42	91.91	91.91
	0.3	1	4.264	4.239	4.242	14.84	12.77	12.80	14.65	14.65
		2	25.25	26.44	26.58	48.39	38.30	38.41	47.76	47.78
		3	66.81	73.47	74.44	57.52[c]	57.28[c]	67.36[c]	57.33[c]	67.36[c]
		4	93.38[a]	———	———	93.25	63.85	64.02	91.45	91.47
	0.5	1	5.398	5.506	5.514	14.89	12.60	12.64	14.47	14.48
		2	30.64	34.23	34.55	48.70	37.79	37.91	47.20	47.24
		3	76.51	94.67	96.75	57.54[c]	57.68[c]	67.86[c]	57.75[c]	67.86[c]
		4	93.54[a]	———	———	94.39	63.03	63.20	90.52	90.57
1	0.1	1	3.561	3.456	3.463	8.516	6.425	6.442	8.485	8.485
		2	21.48	21.39	21.70	31.00	19.28	19.33	30.94	30.94
		3	27.22[a]	———	———	43.56[c]	42.93[c]	67.11[c]	42.99[c]	67.11[c]
		4	54.28[b]	———	———	64.28[d]	———	———	———	———
	0.3	1	4.181	4.229	4.242	8.543	6.385	6.402	8.438	8.439
		2	22.76	26.01	26.58	31.17	19.15	19.21	30.77	30.79
		3	27.42[a]	———	———	43.56[c]	43.01[c]	67.35[c]	43.14[c]	67.35[c]
		4	54.52[b]	———	———	64.29[d]	———	———	———	———
	0.5	1	5.168	5.484	5.514	8.595	6.303	6.320	8.344	8.346
		2	24.66	33.33	34.55	31.50	18.90	18.96	30.45	30.50
		3	28.11[a]	———	———	43.57[c]	43.08[c]	67.83[c]	43.45[c]	67.82[c]
		4	55.03[b]	———	———	64.31[d]	———	———	———	———

[a]Chordwise bending mode
[b]Combined mode
[c]Sideways bending mode
[d]Antisymmetric chordwise bending mode

tangent to the midsurface, with u being parallel to the x-direction.

The present analysis utilizes the well-known Ritz method and is therefore based upon the potential and kinetic energy functionals. The total potential energy of the rotating shell can be written as

$$V = V_1 + V_2 + V_3 + V_4 \tag{16}$$

where V_1 is the strain energy of stretching (see [27-29])

$$V_1 = \frac{Eh}{2(1-\nu^2)} \int_{-b/2}^{b/2} \int_0^a \left\{ (\epsilon_x + \epsilon_y)^2 - 2(1-\nu) \left[\epsilon_x \epsilon_y - \frac{\gamma_{xy}^2}{4} \right] \right\} dxdy \tag{17}$$

and V_2 is the strain energy of bending

$$V_2 = \frac{Eh^3}{12(1-\nu^2)} \int_{-b/2}^{b/2} \int_0^a \left\{ (\nabla^2 w)^2 - 2(1-\nu) \left[\frac{\partial^2 w}{\partial x^2} \frac{\partial^2 w}{\partial y^2} - \left(\frac{\partial^2 w}{\partial x \partial y} \right)^2 \right] \right\} dxdy \tag{18}$$

In the above expressions ϵ_x, ϵ_y and γ_{xy} are the membrane strains given by

$$\epsilon_x = \frac{\partial u}{\partial x} + \frac{w}{R_x}, \epsilon_y = \frac{\partial v}{\partial y} + \frac{w}{R_y}$$
$$\gamma_{xy} = \left(\frac{\partial v}{\partial x} + \frac{\partial u}{\partial y} \right) + 2\frac{w}{R_{xy}} \tag{19}$$

E is Young's modulus and ν is Poisson's ratio.

The functionals V_3 and V_4 are due to the centrifugal forces of rotation, with V_3 being due to the steady, radially directed components of body forces; that is,

$$V_3 = \frac{1}{2} \int_{-b/2}^{b/2} \int_0^a \left\{ N_x^0 \left(\frac{\partial w}{\partial x} \right)^2 + N_y^0 \left(\frac{\partial w}{\partial y} \right)^2 + 2 N_{xy}^0 \frac{\partial w}{\partial x} \frac{\partial w}{\partial y} \right\} dxdy \tag{20}$$

where N_x^0, N_y^0, and N_{xy}^0 are the membrane stress resultants (i.e., force per unit length) caused by the body forces. Finally, V_4 represents the potential of the *displacement dependent* body forces (i.e., components which exist because of vibratory displacements u, v and w), which is formulated in detail in [12]. The functional V_3 is caused predominantly by tensile stresses, and increases the vibration frequencies, whereas V_4 is caused mainly by normal body forces in the direction of positive w, and typically reduces the frequencies [12].

The kinetic energy of vibratory motion is

$$T = \frac{\rho h}{2} \int_{-b/2}^{b/2} \int_0^a (\dot{u}^2 + \dot{v}^2 + \dot{w}^2) dxdy \tag{21}$$

where the dots denote time derivatives of the displacements and ρ is the mass per unit volume. Coriolis effects are neglected.

To solve the free vibration problem for the blade, a Ritz procedure is followed similar to that described in the previous section on beam theory. That is, one takes the vibratory displacements to be sinusoidal functions of time; i.e.,

$$u(x,y,t) = U(x,y)\sin \omega t$$
$$v(x,y,t) = V(x,y) \sin \omega t \tag{22}$$
$$w(x,y,t) = W(x,y) \sin \omega t$$

where ω is the vibration frequency, and U, V, and W are chosen to be the algebraic polynomials

$$U(x,y) = \sum_{i=1}^{I} \sum_{j=0}^{J} A_{ij} x^i y^j, V(x,y) = \sum_{k=1}^{K} \sum_{l=0}^{L} B_{kl} x^k y^l,$$
$$W(x,y) = \sum_{m=2}^{M} \sum_{n=0}^{N} C_{mn} x^m y^n \tag{23}$$

The functional $T_{max} - V_{max}$ is again formed and it is minimized by setting

$$\frac{\partial}{\partial A_{ij}} (T_{max} - V_{max}) = 0, \quad (i = 1, \ldots, I; j = 0, \ldots J)$$
$$\frac{\partial}{\partial B_{kl}} (T_{max} - V_{max}) = 0, \quad (k = 1, \ldots, K; l = 0, \ldots, L)$$
$$\frac{\partial}{\partial C_{mn}} (T_{max} - V_{max}) = 0, \quad \text{(etc.)} \tag{24}$$

yielding a set of $I(J+1) + K(L+1) + (M-1)(N+1)$ linear algebraic equations in the same number of unknowns, and a matrix eigenvalue problem of the same type as in the previously described beam analysis.

Comparisons for Cambered Blades

Convergence studies were made for the beam theories, both including and neglecting shear deformation and rotary inertia, to establish the upper limits of the summations in equations (14) required to obtain desired convergence. Cambered blade configurations as shown in Fig. 2 having a thickness ratio (b/h) of 20 were investigated, having various combinations of aspect ratio (a/b) and shallowness parameter (b/R). It was found that between six and ten terms of the polynomials were needed to yield convergence of the frequencies to four significant figures for the first four modes of each symmetry class, the number required depending upon the particular mode in question. For the cambered blade of Fig. 2, symmetry uncouples v and ϕ_y from u, ϕ_x, and θ.

The accuracy of the beam equations and the computer programming, as well as the rate of convergence of the Ritz method with the algebraic polynomials, was also established by comparison with the numerical results obtained by Subrahmanyam, Kulkarni and Rao [30] for a particular blade (see [30] p. 20). Their results were also obtained by means of the Carnegie equations, but using slightly different displacement functions. Using seven terms for each of the polynomials (14) excellent agreement (<0.1 percent difference) was observed for each of the frequencies (5) found in [30].

A direct comparison of numerical results for the frequencies of cambered blades obtained from beam theory and shell theory is made in Table 1. The nondimensional frequency parameter used in Table 1 is $\omega a^2 \sqrt{\rho h/D}$ which is a traditional one used for flat plates. Because the blade curvatures utilized in Table 1 are all quite shallow (the deepest curvature, $b/R = 0.5$, corresponds to a circular arc measure of 28.9 deg, the plate frequency parameter is appropriate.

All shear deformation theory results in Table 1 are for a thickness ratio $b/h = 20$ and a Poisson's ratio (ν) of 0.3. A shear correction factor $k = 1.2$ was used (note that this is the *reciprocal* of the factor often used in the published literature) which is representative of the cross sections dealt with in this analysis. For comparison, setting $k = \infty$ yields the classical theory results presented in Table 1, and setting $k = 1$ (which is the theoretical lower limit) was found to yield values of less than 0.1 percent different than those given in Table 1 for $k = 1.2$.

Numerical results according to shallow shell analysis are obtained using 54 deg of freedom. This is arrived at from the algebraic polynomials (23) by choosing 6 terms in the x-

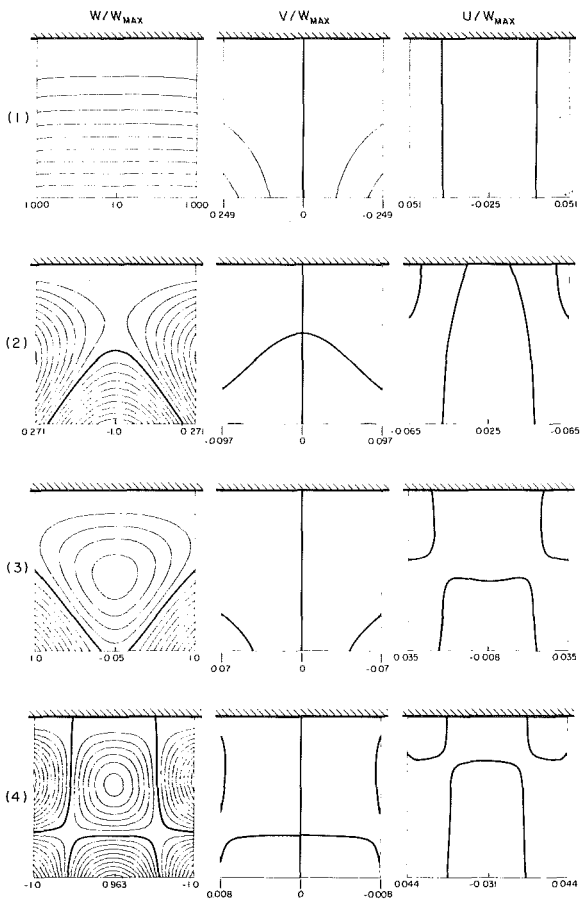

Fig. 3 Symmetric mode shapes for a cambered blade ($b/h = 20$, $a/b = 1$, $b/R = 0.5$)

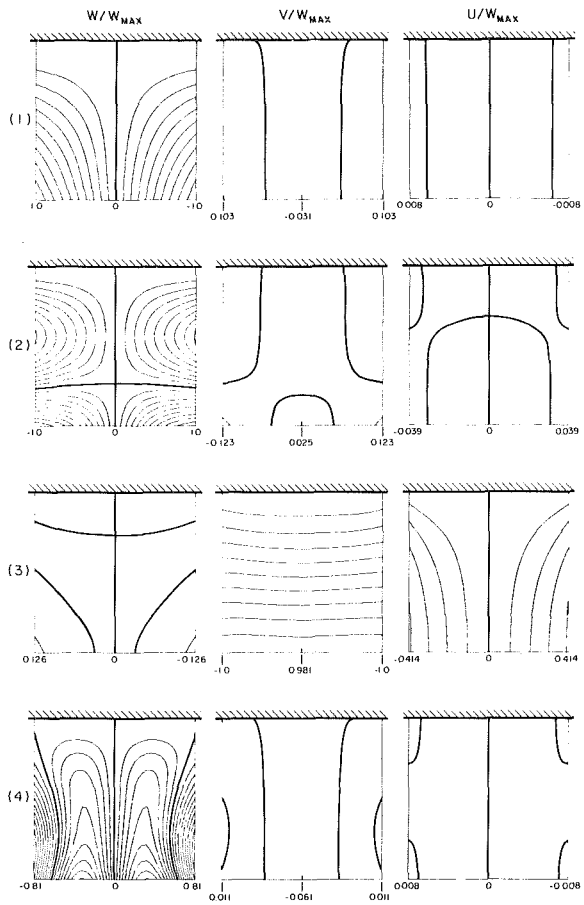

Fig. 4 Antisymmetric mode shapes for a cambered blade ($b/h = 20$, $a/b = 1$, $b/R = 0.5$)

direction (Fig. 2) and 3 terms of even degree in u and w, and odd degree in v in the y-direction for each of the displacements u, v, and w. These results are taken from a previous paper [13], and their convergence was demonstrated there.

Considering first the *symmetric modes* of the large aspect ratio ($a/b = 5$) blades in Table 1, one sees that the frequencies of the first three spanwise bending modes are in reasonably close agreement, although a significant difference between shell and beam theory results of as much as 7 percent occurs for the fourth spanwise bending mode. Of course, for higher modes, the differences would become greater. It is interesting to note that for $b/R = 0.1$, the frequencies predicted by shell theory are greater than those of beam theory, whereas for deeper blades the opposite is true. This may be explained as follows: for a flat (or nearly flat) plate, chordwise bending moments exist, which give the plate additional stiffness unrecognized by beam theory, whereas for deeper blades, warping effects begin to become more important.

Strong warping effects are seen to enter the results for the shorter aspect ratio blades, especially as the curvature increases. For $b/R = 0.5$, for example, and $a/b = 2$ and 1, the beam theories give results for the *second* bending mode frequencies, which are 12 and 35 percent too high, respectively. This reflects the inability of the beam theories to permit cross sectional warping. That is, the beam theory hypothesis that "plane cross sections remain plane during beam deflection" can become significantly violated for small aspect ratio, cambered blades. Or in other words, shear lag effects yield a more flexible system than either beam theory recognizes.

Table 1 also shows that for moderate to low aspect ratios, certain important mode shapes are missed altogether by beam theory. For example, a mode with predominantly normal (w) displacement, and with the greatest curvature changes occuring in the chordwise direction (which we will term "chordwise bending"), is the fourth and third symmetric mode for $a/b = 2$ and 1, respectively, for all the curvatures given. For $a/b = 1$ and significant camber ($b/R = 0.3$ and 0.5) the fourth symmetric mode is a more complex one, also not found by the beam theories.

As an example, Fig. 3 depicts the symmetric mode shapes for the cambered blade having $b/h = 20$, $a/b = 1$, $b/R = 0.5$, corresponding to the last four shell frequency parameters given in Table 1.

Three sketches aligned in a horizontal row are given for each mode shape. The sketches show contour lines of equal displacement, normalized with respect to the maximum normal displacement; that is $W/W_{\max}$, $V/W_{\max}$ and $U/W_{\max}$, in this sequence. Although the W displacements are usually largest during vibration, at least for the lowest frequency modes, the magnitude of the tangential coupling due to U and V displacements can also be seen from the drawings. The contour lines correspond to normalized displacement increments of 0.1, with the lines of zero displacement (node lines) being drawn heavier.

For the short, highly cambered blade of Fig. 3 the first symmetric mode is clearly identifiable as spanwise bending. The second and third modes are mainly second spanwise bending and chordwise bending, respectively, although considerable coupling exists between them. This coupling causes the large differences between the second spanwise

frequencies given in Table 1. The fourth mode is seen in Fig. 3 to be a combined one consisting of both chordwise and spanwise bending.

Table 1 also presents the nondimensional frequency parameters $\omega a^2\sqrt{\rho h/D}$ for the *antisymmetric* modes of the cambered blade. The antisymmetric modes involve coupling between sideways (y-direction) and torsional motions. The two last columns of the antisymmetric mode did not appear for the symmetric modes. They show the effect on the beam frequencies if a torsional warping constant, C_1, (see equation (4)) is added to the analysis. For the blade configurations in Table 1 having $a/b=5$ and 2, the first four antisymmetric modes contain three modes which are predominantly torsional, whereas the remaining one is predominantly sideways bending, as indicated by superscripts. One notes that the torsional frequencies predicted by the classical beam theory are essentially the same as when shear deformation and rotary inertia are included, and would be *exactly* the same if it were not for a small amount of coupling. However, the beam theories give considerably different frequencies for the sideways bending modes, especially for small a/b, as one would expect to find when considering or neglecting shear deformation and rotary inertia effects. For $a/b=1$ the fourth mode is antisymmetric chordwise bending, which the beam theory misses completely. In interpreting Table 1 one must bear in mind that changing a/b corresponds to changing b and keeping a fixed, if the changes in frequencies are to be observed, because the frequency parameter used contains a.

But the most important comparison of antisymmetric frequencies in Table 1 is between the torsional frequencies of shell theory and those of beam theory. If C_1 is not included, one sees large differences, again particularly for small a/b and for the higher modes. The shell theory torsional frequencies are essentially those of flat plates, only slightly affected by the changing cross-sectional arc length caused by changing b/R (b is kept fixed and R changed). These torsional frequencies agree with those readily available for flat plates in the literature (see [31, 32]). Even for a large aspect ratio blade ($a/b=5$), considerable differences (~ 10 percent) are seen to occur between shell and beam frequencies for the third (and higher) torsional modes, as was also found by Carnegie ([3], Figs. 11 and 15) when comparing beam theory frequencies with experimentally measured ones. For $a/b=1$ the third torsional beam frequency in Table 1 is seen to differ from the more accurate shell frequency by about 50 percent.

However, when C_1 is included, the warping constraint is substantially accounted for, and the results of beam theory are seen to agree reasonable well with those of shell theory. In the present analysis the value of C_1 for a thin rectangle ($Eb^3h^3/144$) was used because no proper value for the annular sector is currently known. For small camber however, the approximation as a rectangle should be very good.

The first four antisymmetric modes of the blade having $b/h=20$, $a/b=1$ and $b/R=0.5$ (i.e., the same as for Fig. 3) are depicted by Fig. 4. For the first two modes, which are torsional, the contour lines for the W-displacement agree closely with those of the beam theories. The predominant sidewise bending of the third mode shape and the antisymmetric chordwise bending of the fourth are both clearly seen in Fig. 4.

Comparison for Twisted Blades

Table 2 makes comparisons among the numerical results obtained from the present shell theory, Carnegie's beam theory (including shear deformation and rotary inertia) and those of Petricone and Sisto [33] for a blade having twist only; that is, the curvatures $1/R_x$ and $1/R_y$ in equations (19) are zero, but the twist $1/R_{xy}$ is present. The resulting configuration can be regarded as a flat plate subjected to uniform pretwist, having a twist angle, ϕ, at its free end. Results in Table 2 are for low aspect ratio ($a/b=1$) blades having pretwist angles varying between 0 and 45 deg, with a width/thickness (b/h) ratio of 20 and Poisson's ratio (ν) of 0.3.

The analysis of Petricone and Sisto [33] was based upon helicoidal shell theory, and their numerical results were obtained by means of the Ritz method, using orthogonal polynomials as admissible functions.

Numerical results for the shell theory were typically obtained by taking $i, k = 1,2, \ldots ,5$; $m = 2, 3, \ldots ,6$ and $j, l, n = 0, 2, 4$ (for symmetric modes) or 1, 3, 5 (for antisymmetric modes) in equations (23) yielding frequency determinants of 54th order in size. The convergence accuracy

Table 2 Comparison of $\omega a^2\sqrt{\rho h/D}$ for short, twisted blades ($a/b=1$, $b/h=20$, $\nu=0.3$)

Twist angle, (deg)	Mode number	Symmetric modes: Present shell theory	Symmetric modes: [33]	Symmetric modes: Beam theory	Antisymmetric modes: Present shell theory	Antisymmetric modes: [33]	Antisymmetric modes: Beam theory Without C_1	Antisymmetric modes: Beam theory With C_1
0	1	3.474	———	3.347	8.513	———	6.430	8.474
	2	21.30	———	20.73	30.98	———	19.29	30.91
	3	27.20[a]	———	———	64.27[c]	———	———	———
	4	43.56[b]	———	42.91[b]	71.47	———	32.15	68.86
10	1	3.453	3.48	3.344	9.509	9.58	7.949	9.943
	2	21.10	21.4	20.38	31.66	32.8	23.85	34.76
	3	27.19[a]	27.8	———	64.36[c]	———	———	———
	4	44.25[b]	———	43.39[b]	71.76	———	39.74	73.56
20	1	3.387	3.47	3.336	12.16	12.0	11.34	13.24
	2	20.48	20.6	19.46	33.72	35.2	34.03	43.82
	3	27.32[a]	27.6	———	64.65[c]	———	———	———
	4	46.19[b]	———	44.58[b]	72.71	———	56.72	85.82
30	1	3.265	3.48	3.322	16.08	15.0	15.42	17.23
	2	19.41	19.6	18.21	37.35	37.8	46.27	55.11
	3	27.94[a]	27.9	———	65.21[c]	———	———	———
	4	49.04[b]	———	45.89[b]	74.58	———	77.11	102.4
45	1	2.939	3.51	3.294	24.35	19.3	21.99	23.71
	2	17.18	18.0	16.19	46.45	42.6	65.96	73.77
	3	30.56[a]	28.6	———	66.96[c]	———	———	———
	4	52.46[b]	———	45.56[b]	80.44	———	109.9	131.3

[a] Chordwise bending mode
[b] Sideways bending mode
[c] Antisymmetric chordwise bending mode

of the polynomials for twisted blades has been demonstrated previously [14]. Results for the beam theory were obtained by taking the first ten terms of the algebraic polynomials (14). No significant difference (<4 percent) was found between the classical beam frequencies and those in Table 2, which include shear deformation and rotary inertia, except for sideways bending modes.

Nondimensional frequency parameters $\omega a^2\sqrt{\rho h/D}$ for the *symmetric* modes are listed in one half of Table 2. For a twisted plate the symmetric modes consist of coupled bending involving both v and w displacements (Fig. 2), uncoupled from the torsional modes, which are purely antisymmetric. For all twist angles given, the first two symmetric modes consist predominantly of w-displacements, and are similar to the first two spanwise bending modes of a beam. Table 2 indicates reasonable agreement among the results of shell and beam theories for these two modes. The third symmetric mode is chordwise bending (two mode lines nearly parallel to the length coordinate), which is missed by beam analysis. The fourth mode consists of sideways bending (i.e., predominantly v-displacements), not determined by Petricone and Sisto [33]. Detailed contour plots for the modes in the format of Fig. 3 are available [14] for the case $\phi = 30$ deg.

Considerable disagreement for the *antisymmetric* mode frequencies is observed in Table 2. For each twist angle, the first four antisymmetric modes consist of three torsional and one antisymmetric chordwise bending (i.e., three node lines essentially parallel to the length direction) modes. Beam theory results for the torsional modes are shown in the cases of neglecting warping constraint (without C_1) and including it (with C_1). When warping constraint is neglected the beam theory is observed to yield torsional frequencies which are typically low for small twist angles and too large for the higher modes at large twist angles. When warping constraint is included, the frequencies are all raised, giving good agreement with shell theory results for zero twist, but serious disagreements for $\phi = 20$, 30 and 45 deg. These trends can also be somewhat observed in the results of Carnegie comparing analysis with experiment ([3], Fig. 11), although the latter results were for large aspect ratio ($a/b = 6$) blades.

Beglinger and Schlachter [34] proposed a correction formula of the form

$$\frac{\omega^*}{\omega} = \left[1 + 2\zeta + \zeta^2\left\{1 + \left[\frac{\pi}{2}(2n-1)\right]^2\right\}\right]^{1/2} \tag{25}$$

to account for torsional warping constraint, where n is the torsional mode number ($n = 1,2, \ldots$) and

$$\zeta = \frac{1}{l}\sqrt{\frac{C_1}{C}\,2(1+\nu)} \tag{26}$$

with l being the beam length, and C and C_1 being the torsional rigidity and warping restraint factors, respectively, as used previously in equation (4). For the twisted plate having a rectangular cross-section

$$\zeta = \frac{b}{l}\sqrt{\frac{1+\nu}{24}} \tag{27}$$

and letting $b/l = 1$ and $\nu = 0.3$, the right-hand side of equation (25) becomes 1.286, 1.650, and 2.205 for $n = 1$, 2, and 3, respectively. Applying these correction factors to the torsional frequencies listed in Table 2 for $\phi = 0$ yields 8.269, 31.83 and 70.89, which are seen to compare reasonably with the frequencies both of shell theory and of beam theory (with C_1). However, a cursory inspection of Table 2 also shows that the same factors applied to the beam frequencies for nonzero angles of twist result in large over-corrections to the beam frequencies.

It should be noted that a twist angle of zero degrees in Table 2 yields a flat plate which would be indentical to the cambered blade of Table 1 having $b/R = 0$. Sideways bending modes are symmetric for twisted blades and antisymmetric for cambered blades.

Another set of twisted blades for which both theoretical and experimental results are available is that studied by MacBain [35]. This set consisted of thin ($b/h = 33.4$) plates of moderate aspect ratio ($a/b = 2.33$) pretwisted through various tip angles ($\phi = 0$, 12, 17, 23.5, 30, and 38 deg). MacBain obtained numerical results using the NASTRAN finite element program with 1265 deg of freedom [36] and compared them with data resulting from tests using holography. Frequency parameters $\omega a^2\sqrt{\rho h/D}$ for the plate ($b/R_y = 0$) having a moderate pretwist angle ($\phi = 30$ deg) are presented in Table 3, and compared there with the corresponding results [14] from the present shallow shell theory and with beam theory (including shear deformation and rotary inertia).

As found previously for blades having little or no camber (see Table 2), the spanwise bending mode frequencies given in Table 3 for beam theory are seen to be typically somewhat low, because the beam model does not recognize the additional stiffening capability of sideways bending moments, M_x, induced by Poisson effects. Again the antisymmetric, torsional mode frequencies are predicted somewhat low by beam theory for the fundamental (1A) mode and become too high for higher modes when warping restraint is not accounted for. Including warping constraint (values given in parentheses) results in appropriate correction for the first torsional frequency, but raises the third one to an unacceptable level. But, on the whole, the beam theory results for MacBain's twisted plate are seen to be reasonably acceptable, at least for the first seven modes.

The second part of the Table 3 shows the effects of adding a small amount of camber $b/R_y = 0.215$, or $a/R_y = 0.5$ to the MacBain twisted blade. Generally, the frequencies are increased slightly, but the beam theory results are now seen to deviate considerably from those of the shallow shell theory. In this case the modes involve complete coupling between the bending in two directions and torsion, compared with the uncambered blade which has torsion uncoupled. The magnitude of the coupling can be seen from previously

Table 3 Comparison of $\omega a^2\sqrt{\rho h/D}$ for moderate aspect ratio (a/b = 2.33), twisted (ϕ = 30 deg), thin (b/h = 33.4) blades

b/R_y	Type of Results	$\omega a^2\sqrt{\rho h/D}$							
	Mode	1S	2S	1A	3S	2A	4S[a]	5S	3A
	Present shell theory	3.237	19.46	30.96	57.81	86.60	109.2	124.7	135.2
0	Finite element [35]	3.473	19.56	28.99	57.38	82.08	88.74	116.1	129.3
	Experiment [35]	3.39	19.09	27.54	57.84	76.87	100.2	115.0	123.6
	Beam theory	3.358	18.79	27.80	55.90	83.41	104.9	120.3	139.0
	(with C_1)			(29.48)		(90.63)			(158.0)
	Mode number	1	2	3	4	5	6	7	8
0.215	Present shell theory	3.660	20.99	31.95	60.61	90.74	109.4	122.6	135.0
	Beam theory	4.574	25.48	27.73	75.48	83.11	111.8	138.5	155.1
	(with C_1)	(4.574)	(25.49)	(29.40)	(75.48)	(90.32)	(111.8)	(155.2)	(157.4)

[a] Sideways bending mode

presented mode shapes [14] (somewhat further complicated by the addition of rotational effects).

Conclusions

Beam theory is generally inadequate to determine the free vibraton frequencies and mode shapes of moderate to low aspect ratio turbomachinery blades. It may also be inadequate for large aspect ratio blades if a careful dynamic response analysis is to be made, requiring reasonably accurate knowledge of the first ten or more frequencies and mode shapes.

The inadequacy of beam theory is seen in the following ways:

1 Modes which are predominantly chordwise bending are completely missed while others involving significant amounts of chordwise bending are poorly determined.

2 Frequencies of modes which are essentially either spanwise bending or torsion may be poorly estimated, especially for blades of low aspect ratio, because of other limitations in the analytical model.

3 Typical blades with no symmetry may have strong coupling between all types of spanwise and chordwise bending and torsion, making suitable corrections for above mentioned limitations difficult.

Inaccuracies in the spanwise bending frequencies may be due to any or all of the following:

1 Additional stiffness due to chordwise bending moments induced by Poisson effects

2 Difficulty in determining a proper shear correction factor to utilize with the shear deformation theory

3 The constraint that "plane cross sections remain plane," required by both classical and shear deformation beam theories, which ignores additional flexibility due to cross-sectional warping

The last factor was seen to be particularly important, especially for low aspect ratio blades, and is not considered in any beam model of blade vibrations known to the writers. Large inaccuracies in the torsional frequencies may arise because of:

1 The constraint on cross sectional warping due to a fixed root

2 Inaccuracy in representing additional beam stiffness due to pretwist

Much of the aforementioned inaccuracy in representing the spanwise bending and torsional modes could be eliminated by incorporation of proper correction factors determined from solutions of the classical theory of elasticity.

By contrast the shallow shell theory is straightforwardly applied and is capable of representing all the vibration modes accurately. The theory is capable of considerable generalization beyond that used in the present work in order to represent actual turbomachinery blades more accurately. The generalizations include:

1 Elastic root constraint

2 Attached shrouds

3 Thick shell theory, for thicker blades

4 A deeper "shallow" shell theory (including more terms in the strain-displacement equations, but still relating all equations to the projected base plane), for more highly cambered and/or twisted blades

5 Accurate representation of rotational effects, including Coriolis forces

6 Variable thickness and curvature

7 Nonrectangular blade planforms

8 Anisotropic and/or nonhomogeneous materials such as composites

9 Accurate determination of initial stresses due to rotation, as well as vibratory stresses

10 Structural damping or layered damping treatments

But the one-dimensional beam theory has an important advantage over the two-dimensional shell theory for blades and vibration modes that it is capable of representing: namely, it can do so with fewer degrees of freedom, thus requiring less computer time. Similarly, the shell theory approach has been shown to require significantly less degrees of freedom [12] than finite element models, for the same degree of accuracy. Thus, both approaches have their proper places in blade vibration analysis, particularly in preliminary design where the effects of changing parameters need to be studied.

Acknowledgments

The authors wish to acknowledge the help of Mr. A. J. Wang in obtaining numerical results for the shell analysis. This work was partially supported by the National Aeronautics and Space Administration, Lewis Research Center, under Grant No. NAG 3-36.

References

1 Leissa, A., "Vibrational Aspects of Rotating Turbomachinery Blades," *Applied Mechanics Reviews*, Vol. 34, No. 5, 1981, pp. 629–635.

2 Carnegie, W., "Static Bending of Pretwisted Cantilever Blades," *Proceedings of the Institution of Mechanical Engineers*, Vol. 171, No. 32, 1957, pp. 873–894.

3 Carnegie, W., "Vibrations of Pretwisted Cantilever Blading," *Proceedings of the Institution of Mechanical Engineers*, Vol. 173, No. 12, 1959, pp. 343–374.

4 Carnegie, W., "Vibrations of Rotating Cantilever Blading: Theoretical Approaches to the Frequency Problem Based on Energy Methods," *Journal Mechanical Engineering Science*, Vol. 1, No. 3, 1959, pp. 235–240.

5 Carnegie, W., "Vibrations of Pretwisted Cantilever Blading: An Additional Effect Due to Torsion," *Proceedings of the Institution of Mechanical Engineers*, Vol. 176, No. 13, 1962, pp. 315–322.

6 Carnegie, W., "Vibrations of Pretwisted Cantilever Blading Allowing for Rotary Inertia and Shear Deflection," *Journal Mechanical Engineering Science*, Vol. 6, No. 2, 1964, pp. 105–109.

7 Carnegie, W., "A Note on the Application of the Variational Method to Derive the Equations of Dynamic Motion of a Pretwisted Cantilever Blade Mounted on the Periphery of a Rotating Disc Allowing for Shear Deflection, Rotary Inertia and Torsion Bending," *Bulletin of Mechanical Engineering Education*, Vol. 5, 1966, pp. 221–223.

8 Carnegie, W., "The Application of the Variational Method to Derive the Equations of Motion of Vibrating Cantilever Blading under Rotation," *Bulletin of Mechanical Engineering Education*, Vol. 6, 1967, pp. 29–38.

9 Houbolt, J. C., and Brooks, G. W., "Differential Equations of Motion for Combined Flapwise Bending, Chordwise Bending and Torsion of Twisted Nonuniform Rotor Blades," NACA Report 1346, 1958.

10 Montoya, J., "Coupled Bending and Torsional Vibrations in a Twisted, Rotating Blade," *Brown Boveri Review*, Vol. 53, No. 3, 1966, pp. 216–230.

11 Leissa, A. W., "Vibrations of Turbine Engine Blades by Shell Analysis," *Shock and Vibration Digest*, Vol. 12, No. 11, 1980, pp. 3–10.

12 Leissa, A. W., Lee, J. K., and Wang, A. J., "Rotating Blade Vibration Analysis Using Shells," ASME Paper No. 81-GT-80, *Journal of Engineering for Power* (to appear).

13 Leissa, A. W., Lee, J. K., and Wang, A. J., "Vibrations of Cantilevered Shallow Cylindrical Shells of Rectangular Planform," *Journal of Sound and Vibration* Vol. 78, No. 3, 1981, pp. 311–328.

14 Leissa, A. W., Lee, J. K., and Wang, A. J., "Vibrations of Twisted Rotating Blades," ASME Paper No. 81-DET-127, to be presented at the ASME Vibrations Conference, Hartford, Conn., Sept. 1981 and to be published in the *Journal of Mechanical Design*.

15 Timoshenko, S. P., and Goodier, J. N., *Theory of Elasticity*, 3rd ed., McGraw-Hill, Inc., 1970.

16 Timoshenko, S. P., "On the Correction for Shear of the Differential Equations for Transverse Vibrations of Prismatic Bars," *Philosophical Magazine*, Ser. 6, Vol. 41, 1921, p. 742.

17 Carnegie, W., "Experimental Determination of the Center-of-Flexure and Center-of-Torsion Coordinates of an Asymmetrical Aerofoil Cross Section," *Journal Mechanical Engineering Science*, Vol. 1, No. 3, 1959, pp. 241–249.

18 Carnegie, W., Stirling, C., and Fleming, J., "Vibration Characteristics of Turbine Blading Under Rotation—Results of an Initial Investigation and Details of a High-Speed Test Installation," *Proceedings of the Institution of Mechanical Engineers*, Vol. 180, pt. 31, 1966.

19 Carnegie, W., Dawson, B., and Thomas, J., "Vibration Characteristics

of Cantilever Blading," *Proceedings of the Institution of Mechanical Engineers*, Vol. 180, pt. 31, 1966, p. 71.

20 Carnegie, W., and Dawson, B., "Vibration Characteristics of Straight Blades of Asymmetrical Aerofoil Cross-Section," *Aeronautical Quarterly*, Vol. 20, 1969, pp. 178–190.

21 Rao, J. S., and Carnegie, W., "Solution of the Equations of Coupled-Bending Bending Torsion Vibrations of Turbine Blades by the Method of Ritz-Galerkin," *International Journal of Mechanical Sciences*, Vol. 12, 1970, pp. 875–882.

22 Carnegie, W., and Dawson, B., "Vibration Characteristics of Pretwisted Blades of Asymmetrical Aerofoil Cross Section," *Aeronautical Quarterly*, Vol. 22, 1971, pp. 257–273.

23 Carnegie, W., and Thomas, J., "The Effects of Shear Deformation and Rotary Inertia on the Lateral Frequencies of Cantilever Beams in Bending," *ASME Journal of Engineering for Industry*, 1972, pp. 267–278.

24 Rao, J. S., "Natural Frequencies of Turbine Blading—A Survey," *Shock and Vibration Digest*, Vol. 5, No. 10, 1973, pp. 3–16.

25 Rao, J. S., "Turbine Blading Excitation and Vibration," *Shock and Vibration Digest*, Vol. 9, No. 3, 1977, pp. 15–22.

26 Rao, J. S., "Turbomachine Blade Vibration," *Shock and Vibration Digest*, Vol. 12, No. 2, 1980, pp. 19–26.

27 Goldenveizer, A. L., "Theory of Elastic Thin Shells," English translation, Pergamon Press, 1961.

28 Novozhilov, N. V., *The Theory of Shells* (English translation), P. Noordhoff Ltd., Groningen, The Netherlands, 1959.

29 Leissa, A. W., *Vibration of Shells*, NASA SP-288, U.S. Government Printing Office, 1973.

30 Subrahmanyam, K. B., Kulkarni, S. V., and Rao, J. S., "Coupled Bending-Torsion Vibrations of Rotating Blades of Asymmetric Aerofoil Cross Section with Allowance for Shear Deflection and Rotary Inertia by Use of the Reissner Method," *Journal of Sound and Vibration*, Vol. 75, No. 1, 1981, pp. 17–36.

31 Leissa, A. W., *Vibration of Plates*, NASA SP-160, U.S. Government Printing Office, 1969.

32 Leissa, A. W., "The Free Vibrations of Rectangular Plates," *Journal of Sound and Vibration*, Vol. 31, No. 3, 1973, pp. 257–293.

33 Petricone, R. D., and Sisto, F., "Vibration Characteristics of Low Aspect Ratio Compressor Blades," ASME JOURNAL OF ENGINEERING FOR POWER, Vol. 93, No. 1, 1971, pp. 103–112.

34 Beglinger, V., and Schlachter, W., "Influence of Support Elasticity, Shear Deformation, Rotary Inertia and Cross-Sectional Warping on the Natural Frequencies of Turbomachine Blades," *Sulzer Technical Review*, Research Number 1978, 1978, pp. 19–26.

35 MacBain, J. C., "Vibratory Behavior of Twisted Cantilever Plates," *Journal of Aircraft*, Vol. 12, No. 4, 1975, pp. 343–349.

36 MacBain, J. C., private communication, Apr. 1981.

B. R. Hollworth
Associate Professor.
Mem. ASME

G. Lehmann
Instructor.

J. Rosiczkowski
Instructor.
Assoc. Mem. ASME

Mechanical and Industrial
Engineering Department,
Clarkson College of Technology,
Potsdam, N.Y. 13676

Arrays of Impinging Jets With Spent Fluid Removal Through Vent Holes on the Target Surface, Part 2: Local Heat Transfer

An extensive study was conducted to determine the heat transfer characteristics of arrays of turbulent air jets impinging on perforated target surfaces. Spent air was withdrawn through vent holes on the surface, rather than along one or more of its edges, as had been done in all previous investigations. An earlier publication presented average heat transfer data for such systems; this paper gives results of comprehensive measurements of local heat transfer. Also given are the results of flow visualization studies, and an approximate mathematical model which predicts distributions of local heat transfer which agree satisfactorily with test data.

Introduction

Arrays of impinging fluid jets may be used to obtain high levels of convective heat and mass transfer. Applications range from the drying of paper and films to the cooling of high-power electronic devices. Such systems have, of course, become an accepted technique for cooling components (blades, vanes, tip seals, etc.) in the hot sections of gas turbine engines. A number of studies [1, 2, 3, 4, 5] have been conducted to obtain convective heat transfer data for arrangements of multiple jets; and Martin [6] and Obot et al. [7] have recently assembled comprehensive surveys of the relevant literature.

Figure 1 shows a so-called "hybrid" cooling configuration, wherein a solid surface is cooled by impingement in combination with transpiration and film cooling. Fluid jets impinge on the back face of the panel, and the spent fluid is subsequently vented through holes in the panel and discharged into the hot gas to achieve additional cooling benefit. It is well known that the mode of spent fluid removal influences the flow field near the target surface. This, of course, affects the boundary layer growth and the corresponding distribution of convective heat transfer. All impingement studies to date have been concerned with arrays in which spent fluid was withdrawn along one or more edges of the target surface. It is apparent that such data may not be applied to the design of impingement arrays for hybrid systems, with their unique mode of spent air removal.

A comprehensive investigation was undertaken, therefore, to obtain heat transfer data for arrays of impinging jets with spent fluid removal through an array of vent holes on the target surface. Such information may be used, in conjunction with already available data on transpiration and film cooling, for the design of hybrid systems. More specifically, the goals of this study were:

1 To measure average heat transfer
2 To measure local heat transfer
3 To conduct flow visualization studies to relate heat transfer to details of the fluid flow
4 To generate an analytical model to predict impingement heat transfer

The results of the first phase of the work (i.e., measurements of average heat transfer) have already been reported by Hollworth and Dagan [8]. This paper reports the results of the remaining portions of the program, which help to explain several significant trends associated with the behavior of average heat transfer.

The geometry under consideration was a 4 × 4 square array of circular jets impinging upon a virtually isothermal (see the discussion in the section entitled, Experimental Apparatus and Procedures) vented target plate. Both the orifice plate (which forms the jets) and the target plate are flat surfaces in

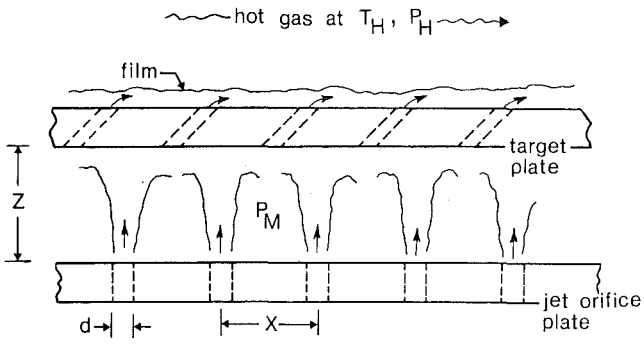

Fig. 1 Hybrid cooling system

Contributed by the Power Division for publication in the JOURNAL OF ENGINEERING FOR POWER. Manuscript received by the Power Division August 24, 1982.

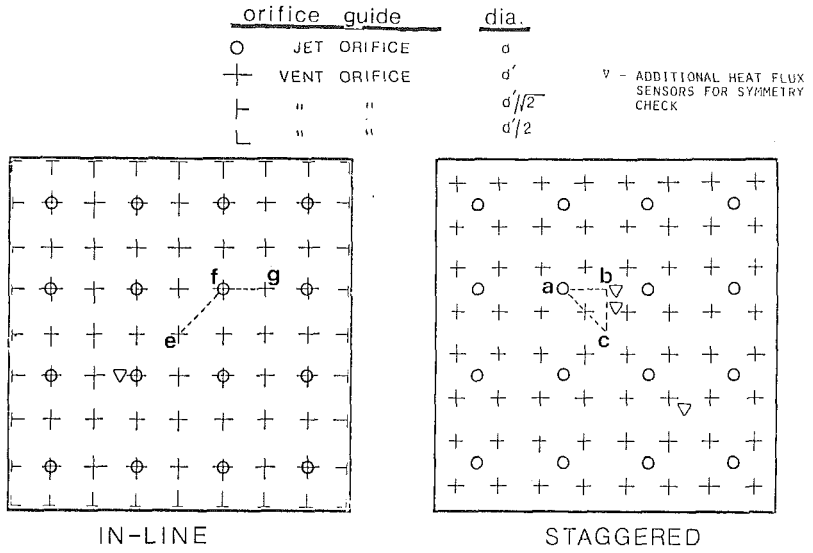

Fig. 2 Vent patterns

the shape of a square having side length $4X \times 4X$, where X is the center-to-center spacing between jet orifices.

Vent holes had the same nominal diameters as jet orifices and were laid out, also, in square arrays. However, the spacing between vents was exactly half that of the jet orifices. The geometry is fairly representative of those which occur in gas turbine applications, as was discussed in some detail in [8]. Jet orifices were square-edged with length/diameter = 1.0. They were calibrated and found to have a discharge coefficient (C_d) of 0.80 over the range of flows used for the heat transfer tests. Vent holes were essentially sharp-edged orifices (as discussed in [9]) with a discharge coefficient (C_d') of 0.62. The vents were drilled with their diameters (d') somewhat larger than those of the jet orifices so that the *effective areas* of both were the same. The vent diameters were thus determined from

$$d' = \sqrt{\frac{C_d}{C_{d'}}}\, d = 1.14\, d \tag{1}$$

Finally, two vent configurations (see Fig. 2) were tested. In the inline arrangement, there is a vent directly opposite each jet orifice; and the staggered arrangement is set up so that there is no vent directly opposite any of the jet orifices. The smaller holes on the periphery of the inline plate serve to simulate the same flow as would occur for an array of infinite extent.

Table 1 Variables and ranges

Nominal jet orifice diameter[a]	d	5.0 mm, 2.5 mm
Jet Reynolds number	Re	3000 – 35000
Jet Prandtl number	Pr	0.71
Nondimensional jet-to-jet spacing	$\bar{X}$	5,10,15,20
Nondimensional standoff between orifice plate and target plate	$\bar{Z}$	$0.5 - \bar{X}$

[a] Actual diameters were 5.08 mm and 2.54 mm

Independent parameters involving system geometry, coolant flow, and fluid properties were varied over ranges generally appropriate to gas turbine cooling applications. These parameters and their ranges are summarized above in Table 1, and the variables are defined in the Nomenclature section. The larger values of $\bar{X}$ (i.e., $\bar{X} = 15,20$) correspond to designs which require a fairly small coolant flow to accompany a large pressure difference across the orifice plate. The hybrid cooling system of Fig. 1 often has such a requirement. The test fluid for the experimental parts of this study was air near S.T.P.[1] and jet velocities were low enough so that compressibility effects were always negligible.

[1] S.T.P. denotes the standard sea level conditions: pressure = 1.01×10^5 N/m^2, temperature = 15°C.

Nomenclature

c = specific heat of fluid, J/Kg•K
c_d = discharge coefficient of jet orifices
c_d' = discharge coefficient of vent holes
d = diameter of jet orifices, m
d' = diameter of vent holes, m
f = friction coefficient
h = local heat transfer coefficient, W/m^2•K
k = thermal conductivity of fluid, W/m•K
$\dot{m}$ = mass flow rate to jet array, Kg/s
Nu = local Nusselt number, hd/k
P = local static pressure, N/m^2
Pr = fluid Prandtl number
q = local heat flux, W/m^2
q_r = local radiation heat flux, W/m^2
r = radial distance from jet stagnation point, m
$\dot{r}$ = r/d
Re = jet Reynolds number, $\dot{m}/(16 \cdot \pi/4\ \mu d)$
St = local Stanton number, $h/\rho c u_m$
T_o = total temperature of jets, C
T_s = impingement surface temperature, C
u_m = velocity at "edge" of boundary layer
x = heat flux sensor coordinate, Fig. 4
y = heat flux sensor coordinate, Fig. 4
$\bar{x}$ = x/d
$\bar{y}$ = y/d
X = center-to-center spacing between jet orifices, m
$\bar{X}$ = X/d
Z = normal distance between jet plate and target plate, m
$\bar{Z}$ = Z/d
δ = hydrodynamic boundary layer thickness, m
μ = dynamic viscosity, Kg/m•s
ν = kinematic viscosity, μ/ρ
ρ = density, Kg/m^3
τ_o = wall shear stress, N/m^2

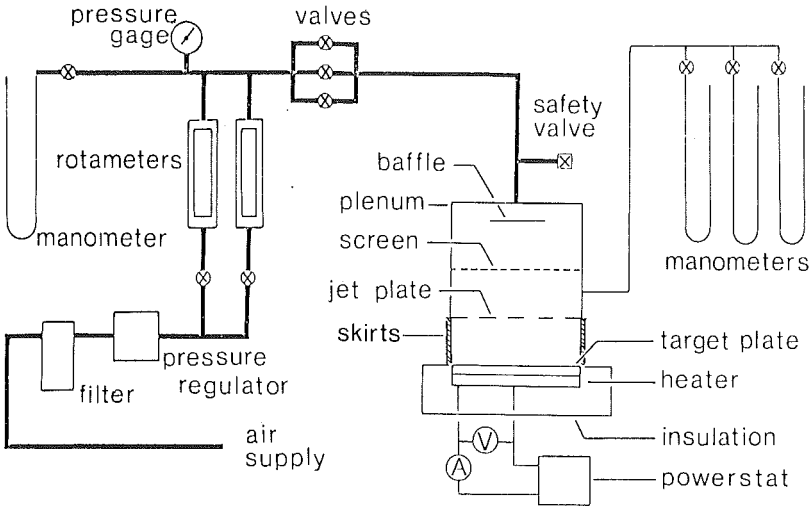

Fig. 3 Test apparatus

Experimental Apparatus and Procedures

The test system for measurements of local heat transfer is shown in Fig. 3. It consists of an air delivery loop, a plenum with interchangeable orifice plates, and an electrically heated target plate on which the jets impinge. Side skirts form an enclosure so all spent air is constrained to exhaust through the vent holes. This is basically the same rig used for earlier experiments [5, 8] to measure average heat transfer.

The air supply loop consists of a reciprocating air compressor (which supplies filtered and dried air at a pressure of approximately 6 bars), along with equipment to control and measure air flow to the heat transfer rig. Air flow is modulated with hand-operated valves, and a pressure regulator maintains the pressure upstream of the test rig – and therefore the flow rate – constant during each test. Flow rate is measured by a bank of rotameters rated accurate to ± 1 percent full scale. A safety valve in the supply line protects against over-pressurizing the plenum.

The jet plenum is an airtight box fabricated from aluminum plate. There are, in fact, two such plenums – a large one to accommodate larger jet array plates, and a smaller box for the smaller arrays. Both contain a baffle and a screen to insure that air is evenly distributed among the several jets orifices, Total temperature is measured with two iron-constantan thermocouples in the plenum, and total pressure is measured with U-tube manometers. Interchangeable orifice plates are used to provide the eight jet arrays (two values of d, four values of $\bar{X}$) indicated in Table 1. The standoff ($\bar{Z}$) between the jet plate and target plate is set and maintained with wooden dowels at the four corners; they are located as far as possible from the vents to minimize interference with the flow. Four side skirts (made from 13-mm thick plexiglas) are used to prevent spent air from exhausting at the edges of the target surface. These are clamped tightly between the jet plate and target plate and all mating surfaces are made airtight using rubber gaskets.

Jets impinge on a flat target consisting of a 6-mm thick copper plate heated by electrical heaters cemented to its back surface. There are two such target plates for each jet plate, one with an inline vent pattern and one with a staggered pattern, as shown in Fig. 2. Each heater/plate assembly is insulated with 50 mm of foam insulation glued to its back surface, to minimize heat loss to the surroundings. Holes, with the same locations as those in the target plate, are bored through the insulation to allow removal of spent air. Each copper plate is instrumented with at least five imbedded iron-constantan thermocouples to measure its temperature distribution. Details concerning the installation and locations of the thermocouples are given in [5].

Measurements of local heat transfer were made using a number of microfoil heat flux sensors attached at sites on the impingement-side of the target plates. These sensors are a special unit (part no. 27022) manufactured by RdF Corp. of Hudson, N.H. Each one consists of three thin layers of Kapton with thermopiles deposited on both faces of the middle layer, which is usually termed the thermal barrier. When the sensor is subjected to a heat flux, the resultant temperature drop across the barrier produces an output emf roughly proportional to the flux. The manufacturer furnishes a calibration with each unit, and specifies ± 5 percent accuracy for them. The calibration includes the device's sensitivity (i.e., volts per W/m^2) at 21°C and a curve to correct the output if its mean temperature differs from 21°C. Output was measured using a digital multimeter accurate to ± 0.04 percent. It was felt that the size of the device's sensing grid (approximately 1.5 mm $\times$ 2.5 mm) was sufficiently small compared to the jet diameter (which may be considered the characteristic length in this experiment) to yield truly "local" heat transfer. Each sensor includes, also, an additional integral thermocouple on the impingement side of the thermal barrier. The reading from this thermocouple may be used to deduce (see Results section) the surface temperature, which is required to calculate the local convection coefficient, h.

After attaching the sensors, the rest of the target surface is masked with a sheet of Kapton having the same thickness (approximately 0.10 mm) as the sensors. This masking serves two functions. First, it produces a smooth surface so that the boundary layer is not locally disturbed as the fluid encounters the edge of each stick-on sensor. Second, the masking has nearly the same thermal impedance as the sensors themselves. Thus, the tendency for local cold spots to occur at each sensor is suppressed, and the entire target is kept more nearly isothermal. It should be pointed out, however, that the thermal impedance of the sensor and the masking (about 0.5°C per Kw/m^2) must be large enough so that the sensors produce an output emf which may be conveniently measured. Because the local h varies over the impingement surface, so must the surface temperature T_s; and the surface tends to be most nonisothermal at high heat fluxes. For these tests, the difference between the (average) surface temperature and the convecting fluid temperature was nominally 50°C. In the worst case, the maximum (or minimum) local T_s differed

from the average value by 8°C. As a rule, the difference was less than 5°C.

Sensors were attached in regions near the centers of the target plates, as shown on Fig. 2. For the staggered array they were located within the area enclosed by dashed line "abca". For a symmetric flow field, any point on the target surface should have an equivalent point within "abca." For the inline array, sensors were attached along dashed line "efg." Additional sensors (denoted by ∇-symbols on Fig. 2) were attached outside of "abca" and off of "efg" to determine if the distribution of heat transfer was, in fact, reasonably symmetric over the entire impingement surface. Table 2 and Fig. 4 give the exact locations of the sensors. The additional sensors used for the abovementioned symmetry check are marked with an asterisk on Fig. 4 and shown next to the corresponding sites within "abca" or on "efg."

Owing to the limited number of sensors available and space limitations, it was impossible to attach a large number of sensors to the plate simultaneously. It required, in fact, three separate tests runs at the same test conditions to generate a complete "map" of local heat transfer. Between runs, some of the sensors were removed from the target plate and reattached at new sites. Sensors were attached to the plate using a thermally sensitive adhesive. They were easily removed without physical damage by heating the plate to a temperature only slightly above the temperature at which heat transfer measurements were made. Local heat transfer measurements were made for wide ranges of jet Reynolds number (Re) and standoff ($\bar{Z}$), but only for inline and staggered arrays with $\bar{X} = 10$, which was felt to be a fairly median geometry.

The test procedure was fairly straightforward. A test geometry was selected and the corresponding rig was assembled and checked for air leaks past the gaskets where the side skirts contacted the orifice plate and target plate. The standoff ($\bar{Z}$) was set using wooden dowels for spacers at the four corners of the enclosure. A flow rate was set for the desired Reynolds number, and the power input to the target plate heaters was adjusted so that the impingement surface temperature (T_s) was approximately 50°C above the jet plenum temperature (T_o). The rig was then allowed to attain steady-state, which generally required 30–45 min. After reaching steady state, the following data were recorded:

- Mass flow rate ($\dot{m}$) of air
- Total temperature, T_o, (measured with two thermocouples in plenum) and total pressure of jets
- Output "emf's" from heat sensors and surface temperature thermocouples built-in to sensors
- Room temperature; ambient pressure, relative humidity
- Temperature readings from several (see [9] for details) thermocouples imbedded in the heated target plate

This procedure was repeated for four values (5500, 10000, 20000, and 35000) of Re and four values (1, 2.5, 5, and 10) of $\bar{Z}$.

The flow visualization method involved seeding one jet near the center of the array with small (dia ≅2 mm) neutrally buoyant Helium bubbles, as discussed in more detail by Rosiczkowski and Hollworth [10]. This technique was used with some success by Colladay and Russel [11] for studies of the flow field in discrete hole film cooling systems. The bubbles are illuminated by a high-intensity lamp and photographed with a 35-mm camera to generate pathline maps of the flow. Light was collimated by a slit to illuminate a "slice" of the region located between the jet plate and the target plate. The slice was 1–2 jet diameters thick, and oriented normal to these two surfaces. The apparatus for this part of the investigation was fabricated entirely of 12-mm thick plexiglass. It was geometrically similar to the heat transfer apparatus, but scaled up in size by a factor of 2.4.

For the flow visualization work, the test fluid remained air near S.T.P. All tests were run at Re = 5500. The intensity (as

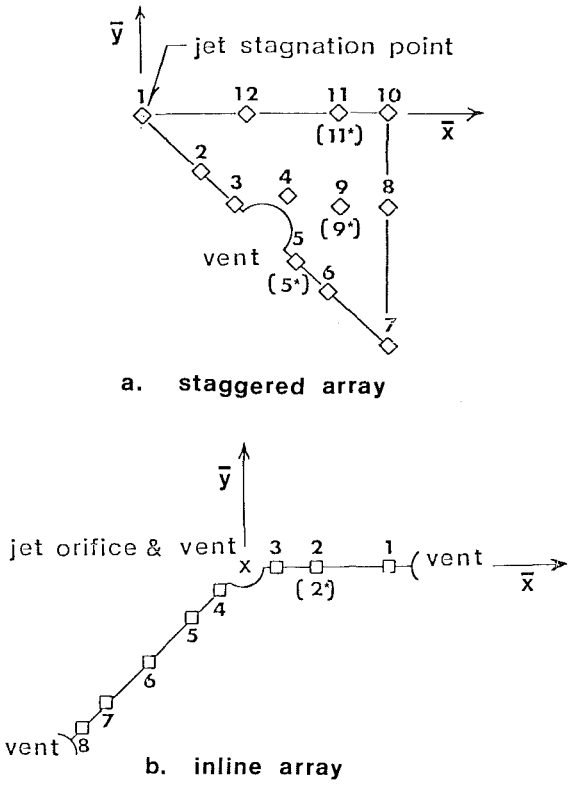

Fig. 4 Locations of heat flux sensors

Table 2 Locations of heat flux sensors[a]

Staggered array			Inline array		
Sensor no.	$\bar{x}$	$\bar{y}$	Sensor no.	$\bar{x}$	$\bar{y}$
1	0.00	0.00	1	3.77	0.00
2	1.20	−1.20	2,2*	1.87	0.00
3	1.90	−1.90	3	0.87	0.00
4	3.00	−1.60	4	−0.62	−0.62
5,5*	3.18	−3.18	5	−1.32	−1.32
6	3.68	−3.68	6	−2.52	−2.52
7	5.06	−5.06	7	−3.59	−3.59
8	5.03	−2.03	8	−4.29	−4.29
9,9*	4.00	−2.00			
10	5.00	0.00			
11,11*	4.00	0.00			

[a] Refer to Fig. 4.

Table 3 Zones for analytical model

Zone no	Zone extent	Description	Characteristics of flow
I	$0 \le r \le 0.046\ Z$	stagnation region	Flow exterior to boundary layer obeys Euler's equation. Velocity, u_m, at "edge" of boundary layer increases linearly with r. Boundary layer is laminar.
II	$0.046Z \le r \le 0.15Z$	transition region	Velocity, u_m, is nearly constant. There is a large pressure gradient with P decreasing exponentially with r. Boundary layer is laminar.
III	$0.15Z \le r \le 0.30Z$	transition region	Velocity, u_m, drops nearly linearly with r. There is a small favorable pressure gradient with P decreasing exponentially with r. Boundary layer is turbulent.
IV	$r \ge 0.30Z$	wall jet region	Velocity, u_m, decays as $1/r$. Pressure gradient vanishes. Boundary layer is turbulent.

well as the length) of the bubble path images was found to depend upon the bubble velocity. At higher Reynolds numbers (i.e., higher velocities) the quality of the resulting photomaps was not acceptable. Using the method discussed above, it was possible to obtain good quality pathline maps using long (on the order of 1.0 s) exposure times. These maps clearly showed several important qualitative features of the flow, though the highly turbulent nature of the flow made it virtually impossible to generate significant quantitative information.

Theoretical Model

An approximate analytical model was developed and used to predict the heat transfer distribution for a single axisymmetric jet impinging normal to a flat plate. These results were then area-averaged mathematically to obtain average heat transfer coefficients. The flow adjacent to the target surface was divided into four distinct zones having the characteristics given in Table 3. The extent of each zone, along with variations of u_m (velocity at "edge" of boundary layer) and P (static pressure) were taken from data given by Poreh and Cermak [12].

The heat transfer coefficient was obtained in the laminar regions using a method based on known wedge flow solutions originally due to Eckert [13]. For radial flows, Kays [14] indicates that the local Stanton number may be determined from

$$\mathrm{St} = \frac{h}{c\rho u_m} = \frac{0.418 \nu^{1/2} r {u_m}^{0.435}}{\left(\int_0^r r^2 {u_m}^{1.87} dr\right)^{0.5}} \tag{2}$$

for $\mathrm{Pr} = 0.7$. Analytical expressions were fitted (see [15] to the u_m (r) data from [12], and used along with equation (2) to determine local heat transfer. In Zone I the result is

$$\frac{\mathrm{Nu}}{\mathrm{Pr}^{1/2}} = \frac{6.78\mathrm{Re}^{1/2}}{\bar{Z}}, \tag{3}$$

and in Zone II the result is

$$\frac{\mathrm{Nu}}{\mathrm{Pr}^{1/3}} = \frac{0.33\left(\frac{3.99}{\bar{Z}}\right)^{1.435} \bar{r}\mathrm{Re}^{1/2}}{\left[0.00027\bar{Z}^{1.13} + 0.33\left(\frac{3.99}{\bar{Z}}\right)^{1.87} (\bar{r}^3 - (0.046\bar{Z})^3)\right]^{0.5}} \tag{4}$$

The method thus yields the familar result that h is constant in the stagnation region, but decays with r in Zone II.

It was assumed that transition to a turbulent boundary layer occurs at $\bar{r} = 1.5$, which is roughly where the flow external to the boundary layer begins to decelerate. This appears to be fairly consistent with experimental results [1, 16] in the literature. Moreover, our own measurements of local heat transfer tend to support this assumption. As a rule, the local heat transfer varies according to $h \sim \mathrm{Re}^m$, where $m = 0.5$ for laminar boundary layers and $m = 0.8$ for turbulent layers. For the heat sensor nearest the stagnation point (at $\bar{r} = 1.70$) the value of m was considerably nearer to 0.8. Thus, it appears that transition occurs at least somewhat inboard of $\bar{r} = 1.70$.

For the two turbulent zones (III and IV) the integral momentum equation was solved numerically and local heat transfer was deduced by analogy. For radially spreading flow on a flat surface, the momentum equation is

$$\frac{u_m}{r}\frac{d}{dr}\left[r\int_0^\delta \rho u dy\right] - \frac{1}{r}\frac{d}{dr}\left[\int_0^\delta \rho^2 u dy\right] = \tau_0 + \delta\frac{dP}{dr} \tag{5}$$

Constant fluid properties were assumed, along with a 1/7 power velocity profile (i.e. $u = u_m(y/\delta)^{1/7}$) in the boundary layer. For such a profile, Kays [14] indicates that the wall shear stress is given by

$$f = \frac{\tau_o}{\frac{1}{2}\rho {u_m}^2} = 0.0456\left[\frac{\delta u_m}{\nu}\right]^{-1/4} \tag{6}$$

Substitution of the assumed velocity profile, equation (6) for the wall shear stress, and expressions for $u_m(r)$ and $P(r)$ from Table 3 finally yield ordinary differential equations for δ in regions III and IV. These differential equations and details are given in [15]. These were solved numerically using a fourth-order Runge-Kutta method.

Once the hydrodynamic boundary layer thickness $(\delta = \delta(r))$ had been determined in this way, equation (6) was used to obtain the local friction factor (f). Finally the local heat transfer coefficient was obtained using the turbulent analogy (due to Martinelli [17]) given by

$$\mathrm{St} = \frac{\sqrt{f/2}}{5\mathrm{Pr} + 5\ln(5\mathrm{Pr} + 1) + \sqrt{2/f} - 14}. \tag{7}$$

The laminar and turbulent solutions were joined by requiring that both yield the same h at $\bar{r} = 1.5$. This gave a starting value of δ for the turbulent solution.

Results and Discussion

A significant result obtained earlier by Hollworth and Dagan [8] was that jet arrays with staggered vents yield substantially higher average heat transfer than do arrays with spent air removal along the four edges of the target or arrays with inline vents. This is shown clearly by Figs. 8 and 6, respectively, in [8].

It was originally hypothesised that the performance advantage of staggered arrays over edge-vented arrays was due to suction near the vent holes, which caused localized thinning of the boundary layer and a corresponding increase in local (and therefore average) h. A major aim in measuring local heat transfer was to test the validity of this hypothesis. Local heat transfer coefficients were determined from measurements of local heat flux (q) using

$$h = \frac{q - q_r}{T_s - T_o}, \tag{8}$$

where T_o is the total temperature of the jets and q_r is a small correction for radiation. The surface temperature, T_s, is obtained (see [9] for details) by applying a correction to the reading of the sensor's integral thermocouple to account for the temperature drop between the thermocouple and the impingement surface.

Figures 5 and 6 are typical "maps" of local heat transfer for arrays with staggered vents. The ◇ symbols indicate locations of heat flux sensors, and the numbers next to each symbol are experimental values of $Nu/Pr^{1/3}$. The Nusselt number is defined as

$$Nu = \frac{hd}{k} \tag{9}$$

and fluid properties are evaluated at a "film" temperature halfway between T_o and T_s. As mentioned previously, it required more than one test tun to generate a complete "map." Between runs, some of the sensors were removed from the target plate and reattached at new sites. There are therefore two values of $Nu/Pr^{1/3}$ next to sensors which *were not* moved between runs; comparing these values gives an indication of the repeatability of the measurements. It should be pointed out that values of $Nu/Pr^{1/3} <$ roughly 10 (which occur only at sites far removed from the jet stagnation point and at low Re) should be regarded only as indicating areas of "greatly diminished" heat transfer. The local h values in such areas are low enough (3–5 times typical free convection values) so that the experimental uncertainty in these data is necessarily high. If one disregards such low $Nu/Pr^{1/3}$, the remaining data are reproducible (on the average) to within ±5 percent; and 80 percent of the data is reproducible to within ±7 percent, which is the uncertainty estimated for this experiment.

Values of $Nu/Pr^{1/3}$ shown in brackets were measured outside of region "abca" (see Fig. 2) and shown next to the corresponding sites within "abca." Sensor pairs such as 9 and 9* and 11 and 11* (see Fig. 2 and Table 2 for locations) were used to determine if the heat transfer distribution in "abca" was representative of all such triangular zones on the impingement plate. These sensors were located at points very close to lines of symmetry in the flow field. As such, their readings are more sensitive than those of other sensors to any minor assymmetries in the flow. An additional test was performed to check symmetry; the entire target was coated with light oil, and talcum powder was injected into the jet plenum and subsequently deposited on the target plate. The result was a fairly high quality trace on the target plate, showing the air flow pattern. From this trace, it was apparent that the entire pattern was generally quite symmetric. At worst, some symmetry lines were displaced 0.2–0.3 d from their "true" positions. While this skewing is not excessive, it may have a relatively large effect at sites 9 and 11, which were located only about one diameter from the nominal position of a line of symmetry. Notwithstanding, the deviation ([max-min)/avg) between readings (averaged over all data) was 13 percent for pair 9/9* and 11 percent for pair 11/11*.

Figures 7 and 8 show the data of Figs. 5 and 6, respectively, replotted as $Nu/Pr^{1/3}$ versus $\bar{r} = r/d$, where r is distance from the jet stagnation point. It shows that the distribution is essentially radially symmetric and that the three sensors nearest the vent (all within 1/2 d of the edge of the vent) indicate no detectable enhancement of heat transfer. This was the case (see [9]) for all tests run for staggered arrays. For larger $\bar{X}$, suction may have a relatively more significant effect as the wall flow associated with the impinging jet diminishes in strength near the vents. However, suction near the vents cannot, in general, account for the level of overall heat transfer increase (as much as 35 percent) observed for staggered arrays relative to edge-vented arrays.

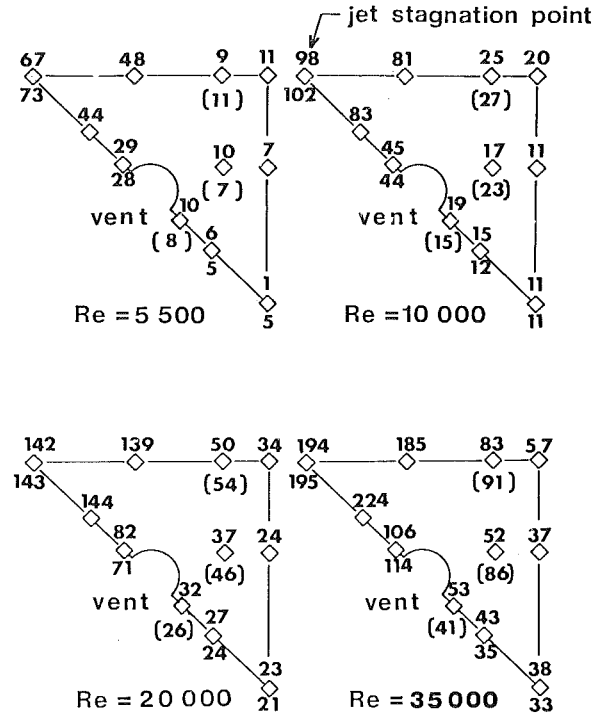

Fig. 5 Distribution of $Nu/Pr^{1/3}$ for staggered array with $\bar{X} = 10$ and $\bar{Z} = 1$

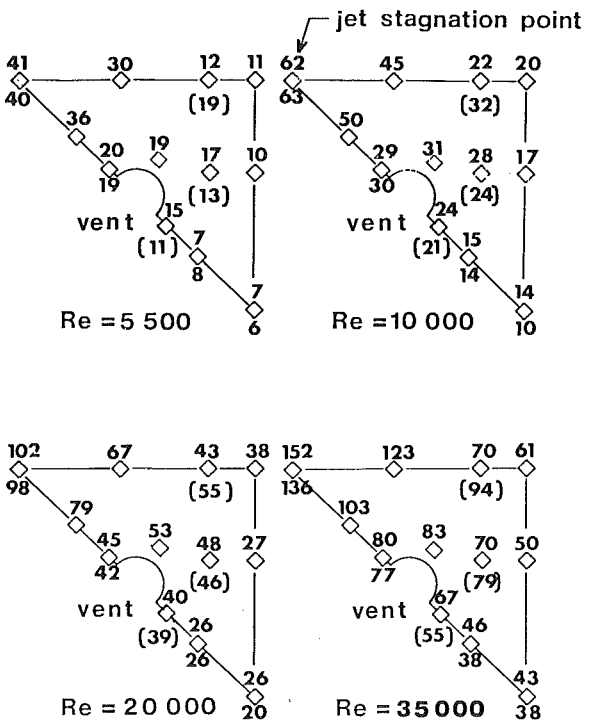

Fig. 6 Distribution of $Nu/Pr^{1/3}$ for staggered array with $\bar{X} = 10$ and $\bar{Z} = 10$

Data taken from [5] for an edge-vented array is shown on Fig. 9, compared to the heat transfer distribution for a staggered array at Re = 20000. Both arrays are otherwise identical, with $\bar{X} = 10$, $\bar{Z} = 5$ and with the same number (i.e, 16) of jets. The higher average h associated with the staggered array appears to be due to higher levels of local h over the

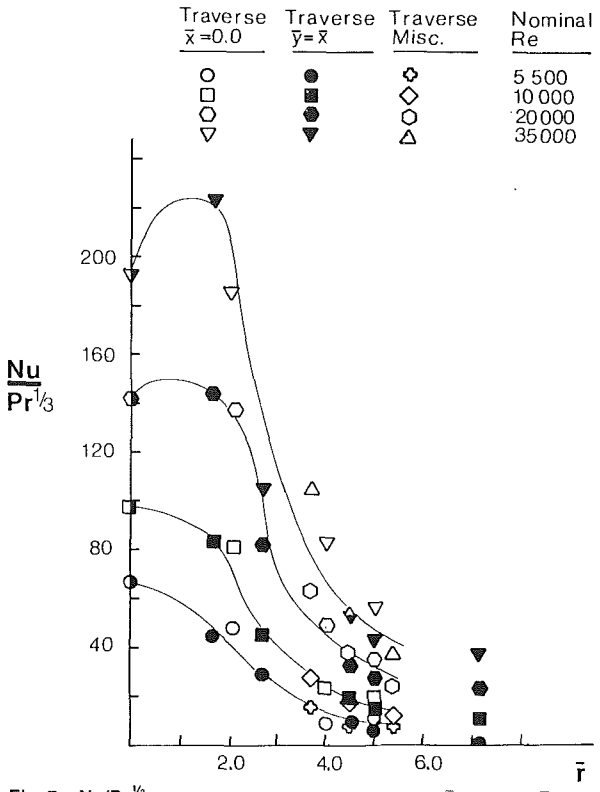

Fig. 7 Nu/Pr$^{1/3}$ versus r for staggered array with $\bar{X} = 10$ and $\bar{Z} = 1$

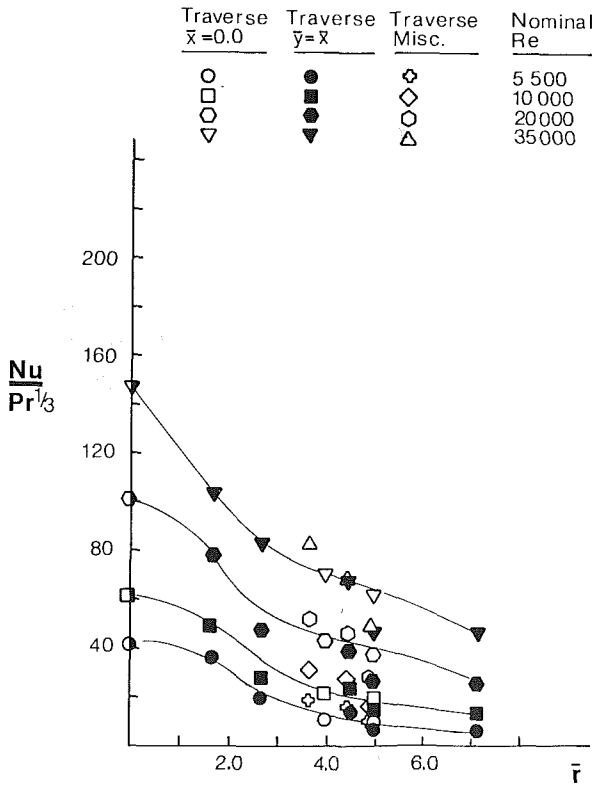

Fig. 8 Nu/Pr$^{1/3}$ versus r for staggered array with $\bar{X} = 10$ and $\bar{Z} = 10$

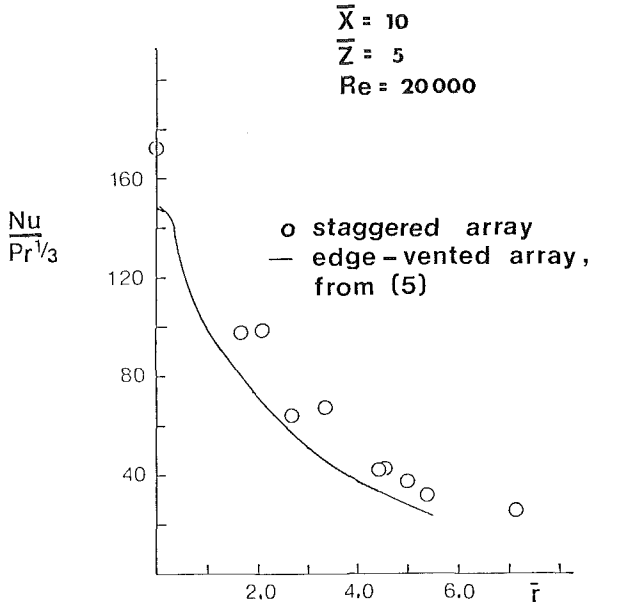

Fig. 9 Heat transfer profiles: staggered array compared to edge-venter array

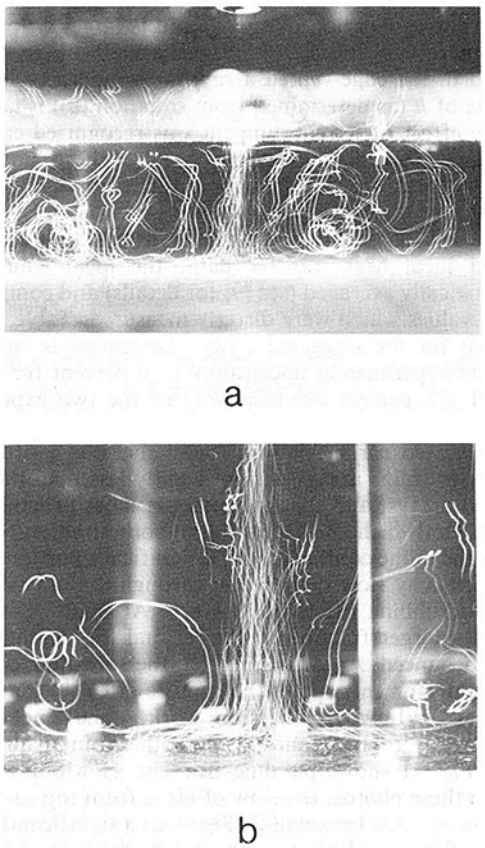

Fig. 10 Flow patterns for jet systems: (*a*) edge-vented array with $\bar{X} = 10$, $\bar{Z} = 5$, (*b*) staggered array with $\bar{X} = 10$, $\bar{Z} = 10$

entire target surface, and not to local effects. The same trend was observed for all conditions at which there was common data. An alternate explanation, based on accepted knowledge of jet behavior and dramatic differences between the flow fields for these two geometrics (as revealed by our flow visualization work) may be put forward. Figure 10(*a*) shows a pathline map for one jet within an edge-vented array. Characteristic of the flow for such geometries is a strong circulation of spent fluid between neighboring jets. For cool jets incident upon a hot surface, this spent fluid may be heated considerably. It is well known that free jets entrain significant amounts of the fluid through which they pass. For the systems

Table 4 Average heat transfer for staggered arrays with $\bar{X} = 10$

$\bar{Z}$	Re	Values of $Nu/Pr^{1/3}$	
		Local measurements, mathematically averaged	Averaged values, measured directly
10	5500	18.4	20.2
	10000	28.9	31.3
	20000	51.2	54.4
	35000	78.5	86.0
5	5500	18.9	22.4
	10000	33.8	34.3
	20000	61.1	60.7
	35000	98.2	94.7
2.5	5500	21.4	21.6
	10000	36.0	35.9
	20000	62.9	64.7
	35000	103.6	102.3
1	5500	20.4	20.5
	10000	35.1	35.8
	20000	65.3	64.7
	35000	97.3	99.7

considered here, the jets are heated by entrainment of the warmer fluid, which reduces the effective ΔT (and hence the heat flux, q) between the jets and the target. Owing to the method used to determine h (see equation (8)), a decrease in q shows up as a decrease in h.

Figure 10(b) shows a typical pathline image for a staggered array. Spent fluid is sucked directly into the four vents around each jet and circulation of spent fluid is largely suppressed. Under these conditions, the "preheating" of jets (which occurred in the edge-vented array) is considerably less, and the value of h (as determined from equation (8)) is larger. In fact, the effect of jet entrainment was recognized earlier by Hollworth [18] who attempted to use these notions in correlating heat transfer data for a single impinging jet in a crosswind.

As a check on both average heat transfer data (reported in [8]) and local heat transfer data, the local values were mathematically averaged (see [9] for details) and compared to average values which were directly measured. Table 4 shows the result for the staggered array. Agreement is within the combined experimental uncertainty (± 6 percent for average h's, and ± 7 percent for local h's) of the two experiments throughout.

As indicated earlier, it was found that the average heat transfer for inline arrays is significantly less than that from staggered arrays, and that the effect is most pronounced at small $\bar{Z}$. Hollworth and Dagan [8] hypothesized, at the time, that for the inline configuration, a significant portion of each cooling jet may flow directly out through the opposing vent without scrubbing the target surface. At small $\bar{Z}$, the vent captures a larger fraction of the jet and the degradation is most procounced. As $\bar{Z}$ is increased, the spreading of the jet (due to entrainment) causes the capture effect to diminish in importance. FLow visualization work, done since [8] appeared, tends to bear out this hypothesis in a qualitative regard. Fig. 11 shows pathlines for one jet within an inline array; in these photos, the flow of air is from top to bottom. It is apparent that for small $\bar{Z}$ (Fig. 11a) a significantly larger fraction of the pathlines are captured by the vent and carried directly out through the target plate.

Local heat transfer was measured also for inline arrays; however, testing was not as extensive as for staggered arrays. The latter geometries were clearly superior and the authors felt, therefore, that they deserved more attention. Figures 12 and 13 are typical heat transfer maps for an inline array. The □ symbols indicate sites where local heat transfer was measured, and the number next to each □ is the local value of $Nu/Pr^{1/3}$. For large $\bar{Z}$ (Fig. 12), the distribution was generally radially symmetric with respect to the center of the jet orifice. For small $\bar{Z}$ (Fig. 13,) however, the distribution was obviously

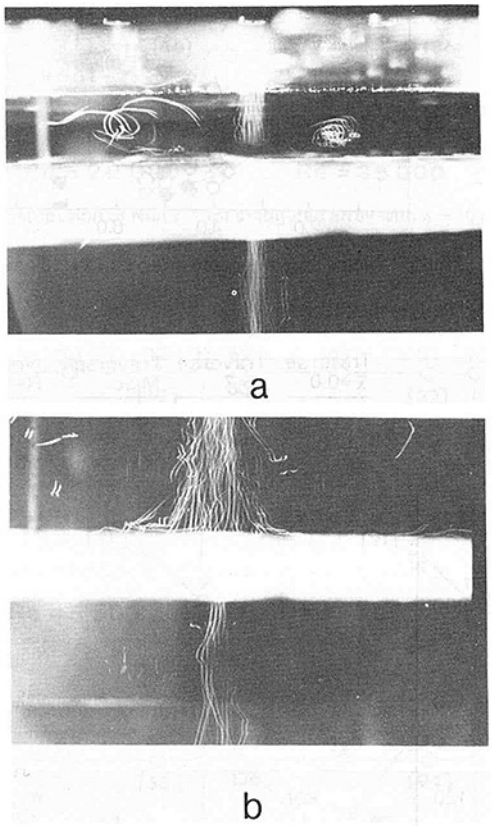

Fig. 11 Pathlines for jet captured by inline vent: (a) $\bar{Z} = 2.5$, (b) $\bar{Z} = 10$

nonsymmetric. This is due to slight misalignment between the jet and vent orifices whose effect is amplified by the capture effect at small $\bar{Z}$, as discussed in some detail in [9].

Figure 14 shows profiles of local heat transfer obtained from the analytical model previously outlined. The pressure and velocity distributions reported by Poreh and Cermak, and used as input for our analysis, are valid only for $8 \leq \bar{Z} \leq 32$. The profiles of Fig. 14 are for $\bar{Z} = 10$, which represents, then, the only value of $\bar{Z}$ at which a direct comparison between theory and test data may be made. As the figure indicates, the analysis tends, in general, to underpredict local heat transfer. A number of investigators have found, likewise, that laminar boundary layer theory predicts lower convective heat transfer in the neighborhood of the stagnation point than is observed experimentally. Typical of these are Donaldson et al. [19],

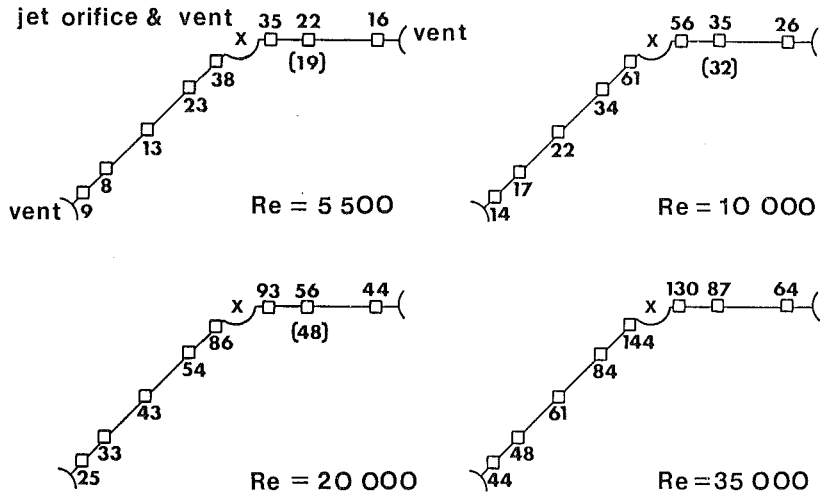

Fig. 12 Distribution of $Nu/Pr^{1/3}$ for inline array with $\bar{X} = 10$ and $\bar{Z} = 10$

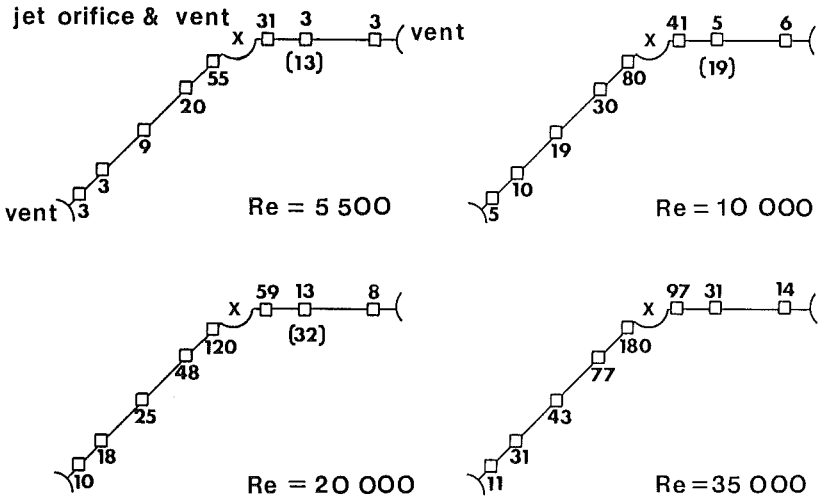

Fig. 13 Distribution of $Nu/Pr^{1/3}$ for inline array with $\bar{X} = 10$ and $\bar{Z} = 2.5$

who attribute this discrepancy to jet turbulence which "imbeds" itself in an otherwise laminar boundary layer and locally enhances heat transfer.

Average heat transfer coefficients were predicted by mathematically area-averaging the local values obtained analytically. The value for an array with jet-to-jet spacing $\bar{X}$ was computed [15] by averaging profiles such as those of Fig. 14 over an "equivalent" circle having the same dimensionless area (i.e., $\bar{X}^2$) as that cooled by a single jet within an array. This was done for spacings $\bar{X} = 10$, 15, and 20 and for Re = 5500, 10000, 20000 and 35000. Average values of $Nu/Pr^{1/3}$ obtained in this fashion were lower than those measured by Hollworth and Dagan [8] by from 2 to 34 percent, depending upon $\bar{X}$ and Re. The mean difference was 21 percent, and better agreement was obtained at large $\bar{X}$ and small Re. Under these conditions, the relative inadequacy of the laminar theory (discussed above) diminishes in importance.

It should be pointed out that the above model is not valid for inline configurations as it does not recognize the "capture" of part of the impinging jet by a vent. Moreover, it is approximate in that axisymmetric flow is assumed, while (in a staggered array) the presence of vents and neighboring jets

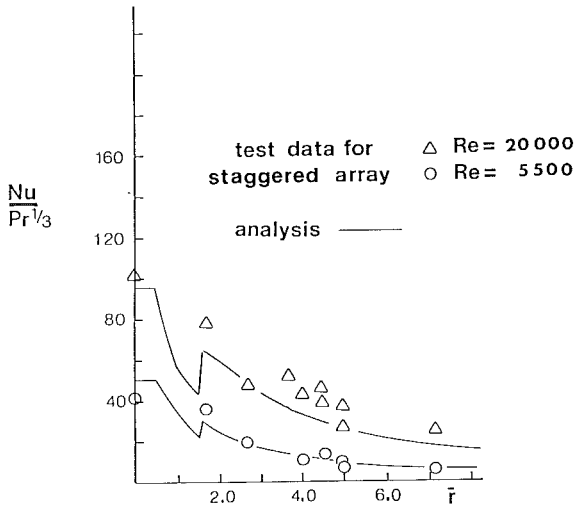

Fig. 14 Comparison of analytical and experimental results for $\bar{X} = 10$ and $\bar{Z} = 10$

serve, of course, to distort the velocity field. Another assumption is that the velocity and pressure distributions measured by Poreh and Cermak [12] for a single unconfined jet could reasonably be applied to a system of multiple jets discharged from an orifice plate. These distributions may, of course, be influenced by interference from neighboring jets and by the confining effect of the orifice plate itself. Our flow visualization work, however, clearly shows that the sort of venting employed here minimizes cross flow of spent fluid. Moreover, very recent work by Obot et al [20] indicates that the effect of confinement by a plate parallel to the target surface is quite small for large $\bar{Z}$ (i.e. $\bar{Z} \geq 8$), which corresponds to the range on which our analysis is presumed to be valid. Undoubtedly this effect would be significant for small plate-to-plate spacing. The model predicts a pronounced heat transfer "spike" where boundary layer transition occurs. The authors believe that this is mainly a consequence of the method (discussed above) used to patch together the laminar and turbulent solutions and does not simulate a real effect. Other investigators [1, 16] have observed similar peaks to occur at small (less than 2-3) $\bar{Z}$. However, they diminish in relative size as $\bar{Z}$ is increased, and degenerate to a slight "kink" in the profile for $\bar{Z} = 10$.

Conclusions

Measurements of local heat transfer were made for arrays of jets impinging on a target plate with an array of vent holes through which spent air was withdrawn. In addition, an extensive flow visualization study was performed. Significant conclusions are the following:

1 The heat transfer advantage of staggered arrays over conventional edge-vented arrays appeared not be due, to any significant degree, to localized enhancement associated with suction near the vents, as had previously [8] been hypothesized. Flow visualization studies revealed, however, that this type of venting suppresses the circulation of spent fluid which (in edge-vented arrays) may "preheat" the jets and thereby reduce heat transfer.

2 Earlier work [8] indicated that staggered arrays were superior to inline arrays in terms of average heat transfer. Flow visualization studies clearly show that inline vents may directly "capture" a large part of each jet (especially at small $\bar{Z}$). The fluid remaining to "scrub" the target surface is reduced, as is the rate of heat transfer.

Acknowledgments

The authors wise to express thanks to the National Science Foundation, who supported this study under Grant No. ENG77-14630.

References

1 Gardon, R., and Cobonpue, J., "Heat Transfer Between a Flat Plate and Jets of Air Impinging Upon It," *International Developments in Heat Transfer, Proceedings, 2nd International Heat Transfer Conference*, ASME, New York, 1962.

2 Kercher, D. M., and Tabakoff, W., "Heat Transfer by a Square Array of Round Air Jets Impinging Perpendicular to a Flat Surface Including the Effect of Spent Air," ASME JOURNAL OF ENGINEERING FOR POWER, Vol. 92, No. 1, Jan. 1970, pp. 73-82.

3 Chance, J. L., "Experimental Investigation of Air Impingement Heat Transfer Under an Array of Round Jets," *Tappi*, Vol. 57, No. 6, 1974, pp. 108-112.

4 Metzger, D. E., and Florschuetz, L. W., "Heat Transfer Characteristics for Inline and Staggered Arrays of Circular Jets with Crossflow of Spent Air," ASME *Journal of Heat Transfer*, Vol. 101, Aug. 1979, pp. 526-531.

5 Hollworth, B. R., and Berry, R. D., "Heat Transfer from Arrays of Impinging Jets with Large Jet-to-Jet Spacing," ASME *Journal of Heat Transfer*, Vol. 100, No. 2, May 1978, pp. 352-357.

6 Martin, H., "Heat and Mass Transfer between Impinging Gas Jets and Solid Surfaces," *Advances in Heat Transfer*, Vol. 13, Academic Press, 1977, pp. 1-59.

7 Obot, N. T., Mujumdar, A. S., and Douglas, W. J. M., "Design Correlations for Heat and Mass Transfer Under Various Turbulent Impinging Jet Configurations," *Drying '80*, Hemisphere, pp. 383-402.

8 Hollworth, B. R., and Dagan, L. S., "Arrays of Impinging Jets With Spent Fluid Removal Through Vent Holes on the Target Surface, Part 1: Average Heat Transfer," ASME JOURNAL OF ENGINEERING FOR POWER, Vol. 102, No. 4, Oct. 1980, pp. 994-999.

9 Lehmann, G., and Hollworth, B., "Arrays of Impinging Jets With Spent Fluid Removal Through Vent Holes on the Target Surface, Part 2: Local Heat Transfer," Department of Mechanical and Industrial Engineering, Clarkson College, Report No. MIE-063, Sept. 1980.

10 Rosiczkowski, J., Hollworth, B., "Arrays of Impinging Jets: Flow Visualization," Department of Mechanical and Industrial Engineering, Clarkson College, Report No. MIE-052, Jan. 1980.

11 Colladay, R. S., and Russel, L. M., "Flow Visualization of Discrete Hole Film Cooling for Gas Turbine Applications," ASME paper No. 75-WA/HT-12, 1975.

12 Poreh, M., and Cermak, J. E., "Flow Characteristics of a Circular Submerged Jet Impinging Normally on a Smooth Surface," *Proceedings of the 6th Midwest Conference on Fluid Mechanics*, 1959, pp. 198-212.

13 Eckert, E. R. G., VDI-Forschungsh, Vol. 416, 1942, pp. 1-24.

14 Kays, W. M., *Convective Heat and Mass Transfer*, McGraw-Hill, 1966, pp. 222-227.

15 Hollworth, B. R., "Arrays of Impinging Jets with Spent Fluid Removal Through Vent Holes on the Target Surface, Part 3: Theoretical Analysis," Department of Mechanical and Industrial Engineer, Clarkson College, Report No. MIE-064.

16 Obot, N. T., Majumdar, A. S., and Douglas, W. J. M., "The Effect of Nozzle Geometry on Impingement Heat Transfer Under a Round Turbulent Jet," ASME Paper No. 79-WA/HT-53, presented at the Winter Annual Meeting, New York, Dec. 2-7, 1979.

17 Martinelli, R. C., ASME *Transactions*, Vol. 69, 1947, p. 947.

18 Hollworth, B. R., "Heat Transfer Characteristics of an Impinging Jet in a Crossflow," Ph.D thesis, M.E. Department, University of Connecticut, 1974.

19 Donaldson, C. D., Snedeker, R. S., and Margolis, D. P., "A Study of Free Jet Impingment, Part 2. Free Jet Turbulent Structure and Impingment Heat Transfer," *Journal of Fluid Mechanics*, Vol. 45, pt. 3, 1971, pp. 477-512.

20 Obot, N. T., Douglas, W. J. M., and Mujumdar, A. S., "Effective of Semiconfinement on Impingment Heat Transfer," *Proceedings of Seventh International Heat Transfer Conference*, Munich, Sept. 1982.